

Beyond Arrhenius: Fluctuation Theory for Dynamics

©2021

Zeke A. Piskulich

Submitted to the graduate degree program in Department of Chemistry and the Graduate Faculty of the University of Kansas in partial fulfillment of the requirements for the degree of Doctor of Philosophy.

Ward H. Thompson, Co-Chairperson

Brian B. Laird, Co-Chairperson

Committee members

Christopher G. Elles

Timothy A. Jackson

James D. Blakemore

Alan M. Allgeier

Date defended: May 7, 2021

The Dissertation Committee for Zeke A. Piskulich certifies
that this is the approved version of the following dissertation :

Beyond Arrhenius: Fluctuation Theory for Dynamics

Ward H. Thompson, Co-Chairperson

Brian B. Laird, Co-Chairperson

Date approved: May 14, 2021

Abstract

A long-standing challenge for simulation and experiment has been the accurate calculation of activation energies and activation volumes *via* Arrhenius analyses which typically require rate constants or dynamical timescales to be resolved over a wide-range of temperatures and pressures to high accuracy. Unfortunately, in some systems timescales can be non-Arrhenius; in others, the system can undergo fundamental changes with temperature (*e.g.* phase transitions, changing solubility). In this thesis, an extension of fluctuation theory from statistical mechanics is developed that allows for the direct calculation of derivatives of dynamical timescales with respect to temperature and pressure, from simulations at a single temperature and pressure. This allows for the direct calculation of activation energies and volumes without requiring the problematic temperature and pressure ranges involved in the traditional Arrhenius approach. Furthermore, these approaches allow for the decomposition of the activation energy into contributions from various molecular interactions to gain deeper mechanistic insight that is otherwise unavailable. Applications to a wide-range of dynamical timescales in liquid water (diffusion, reorientation, hydrogen bond exchanges, and spectral diffusion) are presented. We furthermore demonstrate the ability of these techniques to study water under supercooling and water under pressure, demonstrating that these derivatives can be used to predict the dependence of liquid structure and dynamical timescales with respect to pressure and temperature. We furthermore demonstrate that this method can be used to connect liquid structure and the observed dynamics in liquid water. Finally, we demonstrate that these approaches can be applied to other systems to glean useful, otherwise unobtainable information.

Epigraphs

“And so, does the destination matter? Or is it the path we take? I declare that no accomplishment has substance nearly as great as the road used to achieve it. We are not creatures of destinations. It is the journey that shapes us. Our callused feet, our backs strong from carrying the weight of our travels, our eyes open with the fresh delight of experiences lived.”

— Brandon Sanderson, *The Way of Kings*

“The steady state of disks is full.”

— Ken Thompson

Acknowledgements

I want to begin by thanking both Professors Ward Thompson and Brian Laird for taking me into their groups and welcoming me to the University of Kansas (KU). Both of them have shown me incredible support over the past five years since I first stepped foot on KU's campus, and I have learned so much from them. They have always been the first to suggest conferences for me to attend, and have helped me develop into the scientist that I am today. Brian has continuously pushed me over my time at KU to think more deeply about problems and has gotten me to be *very* comfortable taking Legendre transforms in thermodynamics. He has also helped me broaden my focus as a researcher, bringing me into the world of simulating liquids other than water and teaching me how to think about them. Brian also supported my decision to majorly reformat our Graduate Student organization the same year that he was trying to get all of us moved into a new building as department chair. Likewise, Ward has pushed me to develop as a researcher, as a mentor, and as a time-manager. He put up with five years of late night Slack messages (apparently exceeding 14,000 messages) from me discussing our research.

I would also like to thank the rest of my committee. At different points along my graduate career each member has played an important role in bettering my science through questions at seminars, discussions, and advisory committee meetings.

Over my time at KU I have been supported by a few sources of funding (and computational resources) that I should acknowledge. The overall fluctuation theory project has been supported by a National Science Foundation (NSF) grant (CHE-1800559) which allowed us to purchase nodes on the KU Center for Research Computing (CRC). To that end, I would also like to acknowledge the wonderful staff at the CRC for all of their patience and hard-work helping me troubleshoot compilation and program errors. Over the course of this work, we have also used computational resources from the National Energy Research Scientific Computing Center (NERSC) provided to

us by Dr. Christopher Mundy at Pacific Northwest National Laboratory. Furthermore, I need to acknowledge funding from both the NSF Graduate Research Fellowship Program (grant nos. 1540502 and 1451148) and the NSF Graduate Research Opportunities Worldwide program which allowed me to have deeper freedom in the topics that I studied throughout my time at KU. During my time here, I was also supported by funds from the Gilles fund and graduate studies to attend a number of conferences.

I would like to thank all of the present and former members of my groups. In the Thompson Group, I want to thank Drs. Pansy Patel, Jacob Harvey, Oluwaseun Mesele, Pubudu Wimalasiri, and Camina Mendis, as well as Ankita Katiyar, Ashley Borkowski, Ally Leicht, Paul Burris, Hasini Senanayake, and Sahan Godahewa. In the Laird Group I would like to thank Drs. Pablo Palafox, Peter Barry, and Zhenxing Wang, as well as Seth Martin, Joyce Nguyen, Micah Welsch. I would also like to thank the undergraduates that I have worked with, including Kaylee Barr, Carolyn Smith, Carl Heroneme, Julia Friere-Sovierzoski, Alexey Ermak, Tyler Duncan, and Siddhesh Kulkarni. All of you have been integral to my development into who I am today. I have really appreciated the opportunity to bounce ideas off of each of you, learn from you. My science always ended up better after each discussion we had. I would especially like to thank Pablo, Pansy, and Mesele for being excellent mentors to me when I first joined the group. They always encouraged and pushed me to be the best graduate student that I could be.

My time at KU has also been supported by faculty and staff both in and outside my department. I would like to thank the Chemistry department staff for all of their support. I would especially like to thank Susan Teague, Liz Coleman, and Megan Belaire for their support of my efforts with our graduate student organization. I would also like to thank the Center for Environmentally Beneficial Catalysis at KU for their support during my first year. I would like to thank Drs. Bala Subramaniam, Christopher Lyon, and Claudia Bode for their continued support throughout my time at here.

I would also like to thank Professor Damien Laage and his group for making me feel so incredibly welcome when I visited their group briefly in 2020, as well as for continuing to let me

participate in their group meetings throughout the course of the past year. I have learned a lot from each member of his group. I remain hopeful that I will be able to visit Paris again sometime in the future and continue to learn from everyone there.

I would like to thank Professor Sapna Sarupria for being a mentor to me throughout the last half of my graduate career. Our research and professional development discussions have been valuable to me during my time at KU. I would also like to thank Professor Rick Remsing for his professional advice.

I need to thank Professors Thomas Sewell and Donald Thompson, as well as the members of both of their research groups who trained me as an undergraduate researcher. I would especially thank Drs. Matthew Kroonblawd, Nithin Matthew, and Rezvan Chitsazi for their guidance during this period. I would also like to thank the graduate students who trained me in my first research experience, Drs. Andrew Gillespie and David Stalla, who always pushed me to improve. I am no longer an experimentalist, but many of the lessons that they taught me have been integral to my experience as a graduate student.

I also want to thank the friends, both new and old, who got me through the past five years. Colleen and Kayla thank you for always being friends for me throughout the years to turn to when times got tough. Galina and Sasha, thank you for being such good friends through the past years and for helping us give so much of our stipend to Thai Diner and Jayhawk Tennis. Tal, thank you for being a true friend throughout my time here and bringing me into the extended KU family. Kristen, thank you for everything from the late-night quantum work sessions to the Qdoba/Noodles lunch escapes. Chris, thank you for identifying my ownership of shoes and conscripting me into the chemistry softball team - without it I would not have had nearly the same KU experience. To the game group members, Tal, Tom, Ashley, Hayley, Matt, Ken, Kiersten, and Jake, thank you for being stable supports even in the midst of a global pandemic. Amy, Josh, and Nate, thank you for your friendship during my first years here.

To my family, I cannot thank any of you nearly enough for always believing in me. My parents have always supported me and pushed me to strive to be my best since I was little. Without their

gentle prodding (and sometimes pushing) I would not have ended up where I am today, and for that I am extremely grateful. I would also like to thank my grandmother, Annie Adams, who always offered to help with Ward and Brian's problem sets whenever I came to visit, as well as my step-grandfather, Jack Adams, who passed away during my candidacy exam; he always knew the right joke to tell to make stress melt away. During that period, I got my cat, Lirael, who ended up being an important support to me throughout the remainder of my time at KU. Lastly, I must also thank Kelci Schilly who has been the best teammate through the past four years that anyone could ever ask for. Thank you for always believing in me, and pushing me to be the best that I can be.

To everyone who has helped me get here today, thank you.

Contents

| | |
|------------------------|------------|
| List of Figures | xix |
|------------------------|------------|

| | |
|-----------------------|--------------|
| List of Tables | xxxii |
|-----------------------|--------------|

| | |
|--|----------|
| 1 Introduction and Overview: Activation Energies and Beyond | 1 |
| 1.1 Theory | 3 |
| 1.1.1 Interpretations of the Activation Energy | 3 |
| 1.1.2 Fluctuation Theory for Dynamics | 6 |
| 1.1.2.1 Derivation | 6 |
| 1.1.2.2 Mechanistic Insight | 8 |
| 1.1.2.3 Other Ensembles | 9 |
| 1.2 Activation Energies | 10 |
| 1.2.1 Reaction Rate Constant | 10 |
| 1.2.2 Diffusion Coefficient | 11 |
| 1.2.3 Reorientational Timescales | 14 |
| 1.2.4 Transport Coefficients | 17 |
| 1.2.5 Quantum Dynamics | 18 |
| 1.2.6 Advanced Decompositions | 20 |
| 1.3 Beyond Activation Energies | 21 |
| 1.3.1 Non-Arrhenius Behavior | 21 |
| 1.3.2 Activation Volumes | 23 |
| 1.4 Purpose of the Current Study | 25 |

| | | |
|----------|---|-----------|
| I | Activation Energies of Dynamical Timescales | 28 |
| 2 | Removing the Barrier to the Calculation of Activation Energies | 30 |
| 2.1 | Introduction | 30 |
| 2.2 | Time Correlation Functions (TCFs) and Activation Energies | 32 |
| 2.2.1 | General Expressions | 32 |
| 2.2.2 | Diffusion Coefficients | 33 |
| 2.2.3 | Reorientation Times | 34 |
| 2.3 | Computational Methods | 35 |
| 2.4 | Results | 37 |
| 2.4.1 | Diffusion coefficient activation energy | 37 |
| 2.4.2 | Reorientation time activation energy | 40 |
| 2.4.3 | Energetic decomposition | 42 |
| 2.5 | Conclusion | 45 |
| 3 | The activation energy for water reorientation differs between IR pump-probe and NMR measurements | 46 |
| 3.1 | Introduction | 46 |
| 3.2 | Theory | 49 |
| 3.3 | Computational Methods | 53 |
| 3.4 | Results | 54 |
| 3.4.1 | Reorientation Times and Activation Energies | 55 |
| 3.4.2 | Traditional Arrhenius Analysis | 57 |
| 3.5 | Discussion | 60 |
| 3.5.1 | Contributions to the $\langle \tau_2 \rangle$ Activation Energy | 62 |
| 3.5.2 | Contributions to the $C_2(t)$ Temperature Dependence | 63 |
| 3.5.3 | Activation Energy Decomposition | 65 |
| 3.6 | Conclusions | 68 |

| | | |
|----------|--|------------|
| 4 | Activation Energies and the Extended Jump Model: How Temperature Affects Reorientation and Hydrogen-Bond Exchange Dynamics in Water | 70 |
| 4.1 | Introduction | 70 |
| 4.2 | Theory | 71 |
| 4.2.1 | Water OH Group Reorientation | 72 |
| 4.2.2 | Extended Jump Model for Water Reorientation | 73 |
| 4.2.3 | Activation Energies and the Fluctuation Theory for Dynamics | 75 |
| 4.2.4 | Jump Reorientation | 77 |
| 4.2.5 | Frame Reorientation | 80 |
| 4.3 | Methods | 81 |
| 4.4 | Results and Discussion | 83 |
| 4.4.1 | OH Reorientation | 83 |
| 4.4.2 | Jump Contribution to Reorientation | 85 |
| 4.4.2.1 | H-bond Jump Times | 85 |
| 4.4.2.2 | H-bond Jump Angle Distribution | 88 |
| 4.4.3 | Frame Contribution to Reorientation | 91 |
| 4.4.4 | Tests of the Extended Jump Model | 95 |
| 4.4.4.1 | Prediction of OH Reorientation Times | 95 |
| 4.4.4.2 | Prediction of OH Reorientation Activation Energies | 95 |
| 4.4.4.3 | Jump and Frame Contributions to $E_{a,n}$ | 97 |
| 4.5 | Conclusion | 98 |
| 5 | On the role of hydrogen bond exchanges in the spectral diffusion of water | 100 |
| 5.1 | Introduction | 100 |
| 5.2 | Theory | 104 |
| 5.3 | Computational Methods | 106 |
| 5.3.1 | Simulation Details | 106 |
| 5.3.2 | Vibrational Frequencies | 107 |

| | | |
|---|--|------------|
| 5.4 | Results and Discussion | 108 |
| 5.4.1 | Spectral Diffusion Timescales | 108 |
| 5.4.2 | Activation Energies | 112 |
| 5.4.3 | Mechanistic Insight | 115 |
| 5.5 | Conclusions | 117 |
| II Water Under Extreme Conditions | | 119 |
| 6 Expanding the Calculation of Activation Volumes: Self-Diffusion in Liquid Water | | 121 |
| 6.1 | Introduction | 121 |
| 6.2 | Theory | 124 |
| 6.3 | Computational Methods | 126 |
| 6.4 | Results and Discussion | 127 |
| 6.5 | Summary | 133 |
| 7 The Dynamics of Supercooled Water Can Be Predicted from Room Temperature Simulations | | 135 |
| 7.1 | Introduction | 135 |
| 7.2 | Methods | 137 |
| 7.2.1 | Derivatives of D | 137 |
| 7.2.2 | Derivatives of $\langle \tau_2 \rangle$ and τ_2 | 138 |
| 7.2.3 | Simulation Details | 139 |
| 7.3 | Results | 140 |
| 7.3.1 | Predictions of Dynamical Timescales | 142 |
| 7.3.2 | A Stability Limit Conjecture Description | 144 |
| 7.3.3 | A "Two Liquids" Description | 147 |
| 7.3.4 | Activation Energy Predictions and Decompositions | 151 |
| 7.4 | Discussion | 154 |

| | | |
|-----------|--|------------|
| 7.5 | Conclusions | 156 |
| 8 | On the Temperature Dependence of Liquid Structure | 157 |
| 8.1 | Introduction | 157 |
| 8.2 | Simulation Methods | 159 |
| 8.3 | Results and Discussion | 160 |
| 8.4 | Conclusions | 168 |
| 9 | Temperature Dependence of the Water Infrared Spectrum: Driving Forces, Isosbestic Points, and Predictions | 169 |
| 9.1 | Introduction | 169 |
| 9.2 | Computational Methods | 171 |
| 9.3 | Results and Discussion | 171 |
| 9.4 | Conclusions | 180 |
| 10 | On the Pressure Dependence of Liquid Structure | 181 |
| 10.1 | Introduction | 181 |
| 10.2 | Theory | 182 |
| 10.2.1 | Temperature Derivative | 182 |
| 10.2.2 | Pressure Derivative | 183 |
| 10.2.3 | Thermodynamic Potential | 183 |
| 10.3 | Methods | 185 |
| 10.4 | Results | 185 |
| 10.4.1 | Dependence of Radial Distribution Function on p,T | 185 |
| 10.5 | Discussion | 190 |
| 10.5.1 | Connection to H-Bond Exchanges | 190 |
| 10.5.2 | Predictions of the RDF | 196 |
| 10.6 | Conclusions | 197 |

III Toward A Unified Picture of Water Dynamics **199**

11 Examining the Role of Different Molecular Interactions on Activation Energies and Activation Volumes in Liquid Water **201**

11.1 Introduction 201

11.2 Computational Methods 203

 11.2.1 Force Fields 203

 11.2.2 Fluctuation Theory 207

 11.2.2.1 Diffusion Coefficients 208

 11.2.2.2 Reorientation Times 209

 11.2.2.3 H-bond Jump Times 210

 11.2.2.4 Activation Energy Decompositions 211

 11.2.3 Simulation Details 212

11.3 Results and Discussion 214

 11.3.1 Timescales 214

 11.3.2 Activation Energies 217

 11.3.3 Activation Energy Decomposition 221

 11.3.4 Activation Volumes 225

11.4 Conclusions 228

12 The water hydrogen bond jump activation energy can be inferred from experimental data **230**

12.1 Introduction 230

12.2 Computational Methods 232

12.3 Results and Discussion 232

12.4 Conclusions 241

13 A Dynamical Maxwell Relation **243**

13.1 Introduction 243

| | | |
|--------|---|-----|
| 13.2 | Theory | 245 |
| 13.2.1 | Maxwell Relation for a Dynamical Variable | 245 |
| 13.2.2 | Fluctuation Theory and the Maxwell Relation | 246 |
| 13.3 | Computational Methods | 250 |
| 13.4 | Results and Discussion | 251 |
| 13.4.1 | Contributions to the Maxwell Relation | 251 |
| 13.4.2 | Physically Motivated Description of $D(p, T)$ | 253 |
| 13.5 | Conclusions | 260 |

IV Complex Systems 261

14 Vapor-Liquid Equilibria and Diffusion in CO₂-Expanded Electrolytes 263

| | | |
|----------|--|-----|
| 14.1 | Introduction | 263 |
| 14.2 | Methods | 264 |
| 14.2.1 | Transport Properties | 265 |
| 14.2.2 | Activation Energies | 266 |
| 14.3 | Simulation Details | 267 |
| 14.3.1 | Force Fields | 267 |
| 14.3.2 | Vapor Liquid Equilibrium | 268 |
| 14.3.3 | MD Simulations | 268 |
| 14.3.3.1 | Volume Expansion Simulations | 269 |
| 14.3.3.2 | Transport Calculations | 269 |
| 14.3.3.3 | Activation Energy Calculations | 270 |
| 14.4 | Results and Discussion | 270 |
| 14.4.1 | Viscosity and Diffusion | 271 |
| 14.4.2 | Activation Energies | 275 |
| 14.5 | Discussion | 278 |

| | | |
|-----------|---|------------|
| 14.5.1 | Entropic Origin of Slowed CO ₂ Diffusion | 278 |
| 14.5.2 | Activation Energy Decomposition | 281 |
| 14.6 | Conclusions | 281 |
| 15 | Water Reorientation Times are Invariant with Acrylamide Chain Length | 282 |
| 15.1 | Introduction | 282 |
| 15.2 | Methods | 284 |
| 15.2.1 | System Details | 284 |
| 15.2.2 | Solvation Shell Calculations | 285 |
| 15.2.3 | Reorientation Correlation Function | 286 |
| 15.2.4 | Simulation Details | 286 |
| 15.3 | Theoretical Model | 287 |
| 15.4 | Results and Discussion | 289 |
| 15.4.1 | Categorization of OH groups | 290 |
| 15.4.2 | Reorientation Times | 290 |
| 15.4.3 | Model Parameters | 293 |
| 15.4.4 | Chain Length-Independence | 294 |
| 15.5 | Conclusions | 296 |
| V | End Matter | 297 |
| 16 | Concluding Remarks, Outlook, and Technological Impediments | 298 |
| 16.1 | Activation Energies of Dynamical Timescales | 298 |
| 16.2 | Water Under Extreme Conditions | 299 |
| 16.3 | Toward a Unified Picture of Water Dynamics | 300 |
| 16.4 | Complex Systems | 300 |
| 16.5 | Outlook | 301 |
| 16.5.1 | Maxwell Relations | 301 |

| | | |
|-----------|--|------------|
| 16.5.2 | Jump Diffusion Model | 301 |
| 16.5.3 | Other Quantities | 301 |
| 16.5.4 | Other Derivatives | 302 |
| 16.5.5 | Other Systems | 302 |
| 16.6 | Technological Impediments | 302 |
| 16.6.1 | Size Effects | 302 |
| 16.6.2 | Computational Power and Data Storage | 303 |
| 16.6.2.1 | <i>Ab Initio</i> Molecular Dynamics | 303 |
| 16.6.3 | Thermal Fluctuations | 304 |
| 17 | Future Work | 305 |
| 17.1 | Other Quantities | 305 |
| 17.1.1 | Raman Spectroscopy | 305 |
| 17.1.2 | Dielectric Relaxation | 306 |
| 17.1.3 | Non-Equilibrium Methods | 307 |
| 17.1.4 | Weighted Histogram Analysis Method | 308 |
| 17.2 | Other Derivatives | 309 |
| 17.2.1 | Potential Parameter Derivatives | 309 |
| 17.2.2 | Chemical Potential Derivatives | 311 |
| 17.2.3 | High-Order Derivatives | 312 |
| 17.3 | Other Systems | 313 |
| 17.3.1 | Activation Parameters Near Phase Transitions | 313 |
| 17.3.2 | Liquids at Interfaces | 314 |
| 17.3.3 | Biomolecules | 314 |
| 17.3.4 | Lithium Fluoride Ion Pairing | 315 |
| 17.3.4.1 | Theory | 315 |
| 17.3.4.2 | Methods | 316 |
| 17.3.4.3 | Preliminary Results | 317 |

| | |
|------------------------|------------|
| 17.4 Summary | 319 |
| 18 References | 320 |

List of Figures

- 1.1 Schematic illustration of the fluctuation theory for dynamics. An MD simulation in the canonical ensemble (left) exhibits a distribution of total energies with fluctuations, δH , about the average value (center). Higher energies lead to faster dynamics, such as diffusion (right), while smaller energies lead so slower dynamics. The change in the dynamical timescale, *e.g.*, diffusion coefficient, with the energy is measured by the activation energy. 7
- 1.2 Bottom: The TCFs $MSD(t)$ (black line) and $MSD_H(t)$ (red line) are plotted versus time for the SPC/E water model at 298 K obtained from 2,500 *NVE* trajectories. Top: The ratio $MSD_H(t)/MSD(t)$ (red line) is plotted as a function of time. A fit of this ratio between $t = 15 - 20$ ps to a constant value is also shown (blue dashed line). Note: $MSD(t)$ is in units of $\text{\AA}^2/\text{ps}$, $MSD_H(t)$ in $\text{kcal/mol} \times \text{\AA}^2/\text{ps}$ 12
- 1.3 The contributions to the diffusion TCF $MSD_H(t)$ shown in Fig. 1.2 associated with the kinetic energy (red line), Lennard-Jones potential energy (violet line), and Coulombic potential energy (blue line) are plotted versus time along with the total (black line). 13
- 1.4 OH reorientational correlation function, $C_2(t)$, (black) is shown as a function of time along with a triexponential fit (red), Eq. (1.26). a: $C_2(t)$ is shown on a semi-log scale and the short-time decay is shown in the inset. b: $C_2(t)$ is shown on a linear scale along with its integral (blue, right axis) which equals the average reorientational time, $\langle \tau_2 \rangle$, at long times. Results are from 50,000 *NVE* trajectories with the TIP4P/2005 water model at 298.15 K and 1 bar. 15

| | | |
|-----|---|----|
| 1.5 | The weighted reorientation correlation function $C_{2,H}(t)$ (black) corresponding to Fig. 1.4 is shown along with its contributions from the Lennard-Jones potential energy (indigo), electrostatic potential energy (green), and kinetic energy (red). Fits for each correlation function are included as blue dashed lines. | 17 |
| 1.6 | A deeper decomposition of the activation energies for CO ₂ diffusion in CXEs. Contributions from solvent interactions are included in orange, contributions from electrolyte interactions are included in green. The sum of these contributions are the total potential energy contribution the activation energy (purple). The sum of the potential and kinetic (red) energy equal the total (black). | 20 |
| 1.7 | The second-derivative reorientational TCF, $C_{2,\delta H^2}(t)$, is shown (red line) for SPC/E water at 298 K from 30,000 <i>NVE</i> trajectories along with a fit based on Eq. 1.26 (dashed blue line); $C_2(t)$ is shown for comparison (black line). | 22 |
| 1.8 | The ratio $MSD_V(t)/MSD(t)$, which at long times is equal to the diffusion activation volume, ΔV_D^\ddagger , for 100 bar and $T = 283$ (black), 383 (red), and 473 K (blue) for TIP4P/2005 water from 5,000 <i>NVE</i> trajectories. Dashed lines of the same color indicate the derived ΔV_D^\ddagger from fitting to $t \geq 15$ ps. | 25 |
| 2.1 | A schematic diagram of the nonequilibrium MD simulation approach in which <i>NVE</i> trajectories with different energies are initiated from a single <i>NVT</i> trajectory. | 35 |
| 2.2 | Arrhenius plots for (a) D and (b) τ_2 are presented. Results from the MD simulations (filled black circles) are shown along with linear fits (dashed lines) based on the Arrhenius equation. | 38 |
| 2.3 | Bottom: The TCFs $MSD(t)$ (black line) and $MSD_H(t)$ (red line) are plotted versus time. Top: The ratio $MSD_H(t)/MSD(t)$ (red line) is plotted as a function of time. A fit of this ratio between $t = 15 - 20$ ps to a constant value is also shown (blue dashed line). Note: $MSD(t)$ is in units of $\text{\AA}^2/\text{ps}$, $MSD_H(t)$ in $\text{kcal/mol} \times \text{\AA}^2/\text{ps}$. . . | 39 |

| | | |
|-----|--|----|
| 2.4 | The reorientational TCF $C_2(t)$ (solid black line) is shown as a function of time along with a tri-exponential fit (dashed black line) to Eq. (2.12). The TCF including the energy fluctuation, $C_{2,H}(t)$, is also shown (solid red line) along with the fit (dashed blue line) to Eq. (2.14). | 40 |
| 2.5 | The contributions to the diffusion TCF $MSD_H(t)$ associated with the kinetic energy (red line), Lennard-Jones potential energy (violet line), and Coulombic potential energy (blue line) are plotted versus time along with the total (black line). | 43 |
| 2.6 | The contributions to the reorientational TCF $C_{2,H}(t)$ associated with the kinetic energy (red line), Lennard-Jones potential energy (violet line), and the Coulombic potential energy (blue line) are plotted versus time along with the total (black line). | 44 |
| 3.1 | The OH reorientational correlation function, $C_2(t)$, for TIP4P/2005 water at 298.15 K and 1 bar (black) is shown as a function of time along with a triexponential fit (red), Eq. (3.4). a: $C_2(t)$ is shown on a semi-log scale and the short-time decay is shown in the inset. b: $C_2(t)$ is shown on a linear scale along with its integral (blue, right axis) which equals the average reorientational time, $\langle\tau_2\rangle$, at long times. | 50 |
| 3.2 | The reorientational TCF $C_2(t)$ (black) and the energy fluctuation weighted TCF $C_{2,H}(t)$ (red) are plotted versus time for TIP4P/2005 water at 298.15 K and 1 bar. Fits of each according to Eqs. (3.4) and (3.10) are also shown (blue dashed). | 56 |
| 3.3 | Reorientation time Arrhenius plot calculated from the TIP4P/2005 <i>NPT</i> simulations. Arrhenius fits are included as a black line for the fit of all temperatures, as blue line for the fit of the lowest three temperatures, and as a red line for the fit over the highest three temperatures. A) τ_{lib} and τ_{iner} are shown as diamonds and triangles, respectively. B) A similar analysis is included for τ_2 and $\langle\tau_2\rangle$ which are represented by circles and squares, respectively. | 59 |

| | | |
|-----|--|----|
| 3.4 | The derivative TCF, $C_{2,H}(t)$, (red solid) is compared to its fit, Eq. (3.10), (blue dashed) and the contributions to the fit from the inertial (cyan dashed), librational (violet dashed), and H-bond breaking and making (magenta dashed). The inset shows an expanded view of the the short-time behavior. | 64 |
| 3.5 | The reorientation correlation function $C_2(t)$ weighted by the total energy (black), Lennard-Jones potential energy (indigo), electrostatic potential energy (green), and kinetic energy (red). Fits for each correlation function are included as blue dashed lines. | 67 |
| 4.1 | Water OH group reorientational TCFs, Eq. (4.1), at 298.15 K for $n = 1$ (black), 2 (blue), and 3 (orange); tri-exponential fits using Eq. (4.3) are shown as dashed lines of the same color. Inset shows the results on a semi-log plot. | 73 |
| 4.2 | Schematic illustration of the two components of the extended jump model for OH reorientation: Large-amplitude angular jumps associated with the exchange of H-bond acceptors (left) and the frame reorientation of the intact H-bond pair between jumps (right). | 74 |
| 4.3 | Derivatives of the OH reorientational TCFs with respect to β , Eq. (4.9), for H ₂ O at 298.15 K for $n = 1$ (black), 2 (blue), and 3 (orange); fits to Eq. (4.10) are shown as dashed lines of the same color. | 83 |
| 4.4 | a) Jump TCF, $1-C_{ab}(t)$, (black) and its derivative, $C_{ab,H}(t)$, (red). b) The total energy (black), kinetic energy (red), Lennard-Jones (purple), and Coulombic (green) contributions to the derivative TCF. Calculated TCFs are shown as solid lines and fits as dashed lines of the same color. | 85 |
| 4.5 | Schematic illustration of the potential energy contributions to the jump activation energy. The "reactant" and transition state structures are shown (middle panel) in the context of the radial distribution function and free energy profile. The corresponding changes in the Lennard-Jones (top panel) and Coulombic (bottom panel) interactions are depicted. | 87 |

| | | |
|-----|--|-----|
| 4.6 | a) The jump angle distribution, b) the derivative of the jump angle distribution, and c) the total (black), kinetic energy (red), Lennard-Jones (purple) and Coulombic (green) contributions to the jump angle distribution derivative are presented. | 89 |
| 4.7 | a) Frame reorientational TCF, $C_{n,frame}(t)$ for $n = 1$ (black), 2 (blue), and 3 (orange), and b) Corresponding derivative TCFs, $C_{n,frame,H}(t)$. Fits are shown as dashed lines in the same color. | 91 |
| 4.8 | Decomposition of the derivative frame reorientation TCF, $C_{n,frame,H}(t)$, for a) $n = 1$, b) $n = 2$, and c) $n = 3$. Contributions from kinetic (red), Lennard-Jones (purple), and Coulombic (green) energies are compared to the total (black). Fits are shown as dashed lines of the same color. | 93 |
| 4.9 | Contributions to the OH reorientation activation energy for $n = 1, 2$, and 3 (gray spheres) are compared to the EJM predictions (bars) divided into the jump (red bars) and frame (blue bars) weighted components in Eq. (4.7). | 96 |
| 5.1 | The room temperature frequency-frequency correlation function (black solid line) for SPC/E water is shown along with fits using three (blue dashed line) and four (red dashed line) exponentials. Inset: Semi-log plot. | 109 |
| 5.2 | Same as Fig. 5.1, but for the (a) E3B2 and (b) E3B3 water models. | 111 |
| 5.3 | The β derivative of the FFCF, $\partial C_{\omega}(t)/\partial\beta$, versus time (black solid line) is shown for the (a) SPC/E, (b) E3B2, and (c) E3B3 water models with three- (blue dashed line) and four- (red dashed line) exponential fits, Eq. (5.5). In the latter, the longest timescale is fixed as the jump time, τ_0 | 113 |
| 5.4 | The β derivative of the FFCF, $\partial C_{\omega}(t)/\partial\beta$, versus time (black solid line) and its kinetic (red solid line), Lennard-Jones (violet solid line), and Coulombic (blue solid line) energy contributions for the SPC/E water model. Four-exponential fits, Eq. (5.5), are also shown (dashed lines of the same color; not easily visible because of the high quality of the fit.) | 116 |

| | | |
|-----|---|-----|
| 6.1 | A diagram depicting the production of NVE trajectories sampled along a single NPT trajectory. | 126 |
| 6.2 | A plot of the probability distribution function of the fluctuations in volume of the individual NVE trajectories away from the average volume of the overall NPT trajectory. A gaussian fit has been included as a dashed red line. | 128 |
| 6.3 | The volume-weighted mean-squared displacement $MSD_V(t)$ (red) and the unweighted mean-squared displacement $MSD(t)$ (black) for $p = 100$ bar and 473, 383, and 283 K (top to bottom). | 129 |
| 6.4 | The ratio $MSD_V(t)/MSD(t)$, which at long times is equal to the diffusion activation volume, ΔV_D^\ddagger , for 100 bar and $T = 283$ (black), 383 (red), and 473 K (blue). Dashed lines of the same color indicate the derived ΔV_D^\ddagger from fitting to $t \geq 15$ ps. | 130 |
| 6.5 | (a) Activation volume, ΔV_D^\ddagger , as a function of p and T . The present simulation results (filled symbols) for 283.2 (blue), 298.2 (black), 383.2 (red), and 473.2 K (violet) are compared to experimental data from Ref. 1 (solid lines), Ref. 2 (dashed lines), Ref. 3 (open symbols), and Ref. 4 (dot-dot-dashed lines); see text. Data represented by blue dashed line is for 278.2 K. ² (b) An expanded view of the low temperature results. | 132 |
| 7.1 | (a) Calculated $C_2(t)$ (black solid line) and its tri-exponential fit (red dashed line) with the integral of $C_2(t)$ (blue solid line) which equals $\langle \tau_2 \rangle$ at long times. (b) Calculated $\partial C_2(t)/\partial \beta$ (black solid line) and its fit (red dashed line) to Eq. (7.10) with the integral (blue solid line) that equals $\partial \langle \tau_2 \rangle / \partial \beta$ at long times. (c) Calculated $\partial^2 C_2(t)/\partial \beta^2$ (black solid line) and its fit (red dashed line) to Eq. (7.11) with the integral (blue solid line) that equals $\partial^2 \langle \tau_2 \rangle / \partial \beta^2$ at long times. | 141 |

| | | |
|-----|---|-----|
| 7.2 | (a-c) Calculated $\langle \tau_2 \rangle$, τ_2 , and D (black circle) at different temperatures are compared to the predictions from room temperature simulations (blue solid line). (d-f) Arrhenius plots of $\langle \tau_2 \rangle$, τ_2 , and D calculated from T -dependent simulations (black circle) compared to predictions from room temperature simulations (blue solid line) and the Arrhenius result (red dashed line) from the activation energy at 298.15 K. The melting point of TIP4P/2005 water is also indicated (purple dashed line). ⁵ | 143 |
| 7.3 | Predictions of the temperature dependence of (a) $\langle \tau_2 \rangle$ and (b) D using the two liquids description as given in Eq. (7.17) and described in the text are shown (blue solid line). The results from T -dependent simulations (black circle) are shown along with the measured D (red circle) from Xu <i>et al.</i> ⁶ The melting point of water (magenta dashed line) and TIP4P/2005 water (purple dashed line) water are also indicated. | 149 |
| 7.4 | Temperature-dependent activation energy decompositions are reported for for (a) $\langle \tau_2 \rangle$, (b) τ_2 , and (c) D . The total activation energy (black circle) as well as the the kinetic (red square), Lennard-Jones (purple diamond), and electrostatic contributions (cyan triangle) to the activation energy are presented. The prediction of the total activation energy based on Eqs. (7.12) (blue solid line) and (7.17) (blue dashed line) are also shown. | 151 |
| 8.1 | a: The O-O RDF (black line) and its first derivative (magenta line) calculated from a single simulation at 298.15 K. b: The derivative $\partial g_{OO}(r)/\partial \beta = -g_H(r)$ (magenta line) along with its contributions due to kinetic energy ($X = KE$, red line) and Lennard-Jones ($X = LJ$, violet line) and Coulombic ($X = Coul$, blue line) interactions. | 161 |
| 8.2 | Helmholtz free energy $\Delta A(r)$ (black line) from the O-O RDF is shown along with the internal energy, $\Delta U(r)$, (red line) and entropic, $-T\Delta S(r)$, (blue line) contributions. | 163 |

| | | |
|-----|---|-----|
| 8.3 | a: $g_{OO}(r)$ RDF and b: Helmholtz free energy, $\Delta A_{OO}(r)$, predicted from a single simulation at room temperature (lines) are compared to explicit T -dependent simulations (symbols). | 164 |
| 8.4 | a: Calculated derivative of the O-O RDF, $\partial g_{OO}(r)/\partial\beta = -g_H(r)$, as a function of trajectory length. b: Residual relative to the 50 ns result, $-\Delta g_H(r) = -[g_H(r; t_{traj}) - g_H(r; 50\text{ ns})]$ | 167 |
| 9.1 | (a) HOD in D ₂ O IR spectrum (black), frequency distribution (red), and spectral density (blue) at 298.15 K. The (b) frequency distribution, (c) spectral density, and (d) IR spectrum, with the maximum set to 1, are reproduced (solid black) along with the total derivative with respect to β (dashed black) and the contributions to the derivative from the kinetic (dashed red), Lennard-Jones (dashed violet), and Coulombic (dashed blue) energies. | 172 |
| 9.2 | Free energy ΔA (solid black), internal energy ΔU (dashed black), entropic contribution $-T\Delta S$ (dashed red) are plotted versus frequency along with the Lennard-Jones (dashed violet) and Coulombic (dashed blue) internal energy components for the (a) frequency distribution and (b) IR spectrum at 298.15 K. | 176 |
| 9.3 | Predicted frequency distribution (solid lines) for 280 (blue), 320 (orange), 340 (magenta), and 360 K (red) from the 298.15 K distribution (black) and its derivative; direct calculations at these temperatures are shown as dashed lines of the same color. Results are shown based on (a) first-order Taylor series approximations and (b) van't Hoff predictions, Eq. 9.11. | 178 |
| 9.4 | Predicted IR spectrum (solid lines) for 280 (blue), 320 (orange), 340 (magenta), and 360 K (red) from the 298.15 K spectrum (black) and its derivative; direct calculations at these temperatures are shown as dashed lines of the same color. Both (a) unnormalized and (b) normalized results, Eq. 9.12, are shown (see the text). | 179 |

| | | |
|-------|---|-----|
| 10.1 | a) p -dependence of $g(r)$, b) T -dependence of $g(r)$, c) P -dependence of $g(r)$ T -derivative, d) T -dependence of $g(r)$ T -derivative, e) P -dependence of $g(r)$ P -derivative, and f) T -dependence of $g(r)$ p -derivative. | 186 |
| 10.2 | Dependence of the enthalpy, $\Delta H(r)$, as a function of a) P , and b) T | 187 |
| 10.3 | Dependence of the entropic contribution to the free energy, $-T\Delta S(r)$, as a function of a) P , and b) T | 188 |
| 10.4 | Dependence of the partial molar volume, $\bar{v}(r)$ as a function of a) P , and b) T | 189 |
| 10.5 | Schematic diagram of the enthalpic change associated with a hydrogen bond exchange. | 191 |
| 10.6 | Dependence of the changes in the enthalpy (black) and entropy (red) involved in H-Bond exchanges as a function of a) pressure and b) temperature. | 192 |
| 10.7 | Plot of the OH reorientation activation energy as a function of $\Delta\Delta H$ for TIP4P/2005 water. A linear fit is included as a solid red line. | 193 |
| 10.8 | Dependence of the change in the molar volume as a function of a) pressure and b) temperature. | 194 |
| 10.9 | Dependence of the activation volume, ΔV^\ddagger on the change in the molar volume during an H-bond exchange, $\Delta\Delta\bar{v}$. A linear fit is included as a solid red line. | 195 |
| 10.10 | Predictions of the RDF from 1 bar, 298.15 K as a function of a) pressure, and b) temperature. Predictions are presented as open circles, simulation results are presented as solid lines. | 196 |
| 11.1 | Schematic diagram of interaction sites for the water force fields. | 203 |
| 11.2 | The H-bond jump time τ_0 (black), OH reorientation time τ_2 (red), and diffusion coefficient D (blue) are presented for each water model. Experimental values for the reorientation time ⁷⁻⁹ (red dashed line) and diffusion coefficient ¹⁰ (blue dashed line) are also included. | 214 |

| | | |
|------|--|-----|
| 11.3 | Activation energy decomposition for the studied water models are included for a) the jump time, b) the reorientation time, and c) the diffusion coefficient. The total, kinetic, electrostatic, Lennard-Jones, and other contributions to the activation energy are presented in black, red, blue, purple, and orange, respectively. The experimental values of the diffusion and reorientation activation energies are included as black dashed lines on their respective plots. Experimental uncertainties are included as gray solid lines. | 219 |
| 11.4 | Contributions to the jump (black), reorientation (red), and diffusion (blue) activation energies for the E3B model components (U_2 , U_A , U_B and U_C) for the E3B2 (striped bars) and the E3B3 (empty bars) models. | 223 |
| 11.5 | Activation volumes of the jump time, ΔV_0^\ddagger (black), reorientation time, ΔV_2^\ddagger (red), and diffusion coefficient, ΔV_D^\ddagger (blue). The average experimental diffusion activation volume ^{1,2,4} is also shown (dashed blue line; experimental ranges indicated by gray solid lines). The experimental reorientation activation volume at 450 bar is also listed. ¹¹ | 225 |
| 12.1 | Plots of the liquid water OO a) radial distribution function and b) the β derivative of the RDF, $-g_{H,OO}(r)$, for each model. Insets show a closer view of the first maximum. | 233 |
| 12.2 | Water OO (a) Gibbs free energy, (b) enthalpy, and (c) entropy profiles. (The first minimum is set to zero in each case.) | 235 |
| 12.3 | Schematic of the liquid water OO a) enthalpic and b) entropic contributions to the free energy. Indicated on the plot are the positions r_{1st} , r^\ddagger , and r_{2nd} as well as marking the forward and backward directions over the enthalpic barrier. | 237 |

| | | |
|------|---|-----|
| 12.4 | Plot of the jump, reorientation, and diffusion activation energies plotted for each water model as a function of $\Delta\Delta H$ (top panels) and $\Delta\Delta S$ (bottom panels). Linear fits are included for each panel as a dashed line in the same color. The predicted activation energies from Skinner's X-ray data generated using the correlations of $\Delta\Delta H$ are included on each plot. | 239 |
| 13.1 | Comparison of measured $D(p, T)$ from Woolf ⁴ (circles) compared to its fit (dashed lines) to Eq. (13.24). | 255 |
| 13.2 | Comparison of measured $D(p, T)$ from Krynicky ³ (circles) compared to its fit (dashed lines) to Eq. (13.24) at high (top panel) and low (bottom panel) temperatures. | 256 |
| 13.3 | Comparison of measured $D(p, T)$ from Harris 1980 ¹ (circles) compared to its fit (dashed lines) to Eq. (13.24). | 258 |
| 13.4 | Comparison of measured $D(p, T)$ from Harris 1997 ² compared to its proposed fit to Eq. (13.24). | 258 |
| 14.1 | Left Panel: The vapor-liquid equilibrium for the binary MeCN-CO ₂ mixture is presented. The liquid phase compositions are presented in black, the vapor phase compositions are presented in red. Middle Panel: The volume expansion for the binary mixture is presented. Right Panel: Schematic diagram of the volume expansion observed during the CO ₂ expansion process. | 264 |
| 14.2 | a) Shear viscosities as a function of CO ₂ concentration. b) Diffusion coefficients for MeCN (blue) and CO ₂ (red) and shear viscosities (black) for the "Neutralized" system. c) Diffusion coefficients for the "Charged" system for MeCN (blue) and CO ₂ (red). d) Diffusion coefficients for the "Charged" system for Li ⁺ (indigo) and ClO ₄ ⁻ (green). Electrolyte concentrations are indicated in the figure legends. | 272 |

14.3 a) The ratio $D/D_{0,C}$ is shown on the primary axis. The ratio η/η_0 is shown in black. CO₂ results are shown in red, and MeCN results are shown in blue. Electrolyte concentrations are indicated in the figure legend. b) The ratio $D/D_{0,E}$ is shown. CO₂ results are shown in red, and MeCN results are shown in blue. CO₂ concentrations are indicated in the figure legend. 274

14.4 Activation energies for the highest concentration of electrolyte of a) MeCN, b) CO₂ as a function of pressure. The decomposition of the activation energy is presented in the figure legend. 276

14.5 Comparison of D_f/D_{ref} and the arrhenius exponent corresponding to $\Delta E_a = E_{a,f} - E_{a,ref}$. MeCN results are included in panel a, CO₂ results are included in panel b. Linear fits are included as dashed lines. The line of constant entropy ($y = x$) is included as a solid black line. 279

15.1 The reorientation time (τ_2) is presented for the 1-mer (black circles), 3-mer (red circles), and the 5-mer (blue circles). The neat water reorientation time ($\tau_{2,neat}=2.65$ ps) is included as a dashed black line. 283

15.2 A schematic diagram of the simplified PAAm model, separating the mers into "end" groups (orange) and "middle" groups (green). 288

15.3 Counts (per monomer unit) of (top panel) OHs in the first solvation shell (but not H-bonded to PAAm) and (bottom panel) OHs H-bonded to PAAm. Results are presented for the 1-mer (black), 3-mer (red), and 5-mer (blue). 290

15.4 The categorized reorientation correlation times are presented for the 1-mer (black), the 3-mer (red), and the 5-mer (blue). 1st solvation shell values ($\tau_{2,1st}$) are included as squares, H-bonded values ($\tau_{2,HB}$) are included as diamonds, and bulk values ($\tau_{2,bulk}$) are included as upwards triangles. The neat water value ($\tau_{2,neat}=2.65$ ps) is included as a dashed black line. 291

| | | |
|------|--|-----|
| 15.5 | The total reorientation correlation times (τ_2) are presented for the 1-mer (black), the 3-mer (red), and the 5-mer (blue).The neat water value ($\tau_{2,neat}=2.65$ ps) is included as a dashed black line. We have included the results from our simple model, described by Eq. 15.9 using the parameters from Table 15.4 for the 1-mer (black), 3-mer (red), 5-mer (blue), 7-mer (purple), 9-mer (magenta), 11-mer (orange), and 15-mer (green). The inset figure shows the low concentration data, the main figure shows high concentrations. The 1-mer result corrected by s_{eff} is included as a black dashed line. | 294 |
| 17.1 | The first three derivatives of the reorientation correlation function are included (black) along with their fits (red) for TIP4P/2005 water at room temperature. . . . | 312 |
| 17.2 | The potential of mean force calculated from the AIMD simulations. Harmonic fits of the CIP and SSIP wells are included as red and blue dashed lines, respectively. . | 317 |
| 17.3 | Activation energy decompositions for ion pairing. The total activation energy, the kinetic contribution to the activation energy, and the potential contribution to the activation energy are included in black, red, and blue, respectively. | 318 |

List of Tables

| | | |
|-----|---|----|
| 3.1 | Reorientation times, τ_α , in ps, amplitudes, A_α , amplitude derivatives, $\partial A_\alpha/\partial\beta$, in kcal/mol, and activation energies, E_α , in kcal/mol for the TIP4P/2005 model calculated from the <i>NPT</i> ensemble at 298.15 K and 1 bar. Subscripts indicate uncertainties in the final digit(s). | 54 |
| 3.2 | Simulated reorientation times at different temperatures for TIP4P/2005 water at 1 bar. | 58 |
| 3.3 | Activation energies (kcal/mol) calculated from an Arrhenius analysis of the temperature dependence through fitting different sets of points. The column labeled "All" is a fit of all temperatures 288.15-308.15K, "Middle" is a fit over all temperatures 293.15-303.15K, "Low" is a fit over all temperatures 288.15-298.15K, "High" is a fit over all temperatures 298.15-308.15K, and "Separated" is a fit of 288.15 K, 298.15 K, and 308.15 K. | 58 |
| 3.4 | Contributions to the activation energy, $E_{a,\langle\tau_2\rangle}^{(fit)}$, in kcal/mol, as given in Eq. (3.12). Results are for TIP4P/2005 water at 298.15 K and 1 bar. Last row shows the total associated with each timescale. | 61 |
| 3.5 | Activation energy decomposition, in kcal/mol, calculated from the <i>NPT</i> ensemble at 298.15 K. | 68 |
| 4.1 | Timescales (in ps) calculated from the jump dynamics, jump contribution, frame contribution, total reorientation, and EJM prediction are included along with the jump angle contribution, \bar{w}_n ; see the text for definitions. Subscripts represent the uncertainty in the final digit(s). | 82 |

| | | |
|------|--|-----|
| 4.2 | Activation energies and their kinetic energy (<i>KE</i>), Lennard-Jones (<i>LJ</i>), and Coulombic (<i>Coul</i>) contributions (all in kcal/mol) for the components of the extended jump model for different order <i>n</i> reorientational TCFs. Subscripts indicate the uncertainties in the final digit(s). | 82 |
| 4.3 | The additivity of the activation energies (all in kcal/mol) within the EJM is presented. The directly calculated OH reorientation activation energy ($E_{a,n}$) and its different energetic contributions are compared for each <i>n</i> to the EJM prediction ($E_{a,n}^{EJM}$) and its weighted jump and frame reorientation components in Eq. (4.7). . . | 94 |
| 5.1 | Timescales (in ps) and amplitudes of the FFCF calculated from three- (top) and four- (bottom) exponential fits. Subscripts represent uncertainty in the trailing digit(s). | 110 |
| 5.2 | Activation energies and kinetic (<i>KE</i>), Lennard-Jones (<i>LJ</i>), and Coulombic (<i>Coul</i>) energy components for the jump time τ_0 and the spectral diffusion times obtained from three-, $\tau_\omega^{(3)}$, and four-, $\tau_\omega^{(4)}$, exponential fits of the derivative FFCF, $C_{\omega,H}(t)$. All energies are in kcal/mol; subscripts represent uncertainty in the trailing digit(s). | 114 |
| 6.1 | Calculated and measured activation volumes, ΔV_d^\ddagger , (in cm ³ /mol) for water self-diffusion | 131 |
| 7.1 | Values, derivatives, and activation energies of $\langle \tau_2 \rangle$, τ_2 , and $1/D^a$ at 298.15 K . . . | 143 |
| 7.2 | Comparison of stability limit conjecture parameters [†] with fits to <i>T</i> -dependent data. [‡] | 144 |
| 7.3 | Parameters [†] for the “two-liquids” picture. [‡] | 147 |
| 11.1 | Force field parameters used for each of the water models. | 204 |

| | | |
|------|---|-----|
| 11.2 | H-bond jump time τ_0 , OH reorientation time τ_2 , diffusion coefficients directly from the simulations, D_{PBC} , and corrected for finite-size effects, D , and shear viscosities, η_s for different water models; times are in ps, diffusion coefficients are in 10^{-5} cm ² /s, and shear viscosities are in cP. Subscripts indicate uncertainties in the trailing digit(s). | 215 |
| 11.3 | Activation energies (in kcal/mol) of the jump time, OH reorientation time, and diffusion coefficient. Subscripts indicate uncertainties in the trailing digit(s). | 218 |
| 11.4 | Activation volumes (in cm ³ /mol) of the jump time, ΔV_0^\ddagger , reorientation time, ΔV_2^\ddagger and diffusion coefficient, ΔV_D^\ddagger . Subscripts indicate uncertainties in the trailing digit(s). | 226 |
| 12.1 | E_a , 0, $\Delta\Delta H$, $\Delta\Delta H^\theta$, and $-T\Delta\Delta S$ for each water model and experiment. ¹² | 238 |
| 13.1 | Summary of fits of Eqs. (13.23) and (13.24) to experimental measurements ¹⁻⁴ and direct simulation results for TIP4P/2005 water. Values are for 298.15 K and 1 bar. | 257 |
| 14.1 | Force Field Parameters | 267 |
| 14.2 | GEMC concentrations and volume expansions, as well as solvent numbers. Uncertainties are included as subscripts. | 270 |
| 14.3 | Volume expansions calculated as a function of pressure for each electrolyte concentration, x_{LiClO_4} | 270 |
| 14.4 | Activation energy decompositions for both MeCN and CO ₂ diffusion as a function of pressure and number of ions. Uncertainties in the final digits are included as subscripts. | 275 |
| 15.1 | Compositions and simulation cell side lengths for each of the polymer concentrations and chain-lengths. | 284 |
| 15.2 | Counts (per monomer unit) of OHs H-bonded to PAAm and OHs in the first solvation shell. | 291 |

| | | |
|------|--|-----|
| 15.3 | OH reorientation times calculated for each concentration and chain length of PAAm. Included are reorientation of all OHs (τ_2), OHs in the 1 st solvation shell ($\tau_{2,1st}$), OHs H-bonded to PAAm ($\tau_{2,hbond}$), and OHs that are neither H-bonded to PAAm or in the first solvation shell ($\tau_{2,bulk}$). | 292 |
| 15.4 | Model parameters used for Eq. 15.9. | 293 |
| 17.1 | Activation energies (in kcal/mol) for ion pairing. | 318 |

Chapter 1

Introduction and Overview: Activation Energies and Beyond

The activation energy for a thermal reaction rate constant, $k(T)$, defined as

$$E_a = -\frac{\partial \ln k(T)}{\partial \beta}, \quad (1.1)$$

where $\beta = 1/k_B T$, is one of the most fundamental characteristics of the underlying chemical process. It is most often interpreted in relation to the Arrhenius expression for the rate constant,^{14–17}

$$k(T) = A e^{-E_a/k_B T}, \quad (1.2)$$

where A is the Arrhenius prefactor, or frequency factor, which is assumed to be temperature independent. This empirical relationship between the rate constant and temperature gives rise to the standard approach for determining the activation energy: one constructs an Arrhenius plot of $\ln k(T)$ versus $1/T$ and the slope is then $-E_a/k_B$. The resulting E_a is frequently related to the barrier for the reaction, which can be valuable for gaining insight into the reaction mechanism.

There are important limitations to obtaining the activation energy by an Arrhenius analysis. The requirement that k be measured or calculated over a range of temperatures cannot be met in some cases. For example, near a phase transition an increase or decrease in temperature can lead to a change in k that is due to the phase change rather than the barrier in the state of interest. Proteins and other biomolecules that undergo folding/unfolding transitions represent a special case

Adapted with the permission of Zeke A. Piskulich, Oluwaseun O. Mesele, and Ward H. Thompson and the American Chemical Society from *J. Phys. Chem. A* **123**, 7185-7194 (2019).¹³

of this problem in which only a limited temperature range is available for an Arrhenius analysis. This constraint competes with the requirement that the temperature range must also be sufficiently broad that changes in k are large enough to be resolved by the experimental or simulation approach.

Activation energies are relevant for many timescales other than chemical reaction rate constants and the conflicts inherent in choosing an appropriate temperature range can be particularly prominent in such cases. Diffusion coefficients, reorientation times, viscosity, and dielectric relaxation times are only a few examples of timescales that can be described by an Arrhenius equation analogous to Eq. 1.2. Because the underlying processes do not involve changes in chemical bonding, they typically have smaller activation energies and thus depend more weakly on temperature. Moreover, the interpretation of the activation energy is more challenging in such cases, for which a clear reaction coordinate and barrier are not readily identifiable.

In this Introduction, we briefly discuss the approaches developed within this thesis for avoiding an Arrhenius analysis by direct calculation of the activation energy from simulations at a single temperature. In general terms, these methods focus on calculation of the analytical derivative of an arbitrary dynamical timescale with respect to temperature, in contrast to the numerical derivative obtained in an Arrhenius analysis. Conceptually, the approach is essentially the fluctuation theory of statistical mechanics applied to dynamics. As such, it permits not only computational advantages, but new physical insight that is otherwise inaccessible.

Nearly a century ago, Tolman developed, based on a statistical mechanical analysis, an alternative interpretation of the activation energy as the difference in the average energy of reacting molecules minus the average energy of reactant molecules,¹⁸

$$E_a = \langle E \rangle_{reacting} - \langle E \rangle_r, \quad (1.3)$$

This idea was further developed by Truhlar¹⁹ in terms of the reactive cross sections of gas phase collision theory which improved upon an approximation in Tolman's approach. Note that the focus of Tolman's interpretation is on the energy the reacting species must have to overcome the barrier

rather than the height of the barrier that must be overcome. This is a different perspective than is often used in thinking about activation energies and it opens up new possibilities for physical insight.^{20–22} In particular, it indicates that the activation energy can be decomposed into contributions due to the system interactions (*vide infra*). A given component is then the average energy of the reacting species, relative to that of the reactants, associated with the specific interaction. The contribution to the activation energy is then the measure of how effective additional energy in this interaction is for speeding up the dynamics of interest.

The remainder of this Introduction is organized as follows. We first introduce the Tolman interpretation of activation energy and the fluctuation theory for dynamics approach using simple derivations; the implications for obtaining new mechanistic insight using this method are discussed. Several examples of applications of this fluctuation theory, many of which will be discussed in greater detail in later chapters, are presented to illustrate the generality and flexibility of the method. Prospects for moving beyond the calculation of activation energies are then introduced in terms of both non-Arrhenius behavior and derivatives of dynamical timescales with respect to other thermodynamic variables.

1.1 Theory

1.1.1 Interpretations of the Activation Energy

The Tolman interpretation of the activation energy, discussed above and expressed in Eq. 1.3, is most easily summarized by considering the thermal reaction rate constant written in terms of the cumulative reaction probability, $N(E)$; see, *e.g.*, Ref. 20. In brief, quantum mechanically $N(E)$ is the sum over all state-to-state reaction probabilities at a fixed total energy,²³

$$N(E) = \sum_{\mathbf{n}_r, \mathbf{n}_p} P_{\mathbf{n}_r, \mathbf{n}_p}(E), \quad (1.4)$$

where \mathbf{n}_r and \mathbf{n}_p represent the full set of reactant and product quantum numbers. The classical $N(E)$ can be analogously defined. The reaction rate constant is given by

$$k(T) = \frac{1}{2\pi\hbar Q_r(T)} \int_0^\infty N(E) e^{-\beta E} dE, \quad (1.5)$$

where $Q_r(T)$ is the reactant partition function. Then it is straightforward to see that the activation energy is

$$E_a = \frac{\int_0^\infty N(E) E e^{-\beta E} dE}{\int_0^\infty N(E) e^{-\beta E} dE} + \frac{1}{Q_r} \frac{\partial Q_r}{\partial \beta}. \quad (1.6)$$

The second term can easily be identified as the negative of the average reactant energy, $-\langle E \rangle_r$. If we recognize

$$P_{reacting}(E) = \frac{N(E) e^{-\beta E}}{\int_0^\infty N(E) e^{-\beta E} dE}, \quad (1.7)$$

as the normalized distribution for the probability of reacting with a total energy E , then we can see that the first term in Eq. 1.6 is the average energy of species that react:

$$\langle E \rangle_{reacting} = \int_0^\infty E P_{reacting}(E) dE, \quad (1.8)$$

such that the activation energy is given by Eq. 1.3, as originally obtained by Tolman.¹⁸

It is useful to compare this to the activation energy one obtains from transition state theory^{24,25} (TST) in which the rate constant is approximated as

$$k_{TST}(T) = \frac{k_B T}{h} \frac{Q^\ddagger}{Q_r} e^{-\beta E^\ddagger}, \quad (1.9)$$

where Q^\ddagger and E^\ddagger are the transition state internal partition function and electronic energy, respectively. The activation energy is then given as

$$E_a^{TST} = E^\ddagger + \langle E \rangle_{int,\ddagger} + k_B T - \langle E \rangle_r, \quad (1.10)$$

where $\langle E \rangle_{int,\ddagger} = -\partial \ln Q^\ddagger / \partial \beta$ is the average internal (rotational and vibrational) energy of the

transition state structure or “activated complex.” Comparing this result with Eq. 1.3 indicates that within TST the average energy of reacting species is $\langle E \rangle_{reacting}^{TST} = E^\ddagger + \langle E \rangle_{int,\ddagger} + k_B T$. That is, $\langle E \rangle_{reacting}^{TST}$ is the electronic barrier height plus the average thermal internal energy of the transition state and $k_B T$ associated with kinetic energy along the reaction coordinate.

If we note that the exact rate constant can be written as

$$k(T) = \kappa(T) k_{TST}(T), \quad (1.11)$$

where $\kappa(T)$ is the transmission coefficient, then it is straightforward to see that

$$E_a = E_a^{TST} + E_{a,\kappa}. \quad (1.12)$$

Here, $E_{a,\kappa} = -\partial \ln \kappa / \partial \beta$ is the contribution to the activation energy from the temperature dependence of the transmission coefficient. Since $\kappa(T)$ corrects all sins of the TST approximation, it can include, for example, contributions from both transition state recrossing and quantum mechanical tunneling. Moreover, it is important to note that, like k_{TST} , $\kappa(T)$ depends on the choice of the transition state dividing surface that separates the reactants and products. This is evident from Eq. 1.11 because the exact (measurable) rate constant, $k(T)$, does not depend on any definition of a transition state while $k_{TST}(T)$ naturally does. Consequently, both E_a^{TST} and $E_{a,\kappa}$ are not obtainable from measurements because they depend on the choice of the dividing surface separating reactants and products, while E_a does not.

The above results lead to some of the commonly invoked interpretations of the activation energy that differ from that of Tolman and must be applied with care. For example, the activation energy is often loosely considered to represent the barrier height for the reaction. This is a reasonable extension of Eq. 1.3 because the energy of reacting species above that of reactants is related to the barrier height that must be surmounted to react. However, this equivalence should not be taken too literally; for example, as we show below, the average energy of the reacting species, $\langle E \rangle_{reacting}$, and the reactants, $\langle E \rangle_r$, can be decomposed into various energy components and thus so can the

activation energy, in a way that does not make sense for the barrier height. That is, the activation energy is a measure of the *energy required to surmount the barrier* and not just the electronic (or even thermal) energy of the barrier.

1.1.2 Fluctuation Theory for Dynamics

1.1.2.1 Derivation

Fluctuation theory has been used to great effect in understanding equilibrium statistical thermodynamics,^{26–28} but only recently has it been shown that the same ideas can be extended to understand chemical dynamics. A prototypical example of fluctuation theory is the relation between the heat capacity and energy fluctuations. Namely, the average energy of a system in the canonical ensemble is given by

$$\langle E \rangle = -\frac{\partial \ln Q(N, V, T)}{\partial \beta}, \quad (1.13)$$

where Q is the partition function. Then, the heat capacity, C_V , is obtained by taking the temperature derivative of $\langle E \rangle$ and can be shown to be related to the fluctuations in the energy,²⁶

$$C_V = \left(\frac{\partial \langle E \rangle}{\partial T} \right)_{N, V} = \frac{1}{k_B T^2} [\langle E^2 \rangle - \langle E \rangle^2] = \frac{\langle \delta E^2 \rangle}{k_B T}, \quad (1.14)$$

where $\delta E = E - \langle E \rangle$ is the fluctuation of the system energy from its equilibrium average.

This framework for connecting thermodynamic properties, particularly those that are related to derivatives of averages with respect to thermodynamic variables, can be straightforwardly generalized to dynamical properties. To see this, consider some property $f(t) = f(\mathbf{p}, \mathbf{q}, t)$ that depends on the system momenta (\mathbf{p}) and coordinates (\mathbf{q}). Here, we assume a classical system, though a quantum mechanical version of the following result is obtainable in a completely analogous way.

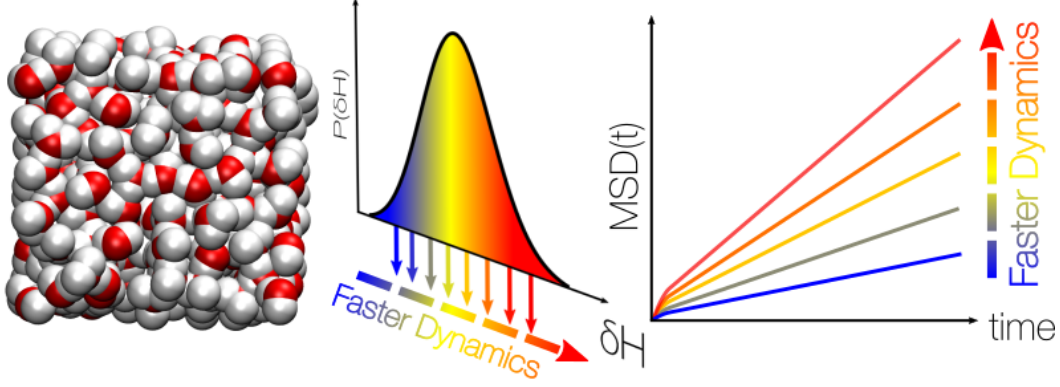


Figure 1.1: Schematic illustration of the fluctuation theory for dynamics. An MD simulation in the canonical ensemble (left) exhibits a distribution of total energies with fluctuations, δH , about the average value (center). Higher energies lead to faster dynamics, such as diffusion (right), while smaller energies lead so slower dynamics. The change in the dynamical timescale, *e.g.*, diffusion coefficient, with the energy is measured by the activation energy.

The average of the property f in the canonical ensemble can then be written as

$$\begin{aligned}
 \langle f(t) \rangle &= \frac{1}{Qh^F} \int \int d\mathbf{p} d\mathbf{q} e^{-\beta H(\mathbf{p}, \mathbf{q})} f(\mathbf{p}, \mathbf{q}, t), \\
 &= \frac{1}{Q} \text{Tr}[e^{-\beta H} f(t)],
 \end{aligned} \tag{1.15}$$

where F is the number of degrees-of-freedom, Q is the canonical partition function, and the second equality defines the trace, Tr , as an average over phase space. Then, because only Q and the Boltzmann weight depend on temperature (note the similarity to Eq. 1.5),

$$\begin{aligned}
 \frac{\partial \langle f(t) \rangle}{\partial \beta} &= -\frac{1}{Q} \frac{\partial Q}{\partial \beta} \langle f(t) \rangle - \frac{1}{Q} \text{Tr}[e^{-\beta H} H(0) f(t)] \\
 &= -\frac{1}{Q} \text{Tr}[e^{-\beta H} \delta H(0) f(t)] \\
 &= -\langle \delta H(0) f(t) \rangle,
 \end{aligned} \tag{1.16}$$

where $\delta H(0) = H(0) - \langle H \rangle$. This result has a simple physical interpretation as discussed in the following section and illustrated in Fig. 1.1. We can also note that if $f(t) = \delta H(0) = \delta E(0)$ then this result is the same as Eq. 1.14 for the heat capacity.

If $f(t)$ is chosen to be a dynamical variable, the resulting derivative in Eq. 1.16 gives the

temperature dependence of the corresponding transport coefficient or dynamical timescale. In one general case, $f(t)$ can represent a time-correlation function (TCF), $C(t) = \langle A(0)B(t) \rangle$, where A and B are two functions of phase space coordinates. Typically, a dynamical constant of interest can be obtained from the time decay or integral of the TCF; several examples are given below. The result in Eq. 1.16 gives the temperature (or, equivalently, β) derivative of the entire TCF as $\frac{\partial C(t)}{\partial \beta} = -\langle \delta H(0)A(0)B(t) \rangle$. In this regard, the fluctuation theory applied to dynamics is quite powerful as it provides more than just an activation energy for a single timescale.

1.1.2.2 Mechanistic Insight

One of the advantages of this fluctuation theory approach is that it can provide physical insight that is not readily available from other methods. For example, the temperature (β) derivative of the average time-dependent property in Eq. 1.16 involves fluctuations in the full, system energy, $\delta H(0)$. The interpretation of this, illustrated in Fig. 1.1, is straightforward: the derivative is a measure of how the dynamics characterized by $\langle f(t) \rangle$ are accelerated or retarded when there is more ($\delta H > 0$) or less ($\delta H < 0$) energy available than average.

The total system energy can also be decomposed into additive components in an almost endless number of ways to provide mechanistic insight. That is, if $H = \sum_{\alpha} H_{\alpha}$, then

$$\frac{\partial \langle f(t) \rangle}{\partial \beta} = -\sum_{\alpha} \langle \delta H_{\alpha}(0) f(t) \rangle. \quad (1.17)$$

Then each term has the interpretation of the contribution of the H_{α} energy to the change in $\langle f(t) \rangle$ with β . Namely, it is a measure of how the dynamics of $\langle f(t) \rangle$ are modified when there is more ($\delta H_{\alpha} > 0$) or less ($\delta H_{\alpha} < 0$) of the H_{α} energy component available relative its average value.²⁹

In the simplest case, one can write the total Hamiltonian in many classical simulations as $H = KE + V_{LJ} + V_{Coul} + V_{intra}$, where KE , V_{LJ} , V_{Coul} , and V_{intra} are the kinetic energy and Lennard-Jones, Coulombic, and intramolecular potential energy terms, respectively. Then, for example, $-\langle \delta V_{Coul}(0) f(t) \rangle$ is the contribution to the β derivative of $\langle f(t) \rangle$ that is associated with the

Coulombic interactions. If $\langle f(t) \rangle$ is related to a dynamical timescale (*e.g.*, rate constant, reorientation time), this provides a way to determine the contributions of the different energetic terms in the system to the activation energy associated with the timescale. In the context of Tolman's interpretation of the activation energy given in Eq. 1.3, this means one can determine, for example, $E_{a,Coul} = \langle E \rangle_{reacting,Coul} - \langle E \rangle_{r,Coul}$, which is the average *Coulombic* energy of reacting molecules minus the average *Coulombic* energy of reactant molecules. Because there are a multitude of ways to additively divide the contributions to the total Hamiltonian, the mechanistic information that can be obtained by this approach is considerable.

1.1.2.3 Other Ensembles

Fluctuation theory can also be applied in ensembles beyond the canonical one. For example, the activation energy for a dynamical process occurring at constant pressure, *i.e.*, in the isothermal-isobaric or *NPT* ensemble, can be obtained as well. In this case, the average of a dynamical property, f , is given by

$$\langle f(t) \rangle_p = \frac{1}{\Delta} \text{Tr}[e^{-\beta(H+pV)} f(t)], \quad (1.18)$$

where $\Delta(N, p, T)$ is the isotherm-isobaric ensemble partition function. Then, it is straightforward to show that the derivative of the average $f(t)$ at constant pressure is

$$\begin{aligned} \frac{\partial \langle f(t) \rangle_p}{\partial \beta} &= -\frac{1}{\Delta} \text{Tr}[e^{-\beta(H+pV)} (\delta H(0) + p\delta V(0)) f(t)], \\ &= -\langle \delta H(0) f(t) \rangle_p - p \langle \delta V(0) f(t) \rangle_p. \end{aligned} \quad (1.19)$$

As will be shown below, the second term is related to the activation volume for the process while the first term is analogous to Eq. 1.16 but evaluated at constant pressure instead of constant volume. The difference between the constant volume and constant pressure activation energy has not received a great deal of attention, but both have been measured in some key cases, *e.g.*, for the diffusion coefficient of water.^{1,3,4,30}

1.2 Activation Energies

To illustrate the potential of this fluctuation theory for dynamics and detail the implementation, we consider some specific examples. In particular, we discuss the theoretical framework for many different dynamical timescales that are frequently of interest and present basic examples of applications to a number of properties.

We have implemented Eq. 1.16 in multiple ways, the key feature of which is that the averages must be evaluated in an ensemble with constant T where fluctuations in the system energy, δH , are present. In principle, this means that a single MD simulation where the temperature is maintained with a thermostat can be used to evaluate activation energies. While this can be straightforwardly implemented,³¹ it is approximate because the thermostat affects the dynamics. In many cases, this approach can be sufficient to determine a reasonable activation energy. However, this issue can be avoided entirely by running a thermostatted trajectory at a temperature T to generate initial conditions for subsequent short, constant energy, NVE , trajectories from which the dynamics and activation energies are obtained. Each short trajectory has its own fixed energy and hence fluctuation from the average of all the trajectories, δH . This approach has no effect from the thermostat (as long as it provides the correct distribution of energies) and has the advantage that the short trajectories are independent and can be run in an embarrassingly parallel fashion. Except where otherwise noted, the data presented here were obtained using this approach.

1.2.1 Reaction Rate Constant

A common approach to calculating the rate constant for a chemical reaction is through reactive flux TCFs,^{32–34} such as

$$k(T) = \lim_{t \rightarrow \text{long}} \langle F_s(0) \mathcal{P}(t) \rangle. \quad (1.20)$$

Here, $F_s = \delta[s(0) - s^\ddagger] v_s(0)$ is the flux through the transition state dividing surface defined in terms of the reaction coordinate s with velocity v_s . The δ -function dictates that trajectories start at time $t = 0$ at the transition state defined by $s = s^\ddagger$ and $\mathcal{P}(t)$ is the characteristic function that is equal to

1 for reactive trajectories, *i.e.*, those that start as reactants in the past ($-t$) and end as products in the future (t), and 0 for non-reactive trajectories. For example, $\mathcal{P}(t) = \Theta[s(t) - s^\ddagger]$, where $\Theta(x)$ is the Heaviside step function, is a common choice for evaluating the characteristic function. The exact classical rate constant is obtained when the trajectories are propagated to a time t long enough that all transition state recrossing has been completed.

The activation energy for the rate constant, Eq. 1.1, is then obtained using Eq. 1.16 as

$$E_a = \frac{\lim_{t \rightarrow \text{long}} \langle \delta H(0) F_s(0) \mathcal{P}(t) \rangle}{\lim_{t' \rightarrow \text{long}} \langle F_s(0) \mathcal{P}(t') \rangle}. \quad (1.21)$$

Such a result was first shown by Dellago and Bolhuis,³⁵ and has been implemented *via* transition path sampling simulations in a several cases.^{36–41}

Mesele and Thompson demonstrated that if this result is compared with the Tolman expression for the activation energy, Eq. 1.3, while noting that in this case of a chemical reaction $\delta H = H - \langle E \rangle_r$, it leads to the result

$$\langle E \rangle_{\text{reacting}} = \frac{\lim_{t \rightarrow \text{long}} \langle H(0) F_s(0) \mathcal{P}(t) \rangle}{\lim_{t' \rightarrow \text{long}} \langle F_s(0) \mathcal{P}(t') \rangle}, \quad (1.22)$$

for the average energy of the reacting species, which is equivalent to Eq. 1.8.³¹

1.2.2 Diffusion Coefficient

The diffusion coefficient, D , is typically calculated from the mean-squared displacement, $MSD(t) = \langle |\vec{r}(t) - \vec{r}(0)|^2 \rangle$, which is a measure of the distance traveled by a molecules in time t . Specifically, the diffusion coefficient is obtained as

$$D(T) = \lim_{t \rightarrow \infty} \frac{MSD(t)}{6t}, \quad (1.23)$$

for motion in three dimensions. Thus, in this case $f(t) = |\vec{r}(t) - \vec{r}(0)|^2$ and Eq. 1.16 leads to

$$\begin{aligned}
 E_{a,D} &= -\frac{\partial \ln D}{\partial \beta} = \frac{\lim_{t \rightarrow \infty} \langle \delta H(0) |\vec{r}(t) - \vec{r}(0)|^2 \rangle}{\lim_{t \rightarrow \infty} \langle |\vec{r}(t) - \vec{r}(0)|^2 \rangle} \\
 &= \frac{\lim_{t \rightarrow \infty} MSD_H(t)}{\lim_{t \rightarrow \infty} MSD(t)}, \tag{1.24}
 \end{aligned}$$

where $MSD_H(t)$, defined by the last equality, is the mean-squared displacement weighted by the energy fluctuations.

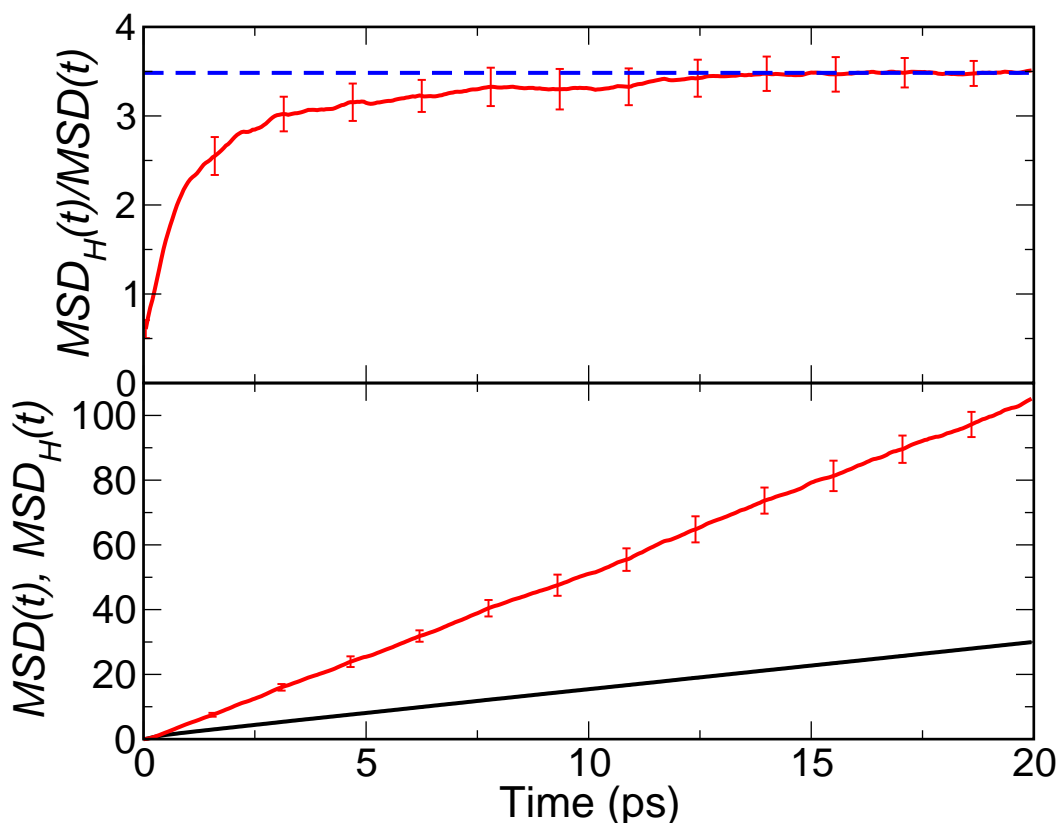


Figure 1.2: Bottom: The TCFs $MSD(t)$ (black line) and $MSD_H(t)$ (red line) are plotted versus time for the SPC/E water model at 298 K obtained from 2,500 *NVE* trajectories. Top: The ratio $MSD_H(t)/MSD(t)$ (red line) is plotted as a function of time. A fit of this ratio between $t = 15 - 20$ ps to a constant value is also shown (blue dashed line). Note: $MSD(t)$ is in units of $\text{\AA}^2/\text{ps}$, $MSD_H(t)$ in $\text{kcal/mol} \times \text{\AA}^2/\text{ps}$.

In practice, Eq. 1.24 is most accurately evaluated by separately fitting $MSD_H(t)$ and $MSD(t)$ each to a line at longer times and then taking the value of the ratio of the slopes. In many cases,

however, the activation energy can be obtained from the ratio of the correlation functions directly at long times. This is illustrated in Fig. 1.2 where the mean-squared displacements (weighted and unweighted) and their ratio are shown for the SPC/E water model⁴² at 298.15 K. From the data presented in Fig. 1.2, the activation energy for water diffusion is found to be $E_{a,D} = 3.48 \pm 0.16$ kcal/mol, in excellent agreement with $E_{a,D} = 3.49 \pm 0.20$ kcal/mol derived from an Arrhenius analysis.

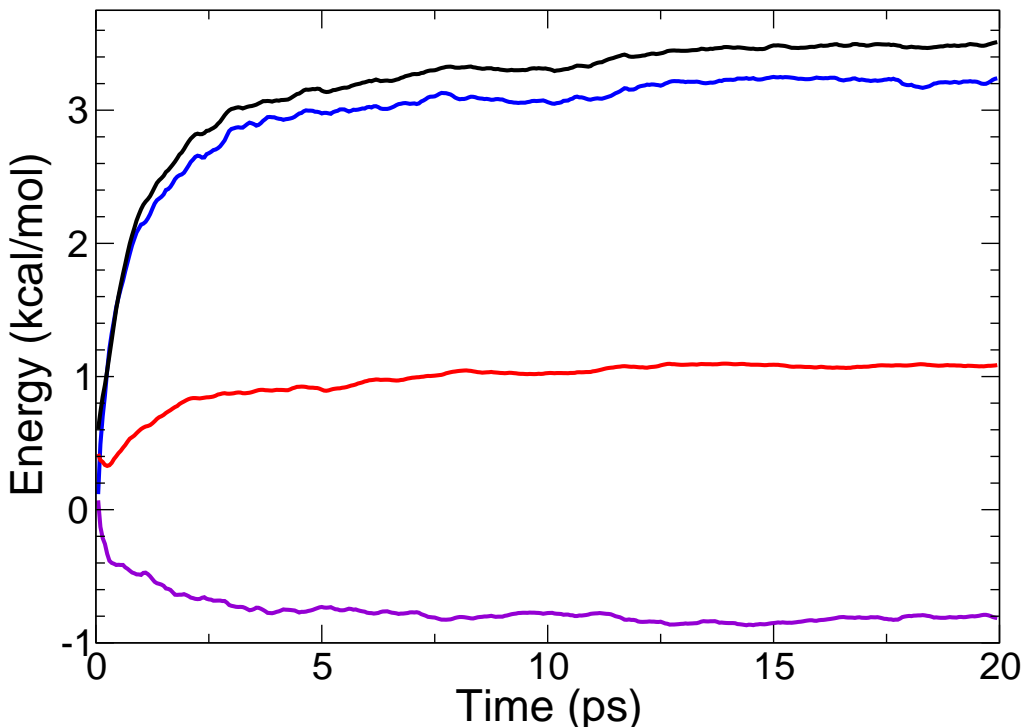


Figure 1.3: The contributions to the diffusion TCF $MSD_H(t)$ shown in Fig. 1.2 associated with the kinetic energy (red line), Lennard-Jones potential energy (violet line), and Coulombic potential energy (blue line) are plotted versus time along with the total (black line).

As mentioned in the above section the fluctuation theory for dynamics offers new opportunities for insights into the mechanisms of diffusion by allowing for a decomposition of activation energies into various energetic contributions. In Fig. 1.3 we present the decomposition of the activation energy for the kinetic, Lennard-Jones, and electrostatic energy components with values of 1.1, -0.8, and 3.2 kcal/mol, respectively. This indicates that electrostatic interactions are the dominant contribution to the diffusion activation energy.

These results are indicative of the central role of hydrogen-bond (H-bond) exchanges in water diffusion, which are primarily governed by the electrostatic interactions. In the context of the Tolman interpretation of activation energies, this indicates that higher Coulombic interaction energy accelerates water diffusion, presumably by destabilizing the water H-bonds. In contrast, increasing the Lennard-Jones energy leads to *slower* diffusion. This competition between the Lennard-Jones and Coulombic contributions to the activation energy will be explored further throughout the first part of this thesis. Furthermore, keeping in mind the Tolman interpretation of activation energies, this indicates that the water molecules with higher kinetic or electrostatic energies will diffuse more quickly on average than those that have larger Lennard-Jones energies.

1.2.3 Reorientational Timescales

Reorientational dynamics, as measured by infrared pump-probe anisotropy and spin-echo NMR, are characterized by the reorientation time correlation function, $C_2(t) = \langle P_2[\vec{e}(0) \cdot \vec{e}(t)] \rangle$. This TCF acts as a measure of the change in the orientation of a particular molecular axis, described by the unit vector \vec{e} , in time t . Here, P_2 denotes the second Legendre polynomial which weights the dynamics in accord with the IR spectroscopy and NMR signals. In this case then, $f(t) = P_2[\vec{e}(0) \cdot \vec{e}(t)]$ and thus from Eq. 1.16 we find that,

$$\frac{\partial C_2(t)}{\partial \beta} = -C_{2,H}(t) = -\langle \delta H(0) P_2[\vec{e}(t) \cdot \vec{e}(0)] \rangle. \quad (1.25)$$

For water reorientational dynamics we choose \vec{e} to be along each OH bond. The OH reorientation dynamics exhibit three timescales: 1) an inertial one (25 fs) associated with water reorienting before it feels any other interactions, 2) a librational one (0.5 ps) associated with water rotations within a particular H-bond, and 3) one associated with H-bond exchange dynamics (~ 3 ps). It is the last of these which is accessible to IR pump-probe anisotropy measurements.

These timescales can be extracted from the C_2 correlation function by fitting to a tri-exponential

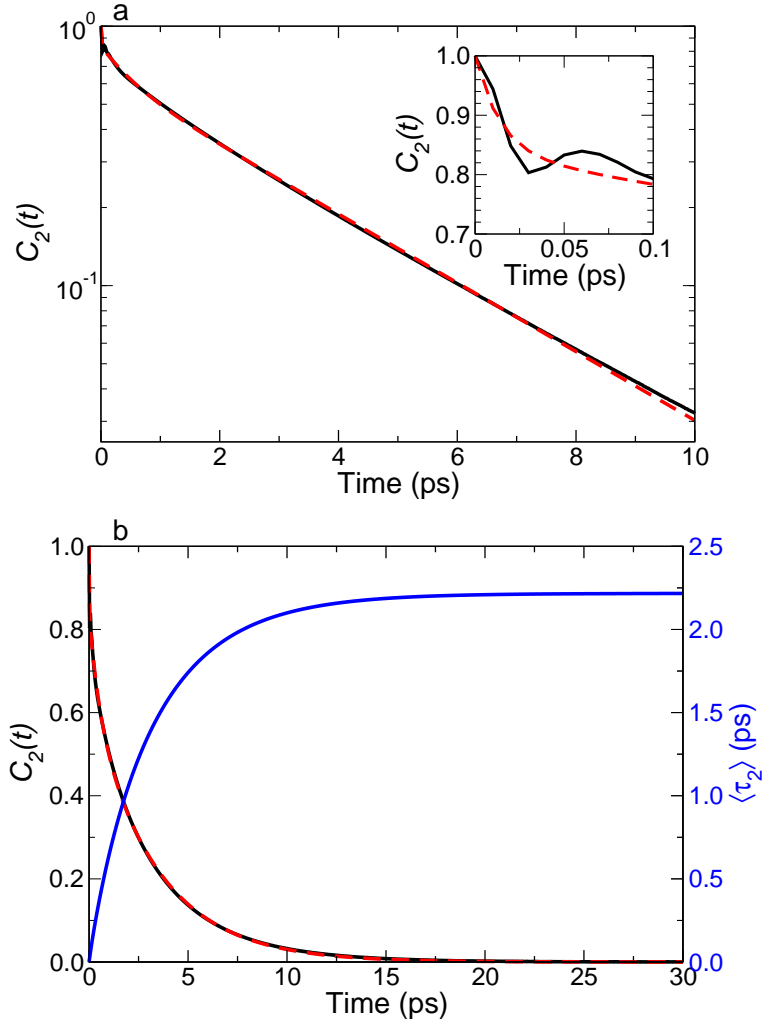


Figure 1.4: OH reorientational correlation function, $C_2(t)$, (black) is shown as a function of time along with a triexponential fit (red), Eq. (1.26). a: $C_2(t)$ is shown on a semi-log scale and the short-time decay is shown in the inset. b: $C_2(t)$ is shown on a linear scale along with its integral (blue, right axis) which equals the average reorientational time, $\langle \tau_2 \rangle$, at long times. Results are from 50,000 *NVE* trajectories with the TIP4P/2005 water model at 298.15 K and 1 bar.

function,

$$C_2(t) = \sum_{\alpha} A_{\alpha} e^{-t/\tau_{\alpha}} = \sum_{\alpha} A_{\alpha} e^{-k_{\alpha} t}, \quad (1.26)$$

where $\alpha = \text{inertial, librational, or } 2$ (associated with H-bond rearrangements) and A_{α} represents the amplitude (or importance) of the α reorientation timescale, $\tau_{\alpha} = 1/k_{\alpha}$. The reorientational TCF, from simulations using the TIP4P/2005 water model,⁵ are shown in Fig. 1.4a along with the fit which yields $\tau_{iner} = 13$ fs, $\tau_{lib} = 0.455$ ps, and $\tau_2 = 3.2$ ps. NMR spin-echo experiments cannot

access the individual timescales but instead measure the average reorientation time,⁴³

$$\langle \tau_2 \rangle = \int_0^\infty C_2(t) dt. \quad (1.27)$$

For water, the integrated reorientation time is 2.2 ps for the TIP4P/2005 water model. Figure 1.4b shows both $C_2(t)$ and its time integral used to calculate this value.

The activation energies and temperature dependence of the amplitudes can be obtained by fitting the derivative TCF, $C_{2,H}(t)$, to the derivative of Eq. 1.26,

$$\frac{\partial C_2(t)}{\partial \beta} = \sum_\alpha \left[\frac{\partial A_\alpha}{\partial \beta} - A_\alpha \frac{\partial k_\alpha}{\partial \beta} t \right] e^{-k_\alpha t}. \quad (1.28)$$

using the amplitudes and timescales obtained from fitting $C_2(t)$ itself. Both the derivative TCF, $C_{2,H}(t)$, and its fit using this equation are shown in Fig. 1.5. From this, the activation energy of each reorientation timescale is calculated as,

$$E_{a,\tau_\alpha} = -\frac{1}{k_\alpha} \frac{\partial k_\alpha}{\partial \beta}, \quad (1.29)$$

Note that the activation energies for τ_{iner} and τ_{lib} are merely effective ones that describe the temperature dependence locally, as these timescales do not exhibit Arrhenius behavior.

The activation energy corresponding to the average reorientation time, $\langle \tau_2 \rangle$, accessed by NMR is given by

$$E_{a,\langle \tau_2 \rangle} = \frac{1}{\langle \tau_2 \rangle} \int_0^\infty \frac{\partial C_2(t)}{\partial \beta} dt. \quad (1.30)$$

We will show in Chapter 3 that there is a quantitative and qualitative difference between the pump-probe activation energy, $E_{a,\tau_2} = 4.28 \pm 0.10$ kcal/mol, and the NMR activation energy, $E_{a,\langle \tau_2 \rangle} = 4.58 \pm 0.11$ kcal/mol.⁴⁴ This difference is associated with the change in the amplitude, A_2 , which enters into the $\langle \tau_2 \rangle$ activation energy.

As in the case of diffusion, the activation energies associated with OH reorientation in water can be decomposed into specific contributions from various components of the total energy. An

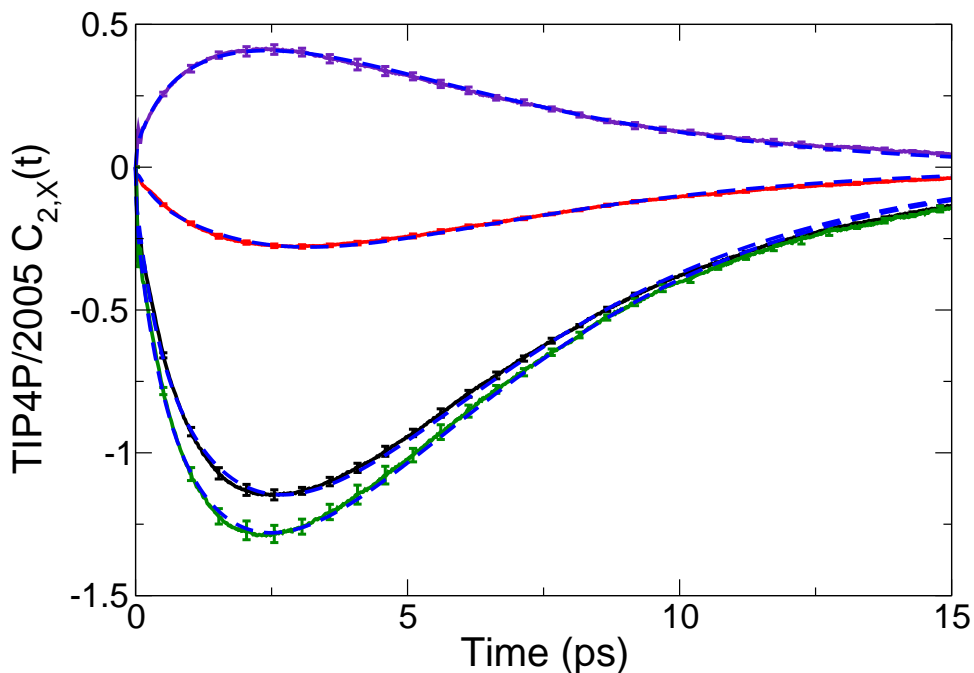


Figure 1.5: The weighted reorientation correlation function $C_{2,H}(t)$ (black) corresponding to Fig. 1.4 is shown along with its contributions from the Lennard-Jones potential energy (indigo), electrostatic potential energy (green), and kinetic energy (red). Fits for each correlation function are included as blue dashed lines.

example is shown in Fig. 1.5, where the weighted correlation functions for the kinetic, Lennard-Jones, and electrostatic energies are presented, corresponding to activation energy contributions of 1.14, -1.31, and 4.38 kcal/mol, respectively. As with diffusion, it is clear that the most important contribution to the activation energy comes from Coulombic interactions. Indeed, the results of this decomposition are in close accord with those from diffusion, reflecting the fact that H-bond exchanges are the key event in both the rotational and translational dynamics of water.

1.2.4 Transport Coefficients

Many important physical quantities may be calculated from the class of time correlation functions obtained as Green-Kubo relations. In a general context, a particular frequency-dependent transport

coefficient can be expressed as a Fourier transform of the appropriate TCF,⁴⁵

$$\sigma(\omega) = \int_0^{\infty} e^{-i\omega t} \langle \dot{A}(0) \dot{B}(t) \rangle dt. \quad (1.31)$$

Frequently, only the zero frequency ($\omega = 0$) value is of interest and then σ is simply the integral of the TCF. (Note the similarity to the average reorientation time, Eq. 1.27.) The generality of the fluctuation theory approach as expressed in Eq. 1.16 means that it can be straightforwardly extended to transport coefficients. Specifically, one obtains

$$\begin{aligned} E_{a,\sigma}(\omega) &= -\frac{1}{\sigma(\omega)} \frac{\partial \sigma(\omega)}{\partial \beta} \\ &= \frac{\int_0^{\infty} e^{-i\omega t} \langle \delta H(0) \dot{A}(0) \dot{B}(t) \rangle dt}{\int_0^{\infty} e^{-i\omega t} \langle \dot{A}(0) \dot{B}(t) \rangle dt}, \end{aligned} \quad (1.32)$$

for the frequency-dependent activation energy, which can be evaluated from simulations at a single temperature.

This expression is sufficiently general that it can be applied to properties including viscosity, conductivity, dielectric relaxation, and even spectroscopy. Indeed, Morita and co-workers have developed similar approaches to calculating the dependence of different vibrational spectra on temperature and other variables.^{46–49} In the case of a number of the transport coefficients, *e.g.*, viscosity, which has been recently studied by our group,⁵⁰ the key difference with the diffusion and reorientational dynamics examples discussed above is that they involve quantities that are global. That is, the quantities A and B in the TCF depend on the full system configuration and are not obtained individually for each molecule. This means that the relevant TCF can require more averaging to converge, though this is in no way prohibitive.

1.2.5 Quantum Dynamics

The fluctuation theory for dynamics approach described above is completely general in that it can be applied to not only classical but also quantum mechanical, semiclassical, or mixed quantum-

classical dynamics. Here we briefly consider the application to quantum dynamics. Consider a general quantum mechanical time correlation function,

$$C(t) = \langle \hat{A}(0) \hat{B}(t) \rangle = \frac{1}{\mathcal{Q}} \text{Tr}[e^{-\beta \hat{H}} \hat{A} \hat{B}(t)], \quad (1.33)$$

where $\hat{B}(t) = e^{i\hat{H}t/\hbar} \hat{B} e^{-i\hat{H}t/\hbar}$, \mathcal{Q} is the quantum mechanical partition function, and Tr is a quantum mechanical trace. Then, just as in the classical case, it is straightforward to show that the derivative with respect to β is given by

$$\frac{\partial C(t)}{\partial \beta} = \frac{1}{\mathcal{Q}} \text{Tr}[e^{-\beta \hat{H}} \delta \hat{H} \hat{A} \hat{B}(t)], \quad (1.34)$$

where $\delta \hat{H} = \hat{H} - \langle \hat{H} \rangle$.

The thermal rate constant for a chemical reaction can be considered as a special example using the results of Miller, Schwartz, and Tromp.²³ They derived several equivalent forms for the formally exact quantum mechanical rate constant, including in terms of the flux-flux TCF,

$$k_{QM}(T) = \int_0^\infty C_{ff}(t) dt = \int_0^\infty \langle \hat{F}_s(0) \hat{F}_s(t) \rangle dt, \quad (1.35)$$

where $\hat{F}_s = i[\hat{H}, \theta(\hat{s} - s^\ddagger)]/\hbar$ is the symmetrized flux operator at the transition state dividing surface located at s^\ddagger . Then, using Eq. 1.34 the activation energy is given by

$$E_{a,QM} = \frac{\int_0^\infty \langle \delta \hat{H}(0) \hat{F}_s(0) \hat{F}_s(t) \rangle dt}{\int_0^\infty \langle \hat{F}_s(0) \hat{F}_s(t) \rangle dt}. \quad (1.36)$$

Note that $E_{a,QM}$ can be evaluated from the calculation of k_{QM} itself by one additional multiplication of the Hamiltonian. Our group has demonstrated the implementation (and accuracy) of this direct calculation of the activation energy for the simple one-dimensional Eckart barrier.³¹ Similar activation energy expressions³¹ can be obtained for each of the various TCFs that can be used to obtain the rate constant.²³

1.2.6 Advanced Decompositions

Simple decompositions of energy into contributions from different molecular interactions as has been described above are not the limit of this fluctuation theory approach. Indeed, in liquids that are made up of a heterogeneous mixture of components, more interesting decompositions can be undertaken. One example of such a system where more interesting decompositions is possible are carbon dioxide (CO_2) expanded electrolytes (CXEs) (for which the standard decomposition of energies will be discussed in detail in Chapter 14 of this thesis). In this system, the liquid phase is a mixture of CO_2 , acetonitrile (MeCN), lithium (Li^+), and perchlorate (ClO_4^-). In this system, each of the components of the activation energy that have been described thus far can be subdivided further, either by species for the kinetic contribution, or by interacting pair for the Lennard-Jones and Coulombic interactions.

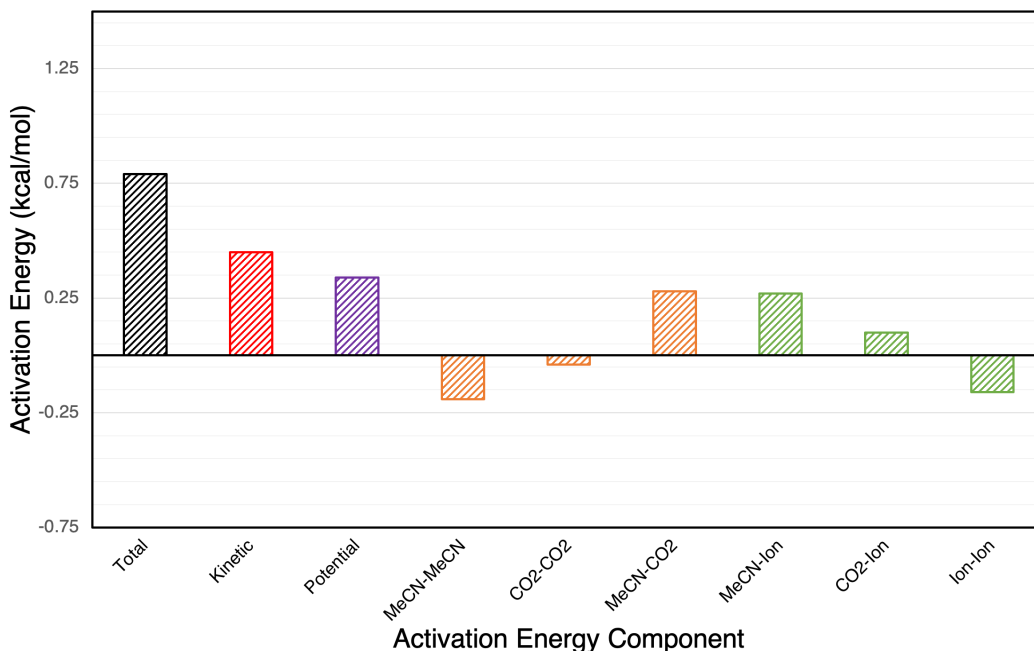


Figure 1.6: A deeper decomposition of the activation energies for CO_2 diffusion in CXEs. Contributions from solvent interactions are included in orange, contributions from electrolyte interactions are included in green. The sum of these contributions are the total potential energy contribution the activation energy (purple). The sum of the potential and kinetic (red) energy equal the total (black).

In Figure 1.6 we have presented an example of a deeper decomposition of the activation ener-

gies for CO₂ diffusion in the above described CXE at a pressure of 50 bar. In particular, we have subdivided the activation energy by overall potential energy contributions from specific interactions. Our results demonstrate a dichotomy in the potential energy contributions to the activation energy where MeCN electrolyte interactions lead to a raised activation energy, but electrolyte electrolyte interactions lead to a lowered activation energy. In Chapter 15 we will demonstrate that the CO₂ activation energy does not change with electrolyte concentration, and will provide an entropic argument based on preferential solvation. It is very likely that these more deeply decomposed activation energy contributions could provide additional information about how these individual components shift while the total activation energy is maintained. Unfortunately, such deeper decompositions require significantly more computational power and averaging the specific fluctuations being examined are correlated with smaller subsections of the system.

1.3 Beyond Activation Energies

1.3.1 Non-Arrhenius Behavior

Thus far our discussion has focused on the temperature dependence of different dynamical quantities in the context of the activation energy. Another key focus of this thesis is to consider the situation where the activation energy is not sufficient to describe the the change in dynamics with temperature, *i.e.*, when it is itself temperature dependent. Indeed, a number of dynamical processes display strong non-Arrhenius behavior, *e.g.*, dynamics governed by low barriers in liquids or reaction rate constants that have a significant contribution from quantum mechanical tunneling. For example, liquid water displays significantly non-Arrhenius behavior in both reorientation dynamics^{51,52} and diffusion,^{1,3,53–56} from the deeply supercooled regime up to the boiling point.

The fluctuation theory for dynamics straightforwardly addresses non-Arrhenius behavior because it determines the analytical temperature derivatives completely locally at a single temperature, *e.g.*, at 298.15 K. In other words, it does not depend on any numerical derivative approximation such as that implicit in an Arrhenius analysis, which can be sensitive to the choice of

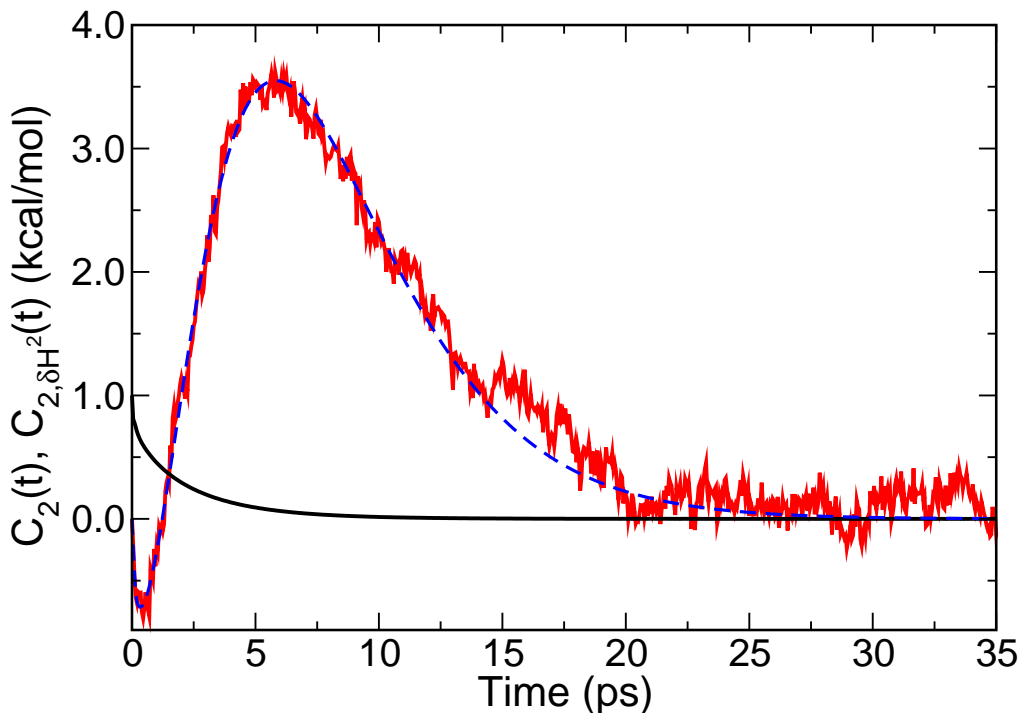


Figure 1.7: The second-derivative reorientational TCF, $C_{2,\delta H^2}(t)$, is shown (red line) for SPC/E water at 298 K from 30,000 *NVE* trajectories along with a fit based on Eq. 1.26 (dashed blue line); $C_2(t)$ is shown for comparison (black line).

temperatures. Moreover, the approach is not limited to the first derivative and higher derivatives can also be calculated. For example, for reorientational dynamics it can be shown that taking the derivative of Eq. 1.25 gives

$$\begin{aligned} \frac{\partial^2 C_2(t)}{\partial \beta^2} &= \langle [\delta H(0)^2 - \langle \delta H^2 \rangle] P_2 [\vec{e}(t) \cdot \vec{e}(0)] \rangle \\ &\equiv C_{2,\delta H^2}(t), \end{aligned} \quad (1.37)$$

which is the first measure of non-Arrhenius behavior. This is analogous to an expression for the temperature derivative of the activation energy developed by Truhlar and Kohen in the context of non-Arrhenius enzyme kinetics.⁵⁷

An example of this non-Arrhenius TCF is shown in Fig. 1.7, where $C_{2,\delta H^2}(t)$ is plotted as a function of time for OH reorientation in water at 298 K. These results were obtained using the same approach described in Ref. 58 with 30,000 short *NVE* trajectories. The expected behavior

of $C_{2,\delta H^2}(t)$ is obtained by taking the second derivative with respect to β of the fitting function for $C_2(t)$ itself, Eq. 1.26. This fit is also presented in Fig. 1.7 and provides an excellent representation of the calculated TCF. The integral of $C_{2,\delta H^2}(t)$ is directly related to the non-Arrhenius behavior of the integrated reorientation time, Eq. 1.27, namely $\partial E_{a,\langle\tau_2\rangle}/\partial\beta$. The SPC/E model gives $\partial E_{a,\langle\tau_2\rangle}/\partial\beta = 4.81$ (kcal/mol)² at room temperature, compared to 7.66 (kcal/mol)² obtained by fitting the measured $\langle\tau_2\rangle$ values of Ludwig *et al.*⁵¹ This is reasonable agreement, but the difference is indicative of the shortcomings of the SPC/E model in terms of describing the water reorientational dynamics over a broader range of temperatures.⁵

1.3.2 Activation Volumes

Furthermore, this thesis will demonstrate that the fluctuation theory for dynamics can be extended to derivatives with respect to other thermodynamic variables.^{37,59} For example, in the isothermal-isobaric ensemble the average of the dynamical quantity $f(t)$, given in Eq. 1.18, can be differentiated with respect to pressure to give

$$\frac{\partial\langle f(t)\rangle}{\partial p} = -\beta\langle\delta V(0)f(t)\rangle_{NpT} \quad (1.38)$$

where $\delta V(0) = V(0) - \langle V\rangle_{NpT}$. Such derivatives are related to the activation volume, which for a rate constant k is given by

$$\Delta V^\ddagger = -RT\frac{\partial\ln k}{\partial p}. \quad (1.39)$$

This measure of the pressure dependence of the rate constant is important in many practical situations of high-pressure chemistry but also interesting from a mechanistic viewpoint.^{60,61} The typical interpretation of ΔV^\ddagger is as a measure of relative size of the transition state and reactant structures. However, Ladanyi and Hynes showed that this perspective is only complete in condensed phases if it includes the surrounding solvent molecules and their arrangement (or packing) around the transition state and reactants.⁶²

The fluctuation theory for dynamics offers an improved method for calculating activation vol-

umes from MD simulations. The typical approach involves calculation of k over a large pressure range (often spanning thousands of bar) to resolve the comparatively modest differences with pressure, which are then used in an Arrhenius analysis to calculate a single activation volume.^{61–64} This assumes that ΔV^\ddagger is p -independent, which is not true in some key cases, such as water diffusion. Alternatively, one can use simulations to estimate the volumes directly,⁶⁵ or calculate k at many pressures and fit the global pressure dependence, which can then be used to determine ΔV^\ddagger .

As an example of the fluctuation theory approach, consider the pressure dependence of the diffusion coefficient. From Eq. 1.38 it can be seen that the pressure derivative of the mean-squared displacement can be written as

$$\begin{aligned}\Delta V_D^\ddagger &= -\frac{\partial \ln D}{\partial p} = \frac{\lim_{t \rightarrow \infty} \langle \delta V(0) |\vec{r}(t) - \vec{r}(0)|^2 \rangle}{\lim_{t \rightarrow \infty} \langle |\vec{r}(t) - \vec{r}(0)|^2 \rangle} \\ &= \frac{\lim_{t \rightarrow \infty} MSD_V(t)}{\lim_{t \rightarrow \infty} MSD(t)},\end{aligned}\tag{1.40}$$

where $MSD_V(t) \equiv \langle \delta V(0) |\vec{r}(t) - \vec{r}(0)|^2 \rangle_{NpT}$ in analogy to $MSD_H(t)$ obtained in deriving the activation energy. Indeed, this result is reminiscent of Eq. 1.24 and the interpretation is analogous. Namely, the activation volume is a measure of how the diffusion speeds up (or slows down) when the system volume is larger ($\Delta V > 0$) or smaller ($\Delta V < 0$) than its average value at the pressure of interest.

The diffusion coefficient of water is a key example of a property that does not exhibit an Arrhenius-like pressure dependence. As the pressure is increased, it is observed that D first increases ($\Delta V_D^\ddagger < 0$) and then decreases ($\Delta V_D^\ddagger > 0$).^{1,3,4,30} The former behavior is attributed to disruption of the H-bonding network, while the latter is ascribed to significant distortion of the network at higher pressures such that the transition state for H-bond exchange requires a larger volume. For a fixed pressure, the activation volume increases with temperature, which is illustrated in Fig. 1.8, where the ratio $MSD_V(t)/MSD(t)$ and the corresponding ΔV_D^\ddagger values are plotted versus time at 100 bar for three temperatures. The activation volumes obtained are within $\sim 25\%$ of the values

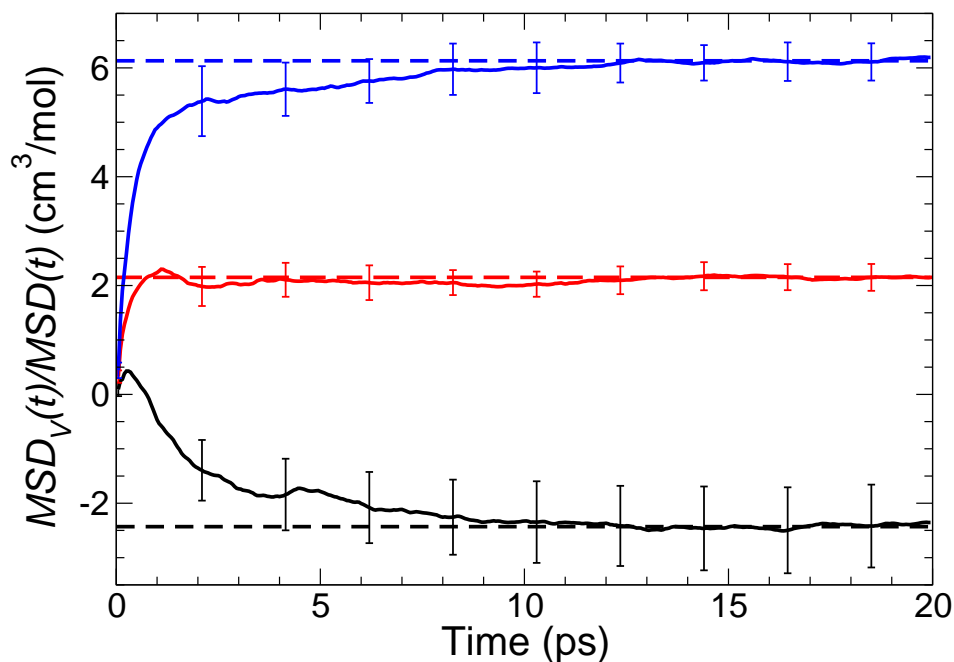


Figure 1.8: The ratio $MSD_V(t)/MSD(t)$, which at long times is equal to the diffusion activation volume, ΔV_D^\ddagger , for 100 bar and $T = 283$ (black), 383 (red), and 473 K (blue) for TIP4P/2005 water from 5,000 NVE trajectories. Dashed lines of the same color indicate the derived ΔV_D^\ddagger from fitting to $t \geq 15$ ps.

obtained experimentally by Krynicki *et al.*³

1.4 Purpose of the Current Study

In this Introductory chapter, approaches for direct calculation of the activation energy for nearly any dynamical timescale of a chemical system from simulations at a single temperature have been presented. These methods directly calculate the analytical derivative with respect to temperature, in contrast to the standard Arrhenius analysis in which the derivative is determined numerically. They are fundamentally an application of fluctuation theory in statistical mechanics applied to dynamical properties and are the basis for the remainder of this thesis.

The fluctuation theory approach enables new mechanistic insight. The activation energy can

be rigorously decomposed into contributions associated with different terms in the Hamiltonian, *i.e.*, interactions present in the system. These are readily understood in the context of Tolman's interpretation of the activation energy as the difference between the average energy of reacting species relative to the average energy of the reactants.¹⁸ Then each contribution is the average energy of a particular interaction (or kinetic energy) for the reacting species relative to that of the reactants. In other words, we can obtain the measure of how effective it is, in terms of accelerating the dynamics of interest, to deposit energy into specific interactions and motions of the molecular system. Throughout this thesis, these decompositions will be important for developing a mechanistic understanding of the studied timescales.

The method is not limited to activation energies. Non-Arrhenius behavior can be probed by calculation of higher derivatives of a timescale with respect to temperature. Moreover, the change in dynamics with respect to nearly any thermodynamic variable can be determined by carrying out simulations in the appropriate ensemble.

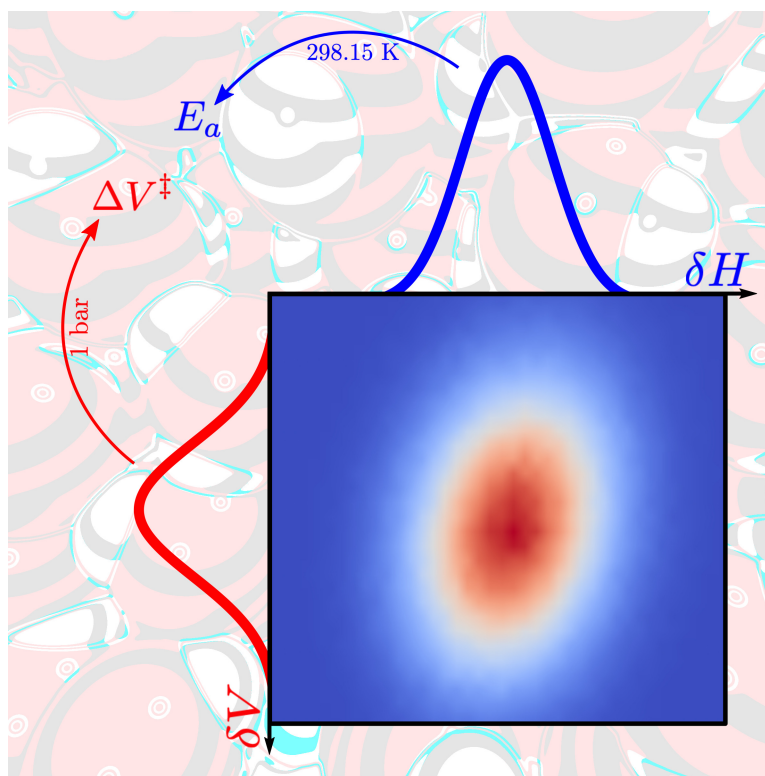
A number of advantages associated with this approach have yet to be fully explored. A key example is that it permits access to activation energies even for systems that are at the point of a thermally-induced transformation, because simulations at only one temperature are required. Thus, an activation energy can be calculated for a liquid close to its boiling point or a protein near its melting temperature; for these systems an Arrhenius analysis is challenging because an increase in temperature generates a phase or structural change. In addition, we have only shown here some of the simplest possible decompositions of the activation energy into broad categories of interactions and the kinetic energy. Significantly more detailed mechanistic insight is available by considering the contributions to the energy of particular atomic or molecular interactions and motions.

In the remainder of this thesis, the concepts developed within this Introduction will be extended and developed in more detail over four parts. The first part, *Activation Energies of Dynamical Timescales*, focuses on the basic development and application of fluctuation theory at ambient conditions to better understand activation energies (and their decompositions) for a wide-variety of timescales. The second part, *Water Under Extreme Conditions*, develops the above discussed ap-

proaches for calculating activation volumes and higher derivatives with respect to pressure in order to better understand water dynamics away from ambient conditions. The third part, *Toward a Unified Picture of Water Dynamics*, focuses on the connection between water structure and dynamics through the lens of fluctuation theory. The final part, *Complex Systems*, describes two non-water systems that have been studied in the course of this thesis for which dynamical timescales can provide valuable information.

Part I

Activation Energies of Dynamical Timescales



In Part 1, methods for applying fluctuation theory to better understand activation energies for a wide range of dynamic timescales are presented, including diffusion (Chapter 2), reorientation (Chapters 2-5), hydrogen-bond exchange dynamics (Chapters 5-6), and spectral diffusion (Chapter 6). Chapter 2 presents the first calculations of diffusion and reorientation activation energies in liquid water using the fluctuation theory approach, as well as the ability to decompose activation energies. In Chapter 3, we found for the first time that reorientation activation energies measured using two commonly used experimental techniques are different. In Chapter 4, we showed that the Extended-Jump Model, which connects water reorientation and hydrogen bond exchanges, is consistent on both the timescale level and the activation energy level. In Chapter 5, we demonstrate that hydrogen bond exchanges are present within the spectral diffusion of liquid water as a fourth timescale distinct from the commonly measured spectral diffusion time.

Chapter 2

Removing the Barrier to the Calculation of Activation Energies

2.1 Introduction

Molecular dynamics (MD) simulations are a ubiquitous tool for understanding the dynamics of chemical systems. In particular, they can be directly connected with experimental measurements by, for example, using time correlation functions (TCFs) to obtain observables ranging from kinetic rate constants to vibrational spectra. Inevitably, the data generated in a MD simulation dwarf the information produced by such analyses. It is thus important to seek methods by which the trajectory data can be examined to take advantage of the significant information content that is generally discarded.

Reaction rate constants, transport coefficients, and other important dynamical timescales for molecular systems are frequently obtained through the calculation of TCFs.^{66–68} For example, the rate constant for a chemical reaction can be determined from the flux-side TCF, $C_{fs}(t)$, as^{23,32,34,69}

$$k = \lim_{t \rightarrow \text{long}} C_{fs}(t) = \lim_{t \rightarrow \text{long}} \langle F_s(0) \theta[s(t) - s^\ddagger] \rangle, \quad (2.1)$$

where s defines a dividing surface between reactants ($s < s^\ddagger$) and products ($s > s^\ddagger$), $\theta(x)$ is the Heaviside step function, and $F_s(0) = \delta[s(0) - s^\ddagger] v_s(0)$ is the flux through the dividing surface with

Adapted with the permission of Zeke A. Piskulich, Oluwaseun O. Mesele, and Ward H. Thompson and AIP Publishing from *J. Chem. Phys.* **2017**, *147*, 134103.⁵⁸

v_s the velocity along s . The activation energy of the reaction,

$$E_a = -\frac{d \ln k(T)}{d\beta}, \quad (2.2)$$

where $\beta = 1/k_B T$, is a quantity that is of significant interest due to the insight it provides into the effective barrier for the reaction. It is typically calculated by constructing an Arrhenius plot of $\ln k(T)$ versus $1/T$ based on measurements (or calculations) at multiple temperatures. In the context of Eq. (2.1), however, E_a is related to the temperature-dependence of a TCF such as $C_{f_s}(t)$. Indeed, it has been shown by Dellago and Bolhuis³⁵ that this perspective can be used to calculate E_a directly from transition path sampling simulations at a single temperature,^{36,37,70} and a related approach has been demonstrated by Morita and co-workers for vibrational spectra.^{46,48,49} We have recently generalized this beyond transition path sampling and to other TCFs from which rate constants can be obtained, including those based on a quantum description.³¹

The measurement and calculation of activation energies by an Arrhenius analysis can raise significant issues due to the need to consider multiple temperatures. For example, many systems have a structure that is highly dependent on temperature, *e.g.*, folded proteins, bilayer membranes or vesicles, and self-assembled structures. This can make construction of an Arrhenius plot problematic by restricting the range of temperatures that can be considered. A similar issue arises even for bulk systems if one is interested in an activation energy at conditions that are near a phase transition. Yet it can be of significant interest to examine the activation energies of dynamical processes in the vicinity of these points of transformation.

It is also important to consider cases where quantities other than a rate constant are of interest, but for which an activation energy can still be measured and calculated. In this Chapter, we do just that by first showing a general expression for the temperature derivative of a TCF and then applying this result to two commonly considered dynamical properties: diffusion coefficients and reorientational timescales. The method is demonstrated by application to the relevant time correlation functions for these attributes in bulk liquid water. In addition, it is shown how deeper physical

insight into these processes can be obtained than is possible from Arrhenius calculations.

2.2 Time Correlation Functions (TCFs) and Activation Energies

2.2.1 General Expressions

A general time correlation function between two dynamical variables A and B in the canonical ensemble, $C_{AB}(t) = \langle A(0)B(t) \rangle$, can be written more explicitly as,

$$C_{AB}(t) = \frac{1}{Q} \text{Tr} \left[e^{-\beta H} A(0)B(t) \right], \quad (2.3)$$

where Q is the partition function, H is the Hamiltonian, and Tr indicates an integration over phase space. In this correlation function expression, only Q and $e^{-\beta H}$ depend on the temperature. Thus, the derivative of $C_{AB}(t)$ with respect to β can be straightforwardly evaluated as

$$\begin{aligned} \frac{\partial C_{AB}(t)}{\partial \beta} &= -\frac{1}{Q^2} \frac{dQ}{d\beta} \text{Tr} \left[e^{-\beta H} A(0)B(t) \right] \\ &\quad - \frac{1}{Q} \text{Tr} \left[e^{-\beta H} H(0)A(0)B(t) \right]. \end{aligned} \quad (2.4)$$

Noting the definition of the average energy, $\langle H \rangle = -d \ln Q / d\beta$, this gives

$$\frac{\partial C_{AB}(t)}{\partial \beta} = -\langle \delta H(0)A(0)B(t) \rangle, \quad (2.5)$$

where $\delta H(0) = H(0) - \langle H \rangle$ is the fluctuation in energy from its average value.

This shows that the temperature dependence of the TCF, and thus any associated timescales, can be determined by evaluating this simple time correlation function that is closely related to $C_{AB}(t)$ itself. Note that the interpretation of this result is intuitive as it relates the derivative to the (continuous) differences between $C_{AB}(t)$ when the system energy is initially greater than average ($\delta H(0) > 0$) and when it is initially less than average ($\delta H(0) < 0$). In this sense, Eq. (2.5) is an analytical derivative instead of the numerical derivative that is obtained from an Arrhenius analysis.

As noted above, an analogous result has already been obtained in the context of reactive flux and other TCFs that can be directly related to rate constants.^{31,35} However, there are many contexts in which timescale or transport coefficients are calculated from a TCF and possess an activation energy, or even simply a dependence on temperature, that is of physical interest. In the following we show how the general result in Eq. (2.5) can be used to evaluate such activation energies for the examples of self-diffusion and OH reorientation in liquid water.

2.2.2 Diffusion Coefficients

We consider, as a first example, the application of this formulation to the activation energy of diffusion. The diffusion coefficient, D , can be calculated from the mean-squared-displacement (MSD) as

$$MSD(t) = \langle |\vec{r}(t) - \vec{r}(0)|^2 \rangle, \quad (2.6)$$

which becomes linear at long times such that

$$D = \lim_{t \rightarrow long} \frac{MSD(t)}{6t}, \quad (2.7)$$

for motion in three dimensions. The activation energy associated with the diffusion coefficient is defined as

$$E_a = -\frac{\partial \ln D}{\partial \beta}. \quad (2.8)$$

Then, taking the derivative of Eq. (2.7) with respect to β and dividing by D yields

$$E_a = -\lim_{t \rightarrow long} \frac{1}{6Dt} \frac{\partial MSD(t)}{\partial \beta}. \quad (2.9)$$

Using Eqs. (2.5)-(2.7) this can be written as,

$$\begin{aligned}
 E_a &= \lim_{t \rightarrow \text{long}} \frac{\langle \delta H(0) |\vec{r}(t) - \vec{r}(0)|^2 \rangle}{\langle |\vec{r}(t) - \vec{r}(0)|^2 \rangle} \\
 &\equiv \lim_{t \rightarrow \text{long}} \frac{MSD_H(t)}{MSD(t)},
 \end{aligned} \tag{2.10}$$

where $MSD_H(t)$, defined by the relation above, is the MSD weighted by the energy fluctuation. Note that the limit of the ratio of the functions equals the ratio of the limits as long as both are well defined and the limit of the denominator is not zero; each condition is met here. Thus, this ratio of TCFs should approach a constant value at longer times that is equal to the diffusion coefficient activation energy.

2.2.3 Reorientation Times

The same approach can also be applied to reorientation dynamics. Reorientation times, denoted τ_ℓ , are typically calculated from the time decay of the ℓ^{th} -order reorientation correlation function,

$$C_\ell(t) = \langle P_\ell [\vec{e}(0) \cdot \vec{e}(t)] \rangle. \tag{2.11}$$

Here P_ℓ is the ℓ^{th} -order Legendre polynomial and \vec{e} is a unit vector pointing along some molecular axis, *e.g.*, the OH bond in a water molecule. The $\ell = 2$ TCF, $C_2(t)$, is of particular interest as it can be directly measured by IR pump-probe anisotropy experiments⁷¹⁻⁷³ and an average rotational time defined as its integral can be obtained from NMR.⁷²⁻⁷⁶

In water and other hydrogen bonding (H-bonding) liquids it has been shown that the $C_2(t)$ TCF is well described by a tri-exponential decay that distinguishes the timescales associated with reorientation due to inertial (τ_{iner}), librational (τ_{lib}), and H-bond making and breaking (τ_2) dynamics.⁷⁷ Taking this form for the general, ℓ^{th} -order, case, the TCF can be written as⁷⁸

$$C_\ell(t) = \sum_{\alpha} A_{\alpha} e^{-t/\tau_{\alpha}}, \tag{2.12}$$

where $\alpha = \text{iner}, \text{lib}$, and ℓ (corresponding to the three timescales), and the A_α represent the amplitudes of the contributions of the three components to the overall reorientation dynamics. Applying the result in Eq. (2.5) to $C_\ell(t)$ gives

$$-\frac{\partial C_\ell(t)}{\partial \beta} = C_{\ell,H}(t) = \langle \delta H(0) P_\ell [\vec{e}(0) \cdot \vec{e}(t)] \rangle, \quad (2.13)$$

where $C_{\ell,H}(t)$ is the reorientational TCF weighted by the energy fluctuation. If the same derivative with respect to β is taken on Eq. (2.12) an additional expression for $C_{\ell,H}(t)$ results:

$$C_{\ell,H}(t) = -\sum_\alpha \left[\frac{\partial A_\alpha}{\partial \beta} - \frac{\partial (1/\tau_\alpha)}{\partial \beta} t A_\alpha \right] e^{-t/\tau_\alpha}. \quad (2.14)$$

Then, Eq. (2.13) can be used to calculate $C_{\ell,H}(t)$ from MD simulations while Eq. (2.14) gives the form to which it can be fit (constrained by the A_α and τ_α obtained by fitting $C_\ell(t)$ itself) to determine the temperature dependence of the amplitudes and timescales and, in some cases, the activation energy of the latter. In particular, an activation energy of one of the timescales can be obtained as

$$E_{a,\alpha} = -\tau_\alpha \frac{\partial (1/\tau_\alpha)}{\partial \beta}. \quad (2.15)$$

This again provides a simple method for calculating an activation energy from a single-temperature MD simulation.

2.3 Computational Methods

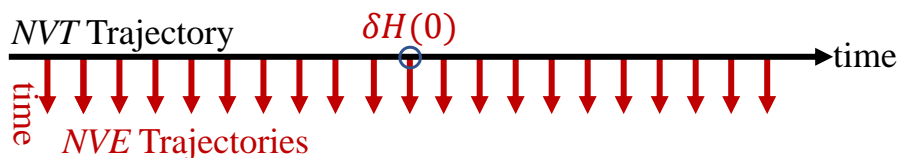


Figure 2.1: A schematic diagram of the nonequilibrium MD simulation approach in which *NVE* trajectories with different energies are initiated from a single *NVT* trajectory.

In principle, the energy fluctuation TCFs, $MSD_H(t)$ and $C_{\ell,H}(t)$, and the associated activation energies can be calculated from a single NVT MD simulation, as we have previously illustrated for H-bond exchange TCFs.³¹ However, there is naturally some effect due to the thermostat used to maintain the temperature that needs to be minimized. Here we adopt a different, nonequilibrium MD, approach to illustrate the method that avoids any effect of the thermostat. Specifically, we sample initial conditions for short constant energy (NVE) trajectories from a long NVT MD simulation as illustrated in Fig. 2.1. Each NVE trajectory has an initial energy, sampled from the canonical ensemble, that defines $\delta H(0)$ that weights the TCF giving $MSD(t)$ or $C_2(t)$.

For the results presented here, 2000 NVE trajectories of 20 ps each were propagated starting from configurations and momenta sampled every 1 ps from a 2 ns NVT trajectory following a 0.1 ns equilibration. For each trajectory $MSD(t)$ and the reorientational TCF, $C_2(t)$, were calculated along with their energy fluctuation versions, $MSD_H(t)$ and $C_{2,H}(t)$. Uncertainties in the results are reported as 95% confidence intervals according to the Student's t -distribution based on block averaging with 8 blocks of 250 trajectories each.

A fully-periodic cubic simulation cell with a side length of 21.725311 Å was filled with 343 water molecules to give a density of 0.997 g/mol. The H₂O molecules were modeled using the SPC/E force field.⁴² This model is a completely rigid, three-site model that treats intermolecular interactions as a combination of Lennard-Jones (LJ) and Coulombic interactions. In this model, point charges are placed on each atom while only oxygen atoms are treated as LJ sites. The Lorentz-Berthelot mixing rules are used to calculate intermolecular interactions between unlike atom types.^{79,80}

The MD simulations were performed using the Large-Scale Atomic/Molecular Massively Parallel Simulator (LAMMPS).⁸¹ A simulation timestep of 1.0 fs was used, with configurations in the NVE trajectories saved every 50 fs for calculation of the correlation functions. The SHAKE algorithm was used to hold the OH bonds and H-O-H angles rigid,⁸² with a tolerance of 0.0001 that specifies the relative error in the iterative solution. Intermolecular interactions were treated with a spherical cutoff of 10.5 Å and long-range electrostatics were described with an Ewald sum-

mation with an accuracy parameter of 0.0001 (that specifies the root-mean-squared error of the per-atom forces relative to a reference system). Canonical (*NVT*) simulations were performed using a Nosé-Hoover thermostat,^{83,84} with a thermostat damping parameter of 100 fs.

For comparison, activation energies were also calculated in the usual way using the Arrhenius equation from *NVT* trajectories at $T = 285, 298.15, 315,$ and 330 K. Each trajectory was propagated for 4.5 ns with the first 0.5 ns used for equilibration. The trajectories were split into ten 0.4 ns blocks for block averaging to obtain 95% confidence intervals from the Student's t -distribution.

The results from the Arrhenius calculations are presented in Fig. 2.2. From linear fits of the Arrhenius plots activation energies of 3.5 ± 0.2 and 3.5 ± 0.1 kcal/mol are calculated for D and τ_2 , respectively, in good agreement with previously reported values.^{85,86} These results will be used as a comparison for calculations using the energy fluctuation method described in Sec. 2.2.

2.4 Results

In this Section, we apply the approaches described above to directly calculate the full temperature-dependence of TCFs and determine the activation energies associated with relevant timescales. We consider two examples involving bulk liquid water: self-diffusion and OH-bond reorientation.

2.4.1 Diffusion coefficient activation energy

Using the nonequilibrium MD simulations described in Sec. 2.3 we have calculated the mean-squared displacement, $MSD(t)$, and the corresponding energy fluctuation TCF, $MSD_H(t)$ for the oxygen atom of water at 298.15 K. The results are presented in Fig. 2.3. A linear fit to $MSD(t)$ at longer times (between 2-20 ps) gives the diffusion coefficient as $D = 2.5 \times 10^{-5}$ cm²/s, in excellent agreement with reported values in the literature for the SPC/E water model.^{42,87} The time-dependence of $MSD_H(t)$ is generally similar to the $MSD(t)$ itself in that, following a short initial period, it is linear with time (with a slope of 5.3 kcal/mol \times Å²/ps).

As shown in Eq. (2.10), the activation energy for the diffusion coefficient can be calculated

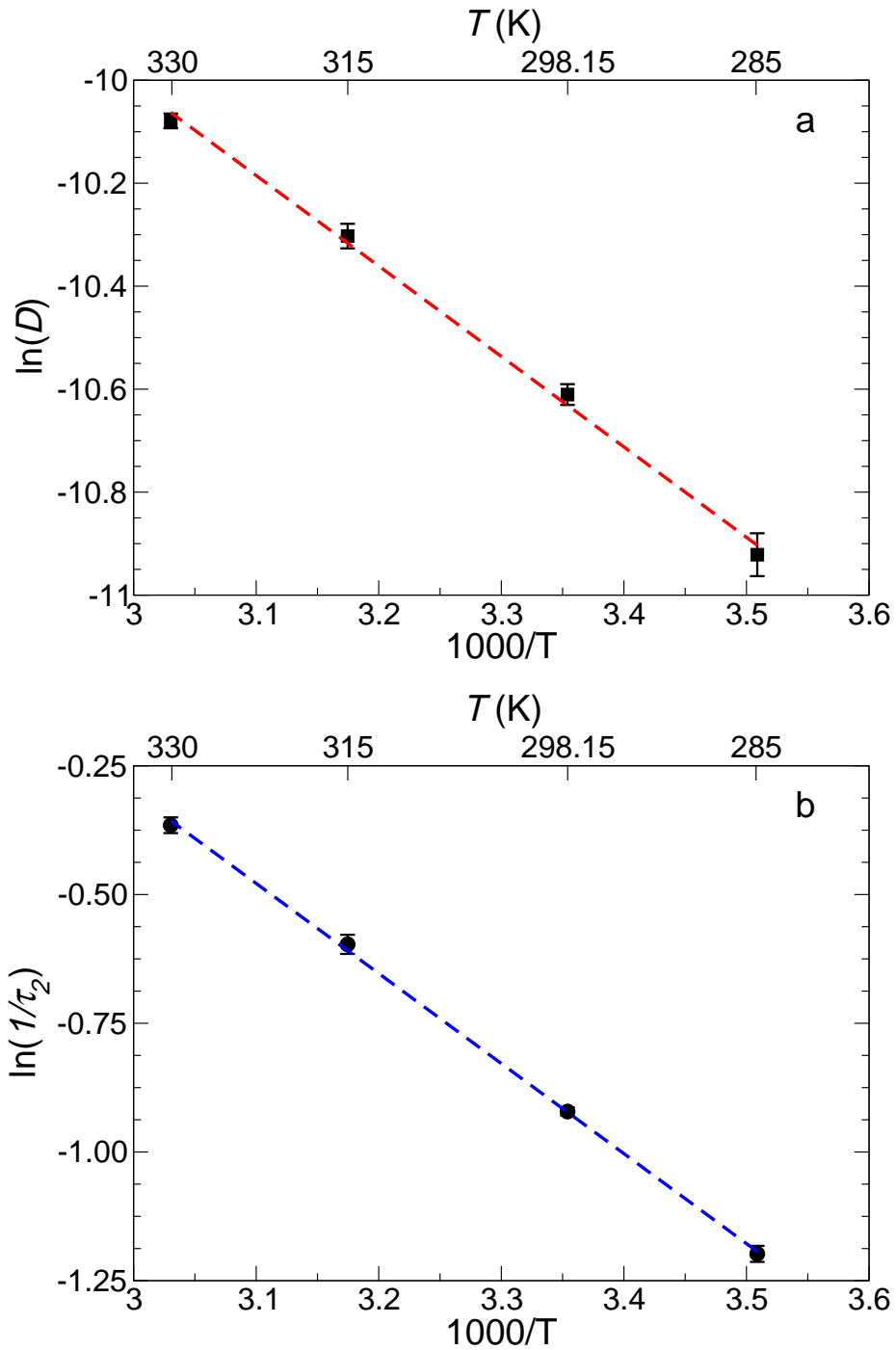


Figure 2.2: Arrhenius plots for (a) D and (b) τ_2 are presented. Results from the MD simulations (filled black circles) are shown along with linear fits (dashed lines) based on the Arrhenius equation.

from the ratio $MSD_H(t)/MSD(t)$ at long times. This ratio is also shown in Fig. 2.3 as a function of time and does indeed reach a constant value for times longer than ~ 12 ps. The value of the

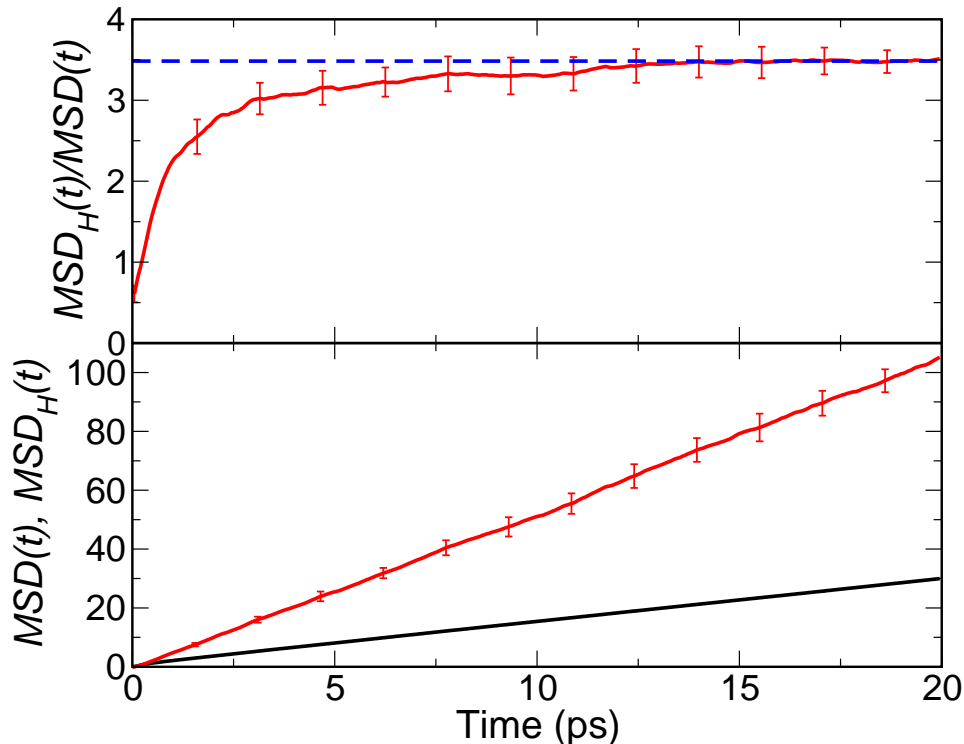


Figure 2.3: Bottom: The TCFs $MSD(t)$ (black line) and $MSD_H(t)$ (red line) are plotted versus time. Top: The ratio $MSD_H(t)/MSD(t)$ (red line) is plotted as a function of time. A fit of this ratio between $t = 15 - 20$ ps to a constant value is also shown (blue dashed line). Note: $MSD(t)$ is in units of $\text{\AA}^2/\text{ps}$, $MSD_H(t)$ in $\text{kcal/mol} \times \text{\AA}^2/\text{ps}$.

activation energy was obtained by fitting the ratio to a constant value for $t = 15 - 20$ ps, yielding, $E_{a,D} = 3.48 \pm 0.16$ kcal/mol. This result is in excellent agreement with the value of 3.5 ± 0.2 kcal/mol obtained from the Arrhenius plot in Fig. 2.2. Note that an alternative method for calculating $E_{a,D}$ would be to use the ratio of the slopes obtained from the linear fits to the respective correlation functions; this yields 3.52 kcal/mol when fit over the time range 15-20 ps.

The calculation of diffusion activation energies in this manner provides an effective alternative to the usual Arrhenius method. Trajectories are required at only a single temperature and thus no choice needs to be made of the conditions for the simulations at other temperatures, *e.g.*, whether to keep the same density (as we have done in our Arrhenius calculations) or modify the density to correspond to the experimental or simulation model result for each value of T . Additionally, as this approach calculates the temperature dependence of the diffusion coefficient it may be used for systems and conditions where the behavior is non-Arrhenius.

2.4.2 Reorientation time activation energy

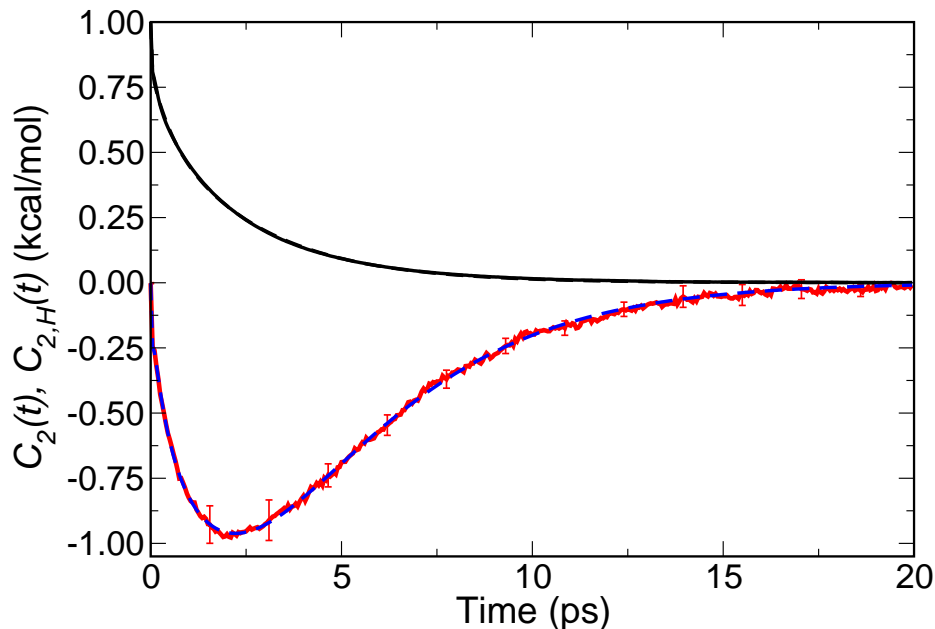


Figure 2.4: The reorientational TCF $C_2(t)$ (solid black line) is shown as a function of time along with a tri-exponential fit (dashed black line) to Eq. (2.12). The TCF including the energy fluctuation, $C_{2,H}(t)$, is also shown (solid red line) along with the fit (dashed blue line) to Eq. (2.14).

The same nonequilibrium MD trajectories used to evaluate the diffusion coefficient were analyzed to calculate the reorientational correlation function, $C_2(t)$, and its temperature dependence *via* the energy fluctuation TCF, $C_{2,H}(t)$. These two TCFs are plotted as a function of time in Fig. 2.4 along with the tri-exponential fit to $C_2(t)$, Eq. (2.12), and the related fit to $C_{2,H}(t)$, Eq. (2.14). The former gives the three timescales for the reorientational dynamics as 25 fs, 0.49 ps, and 2.6 ps, corresponding to inertial, librational, and H-bonding breaking and making dynamics, respectively. These parameters are also used in the fit to $C_{2,H}(t)$ so that the fitting parameters are the derivatives with respect to β of each of the amplitudes and timescales. Note that the fits to both $C_2(t)$ and $C_{2,H}(t)$ are in excellent agreement with the calculated TCFs.

A key focus of the analysis of the temperature dependence of the timescales is on the activation energy associated with the reorientational time τ_2 . The fit to $C_{2,H}(t)$ gives this as $E_{a,2} = 3.67 \pm 0.24$ kcal/mol. This agrees with the result of 3.5 ± 0.1 kcal/mol obtained from the Arrhenius

plot, Fig. 2.2b, as well as prior calculations that also yielded 3.5 kcal/mol.^{85,86} It is notable that the activation energy for OH reorientation is similar to that obtained for self-diffusion. This is indicative of the common molecular origin of the two in the breaking and making of H-bonds. Namely, the exchange (or “jump”) between two different H-bond acceptors that is required for an OH to reorient is also the key molecular event for diffusion of a water molecule.

It is important to note that, because the derivatives with respect to β are obtained from a simulation at a single temperature, they may or may not correspond to an activation energy. That is, it is not possible to determine from the derivative alone whether or not $\ln(1/\tau_\alpha)$ depends linearly on $1/T$. Often one has some prior knowledge, such as in the case of D or τ_2 , that the property is activated. However, this is not true for the inertial and librational timescales, τ_{iner} and τ_{lib} . An indication that they may not obey Arrhenius behavior is that our results give uncertainties that encompass zero activation energy: $E_{a,iner} = 1.6 \pm 1.7$ kcal/mol and $E_{a,lib} = 1.0 \pm 1.2$ kcal/mol. Indeed, plots of $1/\tau_{iner}$ and $1/\tau_{lib}$ versus $1/T$ show that these timescales do not exhibit Arrhenius behavior.

Additional information is available in the form of the amplitude derivatives. The fit to $C_{2,H}(t)$ gives $dA_{iner}/d\beta = -0.11 \pm 0.09$, $dA_{lib}/d\beta = -0.18 \pm 0.09$, and $dA_2/d\beta = 0.29 \pm 0.10$. These indicate that as temperature increases (β decreases) the amplitudes of the inertial and librational components increase and that of the H-bond making and breaking component decreases. This is consistent with linear fits to the amplitudes obtained from the simulations at different temperatures, which give -0.08, -0.12, and 0.20 for A_{iner} , A_{lib} , and A_2 , respectively for $T = 285 - 315$ K. This is not the full temperature range we have simulated, however the estimated derivatives change significantly (to 0.04, -0.12, and 0.08) when $T = 330$ K is included in the fitting. This is a further indication that in the energy fluctuation TCFs we are obtaining local derivatives that can have distinct quantitative and qualitative differences from that obtained from multiple-temperature simulations that can depend on the temperature range considered.

2.4.3 Energetic decomposition

A key advantage of the method proposed in this work is the ability to decompose an activation energy or, more generally, a derivative with respect to temperature, into individual contributions due to each component of the energy. Specifically, we can note that the fluctuation in the energy that appears in $MSD_H(t)$ and $C_{2,H}(t)$ can be written as

$$\delta H(0) = \delta KE(0) + \delta V(0), \quad (2.16)$$

$$= \delta KE(0) + \delta V_{LJ}(0) + \delta V_{Coul}(0). \quad (2.17)$$

Here, $\delta KE(0)$ and $\delta V(0)$ are the fluctuations in the kinetic and potential energy, respectively. The second equality notes that the potential energy fluctuation can be further decomposed into the various types of interactions including this simplest example of the Lennard-Jones, δV_{LJ} , and Coulombic, δV_{Coul} , contributions to the water energy. Then, the activation energy can be likewise divided into such contributions as

$$E_a = E_a^{KE} + E_a^{LJ} + E_a^{Coul}, \quad (2.18)$$

where E_a^{KE} , E_a^{LJ} , and E_a^{Coul} are the components of the activation energy associated with fluctuations in the kinetic energy, LJ potential energy, and Coulombic potential energy, respectively. This approach builds on the pioneering work of Tolman¹⁸ and Truhlar¹⁹ to elucidate the physical interpretation of an activation energy.

In the case of diffusion, the component of the activation energy associated with the Coulombic interactions is, for example, then given by,

$$E_{a,D}^{Coul} = \frac{\langle \delta V_{Coul}(0) |\vec{r}(t) - \vec{r}(0)|^2 \rangle}{\langle |\vec{r}(t) - \vec{r}(0)|^2 \rangle}, \quad (2.19)$$

and similarly for $E_{a,D}^{KE}$ and $E_{a,D}^{LJ}$. Note that this is only one way to obtain insight into the origins of the activation energy, and a particularly simple choice. In general, the energy fluctuation, $\delta H(0)$,

can be divided up in any number of ways to gain insight into the nature of the activated process.

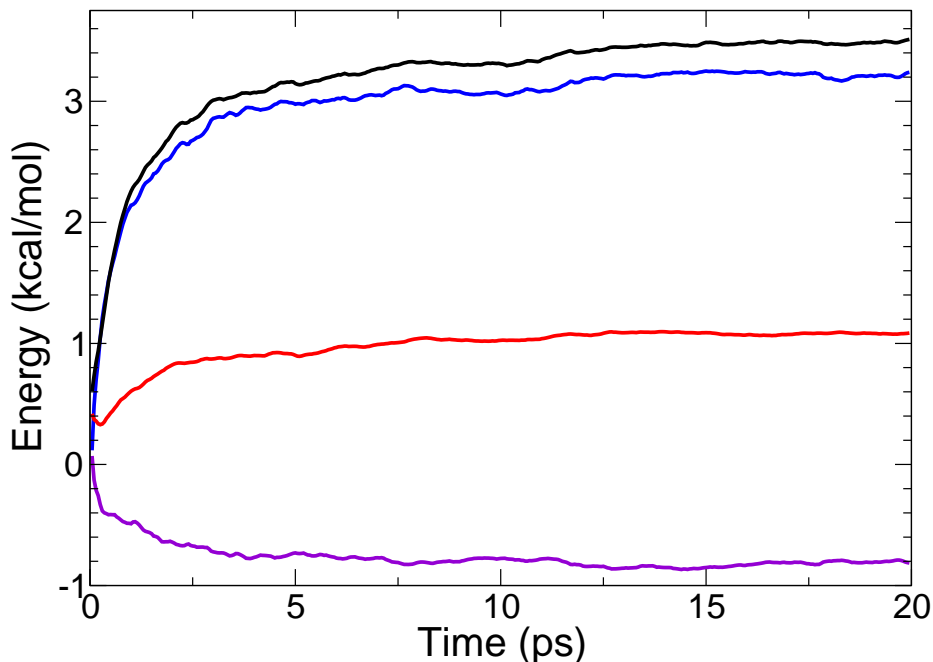


Figure 2.5: The contributions to the diffusion TCF $MSD_H(t)$ associated with the kinetic energy (red line), Lennard-Jones potential energy (violet line), and Coulombic potential energy (blue line) are plotted versus time along with the total (black line).

The resulting TCF for the Coulombic contribution to $MSD_H(t)$ given in Eq. (2.19) is presented as a function of time in Fig. 2.5 along with the LJ and kinetic energy results and the total $MSD_H(t)$. Each contribution to the activation energy can be obtained by fitting the constant value reached at longer times ($t = 15 - 20$ ps); this gives 1.1, -0.8, and 3.2 kcal/mol for the kinetic, Lennard-Jones, and Coulombic energy, respectively. Thus, it is clear from the data that the dominant contribution to the activation energy of diffusion is the Coulombic interactions between water molecules. This is expected given the central role of H-bonding in the mechanism of water diffusion. What is perhaps less obvious is the negative contribution from the Lennard-Jones interactions that are slightly more than cancelled by the kinetic energy component. These results point to the new insight that may be obtained by the present approach.

The same decomposition approach can be applied to the reorientational correlation function,

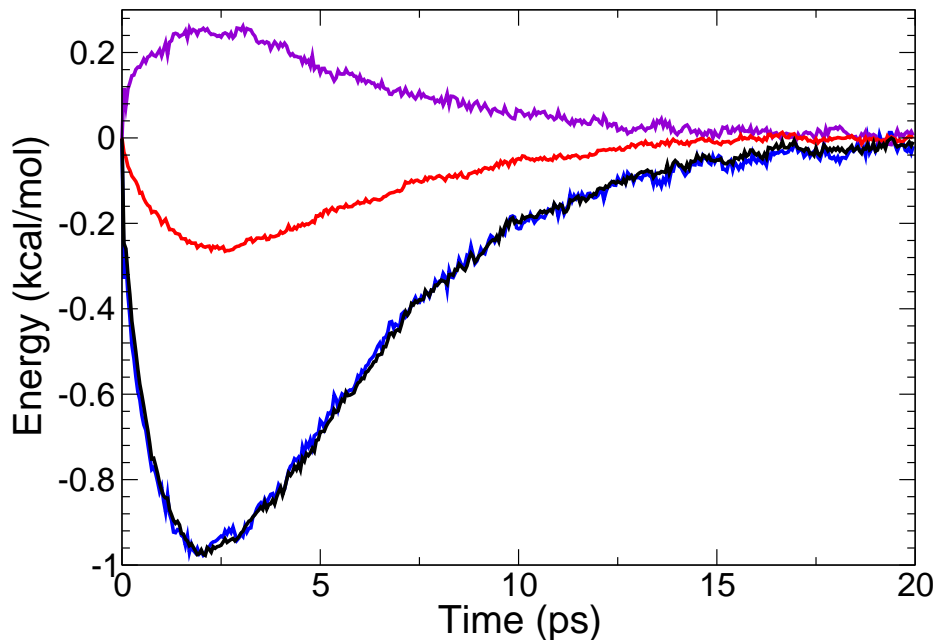


Figure 2.6: The contributions to the reorientational TCF $C_{2,H}(t)$ associated with the kinetic energy (red line), Lennard-Jones potential energy (violet line), and the Coulombic potential energy (blue line) are plotted versus time along with the total (black line).

$C_2(t)$. For example, $C_{2,H}(t)$ given in Eq. (2.13), can be written as the sum of

$$C_{2,Coul}(t) = \langle \delta V_{Coul}(0) P_\ell [\vec{e}(0) \cdot \vec{e}(t)] \rangle, \quad (2.20)$$

and the analogous contributions $C_{2,KE}(t)$, and $C_{2,LJ}(t)$. These three components are shown as a function of time, along with the total $C_{2,H}(t)$, in Fig. 2.6. As with the diffusion constant, the dominant contribution to the activation energy are Coulombic interactions. In fact, there is essentially complete cancellation of the kinetic energy and LJ contributions such that the Coulombic component is nearly equal to the total $C_{2,H}(t)$ for all times. This is again an indication of the central role of H-bond exchanges in OH reorientation in water, which has been extensively explored in the extended jump model of Laage and Hynes.^{85,88}

2.5 Conclusion

This work demonstrates a general approach for evaluating the temperature-dependence of time correlation functions that can also yield the activation energy for transport coefficients or dynamical timescales. A key feature is that the activation energy is obtained from simulations at a single temperature. The method has been demonstrated for the self-diffusion and OH reorientation in bulk liquid water and gives activation energies in agreement with those obtained from standard Arrhenius calculations. The framework, however, is not limited to these examples and can be straightforwardly extended to other transport coefficients, dynamical timescales, or TCFs. Indeed, this approach gives the temperature derivative of a dynamical timescale at a given temperature and it does not require an assumption of Arrhenius behavior.

This approach also provides additional insight into the origins of the activation energy. In particular, we have shown how the activation energy can be decomposed into components associated with the various contributions to the system energy, *e.g.*, kinetic, Lennard-Jones, and Coulombic energies. For both diffusion and reorientation in bulk water, nearly the entire contribution to the activation energy arise from the Coulombic interactions, which is associated with the central role of hydrogen-bond dynamics in both processes. This kind of analysis should lead to a better understanding of the molecular-level interactions that influence the activation energy.

Because the activation energy calculations do not require simulations at multiple temperatures, the present method may be particularly useful in cases where changing the temperature is problematic. For example, biological or self-assembled systems, such as lipid bilayers or reverse micelles, can often display dramatic changes in structure, *e.g.*, protein unfolding, with relatively small temperature changes. Similarly, for systems near a phase transition the range of temperatures for which an Arrhenius analysis can be used is strongly constrained. However, the approach presented here permits the calculation of activation energies or, more generally, the derivative of full time correlation functions with respect to temperature even in such cases.

Chapter 3

The activation energy for water reorientation differs between IR pump-probe and NMR measurements

3.1 Introduction

The reorientational dynamics of water play a central role in many chemical processes. As the solvent in biological systems, water shapes the structure, dynamics, and, ultimately, the function of proteins and DNA.⁸⁹ More generally, water reorientational dynamics, which manifest the underlying structure and rearrangements of the water hydrogen-bonded (H-bonded) network, govern the solvation response of the liquid. Thus, they have been found to be a key element of the mechanisms of, for example, proton transfer,^{90,91} S_N2 ,⁹² and ion-pairing^{93,94} reactions.

Experimentally, reorientational dynamics have been studied in detail by ultrafast infrared pump-probe anisotropy (IR-PP) and NMR spin-echo. These methods have been used particularly to measure the timescales associated with reorientation of particular bond vectors in water over a range of temperatures and pressures.^{51,72,95–98} In isotopically dilute water, *e.g.*, HOD in H₂O, IR-PP measurements provide a femtosecond-resolved view of the reorientational dynamics of the OD bond vector associated with a vibrational transition by measuring the anisotropy decay, $r(t)$, of vibrationally excited water molecules.^{71,99–102} The anisotropy decay is in most cases directly equivalent

Adapted with the permission of Zeke A. Piskulich, and Ward H. Thompson and AIP Publishing from *J. Chem. Phys.* **149**, 164504 (2018).⁴⁴

to the second-order reorientational time correlation function (TCF),⁷¹

$$C_2(t) = \langle P_2 [\vec{e}(0) \cdot \vec{e}(t)] \rangle, \quad (3.1)$$

as $r(t) = 0.4C_2(t)$. Here, \vec{e} represents a unit vector along the relevant bond, OD in the case of HOD in H₂O, P_2 is the second-order Legendre polynomial, and $\langle \dots \rangle$ represents a thermal average. IR-PP measurements and simulations have led to a detailed understanding of the anisotropy decay in water which occurs on three timescales, as discussed in greater detail below. The longest of these, denoted τ_2 , is associated with the exchange of hydrogen-bond (H-bond) partners and has been measured as 2.5 – 2.7 ps in water at room temperature.^{7,8,71,72,101,103–105}

The NMR spin-echo method takes advantage of the relationship between the longitudinal spin relaxation time, T_1 , and the integral of the orientation correlation function to measure an averaged reorientation time,⁴³

$$\langle \tau_2 \rangle = \int_0^\infty C_2(t) dt. \quad (3.2)$$

This averaged, or integrated, time has contributions from all of the timescales on which $C_2(t)$ decays, not just that associated with H-bond breaking and making.^{51,106–108} As a consequence, the measured times for OH reorientation in H₂O from NMR are shorter than that for τ_2 , with $\langle \tau_2 \rangle$ observed to be in the range 1.7 – 2.0 ps.^{51,97,109,110} It is important to note that NMR experiments are unable to measure OH bond reorientation directly, but only that of the OD bond in D₂O, the out-of-plane vector from ¹⁷O NMR, and the H-H vector in H₂O from proton NMR. However, the OH integrated reorientation time can be estimated using some basic assumptions.^{51,52,107,109}

The reorientational correlation function, $C_2(t)$, in Eq. (3.1) can be straightforwardly calculated from molecular dynamics (MD) simulations. The direct connection between the observables probed in these IR-PP and NMR measurements and $C_2(t)$ thus provides a special opportunity for synergy between experimental and theoretical studies to understand reorientation dynamics. Indeed, significant insight has been obtained in the H-bond dynamics in this way. In particular, the extended jump model (EJM) of Laage and Hynes,^{85,88} has elucidated the underlying mechanis-

tic connection between the τ_2 reorientation time and the timescale for an OH group to exchange H-bond acceptors, the “jump” time. In the EJM model, water reorientation is described as a combination of large amplitude angular jumps¹¹¹ that occur when H-bond acceptors are exchanged and diffusive¹¹² “frame” reorientation of the intact H-bonded pair. In water, the former represents the dominant contribution to the OH reorientation and thus there is a clear connection between the reorientational and H-bond dynamics.

An important characteristic of an activated dynamical process is the temperature dependence of the relevant timescale(s). This is typically expressed as the activation energy, E_a , which for a rate constant k is expressed as

$$E_a = -\frac{\partial \ln k}{\partial \beta}, \quad (3.3)$$

where $\beta = 1/k_B T$. While E_a is most precisely described as an expression of the temperature dependence of k , in many cases it can be interpreted in terms of an effective barrier for the process of interest.^{18,19} While there has been ample consideration of the differences between τ_2 and $\langle \tau_2 \rangle$, little attention has been paid to comparing the activation energies for the two timescales. Because τ_2 is one of the components contributing to $\langle \tau_2 \rangle$, independent measurements of E_a for each timescale could yield additional insight into the reorientational dynamics.

In this Chapter, we use precise MD simulation calculations of the timescales obtained from IR-PP and NMR experiments as well as their corresponding activation energies. A recently developed method for calculating activation energies from simulations at a single temperature^{31,58,59} is used to remove any numerical approximations associated with an Arrhenius analysis (and these approximations are also quantified). The calculations are analyzed to provide a framework for understanding the differences between the τ_2 and $\langle \tau_2 \rangle$ activation energies. In particular, the simulations predict that the two timescales should have different activation energies and estimate the experimental precision that will be required to distinguish them. Moreover, the analysis shows what additional information about the reorientational dynamics could be extracted from a quantitative comparison of the τ_2 and $\langle \tau_2 \rangle$ activation energies.

3.2 Theory

The reorientational TCF defined in Eq. (3.1) has been extensively studied for OH reorientation in water both experimentally and by simulation. For concreteness, $C_2(t)$ is plotted versus time in Fig. 3.1 for OH reorientation in water at 298.15 K and 1 bar, calculated with the simulation approach described below in Sec. 3.3. The decay of $C_2(t)$ occurs on three timescales and the TCF is typically fit by a triexponential

$$C_2(t) = \sum_{\alpha} A_{\alpha} e^{-t/\tau_{\alpha}}, \quad (3.4)$$

where α indexes the three timescales, τ_{α} , with amplitudes A_{α} . The fastest timescale, τ_{iner} , observable in the inset of Fig. 3.1a, is associated with inertial motion, *i.e.*, the free, or ballistic, reorientation of the OH that occurs at times short enough that intermolecular interactions are unimportant. The intermediate timescale, τ_{lib} , is characteristic of the librational motion of the OH reorienting within the restrictions of the intact H-bond. Finally, the longest timescale, τ_2 , is associated with the complete OH reorientation accomplished by a combination of rotation of the intact H-bonded pair and large angle “jumps” associated with the exchange of H-bond acceptor.^{85,88} In water at room temperature, the latter mechanism is the dominant contribution to the reorientation. The values obtained from fitting $C_2(t)$ by Eq. (3.4) up to $t = 10$ ps are given in Table 3.1; the time range is chosen to match that typically available in IR-PP measurements, which are limited by the short lifetime of the OH or OD vibrationally excited state in isotopically dilute water ($T_1 = 0.7 - 0.74$ ps^{72,113,114} for HOD in D₂O and $T_1 = 1.7 - 1.8$ ps for HOD in H₂O^{72,103,115}).

The fitting by Eq. (3.4) assumes that the inertial and librational times decay exponentially, which is not the case as evident from Fig. 3.1. The inertial decay is rigorously Gaussian while in water the librational dynamics exhibit a coherent oscillation. These two details are frequently ignored, as we do here. As a check, we have also fit the data with a Gaussian decay for the inertial component and found that it does not change the timescales or the relevant activation energies.

The average, or integrated, reorientational time defined by $\langle \tau_2 \rangle$ in Eq. (3.2) is shown in Fig. 3.1b.

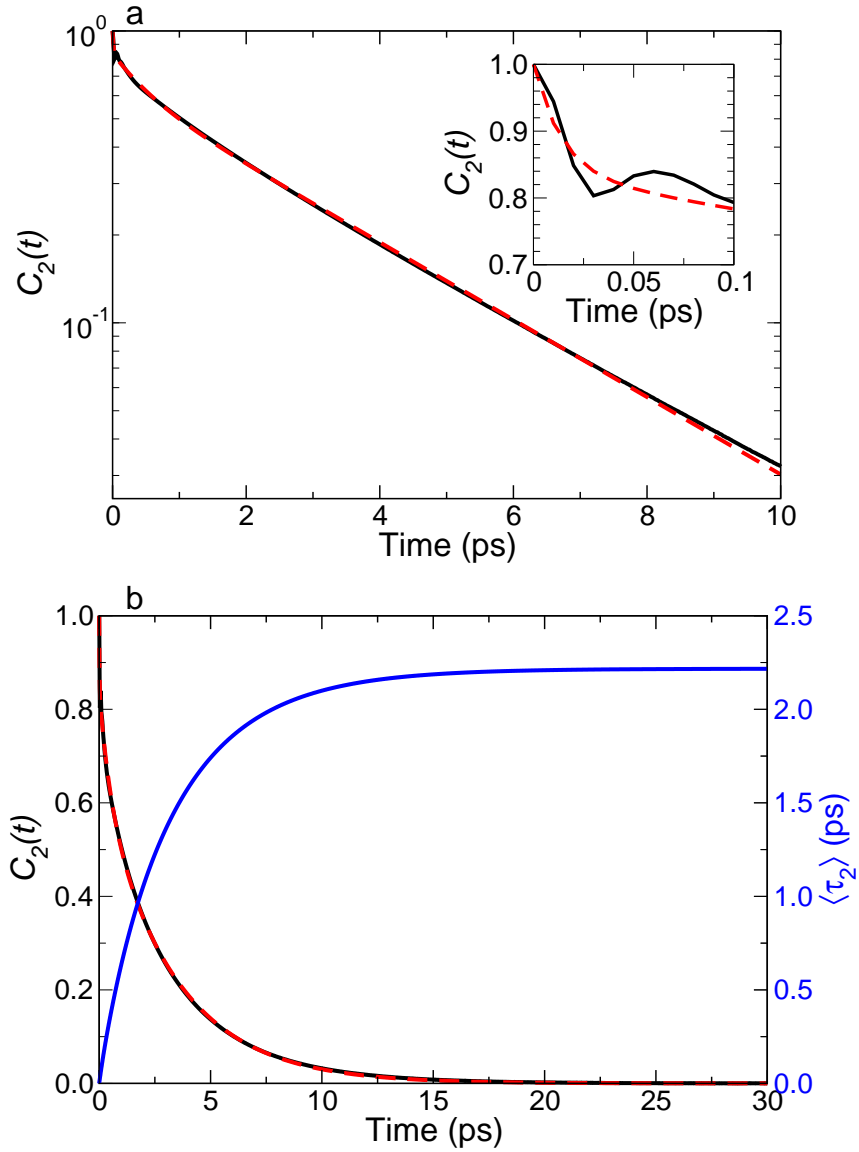


Figure 3.1: The OH reorientational correlation function, $C_2(t)$, for TIP4P/2005 water at 298.15 K and 1 bar (black) is shown as a function of time along with a triexponential fit (red), Eq. (3.4). a: $C_2(t)$ is shown on a semi-log scale and the short-time decay is shown in the inset. b: $C_2(t)$ is shown on a linear scale along with its integral (blue, right axis) which equals the average reorientational time, $\langle \tau_2 \rangle$, at long times.

In the context of the triexponential fit to $C_2(t)$ the average time is given by

$$\langle \tau_2 \rangle = \sum_{\alpha} A_{\alpha} \tau_{\alpha}, \quad (3.5)$$

which indicates its dependence on all three timescales and amplitudes; this relation will be exam-

ined in greater detail in Sec. 3.4.1. It is important to note that $\langle \tau_2 \rangle$ is calculated here, except when otherwise noted, by direct integration of $C_2(t)$ and thus the value is independent of any assumed form for the reorientation TCF.

If the inverse of a timescale, τ_α^{-1} , is assumed to correspond to a rate constant, the activation energy associated with each can be written from Eq. (3.3) as

$$E_{a,\tau_\alpha} = -\tau_\alpha \frac{\partial (1/\tau_\alpha)}{\partial \beta}. \quad (3.6)$$

Note that this activation energy is well-defined even in the case that the timescale does not correspond to a rate constant or does not exhibit Arrhenius behavior. In such a case E_{a,τ_α} may be viewed as an “effective” activation energy that describes the temperature dependence of the timescale, but for which the physical interpretation must otherwise be carefully considered. An activation energy can similarly be defined for the average reorientational time as

$$E_{a,\langle \tau_2 \rangle} = -\langle \tau_2 \rangle \frac{\partial (1/\langle \tau_2 \rangle)}{\partial \beta}. \quad (3.7)$$

This, in principle, has contributions from all of the timescales present in $C_2(t)$, as is evident from consideration of Eq. (3.5).

We have previously shown that the derivative of temperature derivative of $C_2(t)$ can be directly determined from simulations at a single temperature.⁵⁸ The reorientational TCF given in Eq. (3.1) can be written more explicitly as

$$\begin{aligned} C_2(t) &= \frac{1}{Q} \text{Tr} \left[e^{-\beta H} P_2 [\vec{\epsilon}(0) \cdot \vec{\epsilon}(t)] \right], \\ &= \frac{1}{Q h^f} \int d\mathbf{p} \int d\mathbf{q} e^{-\beta H} P_2 [\vec{\epsilon}(0) \cdot \vec{\epsilon}(t)], \end{aligned} \quad (3.8)$$

where, as indicated by the second equality, Tr represents an integration over all of the coordinates and momenta, Q is the partition function, and f is the number of degrees-of-freedom. Since only

Q and the Boltzmann factor, $e^{-\beta H}$, depend on the temperature, it is straightforward to show that

$$-\frac{\partial C_2(t)}{\partial \beta} = C_{2,H}(t) = \langle \delta H(0) P_2 [\vec{e}(0) \cdot \vec{e}(t)] \rangle, \quad (3.9)$$

where $\delta H(0) = H(0) - \langle H \rangle$ is the fluctuation in the total system energy at time $t = 0$. Thus, the temperature dependence of $C_2(t)$ is given by $C_{2,H}(t)$, which is the reorientational TCF weighted by the fluctuation in the initial energy.⁵⁸ In this way, the temperature derivative $\partial C_2(t)/\partial \beta$ can be calculated from the same simulations that give $C_2(t)$, *i.e.*, from consideration of a single temperature without the necessity or approximation of constructing an Arrhenius plot. The implementation of these simulations is described in Sec. 3.3.

The $C_{2,H}(t)$ TCF can be analyzed in a manner consistent with that of $C_2(t)$ by taking the derivative of the fitting function in Eq. (3.4) with respect to β , which gives

$$C_{2,H}(t) = -\sum_{\alpha} \left[\frac{\partial A_{\alpha}}{\partial \beta} - \frac{\partial (1/\tau_{\alpha})}{\partial \beta} t A_{\alpha} \right] e^{-t/\tau_{\alpha}}. \quad (3.10)$$

Here A_{α} and τ_{α} are the parameters calculated from the fit of $C_2(t)$ using Eq. (3.4), while $\partial(1/\tau_{\alpha})/\partial \beta$ and $\partial A_{\alpha}/\partial \beta$ are new fitting parameters representative of the temperature dependence of the amplitudes and timescales for the reorientational dynamics. The former can then be used to calculate the activation energies for each timescale from Eq. (3.6). These represent the activation energies that can be obtained from IR-PP measurements at different temperatures.

By integrating the derivative correlation function $C_{2,H}(t)$ the activation energy associated with the average reorientation time, Eq. (3.7), can be directly calculated as

$$E_{a,\langle \tau_2 \rangle} = \frac{1}{\langle \tau_2 \rangle} \int_0^{\infty} \frac{\partial C_2(t)}{\partial \beta} dt = -\frac{1}{\langle \tau_2 \rangle} \int_0^{\infty} C_{2,H}(t) dt. \quad (3.11)$$

In the context of the fitting of $C_2(t)$ and $C_{2,H}(t)$, the activation energy for $\langle \tau_2 \rangle$ can be derived using

Eqs. (3.10) and (3.11) to give

$$E_{a,\langle\tau_2\rangle}^{(fit)} = \sum_{\alpha} \left[\frac{\partial A_{\alpha}}{\partial \beta} \frac{\tau_{\alpha}}{\langle\tau_2\rangle} + A_{\alpha} \frac{\tau_{\alpha}}{\langle\tau_2\rangle} E_{a,\tau_{\alpha}} \right]. \quad (3.12)$$

From this relationship, it is apparent that $E_{a,\langle\tau_2\rangle}^{(fit)}$ need not be equal to E_{a,τ_2} . The two can only be identical if the amplitudes, timescales, and their temperature derivatives exhibit particular relationships, *i.e.*, it is not generally true. Note that if the assumptions made in the fitting of $C_2(t)$ are correct, then $E_{a,\langle\tau_2\rangle} = E_{a,\langle\tau_2\rangle}^{(fit)}$, which provides a check on the accuracy of Eq. (3.4).

3.3 Computational Methods

The direct fluctuation method derived previously^{31,58,59} and described briefly above is used to calculate the activation energies of the reorientation times for the OH bond in water. The simulations are implemented as follows. A long trajectory in the isobaric-isothermal (*NPT*) ensemble is used to generate initial configurations for a large number of constant energy and volume (*NVE*) trajectories, from which the correlation functions $C_2(t)$ and $C_{2,H}(t)$ are calculated. In this way, the *NVE* trajectories sample over the variations of the system energy, *i.e.*, $\delta H(0)$, in the *NPT* simulation that are representative of the desired temperature (and related to the heat capacity^{5,116,117}), but there is no effect of the thermostat in the *NVE* dynamics from which the TCFs are obtained. We also consider, for comparison, simulations in which the initial configurations are sampled from a canonical ensemble (*NVT*) trajectory.

The MD simulations were performed using the Large-Scale Atomic/Molecular Massively Parallel Simulator (LAMMPS).⁸¹ A simulation cell of 343 water molecules initialized within a fully-periodic box of length 21.725311 Å was initialized to give a density of 0.997 g/mol. The TIP4P/2005⁵ water force field was used in all the simulations. This is a rigid model that has a charge on each atom and a fourth point charge that improves the description of the electrostatic interactions relative to three-site models; it is parameterized to describe the properties of water over a range of temperatures and pressures.⁵ The water molecules were kept rigid using of the SHAKE algorithm

Table 3.1: Reorientation times, τ_α , in ps, amplitudes, A_α , amplitude derivatives, $\partial A_\alpha/\partial\beta$, in kcal/mol, and activation energies, E_α , in kcal/mol for the TIP4P/2005 model calculated from the *NPT* ensemble at 298.15 K and 1 bar. Subscripts indicate uncertainties in the final digit(s).

| Value | τ_{iner} | τ_{lib} | τ_2 | $\langle\tau_2\rangle$ |
|-----------------------------------|---------------------|----------------------|---------------------|------------------------|
| τ_α | 0.013 ₁ | 0.455 ₄ | 3.225 ₈ | 2.218 ₅ |
| A_α | 0.156 ₁ | 0.193 ₁ | 0.651 ₂ | |
| $\partial A_\alpha/\partial\beta$ | -0.072 ₈ | -0.164 ₃₆ | 0.237 ₄₁ | |
| E_α | 0.64 ₁₂ | 1.86 ₂₈ | 4.28 ₁₀ | 4.58 ₁₁ |

with a tolerance of 1.0×10^{-4} .¹¹⁸ Electrostatic interactions from all four sites on the TIP4P/2005 model were included through the use of a standard Coulomb interaction and an Ewald sum calculated using the Particle Particle Particle Mesh (PPPM),^{119–121} with the Ewald accuracy parameter taken as 1.0×10^{-4} . The cutoff for the LJ interactions was 10.5 Å, while that for electrostatic interactions was 8.5 Å.

For each simulation a 50 ns *NPT* (or *NVT*) trajectory was propagated with the temperature maintained by a Nosé-Hoover chain of length three and a thermostat damping parameter of 100 fs; the *NPT* barostat damping parameter was 1 ps.^{83,84} Initial coordinates and momenta for the *NVE* trajectories were saved every 1 ps, giving a total of 50,000 trajectories, each of length 50 ps. All simulations used a timestep of 1 fs and configurations were saved every 10 fs from the *NVE* trajectories. Simulations were divided into ten blocks of 5,000 trajectories each for block averaging to obtain 95% confidence intervals according to the Student’s *t*-distribution,¹²² which are the errors reported on the data.

To compare with the traditional means of calculating activation energies *via* the Arrhenius equation, we have additionally calculated reorientation times using the same simulation approach in the *NPT* ensemble at 1 bar at 288.15, 293.15, 303.15, and 308.15 K.

3.4 Results

3.4.1 Reorientation Times and Activation Energies

The simulation approach just described was used to calculate reorientation times and activation energies for the TIP4P/2005 water model at 298.15 K and 1 bar in the NPT ensemble. The calculated $C_2(t)$ correlation function, Eq. (3.1), is shown in Fig. 3.1 along with the triexponential fit, Eq. (3.4), and the resulting times and amplitudes are given in Table 3.1. The fitting of $C_2(t)$ is restricted to $t \leq 10$ ps as this corresponds to the time range generally accessible in IR-PP measurements due to the OH excited-state vibrational lifetime. The NPT ensemble is used because it most closely corresponds to the typical conditions of IR-PP and NMR experiments. The inertial timescale is found to be $\tau_{iner} = 13$ fs; this timescale is typically not accessible in pump-probe measurements because it is shorter than the IR pulse width. The librational timescale of 455 fs obtained from the fit is longer than the ~ 200 fs timescale typically attributed to librational dynamics.^{8,72}

The longest decay time, associated with H-bond exchanges, is calculated as 3.225 ps, which is longer than that reported in measurements, which fall in the range 2.5-2.7 ps for OD rotation of HOD in H_2O .^{7,8,71,72,101,103-105} Likewise, the average reorientation time obtained is $\langle \tau_2 \rangle = 2.218$ ps (see Fig. 3.1b), which is slightly longer than the values of 1.7-2.0 ps^{51,97,109,110} obtained in NMR measurements. We note that the TIP4P/2005 water model also underestimates the water diffusion coefficient,⁵ suggesting that it generally exhibits hydrogen-bonding dynamics that are slightly too slow compared to experiment. It is noteworthy that $\langle \tau_2 \rangle$ is determined almost completely by τ_2 , *i.e.*, if the contributions of each timescale are considered as expressed in Eq. (3.5), one finds 0.002, 0.09, and 2.10 ps for τ_{iner} , τ_{lib} , and τ_2 , respectively.

The present result is also slightly longer than the values of $\tau_2 = 3.1$ ps and $\langle \tau_2 \rangle = 2.04$ ps reported by Stirnemann and Laage for the TIP4P/2005 water model from an equilibrium NVE simulation.¹⁰⁸ The differences appear to be due to the choice of ensemble. Simulations in the NVT ensemble using the present approach yield $\tau_2 = 3.070$ ps and $\langle \tau_2 \rangle = 2.122$ ps, in excellent agreement with the results of Stirnemann and Laage. This indicates that there are differences in the water reorientational timescales under constant pressure and constant volume conditions, but they are relatively small.

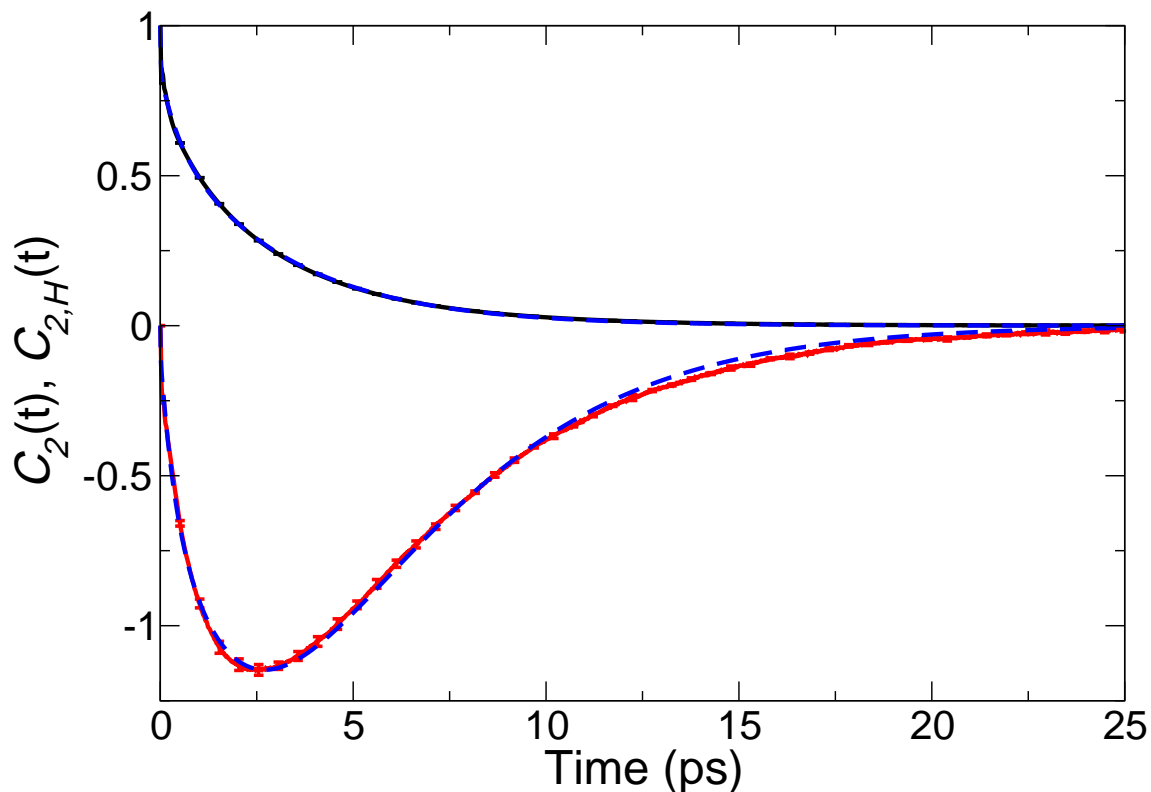


Figure 3.2: The reorientational TCF $C_2(t)$ (black) and the energy fluctuation weighted TCF $C_{2,H}(t)$ (red) are plotted versus time for TIP4P/2005 water at 298.15 K and 1 bar. Fits of each according to Eqs. (3.4) and (3.10) are also shown (blue dashed).

The derivative with respect to β of the reorientational TCF was calculated *via* Eq. (3.9) to determine the activation energies for reorientation. The $C_2(t)$ and the energy fluctuation-weighted TCF, $C_{2,H}(t)$, are presented in Fig. 3.2 for the TIP4P/2005 *NPT* simulation. The derivative correlation function was fit over the 50 ps range using Eq. (3.10) and used to extract activation energies associated with each reorientation timescale, which are given in Table 3.1.

The activation energy for the τ_2 reorientation time associated with H-bond exchanges is found to be 4.28 kcal/mol. This is in very good agreement with the value of 4.1 ± 0.5 kcal/mol measured by Petersen *et al.* in IR-PP experiments,⁷ which also yielded $\tau_2 = 2.5$ ps, shorter than that found in the present simulations. The present E_a is larger than the 3.7 kcal/mol obtained by Nicodemus *et al.*

from 2D-IR measurements of the anisotropy;¹⁰⁵ they found $\tau_2 = 2.9$ ps at 295 K which would predict a value of 2.7 ps at 298.15 K, again smaller than the present simulation result. Both experimental studies measured OD reorientation for HOD in H₂O. The activation energy for the TIP4P/2005 water model is larger than those reported for the SPC/E (3.5 and 3.67 ± 0.24 kcal/mol),^{58,85,86} and E3B (3.82 kcal/mol),¹²³ models as well as TTM3-F evaluated with centroid molecular dynamics (4.1 kcal/mol).¹²⁴

The activation energy associated with $\langle \tau_2 \rangle$ was also calculated using Eq. (3.11) and is presented in Table 3.1. The present result of $E_{a,\langle \tau_2 \rangle} = 4.58$ kcal/mol is in excellent accord with values obtained from NMR experiments, which are in the range of 4.4-4.6 kcal/mol^{51,52,96,125} with uncertainties on the order of ± 0.5 kcal/mol. The same NMR measurements do, however, predict shorter average reorientation times than the simulations, finding $\langle \tau_2 \rangle = 1.67$ and 1.95 ps for H₂O,^{51,52} and 2.21 and 2.37 ps in D₂O.^{52,96}

It is interesting to examine how the amplitudes for the different timescales for decay of $C_2(t)$ change with temperature; these data are also included in Table 3.1. Note that the sum of all of the derivatives should add to zero (since the TCF is normalized) and this is obtained in the fitting without imposing it as a constraint. An important observation is that the amplitude associated with H-bond dynamics, A_2 , is found to increase with temperature (decrease with β) while those corresponding to the inertial and librational timescales decrease.

A key result of this analysis is that the activation energies for τ_2 and $\langle \tau_2 \rangle$ are *not* the same and can be resolved within the present simulations. This observation appears to be consistent with the reported activation energies measured by IR-PP for τ_2 and by NMR for $\langle \tau_2 \rangle$, but the reported uncertainties are too large to make any comparison definitive at present. In Sec. 3.5 below, we examine the origins and implications of the differences in these activation energies.

3.4.2 Traditional Arrhenius Analysis

The direct fluctuation method calculates the derivative of $C_2(t)$, and hence of the underlying timescales, with respect to β in an analytical way. That is, there is no numerical finite differ-

Table 3.2: Simulated reorientation times at different temperatures for TIP4P/2005 water at 1 bar.

| T(K) | τ_{iner} (ps) | τ_{lib} (ps) | τ_2 (ps) | $\langle \tau_2 \rangle$ (ps) |
|--------|--------------------|--------------------|---------------------|-------------------------------|
| 288.15 | 0.014 ₁ | 0.523 ₄ | 4.186 ₁₄ | 2.943 ₁₁ |
| 293.15 | 0.013 ₁ | 0.483 ₆ | 3.653 ₁₂ | 2.541 ₁₁ |
| 298.15 | 0.013 ₁ | 0.455 ₄ | 3.225 ₈ | 2.218 ₅ |
| 303.15 | 0.013 ₁ | 0.421 ₅ | 2.867 ₆ | 1.962 ₄ |
| 308.15 | 0.012 ₁ | 0.397 ₄ | 2.565 ₄ | 1.743 ₄ |

Table 3.3: Activation energies (kcal/mol) calculated from an Arrhenius analysis of the temperature dependence through fitting different sets of points. The column labeled "All" is a fit of all temperatures 288.15-308.15K, "Middle" is a fit over all temperatures 293.15-303.15K, "Low" is a fit over all temperatures 288.15-298.15K, "High" is a fit over all temperatures 298.15-308.15K, and "Separated" is a fit of 288.15 K, 298.15 K, and 308.15 K.

| Timescale | All | Middle | Low | High | Separated |
|--------------------------|--------------------|--------------------|--------------------|--------------------|--------------------|
| τ_{iner} | 1.31 ₁₂ | 1.20 ₂₆ | 1.56 ₁₈ | 1.09 ₂₃ | 1.33 ₁₂ |
| τ_{lib} | 2.43 ₁₈ | 2.42 ₃₇ | 2.38 ₂₇ | 2.49 ₄₅ | 2.42 ₁₄ |
| τ_2 | 4.31 ₆ | 4.28 ₇ | 4.45 ₁₃ | 4.18 ₁₀ | 4.32 ₂₂ |
| $\langle \tau_2 \rangle$ | 4.61 ₇ | 4.57 ₁₁ | 4.83 ₁₃ | 4.40 ₁₁ | 4.63 ₂₁ |

ence approximation to the derivative as is implicit in the use of an Arrhenius analysis. This is, however, *not* the way in which measured activation energies are obtained from IR-PP and NMR experiments. Thus, to gain insight into any differences between the calculated activation energies in Table 3.1 and those determined by a traditional Arrhenius analysis, we have carried out the latter. Namely, the reorientational TCF was calculated at four additional temperatures at 1 bar to give the reorientation timescales over temperatures from 288.15 to 308.15 K in 5 K increments. The results are given in Table 3.2 and presented as Arrhenius plots for each timescale in Fig. 3.3.

All of the reorientation timescales show the expected trend of faster dynamics with increasing temperature and hence positive activation energies. However, even over this relatively narrow temperature range, there is noticeable curvature in the Arrhenius plot for τ_{iner} , in Fig. 3.3a, indicating that the corresponding activation energy should not be interpreted in terms of an Arrhenius equation.

The data in Table 3.2 were used to obtain activation energies by selecting different sets of temperatures to use in the Arrhenius analysis. The corresponding fits are shown in Fig. 3.3 and the

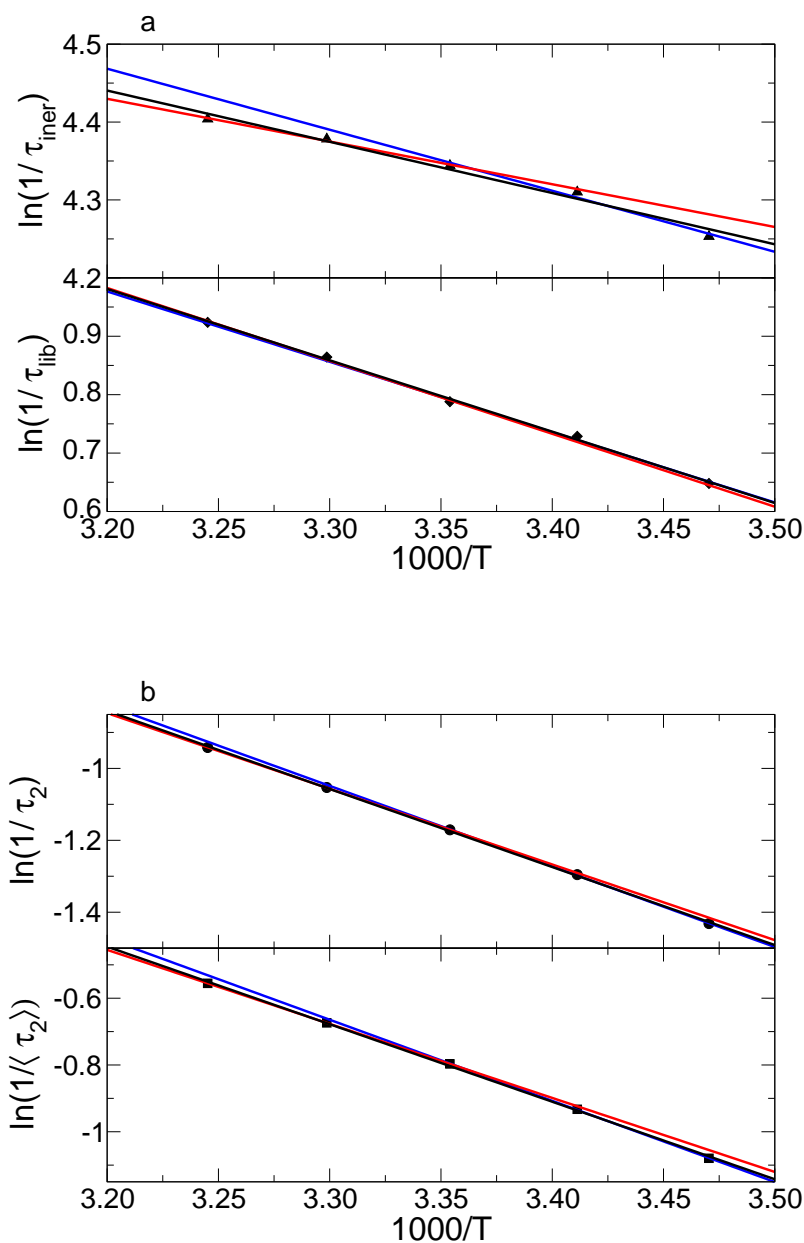


Figure 3.3: Reorientation time Arrhenius plot calculated from the TIP4P/2005 *NPT* simulations. Arrhenius fits are included as a black line for the fit of all temperatures, as blue line for the fit of the lowest three temperatures, and as a red line for the fit over the highest three temperatures. A) τ_{lib} and τ_{iber} are shown as diamonds and triangles, respectively. B) A similar analysis is included for τ_2 and $\langle\tau_2\rangle$ which are represented by circles and squares, respectively.

results are given in Table 3.3. The activation energies for τ_2 and $\langle\tau_2\rangle$ obtained using the narrowest range of temperatures around 298.15 K (the “Middle” fit in Table 3.3) give values in excellent

agreement with the results from the direct calculation of E_{a,τ_2} and $E_{a,\langle\tau_2\rangle}$ in Table 3.1. This result is expected given that this approach minimizes the numerical approximation in the Arrhenius-derived activation energy. Interestingly, there are distinct deviations between the direct and Arrhenius activation energies for τ_{iner} and, for some of the temperatures ranges, τ_{lib} , presumably due to non-Arrhenius behavior.

The Arrhenius analysis gives activation energies for τ_2 that agree with the directly calculated value (Table 3.1) within statistical errors independent of the temperature range used in the calculation (though only barely so for some choices). The non-Arrhenius nature of τ_2 is, however, evident as the activation energy calculated between 288.15–298.15 K is larger, 4.45 ± 0.13 kcal/mol, than that obtained from 298.15–308.15 K, 4.18 ± 0.10 kcal/mol. A similar result is obtained for the integrated time, $\langle\tau_2\rangle$, activation energy.

The difference between the low- and high-temperature fits of the reorientation times are indicative of non-Arrhenius behavior. Indeed, Stirnemann and Laage noted that $E_{a,\langle\tau_2\rangle}$ changes by 8 kcal/mol between 235 K and 350 K.¹⁰⁸ All linear Arrhenius fits within this work are over a significantly smaller temperature range than typically used in experimental works, yet the choice of the temperature range is clearly important. Alternatively, experimental works make assumptions about the functional form of the temperature dependence to evaluate the derivative locally.⁵² A key suggestion from these calculations is that it is important to minimize the temperature range used in the Arrhenius analysis as much as possible to avoid effects due to the temperature-dependence of the activation energies for the water reorientational timescales.

3.5 Discussion

The key result from the simulations presented in Sec. 3.4 is that there is a distinguishable difference in the activation energies associated with τ_2 , $E_{a,\tau_2} = 4.28 \pm 0.10$ kcal/mol, and $\langle\tau_2\rangle$, $E_{a,\langle\tau_2\rangle} = 4.58 \pm 0.11$ kcal/mol. This indicates that IR-PP and NMR experiments are measuring slightly different aspects of the OH reorientation, which we now examine. Moreover, our calculations suggest that experiments need to be able to resolve the τ_2 and the $\langle\tau_2\rangle$ activation energies within

Table 3.4: Contributions to the activation energy, $E_{a,\langle\tau_2\rangle}^{(fit)}$, in kcal/mol, as given in Eq. (3.12). Results are for TIP4P/2005 water at 298.15 K and 1 bar. Last row shows the total associated with each timescale.

| Component | τ_{iner} | τ_{lib} | τ_2 |
|---|----------------------|---------------------|----------------------|
| $\frac{\partial A_\alpha}{\partial \beta} \frac{\tau_\alpha}{\langle\tau_2\rangle}$ | -0.0004 ₁ | -0.034 ₈ | 0.344 ₆₁ |
| $A_\alpha \frac{\tau_\alpha}{\langle\tau_2\rangle} E_{a,\tau_\alpha}$ | 0.0006 ₂ | 0.074 ₁₁ | 4.051 ₉₅ |
| Total | 0.0002 ₂ | 0.040 ₂₂ | 4.395 ₁₆₁ |

~ 0.15 kcal/mol to observe this difference in activation energies.

Before analyzing the differences in the τ_2 and $\langle\tau_2\rangle$ activation energies, it is useful to consider some aspects of the experimental techniques that can affect the measured values. First, in IR-PP measurements, the anisotropic decay is that of a vibrationally excited OH bond, while in NMR experiments the dynamics probed are that of the vibrational ground state. The effect of vibrational excitation on the reorientational dynamics has not been examined in the literature,¹²⁶ but the slightly longer bond distance of the vibrationally excited OH suggests it might lead to a small relative increase in E_{a,τ_2} compared to $E_{a,\langle\tau_2\rangle}$. Further, the IR-PP measurements most directly comparable to the present simulations are in isotopically dilute solutions, specifically, OD reorientation of HOD in H₂O to avoid dynamics associated with resonant vibrational energy transfer. It is noteworthy that, as noted above, experiments find longer reorientational times for HOD in D₂O compared to HOD in H₂O.⁷² Similarly, NMR measurements find longer $\langle\tau_2\rangle$ times for D₂O than H₂O as noted in Sec. 3.4.1.^{51,52,96} An examination of nuclear quantum effects on water reorientational dynamics found no change in the mechanisms and only minor quantitative changes relative to classical simulations.¹²⁷ This demonstrates that the reorientation is influenced more strongly by the isotopic effect of the full solvent than the reorienting bond.

3.5.1 Contributions to the $\langle \tau_2 \rangle$ Activation Energy

To better understand the integrated reorientation time activation energy and its relationship to E_{a,τ_2} , we note that it can be expressed in terms of contributions due to each of the timescales assuming $C_2(t)$ is well described by the tri-exponential fit, Eq. (3.12). The component of $E_{a,\langle \tau_2 \rangle}$ due to each timescale can be further decomposed into two components, the first associated with the temperature dependence of the amplitude, $\partial A_\alpha / \partial \beta$, and the second with the timescale activation energy, E_{a,τ_α} . Each of these contributions is given in Table 3.4. The total integrated time activation energy based on this triexponential fit is $E_{a,\langle \tau_2 \rangle}^{(fit)} = 4.44 \pm 0.09$ kcal/mol, which is in reasonable agreement with the result obtained from direct integration of $C_{2,H}(t)$, $E_{a,\langle \tau_2 \rangle} = 4.58 \pm 0.11$ kcal/mol.

The results in Table 3.4 show that the contribution of the inertial dynamics to the integrated time activation energy is negligible. This is due largely to the $\tau_\alpha / \langle \tau_2 \rangle$ factor that appears in each term. The librational contribution, 0.040 kcal/mol, is significantly larger, but still an order-of-magnitude smaller than that due to τ_2 . It is notable that for both τ_{iner} and τ_{lib} , the term associated with the change in the amplitude with temperature is negative, while that associated with the activation energy is positive so the result for each timescale is reduced by the partial cancellation of these two terms.

The dominant contribution, as expected, is that associated with the τ_2 reorientation time, namely H-bond breaking and making. The largest component of this arises from the term associated with the τ_2 activation energy, but that arising from the temperature dependence of the A_2 amplitude is also significant. This is a clear indication that the activation energy of the integrated reorientation time is not determined solely by that of τ_2 . In particular, the contribution of E_{a,τ_2} appears in $E_{a,\langle \tau_2 \rangle}$ scaled by $A_2 \tau_2 / \langle \tau_2 \rangle = 0.947$, but this reduction is more than compensated by the increase in A_2 with temperature. It is predominantly this effect that makes $E_{a,\langle \tau_2 \rangle}$ greater than E_{a,τ_2} . In other words, the integrated time activation energy includes a significant contribution due to the change with temperature in the amplitude of the H-bond exchange component of the reorientational TCF. Because the inertial and librational contributions are nearly negligible, accurate measurement of the τ_2 and $\langle \tau_2 \rangle$ activation energies would provide an experimental estimate

of the temperature dependence of the amplitude, *i.e.*, $\partial A_2/\partial\beta$. Alternatively, this derivative can, in principle, be obtained from temperature-dependent IR-PP measurements and be used to predict $E_{a,\langle\tau_2\rangle}$.

It is also interesting to consider the perspective wherein $A_2(= 1 - A_{iner} - A_{lib})$ is considered to be determined from the magnitude of the incomplete reorientation completed through inertial and librational motions. Then $\partial A_2/\partial\beta = -\partial A_{iner}/\partial\beta - \partial A_{lib}/\partial\beta$ and the results in Table 3.1 indicate that the librational contribution to the amplitude change is roughly twice that due to inertial motion. Thus, in this viewpoint the difference between E_{a,τ_2} and $E_{a,\langle\tau_2\rangle}$ is associated primarily with the increasing amplitude of librational reorientation as temperature increases along with a smaller contribution from an analogous change in the inertial amplitude.

3.5.2 Contributions to the $C_2(t)$ Temperature Dependence

A different, but related, approach is to evaluate the temperature dependence of the $C_2(t)$ reorientational TCF at a particular time, with the aim to separate the contributions of librational and H-bond breaking and making dynamics by choosing shorter or longer times, respectively.^{8,128} The direct calculation of $\partial C_2(t)/\partial\beta = -C_{2,H}(t)$ along with the decomposition into terms associated with the three timescales given in Eq. (3.10) permits a direct analysis of the TCF derivative. The contributions thus separated into inertial, librational, and H-bond exchange (τ_2) motions are compared to the total $C_{2,H}(t)$ in Fig. 3.4.

It is clear from Fig. 3.4 that the inertial dynamics have a small, short-lived contribution to the temperature dependence of $C_2(t)$. Indeed, the τ_{iner} term is essentially zero for times longer than ~ 50 fs. The librational contribution extends to longer times – it is negligible after ~ 2.5 ps – beyond which the τ_2 term is the only contributor to $\partial C_2(t)/\partial\beta$. As can be seen in the inset of Fig. 3.4, the τ_{lib} and τ_2 terms have opposite signs for times less than 0.2 ps. Thus $\partial C_2(t)/\partial\beta$ evaluated at times shorter than this involves cancellation between contributions due to the two motions, while longer times up to ~ 2.5 ps involve the addition of τ_{lib} and τ_2 components, and beyond this the derivative is determined only by H-bond exchange dynamics.

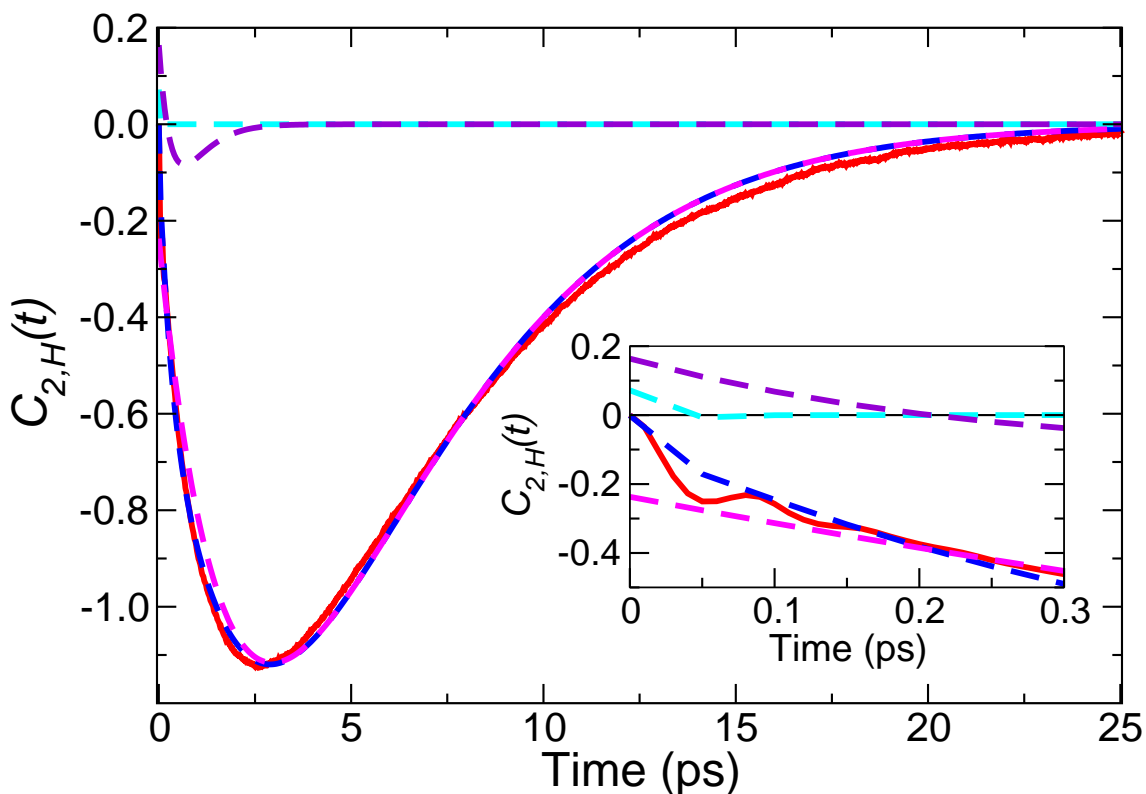


Figure 3.4: The derivative TCF, $C_{2,H}(t)$, (red solid) is compared to its fit, Eq. (3.10), (blue dashed) and the contributions to the fit from the inertial (cyan dashed), librational (violet dashed), and H-bond breaking and making (magenta dashed). The inset shows an expanded view of the the short-time behavior.

It is interesting then to consider what determines the TCF derivative at a short time, *e.g.*, $t^* = 100$ fs. Moilanen *et al.* previously measured $C_2(t^*)$ using IR-PP as a function of the pump frequency and temperature for HOD in H_2O .⁸ They found that $C_2(t^*)$ decreased linearly with the ω_{01} OD vibrational frequency at all temperatures but with different slopes such that at lower frequencies (stronger H-bonds) $C_2(t^*)$ increased with T and at higher frequencies (weaker H-bonds) it decreased with T . The present results, which do not resolve different vibrational frequencies, find $\partial C_2(t)/\partial\beta > 0$ such that $\partial C_2(t)/\partial T$ is negative, consistent with the higher frequency results of Moilanen *et al.* Moreover, we can see from Fig. 3.2 that the sign of $C_{2,H}(t)$ is the same for all

times and thus the qualitative temperature dependence, *i.e.*, sign of $\partial C_2(t)/\partial T$, is the independent of the time at which it is evaluated.

The decomposition of $\partial C_2(t)/\partial \beta|_{t^*}$ for $t^* = 100$ fs can be seen directly from the inset of Fig. 3.4. As noted, the inertial dynamics make a negligible contribution to the total derivative $C_{2,H}(t^*) = -0.245$ kcal/mol. The dominant term is that associated with H-bond exchanges, -0.31 kcal/mol, which is only partially cancelled by the librational component of 0.07 kcal/mol. This result is somewhat surprising because the short-time dynamics of $C_2(t)$ are dominated by the inertial and librational dynamics. However, the larger amplitude and stronger temperature dependence of τ_2 (see Table 3.1) lead to this result *via* Eq. (3.10). Indeed, the results in Fig. 3.4 show that the H-bond exchange contribution is the dominant one at all times, even at $t = 0$. Given the results of Moilanen *et al.*,⁸ it will be interesting to revisit this analysis as a function of the OH (or OD) vibrational frequency.

3.5.3 Activation Energy Decomposition

Additional insight can be obtained by examination of the different energetic contributions to the activation energies. We previously showed that the weighted reorientational TCF, Eq. (3.9), and thus the activation energy, can be rigorously decomposed into contributions due to different kinetic energy and interaction terms.⁵⁸ Namely, the fluctuation in the energy can be written as

$$\delta H(0) = \delta KE(0) + \delta V_{LJ}(0) + \delta V_{Coul}(0), \quad (3.13)$$

where KE is the kinetic energy, V_{LJ} the Lennard-Jones potential, and V_{Coul} the Coulombic interactions. Then,

$$C_{2,H}(t) = C_{2,KE}(t) + C_{2,LJ}(t) + C_{2,Coul}(t), \quad (3.14)$$

where, *e.g.*, $C_{2,LJ}(t) = \langle \delta V_{LJ}(0) P_2[\vec{e}(0) \cdot \vec{e}(t)] \rangle$. In this way, the total activation energy for each timescale and $\langle \tau_2 \rangle$ can be written in terms of the contribution from each component of the Hamiltonian.

It is useful to consider the meaning of these contributions. From Eq. (3.9) it can be seen that $\partial C_2(t)/\partial\beta$ is given by the correlation of the energy fluctuation at $t = 0$ with $P_2[\vec{e}(0) \cdot \vec{e}(t)]$, *i.e.*, how the reorientational dynamics changes when the system has an energy that is greater than ($\delta H > 0$) or less than ($\delta H < 0$) the average value. This same interpretation can be applied to the additive contributions to the total energy. Thus, $C_{2,LJ}(t)$ is a measure of how the reorientational dynamics changes when the system has a total Lennard-Jones interaction energy that is greater than ($\delta V_{LJ} > 0$) or less than ($\delta V_{LJ} < 0$) its average value.

This is consistent with the interpretation of the activation energy by Tolman¹⁸ nearly a century ago, which was subsequently expanded upon by Truhlar.¹⁹ In the context of classical trajectories it can be briefly stated as the activation energy is the average energy of all reactive trajectories minus the average energy of the reactants. For the process of OH reorientation considered here, the “reactant” energy is just the average equilibrium energy. Then, for example, the contribution to E_a from the kinetic energy, $E_{a,KE}$ is the difference in the average *kinetic energy* of all reactive trajectories minus the average *kinetic energy* of the reactants. It is important to note that this is not an indication that the kinetic energy contributes to the barrier, but rather that $E_{a,KE} > 0$ means that increasing the kinetic energy speeds up the process, *i.e.*, assists in surmounting the barrier.

Another way of understanding this decomposition is to generalize the Boltzmann factor in the phase space average (trace) and partition function in Eq. (3.8) as $\exp\{-\beta_{KE}KE - \beta_{LJ}V_{LJ} - \beta_{Coul}V_{Coul}\}$, such that the distribution of each energy term is governed by a separate temperature. In this context then, for example, $C_{2,LJ}(t) = -\partial C_2(t)/\partial\beta_{LJ}$ which thus gives the contribution to the activation energy due to changing the Lennard-Jones “temperature” independent of that associated with the other terms in the Hamiltonian.

This analysis gives otherwise unavailable mechanistic insight into the origins of the activation energy; the component TCFs defined in Eq. (3.14) are plotted in Fig. 3.5. In our previous work we did not observe a difference between the TCF weighted by the total energy, $C_{2,H}(t)$ and the contribution due to the electrostatic interactions, $C_{2,Coul}(t)$ outside the statistical uncertainty. The improved sampling in the present work does resolve a difference between these two weighted

correlation functions and shows a deeper minimum in $C_{2,Coul}(t)$ compared to the total derivative TCF. The results are otherwise essentially the same as previously observed.⁵⁸ Namely, the electrostatic interactions are the dominant contribution to the activation energy, which is anticipated by the extended-jump model for OH reorientation.^{85,88} The kinetic energy and Lennard-Jones contributions largely cancel each other, with the former giving a positive contribution to the activation energies and the latter a negative. In other words, larger instantaneous Lennard-Jones interaction energies lead to slower reorientational dynamics, in contrast to the Coulombic interaction and kinetic energies. The reason for this is not yet clear, but it deserves further study.

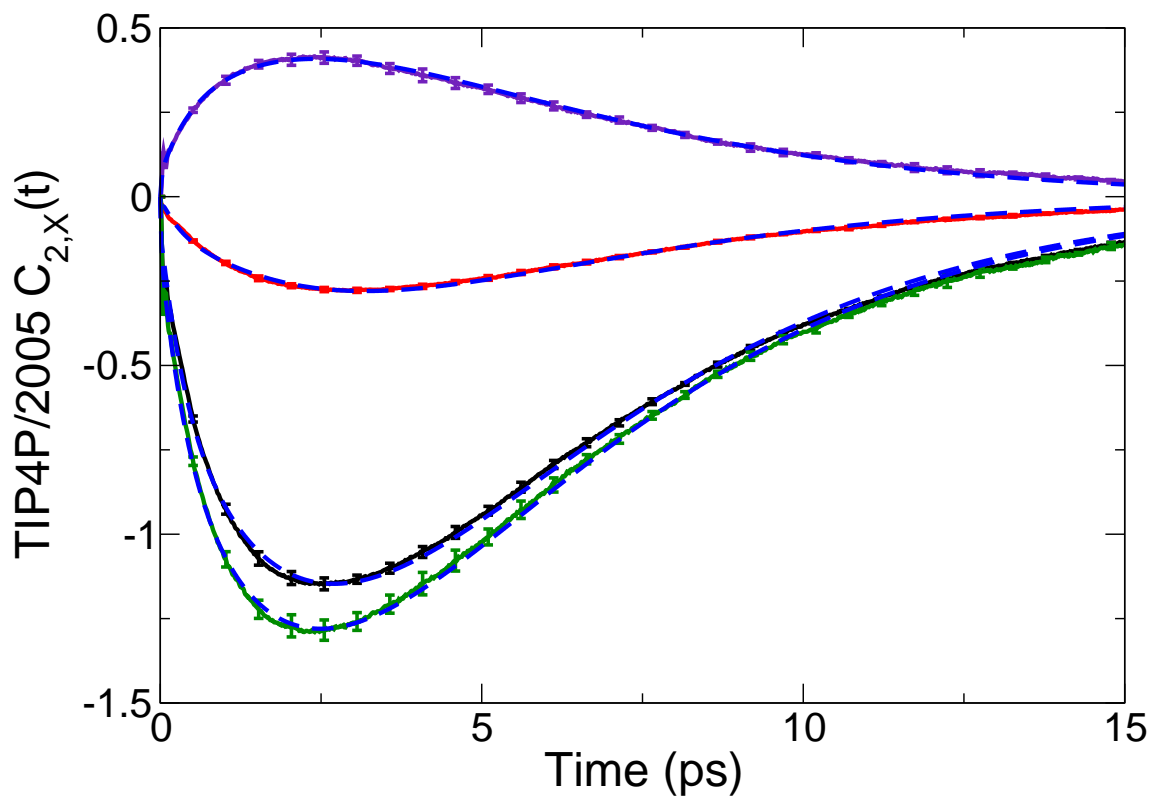


Figure 3.5: The reorientation correlation function $C_2(t)$ weighted by the total energy (black), Lennard-Jones potential energy (indigo), electrostatic potential energy (green), and kinetic energy (red). Fits for each correlation function are included as blue dashed lines.

The contribution of each energetic contribution to the activation energies, of each τ_α and $\langle \tau_2 \rangle$, is

Table 3.5: Activation energy decomposition, in kcal/mol, calculated from the *NPT* ensemble at 298.15 K.

| Value | τ_{iner} | τ_{lib} | τ_2 | $\langle \tau_2 \rangle$ |
|--------------|--------------------|---------------------|--------------------|--------------------------|
| $E_{a,Tot}$ | 0.64 ₁₂ | 1.86 ₂₈ | 4.28 ₁₀ | 4.58 ₁₁ |
| $E_{a,LJ}$ | 0.05 ₁₆ | -0.37 ₂₂ | -1.31 ₆ | -1.54 ₇ |
| $E_{a,Coul}$ | 0.21 ₂₈ | 1.54 ₄₀ | 4.38 ₁₃ | 4.98 ₁₄ |
| $E_{a,KE}$ | 0.37 ₁₀ | 0.70 ₁₀ | 1.21 ₄ | 1.14 ₄ |

obtained by fitting each weighted TCF using Eq. (3.10). The results of this analysis are presented in Table 3.5 and the fits are shown with the calculated TCFs in Fig. 3.5. As expected from the above discussion, the Coulombic interactions give the largest contribution to the activation energy of the τ_{lib} and τ_2 individual timescales in $C_2(t)$ as well as $\langle \tau_2 \rangle$. In contrast, the inertial timescale is dominated by the kinetic energy and also does not exhibit any cancellation between the Lennard-Jones and kinetic energy terms.

The decomposition can be used to examine the origin of the difference between E_{a,τ_2} and $E_{a,\langle \tau_2 \rangle}$. It is notable that each energetic term shows a statistically significant difference between the contribution to the τ_2 and $\langle \tau_2 \rangle$ activation energies. In particular, the Coulombic term is 0.6 kcal/mol larger for $E_{a,\langle \tau_2 \rangle}$ than E_{a,τ_2} . This effect is partially cancelled by the -0.07 and -0.23 kcal/mol differences due to the kinetic energy and Lennard-Jones interactions, respectively. The breakdown of the Coulombic contribution to $C_{2,H}(t)$ into the terms associated with the temperature-dependence of the amplitude and the individual timescale activation energies (not shown) are consistent with those of the total given in Table 3.4. Namely, there are minimal effects due to the inertial and librational contributions and $E_{a,\langle \tau_2 \rangle}$ is larger than $E_{a,\tau_2,Coul}$ due to the contribution of $\partial A_{2,Coul}/\partial \beta$.

3.6 Conclusions

The results of the present simulations show a difference between the activation energy for OH re-orientational dynamics in water measured by pump-probe anisotropy and that obtained in NMR spin-echo experiments. The IR-PP experiments obtain the longest timescale decay, τ_2 , associated with H-bond making and breaking, and its corresponding activation energy. However, NMR mea-

measurements give the average time, $\langle \tau_2 \rangle$. While the $\langle \tau_2 \rangle$ activation energy is dominated by that of τ_2 , it also has a significant contribution due to the change in the τ_2 amplitude with temperature (at the expense of the inertial and librational dynamics amplitudes).

The difference between E_{a,τ_2} and $E_{a,\langle \tau_2 \rangle}$ is calculated as 0.3 kcal/mol for the TIP4P/2005 water model at 298.15 K and 1 bar. This indicates that experimental measurements will need to resolve the τ_2 and $\langle \tau_2 \rangle$ activation energies to uncertainties of ~ 0.15 kcal/mol in order to distinguish the two. The current simulations use the fluctuation method to directly calculate the activation energies from simulations at a single temperature^{31,58,59} with extensive sampling to obtain precise values. A traditional Arrhenius analysis, which gives consistent results, shows that this direct approach yields the activation energy at the particular temperature of interest without invoking a finite difference numerical approximation for the temperature derivative. The non-Arrhenius behavior of the water reorientational dynamics¹⁰⁸ means that the activation energy from an Arrhenius analysis is more accurately determined from a small temperature range.

It remains to be seen if experiments can achieve the precision required to distinguish the τ_2 and $\langle \tau_2 \rangle$ activation energies. Such a result would be an important benchmark for water models, particularly those that aim to describe the water dynamics over a range of temperatures. Moreover, the analysis presented here indicates that an accurate difference in E_{a,τ_2} and $E_{a,\langle \tau_2 \rangle}$ can be used to quantitatively determine how the τ_2 timescale amplitude in $C_2(t)$ changes with temperature.

The present approach can be straightforwardly extended to examine activation energies for reorientation, or other dynamical timescales, in more complex environments. Both IR-PP and NMR measurements have been (or can be) applied to characterize water reorientational dynamics in systems from concentrated ionic solutions^{73,129–132} to reverse micelles.^{128,133,134,134,135} In many such cases, additional timescales appear in the reorientational TCF due to the presence of an interface and the temperature dependence of these new decay times as well as that of their amplitudes should provide new molecular-level insight into the dynamics.

Chapter 4

Activation Energies and the Extended Jump Model: How Temperature Affects Reorientation and Hydrogen-Bond Exchange Dynamics in Water

4.1 Introduction

In liquid water at ambient conditions, a broad range of dynamical processes have been found to exhibit similar temperature dependences. These include, for example, molecular reorientation measured by NMR^{52,137} and femtosecond infrared spectroscopies,^{7,105,138} vibrational frequency dephasing,^{105,138,139} dielectric relaxation,¹⁴⁰ viscosity,^{3,4,141,142} and structural dynamics probed by quasi-elastic neutron scattering.^{143,144} The comparable activation energies measured for these processes imply that the associated energy barriers have similar heights and could thus suggest that they share a common rate-determining elementary step. Hydrogen-bond (H-bond) exchanges are likely this common underlying mechanism, as they have already been shown to be the major reorientation pathway.⁸⁸

However, an important limitation in establishing activation energies in water arises from the markedly non-Arrhenius behavior at ambient conditions.^{6,141,145,146} The traditional determination from a series of measurements at different temperatures is thus ambiguous and sensitively depends on the chosen temperature interval. This issue was recently addressed by a fluctuation theory

Adapted with the permission of Zeke A. Piskulich, Damien Laage, and Ward H. Thompson and AIP Publishing from *J. Chem. Phys.* **153**, 174110 (2020).¹³⁶

approach for dynamics,^{13,31,44,50,58,59,147} which permits the calculation of activation energies from molecular dynamics simulations at a single temperature. This method further provides important insight in the activation energy components, and has been successfully applied to a broad range of dynamical processes in water.

Here, we use the fluctuation theory method to identify the molecular origin of the reorientation activation energy and its connection to hydrogen-bond exchange dynamics. In contrast to the long-held Debye diffusion picture, water reorientation was shown⁸⁸ to be mostly caused by sudden, large-amplitude angular jumps during hydrogen-bond exchanges, along with the slower tumbling of intact hydrogen-bonds, and the extended jump model (EJM) was proposed to connect this mechanism to the water reorientation time. However, while hydrogen-bond jumps have been characterized over a broad temperature range,¹⁰⁸ the EJM has so far mostly been used at ambient temperature. Our present goal is therefore two-fold: 1) we will first assess the EJM's ability to describe the reorientation time temperature dependence and activation energy, and 2) we will use this model to gain a molecular insight in the activation energy's origin as well as its connection with H-bond exchanges.

The remainder of the Chapter is organized as follows. The details of OH reorientation and its description within the extended jump model are presented in Sec. 6.2 with particular attention on the associated activation energies. The details of the molecular dynamics simulations that are used to determine the timescales and activation energies are given in Sec. 4.3. The OH reorientation timescales and their activation energies are presented in Sec. 4.4.1. These are compared quantitatively with the corresponding results for the H-bond jump time, the distribution of jump angles, and the frame reorientation time in the remainder of Sec. 4.4 and the fidelity of the EJM is discussed quantitatively. Finally, conclusions are offered in Sec. 4.5.

4.2 Theory

4.2.1 Water OH Group Reorientation

Water reorientational dynamics are frequently described in terms of the time correlation function (TCF),

$$C_n(t) = \langle P_n[\vec{e}_{OH}(0) \cdot \vec{e}_{OH}(t)] \rangle, \quad (4.1)$$

where P_n is the n^{th} -order Legendre polynomial and $\vec{e}_{OH}(t)$ is the unit vector along the OH bond undergoing reorientation (Figure 4.1). The second-order TCF $C_2(t)$ is accessible experimentally *via* polarization-resolved infrared pump-probe measurements, which under most conditions probe the anisotropy decay $r(t) = 0.4 C_2(t)$.^{71,72} As we have shown previously, this reorientation has a different temperature dependence than that of the integrated reorientation time, $\langle \tau_2 \rangle = \int_0^\infty C_n(t) dt$, which is typically measured in nuclear magnetic resonance experiments.⁴⁴

It is useful, in examining the mechanism(s) underlying the reorientational dynamics, to compare the behavior for different orders, n , of the TCFs and to determine the associated reorientation times. For example, a characteristic feature of systems obeying Debye rotational diffusion is that reorientation times are governed by the rotational diffusion coefficient D_R ,

$$\tau_n^{\text{Debye}} = \frac{1}{n(n+1)D_R}, \quad (4.2)$$

which leads to direct relationships between the reorientational timescales obtained for different orders. That is, $\tau_1^{\text{Debye}} / \tau_2^{\text{Debye}} = 3$ and $\tau_1^{\text{Debye}} / \tau_3^{\text{Debye}} = 6$.

The OH reorientational dynamics in water captured in $C_n(t)$ exhibit three timescales. The fastest of these (tens of fs) is associated with inertial, or ballistic, motion and is followed by slower dynamics (hundreds of fs) due to librational motion of the OH group within the intact H-bond. The longest timescale is 2.5-2.6 ps,^{8,104,114} and is determined by H-bond dynamics. Because of this behavior, $C_n(t)$ can be fit using a sum of three exponentials,

$$C_n(t) = \sum_{\alpha} A_{\alpha,n} e^{-k_{\alpha,n} t}, \quad (4.3)$$

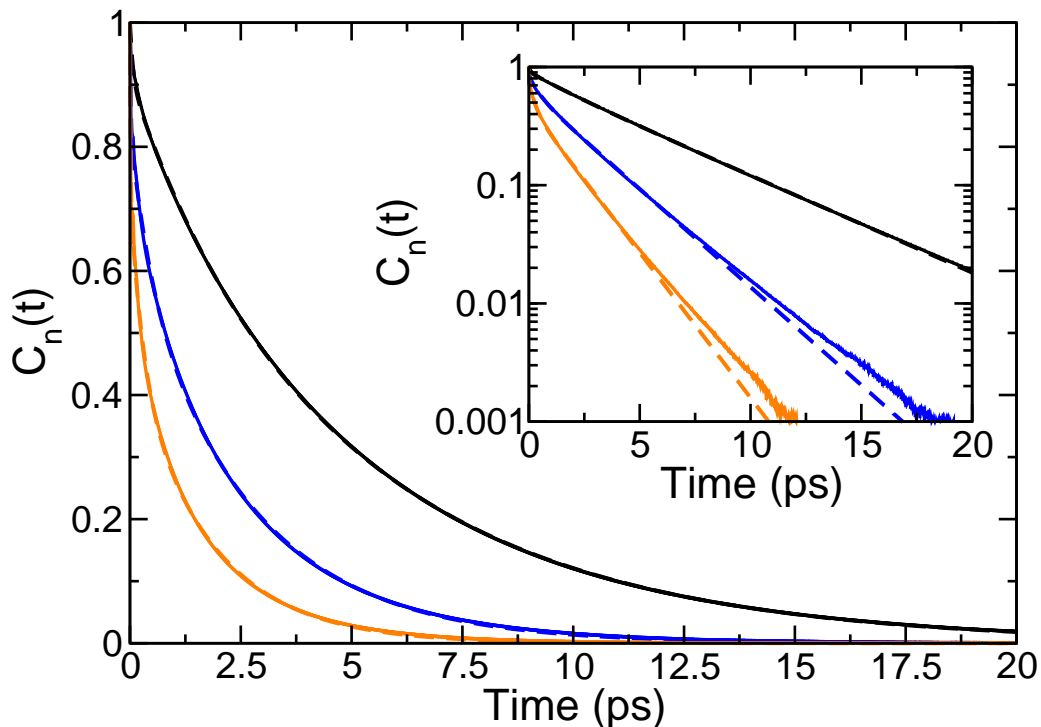


Figure 4.1: Water OH group reorientational TCFs, Eq. (4.1), at 298.15 K for $n = 1$ (black), 2 (blue), and 3 (orange); tri-exponential fits using Eq. (4.3) are shown as dashed lines of the same color. Inset shows the results on a semi-log plot.

where $\alpha = \textit{inertial}$, $\textit{librational}$, and \textit{Hbond} . The last is associated with H-bond breaking and making; it is this reorientational dynamics that the EJM describes and which will thus be the focus of the remainder of this Chapter. For simplicity, we will henceforth omit the “ \textit{Hbond} ” and refer to this rate constant as $k_n = 1/\tau_n$, where τ_n is the corresponding timescale. The $A_{\alpha,n}$ are the amplitudes associated with the three timescales, which for the longest timescale will be referred to as A_n .

4.2.2 Extended Jump Model for Water Reorientation

It is now well-established that water reorientation is not a rotationally diffusive process, but modifications to the overall picture of the mechanism came in steps. Starting from the Debye diffusion picture, which assumes that reorientation proceeds through a succession of infinitesimally small amplitude angular jumps, Ivanov extended this model to describe reorientation through (uncorre-

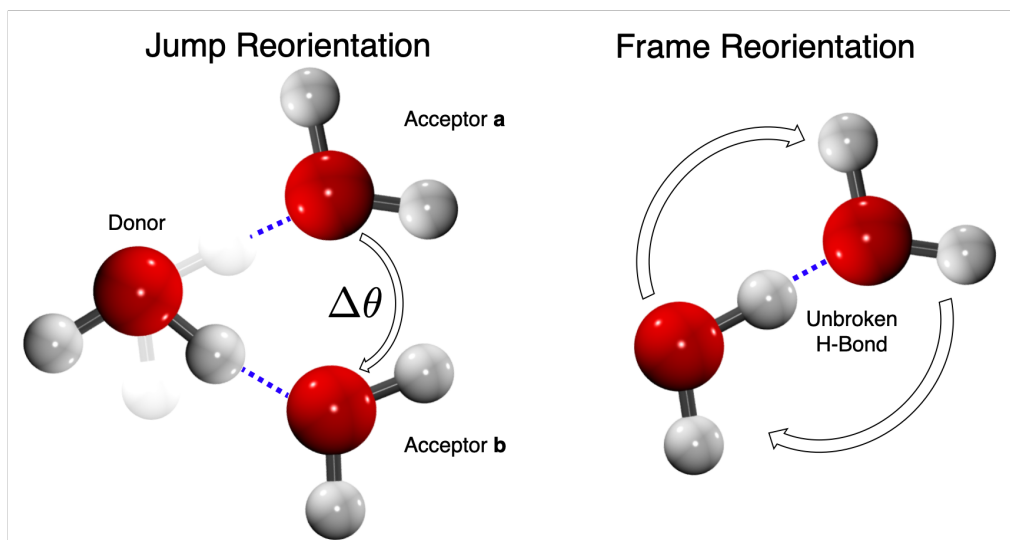


Figure 4.2: Schematic illustration of the two components of the extended jump model for OH reorientation: Large-amplitude angular jumps associated with the exchange of H-bond acceptors (left) and the frame reorientation of the intact H-bond pair between jumps (right).

lated) finite amplitude angular jumps,¹¹¹ but did not apply the resulting theory to any molecular system. The Ivanov model further assumed that the reorientation axis remained fixed and underwent no reorientation between the angular jumps. More recently, Laage and Hynes demonstrated, by analysis of molecular dynamics trajectories, that OH bonds in liquid water *do* reorient through finite amplitude jumps associated with the exchange of H-bond acceptors. The average angle spanned in such jumps is around 70° and this represents the dominant contribution to OH reorientation, but it is not the sole one. They proposed the extended jump model^{73,85,88} (EJM) that included both the H-bond jumps and an additional contribution associated with the reorientation of the intact H-bond in between H-bond exchanges, which is referred to as “frame” reorientation.

The EJM has been used to describe how OH reorientation in water is affected by ions^{73,129,148,149} as well as hydrophobic¹⁵⁰ and amphiphilic¹⁵¹ solutes. In addition, the EJM has been used to gain insight into water reorientational dynamics at interfaces that range from extended aqueous surfaces^{152,153} to biomolecular hydration shells⁸⁹ and confining frameworks including zeolites,¹⁵⁴ reverse micelles,¹³⁵ and mesoporous silica.^{154,155} The EJM has also been extended to describe OH reorientation in alcohols.^{31,86}

The EJM describes the longest OH reorientation timescale as a combination of large-amplitude angular jumps associated with exchange of H-bond acceptor and the frame reorientation of the individual intact H-bond pair, as illustrated in Fig. 4.2. Mathematically, this gives the n^{th} -order reorientational time, τ_n , as

$$\frac{1}{\tau_n} = \frac{1}{\tau_n^{\text{jump}}} + \frac{1}{\tau_n^{\text{frame}}}, \quad (4.4)$$

where τ_n^{jump} and τ_n^{frame} are the jump and frame contributions, defined in greater detail below. Equivalently, this can be written in terms of effective rate constants associated with each timescale,

$$k_n = k_n^{\text{jump}} + k_n^{\text{frame}}, \quad (4.5)$$

where $k_n^X = 1/\tau_n^X$ for each timescale in Eq. (4.4).

4.2.3 Activation Energies and the Fluctuation Theory for Dynamics

The water OH reorientation activation energy is

$$E_{a,n} = -\frac{\partial \ln(1/\tau_n)}{\partial \beta}, \quad (4.6)$$

where $\beta = 1/k_B T$. Within the EJM, $E_{a,n}$ is related to the jump and frame reorientation activation energies *via* Eq. (4.5) as

$$\begin{aligned} E_{a,n} &= \frac{k_n^{\text{jump}}}{k_n} E_{a,n}^{\text{jump}} + \frac{k_n^{\text{frame}}}{k_n} E_{a,n}^{\text{frame}} \\ &= \frac{\tau_n}{\tau_n^{\text{jump}}} E_{a,n}^{\text{jump}} + \frac{\tau_n}{\tau_n^{\text{frame}}} E_{a,n}^{\text{frame}} \end{aligned} \quad (4.7)$$

This contrasts with the activation energies expected within the Debye model Eq. (4.2),

$$E_{a,n}^{\text{Debye}} = -\frac{\partial \ln D_R}{\partial \beta}, \quad (4.8)$$

which are explicitly independent of the order of the TCF.

While the ratios of the reorientation timescales have frequently been used to examine the mechanism of reorientation in liquids,^{85,86,88,114,156–158} the behavior of $E_{\alpha,n}$ on the order n of the TCF has not previously been explored, nor have the relative contributions of the jump and frame reorientations. The following sections lay out a simple technique for calculating each term in Eq. (4.7) using fluctuation theory for dynamics and address these issues.

Fluctuation theory for dynamics yields the analytical derivative of a rate constant or timescale with respect to β rather than the numerical derivative obtained from an Arrhenius analysis. It is thus particularly advantageous when applied to systems that deviate from the Arrhenius relation, as do many dynamical properties of liquid water. Within this framework, we have previously shown that the derivative of Eq. (4.1) with respect to β can be expressed as a new TCF,

$$\frac{\partial C_n(t)}{\partial \beta} = -\langle \delta H(0) P_n[\vec{e}_{OH}(0) \cdot \vec{e}_{OH}(t)] \rangle \equiv -C_{n,H}(t), \quad (4.9)$$

where $\delta H(0) = H(0) - \langle H \rangle$ is the fluctuation in energy. This TCF, like $C_n(t)$ itself, can be evaluated from simulations at a single temperature, avoiding the necessity for an Arrhenius analysis. In other words, Eq. (4.9) gives the analytical derivative of the TCF with respect to temperature in contrast to the numerical derivative obtained from an Arrhenius plot.

The derivative TCF given in Eq. (4.9) can be fit by taking the derivative of Eq. (4.3) with respect to β ,

$$\frac{\partial C_n(t)}{\partial \beta} = \sum_{\alpha} \left[\frac{\partial A_{\alpha,n}}{\partial \beta} - \frac{\partial k_{\alpha,n}}{\partial \beta} A_{\alpha,n} t \right] e^{-k_{\alpha,n} t}, \quad (4.10)$$

where $A_{\alpha,n}$ and $k_{\alpha,n}$ are now constants calculated from the fit of Eq. (4.3) and $\partial A_{\alpha,n}/\partial \beta$ and $\partial k_{\alpha,n}/\partial \beta$ are fitting parameters. The latter can be used to determine the activation energy associated with each timescale as $E_{\alpha,n} = -k_{\alpha,n}^{-1} (\partial k_{\alpha,n}/\partial \beta)$, which is equivalent to Eq. (4.6).¹⁵⁹

A key advantage of the fluctuation theory approach is the additional mechanistic insight it provides. Specifically, the total system energy fluctuation can be decomposed into physically meaningful components, which can be used to determine the contributions to the activation energy for each.^{13,44,50,58,147,160} For example, in the case of the fixed-charge classical MD simulations used

in the present work, it is natural to divide the energy fluctuation as

$$\delta H(0) = \delta KE(0) + \delta V_{LJ}(0) + \delta V_{Coul}(0), \quad (4.11)$$

where KE is the total kinetic energy and V_{LJ} and V_{Coul} are the total Lennard-Jones and Coulombic potential energies. Using this in Eq. (4.9) gives a rigorous decomposition of $\partial C_n(t)/\partial\beta$ into contributions from these components of the energy. By fitting each of these derivative contributions with a function of the form of Eq. (4.10), we can obtain the activation energy components

$$E_{a,n} = E_{a,n}^{KE} + E_{a,n}^{LJ} + E_{a,n}^{Coul}. \quad (4.12)$$

Here, for example, $E_{a,n}^{Coul}$ comes from fitting the TCF in Eq. (4.9) with $\delta H(0)$ replaced by $\delta V_{Coul}(0)$.

The interpretation of this result is best understood in the context of Tolman's analysis of the activation energy.^{13,18–20} Tolman showed that the activation energy for a chemical reaction is the average energy of reacting species minus the average energy of reactants, $E_a = \langle E \rangle_{reacting} - \langle E \rangle_{reactant}$. In this context, one can view, for example, the kinetic energy component of the activation energy as the average kinetic energy of reacting species minus the average kinetic energy of reactants. In other words, the activation energy components are measures of how energy in different motions or interactions helps (or hinders) passage over the barrier for the process. This is how Eq. (4.12) can be understood to provide mechanistic information, information which is not available by other methods. This activation energy decomposition gives an even more detailed test of the EJM as will be discussed below.

4.2.4 Jump Reorientation

The contribution to OH reorientation due to H-bond exchanges involves two factors. The first is the jump time, $\tau_0 = 1/k_0$, which is the inverse rate constant for the "reaction" in which an OH switches from one H-bond acceptor to another. This timescale, unlike the others discussed in this study, is independent of the order n . The second is the effect of the "jump angle," $\Delta\theta$, which is

defined as the effective angle traversed (in a lab-fixed frame) by the OH vector in the process of the exchange of H-bond acceptors.^{85,88} This angle is large, $\sim 70^\circ$ on average. The overall effect of the jumps on the reorientational TCF depends on n and is given by

$$k_n^{jump} = k_0 \bar{w}_n. \quad (4.13)$$

Here, \bar{w}_n is the average value of the weighting function for the jump angle, which was derived by Ivanov,¹¹¹

$$w_n(\Delta\theta) = 1 - \frac{\sin[(2n+1)\Delta\theta/2]}{(2n+1)\sin[\Delta\theta/2]}. \quad (4.14)$$

The average value is obtained by averaging over the distribution of jump angles, $P(\Delta\theta)$,

$$\bar{w}_n = \int_0^\pi w_n(\Delta\theta) P(\Delta\theta) d\Delta\theta. \quad (4.15)$$

Mathematically, the jump angle can be taken as the $O_a \cdots O_d \cdots O_b$ angle at the jump transition state where a and b indicate the original and new H-bond acceptors, respectively, and d the H-bond donor. In practice it is sufficient to calculate this angle at the first timestep at which a new ($O_d - H_d \cdots O_b$) H-bond is formed. Though $w_n(\Delta\theta)$ does not depend on temperature, its average value, \bar{w}_n , does because it involves the jump angle distribution, $P(\Delta\theta)$.

The jump time τ_0 , and associated rate constant k_0 , can be calculated using the stable-states picture³³ for the H-bond exchange process. Specifically, the "side-side" time correlation function,

$$C_{ab}(t) = \langle n_a(0) n_b(t) \rangle, \quad (4.16)$$

is calculated, where n_a (n_b) is equal to 1 if the OH of interest is H-bonded to molecule a (b), and zero otherwise. Absorbing boundary conditions are used such that once an exchange occurs, no further exchanges are considered. The function, $1 - C_{ab}(t)$ then decays at longer times with the timescale τ_0 ; in practice, it is fit to a double exponential to account for transient dynamics at early times.¹⁶¹ In this work, we have defined H-bonds by strict geometric criteria: $R_{O_d-O_a} \leq 3.1 \text{ \AA}$,

$r_{H_d-O_a} \leq 2.0 \text{ \AA}$, and $\alpha_{H_d-O_d-O_a} \leq 20^\circ$.

We have previously shown that the derivative of $1 - C_{ab}(t)$ with respect to β is given by³¹

$$\frac{\partial[1 - C_{ab}(t)]}{\partial\beta} = \langle \delta H(0) n_a(0) n_b(t) \rangle \equiv C_{ab,H}(t). \quad (4.17)$$

In that work, we demonstrated that the derivative correlation function peaks at a time of τ_0 and at a height of $E_{a,0}/e$ (where $E_{a,0}$ is the jump time activation energy and e is Euler's number) if the decay is assumed to be single exponential. Here, we adopt the more accurate approach of a double exponential fit for the decay and hence for the derivative TCF in Eq. (4.17), analogous to Eq. (4.10), which is then used to determine $\partial k_0/\partial\beta$.

Because both k_0 and \bar{w}_n depend on temperature, the derivative of k_n^{jump} with respect to β is

$$\frac{\partial k_n^{jump}}{\partial\beta} = \frac{\partial k_0}{\partial\beta} \bar{w}_n + k_0 \frac{\partial \bar{w}_n}{\partial\beta}. \quad (4.18)$$

The jump contribution activation energy can then be calculated by dividing both sides by $k_n^{jump} = k_0 \bar{w}_n$ and changing the sign, yielding

$$\begin{aligned} E_{a,n}^{jump} &= -\frac{1}{k_0} \frac{\partial k_0}{\partial\beta} - \frac{1}{\bar{w}_n} \frac{\partial \bar{w}_n}{\partial\beta} \\ &\equiv E_{a,0} + E_{a,n}^{\Delta\theta}. \end{aligned} \quad (4.19)$$

Thus, it is the sum of the jump time activation energy, $E_{a,0}$, (which is not to be confused with the jump reorientation contribution activation energy, $E_{a,n}^{jump}$, which includes the jump angle temperature dependence) and the activation energy associated with the jump angle weighting, $E_{a,n}^{\Delta\theta}$. Note that only the latter depends on the order n of the TCF.

The derivative of the average jump angle weighting, Eq. (4.15), can be taken with respect to β to get

$$\frac{\partial \bar{w}_n}{\partial\beta} = \int_0^\pi w_n(\Delta\theta) \frac{\partial P(\Delta\theta)}{\partial\beta} d\Delta\theta, \quad (4.20)$$

where

$$\partial P(\Delta\theta)/\partial\beta = -\langle\delta H(\tau^*)\delta[\Delta\theta - \Delta\tilde{\theta}(\mathbf{Q})]\rangle = -P_H(\Delta\theta), \quad (4.21)$$

is the derivative of the jump angle distribution. Here the energy fluctuation is evaluated at the time of each individual jump (τ^*). For a given *NVE* trajectory, $\delta H(\tau^*) = \delta H(0)$, but the same is not true for the energetic components, *e.g.*, $\delta KE(\tau^*) \neq \delta KE(0)$.

4.2.5 Frame Reorientation

The frame reorientation time is determined by calculating the reorientational TCF for the $O_d \cdots O_a$ vector, which provides the local frame reorientation between successive jumps,

$$C_n^{frame}(t) = \langle P_n[\vec{e}_{OO}(0) \cdot \vec{e}_{OO}(t)] \rangle_{Hbond}, \quad (4.22)$$

where the *Hbond* subscript on the average indicates that only molecules that have not switched H-bond partners between times 0 and t are included in the average. This leads to a time-dependent normalization for the TCF that is equal to the H-bond survival probability; this limits the times over which the TCF can be accurately calculated. The decay of $C_n^{frame}(t)$ is well described by a bi-exponential function with the longer timescale equal to the frame time, τ_n^{frame} .

The derivative of $C_n^{frame}(t)$ is completely analogous to that for OH reorientation given in Eq. (4.9) and can be fit through an expression of the form given in Eq. (4.10) with a sum over only two exponentials. In this approach, the frame activation energy,

$$E_{a,n}^{frame} = -\frac{\partial \ln(1/\tau_n^{frame})}{\partial\beta} \quad (4.23)$$

can then be extracted directly from the fitting of $C_n^{frame}(t)$ and its derivative TCF.

4.3 Methods

The MD simulations were carried out using the Large-scale Atomic/Molecular Massively Parallel Simulator (LAMMPS).⁸¹ A fully-periodic simulation cell of side length 21.725311 Å was filled with 343 SPC/E water molecules,⁴² corresponding to the 298.15 K experimental density of 0.997 g/cm³. All simulations used a timestep of 1 fs, and the electrostatics from all simulations used the Particle-Particle-Particle Mesh Ewald summation method^{119,120} with a tolerance parameter of 1×10^{-4} . The SHAKE algorithm was used to hold the water bonds and angle rigid, the tolerance parameter was 1×10^{-4} . One 50 ns *NVT* trajectory was propagated with positions and momenta saved every 1 ps, yielding 50,000 configurations. The temperature of the simulation was 298.15 K, with initial velocities selected from the Maxwell-Boltzmann distribution and the initial configuration generated by PACKMOL.¹⁶² The Nosé-Hoover thermostat damping parameter was 100 fs.^{83,84}

From each saved configuration, a 50 ps *NVE* simulation was run, from which the dynamical properties were evaluated. Configurations were saved every 10 fs, leading to 5000 total configurations per *NVE* trajectory; this is more than sufficient to resolve both the initial decay dynamics and the jump angle distribution. As has been noted in our prior works, each *NVE* trajectory has a different fluctuation in energy, $\delta H(0)$, from the average energy of the long trajectory. From each of these trajectories the OH reorientation, jump, and frame TCFs are calculated along with the jump angle distribution and each is also weighted by the energy fluctuations to obtain the contribution to their derivative with respect to β as described in Sec. 4.2. These individual correlation functions are then averaged across all the *NVE* trajectories. All reported uncertainties correspond to a 95% confidence interval according to the Student's *t*-distribution¹²² over an average of 10 blocks (each block representing 5,000 *NVE* trajectories).

| Order | τ_0 | \bar{w}_n | τ_n^{jump} | τ_n^{frame} | τ_n | τ_n^{EJM} |
|---------|--------------------|---------------------|--------------------|---------------------|--------------------|--------------------|
| $n = 1$ | 3.141 ₂ | 0.4512 ₂ | 6.961 ₄ | 16.91 ₁₃ | 5.29 ₃ | 4.93 ₂ |
| $n = 2$ | 3.141 ₂ | 0.8819 ₁ | 3.562 ₂ | 5.97 ₃ | 2.618 ₇ | 2.231 ₅ |
| $n = 3$ | 3.141 ₂ | 1.0758 ₁ | 2.920 ₂ | 3.19 ₂ | 1.767 ₄ | 1.523 ₄ |

Table 4.1: Timescales (in ps) calculated from the jump dynamics, jump contribution, frame contribution, total reorientation, and EJM prediction are included along with the jump angle contribution, \bar{w}_n ; see the text for definitions. Subscripts represent the uncertainty in the final digit(s).

| Component | $E_{a,0}$ | $E_{a,n}^{\Delta\theta}$ | $E_{a,n}^{jump}$ | $E_{a,n}^{frame}$ |
|--------------|--------------------|--------------------------|--------------------|---------------------|
| $n = 1$ | | | | |
| <i>Total</i> | 3.31 ₅ | 0.302 ₁₀ | 3.62 ₅ | 3.62 ₂₄ |
| <i>KE</i> | 0.96 ₃ | 0.069 ₇ | 1.03 ₃ | 1.11 ₁₃ |
| <i>LJ</i> | -0.91 ₄ | -0.136 ₁₀ | -1.05 ₄ | -0.92 ₁₆ |
| <i>Coul</i> | 3.27 ₅ | 0.369 ₁₄ | 3.64 ₅ | 3.44 ₂₈ |
| $n = 2$ | | | | |
| <i>Total</i> | 3.31 ₅ | 0.129 ₆ | 3.44 ₅ | 3.66 ₁₁ |
| <i>KE</i> | 0.96 ₃ | 0.021 ₄ | 0.98 ₃ | 1.12 ₈ |
| <i>LJ</i> | -0.91 ₄ | -0.082 ₅ | -1.00 ₄ | -1.02 ₁₅ |
| <i>Coul</i> | 3.27 ₅ | 0.190 ₈ | 3.46 ₅ | 3.57 ₂₄ |
| $n = 3$ | | | | |
| <i>Total</i> | 3.31 ₅ | 0.003 ₂ | 3.31 ₅ | 3.68 ₈ |
| <i>KE</i> | 0.96 ₃ | -0.012 ₂ | 0.95 ₃ | 1.09 ₇ |
| <i>LJ</i> | -0.91 ₄ | -0.032 ₃ | -0.95 ₃ | -1.05 ₁₂ |
| <i>Coul</i> | 3.27 ₅ | 0.047 ₄ | 3.31 ₅ | 3.65 ₁₈ |

Table 4.2: Activation energies and their kinetic energy (*KE*), Lennard-Jones (*LJ*), and Coulombic (*Coul*) contributions (all in kcal/mol) for the components of the extended jump model for different order n reorientational TCFs. Subscripts indicate the uncertainties in the final digit(s).

4.4 Results and Discussion

The timescales and activation energies for the OH reorientational dynamics were computed using the simulation approach described above along with those for the jump time, jump angle, and frame time components of the extended jump model. In the remainder of this Chapter, we present and discuss these results with the aim of both testing the ability of the EJM to accurately describe reorientation activation energies, and identifying the molecular origin of these activation energies.

4.4.1 OH Reorientation

We have calculated the OH reorientation TCF using Eq. (4.1) for $n = 1 - 3$. The three time correlation functions are shown in Fig. 4.1 along with tri-exponential fits, Eq. (4.3). The τ_n timescales are provided in Table 4.1. We note that the $n = 2$ timescales (and activation energies) are in agreement with, but better converged than, our previous results.^{58,85,86,88}

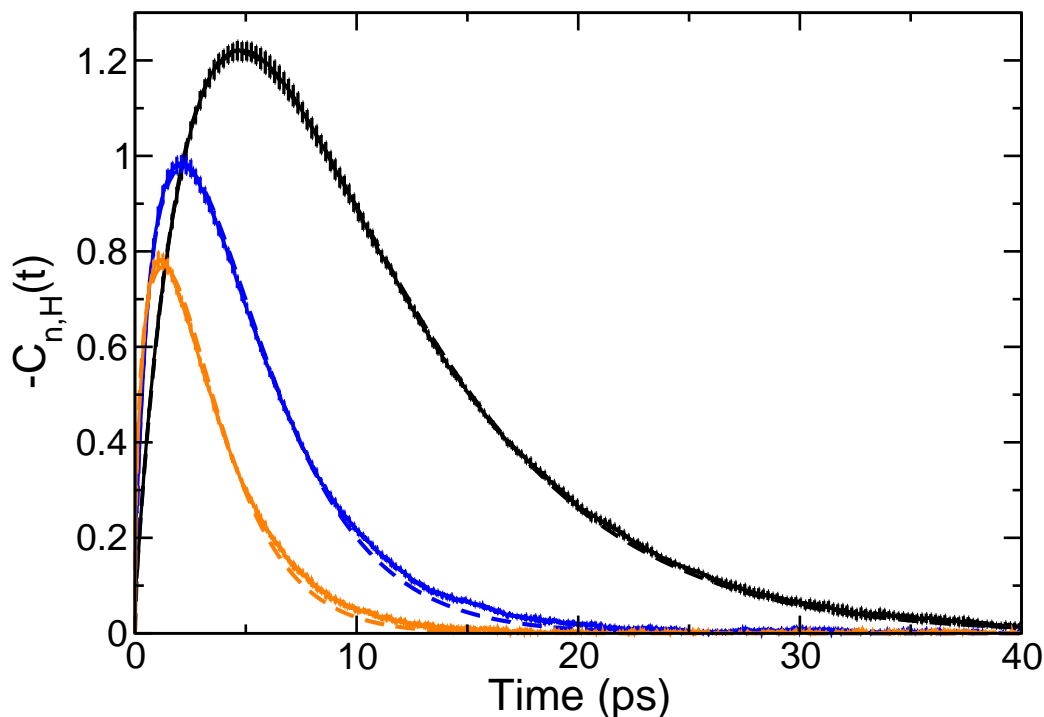


Figure 4.3: Derivatives of the OH reorientational TCFs with respect to β , Eq. (4.9), for H_2O at 298.15 K for $n = 1$ (black), 2 (blue), and 3 (orange); fits to Eq. (4.10) are shown as dashed lines of the same color.

The activation energies of the reorientational timescales are obtained from the corresponding TCFs weighted by the energy fluctuations, $\delta H(0)$, as given by Eq. (4.9). These derivative TCFs are shown in Fig. 4.3 for $n = 1 - 3$ along with their fits to the form in Eq. (4.10) based on a tri-exponential decay of $C_n(t)$. The fits provide an excellent description of the derivative TCFs and are used to obtain the OH reorientational activation energy for each order, $E_{a,n}$, from Eq. (4.6). The resulting values are provided in the two leftmost columns of Table 4.3.

We first use these results to examine the validity of the Debye model. In agreement with prior calculations,^{85,88,156,157} the τ_n reorientation time ratios deviate from the values predicted by the Debye rotational diffusion model: $\tau_1/\tau_2 = 2.02$ and $\tau_1/\tau_3 = 2.99$ are significantly smaller than the ratios of 3 and 6, respectively, given by the diffusive model. The activation energies exhibit more modest differences and are not distinguishable outside the errors. This shows that the reorientation time ratios are expected to be approximately independent of temperature and thus that there is no temperature where these ratios would reach the ideal Debye diffusion values. While activation energies are not as instructive as a test of the Debye model compared to the reorientation timescales, they show that the deviation with respect to the Debye model is present over a broad temperature range in liquid water. In addition, a recent comparison of the activation energies of water reorientation, diffusion, and viscosity found deviations from the Debye-Stokes-Einstein description, which argues against this picture for water reorientation.⁵⁰ Finally, the kinetic, Lennard-Jones, and Coulombic energy contributions to the reorientation activation energy, also reported in Table 4.3, show that these different components are approximately independent of the order n . Their interpretation will be provided below.

We now proceed to test the ability of the extended jump model to describe the reorientation activation energy, and analyze its jump and frame components to provide a molecular understanding of reorientational activation energies.

4.4.2 Jump Contribution to Reorientation

As noted in Sec. 4.2.4, the jump contribution to the reorientational timescale has two components: the jump time and the distribution of jump angles. We consider each in turn.

4.4.2.1 H-bond Jump Times

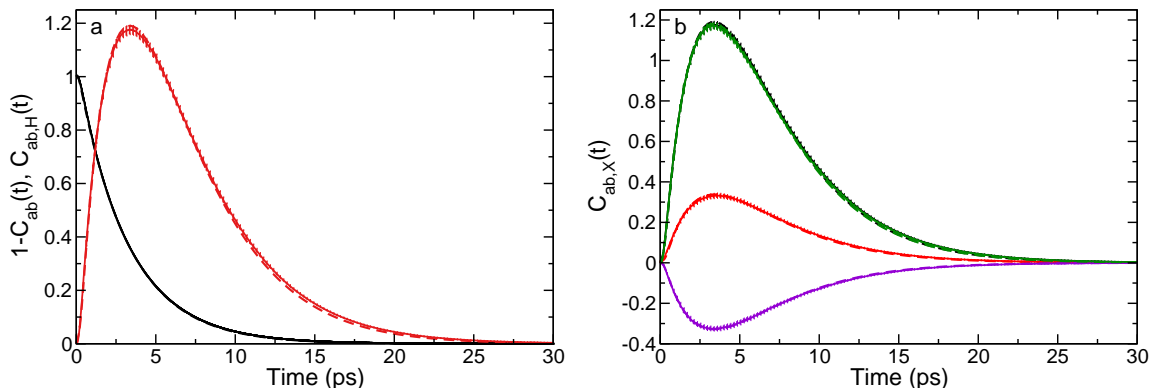


Figure 4.4: a) Jump TCF, $1-C_{ab}(t)$, (black) and its derivative, $C_{ab,H}(t)$, (red). b) The total energy (black), kinetic energy (red), Lennard-Jones (purple), and Coulombic (green) contributions to the derivative TCF. Calculated TCFs are shown as solid lines and fits as dashed lines of the same color.

The stable states TCF introduced in Sec. 4.2.4 was used to calculate the H-bond jump time and its activation energy for water from the same simulations used to obtain the OH reorientational dynamics. The calculated $C_{ab}(t)$, Eq. (4.16), and its bi-exponential fit are shown in Fig. 4.4a. The longer timescale is the jump time, τ_0 , and is found to be 3.142 ± 0.002 ps, which is in excellent agreement with previously reported results.^{31,85,86} Note that τ_0 is the inverse of the rate constant k_0 for an OH to exchange one H-bond acceptor for another and hence is independent of the order n for the reorientational TCF.

The activation energy of the jump time is calculated from the $C_{ab,H}(t)$ correlation function given in Eq. (4.17), which is also plotted in Fig. 4.4a. By fitting this derivative TCF to a bi-exponential form analogous to Eq. (4.10), we obtain $\partial k_0/\partial\beta$ from which we find an activation energy of $E_{a,0} = 3.31 \pm 0.05$ kcal/mol. This is in good agreement with our previously reported values of 2.9 kcal/mol^{31,85} from an Arrhenius analysis and 3.2 kcal/mol from a direct fluctuation

theory calculation.³¹ We note that the non-Arrhenius temperature dependence of water dynamics around ambient conditions makes the results of Arrhenius analyses sensitive to the chosen temperature range.⁴⁴ This jump time activation energy is lower than that for the OH reorientation timescale (independent of the order). This indicates that the latter, which is more easily measured, cannot be used alone to determine the former.

As discussed in Sec. 4.2.1, the fluctuation theory approach provides a rigorous decomposition of the activation energy. We applied this approach to the jump time TCF using the energy components given in Eq. (4.11) and the results are shown in Fig. 4.4b. These are also fit to a bi-exponential form of Eq. (4.10) to extract activation energies associated with each contribution to $E_{a,0}$ as in Eq. (4.12). The activation energies extracted in this way are reported in Table 4.2.

The results in Fig. 4.4b and Table 4.2 are consistent with our previous analyses of water diffusion coefficients,^{13,58,160} reorientational dynamics,^{13,44,58,160} and viscosity.⁵⁰ Namely, the electrostatic contribution dominates with $E_{a,0}^{Coul} = 3.27 \pm 0.05$ kcal/mol, nearly equal to the total activation energy. The kinetic energy contribution is also positive, but smaller (0.96 ± 0.03 kcal/mol) and the Lennard-Jones potential energy contributes a negative activation energy on the same order as the kinetic contribution (-0.91 ± 0.004 kcal/mol). However, this near cancellation of $E_{a,0}^{KE}$ and $E_{a,0}^{LJ}$ is actually fortuitous and it can be seen that it is actually the Coulombic and Lennard-Jones contributions that are in competition.¹⁶⁰

The physical explanation for this competition between the Coulombic and Lennard-Jones interactions can be understood by considering the chemical "reaction" involved in the H-bond jump. This is illustrated schematically in Fig. 4.5. In a typical H-bond the two water molecules sit high up on the repulsive wall of their mutual Lennard-Jones potential, held there by the attractive Coulombic interactions. To exchange H-bond partners, the water molecules must increase their intermolecular distance, moving to the hydrogen bond exchange transition state (a bifurcated hydrogen-bond arrangement; as discussed in Ref. 32, it is unstable in ambient liquid water, in contrast to suggestions of stable overcoordinated water molecules in structures quenched from supercooled trajectories).¹⁶³ This necessarily involves moving lower on the repulsive wall of the Lennard-Jones

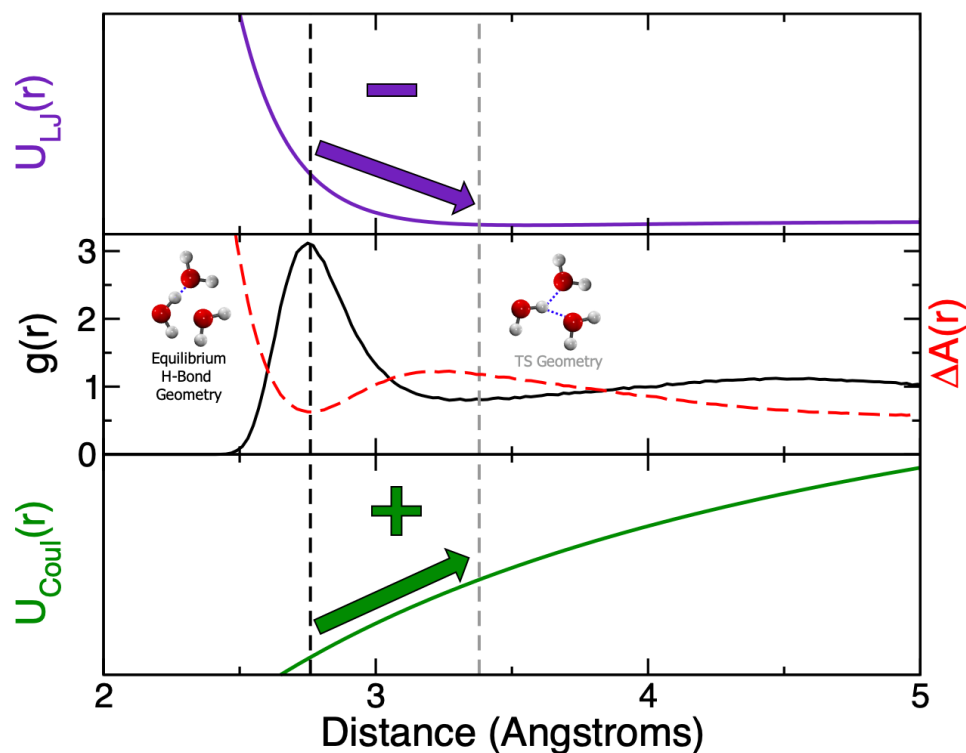


Figure 4.5: Schematic illustration of the potential energy contributions to the jump activation energy. The “reactant” and transition state structures are shown (middle panel) in the context of the radial distribution function and free energy profile. The corresponding changes in the Lennard-Jones (top panel) and Coulombic (bottom panel) interactions are depicted.

potential while simultaneously rising higher on the intermolecular electrostatic potential. This rise in the Coulombic energy and fall in the Lennard-Jones potential associated with the process of an H-bond exchange leads to the positive and negative activation energy components, respectively. However, the electrostatic interactions are dominant and are thus quantitatively larger. The predominance of Coulombic interactions in the water jump and reorientation activation energies is consistent with the marked activation energy increase for water reorientation hydrogen-bonded to anions with increasing charge density,¹⁶⁴ which has been explained by a transition-state H-bond strength effect in the jump mechanism.¹⁴⁸

4.4.2.2 H-bond Jump Angle Distribution

To fully calculate the activation energy for the jump reorientation component, it is also necessary to calculate the temperature-induced changes in the distribution of jump angles as described in Sec. 4.2.4.

We start by calculating the jump angle distribution. From each short *NVE* trajectory, $P(\Delta\theta)$ was calculated using the first H-bond exchange of every initially H-bonded OH group and then results were averaged across all of the trajectories. The distribution is shown in Fig. 4.6a and gives the average angular jump amplitude to be $\langle\Delta\theta\rangle = 70.31^\circ \pm 0.02^\circ$. This is in excellent agreement with the previously reported results by Laage and Hynes,⁸⁵ which gave the average amplitude as 68° . With this jump angle distribution \bar{w}_n can be calculated using Eq. (4.15) for each order of the Legendre polynomial $n = 1, 2, \text{ or } 3$; the resulting values are given in Table 4.1.

The calculated jump angle distribution has two prominent features. The central feature peaks around 52.5° and corresponds to H-bond exchanges in which the new H-bond acceptor is itself H-bonded (either as a donor or acceptor) to the original H-bond acceptor for the OH of interest.¹⁶⁵ The peak at larger jump angles is associated with new acceptors that have no H-bond connection with the current acceptor.

A qualitative connection between the jump angle distribution and the water OO radial distribution function can be suggested. At the jump transition state, a $\Delta\theta$ angle between O^a , O^d and O^b implies that the O^aO^b distance is $2OO^\ddagger \sin(\Delta\theta/2)$ where OO^\ddagger is the $O^dO^{a,b}$ transition state distance. If one adopts the strong approximations that i) the O^aO^b transition-state distribution is similar to the equilibrium OO radial distribution function and ii) that the jump angle probability is only determined by the probability of the presence of the new acceptor O^b , thus ignoring the increase in jump barrier energy with $\Delta\theta$, the jump angle probability is approximately proportional to $g_{OO}(2OO^\ddagger \sin(\Delta\theta/2)) \sin(\Delta\theta)$. This simplified geometric picture can explain the general shape of the jump angle distribution and suggests that the first peak in the jump angle distribution corresponds to the first peak in the OO radial distribution function.

We have further calculated the derivative of the jump angle distribution with respect to β ,

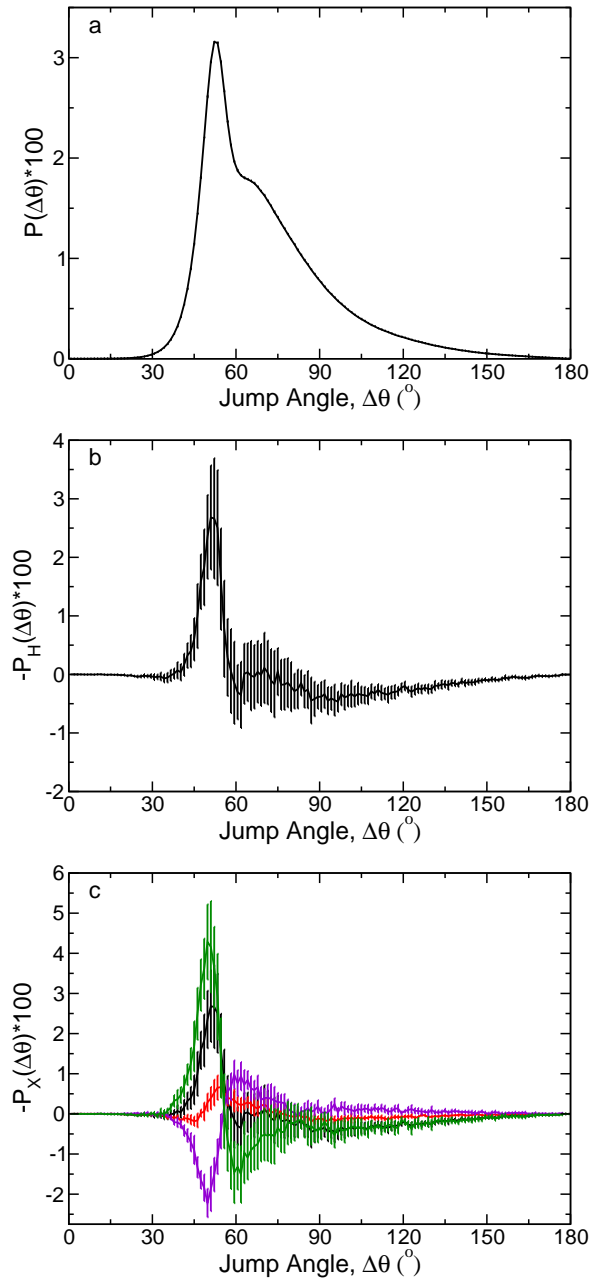


Figure 4.6: a) The jump angle distribution, b) the derivative of the jump angle distribution, and c) the total (black), kinetic energy (red), Lennard-Jones (purple) and Coulombic (green) contributions to the jump angle distribution derivative are presented.

$-P_H(\Delta\theta)$. This derivative distribution is obtained by the same process as that used to calculate $P(\Delta\theta)$, but the contribution of each jump angle is weighted by the energy fluctuation at the time of the jump, $\delta H(\tau^*)$. The derivative of the probability distribution is presented in Fig. 4.6b. To calculate the activation energy associated with changes in the jump angle distribution with tem-

perature, $E_{a,n}^{\Delta\theta}$ in Eq. (4.19), we use Eqs. (4.15) and (4.20). These activation energies, given in Table 4.2, are found to be 0.302 ± 0.010 , 0.129 ± 0.006 , and 0.003 ± 0.002 kcal/mol for $n = 1$, 2, and 3, respectively. Thus, they are at least an order of magnitude smaller than the jump time activation energy, $E_{a,0}$, and represent only a small part of the overall jump contribution to the OH reorientational activation energy $E_{a,n}^{jump}$.

We have also calculated the decomposition of the jump angle distribution derivative with β , denoted as $-P_X(\Delta\theta)$ where $X = KE, LJ$, or *Coul*. These derivative distributions are plotted in Fig. 4.6c and the contributions to the jump angle distribution activation energy are given in Table 4.2. While the scale of the activation energy contributions decrease with increasing orders of the Legendre polynomial, the trends for the components are similar to that of the jump time. Namely, electrostatics represent the largest contribution, partially canceled by the smaller, negative Lennard-Jones component. Coulombic interactions disfavor large amplitude jumps when the temperature decreases, probably because in the transition state configurations for large-angle jumps the OH group that reorients loses its favorable electrostatic interactions with both the initial and final acceptors. The LJ potential disfavors small-angle jumps, presumably because they require small O^aO^b distances that involve significant repulsive LJ interactions.

Interestingly, in contrast to the case of the radial distribution function and other static quantities that depend only on coordinates (not momenta),¹⁴⁷ the kinetic energy contribution to jump angle distribution derivative is non-zero. This is a clear indication that the jump angle distribution is a dynamical quantity. Namely, $P(\Delta\theta)$ effectively depends on the coordinates before and after an H-bond exchange, which leads to a correlation between the system kinetic energy and the jump angle. The KE contribution is effectively zero for large-angle jumps but positive for small-angle ones, suggesting that these dynamical effects depend on the nature of the new acceptor.

Using the calculated activation energies of the jump angle distribution, $E_{a,n}^{\Delta\theta}$, and the characteristic jump timescale, $E_{a,0}$, the total jump contribution to the OH reorientation activation energy, $E_{a,n}^{jump}$, can be calculated from Eq. (4.19). These are found to be 3.62 ± 0.05 , 3.44 ± 0.05 , and 3.31 ± 0.05 kcal/mol, respectively, for $n = 1, 2$, and 3. The full decomposition of these activation

energies are provided in Table 4.2. Note that the change in $E_{a,n}^{jump}$ with the order of the reorientational TCF is associated only with the jump angle distribution (which itself does not depend on n) reflecting different weighting of the large-amplitude angular jumps.

4.4.3 Frame Contribution to Reorientation

The final component of the EJM is the frame reorientation. We have calculated the frame reorientation TCF as described in Sec. 4.2.5 and the results are shown in Fig. 4.7a. Because $C_{n,frame}(t)$ can only be obtained from OH groups that have not exchanged their H-bond acceptor, the TCF can only be calculated for limited times (up to delays on the order of the H-bond jump time). In practice, we find that the time range over which data can be reliably obtained is approximately four times the characteristic jump time τ_0 , or 12.5 ps. At this time, fewer than 2% of the originally H-bonded OH moieties have not switched partners and are thus still contributing to $C_{n,frame}(t)$.

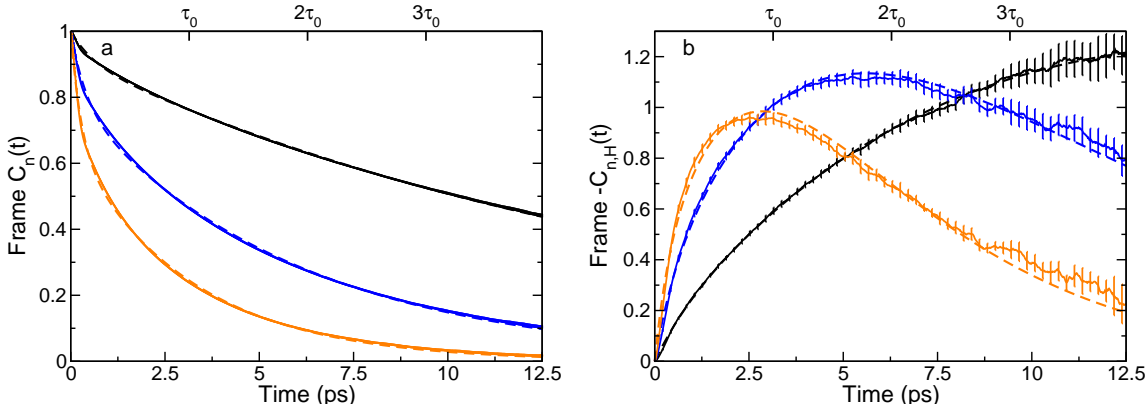


Figure 4.7: a) Frame reorientational TCF, $C_{n,frame}(t)$ for $n = 1$ (black), 2 (blue), and 3 (orange), and b) Corresponding derivative TCFs, $C_{n,frame,H}(t)$. Fits are shown as dashed lines in the same color.

The calculated $C_{n,frame}(t)$ are well described by a bi-exponential fit, also shown in Fig. 4.7a, in which the longer time is the frame reorientation time. We find $\tau_n^{frame} = 16.91 \pm 0.13$, 5.97 ± 0.03 , and 3.19 ± 0.02 ps for $n = 1, 2$, and 3 , respectively.¹⁶⁶ The $n = 1$ and 2 values are in good agreement with the $\tau_1^{frame} = 15.5$ ps and $\tau_2^{frame} = 5.6$ ps previously obtained by Laage and Hynes.⁸⁵

The derivatives of the frame reorientation TCFs,

$$\begin{aligned} \frac{\partial C_n^{frame}(t)}{\partial \beta} &= -\langle \delta H(0) P_n [\vec{e}_{OO}(0) \cdot \vec{e}_{OO}(t)] \rangle_{Hbond} \\ &\equiv C_{n,frame,H}(t), \end{aligned} \quad (4.24)$$

were also calculated and are presented in Fig. 4.7b. We find that the frame activation energies are 3.62 ± 0.24 , 3.66 ± 0.11 , and 3.68 ± 0.08 kcal/mol for $n = 1, 2$, and 3 , respectively.

It has been suggested that, while the mechanism for OH reorientation is not diffusive, the frame reorientation is much closer to the ideal diffusive behavior.⁸⁵ This rotation likely involves, as elementary steps, H-bond exchanges between the central H-bonded partners and the surrounding waters in their first solvation shell (while maintaining the central H-bond). We can examine whether collectively these jumps lead to Debye rotational diffusion for the frame reorientation using the two essential predictions of the timescales and activation energies made by the Debye model in Eq. (4.2). Namely, in terms of the frame reorientation timescales calculated here, we find $\tau_1^{frame} / \tau_2^{frame} = 2.83$, $\tau_1^{frame} / \tau_3^{frame} = 5.30$, and $\tau_2^{frame} / \tau_3^{frame} = 1.87$, which are in reasonable accord with the Debye predictions of 3, 6, and 2, respectively. These timescale ratios thus suggest that the contributions from *multiple* H-bond exchanges with the solvating water molecules leads to primarily diffusive rotational dynamics for the frame.

The activation energies obtained for frame reorientation, Table 4.2, are the same within statistical error, which is also consistent with the Debye model. However, the example of OH reorientation discussed in Sec. 4.4.1, suggests the activation energies may not be instructive for testing the rotational diffusion model.

The derivative TCF for frame reorientation, $C_{n,frame,H}(t)$ can also be decomposed in terms of contributions from the kinetic, Lennard-Jones, and Coulombic energies. These results are shown in Fig. 4.8 and the derived activation energies are given in Table 4.2. The magnitudes and signs of the different components of the frame activation energy follow the same trends observed for the jump time. In addition, as is true for the total $E_{a,n}^{frame}$, each contribution is nearly independent of

the order n of the reorientational TCF.

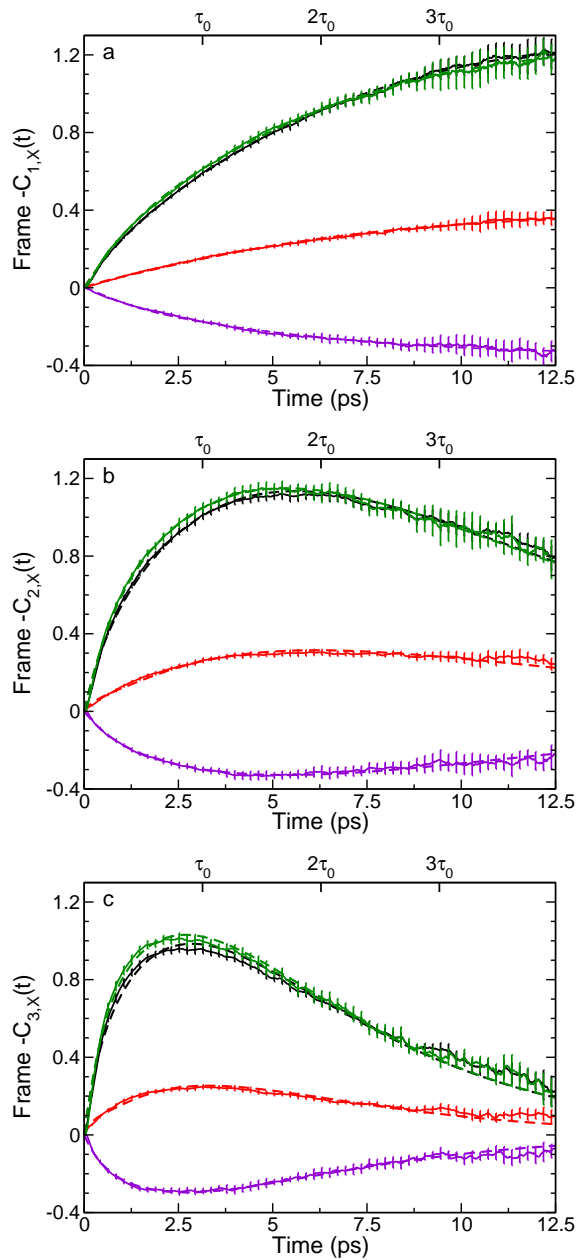


Figure 4.8: Decomposition of the derivative frame reorientation TCF, $C_{n,frame,H}(t)$, for a) $n = 1$, b) $n = 2$, and c) $n = 3$. Contributions from kinetic (red), Lennard-Jones (purple), and Coulombic (green) energies are compared to the total (black). Fits are shown as dashed lines of the same color.

| Component | $E_{a,n}$ Calculated | = | Weighted Jump Contribution | + | Weighted Frame Contribution | = | $E_{a,n}^{EJM}$ Predicted |
|--------------|-------------------------|---|-------------------------------|---|--------------------------------|---|------------------------------|
| <i>n</i> = 1 | | | | | | | |
| <i>Total</i> | 3.70 ₁₁ | = | 2.56 ₄ | + | 1.06 ₇ | = | 3.62 ₈ |
| <i>KE</i> | 1.06 ₉ | = | 0.73 ₂ | + | 0.32 ₄ | = | 1.05 ₄ |
| <i>LJ</i> | -1.01 ₉ | = | -0.74 ₃ | + | -0.27 ₄ | = | -1.01 ₆ |
| <i>Coul</i> | 3.65 ₈ | = | 2.58 ₄ | + | 1.00 ₉ | = | 3.58 ₉ |
| <i>n</i> = 2 | | | | | | | |
| <i>Total</i> | 3.69 ₇ | = | 2.15 ₃ | + | 1.37 ₅ | = | 3.52 ₅ |
| <i>KE</i> | 1.08 ₅ | = | 0.62 ₂ | + | 0.42 ₃ | = | 1.03 ₄ |
| <i>LJ</i> | -1.01 ₇ | = | -0.63 ₁ | + | -0.38 ₅ | = | -1.00 ₆ |
| <i>Coul</i> | 3.61 ₁₀ | = | 2.17 ₃ | + | 1.33 ₉ | = | 3.50 ₁₀ |
| <i>n</i> = 3 | | | | | | | |
| <i>Total</i> | 3.56 ₇ | = | 1.73 ₃ | + | 1.76 ₄ | = | 3.49 ₅ |
| <i>KE</i> | 1.03 ₅ | = | 0.50 ₂ | + | 0.52 ₃ | = | 1.01 ₄ |
| <i>LJ</i> | -0.98 ₇ | = | -0.49 ₂ | + | -0.50 ₅ | = | -1.00 ₆ |
| <i>Coul</i> | 3.51 ₁₁ | = | 1.73 ₃ | + | 1.74 ₉ | = | 3.47 ₉ |

Table 4.3: The additivity of the activation energies (all in kcal/mol) within the EJM is presented. The directly calculated OH reorientation activation energy ($E_{a,n}$) and its different energetic contributions are compared for each n to the EJM prediction ($E_{a,n}^{EJM}$) and its weighted jump and frame reorientation components in Eq. (4.7).

4.4.4 Tests of the Extended Jump Model

In this Section, we address two important features of the extended jump model: 1) its ability to quantitatively predict OH reorientation activation energies, and their components associated with different interactions and motions, and 2) the relative contributions of the jump and frame contributions to temperature dependence of the OH reorientation time. The latter will provide a novel insight in the molecular origins of the reorientation activation energy.

4.4.4.1 Prediction of OH Reorientation Times

The extended-jump model has been demonstrated to describe the timescales and mechanisms of water reorientation in neat water^{85,88} and the jumps have been characterized *via* two-dimensional infrared spectroscopy experiments in aqueous salt solutions.^{134,167} In particular, Laage and Hynes showed that the overall reorientation rate constant is the sum of the jump and frame reorientation rate constants, Eq. (4.4). In Table 4.1 we have included these contributions, τ_n^{jump} and τ_n^{frame} , as well as the predicted OH reorientation timescale, τ_n^{EJM} . It can be seen that the EJM reasonably predicts the OH reorientational timescales for all three orders of the TCF and the results are in good agreement with those previously reported.^{85,88} We note, however, that the EJM prediction is not exact, and the simple consideration of the reorientation times cannot decide whether the small residual discrepancy is caused by some of the EJM approximations (*e.g.*, the assumptions of an isotropic jump axis distribution and of a decoupling between the jumps of the two OH groups in the same water molecule) or by some more fundamental issue with the jump mechanism.

4.4.4.2 Prediction of OH Reorientation Activation Energies

Here, we have presented a different approach for examining the extended jump model by examining its predictions for the temperature dependence of the OH reorientational timescales. Specifically, we have used our calculated results for the activation energies of the jump angle distribution, the jump time, and the frame reorientation time to calculate the OH reorientation activation energy predicted by the EJM in Eq. (4.7). We now compare these predictions to the directly computed

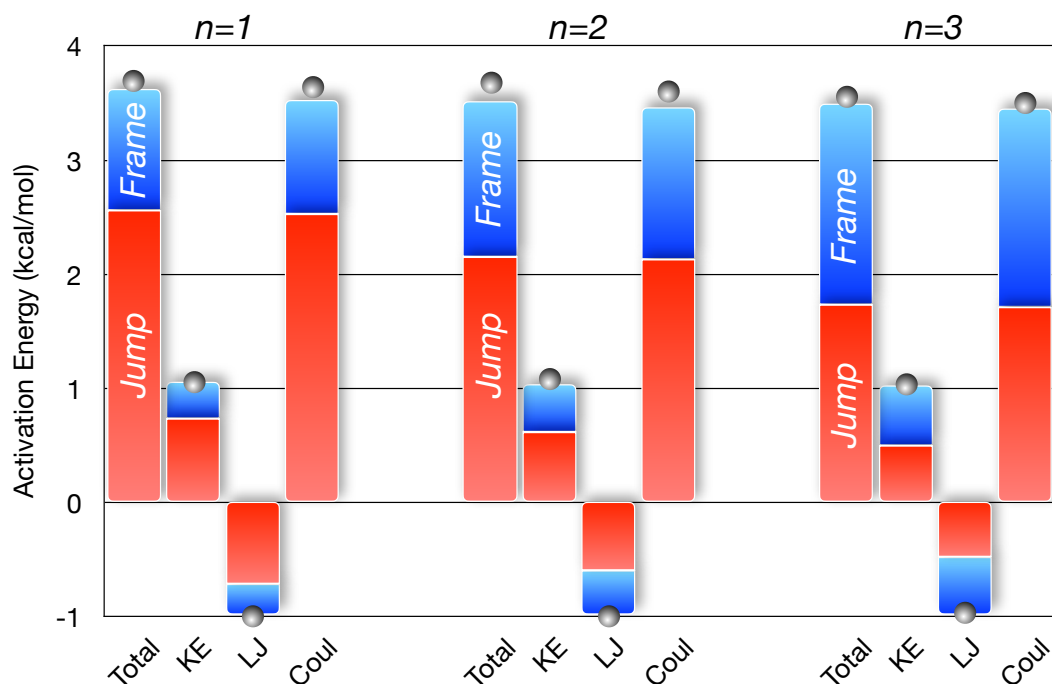


Figure 4.9: Contributions to the OH reorientation activation energy for $n = 1, 2,$ and 3 (gray spheres) are compared to the EJM predictions (bars) divided into the jump (red bars) and frame (blue bars) weighted components in Eq. (4.7).

OH reorientation activation energies. The fluctuation theory approach avoids potential numerical inaccuracies associated with choosing a range of temperatures for an Arrhenius analysis as well as any effects of intrinsic non-Arrhenius behavior. This issue is particularly critical in liquid water, where these non-Arrhenius effects are especially pronounced for dynamical properties.^{6,141,145,146}

In Table 4.3 and Fig. 4.9, we compare the calculated activation energy for each reorientational timescale τ_n to the EJM prediction, which is further broken down into the contributions from H-bond jumps and frame reorientation. Note that the jump and frame contributions to the activation energies include the reweighting by the ratio of the timescales as seen in Eq. (4.7). The results clearly show that the EJM accurately predicts the activation energies of water OH reorientation for all three orders of the TCF. As activation energies are a commonly used measure of the temperature dependence of timescales, this indicates that the EJM not only accurately predicts the OH reorientation time itself, but also the temperature dependence of the reorientation time. This is true for all orders of the reorientational TCF, but most importantly, it is accurate for the $n = 2$ order which is

experimentally accessible *via* both NMR and pump-probe infrared anisotropy experiments.

4.4.4.3 Jump and Frame Contributions to $E_{a,n}$

It is interesting to examine the relative contributions of the jump and frame mechanisms to the OH reorientation activation energy. The jump and frame contributions to the n^{th} -order reorientational time activation energies are given in Table 4.2. As noted above, the frame reorientation activation energy is $E_{a,n}^{\text{frame}} \simeq 3.65$ kcal/mol independent of the order. This is similar in magnitude to the jump contribution, which includes the temperature dependence of both the jump time and the jump angle distribution. For $n = 1$, the overall jump activation energy, Eq. (4.19), is effectively the same as that for frame reorientation ($E_{a,n}^{\text{jump}} = 3.62 \pm 0.05$ kcal/mol). How these two combine to predict the OH reorientation activation energy depends on the relative jump and frame timescales as given in Eq. (4.7). Because the jump contribution to the reorientation time is faster than the frame time, $\tau_n^{\text{jump}} < \tau_n^{\text{frame}}$ (see Table 4.1), the OH reorientation time has a larger contribution from the jumps. This is illustrated in Table 4.3 and Fig. 4.9 where the weighted jump and frame contributions to τ_n given in Eq. (4.7) are shown. For the $n = 1$ reorientational TCF, the weighted jump contribution is ~ 2.5 times larger than the weighted frame contribution.

As the order increases, the jump and frame contributions to τ_n both decrease but also get closer, as shown in Table 4.1. At the same time, the frame activation energy is independent of n while the jump contribution activation energy decreases modestly with n ; see Table 4.2. The effect of these two trends is that the weighted frame contribution to the OH reorientation activation energy grows as the weighted jump contribution shrinks. As given in Table 4.3 and shown in Fig. 4.9, for $n = 2$, the weighted jump contribution is only 1.5 times the weighted frame contribution and, for $n = 3$, the two are equal. Thus, the relative importance of frame reorientation and H-bond jumps to the OH reorientational activation energy $E_{a,n}$ depends on the order n . And it does so primarily because of the difference in how τ_n^{frame} decreases more quickly with n than does τ_n^{jump} .

The close quantitative similarity of the activation energies for the jump and frame contributions to OH reorientation, $E_{a,n}^{\text{jump}}$ and $E_{a,n}^{\text{frame}}$, indicates that their relative importance in determining $E_{a,n}$

will not be strongly temperature dependent. In other words, the effect of H-bond jumps should be the dominant contribution to both τ_n and $E_{a,n}$ for $n = 1$ or 2 over a significant range of temperatures (at least outside the deeply supercooled regime where non-Arrhenius effects are important.)

While it is important that the EJM description of water reorientation accurately predicts the activation energy, it is even more critical that it does so for the right reasons. We have tested this using the decomposition of the calculated $E_{a,n}$ into kinetic, Lennard-Jones, and Coulombic energy contributions in direct comparison to the EJM predictions. These results are also included in Table 4.3 and Fig. 4.9. As with the total activation energy, each component also correctly predicts the reorientation activation energy contribution from that component. Thus, the EJM not only accurately describes the activation energy but also the physical interpretation of its origins.

4.5 Conclusion

This work demonstrates an application of the fluctuation theory for dynamics to the extended jump model of water reorientation. We have calculated the activation energies of the jump reorientation time, the distribution of jump angles, and the frame reorientation time and used them to predict the OH reorientation time in liquid water for multiple orders of the reorientation correlation function. Importantly, the activation energies extracted from both the actual and predicted OH reorientation agree, but they are also in good agreement with experimental results from pump-probe infrared anisotropy experiments,^{7,105,138} supporting the EJM as the physical model underlying water reorientation. Furthermore, the activation energy decomposition indicates that the EJM correctly determines the activation energies for the right reasons as the predicted and the actual decomposition of the OH reorientation activation energy are also in excellent agreement.

The frame reorientation times and activation energies were examined probe the nature of this reorientation. The ratio of timescales of different orders of the reorientational TCF strongly indicate that the frame reorientation is reasonably described by Debye rotational diffusion. This rotational diffusion is likely caused by Brownian orientational motions induced in the frame of the unbroken hydrogen bonds by exchanges within the first solvation shells of the H-bond partners.

It was found that not only the total activation energy, but also the decomposition of the activation energy, was unchanging with the order of the Legendre polynomial; while this result is predicted by the Debye model of rotational diffusion, this behavior of the activation energies does not appear to be significantly different from the predictions of the EJM.

In all, the work presented here provides strong evidence for the EJM description of OH reorientation. Furthermore, for the first time, the contributions to water reorientation from each component of the activation energy has been explained in terms of jump and frame component activation energies. The methods presented here are general and could be easily extended to reorientation of water molecules around a solute or in the first hydration layer of a biomolecule.

Chapter 5

On the role of hydrogen bond exchanges in the spectral diffusion of water

5.1 Introduction

The development of two-dimensional infrared photon-echo (2D-IR) spectroscopy has driven considerable interest in spectral dynamics in liquids and other condensed phase environments.^{72,169–171} This technique provides a method to monitor the fluctuations of a particular vibrational frequency, the spectral diffusion, to gain new insight into the liquid dynamics. This spectral diffusion is described by the frequency-frequency correlation function (FFCF) that represents a quantitative measure of the timescale(s) with which a vibrational mode loses memory of its frequency.

While 2D-IR spectroscopy has been applied across a diverse set of systems, liquid water is perhaps the best studied case. The water OH stretch vibration is of particular interest, because its frequency sensitively depends on the hydrogen-bond (H-bond) strength. The FFCF obtained by 2D-IR spectroscopy thus provides a unique probe of the H-bond fluctuation dynamics in the liquid. Several theoretical and simulation studies^{172–175,175–177} have investigated the molecular origin of the OH frequency dephasing in liquid water, and led to a consensus about the role of H-bond rearrangements. However, different suggestions were made regarding the exact nature of these rearrangements and their short-ranged or collective character.

Adapted with the permission of Zeke A. Piskulich, Damien Laage, and Ward H. Thompson and AIP Publishing from *J. Chem. Phys.* **154**, 064501 (2021).¹⁶⁸

After these pioneering studies of frequency dephasing in water, it was shown^{85,88} that a major contribution to H-bond rearrangements originates from H-bond exchanges, where a water OH group switches H-bond acceptors *via* a sudden angular “jump” of the OH bond. The extended jump model^{85,88} (EJM) combines this jump mechanism with the slower tumbling of the intact H-bond between these jumps and is able to accurately predict not only the timescales of water OH reorientation,^{85,88} but also the associated activation energies.¹³⁶ Additionally, direct evidence of these large-angle jumps in salt solutions was provided by polarization-sensitive 2D-IR spectroscopy measurements.¹⁶⁷

These large-angle jumps occurring with H-bond exchanges represent the main underlying molecular step for much of the dynamics of water, including reorientation,^{85,88} diffusion,^{58,136,178,179} and shear viscosity.^{50,178} Prior studies^{175,175,180} have suggested that H-bond exchanges are also the cause of spectral diffusion, but others have proposed alternative interpretations.^{155,176,177,181–183}

In this Chapter, we carry out a detailed analysis of the FFCF for isotopically dilute liquid water (HOD in D₂O) with the aim of elucidating the dynamics to which it is sensitive. The particular focus is on how H-bond exchange dynamics appears in the spectral diffusion. In addition to the FFCF itself, we investigate its temperature derivative and hence the activation energies associated with the spectral diffusion timescales. This is accomplished by application of the recently developed fluctuation theory for dynamics.^{13,31,44,50,58,59,136,147,160,184}

Before proceeding, we first note that the FFCF exhibits short-time (< 0.5 ps) dynamics, which appears to now be uniformly recognized as associated with underdamped, librational dynamics within the intact H-bond.^{8,172–174,176,177} The focus of the present work, however, is the longer-time (picosecond) spectral diffusion that has been the subject of many studies and for which several interpretations have been proposed. While all studies concur that this timescale reports on water H-bond rearrangement dynamics, it is important to note that the language used to describe the phenomena underlying spectral diffusion dynamics is not unambiguous. Namely, “H-bond dynamics” can encompass multiple physically distinct processes with increasing timescales: 1) the rearrangement of the H-bond geometry without breaking the H-bond itself, 2) transient breaking of H-bonds

that occurs before another H-bond partner is found in an exchange event or that occurs without any exchange at all when an OH returns to its original H-bond acceptor, and 3) H-bond jumps in which the OH group switches from one acceptor to another. All three types of dynamics surely play some role in spectral diffusion and in the following we will attempt to carefully distinguish between them in our discussion.

We first provide a brief overview of the prior studies of water frequency dephasing and their interpretations. In explaining some of the earliest measurements of spectral diffusion, the relationship between the H-bond, O \cdots O, distance and the OH frequency was often invoked, and OH frequency dephasing was attributed to the overdamped O \cdots O bond relaxation caused by the large surrounding solvent friction.^{181–183,185,186}

However, four subsequent parallel studies all found that spectral diffusion in water is not associated with modulation of the H-bond distance but rather with H-bond rearrangement dynamics.

First, Rey, Møller, and Hynes^{172,174} showed that the O \cdots O vibration is underdamped and that the relationship between the OH frequency and this H-bond distance involves considerable dispersion, notably due to the librational motion. By contrasting the frequency dynamics of all water OH groups and that of OH groups engaged in intact H-bonds, they concluded that "...the one-to-one frequency-H-bond length assumption is not valid and that the observed experimental time scale should be interpreted in terms of H-bond-breaking and -making dynamics."¹⁷² This picture sat in contrast to the previous descriptions centered on the H-bond distance alone and stressed the importance of H-bond rearrangement dynamics.

In concurrent work, Lawrence and Skinner^{187,188} simulated both the spectral diffusion and H-bond dynamics and also concluded that "at longer times the decay of the spectral diffusion TCF is due to hydrogen bond breaking and making dynamics."¹⁸⁷ More specifically, they proposed that the spectral diffusion time, τ_ω , is equal to the total rate constant for achieving equilibrium *via* both forward and backward H-bond exchanges. Using the intermittent H-bond lifetime, τ_{HB} , as a proxy for the H-bond exchange time, τ_0 , they argued then the spectral diffusion time is given by $\tau_\omega = \tau_{\text{HB}}/2$. There are, however, at least two unresolved puzzles associated with this viewpoint. First,

subsequent characterization of H-bond exchanges *via* the jump mechanism^{85,88} led to an improved determination of the H-bond exchange time from simulations as $\tau_0 \simeq 3.1 - 3.7$ ps.^{85,127,136} This value is thus significantly longer than the H-bond dynamics considered in Ref. 187, and more than twice slower than the spectral diffusion time of isotopically dilute HOD in D₂O determined in both simulations and measurements to be $\tau_\omega \simeq 1 - 1.5$ ps.^{72,114,176,189} H-bond exchanges are thus too slow to explain the fast frequency dephasing. Second, this would require spectral diffusion to be mostly caused by specific H-bond rearrangements that are only accomplished by an exchange of H-bond partners, even though both initial and final partners are water molecules with identical average properties. The nature of these rearrangements would need to be characterized.

A third contribution by Fecko *et al.*¹⁷⁶ stressed the collective character of the H-bond rearrangements causing the spectral dephasing. They compared the FFCF to the time correlation functions of different contributions to the OH frequency (within a perturbation theory description) and some of the geometric parameters (O···O distance and tetrahedrality parameter, q) and found they all have similar long-time decays. Thus, they concluded that the spectral diffusion "...reflects a variety of relaxation mechanisms, including collective rearrangement of the hydrogen-bond network, as well as density and polarization fields, on length scales greater than a molecular diameter." They further argue that these longer time dynamics, which do include the "...breaking and forming of hydrogen bonds, involve the concerted motions of many molecules."

Finally, a different interpretation was later proposed by Garrett-Roe and Hamm¹⁷⁷ who examined the spectral diffusion dynamics based on MD simulations using the SPC model within a perturbation theory approach. Their analysis was based on the calculation of three-time FFCFs rather than the usual (two-time) measure of spectral dynamics and they found that their results "...show that hydrogen bond rearrangements occur largely perpendicular to the OH stretch frequency axis..." However, the motions causing the OH frequency dephasing were not discussed.

In the remainder of this Chapter, we examine the spectral diffusion and H-bond exchange dynamics for HOD in D₂O to gain greater insight into their connection. These analyses indicate that the spectral diffusion timescale, as it is typically extracted from the long-time decay of the

FFCF, is not consistent with that of an H-bond exchange. Rather, we offer evidence that the H-bond jump timescale *is* present in the FFCF decay, but only as an additional, small-amplitude timescale.

5.2 Theory

Spectral diffusion is most clearly quantified in terms of the normalized frequency-frequency time correlation function (FFCF) given by

$$C_{\omega}(t) = \frac{\langle \delta\omega_{01}(0)\delta\omega_{01}(t) \rangle}{\langle \delta\omega_{01}^2 \rangle}, \quad (5.1)$$

where $\delta\omega_{01}(t) = \omega_{01}(t) - \langle \omega_{01} \rangle$ is the fluctuation in the transition frequency at time t and $\langle \dots \rangle$ represents a thermal average. The spectral diffusion time, which we will refer to as τ_{ω} is typically extracted as either the longest timescale of a tri-exponential fit^{72,114,190} of Eq. (5.1) or the timescale from a single exponential fit to $C_{\omega}(t)$ for long times, *e.g.*, $t > 1.5$ ps.¹²³ Note that the FFCF, under reasonable assumptions (at least for the neat liquid),¹⁹¹ can be extracted from the center-line-slope of a 2D-IR spectrum and is thus experimentally accessible.

In the present analysis, we use a multi-exponential fit,

$$C_{\omega}(t) = \sum_{\alpha} A_{\alpha} e^{-k_{\alpha} t}, \quad (5.2)$$

to describe the FFCF. We consider fits with both three and four exponentials and in all cases the shortest three timescales, $\tau_{\alpha} = 1/k_{\alpha}$, are assigned as the inertial (τ_{iner}), librational (τ_{lib}), and spectral diffusion (τ_{ω}) times, respectively. When fitting to three and four exponentials we will denote the spectral diffusion time as $\tau_{\omega}^{(3)}$ and $\tau_{\omega}^{(4)}$, respectively. When four exponentials are used, the longest timescale will be the separately calculated jump time, τ_0 . Note that the inertial and librational decays are not qualitatively exponential, but Eq. (5.2) provides an adequate description of the associated timescales without adversely affecting the longer timescales that are the focus of

the present investigation.

The jump time characterizing H-bond exchanges can be obtained from the stable-states time correlation function,

$$C_{ab}(t) = \langle n_a(0) n_b(t) \rangle, \quad (5.3)$$

where here n_a (n_b) equals 1 for a given OH if it is H-bonded to acceptor a (b) and is 0 otherwise. Thus, for a given OH initially H-bonded to an acceptor we can denote as a , the contribution to C_{ab} at $t = 0$ is zero and it only changes to 1 when the OH has switched to a new acceptor (b). Thus, $C_{ab}(t)$ rises on a timescale equal to the rate constant for H-bond exchanges. Or, equivalently, $1 - C_{ab}(t)$ decays as an exponential with a timescale equal to the jump time. In practice, some short-time non-exponential dynamics is observed in $C_{ab}(t)$ and we fit it to a bi-exponential where the longer timescale is the jump time τ_0 .

We calculate the activation energy for the spectral diffusion timescales based on the fluctuation theory for dynamics.¹³ This approach directly evaluates the temperature derivative of a time correlation function from simulations at a single temperature. A detailed derivation can be found in Ref. 13. Briefly, for the FFCF in Eq. (5.1), the derivative with respect to $\beta = 1/k_bT$ is given by

$$\begin{aligned} \frac{\partial C_\omega(t)}{\partial \beta} &= - \frac{\langle \delta H(0) \delta \omega_{01}(0) \delta \omega_{01}(t) \rangle}{\langle \delta \omega_{01}^2 \rangle} \\ &+ \frac{\langle \delta H(0) \delta \omega_{01}^2 \rangle \langle \delta \omega_{01}(0) \delta \omega_{01}(t) \rangle}{\langle \delta \omega_{01}^2 \rangle^2} \\ &= -C_{\omega,H}(t), \end{aligned} \quad (5.4)$$

where $\delta H(0) = H(0) - \langle H \rangle$ is the fluctuation in the total system energy. We have noted that T only appears in the Boltzmann weighting and normalizing canonical partition functions implicit in the thermal averages in $C_\omega(t)$. Note that the time-correlation functions in Eq. (5.4) can be evaluated at a single temperature using the same simulations from which $C_\omega(t)$ is obtained (see Sec. 5.3.1). They give the analytical derivative of the FFCF in contrast the numerical derivative obtained an Arrhenius analysis. The second term in Eq. (5.4) represents the temperature dependence of the

FFCF normalization factor while the first correlates the spectral dynamics with $\delta H(0)$, the total energy in the system relative to its average value, *e.g.*, faster (slower) spectral diffusion when more (less) energy is available corresponds to a positive spectral diffusion activation energy.

The derivatives of the timescales are then obtained by fitting Eq. (5.4) to the derivative of the fitting function in Eq. (5.2),

$$\frac{\partial C_\omega(t)}{\partial \beta} = \sum_{\alpha} \left[\frac{\partial A_{\alpha}}{\partial \beta} - A_{\alpha} t \frac{\partial k_{\alpha}}{\partial \beta} \right] e^{-k_{\alpha} t}. \quad (5.5)$$

In fitting $\partial C_\omega(t)/\partial \beta$ the timescales and amplitudes obtained from the fit of $C_\omega(t)$ are used such that the fitting parameters are only $\partial A_{\alpha}/\partial \beta$ and $\partial k_{\alpha}/\partial \beta$. The activation energy associated with the α timescale is then given by

$$E_{a,\alpha} = -\frac{1}{k_{\alpha}} \frac{\partial k_{\alpha}}{\partial \beta}. \quad (5.6)$$

Note that in this approach the activation energy is evaluated from simulations at a single temperature (no Arrhenius analysis is involved).

In an analogous fashion, the derivative of the jump TCF, Eq. (5.3), can be obtained as^{31,136}

$$\frac{\partial [1 - C_{ab}(t)]}{\partial \beta} = \langle \delta H(0) n_a(0) n_b(t) \rangle. \quad (5.7)$$

This derivative is also fit to the form in Eq. (5.5), but with only two timescales. The jump time activation energy, $E_{a,0}$, is then given by Eq. (5.6) for the longer, jump, timescale τ_0 .

5.3 Computational Methods

5.3.1 Simulation Details

The simulations were carried out using the Large-scale Atomic/Molecular Massively Parallel Simulator (LAMMPS).⁸¹ A cubic, fully periodic, simulation cell with side lengths of 21.725311 Å was filled with 343 water molecules described by the SPC/E model,⁴² giving a density of 1.00 g/cm³.

A simulation timestep of 1 fs was used. The Particle-Particle-Particle Mesh Ewald summation method was used to calculate electrostatic interactions, with a tolerance parameter of 1×10^{-4} .^{119,120} Water bonds and angles were held rigid using the SHAKE algorithm with a tolerance parameter of 1×10^{-4} .⁸²

One 200 ns *NVT* trajectory was propagated at 298.15 K, with positions and momenta saved every 1 ps, yielding 200,000 configurations. Initial velocities were selected from a Maxwell-Boltzmann distribution. The initial configuration was generated using PACKMOL. The Nosé-Hoover thermostat damping parameter was 100 fs.^{83,84}

From each saved configuration, a 20 ps *NVE* simulation was run from which time correlation functions were calculated. Configurations from each simulation were saved every 10 fs, giving 2000 total configurations per *NVE* trajectory. Reported TCFs are calculated as the average across the set of *NVE* trajectories and derivatives are calculated by weighting by the energy fluctuation of each trajectory according to Eqs. (5.4) and (5.7). All fits of TCFs were calculated using the Levenberg-Marquardt algorithm.^{192,193} All uncertainties are reported as a 95% confidence interval according to the Student's *t*-distribution over an average of ten blocks (each block representing 20,000 configurations).¹²²

We have repeated the above analysis at room temperature for two other water models developed by Skinner and co-workers, the E3B2 and the E3B3 water models.^{194,195} These models explicitly add 3-body effects on top of existing force fields (TIP4P for E3B2 and TIP4P/2005 for E3B3). In general, the simulation details remain the same as above; however, for the E3B2 and E3B3 models the side lengths were 21.7710 and 21.7799 Å, respectively.

5.3.2 Vibrational Frequencies

The OH vibrational transition frequencies are related to the electric field imposed on the H atom by the water molecules surrounding them, as described by the empirical mapping approach developed by Corcelli, Skinner, and co-workers.^{196–199} In this work, we use maps that have been previously developed for the SPC/E, TIP4P, and TIP4P/2005 force fields.^{198,199} In previous work, Skinner

and co-workers have used the TIP4P map in calculations of the FFCE using the E3B2 and E3B3 models. Each of these maps takes the electric field experienced by each hydrogen atom from waters within 7.831 Å of the H atom, which can be written as

$$\mathcal{E}_i(t) = \vec{e}_{OH,i}(t) \cdot \vec{\mathcal{E}}(\vec{r}_{H,i}, t), \quad (5.8)$$

and correlates it to the transition frequency obtained from density functional theory calculations. In the above expression, the electric field is calculated in atomic units, $\vec{r}_{H,i}$ is the position of the i^{th} H atom, and $\vec{e}_{OH,i}$ is a unit vector pointing along the OH bond.

For SPC/E, the transition frequency $\omega_{01}^i(t)$, in cm^{-1} , of the i th OH at time t can be written as

$$\omega_{01}^i(t) = 3761.6 - 5060.4 \mathcal{E}_i(t) - 86225 \mathcal{E}_i(t)^2. \quad (5.9)$$

Similarly, the TIP4P map (used for both E3B2 and E3B3) is,

$$\omega_{01}^i(t) = 3760.2 - 3541.7 \mathcal{E}_i(t) - 152677 \mathcal{E}_i(t)^2. \quad (5.10)$$

The density functional theory calculations used to obtain these “maps” are obtained from quantum-mechanical/point charge cluster calculations using configurations selected from MD simulations. The one-dimensional OH potential is calculated and the corresponding vibrational Schrödinger equation is solved to obtain the frequency.^{198,199}

5.4 Results and Discussion

5.4.1 Spectral Diffusion Timescales

We begin by considering the spectral diffusion dynamics as described by the FFCE. We have calculated the FFCE for three different water models and the timescales and amplitudes for all the simulations are given in Table 5.1. We first discuss the results for SPC/E water at 298.15 K, which

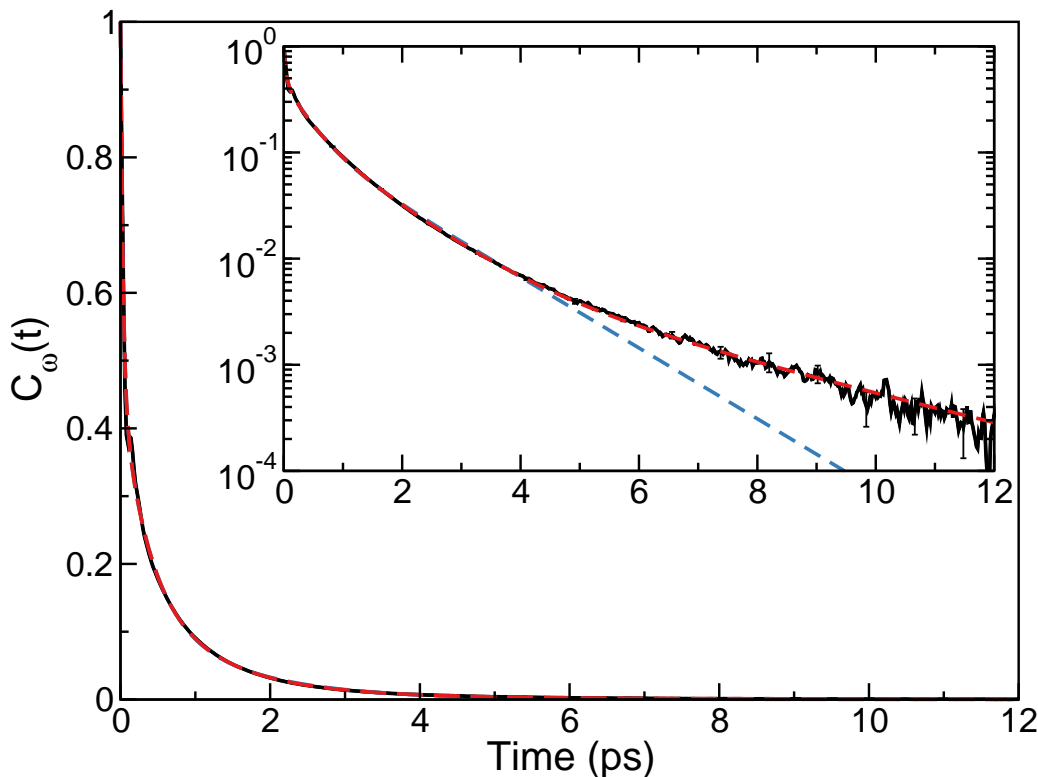


Figure 5.1: The room temperature frequency-frequency correlation function (black solid line) for SPC/E water is shown along with fits using three (blue dashed line) and four (red dashed line) exponentials. Inset: Semi-log plot.

are shown in Fig. 5.1. The fit to a tri-exponential function, Eq. (5.2), is also shown, which gives inertial and librational timescales of 33 and 374 fs, respectively, and a spectral diffusion time of $\tau_{\omega}^{(3)} = 1.30 \pm 0.03$ ps. This last value is consistent with previous simulation studies^{72,190,196,200,201} for SPC/E water that found 0.9,¹⁹⁶ 0.98,¹⁹⁰ and 1.2 ps.²⁰¹ Similarly, photon-echo and 2D-IR measurements have found this timescale to be 0.9, 1.2, or 1.4 ps for HOD/D₂O and 1.7–1.8 ps for HOD/H₂O.^{72,114,130,176,190}

However, it is evident from examination of the FFCF shown on a semi-log scale in the inset of Fig. 5.1 that this tri-exponential description is not accurate at times longer than 4 ps. Rather, the data indicate that an additional timescale is present in the dynamics. Based on the hypothesis that these slower dynamics were in fact those associated with the exchange of H-bond acceptors, we also fit the FFCF with Eq. (5.2) using four exponentials with the longest timescale constrained to

| 3-Exponential Parameters | | | | | | | | | |
|--------------------------|--------|--------------------|--------------------|-----------------------|--------------------|--------------------|--------------------|--------------------|--------------------|
| Model | T (K) | τ_{iner} | τ_{lib} | $\tau_{\omega}^{(3)}$ | A_{iner} | A_{lib} | $A_{\omega}^{(3)}$ | | |
| SPC/E | 298.15 | 0.033 ₁ | 0.374 ₉ | 1.30 ₃ | 0.540 ₂ | 0.316 ₅ | 0.145 ₇ | | |
| E3B2 | 298.15 | 0.033 ₁ | 0.482 ₇ | 2.14 ₄ | 0.547 ₂ | 0.324 ₃ | 0.129 ₄ | | |
| E3B3 | 298.15 | 0.030 ₁ | 0.489 ₃ | 2.27 ₂ | 0.588 ₁ | 0.308 ₁ | 0.104 ₁ | | |
| 4-Exponential Parameters | | | | | | | | | |
| Model | T (K) | τ_{iner} | τ_{lib} | $\tau_{\omega}^{(4)}$ | τ_0 | A_{iner} | A_{lib} | $A_{\omega}^{(4)}$ | A_{τ_0} |
| SPC/E | 298.15 | 0.033 ₁ | 0.320 ₄ | 0.98 ₂ | 3.16 ₁ | 0.532 ₂ | 0.266 ₄ | 0.190 ₄ | 0.013 ₁ |
| E3B2 | 298.15 | 0.031 ₁ | 0.330 ₅ | 1.20 ₂ | 4.59 ₁ | 0.524 ₂ | 0.241 ₃ | 0.209 ₃ | 0.026 ₁ |
| E3B3 | 298.15 | 0.029 ₁ | 0.357 ₃ | 1.19 ₂ | 4.30 ₁ | 0.572 ₁ | 0.233 ₃ | 0.168 ₃ | 0.027 ₁ |

Table 5.1: Timescales (in ps) and amplitudes of the FFCF calculated from three- (top) and four- (bottom) exponential fits. Subscripts represent uncertainty in the trailing digit(s).

the jump time. The jump time was separately calculated as described in Sec. 5.2 from the same simulations and found to be $\tau_0 = 3.16 \pm 0.01$ ps. (We use a strict geometric definition of the H-bond as $R_{O_d \dots O_a} \leq 3.1$ Å, $r_{H \dots O_a} \leq 2.0$ Å, and $\theta_{H-O_d \dots O_a} \leq 20^\circ$, where “d” indicates donor and “a” acceptor.) This four-exponential fit is shown in Fig. 5.1 and provides an excellent description of the full decay of the FFCF (out to 12 ps where the FFCF is less than 0.001). This indicates that H-bond exchanges, *i.e.*, jumps, are indeed present in the FFCF, but only as a long time component described by the jump time and with an amplitude we find to be 1.3% for the SPC/E model. In contrast, the third timescale, $\tau_{\omega}^{(4)}$, has an amplitude of 19.0%.

The tri-exponential fit yields a longest timescale, $\tau_{\omega}^{(3)}$, that represents a mixture of the more rapid spectral diffusion dynamics in between exchanges of H-bond acceptors and that directly associated with H-bond exchanges as described by τ_0 . The mixture is not an even one and the dominant component is that which does not involve H-bond jumps. Because the jump time enters with only a small amplitude, the spectral diffusion timescale is only modestly different in the two descriptions with $\tau_{\omega}^{(4)} = 0.98 \pm 0.01$ ps. Notably, these results indicate that if one only calculates, measures, or fits the FFCF to times less than $\sim 4 - 5$ ps, the resulting timescale is not significantly related to H-bond exchanges. An *f*-test, with a 95% confidence interval, confirms that the 4-exponential fitting function provides a statistically significant improvement in the description of the FFCF over the 3-exponential function.²⁰²

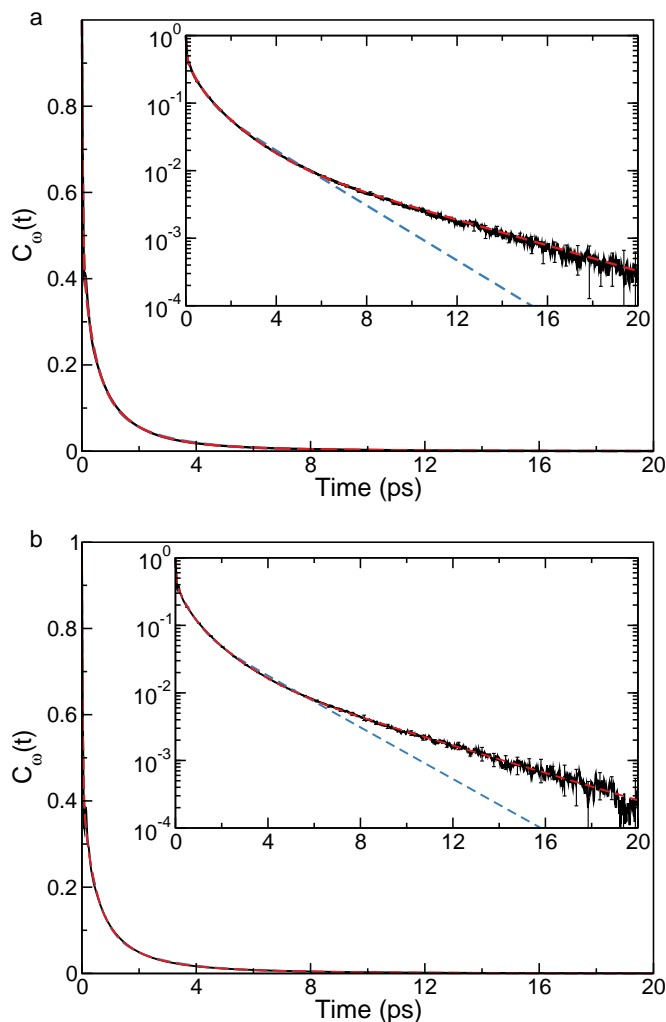


Figure 5.2: Same as Fig. 5.1, but for the (a) E3B2 and (b) E3B3 water models.

It is important to evaluate the generality of this result by considering other water models. To this end, we have carried out the same calculation of the FFCF for the E3B2¹⁹⁴ and E3B3¹⁹⁵ water models, which add three-body interactions to fixed charge models as noted in Sec. 5.3.1. The former has been previously used to investigate water spectral diffusion and its temperature dependence.¹²³ The FFCFs obtained with these models are shown in Fig. 5.2 and the parameters obtained from fitting them are provided in Table 5.1.

The spectral diffusion dynamics for these E3B force fields are qualitatively the same as that observed for SPC/E water in Fig. 5.1. Namely, a tri-exponential fit is consistent with the calculated FFCF only for shorter times, here less than 6 ps. At times longer than this the FFCF decays more

slowly than represented by the spectral diffusion time obtained in the fit, $\tau_{\omega}^{(3)} = 2.1 - 2.3$ ps; see Table 5.1. These times are consistent with the ~ 2 ps previously reported by Ni and Skinner for the E3B2 model.¹²³ This is quantitatively slower than that obtained for the SPC/E model, which represents the primary difference between the descriptions. Because of this behavior, we are able to resolve the FFCF for the E3B models out to longer times than that for SPC/E water.

As with the SPC/E description, these $\tau_{\omega}^{(3)}$ spectral diffusion times are considerably shorter than the calculated jump times, which are also given in Table 5.1. The jump times of $\tau_0 = 4.59$ and 4.30 ps for E3B2 and E3B3, respectively, are significantly larger than the SPC/E value. Using these values as the timescale for an added fourth exponential in fitting $C_{\omega}(t)$ gives excellent agreement over the full time range. However, this jump time contribution to the FFCF is still small, with an amplitude of 2.6 – 2.7% compared to the faster spectral diffusion time amplitude of 21 – 17%. We also note that the addition of this jump time component dramatically reduces the spectral diffusion time obtained to 1.2 ps for both E3B models.

Thus, for all three water models we find the same features in the FFCF that indicate a small role, $< 3\%$ of the total response, for H-bond exchanges that occurs on timescales longer than the dominant component of 1 – 1.2 ps. The latter occurs more rapidly than H-bond exchanges, indicating it has a different physical origin.

5.4.2 Activation Energies

To further explore the role of H-bond exchanges in the spectral diffusion dynamics, we now turn to an examination of the activation energies of the timescales involved. These activation energies can shed light on the mechanistic origins of the decay times present in the FFCF. Most importantly, if the spectral diffusion time is associated with H-bond exchanges, it should exhibit the same activation energy as the jump time.²⁰³ Deviations from this prediction are indicative of a different mechanistic origin (or origins) of the spectral diffusion timescale.

We evaluate this directly by calculating the temperature-, or more precisely, the β -derivative of the full FFCF as described in Sec. 5.2 and expressed in Eq. (5.4). The results are shown in Fig. 5.3

for all three water models along with the fits to the form given in Eq. (5.5). As with the FFCF itself, it is clear that $\partial C_{\omega}(t)/\partial\beta$ is not adequately described at long times by the three-exponential fit, but the agreement is excellent when a small additional component with a timescale equal to the jump time, τ_0 , is included.

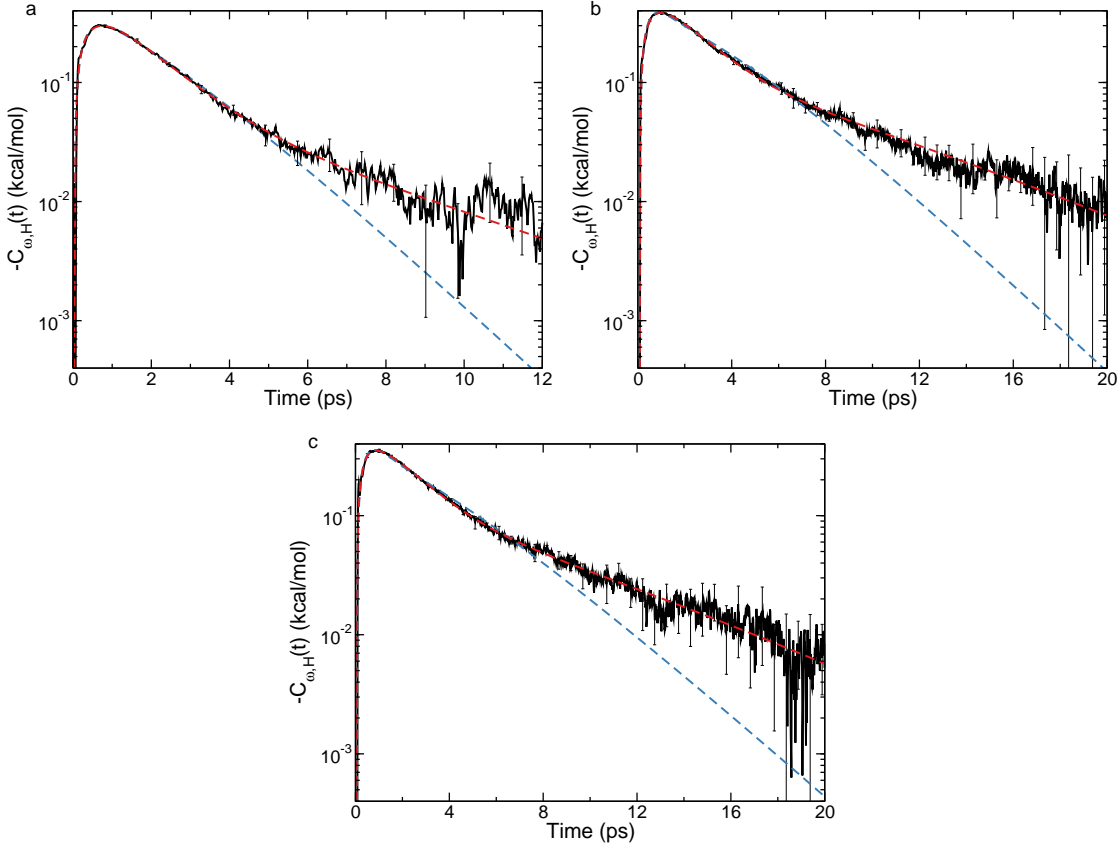


Figure 5.3: The β derivative of the FFCF, $\partial C_{\omega}(t)/\partial\beta$, versus time (black solid line) is shown for the (a) SPC/E, (b) E3B2, and (c) E3B3 water models with three- (blue dashed line) and four- (red dashed line) exponential fits, Eq. (5.5). In the latter, the longest timescale is fixed as the jump time, τ_0 .

As noted in Sec. 5.2, the activation energy of each timescale can be obtained from fitting the derivative FFCF, $C_{\omega,H}(t)$. The results of this analysis are given in Table 5.2. (Note that the four-exponential fits shown in Fig. 5.3 use the jump time τ_0 and its derivative $\partial\tau_0/\partial\beta$, both of which are obtained from a separate analysis of the trajectories.) The calculated activation energies for the spectral diffusion time are not the same as that for the jump time, independent of whether the three- or four-exponential fit is considered. Specifically, the jump time has a significantly

| SPC/E Water Model | | | | |
|---------------------|--------------------|--------------------|---------------------|----------------------|
| Timescale | E_a | KE | LJ | $Coul$ |
| τ_0 | 3.30 ₃ | 0.95 ₁ | -0.88 ₄ | 3.23 ₆ |
| $\tau_\omega^{(3)}$ | 2.24 ₅₁ | 0.51 ₂₀ | -0.60 ₅₀ | 2.33 ₉₈ |
| $\tau_\omega^{(4)}$ | 1.68 ₉₈ | 0.41 ₃₄ | -0.94 ₆₉ | 2.20 _{1.48} |
| E3B2 Water Model | | | | |
| Timescale | E_a | KE | LJ | $Coul$ |
| τ_0 | 4.43 ₂ | 1.10 ₂ | -1.16 ₂ | 4.49 ₂ |
| $\tau_\omega^{(3)}$ | 3.36 ₁₅ | 0.83 ₁₆ | -0.91 ₁₅ | 3.45 ₃₆ |
| $\tau_\omega^{(4)}$ | 2.49 ₂₀ | 0.51 ₁₄ | -0.78 ₂₀ | 2.76 ₄₂ |
| E3B3 Water Model | | | | |
| Timescale | E_a | KE | LJ | $Coul$ |
| τ_0 | 4.14 ₃ | 1.06 ₁ | -1.37 ₃ | 4.45 ₄ |
| $\tau_\omega^{(3)}$ | 2.81 ₃₅ | 0.76 ₉ | -0.94 ₁₇ | 2.98 ₃₆ |
| $\tau_\omega^{(4)}$ | 2.55 ₃₀ | 0.53 ₁₀ | -1.13 ₃₀ | 3.15 ₄₀ |

Table 5.2: Activation energies and kinetic (KE), Lennard-Jones (LJ), and Coulombic ($Coul$) energy components for the jump time τ_0 and the spectral diffusion times obtained from three-, $\tau_\omega^{(3)}$, and four-, $\tau_\omega^{(4)}$, exponential fits of the derivative FFCF, $C_{\omega,H}(t)$. All energies are in kcal/mol; subscripts represent uncertainty in the trailing digit(s).

higher E_a compared to the spectral diffusion time. This difference is increased when the long-time behavior is more accurately described by inclusion of the fourth exponential with timescale τ_0 . This indicates that the spectral diffusion times are determined by a process with a lower effective barrier than that for H-bond exchanges. Consistent with our analysis of the FFCF, this suggests that the spectral diffusion time cannot be solely, or even primarily, associated with H-bond jumps. Furthermore, as was the case for the FFCF, an f -test with 95% confidence intervals confirms that the derivative 4-exponential fitting function provides a statistically significant improvement over the 3-exponential derivative function.²⁰² Importantly, this demonstrates that the explicit inclusion of the jump activation energy in this fit improves the quality of the fit of the long-time behavior of the FFCF.

Ni and Skinner previously reported a spectral diffusion activation energy of 3.85 kcal/mol for the E3B2 water model from an Arrhenius analysis.¹²³ This is most directly comparable to E_a

for $\tau_{\omega}^{(3)}$ in the present calculations, for which we obtain 3.36 ± 0.15 kcal/mol. It is not clear if the two results are statistically different, however, as in Ref. 123 they obtain the timescale from fitting the FFCF for times longer than 1.5 ps to a single exponential and use a wide temperature range (283 – 363 K) for the Arrhenius analysis.²⁰⁴ It is important to note that while these values are similar to activation energies reported for the spectral diffusion time from measurements – values of 3.4 ± 0.5 kcal/mol^{105,138} and 3.5 ± 0.2 kcal/mol¹³⁹ have been reported (though Perakis and Hamm argue that 6.2 ± 0.2 kcal/mol, taken under different polarization conditions, is a better estimate¹³⁹) – they are not in agreement with the jump time activation energy obtained from the same water model, $E_{a,0} = 4.43 \pm 0.02$ kcal/mol. Thus our present results indicate that the spectral diffusion activation energy is *not* the same as the jump activation energy, and thus it is not associated with H-bond exchanges.

5.4.3 Mechanistic Insight

The fluctuation theory approach provides a rigorous way to decompose the activation energy into contributions from different components of the total energy by recognizing that $\delta H(0) = \delta KE(0) + \delta U_{LJ}(0) + \delta U_{Coul}(0)$, where $\delta KE(0)$, $\delta U_{LJ}(0)$, and $\delta U_{Coul}(0)$ are the kinetic, Lennard-Jones, and Coulombic energy fluctuations, respectively. This sum can be used to replace $\delta H(0)$ in Eqs. (5.4) and (5.7) to yield three separate derivative time correlation functions, each of which can then be fit with Eq. (5.5) to extract the activation energy contributions associated with each term. These contributions can be interpreted based on Tolman’s perspective.¹⁸ Tolman showed that for a chemical reaction, the activation energy can be rigorously written as $E_a = \langle H \rangle_{reacting} - \langle H \rangle_{reactants}$, *i.e.*, the average energy of the species that react minus the average energy of reactants. In this context, the Lennard-Jones contribution to the activation energy is $E_{a,LJ} = \langle U_{LJ} \rangle_{reacting} - \langle U_{LJ} \rangle_{reactants}$ or the average Lennard-Jones energy of reacting species minus the average Lennard-Jones energy of reactants. Thus, such decompositions provide otherwise unavailable mechanistic insight into how different kinds of energy in the system promote or inhibit the process of interest.

The decomposition of the FFCF derivative, $\partial C_{\omega}(t)/\partial \beta$, into its kinetic, Lennard-Jones, and

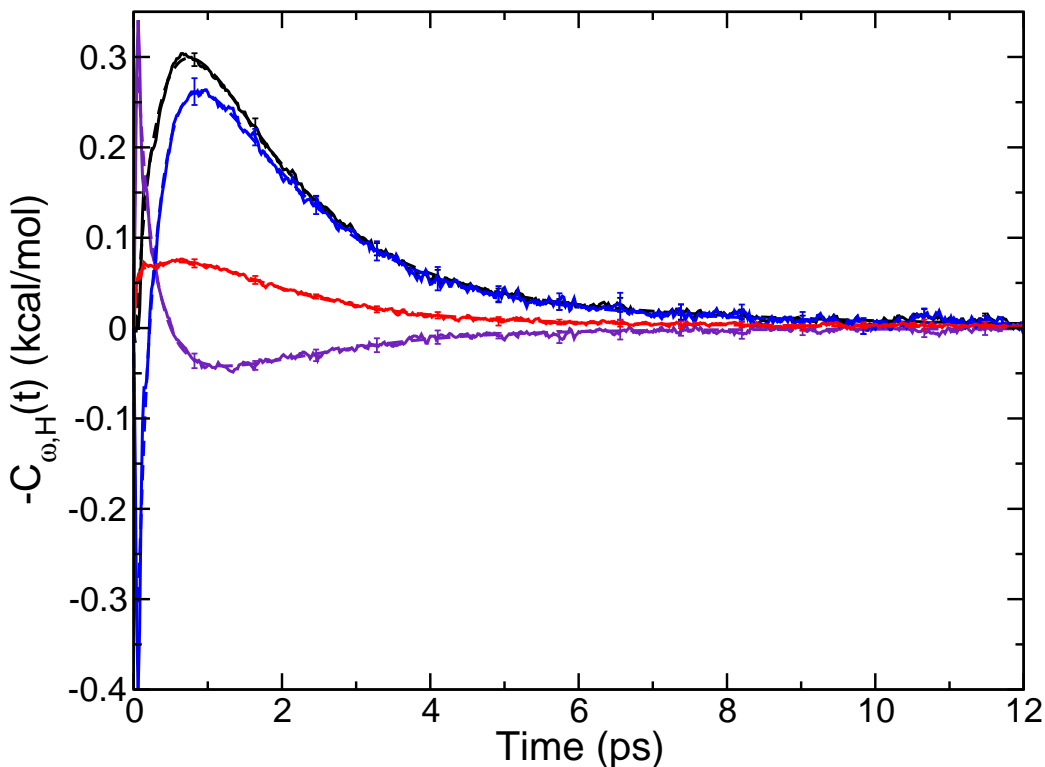


Figure 5.4: The β derivative of the FFCF, $\partial C_{\omega}(t)/\partial\beta$, versus time (black solid line) and its kinetic (red solid line), Lennard-Jones (violet solid line), and Coulombic (blue solid line) energy contributions for the SPC/E water model. Four-exponential fits, Eq. (5.5), are also shown (dashed lines of the same color; not easily visible because of the high quality of the fit.)

Coulombic contributions is shown in Fig. 5.4 for SPC/E water. The activation energy components obtained from the fitting are given in Table 5.2, where E3B2 and E3B3 results are also listed. Consistent with what we have previously found for the activation energies for OH reorientation,^{44,58} diffusion,^{58,160} viscosity,⁵⁰ and H-bond jumps of water,¹³⁶ the Coulombic interactions represent the dominant contribution, though they are in competition with the smaller Lennard-Jones component. Indeed, $E_{a,Coul}$ is nearly equal to the total activation energy for the spectral diffusion timescale if a three-exponential fit is used and larger than it in the four-exponential fitting. On the other hand, $E_{a,LJ}$ is negative, reflecting the natural tension between the Coulombic and Lennard-Jones interactions in an H-bond. However, the Lennard-Jones contribution is significantly smaller than $E_{a,Coul}$, as is the positive kinetic energy component.

The decomposition of the activation energies for the SPC/E model are suggestive of differences

between the results for the H-bond jump and spectral diffusion times. However, the comparatively large statistical uncertainties do not allow them to be distinguished except for the total activation energy and the kinetic energy component; these are both higher for the jump time than the spectral diffusion result. For the E3B models, the errors are smaller (particularly for the $\tau_{\omega}^{(4)}$ timescale due to its larger amplitude) and it is then clear that the differences observed in the total jump and spectral diffusion activation energies are also present in the kinetic, Lennard-Jones, and Coulombic components. In all cases, the jump time has components that are larger in absolute value compared to the spectral diffusion results (independent of the fitting method). This is suggestive of weaker energetic barriers for spectral diffusion compared to H-bond exchanges.

5.5 Conclusions

We have examined the connection between spectral diffusion and H-bond exchange dynamics in three water models by calculating and analyzing the frequency-frequency correlation function for the OH vibration of an HOD in D₂O. We find that the long-time decay of this FFCF is not adequately described by a single spectral diffusion timescale. However, inclusion of an additional decay component with a timescale equal to the H-bond exchange time, τ_0 , yields an excellent fit of the calculated FFCF. This exchange time component has a small amplitude (< 3%) and is thus a minor component of the spectral diffusion dynamics. The remaining spectral diffusion timescale is found to be $\sim 1 - 1.2$ ps, consistent with experimental measurements,^{114,176} but significantly faster than the H-bond exchange time.

We have also used dynamical fluctuation theory to calculate and compare the spectral diffusion and H-bond jump activation energies from the temperature (or β) derivative of the FFCF. This derivative time correlation function is also only well described when a small-amplitude decay based on the H-bond jump time is included. Moreover, the resulting activation energies are different for the spectral diffusion time and the H-bond jump time. The same is true for the components of the two activation energies (available within the fluctuation theory) associated with

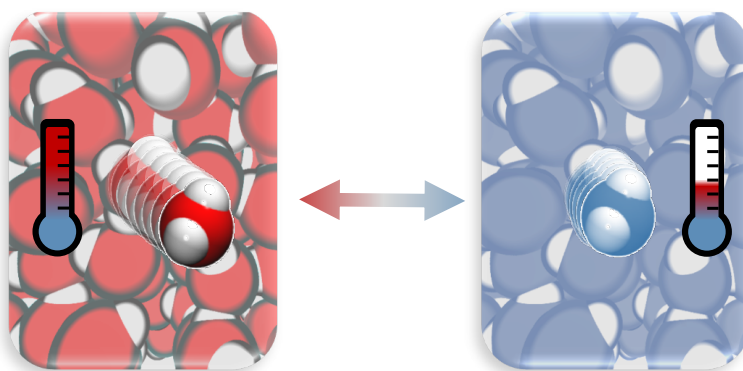
kinetic, Coulombic, and Lennard-Jones energies in the system.

The results show that the spectral diffusion time is shorter than that for H-bond exchanges and it has a smaller activation energy. Thus, it clearly corresponds to processes that happen in between H-bond exchanges and require less energy than that necessary to fully break one H-bond and form another. This implicates rearrangements of the H-bond structure within the intact H-bond and transient breaking of H-bonds (in which the OH returns to its original H-bond acceptor) as the motions associated with the spectral diffusion time. While H-bond exchanges also contribute to the spectral diffusion, they do so at longer times and with a comparatively small amplitude.

This minor contribution of H-bond jumps to the spectral diffusion is consistent with a picture in which only jumps between acceptors that yield different H-bonding structures are expected to lead to a difference in the equilibrium OH frequency. While this is the case in aqueous solutions containing different types of H-bond acceptors,^{134,205} in neat liquid water most of the frequency dephasing can be accomplished by rearrangements of the H-bonding arrangement either without breaking the original H-bond (through motions of the surrounding waters) or by transiently breaking and reforming the H-bond with the original acceptor. These motions occur on a picosecond timescale, more than three times faster than that for H-bond exchanges.

Part II

Water Under Extreme Conditions



In Part 2, we apply fluctuation theory to study water under extreme conditions (*i.e.* away from 298 K and 1 bar), again studying diffusion (Chapters 6-7), reorientation (Chapter 7), Liquid Structure (Chapters 8 and 10), and the infrared HOD/D₂O spectrum (Chapter 9). Chapter 6 is the first direct calculation of activation volumes (and pressure derivatives) using a fluctuation theory approach, Chapter 7 develops a technique for calculating high-order temperature derivatives at room temperature and using them to predict the diffusion coefficient and reorientation time down into the supercooled regime of water (*circa* 125 K). Chapter 8 applies fluctuation theory to the radial distribution function which describes water liquid structure and uses it to predict the radial distribution function down to 235 K from simulations at room temperature. This chapter also develops a technique for using these derivatives to directly calculate the internal energy and entropy along the OO coordinate in liquid water. Chapter 9 examines the origins of isosbestic points in the infrared spectra and illustrates that these spectra can also be predicted from room temperature. Chapter 10 demonstrates the application of pressure derivatives to liquid structure and how they can be used to make predictions of its pressure dependence.

Chapter 6

Expanding the Calculation of Activation Volumes: Self-Diffusion in Liquid Water

6.1 Introduction

Theoretical chemical dynamics is now a mature and thriving field that serves as a critical complement to experimental studies of properties ranging from transport coefficients to nonlinear spectroscopic signals. Simulations can provide mechanistic insight as well as predictions of measurable properties that can guide future experiments. The centerpiece of these approaches are the theories that relate equilibrium dynamics at the molecular level to the desired observable, typically through a time correlation function (TCF) or other statistical mechanical average of a time-dependent quantity.⁶⁸

Key examples include, but are by no means limited to, the Green-Kubo formulas²⁰⁶ that relate macroscopic transport coefficients to integrals, or Fourier transforms, of TCFs and reactive flux correlation functions^{32–34,69} that provide reaction rate constants from TCFs involving the flux through a transition state dividing surface. In this Chapter, we will consider the diffusion coefficient, which can be obtained from the long-time behavior of the mean-squared displacement, $MSD(t) = \langle |r(t) - r(0)|^2 \rangle$, as

$$D = \lim_{t \rightarrow long} \frac{MSD(t)}{6t}, \quad (6.1)$$

This work adapted with the permission of Zeke A. Piskulich, Oluwaseun O. Mesele, and Ward H. Thompson and AIP Publishing from *J. Chem. Phys.* **148**, 134105 (2018).⁵⁹

for motion in three dimensions, where D is the diffusion coefficient, and t is the time.

An issue that is frequently of central importance in the exploration of chemical dynamics is how does the quantity of interest, *e.g.*, the diffusion coefficient, depend on the macroscopic thermodynamic conditions such as temperature, pressure, and chemical potential. Indeed, activation energies derived from the temperature dependence of a relevant timescale are a staple of dynamics studies and provide critical mechanistic insight through their relationship to the rate-limiting barrier height. As an example, the activation energy of diffusion, $E_{a,D}$, is defined by the expression

$$E_{a,D} = -\frac{d \ln D}{d\beta}, \quad (6.2)$$

where $\beta = 1/k_b T$. The activation energy is typically obtained from the slope of an Arrhenius plot of $\ln D$ versus $1/T$ based on measurements or simulations at multiple temperatures. However, this approach can be complicated by temperature-induced changes in the system properties, *e.g.*, the density or composition, that must be considered. In some cases, the problem is acute such as when near a phase transition or for solutes like folded proteins or non-covalent assemblies.

Dellago and Bolhuis addressed this issue by demonstrating how the activation energy for a reaction rate constant can be obtained from transition path sampling simulations at a single temperature.³⁵ Similarly, Morita and co-workers have examined direct approaches for determining the temperature dependence of vibrational spectra.^{46,46,48,49} More recently, we have shown how an activation energy can be obtained from single-temperature simulations for essentially any dynamical timescale, classical or quantum mechanical.^{31,58} Further, we developed rigorous expressions for the contributions to the activation energy from the various components of the total system energy, which provides detailed mechanistic information that is not available by other methods (simulation or experiment).⁵⁸

In the remainder of this Chapter, we further generalize such an approach beyond temperature dependence. Specifically, we show how derivatives of dynamical timescales with respect to macroscopic, thermodynamic variables can be straightforwardly determined through MD simu-

lations. We illustrate the method by applying it to the calculation of the activation volume for self-diffusion in liquid water.

The activation volume for a rate constant, k , or other dynamical timescale is given by its pressure dependence,²⁰⁷

$$\Delta V^\ddagger = -RT \frac{\partial \ln k}{\partial p}, \quad (6.3)$$

and is a key quantity of interest in a variety of chemistries.^{61,208} In addition to providing a quantitative measure of the effect of pressure, ΔV^\ddagger can be useful in understanding chemical mechanisms.⁶¹ It is typically interpreted as the relative size of the transition state and reactant structures. However, Ladanyi and Hynes have pointed out that this geometric interpretation is not always supported by a detailed analysis in liquid systems and is inconsistent with any pressure dependence of the activation volume.⁶² Instead, they noted that ΔV^\ddagger can reflect the rearrangement of the solvent (packing) around the transition state.

Activation volumes have attracted particular attention for ion pairing and hydration shell dynamics with a significant number of experiments^{61,209–212} and simulations^{63,64,64,213–218,218–220} of activation volumes. Most of the experiments have focused on solvent exchange around transition metal ions while the simulations have primarily examined water exchange around alkali or alkaline earth metals and sometimes halides. Activation volumes can provide important insight into the mechanism of solvent exchange by identifying the dissociative or associative nature of the exchange.⁶¹ In the former case, a solvent molecule departs the solvation shell before a new molecule enters, while the order of these events are reversed in the latter instance; the two mechanisms thus lead to opposite signs in ΔV^\ddagger .

Activation volumes can be challenging to measure accurately, but they are particularly difficult to calculate. Typically, they are obtained from calculations of the rate constant at a range of pressures, the results of which are used to generate an Arrhenius-like plot of $\ln k$ versus p , the slope of which gives ΔV^\ddagger via Eq. 6.3. Because k depends weakly on p , the range of pressures used is substantial – often spanning a thousand bar or more – to adequately observe the small changes in k . However, for some systems $\ln k$ varies nonlinearly with the pressure, which can lead to significant

errors using this approach. One key example is the self-diffusion of liquid water,^{1-4,221-223} which is considered in this work. This provides a significant impetus to develop methods for calculating ΔV^\ddagger and related quantities *directly* to avoid such issues. In the case of the activation volume, this means calculating it from simulations carried out at a single pressure.

6.2 Theory

We can write the average of a variable of interest, f , at some time t in a general ensemble as

$$\langle f(t) \rangle = \frac{1}{\Theta} \text{Tr} \left[e^{-\beta(H+\mathbf{b}\cdot\mathbf{X})} f(t) \right]. \quad (6.4)$$

Here, H is the system Hamiltonian and $\Theta = \text{Tr}[e^{-\beta(H+\mathbf{b}\cdot\mathbf{X})}]$ is the partition function. The vectors \mathbf{b} and \mathbf{X} contain as elements the intensive and extensive thermodynamic variables that define the particular ensemble beyond the temperature (β) and Hamiltonian. For example, $\mathbf{b} = (p)$ and $\mathbf{X} = (V)$ for the isothermal-isobaric ensemble and $\mathbf{b} = (\mu_1, \mu_2)$ and $\mathbf{X} = (N_1, N_2)$ for the grand canonical ensemble with two components. It is easy to see, however, that only Θ and the exponential factor depend on the intensive variables, \mathbf{b} and thus, the derivative of the the average value of $f(t)$ with one of these, b_j , is

$$\begin{aligned} \frac{\partial \langle f(t) \rangle}{\partial b_j} &= \beta \langle X_j \rangle \langle f(t) \rangle - \beta \frac{1}{\Theta} \text{Tr} \left[e^{-\beta(H+\mathbf{b}\cdot\mathbf{X})} X_j(0) f(t) \right] \\ &= -\beta \langle \delta X_j(0) f(t) \rangle. \end{aligned} \quad (6.5)$$

Here, $\delta X_j(0) = X_j(0) - \langle X_j \rangle$ and we have used the result that

$$\frac{\partial \Theta^{-1}}{\partial b_j} = \beta \frac{1}{\Theta^2} \text{Tr} [e^{-\beta(H+\mathbf{b}\cdot\mathbf{X})} X_j] = \beta \frac{1}{\Theta} \langle X_j \rangle. \quad (6.6)$$

Such fluctuation equations are far from new, apparently first introduced by Greene and Callen.²⁸ For example, if $f(t) = V(0)$ in the isothermal-isobaric ensemble, Eq. 6.5 can be used to relate the isothermal compressibility to the volume fluctuations.²⁷ However, these relationships have

been generally neglected in understanding how dynamical timescales change with the underlying thermodynamic conditions.

Dynamical timescales are frequently obtained from MD simulations through computation of time correlation functions of the general form $C_{AB}(t) = \langle A(0)B(t) \rangle_{\Theta}$, where A and B are functions of the phase space variables and the subscript Θ indicates that the average is taken in a particular ensemble. Applying Eq. 6.5 to the TCF gives

$$\frac{\partial C_{AB}(t)}{\partial b_j} = -\beta \langle \delta X_j(0) A(0) B(t) \rangle_{\Theta}. \quad (6.7)$$

Thus, the derivative of the TCF with respect to the intensive variable is given by the TCF weighted by the fluctuation in the corresponding extensive variable. This weighted TCF can be calculated within the same simulation from which $C_{AB}(t)$ itself is obtained, as we have previously demonstrated for the activation energy ($b_j = \beta$).^{31,58}

As one key example of Eq. 6.5, consider the isothermal-isobaric ensemble and pressure as the intensive variable. Then, the pressure dependence of $\langle f(t) \rangle$ is simply

$$\frac{\partial \langle f(t) \rangle}{\partial p} = -\beta \langle \delta V(0) f(t) \rangle_{NpT}. \quad (6.8)$$

As we will illustrate below for the example of diffusion in water, this relation provides a way to calculate the the derivative of the diffusion coefficient, D , with respect to pressure from simulations at a single p and within the same framework that gives D itself. Borrero and Dellago have previously implemented an analogous approach for a reaction rate constant in a model system within the context of a transition path sampling approach.³⁷ However, the simple derivation above indicates the general nature of this result.

Another interesting special case of Eq. 6.5 is in the grand canonical ensemble for a binary mixture, taking the intensive variable to be one of the species' chemical potential. Then, it is straightforward to see that

$$\frac{\partial \langle f(t) \rangle}{\partial \mu_j} = -\beta \langle \delta N_j(0) f(t) \rangle_{\mu_1 \mu_2 VT}. \quad (6.9)$$

This indicates that the changes in the dynamics described by $\langle f(t) \rangle$ due to shifts in the phase equilibria can be determined from a single thermodynamic phase point. The implementation of such an approach is ongoing work in our group.

As an illustration of the general concepts just outlined, we consider the specific case of the activation volume of the self-diffusion coefficient, D , of liquid water. As noted in Eq. 6.1, the diffusion coefficient can be calculated from the mean-squared displacement. The activation volume for D can then be obtained from Eq. 6.3 as

$$\begin{aligned} \Delta V_D^\ddagger &= -RT \lim_{t \rightarrow \text{long}} \frac{1}{6Dt} \frac{\partial \text{MSD}(t)}{\partial p} \\ &= \lim_{t \rightarrow \text{long}} \frac{\langle \delta V(0) |\vec{r}(t) - \vec{r}(0)|^2 \rangle_{NpT}}{6Dt}, \end{aligned} \quad (6.10)$$

using Eq. 6.5. Defining $\text{MSD}_V(t) \equiv \langle \delta V(0) |\vec{r}(t) - \vec{r}(0)|^2 \rangle_{NpT}$, this yields the simple expression for the activation volume²²⁴

$$\Delta V_D^\ddagger = \lim_{t \rightarrow \text{long}} \frac{\text{MSD}_V(t)}{\text{MSD}(t)}. \quad (6.11)$$

That is, it can be obtained from the long-time limit of the ratio of the MSD weighted by the volume fluctuations to the unweighted MSD. This provides a convenient means by which activation volumes can be extracted from molecular simulation.

6.3 Computational Methods

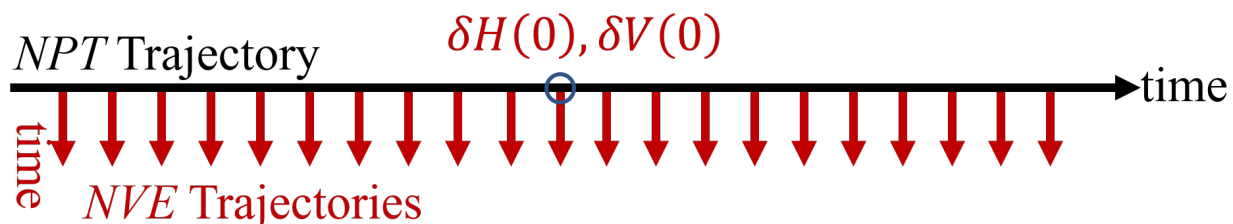


Figure 6.1: A diagram depicting the production of NVE trajectories sampled along a single NPT trajectory.

A practical implementation of the calculation of the activation volume via Eq. (6.11) is illus-

trated schematically in Fig. 6.1. Specifically, an NpT trajectory (using a thermostat and a barostat) is used to generate initial conditions for short, constant energy and volume (NVE) trajectories from which $MSD(t)$ and $MSD_V(t)$ are both calculated. In this way, the dynamics are not influenced by the thermostat or barostat algorithm or parameters as long as they give the correct energy and volume distributions.²²⁵ The NpT trajectory gives configurations that vary in the volume such that each NVE trajectory has a particular fluctuation in the system volume, $\delta V(0)$, relative to the average volume for all the trajectories. (We note that this approach also leads to fluctuations in the initial energies, $\delta H(0)$, as well that can be related to the activation energy.⁵⁸) The distribution of volume fluctuations obtained from the present simulations is shown in Fig. 6.2; as expected the distribution is Gaussian with a width that is related to the isothermal compressibility of the liquid.²⁰⁶

The MD simulations were performed using the Large-Scale Atomic/Molecular Massively Parallel Simulator (LAMMPS).⁸¹ Simulations used 256 water molecules using the TIP4P/2005 model⁵ and volume fluctuations were captured from a 5 ns in the NpT ensemble using a Nosé-Hoover thermostat, with a damping parameter of 100 fs, and a Nosé-Hoover barostat, with a damping parameter of 1 ps.^{83,84,226,227} Every 1 ps, the coordinates and momenta were extracted to serve as the initial conditions for a separate 20 ps constant energy (NVE) trajectory from which the dynamics were obtained from configurations saved every 50 fs; 5000 total NVE trajectories were propagated. In all simulations, the integration timestep was 1 fs timestep, the SHAKE algorithm was used in order to enforce the rigid bonds present within the TIP4P/2005 model,⁵ and electrostatic interactions were calculated using the particle-particle-particle mesh Ewald summation with an accuracy parameter of 10^{-5} .^{119,120}

6.4 Results and Discussion

Using this MD simulation procedure, we have calculated the activation volume of water diffusion at a variety of temperatures and pressures for which experimental data have been reported.¹⁻⁴ Examples of the results are shown in Fig. 6.3 for $p = 100$ bar and three different temperatures,

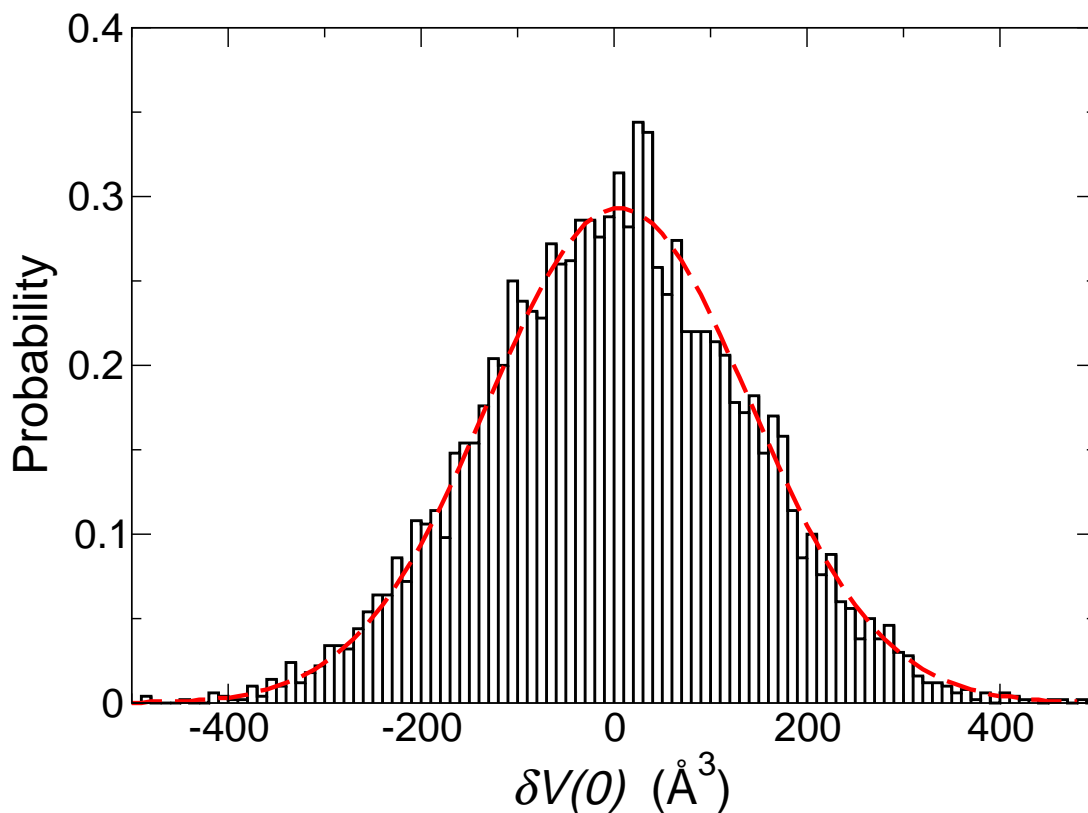


Figure 6.2: A plot of the probability distribution function of the fluctuations in volume of the individual NVE trajectories away from the average volume of the overall NPT trajectory. A gaussian fit has been included as a dashed red line.

283.2, 383.2, and 473.2 K. Specifically, the calculated $MSD(t)$ and $MSD_V(t)$ are shown for each temperature as a function of time. As expected, the volume fluctuation-weighted mean-squared-displacement, $MSD_V(t)$, depends linearly on time, with a slope that equals $6\partial D/\partial p$. This leads to a constant value at longer times for the ratio $MSD_V(t)/MSD(t)$ from which the activation volume can be obtained directly. This ratio, and the corresponding activation volume derived from its limit, is shown for $p = 100$ bar at each of the temperatures in Fig. 6.4. In each case the ratio reaches a constant value at longer times that permits the direct determination of ΔV_D^\ddagger . The present calculations give $\Delta V_D^\ddagger = -2.43 \pm 0.79$, 2.15 ± 0.25 , and 6.13 ± 0.33 cm^3/mol for 283.2, 383.2, and 473.2 K, respectively. These values are in very good agreement with the experimental results of

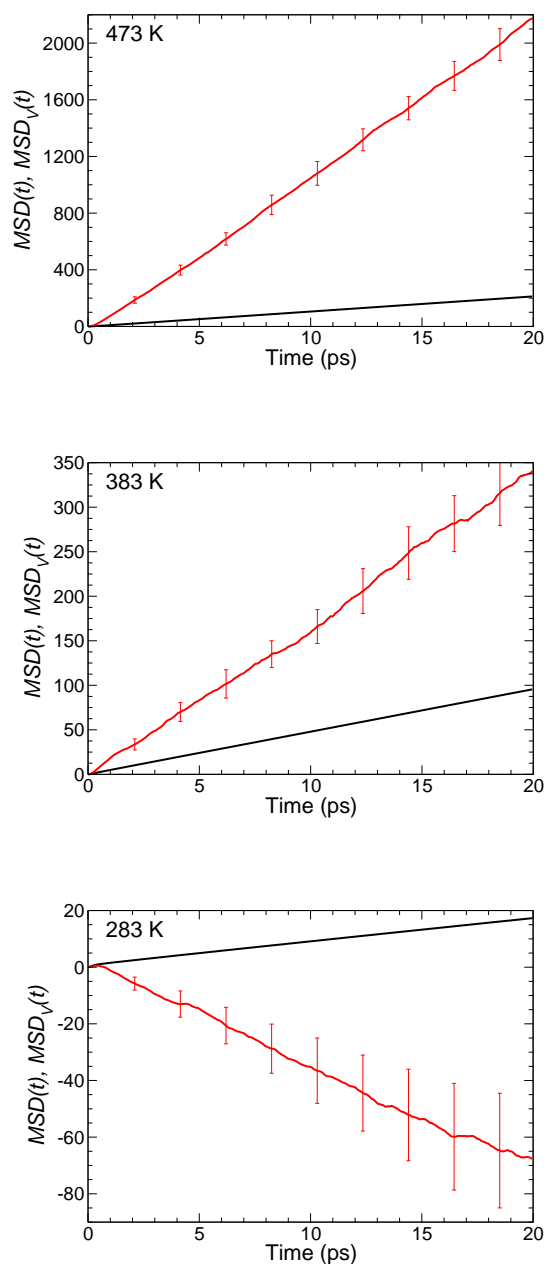


Figure 6.3: The volume-weighted mean-squared displacement $MSD_V(t)$ (red) and the unweighted mean-squared displacement $MSD(t)$ (black) for $p = 100$ bar and 473, 383, and 283 K (top to bottom).

-2.7, 1.7, and 5.5 cm^3/mol reported by Krynicki *et al.*³ for the same three temperatures. At the lowest temperature, we note that Woolf also reported a $\Delta V_D^\ddagger = -2.8 \text{ cm}^3/\text{mol}$ at 277 K.⁴ In addition, we have extracted similar values of -1.9 and -2.9 cm^3/mol from the $D(p, T)$ measurements in Refs.

1 (283 K) and 2 (278 K), respectively.²²⁸

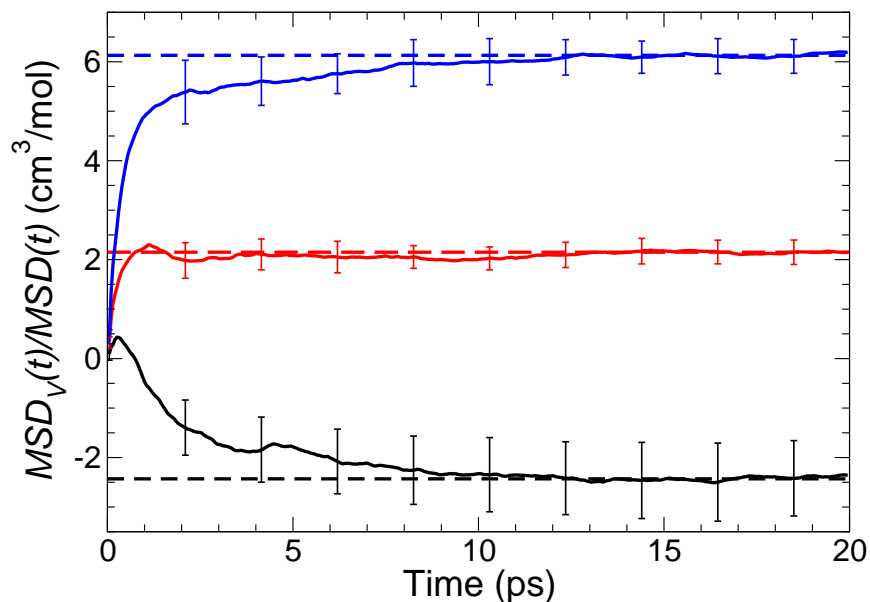


Figure 6.4: The ratio $MSD_V(t)/MSD(t)$, which at long times is equal to the diffusion activation volume, ΔV_D^\ddagger , for 100 bar and $T = 283$ (black), 383 (red), and 473 K (blue). Dashed lines of the same color indicate the derived ΔV_D^\ddagger from fitting to $t \geq 15$ ps.

As noted above, a key feature of the water diffusion coefficient is that the pressure dependence of $\ln D$ is not linear, *i.e.*, the activation volume changes with pressure.^{1–4,221–223} In particular, at lower temperatures (less than ~ 325 K),³ the diffusion coefficient passes through a maximum as the pressure is increased; the value of p at the maximum decreases with temperature such that at higher T the diffusion coefficient decreases monotonically with p . Thus, at lower temperatures, the sign of ΔV_d^\ddagger changes from negative at lower pressures to positive at higher p , while it is uniformly positive at higher T . This behavior is generally attributed to the effect of pressure on the hydrogen-bonding (H-bonding) structure.⁴ Namely, at lower temperatures and pressures, the transition state (including the surrounding “solvent” waters⁶²) associated with an exchange of H-bond acceptors,⁸⁵ involves a reduction in volume and hence $\Delta V_D^\ddagger < 0$. However, as p increases the resulting distortion of the H-bonds reduces this effect and eventually leads to a positive activation

volume.^{4,73} We have explored the variations in ΔV_d^\ddagger by calculating it at several temperatures and pressures. The results are presented in Fig. 6.5 and Table 6.1 along with experimental data reported in the literature³ and values extracted from measurements of $D(p, T)$.^{1,2,4,228}

Table 6.1: Calculated and measured activation volumes, ΔV_d^\ddagger , (in cm^3/mol) for water self-diffusion

| T (K) | p (bar) | Present Simul. | Measurements | | | |
|---------|-----------|------------------|--------------|--------|--------|----------|
| | | | Ref. 3 | Ref. 4 | Ref. 1 | Ref. 2 |
| 283.2 | 100 | -2.43 ± 0.79 | -2.6 | -3.0 | -1.9 | -2.1^a |
| 283.2 | 650 | -1.56 ± 0.48 | 0.0 | -0.9 | -0.8 | -1.0^a |
| 283.2 | 1700 | -0.33 ± 0.21 | 2.7 | 0.5 | 0.5 | 0.4^a |
| 298.2 | 1 | -1.40 ± 0.15 | | -1.6 | -1.3 | -1.3 |
| 298.2 | 650 | -0.60 ± 0.26 | | -0.4 | -0.1 | -0.2 |
| 298.2 | 1700 | 0.23 ± 0.23 | | 0.4 | 0.9 | 0.9 |
| 383.2 | 100 | 2.15 ± 0.25 | 1.7 | | | |
| 383.2 | 1700 | 1.90 ± 0.22 | 2.8 | | | |
| 473.2 | 100 | 6.13 ± 0.33 | 5.5 | | | |
| 473.2 | 1700 | 3.69 ± 0.36 | 11.1 | | | |

^aValues listed under $T = 283.2$ K are for 278.2 K.

The results presented in Fig. 6.5 and Table 6.1 show mixed agreement with experiment for the TIP4P/2005 water model. At low temperatures, 283.2 and 298.2 K, highlighted in Fig. 6.5b, the calculated values are in quite reasonable agreement with measurements. Both show an increasing activation volume with pressure, though the simulations generally rise more slowly and thus underestimate ΔV_d^\ddagger at high p . To our knowledge, only Krynicki *et al.* have measured data above 350 K. As noted above, the simulations are in very good agreement for these higher temperatures with their reported values at 100 bar. However, Krynicki *et al.* find that ΔV_d^\ddagger still increases with p at these temperatures while the simulations predict that it becomes smaller. Thus, the two disagree significantly at 1700 bar. We note that at lower temperatures such as 283 and 298 K where multiple other measured values are available (Table 6.1), the ΔV_d^\ddagger of Krynicki *et al.* are significantly higher than those from other experiments at 650 and 1700 bar. At the same time, the present simulations with the TIP4P/2005 model yield activation volumes that are lower than the measurements at these higher pressures. This suggests accurate ΔV_d^\ddagger at 1700 bar and higher temperatures may lie between the predictions and Krynicki *et al.* measurements. Resolving this issue, however, may require new

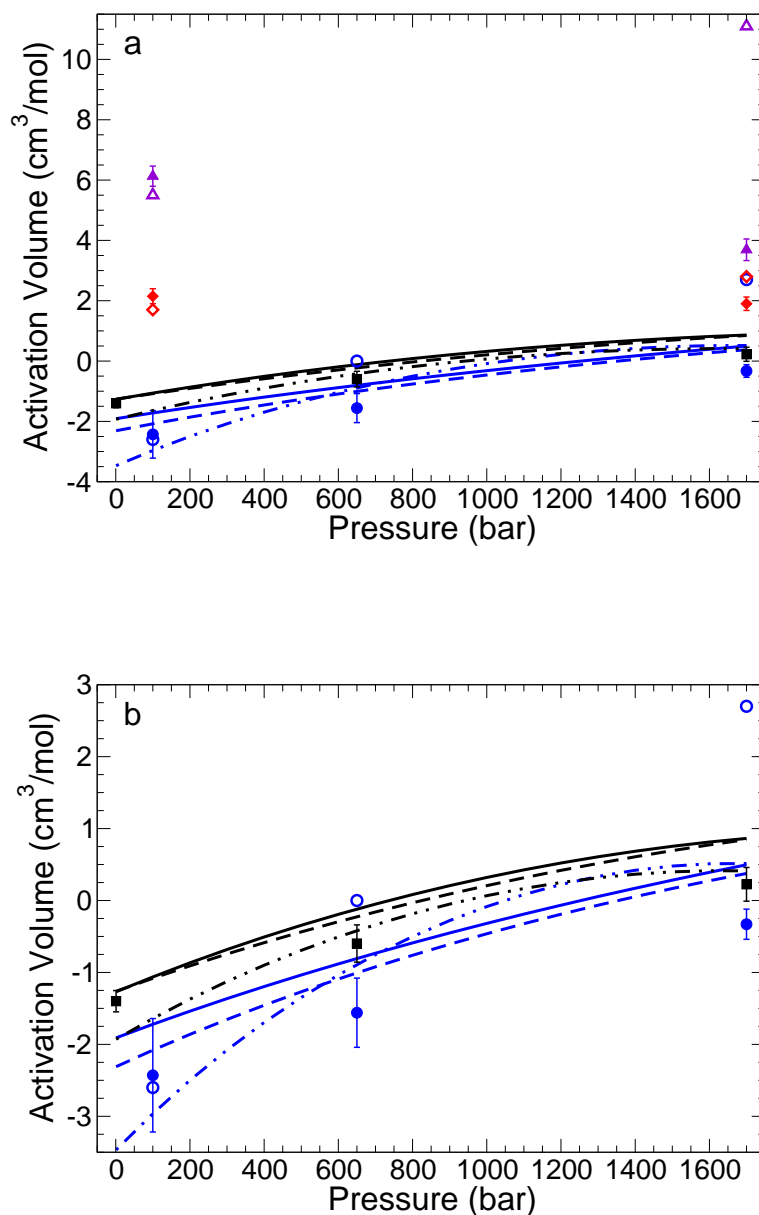


Figure 6.5: (a) Activation volume, ΔV_D^\ddagger , as a function of p and T . The present simulation results (filled symbols) for 283.2 (blue), 298.2 (black), 383.2 (red), and 473.2 K (violet) are compared to experimental data from Ref. 1 (solid lines), Ref. 2 (dashed lines), Ref. 3 (open symbols), and Ref. 4 (dot-dot-dashed lines); see text. Data represented by blue dashed line is for 278.2 K.² (b) An expanded view of the low temperature results.

measurements and simulations with other water models.

It is useful to consider the computational effort required to calculate the activation volumes

presented here. For each p and T , the total simulation time was 105 ns (a 5 ns NpT simulation followed by 5,000 embarrassingly parallel 20 ps NVE simulations). The potential alternative for determining ΔV_d^\ddagger from simulations is to calculate the diffusion constant at several pressures for each temperature; based on experimental studies,^{1-4,221} values at $\sim 8 - 10$ pressures are required. The $D(p; T)$ data can then be fit to a functional form from which the activation volume as a function of pressure at that T can be determined. We are not aware of any applications of this kind of direct simulation approach except for cases where $\ln k$ is linear in p ,²¹⁶ but it has been used in studies where rate constants are obtained from, *e.g.*, transition state theory calculations.⁶²

The diffusion coefficient converges more rapidly than ΔV_d^\ddagger in the present simulations, with a reasonable value for D obtained using only 500 NVE trajectories. However, because D varies weakly with pressure (*e.g.*, increasing p by 200 bar typically leads to changes in D of less than 1%,^{1-4,221}) a more precise value would almost certainly be required to accurately determine the activation volume. With 5000 NVE trajectories we find uncertainties in D that are less than $\tilde{0}.1\%$, which is probably more than sufficient but would need to be repeated for several pressures to determine one activation volume. On the other hand, calculation of the activation volume from the first 500 NVE trajectories gives values for ΔV_d^\ddagger that are within $0.7 \text{ cm}^3/\text{mol}$ of the converged results presented in Table 6.1. Thus, the direct approach presented here should be at least competitive with and likely more efficient than the traditional brute force methods (and additionally requires no assumption about the functional form of the diffusion coefficient with respect to pressure).

6.5 Summary

We have presented a generalized method by which derivatives of TCFs may be taken with respect to a variety of macroscopic variables. We have illustrated this approach by applying it to the calculation of the activation volumes of water self-diffusion and obtained generally good agreement with previous spin-echo NMR measurement results. A key advantage is that this method allows the activation volume to be obtained from simulations at a single pressure. This is particularly important for water diffusion, which exhibits a nonlinear dependence of $\ln D$ on the pressure. However,

the approach is general, both in terms of the dynamical quantity and the macroscopic variable of interest, and is easily implemented within nearly any simulation scheme. It should thus be widely applicable.

Chapter 7

The Dynamics of Supercooled Water Can Be Predicted from Room Temperature Simulations

7.1 Introduction

Significant effort over the past thirty years has been aimed at understanding the complex behavior of liquids in supercooled or glassy states.^{145,229,230} Cooled below its melting point at ambient pressure, water is a metastable liquid that exhibits several anomalous properties. These include a maximum in the isothermal compressibility, an apparent divergence in dynamical timescales such as the diffusion coefficient, and a breakdown of the Stokes-Einstein relation. The origin of these features has attracted significant attention, complicated by the lack of experimental data in the so-called “No Man’s Land” of water’s phase diagram below ~ 230 K where spontaneous crystallization inhibits measurements.

The peculiar trends of structural and dynamical properties in supercooled water¹⁴⁵ have frequently been attributed to either significant changes in the hydrogen bond (H-bond) network^{231–237} or increasing dynamical heterogeneity^{108,234} upon cooling. A particular focus in recent years is the connection to a phase transition between a high-density liquid (HDL) and a low-density liquid (LDL) that occurs at higher pressures ($\gtrsim 1$ kbar).^{238–240} The HDL-LDL coexistence curve terminates at a liquid-liquid critical point (LLCP), the precise location of which is still a matter

Adapted with the permission of Zeke A. Piskulich, and Ward H. Thompson and AIP Publishing from *J. Chem. Phys.* **152**, 074505 (2020).¹⁶⁰

of debate.¹⁴⁶ The extension of this coexistence curve beyond the critical point to lower pressures represents the Widom line, which approximately divides the region in pressure and temperature where the behavior is more HDL-like from that where it is more LDL-like. Thus, the temperature-dependent behavior of supercooled water at ambient pressure can, in this viewpoint, be explained by changes related to crossing the Widom line.

In support of this “two liquids,”¹⁴⁵ HDL-LDL, description of supercooled water are suggestions in experimental and simulation data of a smooth variation in dynamical timescales upon supercooling including viscosity,^{141,223,241,242} diffusion,^{6,146,236,242,243} and reorientation.¹⁰⁸ These results are in sharp contrast to the apparent divergence of timescales^{56,221,244,245} at a temperature $T_s \simeq 228$ K that represents the limit of stability for supercooled water,²⁴⁶ beyond which water dynamics are arrested and not accessible either by experiment or simulation. This perspective has been shown to be incompatible with the known thermodynamic properties of supercooled water,²³⁰ but nevertheless provides a useful mathematical description of water dynamics in the weakly supercooled regime.

In this Chapter, we examine the dynamics of supercooled water, focusing on the diffusion coefficient and reorientational timescales, as a function of temperature. These are among the dynamical properties most frequently used to characterize supercooled water as both can be characterized by experiments and simulations even as they change by orders-of-magnitude. The anomalies of supercooled water dynamics and thermodynamics are often viewed as determining the behavior of water under ambient conditions. If the two are indeed related, this relationship must be reciprocal, *i.e.*, the properties of ambient liquid water can inform us about supercooled water behavior. Here, we demonstrate that this is the case. We apply fluctuation theory for dynamics¹³ to calculate each timescale and its first two derivatives with respect to inverse temperature from simulations at room temperature. This information is then used to parameterize physically-motivated functional forms for the temperature dependence of the timescale that are accurate to low temperatures; expressions based on both the stability limit conjecture and the two-liquids description are considered. These results have implications for both calculating and interpreting dynamics of supercooled water and

other liquids.

7.2 Methods

7.2.1 Derivatives of D

The diffusion coefficient is obtained from the slope of the mean-squared displacement (MSD) evaluated at long times,

$$D = \lim_{t \rightarrow \infty} \frac{\langle |\vec{r}(t) - \vec{r}(0)|^2 \rangle}{6t}. \quad (7.1)$$

Here, t is time, $\vec{r}(t)$ is the time-dependent position, and $\langle \dots \rangle$ indicates an ensemble average at constant pressure and temperature.

In the present simulations, D is calculated from the water oxygen atom mean-squared displacement; for simplicity system size corrections²⁴⁷ are neglected. We have previously shown that the derivatives with respect to $\beta = 1/k_B T$ are given by^{13,58}

$$\frac{\partial MSD(t)}{\partial \beta} = -\langle \delta H(0) |\vec{r}(t) - \vec{r}(0)|^2 \rangle, \quad (7.2)$$

and

$$\frac{\partial^2 MSD(t)}{\partial \beta^2} = \langle [\delta H(0)^2 - \langle \delta H^2 \rangle] |\vec{r}(t) - \vec{r}(0)|^2 \rangle, \quad (7.3)$$

where H is the total energy and $\delta H(0) = H(0) - \langle H \rangle$ is the fluctuation in energy. The two time correlation functions (TCFs) described in Eqs. (7.2)-(7.3) can be obtained in the same, single temperature, simulations as the MSD itself. Effectively, this involves reweighting the mean-squared displacements that are being averaged by the fluctuations in the total system energy at $t = 0$. Derivatives of the diffusion coefficient are then calculated using the slope of each derivative correlation function at long time. Similarly, the activation energy is obtained as

$$E_{a,D} = -\frac{\partial \ln D}{\partial \beta} = \frac{\lim_{t \rightarrow \infty} \langle \delta H(0) |\vec{r}(t) - \vec{r}(0)|^2 \rangle}{\lim_{t \rightarrow \infty} \langle |\vec{r}(t) - \vec{r}(0)|^2 \rangle}. \quad (7.4)$$

7.2.2 Derivatives of $\langle \tau_2 \rangle$ and τ_2

The water reorientational dynamics are typically described by the TCF

$$C_2(t) = \langle P_2[\vec{e}_{OH}(0) \cdot \vec{e}_{OH}(t)] \rangle, \quad (7.5)$$

where P_2 is the second Legendre polynomial, and \vec{e}_{OH} is a unit vector pointing along a particular OH bond. $C_2(t)$ decays on multiple timescales, the longest of which, typically labeled τ_2 , is that associated with reorientation due to H-bond making and breaking. Experimentally, τ_2 can be measured *via* infrared pump-probe anisotropy spectroscopy.⁷¹ However, slow reorientation times are challenging to determine because the method is limited by the excited vibrational state relaxation time, which is 0.7-1.8 ps depending on the isotopic combination used.⁷² Additionally, the qualitative behavior of the $C_2(t)$ decay changes in the supercooled regime, as discussed in greater detail below. The integrated, or average, reorientation time measured by spin-echo NMR experiments is also obtained from this TCF as⁴³

$$\langle \tau_2 \rangle = \int_0^\infty C_2(t) dt. \quad (7.6)$$

We have previously shown that the first- and second-derivatives of the reorientational TCF can be expressed as^{13,44,58}

$$\frac{\partial C_2(t)}{\partial \beta} = -\langle \delta H(0) P_2[\vec{e}_{OH}(0) \cdot \vec{e}_{OH}(t)] \rangle, \quad (7.7)$$

and

$$\frac{\partial^2 C_2(t)}{\partial \beta^2} = \langle [\delta H(0)^2 - \langle \delta H^2 \rangle] P_2[\vec{e}_{OH}(0) \cdot \vec{e}_{OH}(t)] \rangle. \quad (7.8)$$

Because the integrated reorientation time is the time integral of $C_2(t)$, the first- and second-derivatives of $\langle \tau_2 \rangle$ are the time integrals of Eqs. (7.7) and (7.8), respectively.

The water OH reorientational TCF $C_2(t)$ decays on multiple timescales that are associated with rapid (< 50 fs) inertial dynamics, sub-picosecond librational dynamics within an intact H-bond,

and longer-time reorientation associated with H-bond exchanges. Thus, the TCF can be fit as

$$C_2(t) = \sum_{\alpha} A_{\alpha} e^{-t/\tau_{\alpha}}, \quad (7.9)$$

where $\alpha = \text{inertial, librational, and } 2$. The last timescale, τ_2 , is the one of interest here. The derivatives of $C_2(t)$ can then be described by the derivatives of this tri-exponential fitting function, which yields for the first derivative

$$\frac{\partial C_2(t)}{\partial \beta} = \sum_{\alpha} \left[\frac{\partial A_{\alpha}}{\partial \beta} + \frac{\partial(1/\tau_{\alpha})}{\partial \beta} t A_{\alpha} \right] e^{-t/\tau_{\alpha}}. \quad (7.10)$$

The A_{α} and τ_{α} are those obtained from fitting $C_2(t)$ itself and $\partial(1/\tau_{\alpha})/\partial \beta$ and $\partial A_{\alpha}/\partial \beta$ are then generated by fitting $\partial C_2(t)/\partial \beta$.⁴⁴ Similarly, the second derivative can be fit by

$$\begin{aligned} \frac{\partial^2 C_2(t)}{\partial \beta^2} = & \sum_{\alpha} \left[\frac{\partial^2 A_{\alpha}}{\partial \beta^2} \right. \\ & - t \left\{ A_{\alpha} \frac{\partial^2(1/\tau_{\alpha})}{\partial \beta^2} + 2 \frac{\partial A_{\alpha}}{\partial \beta} \frac{\partial(1/\tau_{\alpha})}{\partial \beta} \right\} \\ & \left. + t^2 A_{\alpha} \left(\frac{\partial(1/\tau_{\alpha})}{\partial \beta} \right)^2 \right] e^{-t/\tau_{\alpha}}, \end{aligned} \quad (7.11)$$

from which $\partial^2(1/\tau_{\alpha})/\partial \beta^2$ and $\partial^2 A_{\alpha}/\partial \beta^2$ are obtained.

For the calculation of $E_{a, \langle \tau_2 \rangle}$ at temperatures below 250 K, we fit the long-time decay of the $\partial C_2(t)/\partial \beta$ TCF to a single exponential to obtain the contribution for times greater than 300 ps.

7.2.3 Simulation Details

Predictions of transport properties were made using our previously published methods for calculating the first- and second-derivatives of the time correlation functions.^{44,50,58,59} Twenty separate 50 ns *NPT* trajectories at 1 bar and 298.15 K were propagated to generate a total of 1,000,000 initial configurations from which 50 ps *NVE* trajectories were propagated. A three-chain Nose-Hoover thermostat was utilized in the *NPT* trajectories to hold the temperature constant. The

thermostat and barostat damping parameters were 100 fs, and 1 ps, respectively.^{83,84} A simulation timestep of 1 fs was used. The TIP4P/2005 water model was used for all simulations, and was held rigid by the SHAKE algorithm.^{5,82} The simulation cell was made up of 343 water molecules. The Particle Particle Particle Mesh (PPPM) method was used to calculate long-range electrostatic interactions.^{119,120} The tolerance of both the SHAKE algorithm and the PPPM method was set to 1.0×10^{-4} . The Lennard-Jones interaction cutoff was set to 10.5 Å. All uncertainties are calculated over 5 blocks and represent a 95% confidence interval as taken from the Student's *t*-Distribution.¹²²

The same method was used to calculate the dynamical timescales at 235, 240, 250, 280, 320, 340, and 360 K (all at 1 bar) to provide accurate temperature-dependent results with the same force field and simulation protocol used for the predictions. However, for these calculations only 50,000 short *NVE* trajectories were used. Due to the longer timescales for dynamics in the supercooled region, the *NVE* trajectories at 235 K, 240 K, and 250 K were propagated for 300, 300, and 150 ps, respectively. We note that these simulations extend only to the weakly supercooled regime, ~ 20 K below the TIP4P/2005 model melting temperature, to test the predictions in this range; lower temperatures have been simulated by others but require significant additional computational effort.^{146,236}

7.3 Results

We have used MD simulations of TIP4P/2005 water⁵ at ambient conditions (298.15 K and 1 bar) to calculate the diffusion coefficient and OH reorientation times along with their first- and second-derivatives with respect to β as described in Sec. 7.2. The reorientational TCF, $C_2(t)$, obtained from these simulations is shown in Fig. 7.1a along with a fit to the tri-exponential function Eq. (7.9) with $\tau_2 = 3.271$ ps (see Table 7.1). The running integral, Eq. (7.6), obtained from the simulated $C_2(t)$ at room temperature is shown in Fig. 7.1a and the resulting $\langle \tau_2 \rangle$ from the long-time limit is given in Table 7.1.

The first- and second-derivative of $C_2(t)$ with respect to β are calculated according to Eqs. (7.7) and (7.8) from the simulations described in Sec. 7.2.3. The results are shown in panels b and c of

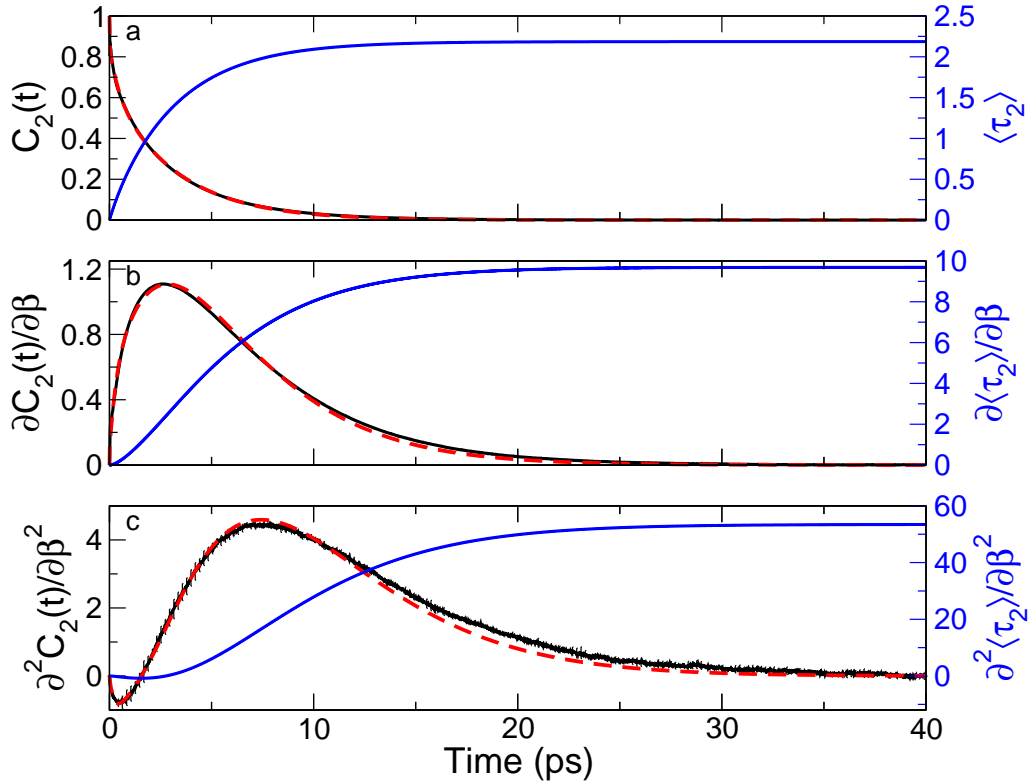


Figure 7.1: **(a)** Calculated $C_2(t)$ (black solid line) and its tri-exponential fit (red dashed line) with the integral of $C_2(t)$ (blue solid line) which equals $\langle \tau_2 \rangle$ at long times. **(b)** Calculated $\partial C_2(t)/\partial \beta$ (black solid line) and its fit (red dashed line) to Eq. (7.10) with the integral (blue solid line) that equals $\partial \langle \tau_2 \rangle / \partial \beta$ at long times. **(c)** Calculated $\partial^2 C_2(t) / \partial \beta^2$ (black solid line) and its fit (red dashed line) to Eq. (7.11) with the integral (blue solid line) that equals $\partial^2 \langle \tau_2 \rangle / \partial \beta^2$ at long times.

Fig. 7.1 along with the integral of each derivative TCF which gives, at long times, the first- and second-derivatives of $\langle \tau_2 \rangle$ with respect to β . Note that the derivatives of τ_2 are obtained by fitting $\partial C_2(t)/\partial\beta$ and $\partial^2 C_2(t)/\partial\beta^2$ by Eqs. (7.10) and (7.11). These fits are shown in Fig. 7.1 and represent the derivative TCFs to a good approximation.

The values of the calculated water diffusion coefficient and reorientational timescales obtained from explicit simulations at different temperatures (hereafter referred to as “ T -dependent simulations”) are plotted as a function of T and $1000/T$ in Fig. 7.2 and the values at 298.15 K are given in Table 7.1. The expected temperature dependence based on Arrhenius behavior, obtained from the directly calculated derivative at 298.15 K, is also shown for comparison. The Arrhenius approximation deviates from the T -dependent simulation results for all three timescales at both higher and lower temperatures. We have previously observed that this non-Arrhenius behavior is even evident for reorientational timescales within small temperature ranges of 20 K around room temperature.⁴⁴ It is thus interesting to consider to what extent information about the non-Arrhenius behavior of supercooled water is available in the liquid at ambient conditions.

7.3.1 Predictions of Dynamical Timescales

We now show how room temperature simulations alone can be used to predict the dynamics of supercooled water. The approach is the previously developed fluctuation theory for dynamics^{13,31,44,50,58} that enables the calculation of the activation energy of a timescale from simulations at a single temperature; these represent the analytical derivatives with respect to inverse temperature and thereby avoid the implicit numerical derivative of an Arrhenius analysis. We have used this method to calculate the first- and second-derivative with respect to β of the diffusion coefficient and reorientation timescales for water from simulations at room temperature as described in Sec. 7.2. The resulting values are provided in Table 7.1 along with the activation energy for each timescale.

Our approach is to use each timescale and its first two derivatives to parametrize a physically-motivated formula for the temperature dependence. The non-Arrhenius behavior of water dynam-

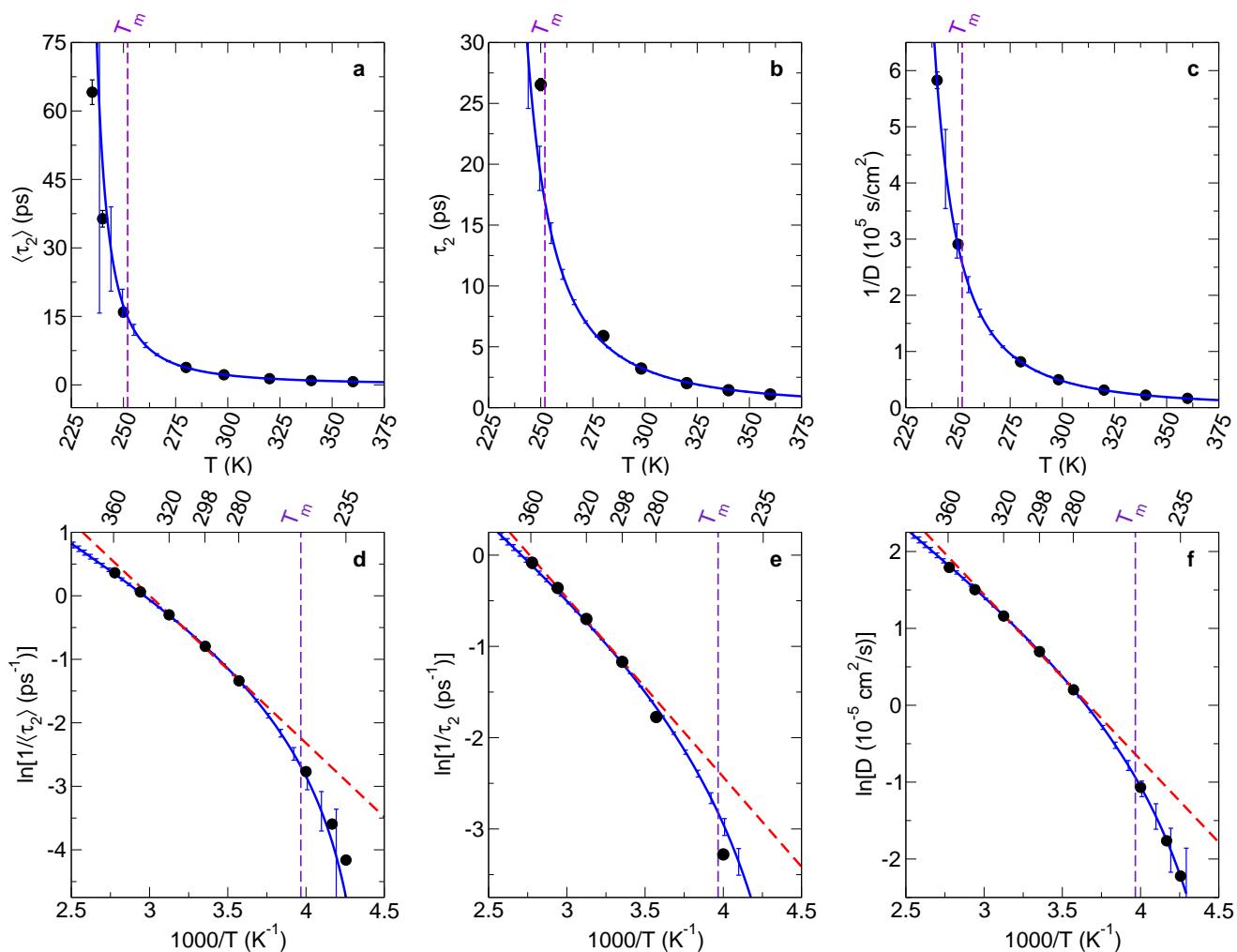


Figure 7.2: **(a-c)** Calculated $\langle \tau_2 \rangle$, τ_2 , and D (black circle) at different temperatures are compared to the predictions from room temperature simulations (blue solid line). **(d-f)** Arrhenius plots of $\langle \tau_2 \rangle$, τ_2 , and D calculated from T -dependent simulations (black circle) compared to predictions from room temperature simulations (blue solid line) and the Arrhenius result (red dashed line) from the activation energy at 298.15 K. The melting point of TIP4P/2005 water is also indicated (purple dashed line).⁵

| Timescale | τ | $1/\tau$ | $\partial\tau/\partial\beta$ | $\partial^2\tau/\partial\beta^2$ | E_a |
|--------------------------|---------------------|----------------------|------------------------------|----------------------------------|---------------------|
| $\langle \tau_2 \rangle$ | 2.215 ₁ | 0.4515 ₅₀ | 10.00 ₃ | 58.1 _{2,3} | 4.514 ₁₂ |
| τ_2 | 3.271 ₂ | 0.3057 ₂ | 13.57 ₄ | 71.0 _{2,3} | 4.149 ₉ |
| $1/D$ | 0.4973 ₃ | 2.011 ₁ | 2.122 ₅ | 11.1 ₄ | 4.267 ₉ |

^a $\langle \tau_2 \rangle$ and τ_2 are in units of ps, D in units of 10^{-5} cm²/s, β and E_a in units of kcal/mol.

Table 7.1: Values, derivatives, and activation energies of $\langle \tau_2 \rangle$, τ_2 , and $1/D$.^a at 298.15 K

| | | Integrated Reorientation Time, $\langle\tau_2\rangle$ | | |
|------------|-----------------|---|--------------------|--------------------|
| Source | Range (K) | T_s (K) | γ | τ_s |
| Prediction | 298.15 | 226.9 _{6.3} | 1.82 ₁₆ | 3.73 ₁₁ |
| Fit | 235.00 – 360.00 | 221.1 | 2.00 | 3.74 |
| | | Reorientation Time, τ_2 | | |
| Source | Range (K) | T_s (K) | γ | τ_s |
| Prediction | 298.15 | 220.3 _{7.0} | 1.83 ₁₇ | 2.05 ₁₃ |
| Fit | 250.00 - 360.00 | 224.37 | 1.96 | 2.63 |
| | | Inverse Diffusion Coefficient, $1/D$ | | |
| Source | Range (K) | T_s (K) | γ | τ_s |
| Prediction | 298.15 | 216.4 _{7.0} | 1.97 ₁₇ | 0.073 ₅ |
| Fit | 235.00 – 360.00 | 218.4 | 1.91 | 0.073 |

† Calculated from Eqs. (7.13)-(7.15); τ_s has units of ps for reorientation and 10^5 s/cm² for diffusion.
‡ Subscripts represent the uncertainties in the trailing digits.

Table 7.2: Comparison of stability limit conjecture parameters[†] with fits to T -dependent data.[‡]

ics has been frequently noted and several models have been proposed to describe the temperature-dependence in the supercooled regime.^{146,223,241,246,248–252} We focus primarily on two such descriptions, one obtained from the stability limit conjecture²⁴⁶ that predicts a divergence in the timescale upon supercooling, and another that assumes a transition from HDL to LDL water so that the timescale changes smoothly.^{146,223,241} The present calculations are not aimed at establishing the accuracy of either description, rather we demonstrate that, given a physical description, one can predict the dynamical properties of water well below its melting point from room temperature simulations.

7.3.2 A Stability Limit Conjecture Description

A prediction for the temperature dependence of a timescale was proposed by Speedy based on the assumption of a stability limit at a temperature T_s ;²⁴⁶ an analogous result has been obtained from mode-coupling theory.²⁴⁸ This predicts a power-law dependence of a timescale τ on the temperature:

$$\tau(T) = \tau_s \left(\frac{T}{T_s} - 1 \right)^{-\gamma} \quad (7.12)$$

where T_s , τ_s , and γ are the divergence/stability limit temperature, reference timescale, and power-law exponent, respectively. In this work we consider $\tau = \langle \tau_2 \rangle$, τ_2 , or $1/D$; while $1/D$ is not explicitly a timescale it behaves as one in its temperature dependence (*vide infra*). This stability limit description has been used extensively in the literature to describe the temperature dependence of water in its supercooled state above T_s ,^{52,56,145,221,236,244,253–256} though it is better viewed as a mathematical model than a physically accurate one.^{6,145,230}

The stability limit prediction for a given timescale, Eq. (7.12), can be fully determined by the timescale and its first two derivatives. For a dynamical timescale, τ , we define the first and second derivatives of its natural logarithm as $(\ln \tau)' = \partial \ln \tau / \partial \beta$ and $(\ln \tau)'' = \partial^2 \ln \tau / \partial \beta^2$, respectively. Along with τ , these derivatives can be used to solve for the parameters in Eq. (7.12) as

$$T_s = \frac{(\ln \tau)' + \beta(\ln \tau)''}{2(\ln \tau)'k_b\beta + k_b\beta^2(\ln \tau)''}, \quad (7.13)$$

$$\gamma = \beta(1 - k_b T_s \beta) (\ln \tau)', \quad (7.14)$$

and

$$\tau_s = \tau \left(\frac{T}{T_s} - 1 \right)^\gamma. \quad (7.15)$$

Furthermore, because the activation energy of the effective rate constant, $k = 1/\tau$ is just $(\ln \tau)'$, it can be obtained in terms of the stability limit parameters directly from Eq. (7.14) as

$$E_{a,\tau} = \frac{\gamma}{\beta(1 - k_b T_s \beta)}. \quad (7.16)$$

The parameters obtained in this way are listed in Table 7.2. These parameterizations provide extrapolative predictions of the temperature dependence of the reorientation and diffusion timescales (along with their activation energies) over a range of temperatures from 360 K down to ~ 220 K.

These predictions are compared to the timescales calculated from the T -dependent simulations in Fig. 7.2. The predictions provide a highly accurate picture of the temperature dependence of these timescales, which exhibit clearly non-Arrhenius behavior. The timescales themselves display

moderate lengthening as the temperature is reduced before a sharp increase occurs as $T \rightarrow T_s$ (top panels of Fig. 7.2). In the case of the integrated reorientation time, this leads to an increase in $\langle \tau_2 \rangle$ by a factor of nearly 30 from 298.15 to 235 K. The prediction of $\langle \tau_2 \rangle$ at 235 K from the room temperature simulations overestimates this slowdown due to uncertainty in the value of T_s , which shifts the location of the divergence. In the case of τ_2 , both the T -dependent simulations and the predictions from room temperature simulations using Eq. (7.12) cannot be extended below 250 K because the reorientational correlation function exhibits a significant stretched-exponential character at lower temperatures. That is, the functional form of $C_2(t)$ changes in the supercooled regime so that τ_2 is not well-defined. In the case of the diffusion coefficient, the agreement between the T -dependent simulations and the predictions from room temperature simulations is excellent (Fig. 7.2c, f). Both find an increase in $1/D$ by a factor of 18.5 as the temperature is reduced from 298.15 to 235 K.

From our predictions, it is clear that significant, even complete, information about dynamics in the weakly supercooled regime is accessible from room temperature simulations. This is not consistent with the viewpoint that there are inherent structural differences present within the supercooled liquid that are not present in the room temperature liquid. Rather, as is discussed in detail below, it indicates that there is not a significant change in mechanism of reorientation and diffusion between the room temperature and supercooled liquids. Regardless of the specific origin of the peculiar temperature dependence of liquid water, these predictions clearly indicate that information about this origin must be present within the ambient liquid.

The parameters for the stability limit equation calculated from our room temperature simulations are in good agreement with values obtained by fitting the results of our T -dependent simulations (see Table 7.2) as well as experimental and simulation results in the literature.^{3,51,53,54,244,256–261} For example, the divergence temperature, T_s , is predicted from the room temperature simulations to be between 216.4 K and 226.9 K, depending on the timescale considered. The average of predicted values of T_s for the diffusion coefficient from the literature^{3,53,54,244,257–260} is 217.9 K which is only 1.5 K higher than our predicted value for this property. Similarly, the values of γ lie be-

| Inverse Integrated Reorientation Time, $1/\langle\tau_2\rangle$ | | | | | |
|---|-----------------|--------------------------------------|----------------------|--------------------------------------|----------------------|
| Source | Range (K) | $1/\tau_{2,0,H}$ (ps ⁻¹) | $E_{a,H}$ (kcal/mol) | $1/\tau_{2,0,L}$ (ps ⁻¹) | $E_{a,L}$ (kcal/mol) |
| Prediction | 298.15 | 380 ₅₄ | 3.88 ₉ | 17.9 _{4.0} | 7.3 ₇ |
| Diffusion Coefficient, D | | | | | |
| Source | Range (K) | $D_{0,H}$ (cm ² /s) | $E_{a,H}$ (kcal/mol) | $D_{0,L}$ (cm ² /s) | $E_{a,L}$ (kcal/mol) |
| Prediction | 298.15 | 0.0156 ₂ | 3.84 ₇ | 4.8 ₇ | 10.4 ₆ |
| Ref. ^{146*} | 125.00 – 273.15 | 0.0111 | 3.61 | 6.152 | 10.49 |

[†]Subscripts represent the uncertainties in the trailing digits.
[‡]Fit of Eq. (7.17) and its first two derivatives; see Sec. 7.2.
^{*}Fit to the measured data of Ref. 6.

Table 7.3: Parameters[†] for the “two-liquids” picture.[‡]

tween 1.82 and 1.97 and are within overlapping uncertainty of one another for all three dynamical timescales, which is also in excellent agreement with the range of values found in the literature. This agreement indicates that the information contained in the ambient liquid is sufficient to quantitatively describe the dynamical behavior upon supercooling. Additionally, all three dynamical timescales have similar values of T_s and γ indicating that they are likely governed by the same process upon cooling, *i.e.*, H-bond exchanges.^{85,108}

7.3.3 A “Two Liquids” Description

The anomalous, non-Arrhenius dynamics of supercooled water has frequently been explained as a coexistence of the HDL and LDL phases. A number of groups have proposed a description of water properties, including viscosity and diffusion coefficient, down to low temperatures based on HDL and LDL dynamics weighted by a switching function.^{146,223,241,242,262–264} This represents an alternative to the timescale divergence of the stability limit description and is consistent with the experiments of Xu *et al.*⁶ The latter were able to measure the diffusion coefficient of water down to 126 K and observed a continuous change with no divergence. Within this two liquids description, the apparent divergence in $1/D$ is associated with a transition from primarily HDL above the Widom line (which occurs around 229 K at 1 bar) to primarily LDL at temperatures well below it. Because HDL and LDL water have different diffusion activation energies, the transition region between the two gives rise to behavior that has the appearance of a divergence, *i.e.*, an

apparent activation energy in the transition region that is substantially higher than that for either HDL or LDL water. Recently, Hestand and Skinner showed that $\ln D(T)$ data obtained by Xu *et al.* can be fit by assuming a two liquids behavior,¹⁴⁶

$$\ln D(T) = s(T) \ln D_L(T) + [1 - s(T)] \ln D_H(T), \quad (7.17)$$

where $s(T) = [1 + e^{4.394(T-T_0)/\Delta T}]^{-1}$ is a smooth function that switches $D(T)$ from HDL Arrhenius behavior above the Widom line, $D_H(T) = D_{0,H} e^{-\beta E_{a,H}}$ to LDL Arrhenius behavior, $D_L(T) = D_{0,L} e^{-\beta E_{a,L}}$ below it.

We have used the inverse timescales $1/\langle\tau_2\rangle$ and D along with their first- and second-derivatives calculated at room temperature to fit the two liquids description given in Eq. (7.17). Unlike the stability limit result, the physical model for the two liquids picture as described in Eq. (7.17) depends on six parameters which are typically fit to experimental measurements or simulations of temperature-dependent data. With only two derivatives and the original timescale, an analytical solution cannot be extracted as in the case of the stability limit conjecture. Instead, Eq. (7.17) and its first two analytical derivatives were fit to these three pieces of information. Fitting of all six parameters gives reasonable estimates of the parameters, but with values that do depend somewhat on the choice of initial values; details for D are given in the supplementary material. An average of the values obtained with different initial parameters and ignoring unphysical results gives $D_{0,H} = 0.0154 \text{ cm}^2/\text{s}$, $E_{a,H} = 3.83 \text{ kcal/mol}$, $D_{0,L} = 4.96 \text{ cm}^2/\text{s}$, $E_{a,L} = 11.6 \text{ kcal/mol}$, $T_0 = 207 \text{ K}$, and $\Delta T = 82.3 \text{ K}$. Additional details are provided in the supplementary material.

Consistent, but more precise, values of the LDL characteristics are obtained with the switching function chosen to have the same parameters found by Hestand and Skinner in their work ($T_0 = 213 \text{ K}$ and $\Delta T = 75 \text{ K}$), reducing the fit to four unknown parameters,¹⁴⁶ those describing the HDL and LDL behavior ($D_{0,H}$, $E_{a,H}$, $D_{0,L}$, $E_{a,L}$).¹⁴⁶ Parameters were fit from our calculated values at room temperature using a ‘‘Nelder-Mead’’ minimization. Reported results for the diffusion coefficient were generated from initial values taken from Hestand and Skinner;¹⁴⁶ different

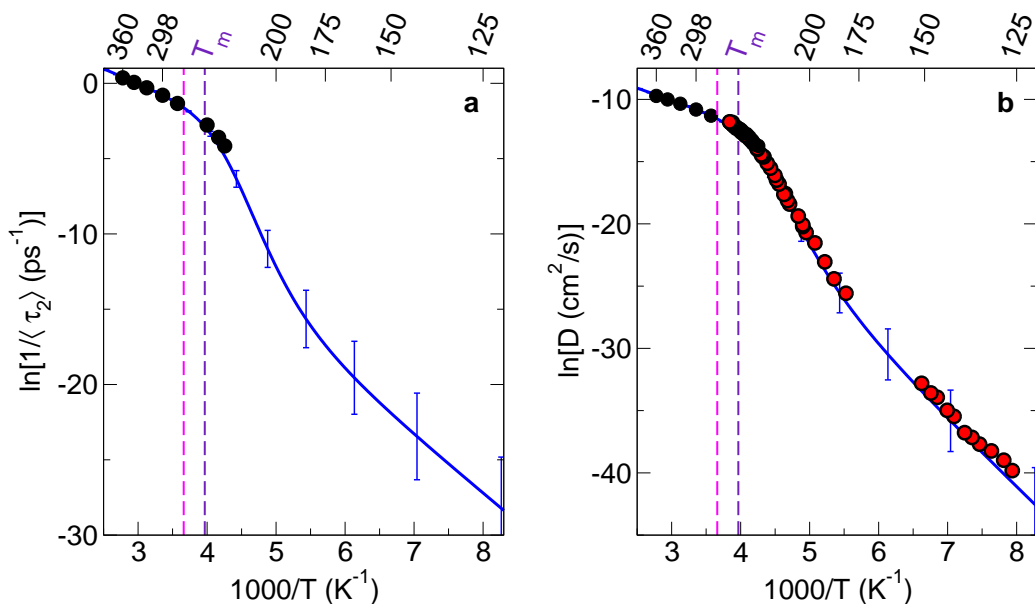


Figure 7.3: Predictions of the temperature dependence of (a) $\langle\tau_2\rangle$ and (b) D using the two liquids description as given in Eq. (7.17) and described in the text are shown (blue solid line). The results from T -dependent simulations (black circle) are shown along with the measured D (red circle) from Xu *et al.*⁶ The melting point of water (magenta dashed line) and TIP4P/2005 water (purple dashed line) water are also indicated.

physically reasonable initial guesses gave very similar, but not identical, fitted parameters (results for the diffusion coefficient case are presented in the supplementary material). For the integrated reorientation time, initial guesses were $1/\tau_{2,0,H} = 1000 \text{ ps}^{-1}$ and $1/\tau_{2,0,L} = 10 \text{ ps}^{-1}$ and the diffusion activation energies from Ref. 146. The results are shown in Fig. 7.3 for $1/\langle\tau_2\rangle$ and D and the parameters are given in Table 7.3; we have not attempted to fit τ_2 to such an expression because, as noted above, it is ill-defined below 250 K.

The predictions obtained by fitting the timescale and its derivatives to Eq. (7.17) are in good agreement with both the T -dependent simulation results and the measured diffusion coefficients.⁶ It is important to note that because the T_0 and ΔT values are obtained by fitting the experimental data,¹⁴⁶ these do not represent predictions solely based on the room temperature simulations. Nevertheless, they show how ambient water dynamics can provide insight into deeply supercooled water by determination of the LDL Arrhenius parameters. Specifically, the fit for the diffusion coefficient gives $E_{a,L} = 10.4 \pm 0.6 \text{ kcal/mol}$ and $D_{0,L} = 4.8 \pm 0.7 \text{ cm}^2/\text{s}$ (Table 7.3), which are

in excellent agreement with the values of 10.5 kcal/mol and 6.152 cm²/s, respectively, obtained by fitting the data of Xu *et al.* directly.¹⁴⁶ Similarly, the HDL behavior is also well reproduced with the fit yielding $E_{a,H} = 3.84 \pm 0.07$ kcal/mol and $D_{0,H} = 0.0156 \pm 0.002$ cm²/s, compared to 3.61 kcal/mol and 0.0111 cm²/s, respectively, from the direct fitting.¹⁴⁶

The integrated reorientation time exhibits similar behavior to the diffusion coefficient, with the two liquids prediction in good agreement with the T -dependent simulation data. The fitting gives the $1/\langle\tau_2\rangle$ activation energy for LDL water as 7.3 ± 0.7 kcal/mol, significantly larger than the 3.88 ± 0.09 kcal/mol obtained for HDL water. We are unaware of measurements of the integrated reorientation time below ~ 220 K that would provide a test of the behavior predicted in Fig. 7.3a.

It is interesting to compare the LDL activation energies for diffusion and reorientation. Qvist *et al.* found through both NMR measurements and simulations that reorientational dynamics slow more quickly than translational diffusion as the temperature is lowered.⁵² This is consistent with the larger divergence temperature (T_s given in Table 7.2) we find for $\langle\tau_2\rangle$ compared to that for D . Similarly, the activation energies as a function of temperature presented below in Sec. 7.3.4 also indicate that the HDL-LDL transition temperature, T_0 , may be higher for reorientation than diffusion. However, it is important to note that this does not have any clear implication for the LDL activation energy. In the two liquids description, the lengthening of the timescale and associated rise in activation energy as T_0 is approached is due to the HDL-LDL transition as represented by the switching function, $s(T)$, in Eq. (7.17). Indeed, the activation energy is larger in this switching region than in *either* the LDL or HDL regimes precisely due to $s(T)$. Thus, it is not possible to infer $E_{a,L}$ from this behavior; if T_0 is larger for reorientation than diffusion this does not clearly indicate that the LDL activation energy for reorientation should be higher than that for diffusion.

It is possible to fully determine the two liquids description by, *e.g.*, calculating higher derivatives at room temperature or including the timescale and first two derivatives at another temperature (above the melting point). The latter is likely more practical. However, a common aspect of both the stability limit and HDL-LDL phase transition descriptions is that they treat the temperature dependence of the room temperature liquid and the supercooled liquid within a single framework.

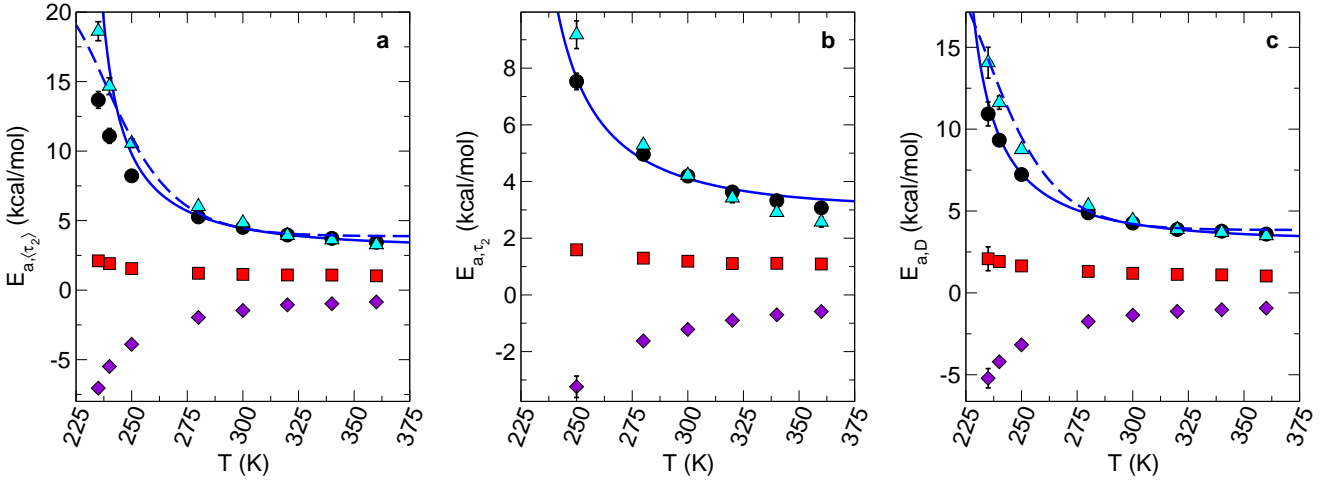


Figure 7.4: Temperature-dependent activation energy decompositions are reported for for (a) $\langle \tau_2 \rangle$, (b) τ_2 , and (c) D . The total activation energy (black circle) as well as the kinetic (red square), Lennard-Jones (purple diamond), and electrostatic contributions (cyan triangle) to the activation energy are presented. The prediction of the total activation energy based on Eqs. (7.12) (blue solid line) and (7.17) (blue dashed line) are also shown.

This implicitly assumes that these quantities vary smoothly with temperature until, in some cases, a divergence at T_s is observed.^{265–267} The notion that supercooled water has distinct structures that are not present in room temperature water appears to be at odds with these models. This is particularly true for the description of supercooled water in terms of an HDL-LDL transition, in which the temperature dependence down to ~ 125 K can be determined from simulations at room temperature.

7.3.4 Activation Energy Predictions and Decompositions

Additional insight into the underlying barrier, and hence the mechanism, associated with a given timescale, τ , can be obtained from the corresponding activation energy,

$$E_{a,\tau} = -\frac{\partial \ln(1/\tau)}{\partial \beta} = \frac{1}{\tau} \frac{\partial \tau}{\partial \beta}, \quad (7.18)$$

which measures the rate of change with temperature. To further explore the behavior of supercooled water, we have calculated the activation energies directly from each of our T -dependent

simulations. In addition, because Eqs. (7.12) and (7.17) give the temperature dependence of the timescale, we have also used the room temperature simulations to predict how the activation energies for water reorientational dynamics and diffusion change upon cooling.

The activation energies for $\langle\tau_2\rangle$, τ_2 , and $1/D$ calculated in these three ways are presented in Fig. 7.4. As is evident from the apparent divergence of the timescales, illustrated in Fig. 7.2, there is a significant increase in these activation energies upon cooling down to 235 K. Similar to the prediction of the timescales above, the predicted and calculated activation energies are in quite good agreement. The predicted $\langle\tau_2\rangle$ activation energy is in excellent agreement with the T -dependent simulation results for $T \geq 280$ K, but overestimates the values at lower temperatures. For τ_2 and $1/D$ the predicted activation energies based on the stability limit conjecture are in good accord with the explicit calculations, slightly overestimating E_{a,τ_2} at higher T . The two liquids description somewhat overestimates the activation energy of both timescales at lower temperature, which may be due to the assumption of the transition temperature value. The accuracy of the predicted activation energies further supports the notion that the water dynamics in the supercooled regime is governed by mechanisms and structural features that are also present at room temperature.

We have previously shown that the direct calculation of the activation energy using the fluctuation theory for dynamics can be used to rigorously decompose it into components.^{13,31,44,50,58} Specifically, the fluctuation in the total energy can be written as $\delta H(0) = \delta KE(0) + \delta U_{LJ}(0) + \delta U_{elec}(0)$, where the three terms are the fluctuations in the kinetic, Lennard-Jones, and electrostatic energies, respectively. Then, the activation energies obtained from Eqs. (7.2) and (7.7), can be written as a sum of contributions associated with each of these components of the total energy, *e.g.*, $E_{a,D} = E_{a,D}^{KE} + E_{a,D}^{LJ} + E_{a,D}^{elec}$. These three contributions, obtained from the T -dependent simulations, are shown for each timescale along with the total activation energy in Fig. 7.4.

These components can be interpreted in terms of Tolman's picture of the activation energy.^{13,18,19} Tolman showed that the activation energy can be written as the difference between the average energy of reactive trajectories and the average reactant energy, *i.e.*, $E_a = \langle E \rangle_{reacting} - \langle E \rangle_{reactant}$. In this context, for example, $E_a^{KE} = \langle KE \rangle_{reacting} - \langle KE \rangle_{reactant}$, which is the average *kinetic* energy

of species crossing the barrier minus the average *kinetic* energy of reactants. These contributions thus indicate the excess energy needed in a particular type of kinetic or interaction energy to surmount the barrier to the process. In this perspective, positive activation energy contributions (*e.g.*, E_a^{elec}) indicate that higher energies in those energy components lead to faster dynamics, while for negative activation energy contributions (*e.g.*, E_a^{LJ}) it leads to slower dynamics.

The decompositions of the activation energies presented in Fig. 7.4 show that electrostatics are the dominant contribution to the total activation energy for both water reorientation and diffusion. Moreover, the electrostatic component increases upon cooling, driving the rise in the total activation energy for each timescale; for example, $E_{a,\langle\tau_2\rangle}$ and $E_{a,D}$ increase by 13.8 and 9.6 kcal/mol, respectively, upon cooling from room temperature to 235 K. The kinetic energy contribution is significantly smaller and is relatively independent of temperature, changing by ~ 1 kcal/mol over the entire temperature range. The Lennard-Jones contribution is negative, indicating that the dynamics are accelerated when this component of the energy is smaller.

It is notable that the activation energies for the three dynamical timescales are in general qualitative and quantitative accord. We have previously found that the reorientation and diffusion activation energies and their components are very similar to each other at room temperature,^{44,50} indicative of a common underlying barrier associated with H-bond exchanges.^{85,88}

As the temperature is reduced, the Lennard-Jones component becomes more negative while the electrostatic contribution increases. This indicates a cancellation between these two that can be understood based on the liquid structure. The first solvation shell of a water molecule is sufficiently close (the OO radial distribution function peaks around 2.75 Å) that these H-bonded waters are on the repulsive wall of the Lennard-Jones potential ($\sigma_{TIP4P/2005} = 3.1589$ Å). Thus, to exchange H-bond partners two waters must first increase the OO distance,⁸⁵ thereby decreasing the Lennard-Jones energy and leading to a negative E_a^{LJ} . The water structure is determined by the tension between these repulsive Lennard-Jones interactions and attractive electrostatic forces. In the process of exchanging H-bond partners, the expansion of the OO distance is associated with an increase in the water-water electrostatic interaction energy, giving a positive E_a^{elec} . Upon cooling

the liquid is increasingly ordered leading to lower (more favorable) electrostatic energy and more repulsive Lennard-Jones interactions, which is reflected in the activation energy components.

In accord with the physical pictures discussed in the preceding sections, the ability to predict reasonable activation energies using both the stability limit and two liquids formalisms indicates that the room temperature liquid contains information about the underlying barriers associated with these dynamical timescales. Additionally, it is clear that these barriers are heavily reweighted upon cooling into the supercooled regime from room temperature; however, this reweighting is a continuation of a trend already present in the ambient liquid. Specifically, the increase in the activation energy witnessed in the weakly supercooled regime is due to a rise in the electrostatic contribution that occurs more rapidly than the simultaneous decrease in the Lennard-Jones contribution, which are both associated with changes in the liquid structure. In the case of the stability limit description the activation energy reported is related to the physical barrier for water diffusion, whereas in the two-liquids picture it represents a weighted average of the HDL and LDL activation energies plus a term associated with the transition between HDL and LDL structures (as described by the switching function). In either case, this indicates that there is significant, even complete, information about the supercooled dynamics that can be obtained from the room temperature liquid.

7.4 Discussion

The predictions in Figs. 7.2-7.4 indicate that the key structural motifs that lead to retarded dynamics in supercooled water are also present in the room temperature liquid. Such structures then appear with increasing probability as the liquid is cooled. This interpretation is consistent with recent vibrational spectroscopic measurements by Taschin and co-workers which indicate that there is a reweighting of structures present in the room temperature liquid upon supercooling.²³³

Similarly, Stirnemann and Laage report an increase in dynamical heterogeneity in water reorientation dynamics upon supercooling.¹⁰⁸ In particular, they analyzed the H-bond exchanges that are directly related to the reorientation timescales,^{85,88} and showed that the non-Arrhenius behavior could be understood in terms of the asphericity of the water structure in the first solvation shell.

For a given asphericity, the activation energy was observed to be constant and the non-Arrhenius temperature dependence was associated with the changes in the distribution of asphericities upon cooling (favoring more tetrahedral environments) and the structural fluctuations within that distribution. While their results are not consistent with a divergence in the reorientational timescales, the data also did not provide evidence for an HDL-LDL phase transition by indication of two distinct local structures.

Saito *et al.* carried out MD simulations for TIP4P/2005 water down to 130 K, including calculations of the diffusion coefficient.²³⁶ They observed a dynamical transition, based on the self-intermediate scattering function, around the expected location of the Widom line at ambient pressure, ~ 220 K. They identified the fragmentation and isolation of structural defects, particularly three-coordinated waters, in the increasingly tetrahedral H-bond network as associated with this transition as the temperature is lowered.

Other models for the temperature dependence have been proposed, such as the Vogel-Fulcher-Tammann (VFT) equation,^{236,250–252} which has an exponential temperature dependence $D_{VFT}(T) = D_0 e^{-B/(T-T_0)}$, similar to the Arrhenius result but with a divergence in the timescale as the temperature is reduced. We have found that it provides a poorer description of the slowdown in diffusion and reorientation timescales than the stability limit results shown in Fig. 7.2. It has also been noted by some that the diffusion coefficient and reorientation time temperature dependence can be described adequately by a fourth- (or higher-) order polynomial;²⁴⁹ this Taylor series description, because it is not physically motivated, requires more information to parameterize for a given temperature range. However, the present approach is general in that a timescale and its derivatives with respect to inverse temperature can be used to parameterize, directly or through fitting, physical models that describe its behavior over a broad range of temperatures.

Finally, we note that the approach presented here can, in principle, be used to directly address the accuracy of the two liquids description (within a given simulation model). Specifically, this picture predicts a change in the sign of the second derivative of the timescale with respect to inverse temperature below the transition temperature, T_0 . This could be directly tested from simu-

lations at ~ 200 K; MD simulations at these conditions, which themselves support the two liquids description, have previously been reported.^{146,236,268}

7.5 Conclusions

We have shown how the the temperature dependence of the reorientation time, integrated reorientation time, and diffusion coefficient of water can be predicted over a large temperature range that extends into the supercooled regime from simulations at room temperature. Our predictions match with both experimental and simulation trends, and are in excellent quantitative agreement with results calculated from T -dependent simulations with the same water model. Similarly, we have quantitatively predicted the temperature dependence of the activation energies.

These calculations are enabled by the fluctuation theory for dynamics approach that gives, at a single temperature, the analytical derivatives of the timescales with respect to (inverse) temperature. This method also provides a rigorous decomposition of the activation energy, which we have used to determine the contributions due to the kinetic, Lennard-Jones, and electrostatic energies from simulations at different temperatures. The largest contribution to the activation energy is due to electrostatic interactions and it rises significantly upon cooling below the melting temperature. This is partially cancelled by the negative Lennard-Jones component, which increases in magnitude as the temperature is reduced. These contributions are indicative of the shifting structures explored as the liquid is supercooled. The relative contributions are very similar for reorientation and diffusion, indicating a common underlying barrier associated with H-bond exchange.

The results presented here demonstrate that, assuming a continuous temperature dependence,²⁶⁹ the structural and dynamical features that control the behavior of supercooled water are present in the room temperature liquid. This should provide insight into the development and interpretation of experiments and molecular-level models for supercooled liquid structure and dynamics.

Chapter 8

On the Temperature Dependence of Liquid Structure

8.1 Introduction

How the properties of molecular systems change with temperature is one of the most fundamental issues in chemistry. Knowledge of this behavior has not only practical implications, but fundamental ones, as it typically permits the separation of energetic and entropic driving forces. Unfortunately, the typical approaches for determining the temperature-dependence is to explicitly carry out measurements or calculations at a range of temperatures and compute effectively numerical derivatives characterizing the rate of change. However, recently there have been several new simulation approaches that determine the change with respect to temperature of both static^{270,271} and dynamical^{13,31,35,37,44,50,58,59} properties directly, by calculation of the analytical derivative. In this Chapter, we present another member of this class of approaches and illustrate it by application to the temperature dependence of the structure of liquid water.

From molecular dynamics (MD) simulations, the radial pair distribution function (RDF) is frequently used to characterize the structure of liquids, as²⁷²

$$g(r) = \frac{V}{N^2} \left\langle \sum_i \sum_{j \neq i} \delta(r - |\vec{r}_{ij}|) \right\rangle, \quad (8.1)$$

where $\vec{r}_{ij} = \vec{r}_j - \vec{r}_i$ is the intermolecular distance between sites i and j , V the volume, N the number

Adapted with the permission of Zeke A. Piskulich and Ward H. Thompson and AIP Publishing, *J. Chem. Phys.* **152**, 011102 (2020).¹⁴⁷

of molecules, and $\langle \dots \rangle$ represents an ensemble average. Experimentally, RDFs can be obtained, for example, from the Fourier transform of the structure factor measured by neutron^{231,273,274} and X-ray^{12,274–276} scattering.

The dependence on temperature of the RDF in the canonical ensemble can be seen more clearly by making explicit the average in Eq. (8.1),

$$g(r) = \frac{V}{N^2} \frac{1}{Q} \frac{1}{h^F} \int d\mathbf{p} \int d\mathbf{q} e^{-\beta H} \sum_i \sum_{j \neq i} \delta(r - |\vec{r}_{ij}|), \quad (8.2)$$

where H is the Hamiltonian, $\beta = 1/k_B T$, \mathbf{q} and \mathbf{p} the system coordinates and momenta, h Planck's constant, and F the number of degrees-of-freedom. In evaluating the temperature dependence of $g(r)$ it is notable that T only appears in the canonical partition function, Q , and the Boltzmann weighting, $e^{-\beta H}$. Thus, taking the derivative with respect to β yields

$$\frac{\partial g(r)}{\partial \beta} = -\frac{V}{N^2} \left\langle \delta H \sum_i \sum_{j \neq i} \delta(r - |\vec{r}_{ij}|) \right\rangle \equiv -g_H(r), \quad (8.3)$$

where $\delta H = H - \langle H \rangle$ is the fluctuation in the total system energy from its average value, $\langle H \rangle = -\partial \ln Q / \partial \beta$. The second equality defines $g_H(r)$. Note that this expression gives the derivative of the RDF with respect to β by weighting the distribution of site-site distances by the fluctuation in total energy at that configuration, when $\delta H > 0$ the distribution is weighted by a positive number and when $\delta H < 0$ it is weighted by a negative number. In this way, the analytical derivative of the RDF is obtained, in contrast with the usual numerical derivatives calculated from simulations of the RDF at different temperatures.

We note that the result in Eq. (8.3) is a straightforward example of fluctuation theory,^{26,28,206} *e.g.*, relating the heat capacity to the fluctuations in the energy. As such, it can be readily extended to derivatives with respect to other thermodynamic variables including pressure or chemical potential. Similar results have been previously derived for various static and dynamical properties,^{13,26,28,31,35,37,44,50,58,59,206,270,271} including for the RDF by Mahynski *et al.*²⁷¹ In the following we show that this derivative can be used to obtain the energetic and entropic driving forces, predict

$g(r)$ over a large temperature range, and extract mechanistic insight.

An additional advantage of this approach is that δH can be decomposed into any additive sum of terms to gain insight into the origin of the temperature dependence. For example, for a typical fixed charge MD simulation, one can write

$$\delta H = \delta KE + \delta V_{LJ} + \delta V_{Coul}, \quad (8.4)$$

where KE , V_{LJ} , and V_{Coul} are the kinetic, Lennard-Jones, and Coulombic energies. Using this in Eq. (8.3) gives

$$g_H(r) = g_{KE}(r) + g_{LJ}(r) + g_{Coul}(r), \quad (8.5)$$

where each term on the right-hand-side is given by the expression in Eq. (8.3) with δH replaced by the respective energy component fluctuation, *e.g.*, δV_{LJ} for $g_{LJ}(r)$. We note that, because the RDF does not involve an average over any \mathbf{p} -dependent property, it is straightforward to show that $g_{KE}(r) = 0$.

In the following, we apply this approach to investigate the structure and free energetics of water using only a simulation at room temperature (298.15 K). The focus is the oxygen-oxygen RDF and its derivative calculated from Eq. (8.3). To test the predictions, additional simulations have been carried out at different temperatures from 235 to 360 K, hereafter referred to as “*T*-dependent Simulations.”

8.2 Simulation Methods

The results presented here were obtained from MD simulations of 343 TIP4P/2005 water molecules⁵ using the LAMMPS program.⁸¹ A 50 ns *NVT* trajectory with 1 fs timestep was propagated at 298.15 K with a density of 0.997 g/cm³ to produce 1,000,000 configurations from which quantities were averaged. As discussed below, while greater sampling is needed to determine the temperature derivative of the RDF (and its decomposition) compared to the RDF itself, such a long trajectory is

not necessary as the convergence is reasonably rapid. A three-chain Nosé-Hoover thermostat^{83,84} was utilized to hold simulations at a constant temperature, with a damping parameter of 100 fs. The water molecules were held rigid by the SHAKE algorithm.⁸² The Particle Particle Particle Mesh (PPPM) method was used to calculate the long-range electrostatic interactions.^{119,120} The SHAKE and PPPM tolerances were both set to 1.0×10^{-4} . The Lennard-Jones interaction cutoff was 10.5 Å and long-range tail corrections were used. In addition to the room temperature simulation, 5 ns simulations using the same protocol were run at 235, 250, 280, 320, and 360 K; results were calculated from 50,000 configurations. Reported uncertainties are calculated from block averages using five blocks and reported as 95% confidence intervals according to the Student's *t*-Distribution.¹²²

8.3 Results and Discussion

The room temperature O-O RDF is shown along with its derivative with respect to β in Figure 8.1a. The derivative, $\partial g_{OO}(r)/\partial\beta$, has a strong positive peak at 2.7 Å in the first solvation shell and a weaker local maximum in the second solvation shell at 4.4 Å. Between the solvation shells, at 3.1 and 5.7 Å, the derivative is negative where $g_{OO}(r)$ itself is a local minimum. Thus, the derivative indicates that as temperature decreases (β increases) water becomes increasingly structured, *i.e.*, the first and second solvation shell peaks increase in amplitude while the minima are lowered. This derivative, or a closely related quantity, has been previously obtained numerically from experimental measurements.²⁷⁷

Insight into the origin of these changes can be obtained by examining the components of the derivative due to energy contributions, shown in Figure 8.1b. As noted above, the kinetic energy term, $g_{KE}(r)$, is rigorously zero. The potential energy contributions are both significant in magnitude but with opposing signs. In particular, the Coulombic component is the dominant term and displays the same behavior as the total derivative. The Lennard-Jones contribution is opposite in sign at all distances, but smaller than $g_{Coul}(r)$. Thus, it only acts to diminish the magnitude of the derivative relative to the Coulombic term alone.

This behavior can be understood in the context of the RDF itself. The first solvation shell

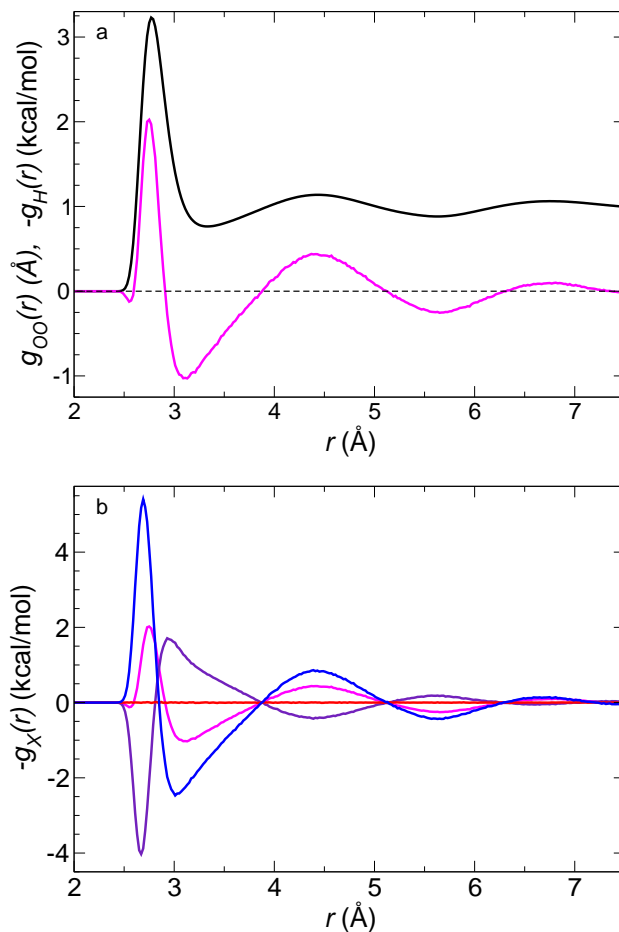


Figure 8.1: a: The O-O RDF (black line) and its first derivative (magenta line) calculated from a single simulation at 298.15 K. b: The derivative $\partial g_{OO}(r)/\partial\beta = -g_H(r)$ (magenta line) along with its contributions due to kinetic energy ($X = KE$, red line) and Lennard-Jones ($X = LJ$, violet line) and Coulombic ($X = Coul$, blue line) interactions.

is peaked at 2.75 Å, which is within the repulsive region of the Lennard-Jones potential with $\sigma = 3.1589$ Å, held there by favorable Coulombic interactions. As the temperature is lowered, the liquid becomes more structured as this lowers the electrostatic potential energy at the expense of the already unfavorable Lennard-Jones interactions.

A particularly interesting feature of the decomposition of $g_H(r)$ is that, for distances beyond the first solvation shell, where the total derivative is zero both $g_{Coul}(r)$ and $g_{LJ}(r)$ are also zero (or nearly so). The distances at which the derivative $\partial g_{OO}(r)/\partial\beta = 0$ are ones where the RDF itself is then effectively independent of temperature. These isosbestic points in the water $g_{OO}(r)$ have been previously observed in both experimental and simulation studies,^{12,276,277} particularly one

obtained in the first solvation shell coordination number. In the present calculations, the isosbestic point related to the first solvation shell occurs where $g_H(r) = 0$ around 2.9 Å; this occurs by a cancellation of non-zero contributions of $g_{Coul}(r)$ and $g_{LJ}(r)$ of opposite signs, in contrast to that observed at larger O-O distances.

It is also instructive to examine the free energy profile that is directly obtained from the RDF as

$$\Delta A(r) = -k_B T \ln g(r) - 2k_B T \ln r, \quad (8.6)$$

where $\Delta A(r)$ is the (constant volume, Helmholtz) free energy as a function of the site-site distance. The first term is the potential of mean force²⁰⁶ and the second term accounts for the increasing volume available for other waters as the intermolecular distance, r , increases. It is straightforward to obtain the derivative of ΔA with respect to β as

$$\frac{\partial A(r)}{\partial \beta} = k_B T \left[\frac{g_H(r)}{g(r)} - \Delta A(r) \right], \quad (8.7)$$

which can be calculated from Eqs. (8.3) and (8.6). Noting that $\Delta A(r) = \Delta U(r) - T\Delta S(r)$, where U and S are the internal energy and entropy, respectively, this derivative can be used to determine both terms. Namely, assuming that both $\Delta U(r)$ and $\Delta S(r)$ are temperature independent, one obtains

$$\Delta S(r) = \frac{1}{k_B T^2} \frac{\partial A(r)}{\partial \beta}, \quad (8.8)$$

and

$$\Delta U(r) = \frac{g_H(r)}{g(r)}. \quad (8.9)$$

Thus, the RDF and its derivative from Eq. (8.3) provide the energetic and entropic driving forces for the liquid structure under the van't Hoffian assumption that they do not change with temperature. Unlike the standard approach, in which $\Delta S(r)$ is obtained from the slope of $\Delta A(r)$ with T at each r followed by calculation of $\Delta U(r) = \Delta A(r) + T\Delta S(r)$, Eqs. (8.8) and (8.9) can be evaluated from a simulation at a single temperature.

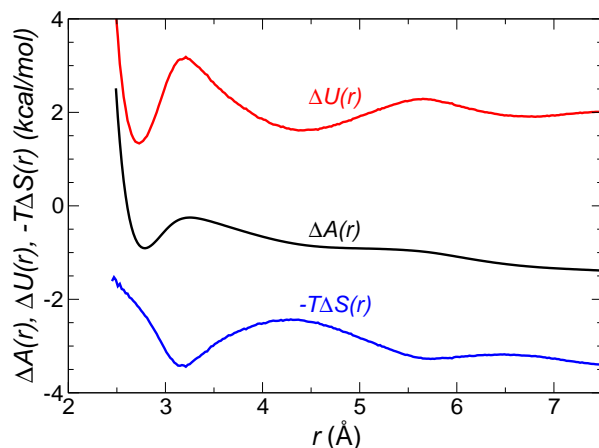


Figure 8.2: Helmholtz free energy $\Delta A(r)$ (black line) from the O-O RDF is shown along with the internal energy, $\Delta U(r)$, (red line) and entropic, $-T\Delta S(r)$, (blue line) contributions.

The entropy and internal energy profiles as a function of O-O distance in water are shown in Fig. 8.2 along with the free energy. The internal energy exhibits minima at the location of the solvation shells, the peaks in $g_{OO}(r)$, at 2.7, 4.4, and 6.7 Å, with the depth of each minimum decreasing with the O-O distance. We can note that the derivative decomposition also gives the contributions to $\Delta U(r)$ given Eq. (8.9) and $g_H(r) = g_{Coul}(r) + g_{LJ}(r)$. Then, Fig. 8.1b shows that the location of the solvation shells follows the dominant electrostatic interactions with the well depths determined further by the direct competition with the Lennard-Jones interactions. The isosbestic points in the O-O RDF occurs where the $g_H(r) = 0$ and hence where $\Delta U(r)$ equals its asymptotic limit. The results in Fig. 8.1b indicate that, beyond the first solvation shell, the Coulombic and Lennard-Jones interactions are directly opposed such that when one favors association (lowers the internal energy) the other disfavors it. Hence, in this region the isosbestic points occur where $g_{Coul}(r) = g_{LJ}(r) = 0$.

The entropic contribution to the free energy, $-T\Delta S(r)$, decreases across the first solvation shell from 2.5 to a minimum at 3.1 Å, *i.e.*, the entropy increases with O-O distance with a maximum at the position of the barrier for a water to move between the first two solvation shells (a key component of hydrogen bond exchange^{85,88}). Following this, energy-entropy compensation is observed with local maxima in $-T\Delta S(r)$ matching the locations of the minima in $\Delta U(r)$ along with an overall decrease associated with the volume term ($-2k_B T \ln r$).

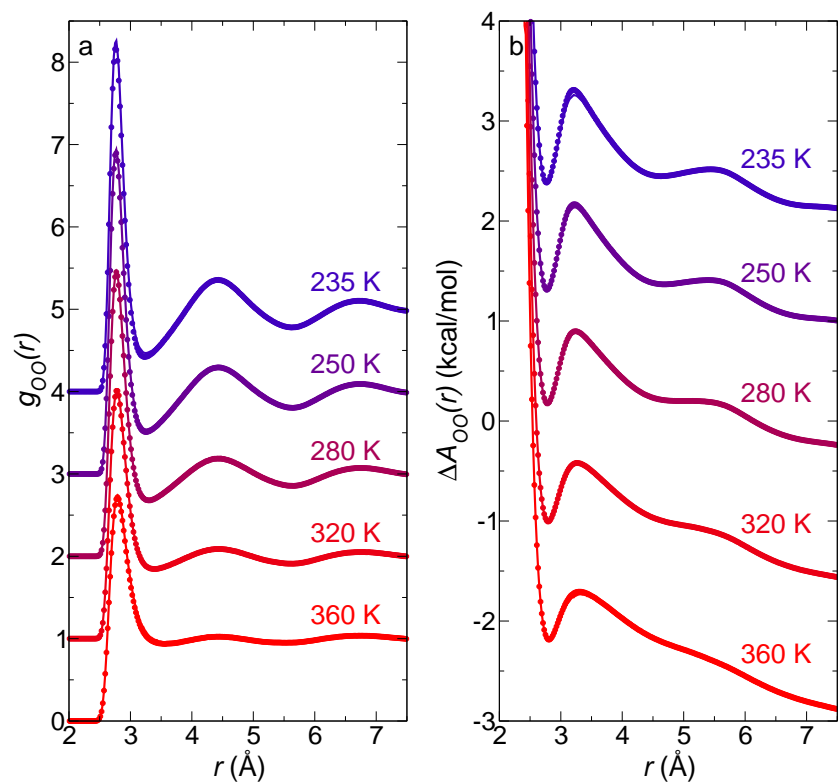


Figure 8.3: a: $g_{OO}(r)$ RDF and b: Helmholtz free energy, $\Delta A_{OO}(r)$, predicted from a single simulation at room temperature (lines) are compared to explicit T -dependent simulations (symbols).

The internal energy and entropy profiles can be used to predict the temperature dependence of both the free energy curve and the RDF. Solving Eq. (8.6) for the RDF gives

$$g(r; \beta) = \frac{C}{r^2} e^{-\beta \Delta A(r)} = \frac{C}{r^2} e^{-\beta \Delta U(r)} e^{\Delta S(r)/k_B}, \quad (8.10)$$

where C is a constant that ensures the normalization of $g(r)$ at large r and represents a choice of the zero of energy for $\Delta A(r)$. If the entropy and internal energy are calculated *via* Eqs. (8.8) and (8.9) at one temperature, then $g(r)$ can be determined at another T , or β , by Eq. (8.10). This enables the prediction of the RDF over a wide range of temperatures from simulations at a single T and the free energy profile – or any other quantity derived from $g(r)$, *e.g.*, coordination number, configurational entropy – can be obtained in an analogous way.

Unlike previous approaches based on Taylor series expansions,^{270,271} Eq. (8.10) rigorously describes the temperature dependence in terms of the energetic and entropic driving forces from the calculation of a single temperature derivative. If $\Delta U(r)$ and $\Delta S(r)$ do not depend significantly on temperature (as the results below indicate is the case), the higher derivatives used in a Taylor series expansion of $g(r)$ as given in Eq. (8.10) provide only information redundant with $\partial g(r)/\partial \beta$. In other words, the primary effect of temperature on the RDF is the explicit T -dependence present within the Helmholtz free energy. Similarly, this global description of $g(r)$ avoids the requirement of Boltzmann reweighting methods²⁷⁸ that the temperatures of interest have overlapping energy distributions. For example, here we make predictions at 235 K from 298.15 K simulations and these two temperatures have total energy distributions that do not overlap.

The predictions calculated with this approach for the O-O RDF in water are presented in Fig. 8.3a for temperatures from 235 to 360 K. These results are obtained from the $g(r)$ and $g_H(r)$ presented in Fig. 8.1a calculated from a simulation at 298.15 K. They are compared to the explicit, T -dependent simulations of the RDF at each of the temperatures shown. The RDFs predicted from the room temperature simulations are in excellent agreement with the directly calculated ones for temperatures from 360 to 235 K. The largest deviation is observed for 235 and 250 K in the min-

imum at $\sim 3.2 \text{ \AA}$ following the first solvation shell, where the predicted $g_{OO}(r)$ is slightly larger than that observed in the T -dependent simulations. This indicates that both the internal energy and entropy profiles are nearly unchanged over a wide range of temperatures, with only small effects seen in this weakly supercooled regime.

We note that these predictions assume that the temperature dependence in the RDF arises from that explicit in the Helmholtz free energy, $\Delta A(r) = \Delta U(r) - T\Delta S(r)$, and thus that the internal energy and entropy are independent of temperature. Based on the results in Fig. 8.3, this is an accurate description of water from near its boiling point to well into the supercooled regime.

Both the RDF and $\Delta A(r)$ results show an increase in the water structuring with decreasing T as evidenced by the increasing amplitude of the solvation shell peaks and the deeper minima in $g_{OO}(r)$ in between these. Both this trend and the agreement between the predicted and explicitly calculated results are also observed when the results are plotted as free energy profiles, $\Delta A_{OO}(r)$ in Fig. 8.3b. Here, the structuring is clearly observed in the increasing depth of the solvation shell minima and the rising barriers for a water to move between solvation shells as the temperature is decreased.

Moreover, because the free energy barriers in $\Delta A(r)$ correspond to those for a water to move between solvation shells, these predictions provide insight into dynamical processes as well that involve such movements, such as a. This includes the exchange of hydrogen bond partners^{85,88} and allied processes such as diffusion and OH reorientation.

It is useful to consider the convergence of the derivative with the length of the trajectory. This is illustrated in Fig. 8.4a where the derivative $\partial g_{OO}(r)/\partial\beta$ is plotted as a function of the total trajectory time. In each case, the calculation is carried out using frames saved every 50 fs, so the trajectory time is proportional to the number of configurations used in the average. The convergence is also affected by the bin width used in the histogramming, here 0.02 \AA . The error, calculated as the difference with the 50 ns result, is shown in Fig. 8.4b to give a more quantitative measure of the convergence. The general behavior of the derivative is already obtained with a 0.5 ns trajectory and well determined at simulation times of 2.0 ns or longer, where the errors are

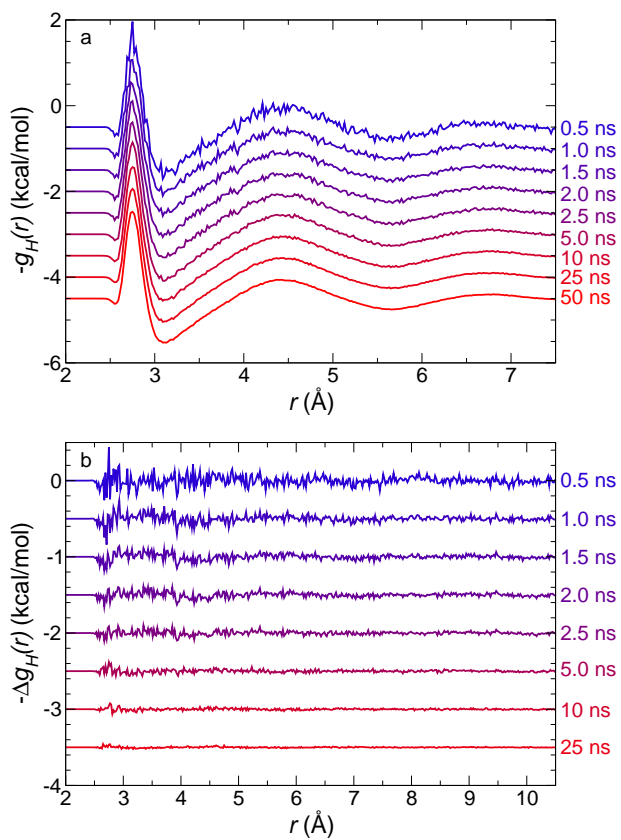


Figure 8.4: a: Calculated derivative of the O-O RDF, $\partial g_{OO}(r)/\partial\beta = -g_H(r)$, as a function of trajectory length. b: Residual relative to the 50 ns result, $-\Delta g_H(r) = -[g_H(r; t_{traj}) - g_H(r; 50\text{ns})]$.

generally less than 0.1 kcal/mol; these errors are decreased if less spatial resolution is required. These results show that the temperature derivative of the RDF is accessible with typical simulation times.

8.4 Conclusions

In summary, we have presented a simple method for calculating the derivative of the radial distribution function with respect to inverse temperature. This derivative is directly related to the internal energy (or, in a constant pressure ensemble, the enthalpy), which further provides access to the entropy. Together, these properties can be used to predict the behavior of the liquid structure over a wide range of temperatures. The approach is a straightforward extension of fluctuation theory and is thus completely general. It can be applied to any equilibrium distribution or average within any ensemble and to other thermodynamic variables. The method is highly accurate over temperature ranges in which the internal energy and entropy do not change with temperature, or do so only weakly. Thus, for example, it cannot be used to predict behavior across a first-order phase transition, as it will instead predict the metastable, *e.g.* supercooled/superheated, behavior. A key advantage is the mechanistic insight it can provide through the decomposition of the derivative into contributions from different interactions present in the system. This approach can be straightforwardly implemented in common simulation protocols to provide additional information that is currently being neglected.

Chapter 9

Temperature Dependence of the Water Infrared Spectrum: Driving Forces, Isosbestic Points, and Predictions

9.1 Introduction

The behavior of liquid water vibrational spectra with temperature has long been of interest because of the potential insight it can offer into the underlying driving forces for the liquid structure and dynamics.^{46,46,48,49,105,124,138,197,279–284,284–286,286–295} Among the prominent features observed are isosbestic points found in the IR^{282,286,286,287} and Raman^{280,284,284,288,289,291–295} spectra as temperature is varied. These have been used to argue for two-state models of the water hydrogen-bond (H-bond) network,^{282,284–287} but more recently it has been shown they instead arise as a natural feature of inhomogeneous broadening.^{291–293}

In this Chapter, we investigate the energetic origins of the temperature dependence of the IR spectrum of dilute HOD in D₂O to shed new light on these issues. Specifically, we directly calculate the temperature derivative of the IR spectrum using molecular dynamics (MD) simulations. The theoretical approach is an application of fluctuation theory to dynamics,^{13,31,35,58} similar to that previously described by Morita and co-workers.^{46,46,48,49} This method provides new mechanistic insight into the energetic driving forces – *e.g.*, kinetic energy, Coulombic and Lennard-Jones interactions – behind spectral changes with temperature, including the nature and origin of the

Adapted with the permission of Zeke A. Piskulich, and Ward H. Thompson and the American Chemical Society from *J. Phys. Chem. Lett.* **11**, 7762-7768 (2020).¹⁸⁴

isosbestic point. We show that the effects can be characterized by an (effective) internal energy as a function of frequency, which itself can be used to predict the IR spectrum for temperatures spanning at least 80 K.

We calculate the IR lineshape from the Fourier transform

$$I(\omega) = \frac{1}{2\pi} \int_{-\infty}^{\infty} e^{-i\omega t} \phi(t) dt, \quad (9.1)$$

of the dipole-dipole response function,

$$\phi(t) = \left\langle \vec{\mu}_{01}(0) \cdot \vec{\mu}_{01}(t) e^{i \int_0^t \omega_{01}(\tau) d\tau} \right\rangle e^{-|t|/2T_1}. \quad (9.2)$$

Here $\vec{\mu}_{01}(t) = \langle 1 | \hat{\mu} | 0 \rangle = \mu_{01}(t) \vec{e}_{OH}(t)$ is the matrix element of the transition dipole moment vector for the OH bond at time t , $\omega_{01}(t)$ is the $0 \rightarrow 1$ vibrational frequency at time t , and T_1 is the $n = 1$ vibrational relaxation lifetime. The brackets $\langle \dots \rangle$ indicate a thermal average.

It is within this thermal average that the temperature dependence of the IR spectrum appears in two factors: the Boltzmann weighting factor in the average and the canonical partition function that normalizes it.^{13,31} Thus, taking the derivative of the IR lineshape gives a simple expression

$$\frac{dI(\omega)}{d\beta} = -\frac{1}{2\pi} \int_{-\infty}^{\infty} e^{-i\omega t} \phi_H(t) dt, \quad (9.3)$$

where $\beta = 1/k_B T$ with k_B Boltzmann's constant and $\phi_H(t)$ is, within a sign, the β derivative of $\phi(t)$,

$$\frac{d\phi(t)}{d\beta} = -\left\langle \delta H(0) \vec{\mu}_{01}(0) \cdot \vec{\mu}_{01}(t) e^{i \int_0^t \omega_{01}(\tau) d\tau} \right\rangle e^{-|t|/2T_1} = -\phi_H(t). \quad (9.4)$$

Here, $\delta H(0) = H(0) - \langle H \rangle$ is the fluctuation in the total system energy from its average value. For simplicity, we neglect the temperature dependence of T_1 and use the value of 700 fs from Fecko *et al.*¹¹⁴

In this work, we evaluate these quantities using the empirical mapping approach^{196,197,199} from a classical MD simulation of H₂O, considering each OH bond as independent and isotopically di-

lute (*i.e.*, neglecting vibration-vibration coupling) to effectively model dilute HOD in D₂O.¹⁹⁷ In this approach, ω_{01} and μ_{01} are obtained from the electric field along the OH bond, exerted by the surrounding waters on the H atom of interest, as determined by a correlation with electronic structure results. This approach has been shown to be accurate for a water in a variety of environments¹⁹⁹ and over a wide range of temperatures.^{197,296}

9.2 Computational Methods

MD simulations of 343 TIP4P/2005⁵ molecules in a periodic simulation cell of side length 21.725311 Å ($\rho = 0.997 \text{ g/cm}^3$) were carried out using the Large-scale Atomic/Molecular Massively Parallel Simulator (LAMMPS).⁸¹ A 1 fs timestep was used with the SHAKE algorithm to hold the water bonds and angle rigid (tolerance of 1×10^{-4}) and the electrostatics described with the Particle-Particle Mesh Ewald summation method^{119,120} (tolerance of 1×10^{-4}). At 298.15 K, six 4 ns *NVT* trajectories were propagated with positions and energies saved every 4 fs; the IR spectra was calculated at 280, 320, 340, and 360 K from one 4 ns *NVT* trajectory at each temperature. Temperature was maintained with a Nosé-Hoover thermostat^{83,84} with a damping parameter of 2 ps, long enough to avoid thermostat effects on the response functions $\phi(t)$ and $\phi_H(t)$. All reported uncertainties correspond to a 95% confidence interval according to the Student's *t*-distribution¹²² over an average of six blocks (each block representing a 4 ns trajectory).

9.3 Results and Discussion

The simulated IR lineshape for HOD in D₂O is presented in Fig. 9.1a. The peak maximum is at 3382 cm⁻¹ and the full-width half-maximum (FWHM) is 270 cm⁻¹. It is interesting to compare the IR lineshape with the distribution of frequencies, $P(\omega) = \langle \delta[w - w_{01}(\mathbf{Q})] \rangle$, which is also plotted in Fig. 9.1a. $P(\omega)$ is notably blueshifted, with a maximum at 3465 cm⁻¹, broader (FWHM = 382 cm⁻¹), and more asymmetric with a long tail to lower frequencies. The differences are partially a result of non-Condon effects, *i.e.*, the transition dipole moment that gov-

erns the IR intensity is larger for stronger H-bonds, which are captured in the spectral density, $P_{\mu}(\omega) = \langle |\mu_{01}(\mathbf{Q})|^2 \delta[w - w_{01}(\mathbf{Q})] \rangle$. The spectral density is also plotted in Fig. 9.1a and more closely resembles the IR lineshape: it peaks at 3385 cm^{-1} but is still broader (FWHM = 361 cm^{-1}). The difference between the the IR lineshape and spectral density can be attributed primarily to dynamical effects, particularly motional narrowing resulting from rapid fluctuations of the vibrational frequency.²⁹⁷

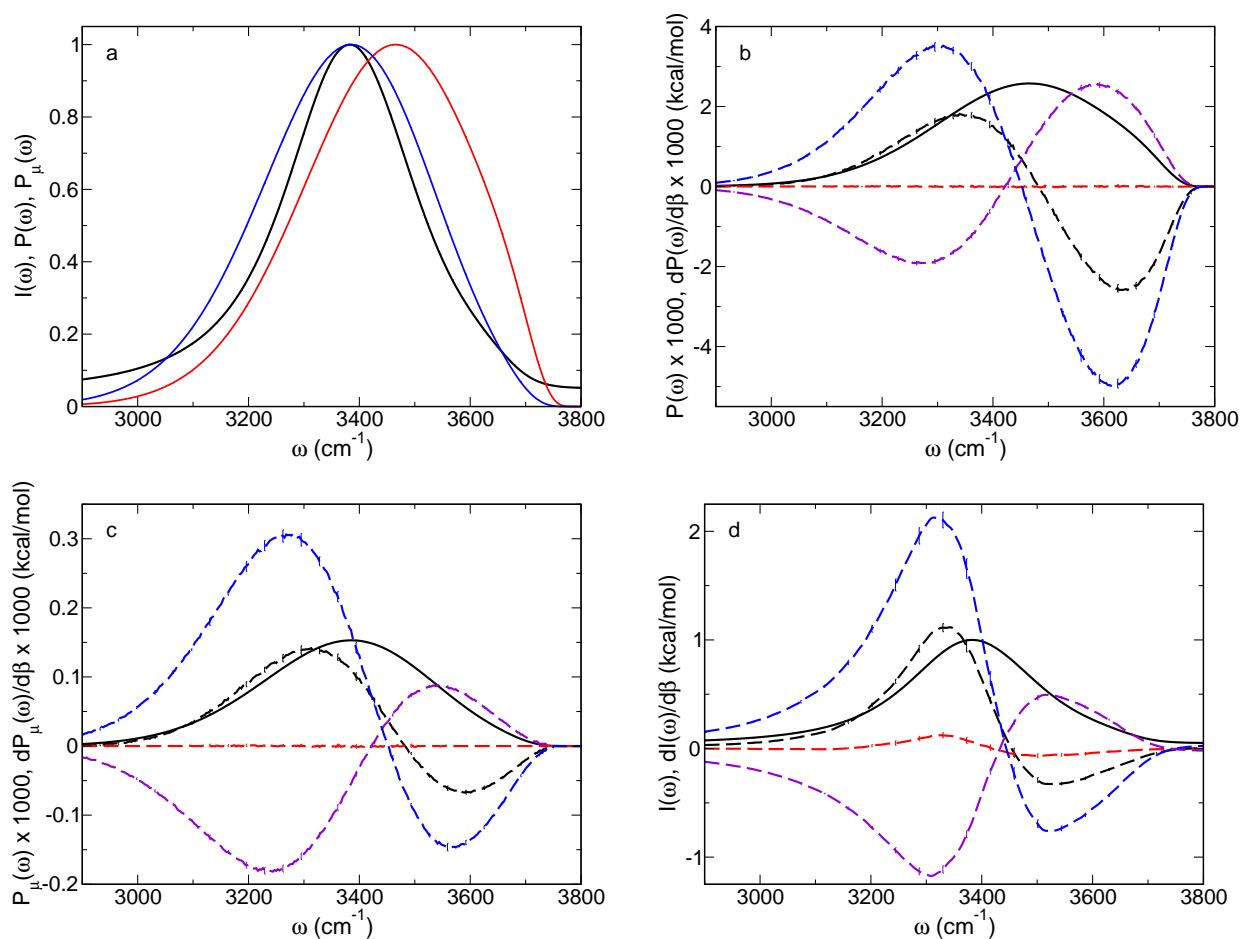


Figure 9.1: (a) HOD in D_2O IR spectrum (black), frequency distribution (red), and spectral density (blue) at 298.15 K. The (b) frequency distribution, (c) spectral density, and (d) IR spectrum, with the maximum set to 1, are reproduced (solid black) along with the total derivative with respect to β (dashed black) and the contributions to the derivative from the kinetic (dashed red), Lennard-Jones (dashed violet), and Coulombic (dashed blue) energies.

The temperature (or β) derivative of the frequency distribution and spectral density can be

calculated like that for $I(\omega)$,

$$\frac{dP(\omega)}{d\beta} = -\langle \delta H \delta[w - w_{01}(\mathbf{Q})] \rangle \equiv -P_H(\omega), \quad (9.5)$$

and

$$\frac{dP_\mu(\omega)}{d\beta} = -\langle \delta H |\mu_{01}|^2 \delta[w - w_{01}(\mathbf{Q})] \rangle \equiv -P_{\mu,H}(\omega). \quad (9.6)$$

A key advantage of this approach is that it provides additional mechanistic information because the system energy is divisible into physically meaningful components, *e.g.*, $\delta H(0) = \delta KE(0) + \delta V_{LJ}(0) + \delta V_{Coul}(0)$, yielding the contributions to the derivative from each of these motions or interactions, *e.g.*, $P_H(\omega) = P_{KE}(\omega) + P_{LJ}(\omega) + P_{Coul}(\omega)$. Here, KE is the kinetic energy and V_{LJ} and V_{Coul} are the Lennard-Jones and Coulombic potential energies. It should be noted that other decompositions are possible as long as the terms sum to the total energy; though for the present work we consider the simple decomposition above. The total temperature derivatives of $P(\omega)$, $P_\mu(\omega)$, and $I(\omega)$ are shown in Fig. 9.1b-d along with the contributions to each derivative from the different energy components.

Considering the frequency distribution first, Fig. 9.1b shows that the total derivative is positive at lower frequencies (*i.e.*, the amplitude in this region will grow as β increases and T decreases) and negative at higher frequencies. Note that because $P(\omega)$ is a normalized probability distribution, its derivative must integrate to zero. This gives rise to at least one frequency where the derivative is zero and therefore where $P(\omega)$ is unchanged by temperature (at least over some interval). Geissler has previously pointed this out in the context of understanding isosbestic points that have been observed in the Raman and IR spectra of water,^{291–293} the former of which can often be well described by the frequency distribution.

New insight into the origin of the isosbestic point is offered by the energetic contributions to the derivative. Because $P(\omega)$ depends only on configurational variables, the kinetic energy contribution is rigorously zero. The total derivative, $dP(\omega)/d\beta$, is thus determined by the direct competition of the Lennard-Jones and Coulombic interactions. Namely, in an H-bond the waters

sit on the repulsive wall of the Lennard-Jones potential, held there by the attractive Coulombic attraction between the donor H atom and the accepting O atom. The frequency distribution captures a continuum of H-bond structures with lower frequencies corresponding to greater electrostatic stabilization and larger Lennard-Jones repulsion. Conversely, the highest frequencies, which reflect weak or even transiently broken H-bonds, involve more favorable Lennard-Jones and poorer Coulombic interactions. This behavior is reflected in the Lennard-Jones and Coulombic contributions to the $P(\omega)$ derivative shown in Fig. 9.1b. The former favors higher frequencies and the latter favors lower frequencies as T decreases. The electrostatic interactions are dominant, so the total derivative reflects the partial cancellation of the Coulombic contribution by the Lennard-Jones term.

The frequency where the total derivative is zero, the isosbestic point for $P(\omega)$ with changes in T , is thus determined by the competition between the Coulombic and Lennard-Jones interactions that are held in tension in an H-bond.^{136,147,160} The same battle between these interactions explains an analogous isosbestic point in the water O–O radial distribution function,¹⁴⁷ which has been observed in both measurements and simulations.^{12,276,277,298}

The IR spectrum differs from the frequency distribution due to both non-Condon and dynamical effects (Fig. 9.1a). The effect of the former on the temperature dependence is explored in Fig. 9.1c, where the spectral density derivative, $dP_\mu(\omega)/d\beta$, is shown along with its kinetic, Lennard-Jones, and Coulombic energy contributions. These are qualitatively similar to those for the frequency distribution. Indeed, the spectral density is the frequency distribution weighted by the average square transition dipole moment at each frequency, increasing the relative amplitude of both $P_\mu(\omega)$ and its derivatives at lower frequencies compared to $P(\omega)$. The temperature dependence of $P_\mu(\omega)$ and $P(\omega)$ thus only differ if $\langle |\mu_{01}|^2 \rangle(\omega)$ changes with temperature. Within the empirical mapping description this is not the case and there is no temperature dependence of the non-Condon effect itself.

Because the IR spectrum includes dynamical effects that significantly affect the lineshape, it is perhaps not obvious that it would retain an isosbestic point. This is explored in Fig. 9.1d, which

shows the total derivative of $I(\omega)$ with respect to β and its energetic components. The total derivative is in general agreement with that previously reported by Joutsuka and Morita using a flexible, polarizable water model to directly describe the frequencies;⁴⁸ they did not report energetic decompositions. The results clearly show that the general shape of $dI(\omega)/d\beta$ is similar to that for the frequency distribution and spectral density, including the presence of a frequency at which the derivative is zero, indicative of an (at least local) isosbestic point at 3454 cm^{-1} , which is redshifted relative to the 3482 cm^{-1} found for $P(\omega)$ and $P_\mu(\omega)$; experiments on H_2O find an isosbestic point at 3460 cm^{-1} .²⁸⁶ As with the frequency distribution, this can be understood based on the energetic contributions to the derivative, which measure how the interactions drive the changes in $I(\omega)$ with T . The dynamical nature of the IR lineshape means that the kinetic energy contribution to the derivative is non-zero, but it remains quite small. Thus, $dI(\omega)/d\beta$ is largely determined by the competition between the Coulombic and Lennard-Jones interactions of the water molecules that, as T is decreased, favor lower and higher OH frequencies, respectively.

It is interesting and useful to examine the thermodynamics that underlie the frequency distribution by considering the corresponding (Helmholtz) free energy profile as a function of frequency,

$$\Delta A(\omega) = -k_B T \ln P(\omega) = \Delta U(\omega) - T \Delta S(\omega), \quad (9.7)$$

where $\Delta U(\omega)$ and $\Delta S(\omega)$ are the internal energy and entropy. It is straightforward to show that, within the van't Hoffian assumption that $\Delta U(\omega)$ and $\Delta S(\omega)$ are temperature independent,¹⁴⁷

$$\Delta U(\omega) = \frac{P_H(\omega)}{P(\omega)}. \quad (9.8)$$

The entropic contribution can be directly obtained from $\Delta A(\omega)$ and $\Delta U(\omega)$. Geissler derived an analogous expression to Eq. 9.8 in explaining the ubiquity of isosbestic points.^{292,293} (The spectral density free energy is the same as that for $P(\omega)$ within the present model.) In addition, because $P_H(\omega)$ can be decomposed into Lennard-Jones and Coulombic contributions, so can the internal

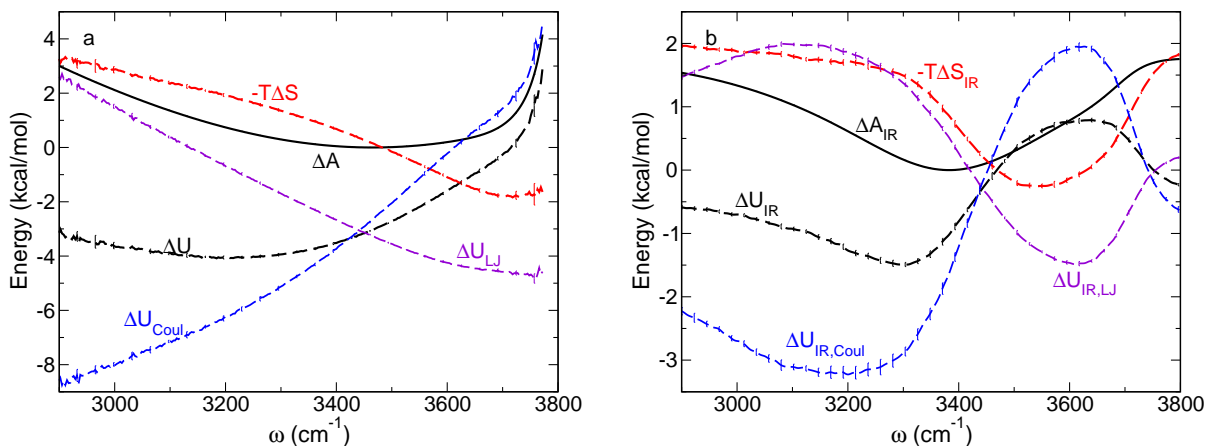


Figure 9.2: Free energy ΔA (solid black), internal energy ΔU (dashed black), entropic contribution $-T\Delta S$ (dashed red) are plotted versus frequency along with the Lennard-Jones (dashed violet) and Coulombic (dashed blue) internal energy components for the (a) frequency distribution and (b) IR spectrum at 298.15 K.

energy. Namely,

$$\Delta U(\omega) = \frac{P_{LJ}(\omega)}{P(\omega)} + \frac{P_{Coul}(\omega)}{P(\omega)} = \Delta U_{LJ}(\omega) + \Delta U_{Coul}(\omega), \quad (9.9)$$

providing additional insight into the energetic driving forces.

The free energy, internal energy, entropy, and internal energy components for the frequency distribution are shown in Fig. 9.2a. The internal energy $\Delta U(\omega)$ has a broad minimum around 3200 cm^{-1} resulting from the competition between the Coulombic and Lennard-Jones contributions. The former decreases monotonically toward lower frequencies, *i.e.*, more redshifted, strongly hydrogen-bonded OH groups, while the latter decreases monotonically as the frequency increases. The entropic contribution, $-T\Delta S(\omega)$, also favors higher frequencies, further indicating that they correspond a more disordered H-bonding arrangement involving weaker, or even transiently broken, H-bonds.

The IR spectrum, as a dynamical quantity, cannot be rigorously converted to a free energy, but we can consider an effective free energy defined in analogy to Eq. 9.7:

$$\Delta A_{IR}(\omega) = -k_B T \ln I(\omega) = \Delta U_{IR}(\omega) - T\Delta S_{IR}(\omega). \quad (9.10)$$

Analogous to the frequency distribution, the internal energy can be decomposed as $\Delta U_{IR}(\omega) = \Delta U_{IR,KE}(\omega) + \Delta U_{IR,LJ}(\omega) + \Delta U_{IR,Coul}(\omega)$, noting that the kinetic energy contribution is non-zero.

These effective free energy, internal energy, entropy, and internal energy components for the IR spectrum are shown in Fig. 9.2b. They exhibit behavior that is generally the same as for the frequency distribution, with the primary difference occurring at the highest and lowest frequencies. Namely, $\Delta A_{IR}(\omega)$ asymptotically approaches constant values at the limits of the spectrum. Similarly, $\Delta U_{IR}(\omega)$ and $-T\Delta S_{IR}(\omega)$ exhibit local maxima and minima due to this behavior. This difference in shapes with the $P(\omega)$ results is due to both non-Condon effects, which appear only in the free energy and entropy, because the transition dipole moment is not T dependent, and dynamical effects such as motional narrowing (see Fig. 9.1a); the latter make these only effective energy curves. Otherwise, the results for the IR spectrum show the same competition between Coulombic and Lennard-Jones interactions as well as between internal energy and entropic factors.

Effective internal energy curves have been previously reported by Hare and Sorenson²⁸⁴ and Walrafen²⁸⁹ obtained from numerical derivatives of the water Raman spectrum. They obtained shapes quite similar to the $\Delta U_{IR}(\omega)$ shown in Fig. 9.2b. They assigned the energy difference between the maximum and minimum in $\Delta U_{IR}(\omega)$ to that required to break an H-bond; here we find that difference to be 2.3 kcal/mol whereas they obtained 3.2 and 5.1 ± 0.5 kcal/mol.^{284,289} We have separately calculated the activation energy for an H-bond exchange, or "jump," (see Ref. 136) and find $E_{a,jump} = 3.79 \pm 0.06$ kcal/mol. Thus, the present results are not consistent with such an interpretation, though this may be related to the larger non-Condon effects present in the IR spectrum.

A key advantage of calculating $\Delta U(\omega)$ is that it provides a van't Hoff approach to predict $P(\omega)$ at different temperatures from a single temperature simulation as

$$P_{pred}(\omega; T_b) = \frac{P(\omega; T_a) e^{-(\beta_b - \beta_a)\Delta U(\omega)}}{\int P(\omega; T_a) e^{-(\beta_b - \beta_a)\Delta U(\omega)} d\omega}. \quad (9.11)$$

The denominator is included to account for the fact that $\exp\{-(\beta_b - \beta_a)\Delta U(\omega)\}$ is not norm

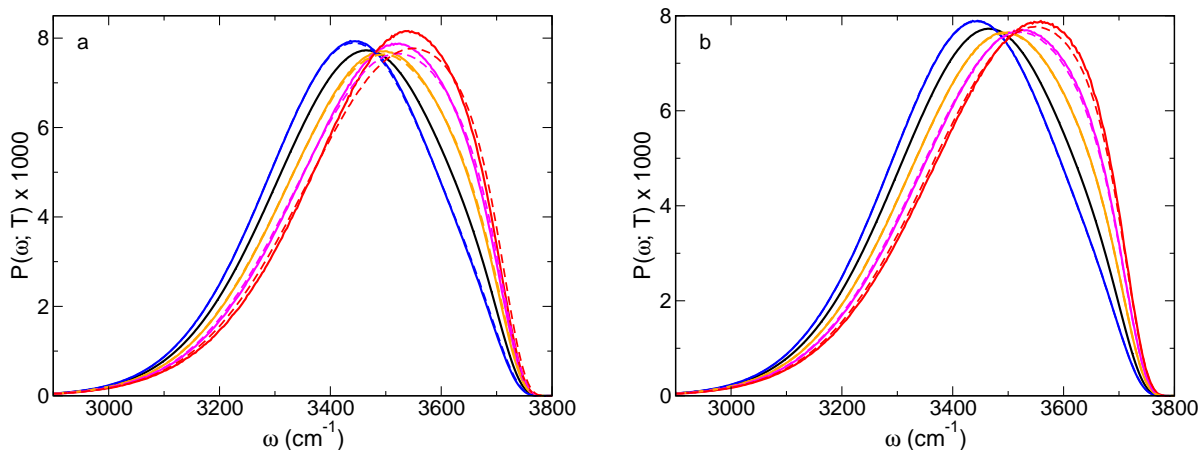


Figure 9.3: Predicted frequency distribution (solid lines) for 280 (blue), 320 (orange), 340 (magenta), and 360 K (red) from the 298.15 K distribution (black) and its derivative; direct calculations at these temperatures are shown as dashed lines of the same color. Results are shown based on (a) first-order Taylor series approximations and (b) van't Hoff predictions, Eq. 9.11.

conserving. Here the a and b subscripts label the simulation and predicted temperature, respectively. The frequency distribution at other temperatures predicted from Eq. 9.11 based on $P(\omega)$ and $\Delta U(\omega)$ calculated at 298.15 K are shown in Fig. 9.3b and compared to the distributions calculated directly at the same temperatures. The agreement is excellent. Only for the highest temperature, 360 K, are there any significant differences between the predicted and directly calculated distributions, where the predicted distribution is slightly too narrow. These shortcomings of the predictions are indicative of non-van't Hoff behavior, *i.e.*, temperature dependence of $\Delta U(\omega)$ and $\Delta S(\omega)$.

The directly calculated and predicted frequency distributions do not exhibit a precise isosbestic point, but only an approximate one, which is a consequence of the normalizing denominator in Eq. 9.11. Without it, the frequency distribution would have a rigorous isosbestic point at the frequency where $\Delta U(\omega) = 0$, *i.e.*, where $dP(\omega)/d\beta = 0$. Note that a first-order Taylor series expansion of the exponential in Eq. 9.11, $P_{1st-order}(\omega; T_b) = P(\omega; T_a)[1 - (\beta_b - \beta_a)\Delta U(\omega)]$, does conserve the normalization of the distribution, illustrating the local nature of the isosbestic point. Results from this description are shown in Fig. 9.3a. The approximation is reasonable for approximately ± 20 K from the temperature at which the derivative is calculated, but leads to significant deviations for larger variations in the temperature.

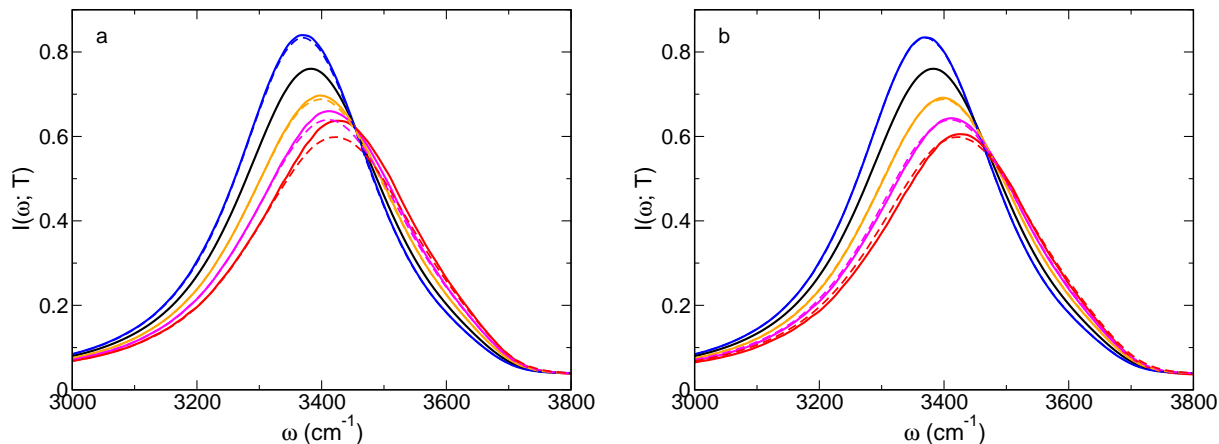


Figure 9.4: Predicted IR spectrum (solid lines) for 280 (blue), 320 (orange), 340 (magenta), and 360 K (red) from the 298.15 K spectrum (black) and its derivative; direct calculations at these temperatures are shown as dashed lines of the same color. Both (a) unnormalized and (b) normalized results, Eq. 9.12, are shown (see the text).

The temperature dependence of the IR spectrum is naturally of greater interest. A key difference with $P(\omega)$ is that the spectrum is not normalized and thus we cannot simply substitute $I(\omega)$ for $P(\omega)$ in Eq. 9.11. One approach is to use the unnormalized spectrum obtained as $I(\omega; T_b) = I(\omega; T_a) e^{-(\beta_b - \beta_a) \Delta U_{IR}(\omega)}$, the results of which are shown in Fig. 9.4a. The spectra predicted this way are in reasonable agreement with those calculated explicitly at the different temperatures. The key differences are, however, an issue of the overall intensity. This can be reasonably remedied by using the change in the frequency distribution normalization as a proxy, namely,

$$I_{pred}(\omega; T_b) = \frac{I(\omega; T_a) e^{-(\beta_b - \beta_a) \Delta U_{IR}(\omega)}}{\int P(\omega; T_a) e^{-(\beta_b - \beta_a) \Delta U(\omega)} d\omega}. \quad (9.12)$$

The results for this approach are presented in Fig. 9.4b. They are in excellent agreement with the explicit calculations of $I(\omega, T)$, with only slight differences for $T \geq 340$ K in the width of the spectrum. As with $P(\omega)$, this renormalization provides a better description of the T -dependent spectra, but also results in an only approximate isosbestic point (Fig. 9.4b) rather than a precise one (Fig. 9.4a).

9.4 Conclusions

In summary, we have directly evaluated the temperature derivatives of the OH frequency distribution and IR spectrum of HOD in D₂O and shown how they can be used to predict the behavior over a wide range of temperatures (*e.g.*, 280-360 K) using a van't Hoff relation. The competition between Coulombic and Lennard-Jones interactions underlies the spectral properties, including the location of a (near) isosbestic point. A precise isosbestic point is not observed due to a subtle renormalization of the non-norm-conserving van't Hoff factor. The approaches described here should be useful in understanding and predicting the temperature dependence for a wide range of spectroscopic measurements probing liquids, including Raman and two-dimensional IR photon echo spectra.

Chapter 10

On the Pressure Dependence of Liquid Structure

10.1 Introduction

Many of liquid water's anomalous features at low temperatures are thought to originate from the presence of a transition between a low-density liquid (LDL) phase and a high-density liquid (HDL) phase located deep within the supercooled regime of water's phase diagram at high pressures.^{240,253,299} At pressures below the liquid-liquid critical point which is thought to be around 170 K and 1.95 kbar,^{240,268,300} the structure of liquid water is made up of both LDL-like (tetrahedral) and HDL-like (distorted tetrahedral) configurations.^{234,301,302} As temperature increases, the liquid structure becomes increasingly HDL-like.^{147,160}

Recently, a van't Hoff approach to predicting the dependence of the radial distribution function (RDF) of liquid water was developed for the canonical (NVT , constant volume and temperature) ensemble.¹⁴⁷ Real experiments, however, are typically not carried out under these conditions and instead occur in the isothermal-isobaric (NpT , constant pressure and temperature) ensemble. In this ensemble, the simulation cell is able to freely adjust to changes to the hydrogen bond (H-bond) network leading to more natural arrangements within this network. Importantly, it is likely that constant pressure is necessary for adequately capturing the reweighting between LDL-like and HDL-like configurations.

In the present work, we have developed an analogous approach to predict the temperature dependence of the RDF in the NpT ensemble from simulations at room temperatures. We also demonstrate for the first time a method for determining the molar volume between water molecules and using this quantity to predict the pressure-dependence of the RDF. We also demonstrate how

the change in the enthalpy and the molar volume associated with H-bond exchanges can be calculated, and that changes in these quantities are consistent with changes observed in the reorientation activation energy and the diffusion activation volume.

10.2 Theory

The RDF can be calculated in the NPT ensemble, as

$$g_{OO}(r) = \left\langle \frac{V}{N^2} \sum_i \sum_{j \neq i} \delta(r - |\vec{r}_{ij}|) \right\rangle, \quad (10.1)$$

where V is the volume, N is the number of molecules, and r is the location along the OO coordinate. Here, $\langle \dots \rangle$ represents a thermal average, which can be rewritten in terms of the isobaric-isothermal (NpT) ensemble partition function, Δ , as

$$g(r) = \frac{1}{\Delta} \text{Tr} \left[e^{-\beta(H+pV)} \frac{V}{N^2} \sum_i \sum_{j \neq i} \delta(r - |\vec{r}_{ij}|) \right], \quad (10.2)$$

where $\beta = 1/(k_b T)$ is the inverse of Boltzmann's constant times temperature, H is the Hamiltonian, p is the pressure, and Tr is an integral over configurations and momenta.

10.2.1 Temperature Derivative

It should be noted that in the above expression only Δ and $e^{-\beta(H+pV)}$ depend on temperature, so the derivative with respect to β is the product rule,

$$\begin{aligned} \left(\frac{\partial g(r)}{\partial \beta} \right)_{N,p} &= -\frac{1}{\Delta^2} \frac{\partial \Delta}{\partial \beta} \text{Tr} \left[e^{-\beta(H+pV)} \frac{V}{N^2} \sum_i \sum_{j \neq i} \delta(r - |\vec{r}_{ij}|) \right] \\ &+ \frac{1}{\Delta} \text{Tr} \left[(H + pV) e^{-\beta(H+pV)} \frac{V}{N^2} \sum_i \sum_{j \neq i} \delta(r - |\vec{r}_{ij}|) \right] \\ &= -\left\langle \delta H \frac{V}{N^2} \sum_i \sum_{j \neq i} \delta(r - |\vec{r}_{ij}|) \right\rangle - p \left\langle \delta V \frac{V}{N^2} \sum_i \sum_{j \neq i} \delta(r - |\vec{r}_{ij}|) \right\rangle. \end{aligned} \quad (10.3)$$

Here, we have recognized that $1/\Delta\partial\Delta/\partial\beta = \langle H \rangle + p\langle V \rangle$, and have defined $\delta H = H - \langle H \rangle$ and $\delta V = V - \langle V \rangle$ as the fluctuations in energy and volume, respectively. It should furthermore be noted that the first term of the final result (that depends on the energy fluctuation) is similar in form to the result found previously for the NVT ensemble;¹⁴⁷ however, the second term accounts for the effect of volume fluctuations on the temperature derivative. It should be noted that for p in bar, and V in \AA^3 , the conversion factor for the second term to units of kcal/mol is 1.4394×10^{-5} , so except at high pressures, this term contributes only small amounts to the temperature dependence.

10.2.2 Pressure Derivative

The same approach may be applied to calculate the derivative with respect to pressure, which following similar steps to those above works out to

$$\left(\frac{\partial g(r)}{\partial p}\right)_{N,T} = -\beta \left\langle \delta V \frac{V}{N^2} \sum_i \sum_{j \neq i} \delta(r - |\vec{r}_{ij}|) \right\rangle. \quad (10.4)$$

which should be recognized as essentially the second term of Eq. 10.4 divided by p . This term's units depend on those of $\beta \delta V$ which in units of kcal/mol and \AA^3 can be conveniently converted to units of bar^{-1} using the same conversion factor 1.4394×10^{-5} .

10.2.3 Thermodynamic Potential

In the NpT ensemble, the underlying thermodynamic potential is the Gibbs free energy ($\Delta G(r)$) which can be calculated along the r coordinate of $g(r)$ through the equation

$$\Delta G(r) = -k_b T \ln g(r) - 2k_b T \ln r \quad (10.5)$$

where the first term is the potential of mean force (PMF) along the r coordinate, and the second term is related to the increase in volume corresponding to moving further along the r coordinate.

The derivative of the Gibbs free energy with respect to temperature can be expressed as,

$$\frac{\partial \Delta G(r)}{\partial \beta} = -k_B T \left[\frac{1}{g(r)} \frac{\partial g(r)}{\partial \beta} + \Delta G(r) \right]. \quad (10.6)$$

Recall that $\Delta G(r) = \Delta H(r) - T \Delta S(r)$ where $\Delta H(r)$ is the enthalpy, and $\Delta S(r)$ is the entropy. If ΔS and ΔH are weakly (or independent) of T , it can be shown that

$$\Delta H(r) = \frac{-1}{g(r)} \frac{\partial g(r)}{\partial \beta} \quad (10.7)$$

and

$$\Delta S(r) = \frac{1}{k_B T^2} \frac{\partial \Delta G(r)}{\partial \beta}. \quad (10.8)$$

These results are essentially identical to those observed for the Helmholtz free energy in the NVT ensemble; however, they differ by the inclusion of the effect of volume fluctuations on the temperature derivative.

Turning to the derivative with respect to pressure, further thermodynamic information is available by recalling that

$$\begin{aligned} dG &= \mu \delta N + \bar{v} \delta p - S \delta T \\ &= \left(\frac{\delta G}{\delta N} \right) \delta N + \left(\frac{\delta G}{\delta p} \right) \delta p + \left(\frac{\delta G}{\delta T} \right) \delta T, \end{aligned} \quad (10.9)$$

where μ is the chemical potential, and \bar{v} is the molar volume for two water molecules separated by a distance r . This molar volume can be calculated as

$$\bar{v} = \frac{\partial \Delta G}{\partial p} = \frac{-1}{\beta g(r)} \frac{\partial g(r)}{\partial p}, \quad (10.10)$$

which can be evaluated directly from a simulation at a single temperature.

10.3 Methods

Molecular dynamics simulations were conducted using the Large-Scale Atomistic/Molecular Massively Parallel Simulator (LAMMPS) in the isothermal-isobaric (NpT) ensemble.⁸¹ Simulations were run at a variety of temperatures ($T=220, 235, 250, 280, 298.15, 320, 360$ K) and pressures ($P=0.001, 0.5, 1, 2.5, 5.0, 7.5, 10.0$ kbar). We have also evaluated these derivatives for a variety of water models at ambient conditions (SPC/E,⁴² SPC/Fw,³⁰³ TIP3P-PME,^{304,305} TIP3P-PME/Fw,^{304,305} OPC3,³⁰⁶ TIP4P/2005,⁵ TIP4P/Ew,³⁰⁷ E3B2,¹⁹⁴ E3B3¹⁹⁵) A three-chain Nosé-Hoover thermostat was used to maintain the temperature with a damping parameter of 0.1 ps,^{83,84} a three-chain barostat was used to maintain pressure, with a 1.0 ps damping parameter.^{226,227} A fully periodic simulation cell was filled with 343 TIP4P/2005 water molecules using PACKMOL.¹⁶² The SHAKE algorithm was used with a tolerance of 10^{-4} to hold the water OH bonds and angles rigid.⁸² Initial velocities were randomly selected from the Maxwell-Boltzman distribution at the appropriate temperature. A simulation timestep of 1.0 fs was used for all simulations. Each simulation was made up of a 1 nanosecond equilibration period, followed by a 50 nanosecond production run from which configurations were output every 50 fs which were used for calculation of the values in the present study.

10.4 Results

10.4.1 Dependence of Radial Distribution Function on p, T

We have calculated the water oxygen-oxygen RDF, $g(r; T, p)$ as a function of temperature and pressure moving away from ambient conditions and have included $g(r; T = 298.15\text{K}, p)$ in Figure 10.1a, and $g(r; T, p = 1\text{bar})$ in Figure 10.1b, respectively. We have also evaluated the derivative with respect to temperature (Figure 10.1c and Figure 10.1d) and pressure (Figure 10.1e and Figure 10.1f) over those same ranges.

If we first consider the T -dependence of the RDF, we find that the results are reasonably similar to those that we found previously for the NVT ensemble;¹⁴⁷ however, the present results exhibit

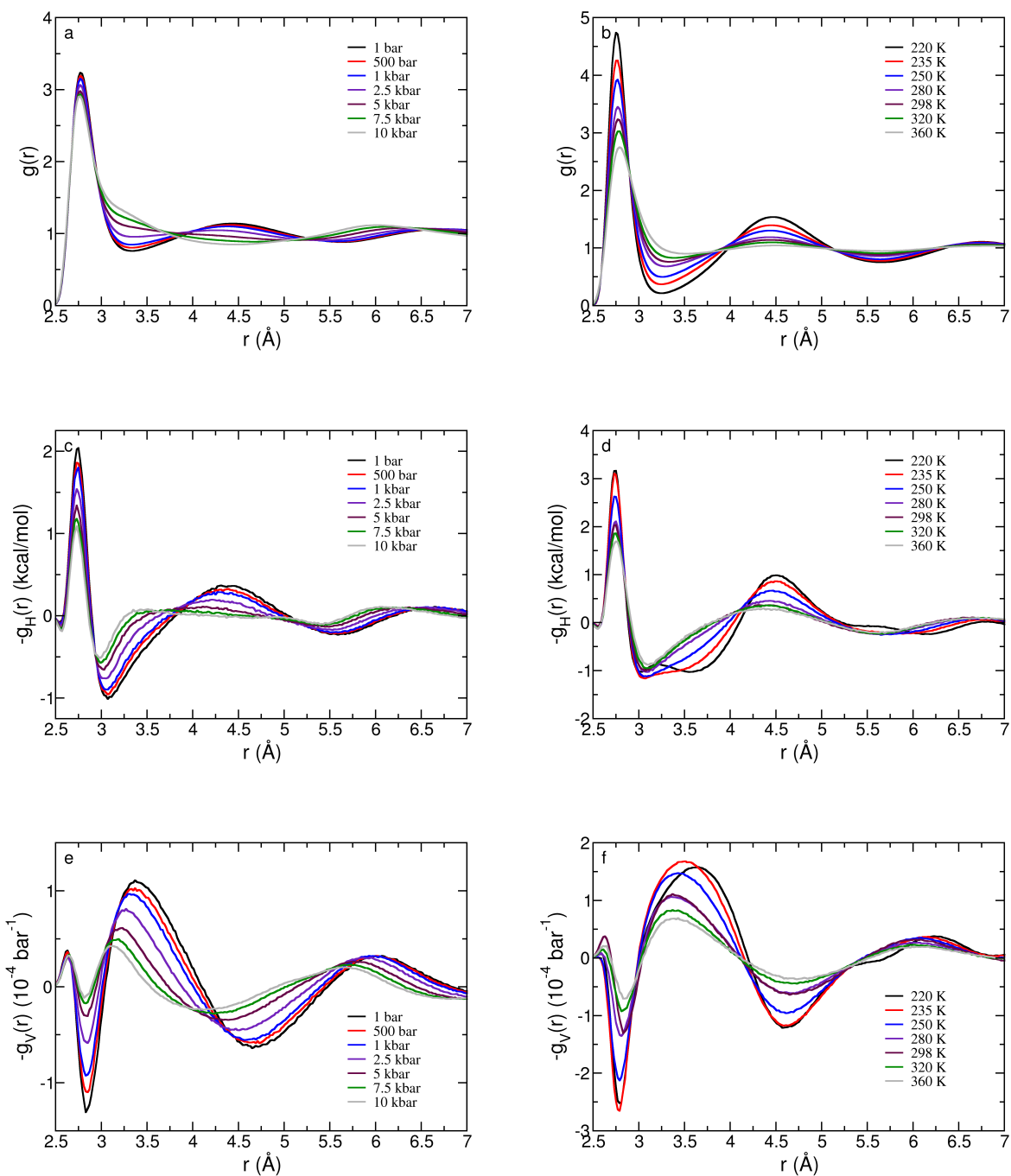


Figure 10.1: a) p -dependence of $g(r)$, b) T -dependence of $g(r)$, c) P -dependence of $g(r)$ T -derivative, d) T -dependence of $g(r)$ T -derivative, e) P -dependence of $g(r)$ P -derivative, and f) T -dependence of $g(r)$ p -derivative.

slightly more structuring than our previous results (Chapter 8). We also note that the isosbestic point in the second solvation shell in the NPT ensemble is more approximate than was observed in the

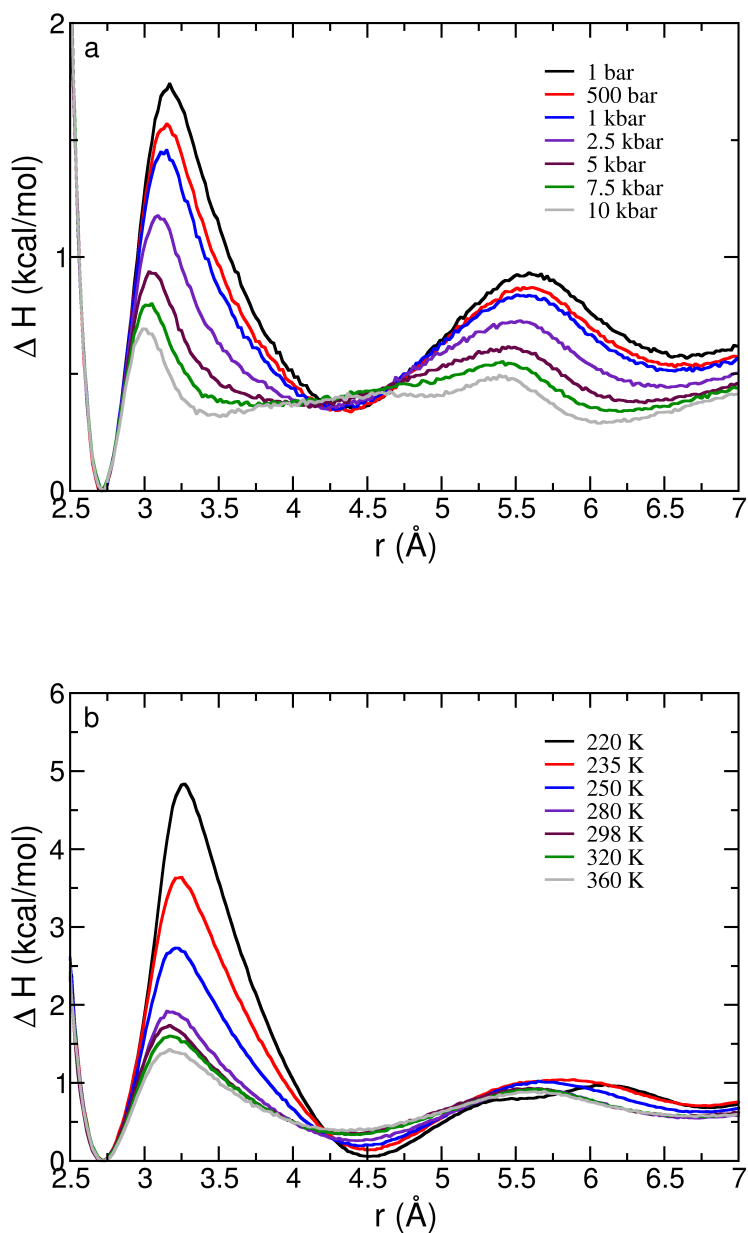


Figure 10.2: Dependence of the enthalpy, $\Delta H(r)$, as a function of a) P , and b) T .

NVT ensemble. With the P -dependent calculations of the RDF we observe that the first peak of the RDF decreases as pressure is increased, and that there appears to be an overall contraction in the liquid structure with pressure. We observe a phenomenologically different behavior at pressures above 2.5 kbar than at pressures below it starting at the minimum separating the first and second

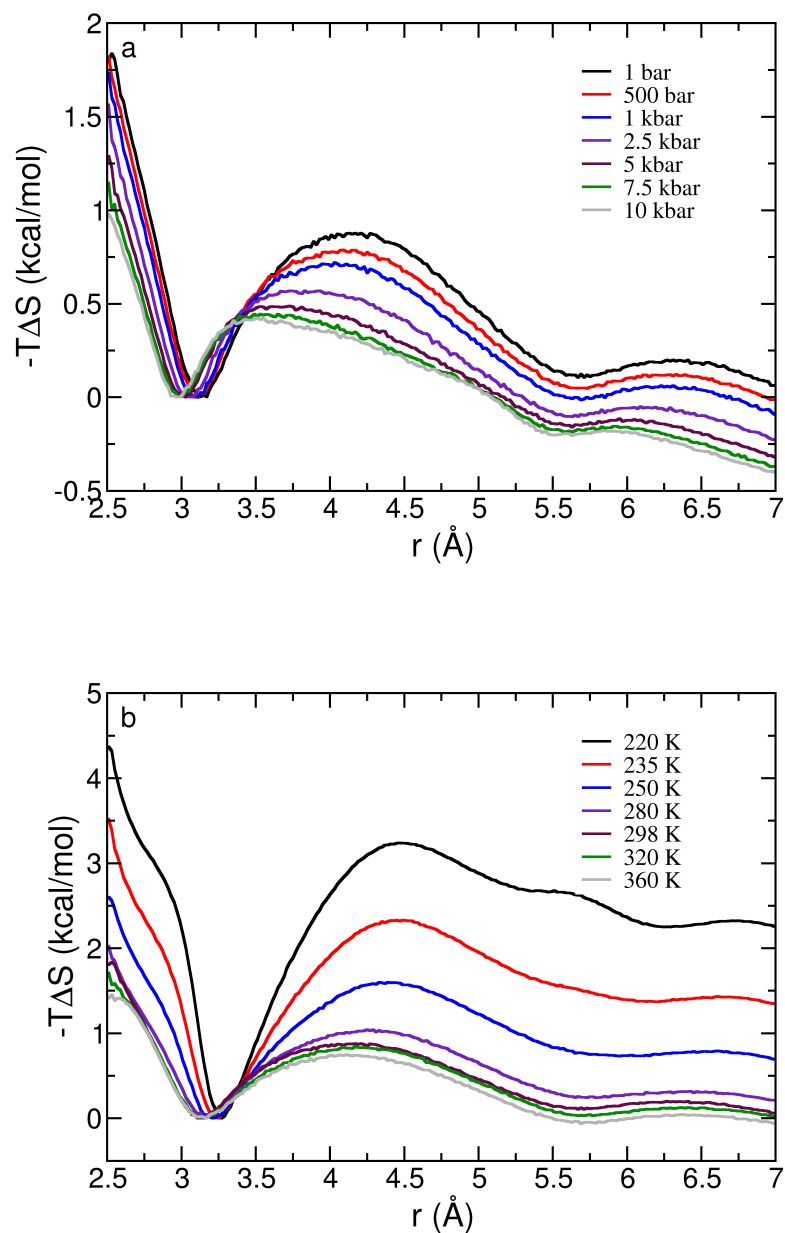


Figure 10.3: Dependence of the entropic contribution to the free energy, $-T\Delta S(r)$, as a function of a) P , and b) T .

solvation shells caused by a distortion of the water H-bond network and a growing population of 5th-neighbor water molecules in this region as has been recently noted by Teng and co-workers for other water models.³⁰⁸

Turning to the derivatives with respect to β plotted in Figure 10.1c-d, we find that as pressure

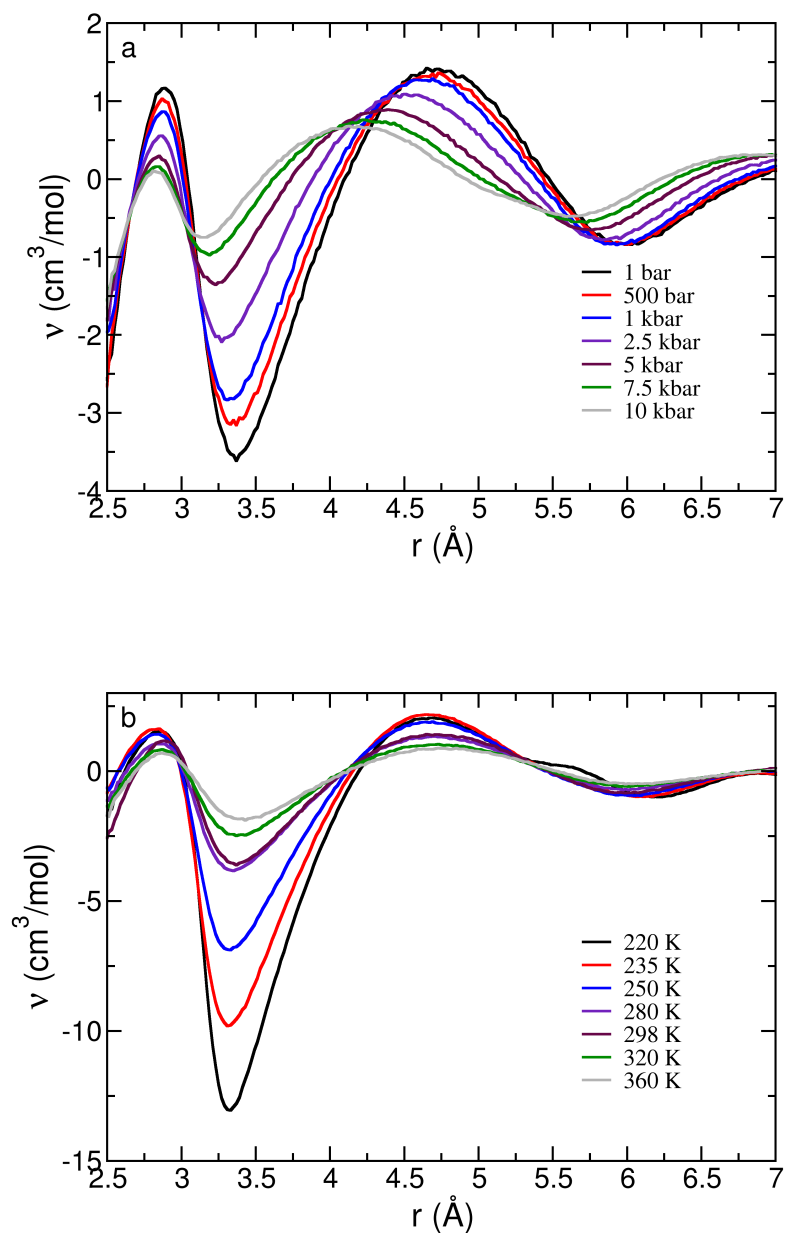


Figure 10.4: Dependence of the partial molar volume, $\bar{v}(r)$ as a function of a) P , and b) T .

is increased the derivative in the second solvation shell becomes weaker (and essentially zero at the 7.5 kbar and 10 kbar). We find that the lowest temperatures exhibit the strongest dependence on β , with 220 K and 235 K exhibiting a more complicated dependence than higher temperatures, potentially related to the larger prevalence of *LDL*-like configurations under these conditions. The

derivatives with respect to p (Figures 10.1e-f) generally vary smoothly, with increases in p leading to an increase in the region separating the first and second solvation shells, consistent with the observations made about the P dependence in this region above. We have used these derivatives to evaluate the enthalpy (Figure 10.2), the entropy (Figure 10.3), and the molar volume (Figure 10.4).

10.5 Discussion

In the remainder of this chapter, we present a calculation of the enthalpic, entropic, and volumetric changes associated with H-bond exchanges and demonstrate their dependence on T , P . We will then demonstrate the use of the enthalpy and molar volume to predict the dependence of the RDF on T , P , respectively.

10.5.1 Connection to H-Bond Exchanges

H-bond exchanges are an essential step in most dynamical processes with liquid water, and have been suggested by Laage and Hynes to be closely linked with the energetics of liquid structure.⁸⁵ In particular, these exchanges involve a new acceptor moving from the second solvation shell to the first, and the old acceptor leaving.

Enthalpically, this can be described by the quantity $\Delta\Delta H = \Delta H_{orig}^{\ddagger} + \Delta H_{new}^{\ddagger}$ where $\Delta H_{orig}^{\ddagger}$ is the barrier to the original acceptor leaving the first solvation shell, and $\Delta H_{new}^{\ddagger}$ is the barrier to the new acceptor entering the first solvation shell. These can be calculated from the RDF as

$$\begin{aligned}\Delta H_{orig}^{\ddagger} &= \Delta H_{OO}(r^{\ddagger}) - \Delta H_{OO}(r_{1st}) \\ \Delta H_{new}^{\ddagger} &= \Delta H_{OO}(r^{\ddagger}) - \Delta H_{OO}(r_{2nd}),\end{aligned}\tag{10.11}$$

where r_{1st} , r_{2nd} , and r^{\ddagger} are the locations of the enthalpic minima of the first and second solvation shells, as well as the maxima of the transition state separating them. We have illustrated this schematically in Figure 10.5. Using these locations from the enthalpic surfaces, we can also calculate the change in entropy ($\Delta\Delta S$) associated with an H-bond exchange. We have plotted both of

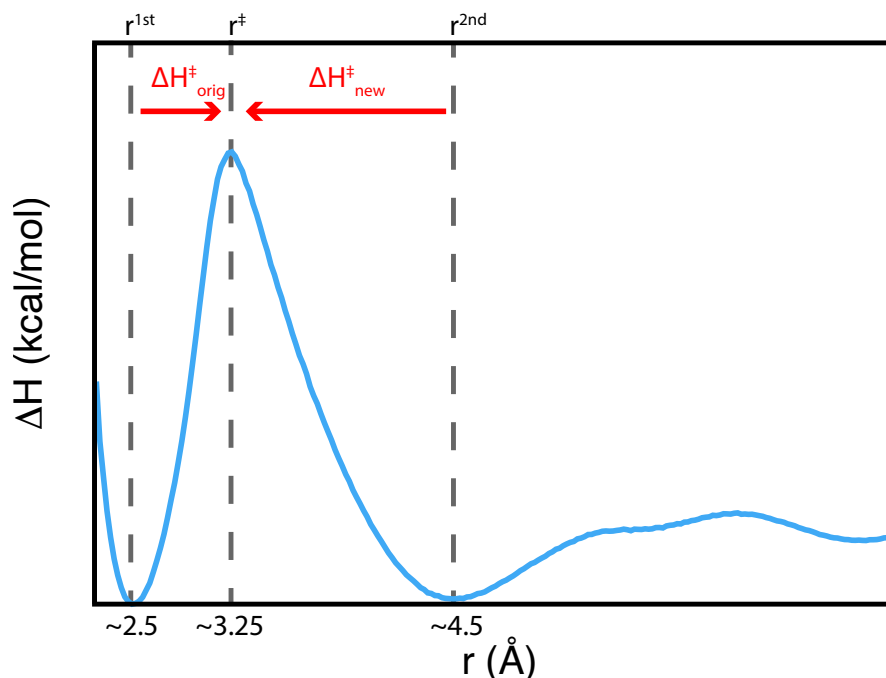


Figure 10.5: Schematic diagram of the enthalpic change associated with a hydrogen bond exchange.

these as a function of pressure in Figure 10.6a and temperature in Figure 10.6b.

The H-bond exchange enthalpy decreases smoothly as the pressure increases, likely due to pressure-induced distortions in the H-bond network. This decrease is consistent with a decrease in the diffusion activation energies (which depends on H-bond exchanges as a fundamental step) that has been observed experimentally. Over this pressure range, we see the entropy change $\Delta\Delta S$ decreases as well.

The dependence of the H-bond exchange enthalpy on temperature is consistent with past simulation measurements that the activation energies of various dynamical timescales (*e.g.* water re-orientation) grow significantly as the simulation temperature decreases. Interestingly, the present results indicate that the Van't Hoffian approach¹⁴⁷ that has been used previously to predict the RDF from room temperature simulations is unlikely to work well down to the lowest temperatures as our results indicate that in the supercooled regime $\Delta\Delta H$ (and $\Delta\Delta S$) exhibit strong temperature dependence.

This temperature dependence of $\Delta\Delta H$ is likely the origin of the increasingly non-Arrhenius

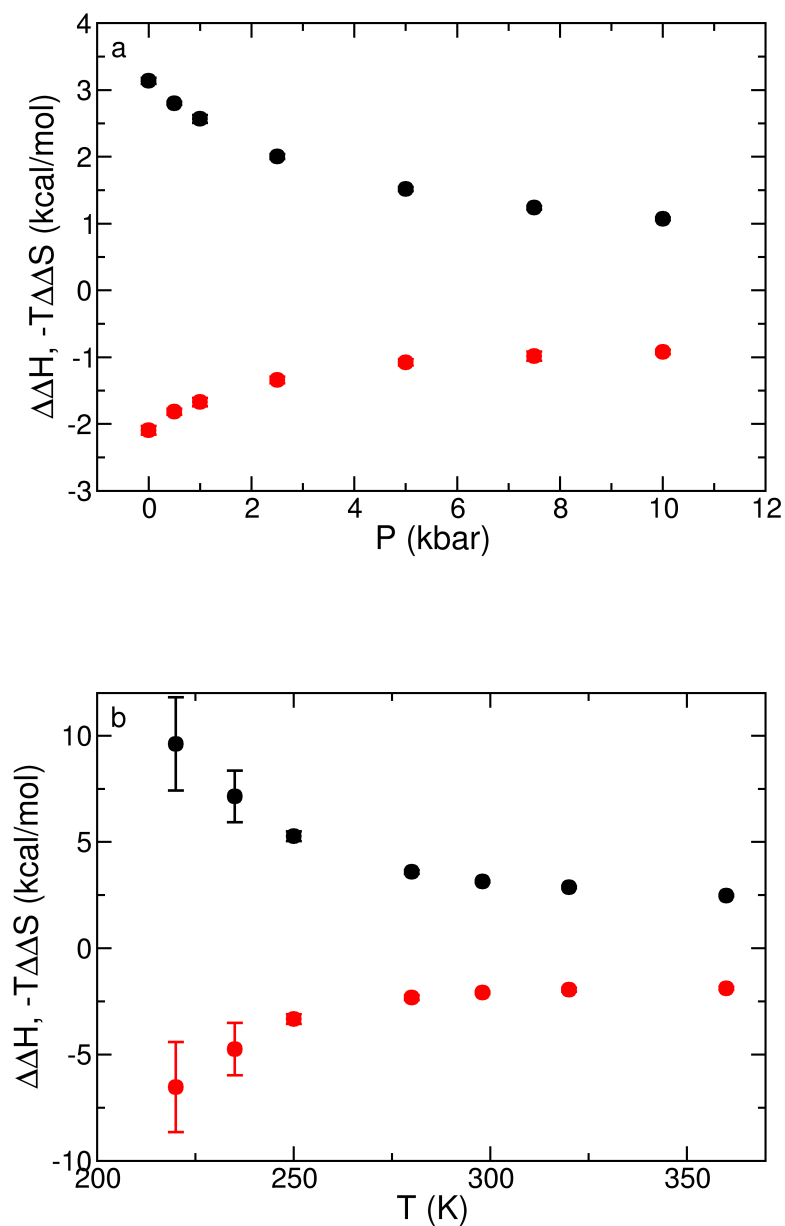


Figure 10.6: Dependence of the changes in the enthalpy (black) and entropy (red) involved in H-Bond exchanges as a function of a) pressure and b) temperature.

nature of dynamical timescales observed in the supercooled regime. A recent study from our group (Chapter 7) has calculated the OH reorientation activation energies using the same water model as our current results, and thus we have plotted those activation energies, E_{a,τ_2} , as a function of our values of $\Delta\Delta H$ in Figure 10.7. We find that these values have a strong, linear correlation

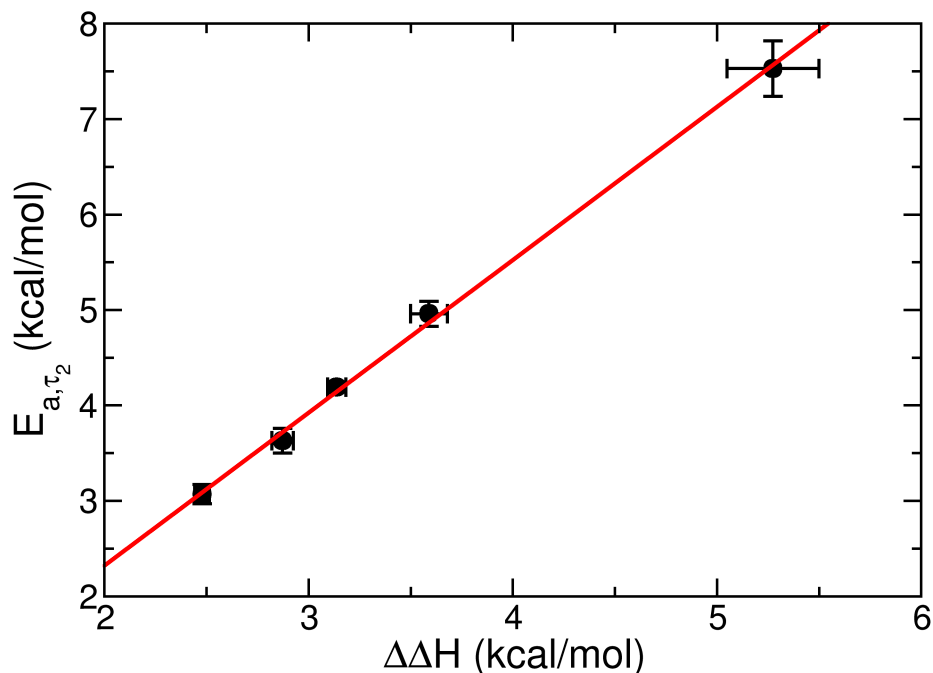


Figure 10.7: Plot of the OH reorientation activation energy as a function of $\Delta\Delta H$ for TIP4P/2005 water. A linear fit is included as a solid red line.

($R^2 = 0.998$). This is unsurprising, as H-bond exchanges are known to be a key underlying step in water reorientation; however, this lends support to the idea that structural changes (*i.e.* an increasing fraction of LDL-like configurations) are a key contributor to the non-Arrhenius effects observed for dynamical timescales in the supercooled regime.

A similar analysis can be done by calculating $\Delta\Delta\bar{v}$, which is the change in the molar volume over the course of an H-bond exchange. We have again included the dependence of this quantity as a function of pressure and temperature in Figure 10.8a and Figure 10.8b. As pressure increases, we find that the H-bond exchange molar volume becomes less negative, indicating that the H-bond exchange transition state (a bifurcated H-bond) increases in volume with pressure. A similar dependence on increasing temperature is noted, with higher temperatures having smaller (less negative) molar volumes. This behavior is consistent with a more distorted H-bond network at higher pressures and temperatures, whereas lower temperatures and pressures favor increasing

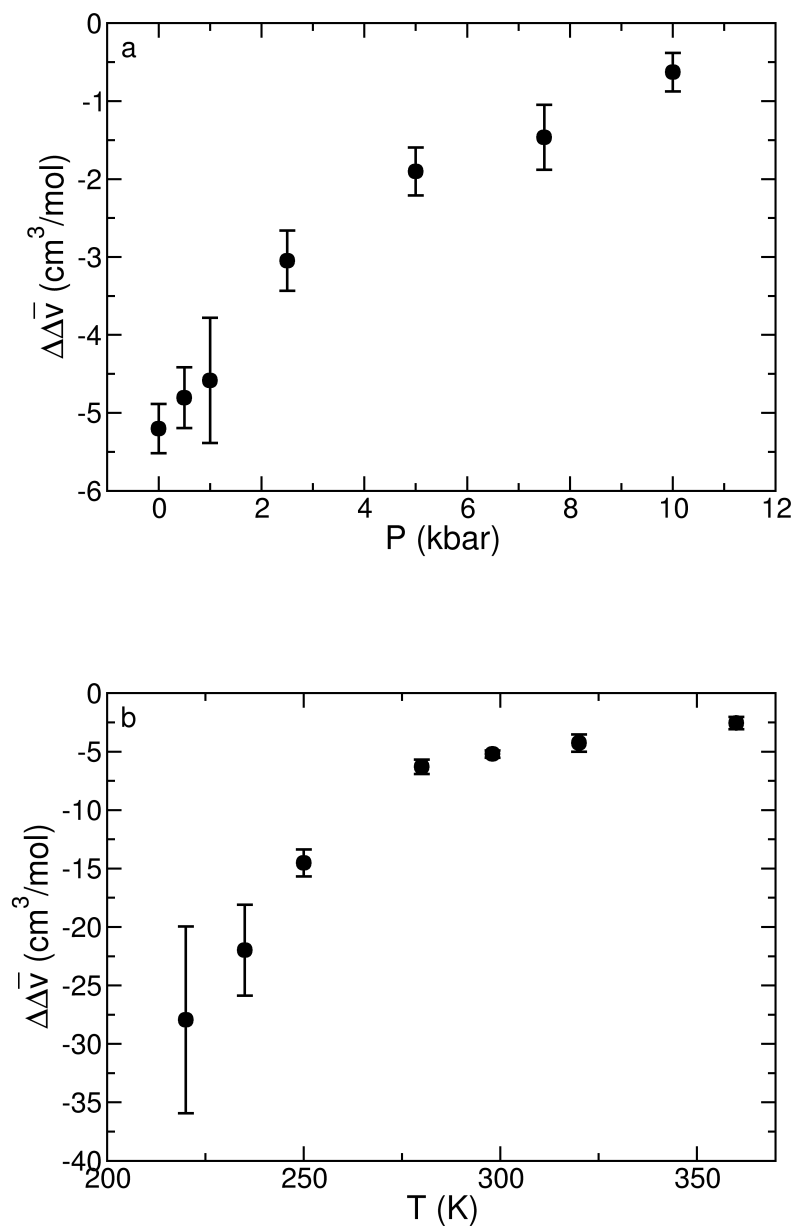


Figure 10.8: Dependence of the change in the molar volume as a function of a) pressure and b) temperature.

structuring.

A similar connection to that made between $\Delta\Delta H$ and E_{a,τ_2} can be made for the activation volume, ΔV^\ddagger , and $\Delta\Delta\bar{v}$ as both are essentially measures of the relative size of the transition state compared to the reactant state. In a recent study (Chapter 6), a number of diffusion activation

volumes were calculated for the same water model used in our present study.⁵⁹ In that study we observed that as pressure increased at room temperature there was an increase in the activation volume consistent with the trends we have observed in $\Delta\Delta\bar{v}$. We similarly found that as temperature increased so did the activation volume, consistent with the present T-dependence of $\Delta\Delta\bar{v}$. We have

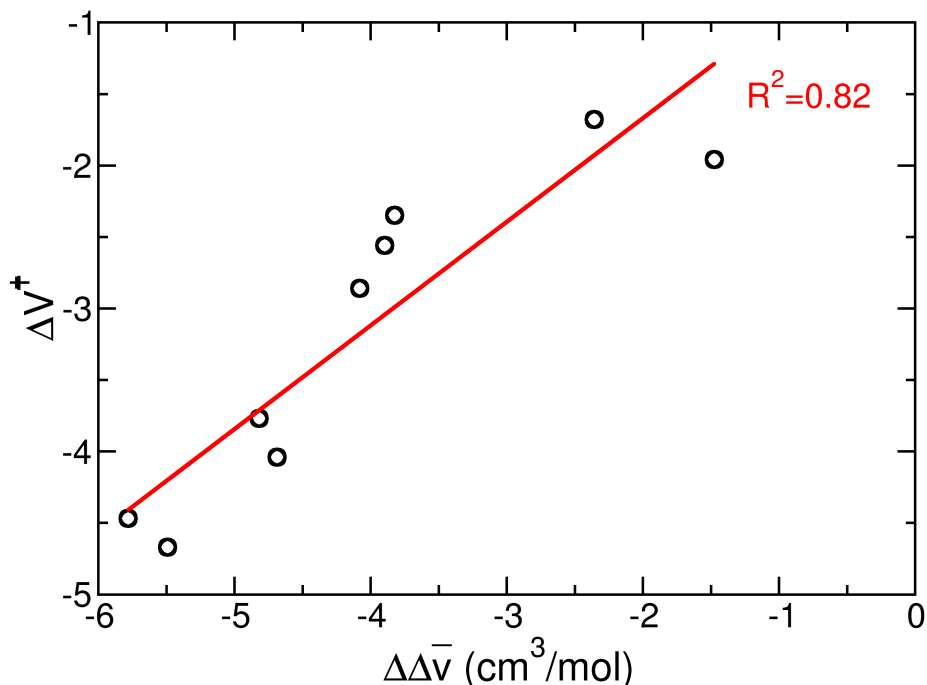


Figure 10.9: Dependence of the activation volume, ΔV^\ddagger on the change in the molar volume during an H-bond exchange, $\Delta\Delta\bar{v}$. A linear fit is included as a solid red line.

furthermore evaluated the value of $\Delta\Delta v$ for a variety of water models, and correlated these values with the published activation volumes of H-Bond jumps for these models (Chapter 11).³⁰⁹ We have included these results in Figure 10.9. We find that there is a linear correlation ($R^2 = 0.88$) between these values, which further demonstrates the connection of the liquid structure to the dynamics of H-bond exchanges. The relative weakness (though it is still quite strong) of the present correlation compared to the above correlation for $\Delta\Delta H$ is likely due to the fact that the activation volume describes the relative size of the transition state, *including the surrounding water molecules*, compared to that of the reactant state. It is unlikely that this can be fully described

by a single coordinate like r_{OO} as we have done here; however, as a first description this works relatively well.

10.5.2 Predictions of the RDF

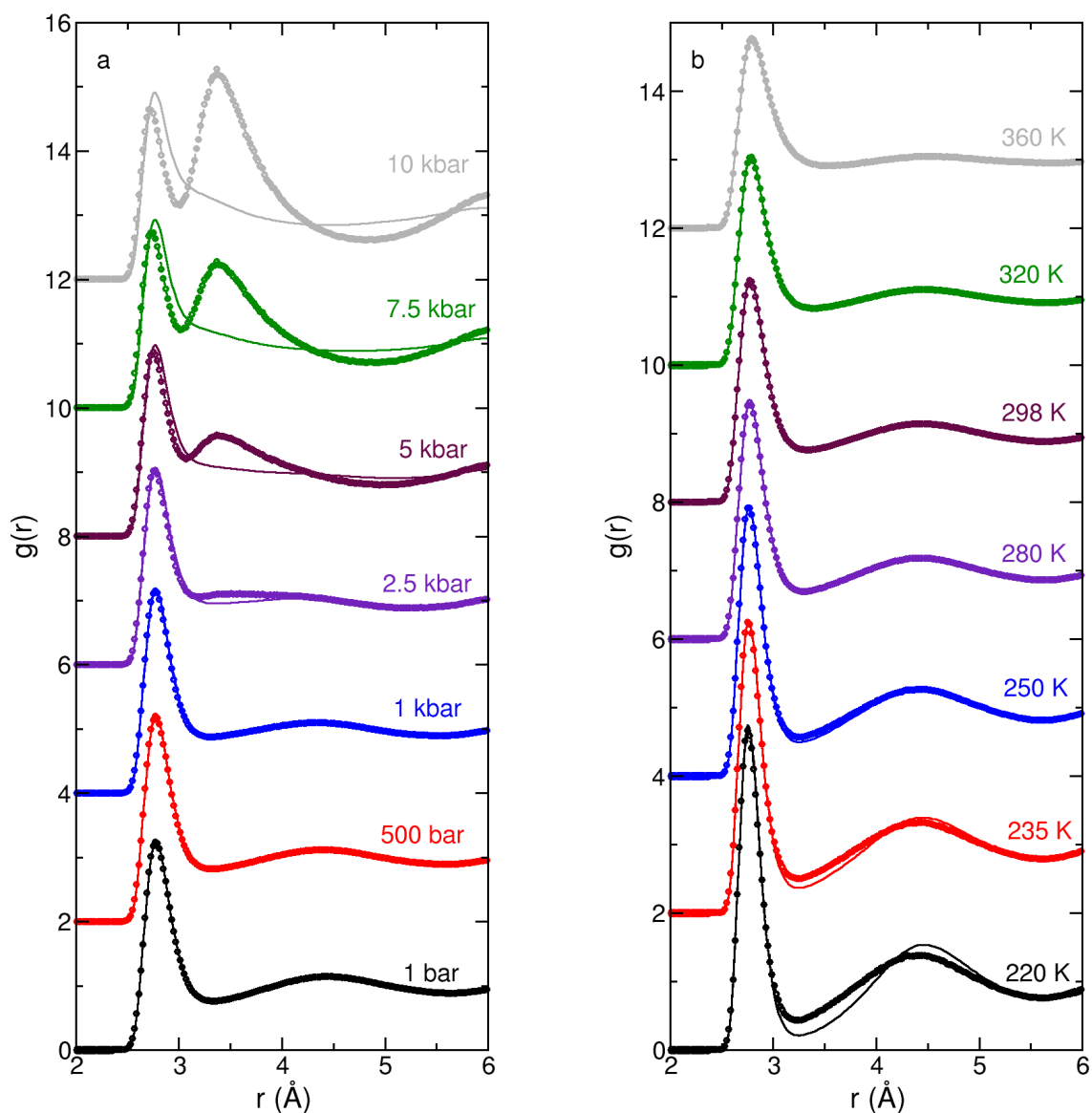


Figure 10.10: Predictions of the RDF from 1 bar, 298.15 K as a function of a) pressure, and b) temperature. Predictions are presented as open circles, simulation results are presented as solid lines.

In a recent study, we demonstrated a Van't Hoff approach to predicting the temperature depen-

dence of the RDF in the NVT ensemble. In the NpT ensemble a similar expression can be derived, as

$$g(r; \beta) = g(r; \beta_0) e^{-(\beta - \beta_0) \Delta H(r)} \quad (10.12)$$

where here $g(r; \beta_0)$ is the RDF at the reference temperature, β_0 . Here, we have made the assumption that $\Delta H(r)$ and $\Delta S(r)$ are only weakly T-dependent (though Figures 10.2b and 10.6b indicate that while appropriate at temperatures near β_0 , this is unlikely to hold over the entire considered range). A similar expression can be derived for predicting the P dependence, as

$$g(r; p) = g(r; p_0) e^{-(p - p_0) \beta \Delta \bar{v}(r)} \quad (10.13)$$

where here $g(r; p_0)$ is now the RDF at the reference pressure, p_0 . We have again assumed that $\Delta \bar{v}(r)$ is weakly dependent on pressure (which again our results in Figure 10.4a, and Figure 10.8a indicate may be appropriate at pressures nearby p_0).

We have presented our predictions with respect to pressure and temperature (made from 1 bar) in Figures 10.10a and 10.10b, respectively. As expected, predictions with respect to pressure work well over only a narrow range (up to 1 kbar); at higher pressures the present method predicts a peak growing in around 3.5 Å that corresponds with the minima in the molar volume. It is likely that the explicit p -dependence of the molar volume must be included in order to predict pressures further away. The method performs significantly better for predicting the temperature dependence, as it did for the NVT ensemble, with the prediction only starting to deviate in the supercooled regime. At 235 K, however, these deviations are larger than were present in that ensemble, likely due to a more significant change in the enthalpy.

10.6 Conclusions

In the present work we have demonstrated the calculation of derivatives of the radial distribution function with respect to pressure and temperature, and how these allow the direct evaluation of the

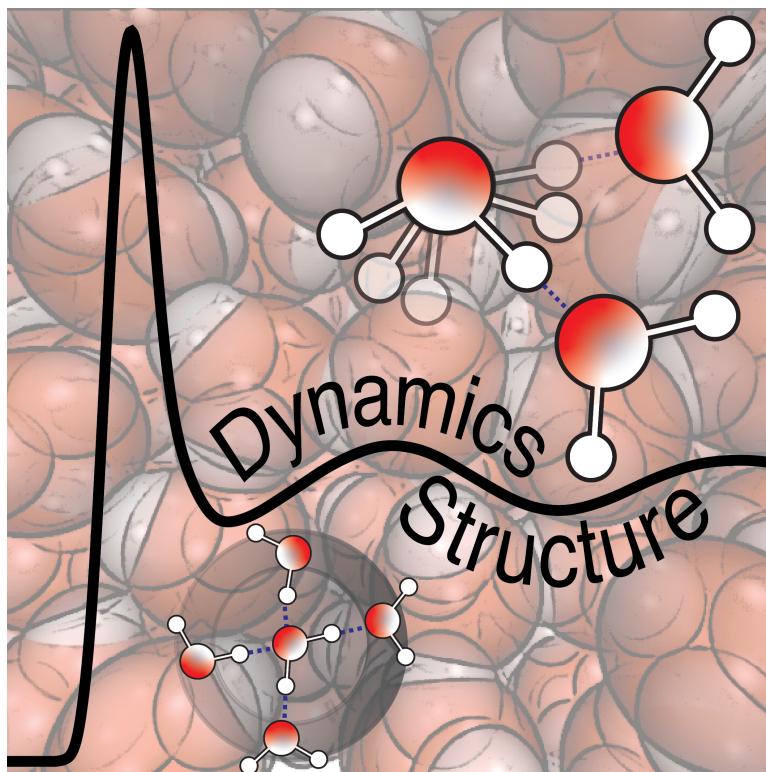
enthalpy, entropy, and the molar volume. We then use these parameters to calculate the change in these parameters over the course of a hydrogen-bond exchange as a function of pressure and temperature. We demonstrate that increasing pressure leads to a decrease in the enthalpy, and the entropy associated with H-bond exchanges, along with a smaller (less negative) molar volume, consistent with a distorted H-bond network leading to a less-structured liquid state. Similarly, we find similar trends with respect to increasing temperature, consistent with a picture of the liquid becoming less tetrahedral as the liquid is heated from the supercooled regime.

We then demonstrated the use of the enthalpy and the molar volume in order to predict the dependence of the RDF on temperature, and pressure, respectively. We found that the prediction performed reasonably well with respect to temperature, with deviations appearing only deep within the supercooled regime. On the other hand, the predictions with respect to pressure perform comparably poorly, only accurately predicting up to 1 kbar. In the future, higher derivatives could be used to account for changes in the molar volume and enthalpy with respect to pressure, and temperature, respectively.

Part III

Toward A Unified Picture of Water

Dynamics



In Part 3, we use large fluctuation theory calculations that span a variety of water models and time correlation functions that have been discussed in the previous parts and use them to develop an underlying picture of water dynamics. Chapter 11 demonstrates the activation energies and activation volumes for a wide range of water models, and Chapter 12 demonstrates how these activation energies can be combined with enthalpies calculated from the radial distribution function to predict experimental activation energies of diffusion, reorientation, and hydrogen bond exchanges. Chapter 13 demonstrates that fluctuation theory can be used to write down a dynamical Maxwell relation that unifies pressure and temperature derivatives; we use it to propose a global fitting function of dynamics in liquid water.

Chapter 11

Examining the Role of Different Molecular Interactions on Activation Energies and Activation Volumes in Liquid Water

11.1 Introduction

Liquid water plays a vital role in many processes in chemistry and biology. It is thus of no surprise that a plethora of approaches have been developed to describe its interactions in the neat liquid,^{5,42,303,307} in solution,³¹⁰ and near proteins.^{304,311,312} These models are typically developed to recreate a specific subset of the features of liquid water (*e.g.*, density maximum, melting temperature, vaporization enthalpy), sometimes at the expense of other properties. Regardless of these limitations, empirical water models have been widely successful in developing our understanding of water as a neat liquid,^{85,88,124,174,190,313–315} under extreme conditions,^{145,146,240,299} and in complex environments.^{89,316–320}

Most water models, however, do not directly incorporate dynamical quantities into their parameter optimization and even fewer use the temperature or pressure dependence of these quantities.^{194,195,303,306} These dependencies are omitted both because their inclusion would significantly increase the complexity of fitting force-field parameters and the difficulty of computing the properties, *e.g.*, the modification of dynamical timescales with pressure typically requires precise calculations over a large range of pressures. This has led to a situation where many empirical water

Adapted with the permission of Zeke A. Piskulich, and Ward H. Thompson and the American Chemical Society from *J. Chem. Theor. Comput.* **17**, p. 2659-2671 (2021).³⁰⁹

models accurately describe the self-diffusion coefficient in the bulk liquid at 298.15 K and 1 bar but display variable success in reproducing the behavior under other conditions. Activation energies and volumes are the key measures of the temperature and pressure dependence of dynamical timescales, indicating how they behave at nearby conditions.

The activation energy of a dynamical timescale τ ,

$$E_a = -\frac{\partial \ln(1/\tau)}{\partial \beta}, \quad (11.1)$$

where $\beta = 1/(k_b T)$ with k_b Boltzmann's constant and T temperature, represents the first-order description of the timescale's temperature dependence. Typically, activation energies are calculated numerically from experimental or simulation T -dependent data using the Arrhenius equation, $k(T) = A e^{-\beta E_a}$, where the prefactor A and E_a are assumed to be temperature independent.

Similarly, the activation volume of a timescale,

$$\Delta V^\ddagger = -k_b T \frac{\partial \ln(1/\tau)}{\partial p}, \quad (11.2)$$

is the first-order description of the timescale's dependence on the pressure p . As is the case for the activation energies, a numerical approach involving experiments or simulations over a range of pressures is typically used.^{61,64,218} However, such an analysis can be significantly more complicated because large pressure ranges – on the order of thousands of bar – are often required to resolve changes in the timescale.

While both activation parameters provide only a local viewpoint of the T and p dependence of these timescales and ignore non-Arrhenius effects, they are the primary contributors to these dependence and thus must be accurate for a model to perform well at other conditions.

In this Chapter, we examine three key timescales for liquid water – the H-bond exchange, or “jump” time, the OH reorientation time, and the self-diffusion coefficient – and the corresponding activation parameters for the SPC/E,⁴² SPC/Fw,³⁰³ TIP3P-PME,^{304,305} TIP3P-PME/Fw,^{304,305} OPC3,³⁰⁶ TIP4P/Ew,³⁰⁷ TIP4P/2005,⁵ E3B2,¹⁹⁴ and E3B3¹⁹⁵ water models using the recently de-

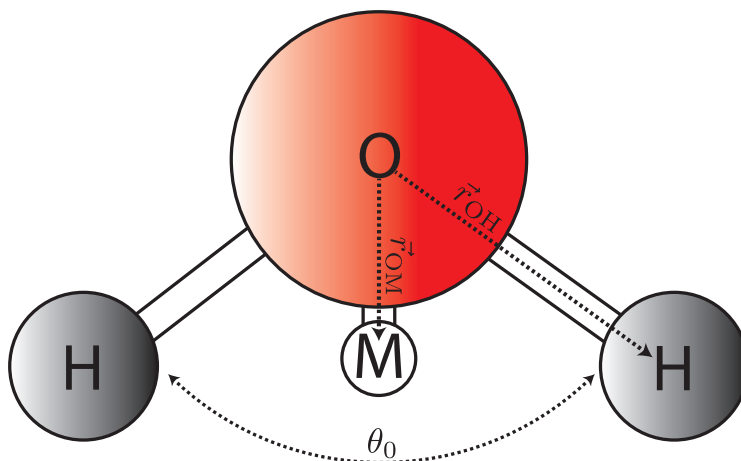


Figure 11.1: Schematic diagram of interaction sites for the water force fields.

veloped fluctuation theory for dynamics.^{13,31,44,50,58,136,147,160,184} This method allows E_a and ΔV^\ddagger to be calculated directly using simulations at a single temperature and pressure rather than the numerical Arrhenius approach. Thus, it provides the activation energy and activation volume to high precision. In addition, it provides a route to otherwise unavailable mechanistic information through a rigorous decomposition of the activation energy into components associated with the motions and interactions present in the system.

11.2 Computational Methods

11.2.1 Force Fields

In the present work we have selected several commonly used water force fields^{5,42,194,195,303–307} used in molecular dynamics (MD) simulations. These include three- and four-site models, rigid and flexible models, and some that include three-body effects. While these models reflect only a small subset of the vast number of available force fields, they are widely used in describing water in the neat liquid, in complex environments, and in biomolecular simulations.

All of the models use an oxygen-oxygen Lennard-Jones potential to describe the van der Waals

| Water Model | σ_{OO} (Å) | ϵ_{OO} (kcal/mol) | q_O (e) | q_H (e) | r_0 (Å) | k_{OH} (K) | θ_0 (degrees) | k_θ (K) | r_{OM} (Å) | q_M (e) |
|---------------------------------|----------------------|-------------------------------|--------------|--------------|--------------|-----------------|-------------------------|-------------------|-----------------|--------------|
| SPC/E ⁴² | 3.166 | 0.155 | -0.8476 | 0.4238 | 1.0 | - | 109.47 | - | - | - |
| SPC/Fw ³⁰³ | 3.165 | 0.155 | -0.82 | 0.41 | 1.012 | 1059.162 | 113.24 | 75.90 | - | - |
| TIP3P-PME ^{304,305} | 3.188 | 0.102 | -0.83 | 0.415 | 0.9572 | - | 104.52 | - | - | - |
| TIP3P-PME/Fw ^{304,305} | 3.188 | 0.102 | -0.83 | 0.415 | 0.9572 | 900 | 104.52 | 110 | - | - |
| OPC3 ³⁰⁶ | 3.17427 | 0.16341 | -0.89517 | 0.447585 | 0.97888 | - | 109.47 | - | - | - |
| E3B2 ¹⁹⁴ | 3.1536 | 0.1550 | 0.0 | 0.520 | 0.9572 | - | 104.52 | - | 0.1550 | -1.040 |
| E3B3 ¹⁹⁵ | 3.1589 | 0.1852 | 0.0 | 0.5564 | 0.9572 | - | 104.52 | - | 0.1546 | -1.1128 |
| TIP4P/2005 ⁵ | 3.1589 | 0.1852 | 0.0 | 0.5564 | 0.9572 | - | 104.52 | - | 0.1546 | -1.1128 |
| TIP4P/Ew ³⁰⁷ | 3.16435 | 0.16275 | 0.0 | 0.5242 | 0.9572 | - | 104.52 | - | 0.1250 | -1.0484 |

Note: σ_{HH} and ϵ_{HH} are zero for all models.

| Water Model | ϵ_2 kcal/mol | k_2 Å ⁻¹ | ϵ_a kJ/mol | ϵ_b kJ/mol | ϵ_c kJ/mol | k_3 Å ⁻¹ |
|-------------|--------------------------|--------------------------|------------------------|------------------------|------------------------|--------------------------|
| E3B2 | 2.349×10^6 | 4.872 | 1745.7 | -4565.0 | 7606.8 | 1.907 |
| E3B3 | 0.453×10^6 | 4.872 | 150.0 | -1005.0 | 1880.0 | 1.907 |

Table 11.1: Force field parameters used for each of the water models.

interactions,

$$U_{LJ}(r_{OO}) = 4\epsilon_{OO} \left[\left(\frac{\sigma_{OO}}{r_{OO}} \right)^{12} - \left(\frac{\sigma_{OO}}{r_{OO}} \right)^6 \right], \quad (11.3)$$

where r_{OO} is the O–O distance, ϵ_{OO} the depth of the well, and σ_{OO} the site diameter. Note, each of the present calculations also use the long-range tail corrections to the energy and pressure described by Sun.³²¹ The electrostatic interactions are calculated using Coulomb’s law, as

$$U_{Elec}(r_{ij}) = \sum_i \sum_j \frac{q_i q_j}{4\pi\epsilon_0 r_{ij}}, \quad (11.4)$$

where q_i and q_j are the charges of the i^{th} and j^{th} atoms separated by distance r_{ij} , and ϵ_0 is the permittivity of free space. The long-range electrostatics are described using the Particle-Particle-Particle-Mesh Ewald (PPPM) summation method.^{119,120} We have included in Table 11.1 the potential parameters for each model investigated in the present work.

In three of the water models studied (SPC/E, TIP3P-PME, and OPC3) the molecular interactions are fully described by Eqs. (11.3) and (11.4) with the SHAKE algorithm⁸² used to hold the bonds and angles at their equilibrium values.

Two other models (SPC/Fw and TIP3P-PME/Fw) incorporate flexibility in the form of har-

monic bond stretches and angle bends, as

$$U_{bond}(r_{OH}) = \frac{1}{2}k_{OH}(r_{OH} - r_0)^2, \quad (11.5)$$

and

$$U_{angle}(\theta) = \frac{1}{2}k_{\theta}(\theta_{HOH} - \theta_0)^2, \quad (11.6)$$

where k_{OH} (k_{θ}) is the bond (angle) force constant, r_{OH} (θ_{HOH}) is the instantaneous bond length (angle), and r_0 (θ_0) is the equilibrium bond length (angle). For SPC/Fw the force field was obtained by a reparameterization of the SPC/E Lennard-Jones parameters while adding flexibility,³⁰³ while for TIP3P-PME/Fw flexibility was added without other changes from the TIP3P-PME parameters.^{304,305} It should be noted that the PME variant of TIP3P uses the corrected parameters developed by Price and Brooks in Ref. 305 which account for the inclusion of long-range electrostatics in the calculations. Previous studies indicate that the original TIP3P parameterization has even faster dynamics than TIP3P-PME.^{304,305}

Two additional models use a 4-site description of water (TIP4P/Ew and TIP4P/2005) in which the oxygen retains its Lennard-Jones site but the oxygen charge is moved a distance r_{OM} away from the oxygen atom along the bisector of the HOH angle between the hydrogen atoms. This is depicted schematically in Fig. 11.1. These interactions are still calculated from Eqs. (11.3) and (11.4), but with the modified oxygen charge position.

The models listed above are completely pairwise, with many-body effects included only in an average way by virtue of the fitting to experimental data. The E3B models developed by Tainter *et al.*^{194,195} are built on top of existing 4-site descriptions of the pairwise interactions to include explicit three-body cooperativity as part of the model. The total potential energy of each E3B model may be written in terms of the above equations as

$$U_{E3B} = U_{base} + U_2 + U_{3-body}, \quad (11.7)$$

where here U_{base} is the potential energy described by the TIP4P model (E3B2) or the TIP4P/2005 model (E3B3).

This first term in the three-body part,

$$U_2(r_{ij}) = \mathcal{E}_2 \sum_{i,j} e^{-k_2 r_{ij}}, \quad (11.8)$$

removes the many-body interactions typically built into two-body potentials implicitly. Here \mathcal{E}_2 and k_2 are constants and r_{ij} is the distance between the two oxygen atoms. The explicit 3-body part of the potential is

$$U_{3-body} = U_A + U_B + U_C \quad (11.9)$$

where A , B , and C are labels for anti-cooperative double H-bond donor interactions (central water donates H-bonds to two other waters), cooperative interaction of molecules that donate and accept an H-bond (central water donates to one water, accepts from another), and the anti-cooperative double H-bond acceptor interactions (central water accepts from two other waters), respectively. These three configurations are illustrated below in Fig. 11.4. The terms U_A , U_B , and U_C are calculated as

$$U_X = \mathcal{E}_X \sum_{i,j,k,l} f(r_{ij})f(r_{kl}), \quad (11.10)$$

where $X = A, B$, or C , and r_{ij} and r_{kl} are the $H_d \cdots O_a$ hydrogen bond distances connecting the central water molecule to the two other water molecules in the triad interaction.

The function $f(r)$ is given by

$$f(r) = e^{-k_3 r} s(r), \quad (11.11)$$

where $s(r)$ is the switching function,

$$s(r) = \begin{cases} 1 & r < r_s \\ \frac{(r_f - r)^2 (r_f + 2r - 3r_s)}{(r_f - r_s)^3} & r_s \leq r \leq r_f \\ 0 & r > r_f \end{cases} \quad (11.12)$$

which smoothly truncates the calculation of 3-body interactions at OH distances between $r_s = 5.0 \text{ \AA}$ and $r_f = 5.2 \text{ \AA}$. This term is included because the summations in Eqs. (11.9) and (11.10) include 42 terms, which fall off nearly to zero beyond 5.0 \AA , thus these terms are excluded at greater distances for computational efficiency.

11.2.2 Fluctuation Theory

Recently, we have shown how the temperature and pressure dependence for a general property can be obtained from simulations at a single p and T using fluctuation theory for dynamics.^{13,31,44,50,58,136,147,160,184} To illustrate the approach, we can consider a general time-dependent property, $f(t)$, and its average in the isobaric-isothermal (NpT) ensemble, $\langle f(t) \rangle$. It is straightforward to show that the temperature derivative of the average is given by

$$\frac{\partial \langle f(t) \rangle}{\partial \beta} = -\langle [\delta H(0) + p \delta V(0)] f(t) \rangle, \quad (11.13)$$

where $\delta H(0) = H(0) - \langle H \rangle$ and $\delta V(0) = V(0) - \langle V \rangle$ are the fluctuations in energy and volume, respectively, at $t = 0$. We note that at 1 bar, the $p \delta V$ term is approximately $10^4 - 10^5$ times smaller than the $\delta H(0)$ contribution and thus can be neglected at low pressures. Thus, in this work we take

$$\frac{\partial \langle f(t) \rangle}{\partial \beta} = -\langle \delta H(0) f(t) \rangle. \quad (11.14)$$

The pressure derivative can similarly be expressed as⁵⁹

$$\frac{\partial \langle f(t) \rangle}{\partial p} = -\beta \langle \delta V(0) f(t) \rangle. \quad (11.15)$$

A key feature of the expressions in Eqs. (11.14) and (11.15) is that they can be evaluated from the same simulations, at a single p and T , used to calculate $\langle f(t) \rangle$ itself. That is, they are the analytical derivatives with respect to β and p in contrast to the numerical derivative obtained from an Arrhenius analysis in either T or p .

In the following, we describe how this dynamical fluctuation theory can be straightforwardly applied to determine the temperature and pressure dependence of the diffusion coefficient, the OH reorientation time, and the H-bond exchange jump time.

11.2.2.1 Diffusion Coefficients

A key measure of water dynamics is contained in the self-diffusion coefficient, D , which can be obtained experimentally from quasi-elastic neutron scattering,¹⁴⁴ tracer studies,^{4,322} or Nuclear Magnetic Resonance (NMR) measurements.^{2,3,54,267} In MD simulations, the diffusion coefficient is obtained from the long-time behavior of the average mean-squared displacement, $\langle MSD(t) \rangle = \langle |\vec{r}(0) - \vec{r}(t)|^2 \rangle$,

$$D = \lim_{t \rightarrow \infty} \frac{\langle MSD(t) \rangle}{6t}, \quad (11.16)$$

where $\vec{r}(t)$ is the molecule position, here defined by the location of the oxygen atom, at time t .

Taking the derivative of D in Eq. (11.16) with respect to β gives a result analogous to that in Eq. (11.14),

$$\frac{\partial D}{\partial \beta} = - \lim_{t \rightarrow \infty} \frac{\langle \delta H(0) |\vec{r}(0) - \vec{r}(t)|^2 \rangle}{6t}, \quad (11.17)$$

so that the activation energy associated with the diffusion coefficient is

$$E_{a,D} = \frac{\lim_{t \rightarrow \infty} \langle \delta H(0) |\vec{r}(0) - \vec{r}(t)|^2 \rangle}{\lim_{t \rightarrow \infty} \langle |\vec{r}(0) - \vec{r}(t)|^2 \rangle}. \quad (11.18)$$

In practice, the ratio of the slopes (at long times) of the numerator and denominator are used to determine $E_{a,D}$. Analogous results are obtained for the pressure derivative giving

$$\Delta V_D^\ddagger = \frac{\lim_{t \rightarrow \infty} \langle \delta V(0) |\vec{r}(0) - \vec{r}(t)|^2 \rangle}{\lim_{t \rightarrow \infty} \langle |\vec{r}(0) - \vec{r}(t)|^2 \rangle}. \quad (11.19)$$

for the activation volume for diffusion.

It is well known that D is underestimated in periodic-boundary condition (PBC) simulations

such as those used here. This can be corrected using^{247,323}

$$D = D_{PBC} + \frac{2.837297k_B T}{6\pi\eta_s L}, \quad (11.20)$$

where D_{PBC} is the value calculated from Eq. (11.16) in PBC simulations, η_s is the shear viscosity, and L is the side length of the PBC simulation cell. From a simulation, the shear viscosity is evaluated from the Green-Kubo relation,

$$\eta_s = \frac{V}{k_B T} \int_0^\infty \langle P_{\alpha\beta}(0)P_{\alpha\beta}(t) \rangle dt, \quad (11.21)$$

where here the repeated $\alpha\beta$ subscript denotes an average of the five correlation functions constructed from the stress tensor: $(P_{xx} - P_{yy})/2$, $(P_{yy} - P_{zz})/2$, P_{xy} , P_{yz} , and P_{xz} . We have previously shown $E_{a,D}$ is unaffected by this correction if the Stokes-Einstein relation holds and only minimally affected if it does not,⁵⁰ so no corrections are used.

We have previously reported diffusion activation energies for SPC/E and TIP4P/2005 water using this method^{58,160} as well as activation volumes for TIP4P/2005 water.⁵⁹

11.2.2.2 Reorientation Times

The OH reorientational dynamics of water are most frequently characterized by the second-order reorientation time correlation function (TCF),

$$C_2(t) = \langle P_2[\vec{e}_{OH}(0) \cdot \vec{e}_{OH}(t)] \rangle, \quad (11.22)$$

where \vec{e}_{OH} is a unit vector along the OH bond and P_2 is the 2nd Legendre polynomial. The dynamics can be measured by infrared pump-probe anisotropy experiments, which determine the anisotropy decay, $r(t) = 0.4C_2(t)$,⁷¹ or NMR measurements that yield the average reorientation time given by the integral of $C_2(t)$.⁴³

In water, $C_2(t)$ decays on three timescales which can be attributed to inertial, librational, and

reorientation associated with H-bond dynamics. It is this last, denoted as τ_2 , which is of greatest interest and the focus of the present work. The timescales can be obtained by fitting $C_2(t)$ to a tri-exponential function

$$C_2(t) = \sum_{\alpha} A_{\alpha} e^{-t/\tau_{\alpha}}, \quad (11.23)$$

where $\alpha = \text{iner}, \text{libr},$ and 2. Following Eqs. (11.14) and (11.15), it is straightforward to show that

$$\frac{\partial C_2(t)}{\partial \beta} = -\langle \delta H(0) P_2 [\vec{e}_{OH}(0) \cdot \vec{e}_{OH}(t)] \rangle, \quad (11.24)$$

and

$$\frac{\partial C_2(t)}{\partial p} = -\beta \langle \delta V(0) P_2 [\vec{e}_{OH}(0) \cdot \vec{e}_{OH}(t)] \rangle. \quad (11.25)$$

These derivative TCFs can be fit to the corresponding derivative of Eq. (11.23),

$$\frac{\partial C_2(t)}{\partial x} = \sum_{\alpha} \left[\frac{\partial A_{\alpha}}{\partial x} - A_{\alpha} t \frac{\partial (1/\tau_{\alpha})}{\partial x} \right] e^{-t/\tau_{\alpha}}, \quad (11.26)$$

where $x = \beta$ or p . In the fitting, the amplitudes A_{α} and timescales τ_{α} are constrained to the values obtained in fitting $C_2(t)$ to Eq. (11.23) so that their derivatives are the fitting parameters. Given the timescale and its derivatives, the reorientational activation energy, $E_{a,2}$, and activation volume, ΔV_2^{\ddagger} , can be obtained. We have previously calculated reorientation activation energies in this way for the SPC/E^{58,136} and TIP4P/2005⁴⁴ models, but have never reported reorientation activation volumes.

11.2.2.3 H-bond Jump Times

The fundamental molecular mechanism underlying both diffusion and reorientation in water is the exchange of H-bond partners.^{85,88,178} These exchanges, or "jumps," can be thought of as a kind of chemical reaction in which an OH group breaks one H-bond and forms another. The corresponding

rate constant can be obtained from the stable-states, side-side, time correlation function,

$$C_{ab}(t) = \langle n_a(0)n_b(t) \rangle \quad (11.27)$$

where $n_a = 1$ ($n_b = 1$) if the OH is H-bonded to acceptor a (b). Thus, for an OH initially H-bonded to an acceptor labeled a , $C_{ab}(t)$ is zero at $t = 0$ when $n_a = 1$ and $n_b = 0$, but rises as OH groups switch to new acceptors. The time dependence is such that $1 - C_{ab}(t)$ decays with the jump time τ_0 , which is the inverse of the rate constant for the H-bond exchange. In practice, there is also some small-amplitude, short-time dynamics not associated with the H-bond jumps so that $1 - C_{ab}(t)$ is accurately fit by Eq. (11.23) with two exponentials and the longer timescale equal to τ_0 .

The derivatives of the stable-states TCF are obtained from Eqs. (11.14) and (11.15) as

$$\frac{\partial[1 - C_{ab}(t)]}{\partial\beta} = \langle \delta H(0) n_a(0) n_b(t) \rangle, \quad (11.28)$$

and

$$\frac{\partial[1 - C_{ab}(t)]}{\partial p} = \beta \langle \delta V(0) n_a(0) n_b(t) \rangle. \quad (11.29)$$

In analogy to the reorientational dynamics, these derivative TCFs can be fit to Eq. (11.26) to obtain $\partial(1/\tau_0)/\partial\beta$ and $\partial(1/\tau_0)/\partial p$ and then the jump time activation energy, $E_{a,0}$, and activation volume, ΔV_0^\ddagger . It should be noted that for both reorientational and jump dynamics, finite simulation size effects are not expected to play as large a role as they do for diffusion due to the small volume of each water molecule.³²⁴ We have recently carried out a detailed investigation of the jump activation energies for SPC/E water.¹³⁶

11.2.2.4 Activation Energy Decompositions

A key feature of fluctuation theory for dynamics is the ability to decompose the activation energy by separating the energy fluctuation into components, *e.g.*, $\delta H = \delta KE + \delta U_{LJ} + \delta U_{Elec} + \delta U_{Bond} + \delta U_{Angle} + \delta U_2 + \delta U_{3-body}$. This allows the calculation of different contributions to the activation

energy as

$$\begin{aligned}
 E_a &= E_a^{KE} + E_a^{LJ} + E_a^{Elec} \\
 &+ E_a^{Bond} + E_a^{Angle} \\
 &+ E_a^{U_2} + E_a^{3-body}.
 \end{aligned}
 \tag{11.30}$$

These different contributions to the activation energy can be understood in terms of Tolman’s (rigorous) perspective in which the activation energy is equal to the average energy of reacting species minus the average energy of reactant species.¹⁸ That is, rather than the energy of the barrier itself, E_a is the energy required to overcome the barrier and hence is decomposable.

As an example, the kinetic energy contribution to the diffusion activation energy can be calculated by replacing $\delta H(0)$ with $\delta KE(0)$ in the derivative of the mean-squared displacement. Then, the kinetic energy contribution is given by

$$E_{a,D}^{KE} = \frac{\lim_{t \rightarrow \infty} \langle \delta KE(0) |\vec{r}(0) - \vec{r}(t)|^2 \rangle}{\lim_{t \rightarrow \infty} \langle |\vec{r}(0) - \vec{r}(t)|^2 \rangle},
 \tag{11.31}$$

and can be interpreted as the average kinetic energy of diffusing molecules minus the average kinetic energy of all molecules.

Extracting activation energy contributions to the jump or reorientation derivative TCFs are likewise straightforward. The relevant component of the derivative of the timescale, *e.g.*, $\partial(1/\tau_0)/\partial\beta^{KE}$, is extracted as discussed by fitting the contribution TCF, *e.g.*, $\langle \delta KE(0) n_a(0) n_b(t) \rangle$ to Eq. (11.26) just as the total derivative TCF is fit. This derivative value is then used to calculate the activation energy component, $E_{a,0}^{KE} = (1/\tau_0)[\partial(1/\tau_0)/\partial\beta^{KE}]$.

11.2.3 Simulation Details

For each model, we used PACKMOL¹⁶² to generate initial configurations and necessary data files for MD simulations. Initial velocities were generated from the room temperature Maxwell-

Boltzmann distribution. Simulations were run using the Large-Scale Atomic/Molecular Massively Parallel Simulator (LAMMPS).⁸¹ An isothermal-isobaric, NpT , ensemble trajectory was propagated at 1 bar and 298.15 K for 1 ns to reach equilibrium, and then production simulations were run for 50 ns.^{226,227} A Nosé-Hoover thermostat and barostat were used, both of chain length 3, with damping parameters of 100 fs and 1000 fs, respectively.^{83,84} From these production simulations, configurations and velocities were output every 1 ps, for a total of 50,000 configurations for each water model.

From each of these saved configurations a 20 ps constant energy, NVE , simulation was propagated with configurations dumped every 10 fs, from which the TCFs were calculated. Reported values were obtained by averaging these TCFs across all 50,000 trajectories, and then fitting these averaged results. Similarly, derivative correlation functions were calculated in the same way with each trajectory's contribution to the average weighted by the fluctuation in the energy. Uncertainties in the fluctuation calculation are reported using block averaging over 10 blocks, and represent a 95% confidence interval according to Student's t -distribution.¹²²

We have additionally calculated the viscosity of each water model from additional MD simulations. For these simulations, five sets of equilibrium configurations and velocities were used as starting points for 1 ns NVT simulations, from which viscosities were calculated using the Green-Kubo formalism described in Sec. 11.2.2.1. Each trajectory was used as a block for block averaging and values are again reported as a 95 % confidence interval. For TIP3P-PME/Fw the pressure tensor was output every 4 ps as it was required to accurately capture the oscillations in the correlation function. For all other models the pressure tensor was output every 10 ps. For all models the viscosity time-correlation function was calculated over 5 ps, with time origins separated every 100 fs.

For all simulations, the timestep was 1 fs and the PPPM method^{119,120} was used for the calculation of electrostatic interactions, with a tolerance parameter of 1×10^{-4} . For simulations involving rigid water molecules, the SHAKE algorithm⁸² was used to hold bonds and angles constant, also with a tolerance of 1×10^{-4} .

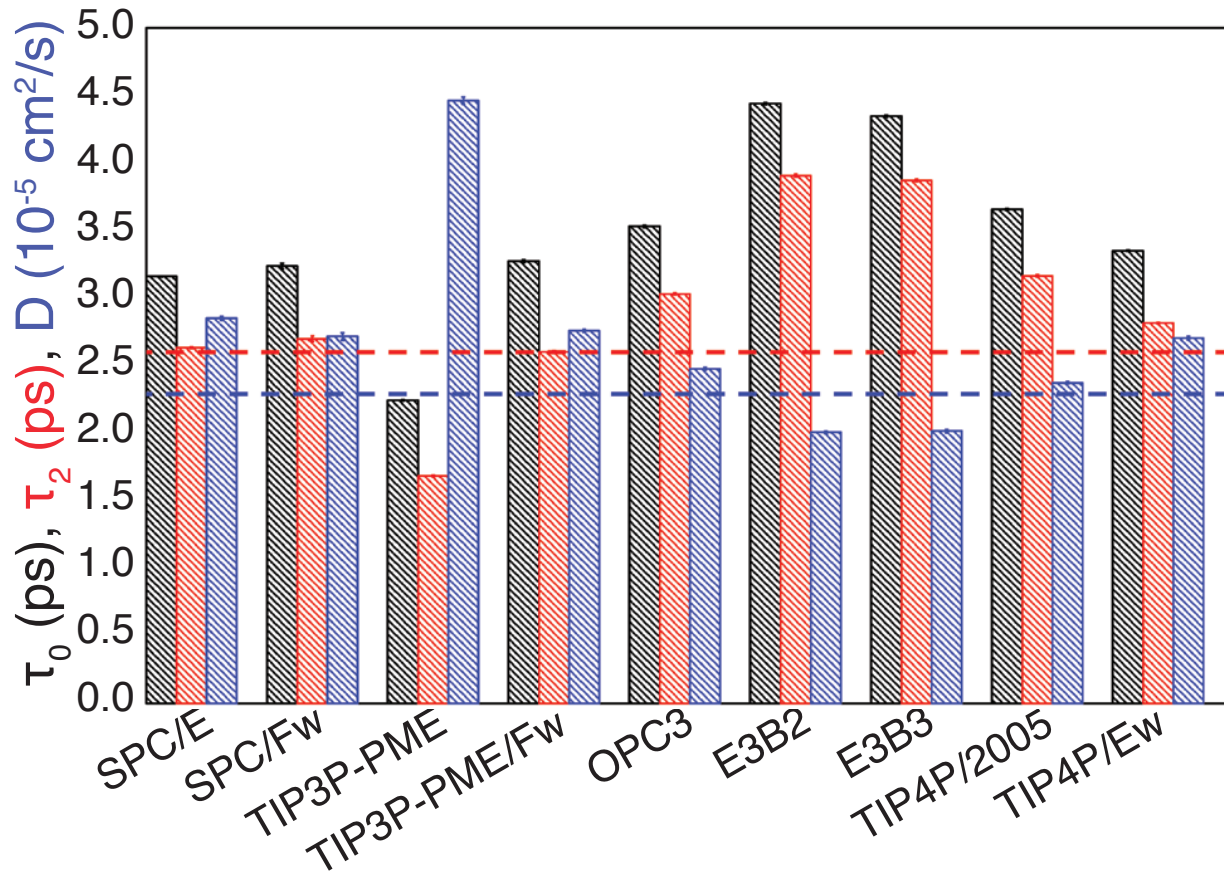


Figure 11.2: The H-bond jump time τ_0 (black), OH reorientation time τ_2 (red), and diffusion coefficient D (blue) are presented for each water model. Experimental values for the reorientation time⁷⁻⁹ (red dashed line) and diffusion coefficient¹⁰ (blue dashed line) are also included.

11.3 Results and Discussion

We have evaluated the jump time τ_0 , the reorientation time τ_2 , and the diffusion coefficient D along with their activation energies and volumes calculated using dynamical fluctuation theory. In the following, we present and discuss the values obtained for these properties from the different water models and compare with available experimental results.

11.3.1 Timescales

We begin by examining the jump time, reorientation time, diffusion coefficient, and viscosity calculated from the simulations described in Sec. 11.2 for each studied force field. We have reported these timescales for each model in Table 11.2 and plotted them in Fig. 11.2. For comparison, we

| Model | τ_0 | τ_2 | D_{PBC} | D | η_s |
|---------------------------|---------------------|---------------------|---------------------|-------------------|-------------------|
| SPC/E | 3.160 ₃ | 2.633 ₄ | 2.437 ₄ | 2.85 ₂ | 0.71 ₃ |
| SPC/Fw | 3.237 ₂₀ | 2.699 ₂₁ | 2.358 ₁₈ | 2.72 ₃ | 0.82 ₅ |
| TIP3P-PME | 2.245 ₃ | 1.686 ₇ | 3.823 ₆ | 4.46 ₃ | 0.46 ₂ |
| TIP3P-PME/Fw | 3.273 ₁₀ | 2.603 ₁₀ | 2.391 ₅ | 2.76 ₁ | 0.80 ₂ |
| OPC3 | 3.531 ₇ | 3.031 ₈ | 2.120 ₄ | 2.48 ₁ | 0.82 ₂ |
| E3B2 | 4.440 ₇ | 3.907 ₁₁ | 1.721 ₃ | 2.00 ₁ | 1.03 ₃ |
| E3B3 | 4.346 ₇ | 3.871 ₁₁ | 1.727 ₄ | 2.02 ₂ | 1.01 ₄ |
| TIP4P/2005 | 3.657 ₇ | 3.165 ₈ | 2.030 ₄ | 2.37 ₁ | 0.85 ₂ |
| TIP4P/Ew | 3.351 ₄ | 2.815 ₆ | 2.314 ₃ | 2.70 ₂ | 0.75 ₃ |
| Expt. ^{7-10,141} | – | 2.6 | | 2.30 | 0.8903 |

Table 11.2: H-bond jump time τ_0 , OH reorientation time τ_2 , diffusion coefficients directly from the simulations, D_{PBC} , and corrected for finite-size effects, D , and shear viscosities, η_s for different water models; times are in ps, diffusion coefficients are in 10^{-5} cm²/s, and shear viscosities are in cP. Subscripts indicate uncertainties in the trailing digit(s).

have included available experimental literature results, Note that pump-probe IR anisotropy results have yielded $\tau_2 = 2.5$,⁷ 2.6,⁸ and 2.7 ps;⁹ in the following we use the average of these results, 2.6 ps, as the experimental value.

We first consider the rigid 3-site water models, SPC/E, TIP3P-PME, and OPC3. These models give some of the shortest reorientation and jump times and some of the largest diffusion coefficients. In particular, the τ_2 value predicted by the SPC/E (2.63 ps) model is in excellent agreement with the measured result of 2.6 ps. In contrast, the OPC3 (3.03 ps) predicts slower dynamics than measured while the TIP3P-PME reorientation time of 1.67 ps is dramatically lower.

The H-bond jump time cannot be directly extracted from experimental measurements and thus we do not have an unambiguous way to use it to test the models. However, because the OH reorientation time is dominated by the timescale for H-bond jumps,^{85,88} it is a reasonable assumption that the models which describe τ_2 well should yield the most accurate jump time. This yields an inference that the “experimental” τ_0 is approximately 3.2 – 3.3 ps, based on the SPC/E, SPC/Fw, and TIP3P-PME/Fw results.

The diffusion coefficients for the rigid 3-site models overestimate the experimental value. The SPC/E and OPC3 do so modestly, yielding values that are 24 and 8% larger than the measured D . As with the other timescales, the TIP3P-PME model predicts grossly accelerated diffusive dynamics with D more than 93% too big. The viscosities of these models are consistent with

this as they have significantly lower values than that reported experimentally.¹⁴¹ It is certainly interesting that a model like SPC/E correctly predicts τ_2 , but overestimates D . Both quantities have H-bond exchanges as the underlying process, but diffusion involves a component related to the size of the translational “jump” upon exchange¹⁷⁸ and perhaps it is this structural quantity that is not properly described within the SPC/E model.

The impact of the faster dynamics in the TIP3P-PME model should be clearly recognized given that it is one of the most frequently used models for biomolecular simulations. The present results indicate that not only does the TIP3P-PME model diffuse and reorient more quickly than real water as has been frequently reported in the literature,^{311,325,326} it likely also exchanges H-bond partners more quickly than real water. This could have important implications for studies of processes influenced by these motions, *e.g.*, water dynamics involved in enzymatic reactions and in hydration of proteins.

Two of the models studied, SPC/Fw and TIP3P-PME/Fw, involve the addition of bond and angle flexibility to a rigid 3-site model. Interestingly, the addition of flexibility appears to fix many of the sins of the TIP3P-PME model. TIP3P-PME/Fw gives a reorientation time in perfect agreement with the experimental result and has a diffusion coefficient that is significantly more reasonable. Furthermore, the viscosity of TIP3P-PME/Fw is nearly double that of TIP3P-PME, bringing it in line with the other 3-site models studied. Interestingly, the SPC/Fw model, which both adds flexibility and reparameterizes the intramolecular interactions, provides only minimal differences in the timescales when compared with the SPC/E model though it does slightly increase the models viscosity.

Compared with the 3-site models, the dynamics of the 4-site models, TIP4P/2005 and TIP4P/Ew, are generally slower. We find OH reorientation times of 2.82 ps for TIP4P/Ew and 3.17 ps for TIP4P/2005, which are longer than the measured τ_2 . This suggests that these models also overestimate the H-bond jump time. On the other hand, the TIP4P/2005 diffusion coefficient, 2.37×10^{-5} cm²/s, is the closest to the experimental value out of all the force fields studied and TIP4P/Ew gives a reasonable result (2.70×10^{-5} cm²/s). Likewise, the TIP4P/2005 viscosity is the closest to

the experimental value of all the water models. Like the 3-site models, the 4-site model with the most accurate reorientation time, TIP4P/Ew, gives a diffusion coefficient that is too large, while the excellent prediction of D by TIP4P/2005 is accompanied by a reorientation time that is 22% larger than obtained in experiments.

The addition of 3-body interactions in the E3B2 and E3B3 models leads to slower dynamics compared to the pairwise 4-site models. They exhibit reorientation times that are too long by more ~ 1.2 ps (50%) and diffusion coefficients that are underestimated, unlike all the other force fields considered. The predicted D are, however, quite reasonable, providing the second best agreement behind the TIP4P/2005 model (upon which the E3B3 model is based). The slower D than experiment is consistent with our calculated values of the viscosity, which indicate that both E3B variants are more viscous than experiment.

Overall, the results show that the best models to use to obtain the correct OH reorientation time at 298.15 K and 1 bar are the rigid 3-site SPC/E and the flexible variants SPC/Fw and TIP3P-PME/Fw. For diffusion, the TIP4P/2005 force field provides the most faithful reproduction of the experimental D .

11.3.2 Activation Energies

We next turn to an investigation of the temperature dependence of each water model as measured by the activation energies of the jump time, the OH reorientation time, and the diffusion coefficient at ambient conditions (298.15 K, 1 bar). The calculated activation energies (and their decompositions) are provided in Table 11.3 and plotted them in Fig. 11.3.

Measured activation energies have been reported for the reorientation time and diffusion coefficient. In the former case, $E_{a,2} = 4.1 \pm 0.5$ kcal/mol was obtained by Petersen *et al.*⁷ and 3.7 ± 0.5 kcal/mol by Nicodemus *et al.*¹⁰⁵ Several measurements of the diffusion activation energy have been reported including 4.2,³²² 4.3,³ 4.4,⁴ 4.5,⁵⁴ and 4.6 kcal/mol,⁵³ and thus we take 4.4 kcal/mol as the experimental value in Fig. 11.3.

We first examine the reorientation activation energies, $E_{a,2}$, which range from 2.98 to 4.69 kcal/-

| Jump Time, τ_0 | | | | | | | | | | | |
|--|--------------------|-------------------|--------------------|---------------------|--------------------|-------------------|--------------------|--------------------|--------------------|--------------------|---------------------|
| Model | Total | KE | Elec | LJ | Bond | Bend | E3B | E_2 | E_a | E_b | E_c |
| SPC/E | 3.09 ₄ | 0.95 ₂ | 2.85 ₅ | -0.72 ₄ | - | - | - | - | - | - | - |
| SPC/Fw | 3.27 ₆ | 1.02 ₂ | 2.98 ₁₃ | -0.71 ₅ | -0.14 ₇ | 0.13 ₂ | - | - | - | - | - |
| TIP3P-PME | 2.71 ₅ | 0.88 ₃ | 2.30 ₄ | -0.47 ₃ | - | - | - | - | - | - | - |
| TIP3P-PME/Fw | 3.38 ₆ | 1.04 ₃ | 3.02 ₁₀ | -0.69 ₅ | -0.09 ₃ | 0.10 ₂ | - | - | - | - | - |
| OPC3 | 3.26 ₆ | 0.98 ₃ | 3.02 ₇ | -0.74 ₄ | - | - | - | - | - | - | - |
| E3B2 | 4.11 ₆ | 1.09 ₃ | 3.99 ₅ | -1.25 ₂ | - | - | 0.28 ₁ | -0.31 ₁ | 0.01 ₁ | -0.12 ₆ | 0.7 ₅ |
| E3B3 | 4.03 ₂ | 1.07 ₄ | 4.16 ₁₁ | -1.29 ₅ | - | - | 0.09 ₁ | -0.04 ₁ | 0.01 ₁ | -0.15 ₂ | 0.28 ₂ |
| TIP4P/2005 | 3.63 ₅ | 1.04 ₄ | 3.69 ₈ | -1.10 ₆ | - | - | - | - | - | - | - |
| TIP4P/Ew | 3.52 ₆ | 1.00 ₃ | 3.54 ₈ | -1.01 ₅ | - | - | - | - | - | - | - |
| Reorientation Time, τ_2 | | | | | | | | | | | |
| Experiment: ^{7,105} 4.1 ± 0.5, 3.7 ± 0.5 kcal/mol | | | | | | | | | | | |
| Model | Total | KE | Elec | LJ | Bond | Bend | E3B | E_2 | E_a | E_b | E_c |
| SPC/E | 3.54 ₅ | 1.08 ₄ | 3.33 ₆ | -0.86 ₇ | - | - | - | - | - | - | - |
| SPC/Fw | 3.69 ₉ | 1.17 ₅ | 3.34 ₂₁ | -0.83 ₉ | -0.14 ₉ | 0.15 ₂ | - | - | - | - | - |
| TIP3P-PME | 2.98 ₇ | 0.94 ₆ | 2.64 ₁₁ | -0.60 ₉ | - | - | - | - | - | - | - |
| TIP3P-PME/Fw | 3.79 ₅ | 1.18 ₄ | 3.41 ₁₄ | -0.86 ₁₀ | -0.06 ₄ | 0.11 ₂ | - | - | - | - | - |
| OPC3 | 3.71 ₅ | 1.13 ₃ | 3.45 ₁₂ | -0.87 ₇ | - | - | - | - | - | - | - |
| E3B2 | 4.69 ₁₀ | 1.26 ₅ | 4.53 ₈ | -1.42 ₆ | - | - | 0.32 ₂ | -0.39 ₃ | -0.04 ₂ | 0.39 ₁₃ | 0.35 ₁₀ |
| E3B3 | 4.55 ₈ | 1.24 ₅ | 4.66 ₁₁ | -1.44 ₆ | - | - | 0.10 ₁ | -0.05 ₁ | 0.00 ₁ | -0.06 ₄ | 0.21 ₄ |
| TIP4P/2005 | 4.12 ₁₀ | 1.21 ₅ | 4.19 ₁₄ | -1.28 ₈ | - | - | - | - | - | - | - |
| TIP4P/Ew | 3.98 ₁₀ | 1.12 ₅ | 3.98 ₁₂ | -1.13 ₈ | - | - | - | - | - | - | - |
| Diffusion Coefficient, D | | | | | | | | | | | |
| Experiment: ^{3,4,53,54,322} 4.2-4.6 kcal/mol | | | | | | | | | | | |
| Model | Total | KE | Elec | LJ | Bond | Bend | E3B | E_2 | E_a | E_b | E_c |
| SPC/E | 3.61 ₉ | 1.07 ₄ | 3.49 ₁₂ | -0.96 ₆ | - | - | - | - | - | - | - |
| SPC/Fw | 3.80 ₁₀ | 1.17 ₃ | 3.64 ₂₁ | -0.98 ₇ | -0.15 ₇ | 0.13 ₄ | - | - | - | - | - |
| TIP3P-PME | 3.26 ₈ | 0.94 ₄ | 3.14 ₈ | -0.82 ₃ | - | - | - | - | - | - | - |
| TIP3P-PME/Fw | 4.04 ₈ | 1.30 ₅ | 3.53 ₁₂ | -0.95 ₆ | 0.07 ₄ | 0.10 ₃ | - | - | - | - | - |
| OPC3 | 3.84 ₇ | 1.11 ₃ | 3.78 ₁₀ | -1.05 ₆ | - | - | - | - | - | - | - |
| E3B2 | 4.73 ₉ | 1.27 ₄ | 4.62 ₁₁ | -1.48 ₆ | - | - | 0.31 ₁₁ | -0.52 ₃ | -0.18 ₂ | 1.86 ₁₄ | -0.85 ₁₀ |
| E3B3 | 4.59 ₁₁ | 1.23 ₅ | 4.74 ₁₀ | -1.48 ₈ | - | - | 0.09 ₁ | -0.07 ₁ | -0.01 ₁ | 0.24 ₃ | -0.07 ₃ |
| TIP4P/2005 | 4.10 ₅ | 1.16 ₄ | 4.18 ₆ | -1.24 ₅ | - | - | - | - | - | - | - |
| TIP4P/Ew | 4.03 ₉ | 1.14 ₄ | 4.10 ₁₂ | -1.21 ₉ | - | - | - | - | - | - | - |

Table 11.3: Activation energies (in kcal/mol) of the jump time, OH reorientation time, and diffusion coefficient. Subscripts indicate uncertainties in the trailing digit(s).

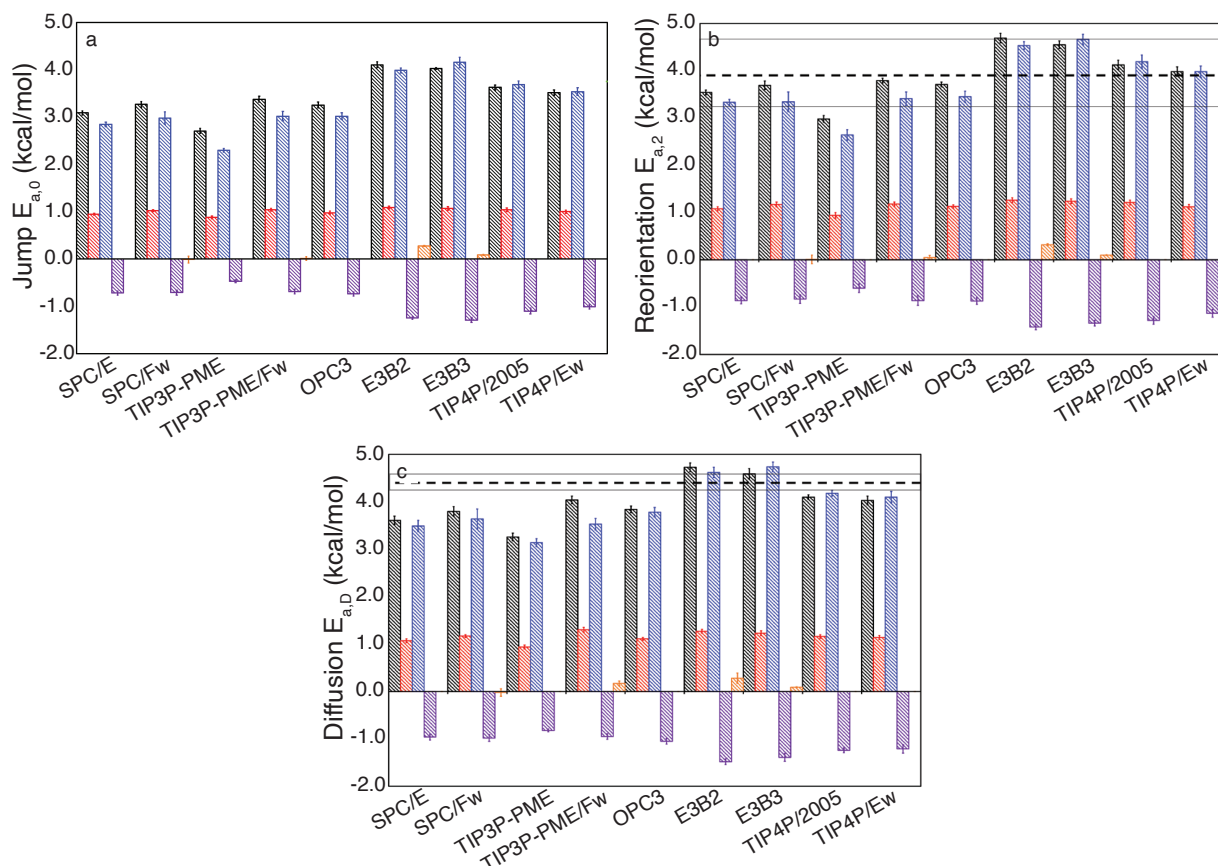


Figure 11.3: Activation energy decomposition for the studied water models are included for a) the jump time, b) the reorientation time, and c) the diffusion coefficient. The total, kinetic, electrostatic, Lennard-Jones, and other contributions to the activation energy are presented in black, red, blue, purple, and orange, respectively. The experimental values of the diffusion and reorientation activation energies are included as black dashed lines on their respective plots. Experimental uncertainties are included as gray solid lines.

mol. All of the models, except TIP3P-PME which has the lowest activation energy, are in agreement, within errors, of one of the reported measured values. However, this is largely due to the significant difference between the two reported experimental $E_{a,2}$ results and their sizable error uncertainties. As with the reorientation timescales, the calculated activation energies appear to fall into two general categories. Namely, the rigid and flexible 3-site models (excepting TIP3P-PME) give $E_{a,2} \simeq 3.5 - 3.8$ kcal/mol, while the 4-site and E3B force fields yield larger activation energies of $4.0 - 4.7$ kcal/mol. Unfortunately, it is not possible to determine which is a better description of the true temperature dependence of liquid water with the currently available experimental data.

The picture for diffusion is somewhat clearer. The TIP3P-PME model gives an $E_{a,D}$ that is

lower by more than 0.3 kcal/mol than that for any other force field. Otherwise, the same division of the results into 3-site models that give lower activation energies, 3.6 – 4.0 kcal/mol and 4-site and 3-body models that give higher activation energies, 4.0 – 4.7 kcal/mol is apparent, though with values that overlap. The latter group is in better accord with the measured diffusion activation energy, suggesting that these force fields better represent the temperature dependence of water diffusion.

No experimental value exists to which we can compare the calculated jump activation energies, but we find that the ordering of the activation energies in these models is similar to that of $E_{a,2}$. The TIP3P-PME result lies significantly outside the range of the other models. The 3-site models predict a weaker temperature dependence of the H-bond jump time, $E_{a,0} \simeq 3.1 - 3.4$ kcal/mol compared to the TIP4P- and E3B-based descriptions which give 3.5 – 4.1 kcal/mol.

We have recently shown¹³⁶ that $E_{a,2}$ may be calculated based on the extended jump model,^{85,88} which gives it as a contribution from two terms. The first is the contribution due to jumps including $E_{a,0}$ and a measure of the temperature dependence of the size of the angular jump. The second is the activation energy of the unbroken H-bond, or “frame,” reorientation obtained from the $C_2(t)$ TCF based on the $O_d \cdots O_a$ vector for H-bonded pairs between jumps. In that work we found that the jump term for the SPC/E model contributed 2.56 kcal/mol to the reorientation activation energy while the frame reorientation added 1.37 kcal/mol. In the present work, we have not calculated these contributions, but it is interesting to consider that different water models might predict different relative jump and frame contributions to $E_{a,2}$.

The addition of 3-body contributions in the E3B2 and E3B3 models raises the activation energies of all three timescales significantly by about 0.4 – 0.7 kcal/mol compared to the 4-site descriptions. Experimental uncertainty does not allow us to differentiate between these values based on measurements.

The present results indicate that the 4-site and 3-body force fields provide better descriptions of the diffusion coefficient and the corresponding activation energy. The TIP4P/2005 model appears to give the best agreement with measurements of these quantities. This is consistent with its wide

use in modeling the T -dependence of water dynamics, including at temperatures far from ambient conditions.^{160,236,327} However, as noted above, 3-site models like SPC/E and TIP3P-PME/Fw are superior at describing the OH reorientation time, but unfortunately we cannot use experimental measurements of the associated activation energy to determine if they also properly describe the temperature dependence.

11.3.3 Activation Energy Decomposition

As we have noted, a key advantage of the fluctuation theory for dynamics approach is the mechanistic insight it generates *via* a rigorous decomposition of the activation energy based on the motions and interactions present in the system. To explore possible differences in the activation energy origins for the different water models we have decomposed them into contributions from the inter- and intramolecular interactions as described in Sec. 11.2.2.4. The results are given in Table 11.3 and Fig. 11.3.

We first note that every model exhibits the same qualitative, even semi-quantitative behavior, in which the dominant contribution is associated with electrostatics, the kinetic energy is a more modest, positive component, and the Lennard-Jones interactions reduce the activation energy. We have previously observed this behavior for the SPC/E and TIP4P/2005 models^{13,44,50,58,136,160} Specifically, we found that the competition between E_a^{Elec} and E_a^{LJ} can be understood by the interactions involved in breaking an H-bond. During an H-bond exchange, the H-bond acceptor moves out of the first solvation shell of the donor water molecule. This requires an increase in the electrostatic energy between the two molecules but a decrease in the Lennard-Jones interactions, which lie on the repulsive wall of the potential in the intact H-bond. The present results indicate that, despite the relatively wide ranges of timescales and activation energies calculated from these models, they treat the underlying competition between these contributions in a similar way.

Considering specifically the kinetic energy contribution to the activation energies, we see (Table 11.3) that it lies in the range 0.88 – 1.3 kcal/mol over the full set of models and timescales. The smallest kinetic energy contributions occur for the TIP3P-PME model in every case, which

we noted above significantly underestimates every activation energy. Ignoring this model we find that the range of values is even smaller for a given timescale where for the jump time $E_{a,0}^{KE} = 0.95 - 1.09$ kcal/mol, for the reorientation time $E_{a,2}^{KE} = 1.08 - 1.26$ kcal/mol, and for the diffusion coefficient $E_{a,D}^{KE} = 1.07 - 1.30$ kcal/mol. While these differences are small, the E3B models consistently have the largest kinetic energy contribution and the SPC/E, OPC3, and TIP4P/Ew force fields have the smallest.

Examination of the electrostatic contributions also yields a consistent picture. It is not only the largest contribution but quite close to the total activation energy, within ~ 0.4 kcal/mol, in every case. In this way it closely tracks the trends in the activation energy for the different models that are discussed above. As would be expected from the physical picture of competition between the electrostatic and Lennard-Jones interactions we have just described, we find E_a^{Elec} and E_a^{LJ} are anti-correlated. Smaller electrostatic contributions, which occur particularly for the rigid and flexible 3-site models, are accompanied by smaller in magnitude (less negative) Lennard-Jones components. In contrast, for the 4-site and 3-body force fields we find the electrostatic component of the activation energy is larger and the corresponding Lennard-Jones term is bigger in magnitude (more negative).

It is also interesting to consider the other contributions to the activation energy associated with flexibility or 3-body interactions that are not shared by every model. Interestingly, the bending and stretching contributions to the activation energy of SPC/Fw essentially cancel each other for every timescale so that the molecular flexibility has no direct effect on the activation energy. This is also true for the TIP3P-PME/Fw model for the jump and reorientation time activation energies, but they combine to increase $E_{a,D}$ in the case of diffusion. More importantly, these results indicate that the differences in the E_a predicted by the SPC/E and SPC/Fw models, which are modest, and those between the TIP3P-PME and TIP3P-PME/Fw models, which are significant, must be attributed to underlying changes in the liquid structure induced by the addition of flexibility rather than a direct role in the dynamics.

In the E3B2 and E3B3 models, the activation energy contributions that come from the addition

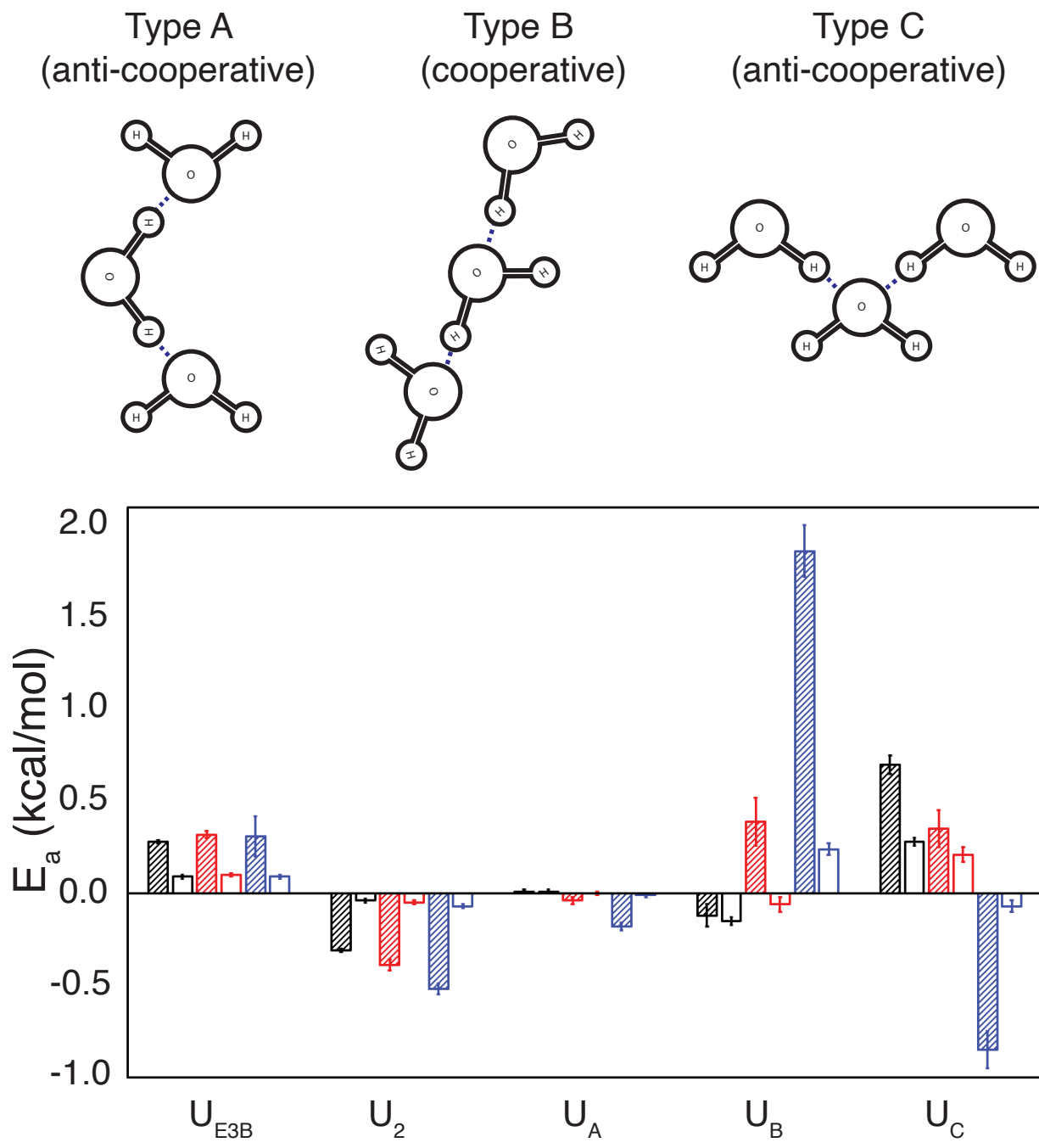


Figure 11.4: Contributions to the jump (black), reorientation (red), and diffusion (blue) activation energies for the E3B model components (U_2 , U_A , U_B and U_C) for the E3B2 (striped bars) and the E3B3 (empty bars) models.

of 3-body interactions likewise do not add up to the total difference in the activation energy when compared with their base models (TIP4P/2005 for E3B3). Indeed, the 3-body terms add ~ 0.3 and

0.1 kcal/mol to the activation energy of each timescale for the E3B2 and E3B3 model, respectively. Note that, in the case where a direct comparison is possible, the overall activation energies are 0.39 – 0.43 kcal/mol higher for the E3B3 force field than for the base TIP4P/2005 description. Thus, as was the case for the effect of molecular flexibility, it is apparent that the key effect of including 3-body interactions is the modification of the liquid structure.

The 3-body contribution to the activation energy can be further decomposed into the components due to the many-body correction to the pairwise potential ($E_a^{U_2}$), anti-cooperative arrangements ($E_a^{U_A}$ and $E_a^{U_C}$), and cooperative arrangements ($E_a^{U_B}$). We have plotted this decomposition for both E3B2 and E3B3 in Fig. 11.4 along with a schematic illustration of the latter three interactions. For both models, the $E_a^{U_2}$ represents a small negative contribution to the activation energy, but the magnitude for E3B2 is significantly greater than that of E3B3. Because the U_2 term is designed to remove the many-body effects implicitly included in the base pairwise force field,^{194,195} this term provides insight into the approximate magnitude of the base model activation energy associated with those many-body effects. Thus, the negative values of $E_a^{U_2}$ indicates that the base 4-site potentials (TIP4P, TIP4P/2005) would have lower activation energies if many-body effects were not included implicitly.

For both models, the anti-cooperative arrangement term $E_a^{U_A}$ contributes the least to the activation energy, with only reorientation and diffusion having slight negative contributions for the E3B2 model. This suggests that the base 4-site models accurately describe the T -dependence of the Type A, anti-cooperative, arrangements without explicit inclusion of 3-body effects. The majority of the remaining contribution to the activation energy comes from the Type B and Type C arrangements, which are (generally) in opposition to one another for each timescale. Interestingly, the Type B (cooperative) configurations appear to strongly increase the T -dependence of the diffusion coefficient, while decreasing the T -dependence of the jump time. Meanwhile, the Type C (anti-cooperative) configurations display the opposite effect. The reorientation activation energy displays behavior intermediate between that of the H-bond jump time and the diffusion coefficient.

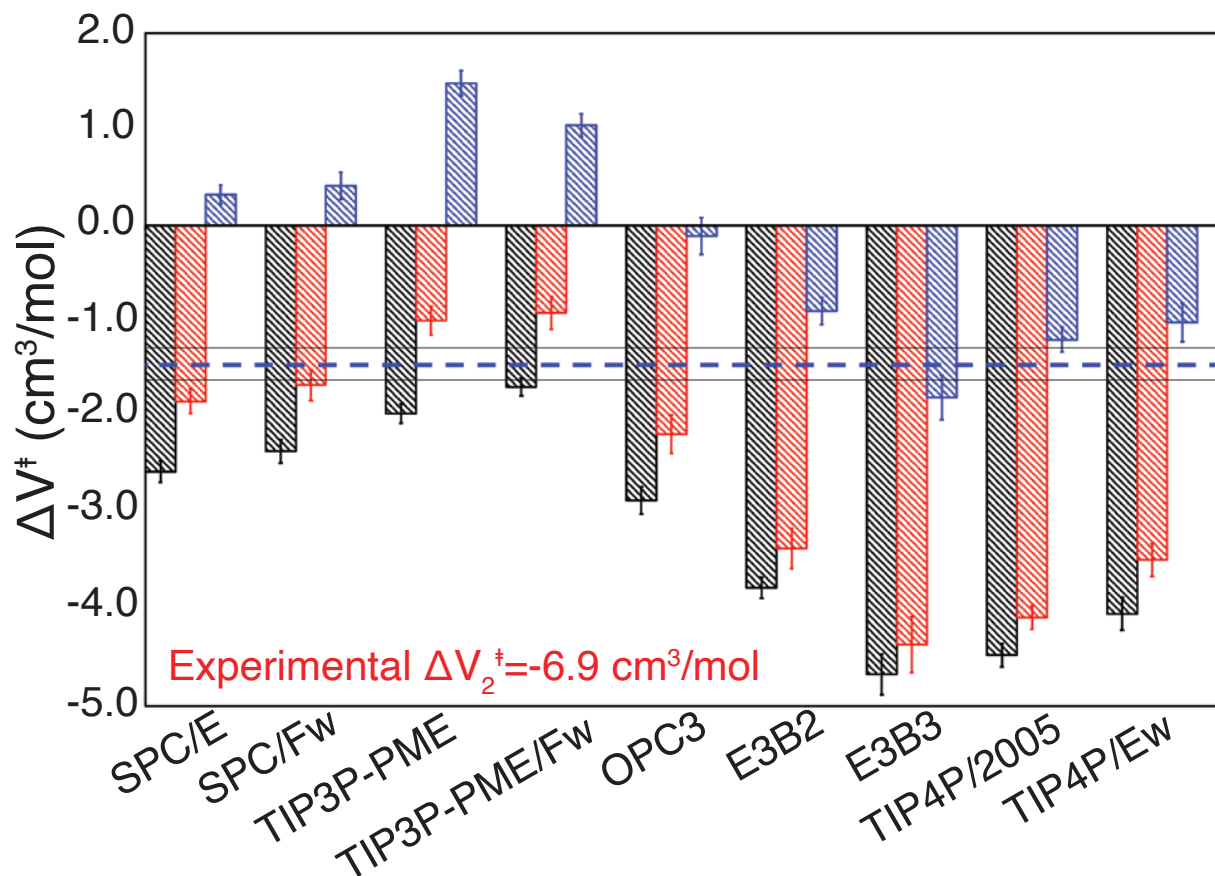


Figure 11.5: Activation volumes of the jump time, ΔV_0^\ddagger (black), reorientation time, ΔV_2^\ddagger (red), and diffusion coefficient, ΔV_D^\ddagger (blue). The average experimental diffusion activation volume^{1,2,4} is also shown (dashed blue line; experimental ranges indicated by gray solid lines). The experimental reorientation activation volume at 450 bar is also listed.¹¹

11.3.4 Activation Volumes

Finally, we examine the pressure dependence of the dynamical timescales predicted by the different water models as represented by the activation volumes. Specifically, we have calculated the activation volumes at 298.15 K and 1 bar of the H-bond jump time, OH reorientation time, and diffusion coefficient. The values are provided in Table 11.4 and the results are plotted in Fig. 11.5. We compare with experimental results based on fitting to NMR measurements of D at a series of pressures.^{1,2,4} Recently, Fanetti *et al.* have published pump-probe anisotropy measurements of the reorientation time over a wide range of pressures.¹¹ We have used their values of the reorientation time at 1 bar, 600 bar, and 900 bar to evaluate the reorientation activation volume (ΔV_2^\ddagger) numer-

| Model | ΔV_0^\ddagger | ΔV_2^\ddagger | ΔV_D^\ddagger |
|---------------------------|-----------------------|-----------------------|-----------------------|
| SPC/E | -2.56 ₁₁ | -1.83 ₁₃ | 0.32 ₁₀ |
| SPC/Fw | -2.35 ₁₂ | -1.66 ₁₆ | 0.41 ₁₄ |
| TIP3P-PME | -1.96 ₁₀ | -0.99 ₁₅ | 1.48 ₁₃ |
| TIP3P-PME/Fw | -1.68 ₉ | -0.91 ₁₇ | 1.04 ₁₂ |
| OPC3 | -2.86 ₁₄ | -2.17 ₂₀ | -0.11 ₁₉ |
| E3B2 | -3.77 ₁₁ | -3.36 ₂₁ | -0.89 ₁₄ |
| E3B3 | -4.67 ₂₁ | -4.36 ₂₉ | -1.79 ₂₃ |
| TIP4P/2005 | -4.47 ₁₂ | -4.08 ₁₂ | -1.19 ₁₃ |
| TIP4P/Ew | -4.04 ₁₇ | -3.48 ₁₇ | -1.01 ₂₀ |
| Expt. ^{1,2,4,11} | - | -6.9 ^a | (-1.3)-(-1.6) |

^aAt 450 bar.

Table 11.4: Activation volumes (in cm³/mol) of the jump time, ΔV_0^\ddagger , reorientation time, ΔV_2^\ddagger and diffusion coefficient, ΔV_D^\ddagger . Subscripts indicate uncertainties in the trailing digit(s).

ically, for which we have found a value of -6.9 cm³/mol. To the best of our knowledge, this is the first experimental value for the activation volume of the τ_2 timescale. We are unaware of any measurements for τ_0 .

We first note the general features of the results. We find that the activation volumes for the H-bond jump time, ΔV_0^\ddagger , and the OH reorientation time, ΔV_2^\ddagger are negative for all of the models and that, in every case, ΔV_0^\ddagger is larger in magnitude (more negative) than ΔV_2^\ddagger . The negative activation volumes here correspond to an increase (decrease) in the corresponding rate constant (timescale) with increasing pressure. However, for the diffusion coefficient the 3-site models predict an activation volume that is positive or zero (within errors) but the 4-site and 3-body models yield a negative activation volume. This is an interesting contrast with the activation energy, where we observed comparatively small quantitative differences between the results for the different timescales, particularly for $E_{a,2}$ and $E_{a,D}$. We note that the diffusion activation volume, ΔV_D^\ddagger , changes sign with both pressure and temperature,^{3,10} so that the quantitative results here apply only for the ambient conditions at which they were evaluated.

While the experimental ΔV_2^\ddagger for reorientation is not centered around 1 bar,¹¹ it is still in reasonable agreement with our calculated results. Importantly, it suggests that the stronger pressure effect observed in the simulations for the reorientation time compared to the diffusion coefficient matches the available experimental data showing $|\Delta V_2^\ddagger| > |\Delta V_D^\ddagger|$. Fanetti *et al.* also reported the

p -dependence of τ_2 for the ASAP water force-field,³²⁸ using their values and an Arrhenius-type numerical procedure we estimate an activation volume of $\Delta V_2^\ddagger = -3.7 \text{ cm}^3/\text{mol}$, which is in general agreement with the present, directly calculated, results for different models.

We note that the activation volume measures the difference in volume of the transition state and reactant structures, broadly defined in that it contains any changes in the surrounding solvent arrangement as well.⁶² Thus, a negative (positive) activation volume corresponds to a reduction (increase) in size moving from the reactant state to the transition state. The present results suggest that the volume of the transition state for diffusion is distinctly different than that for reorientation and H-bond jumps despite the fact that the activation energies are quite similar. The latter is understood as a signature of the fact that both reorientation and diffusion have H-bond exchanges as their underlying fundamental process. A key difference between the processes is that diffusion has a component associated with a translational jump accompanying the exchange¹⁷⁸ while reorientation involves one due to an angular jump. While an extended jump model has been developed for OH reorientation,^{85,88} a similar rigorous description is lacking for diffusion; the present results indicate that an accurate reproduction of the diffusion activation volume and its connection to the jump activation volume should be key targets of such a model.

Comparing the results from the different water models does give a consistent picture across the three timescales. Namely, the 3-site models predict larger (positive or less negative) activation volumes in all cases. For diffusion, this means that the 3-site models incorrectly predict the relative size of the transition state and reactant arrangements. The 4-site and 3-body models give $\Delta V_D^\ddagger \simeq -0.9$ to $-1.8 \text{ cm}^3/\text{mol}$, which is in reasonable agreement with the range of experimental values. The TIP4P/2005 ($-1.19 \pm 0.13 \text{ cm}^3/\text{mol}$) and E3B3 ($-1.79 \pm 0.23 \text{ cm}^3/\text{mol}$) force fields give the overall best results and the only ones that overlap, within error, with the measurements.

In the case of the activation volumes for τ_0 and τ_2 , the 3-site models are quantitatively, but not qualitatively, different. They predict negative activation volumes, but ones that are as much as 3 – 4 times smaller than the 4-site and 3-body models. Interestingly, the two 3-body models yield significantly different activation volumes, with the E3B2 model giving results $\sim 0.9 - 1.0 \text{ cm}^3/\text{mol}$

larger than the E3B3 values for every timescale. This leads to E3B2 activation volumes that are less negative than the 4-site (TIP4P/2005 and TIP4P/Ew) models, but more negative E3B3 activation volumes. It is tempting to speculate that this is associated with the larger contributions of the Type B and Type C configurations in the E3B2 model as observed in the activation energy decompositions, Fig. 11.4, but we do not currently have an approach for evaluating such a hypothesis.

The TIP3P-PME and TIP3P-PME/Fw models are the largest outliers as they predict the most positive ΔV_D^\ddagger and the smallest magnitude ΔV_0^\ddagger and ΔV_2^\ddagger . The diffusion result is furthest from the measured values and indicates that these force fields do not adequately describe the pressure dependence. It is interesting that, while the TIP3P-PME/Fw model substantially improves on the deficiencies of TIP3P-PME with respect to timescales (Table 11.2) and activation energies (Table 11.3), it does not notably improve upon the pressure dependence.

11.4 Conclusions

In the present work, we have used dynamical fluctuation theory to evaluate the timescales, activation energies, and activation volumes of the H-bond exchange, or “jump,” time, the OH reorientation time, and the diffusion coefficient for several commonly used water models. While these timescales are non-Arrhenius in water, these activation parameters provide a good measure of the local temperature/pressure dependencies (for example, the activation energy provides a good estimate for the T -dependence¹⁶⁰ of these timescales over a range $\sim 280 - 340$ K). To our knowledge, this is the first calculation of the jump and reorientation activation volumes. We do note that, in this first comparison between models, we have not considered polarizable models, models with more than four sites, electronic structure-based descriptions, or potentials that include more than 3-body effects,³²⁹ which could provide improvement to some or all of the quantities calculated in the present work.

The results show that SPC/E, SPC/Fw, and TIP3P-PME/Fw provide the best description of reorientation timescales in liquid water whereas TIP4P/2005 most faithfully reproduces the measured diffusion coefficient. The four-site and three-body models more accurately predict the diffusion

activation energy, and thus at least the local temperature dependence of diffusion, compared to any of the 3-site models. The TIP3P-PME force field does a universally poor job of describing timescales, activation energies, and activation volumes. We are unable to distinguish between the other models based on the reorientation or jump time activation energies, due to the significant uncertainty in the experimental result for the former and the lack of measurements for the latter.

We have decomposed the activation energies and found that all of the models share the same underlying mechanistic origin of the water dynamics. Namely, a strong competition is observed between the electrostatic and Lennard-Jones interactions with the former representing the dominant contribution. Molecular flexibility and 3-body effects both provide a small direct contribution to the activation energy, but also lead to other changes, e.g., in the liquid structure, that more significantly affect the activation energy.

The superior description of the four-site and 3-body models also extends to the pressure dependence, where the activation volumes for both the reorientation time and diffusion coefficient are in significantly better agreement with experiment than those of the 3-site models. Surprisingly, the activation volumes for the OH reorientation and H-bond jump times are substantially more negative than those for the diffusion coefficient.

Overall, of the force fields examined, TIP4P/2005 and E3B3 (which adds three-body interactions to the TIP4P/2005 model) give the best representation of the dynamical properties and their temperature and pressure dependence. However, this conclusion comes with qualifications. These models overestimate the OH reorientation timescale (and presumably the H-bond jump time) while simultaneously matching experimental measurements of the diffusion coefficient, its activation energy, and its activation volume. The reorientation time is more accurately predicted by the three-site SPC/E, SPC/Fw, and TIP3P-PME/Fw models that, however, predict diffusion that is too fast and a diffusion activation energy that is too low.

Chapter 12

The water hydrogen bond jump activation energy can be inferred from experimental data

12.1 Introduction

One of the hallmarks of liquid water is its extensive hydrogen bond (H-Bond) network. The ability of this network to quickly exchange these H-bonds is responsible for many of the noteworthy features of the neat liquid.^{8,172,174,176} Under ambient conditions, H-bond exchanges play a critical role in most dynamical processes including diffusion,³¹⁵ reorientation,^{85,104} viscosity,^{3,4,141,142} spectral diffusion,^{123,138,330} dielectric relaxation,^{140,331} structural rearrangements,^{143,144} and chemical reactions.^{90–92} As these exchanges play such a ubiquitous role, it is not surprising that they have been characterized in great detail.

Laage and Hynes developed a theoretical treatment of these H-bond exchanges, called the Extended-Jump Model, was developed to describe the reorientation of water molecules in terms of finite amplitude “jumps” between H-bond partners as well as a part that comes from the reorientation of the unbroken $O_d \cdots O_a$ “frame”.^{85,88} The reorientation time, which is measured in pump-probe Infrared anisotropy experiments,⁷¹ can be expressed in terms of these components as,

$$\frac{1}{\tau_2} = \frac{1}{\tau_2^{jump}} + \frac{1}{\tau_2^{frame}} \quad (12.1)$$

where τ_2^{frame} is the frame reorientation time, $\tau_2^{jump} = \tau_0/\bar{w}_2$ is the jump contribution to the reorientation time. Here, τ_0 is the characteristic “jump” time of H-bond exchanges, and \bar{w}_2 is the average

value of the jump angle weighting function derived by Ivanov.¹¹¹

This jump timescale measures the survival lifetime of a hydrogen bond, and is one of the fundamental timescales of liquid water. From a molecular simulation, τ_0 can be calculated from the stable states picture³³ using the “side-side” correlation function, as

$$C_{ab}(t) = \langle n_a(0)n_b(t) \rangle, \quad (12.2)$$

where n_a (n_b) is equal to 1 if the chosen OH is H-bonded to molecule a (b), and is otherwise zero. Absorbing boundary conditions are used so that after an exchange occurs, that molecule’s contribution remains zero regardless of whether it switches back to its original H-bond partner due to a further exchange. The function $1 - C_{ab}(t)$ decays exponentially at longer times with the timescale τ_0 (which in practice is fit with a double exponential to allow for transient behavior at early times).

While this theoretical framework provides powerful insights into water H-bond dynamics within molecular dynamics simulations, it is surprising that a method for measuring τ_0 experimentally has not yet been developed. This has not only restricted the ability to measure this timescale, but it has also made experimental measurements of the jump activation energy,

$$E_{a,0} = -\frac{\partial \ln(1/\tau_0)}{\partial \beta}, \quad (12.3)$$

impossible. Here $\beta = 1/(k_b T)$, k_b is Boltzmann’s constant and T the temperature. As jumps are the elementary steps in many dynamic processes in liquid water and aqueous solutions, their present immeasurability presents an important challenge to be overcome.

In the present work, we present a theoretical development that allows for the experimental jump activation energy to be estimated using information available from correlations between structure and dynamics present within molecular dynamics simulations and applying them to the experimental liquid structure. Specifically, the present work identifies a linear relationships between the enthalpies and entropies associated with exchanging H-bonds and calculated activation energies of

dynamic timescales from a variety of molecular models of liquid water. These relationships are then used along with experimental values of the aforementioned enthalpies and entropies to predict the jump activation energy.

12.2 Computational Methods

For each model, we generated configurations using PACKMOL¹⁶² to generate initial configurations and necessary data files for molecular dynamics simulations. Initial velocities were generated from the room temperature Maxwell-Boltzmann distribution. Molecular dynamics simulations were run using the Large-Scale Atomic/Molecular Massively Parallel Simulator (LAMMPS).⁸¹ Liquid structures were calculated from separate long trajectories, propagated for 50 ns in the NpT ensemble at 1 bar and 298.15 K after a 1 ns equilibration. For these trajectories, configurations were output every 100 fs (in total 500,000 configurations) from which the radial distribution function and its derivative were calculated.

A Nosé-Hoover thermostat and barostat were used, both of chain length 3, with damping parameters of 100 fs and 1000 fs, respectively.^{83,84} For all simulations, the Particle-Particle-Particle Mesh (PPPM) Ewald summation method was used for the calculation of electrostatic interactions, with a tolerance parameter of 1×10^{-4} .^{119,120} For simulations involving rigid water molecules, the SHAKE algorithm was used to hold bonds and angles constant, also with a tolerance of 1×10^{-4} .⁸²

12.3 Results and Discussion

In a recent study, we have directly calculated the activation energy for water diffusion, OH reorientation, and H-bond exchanges using the fluctuation theory for dynamics approach for a wide range of water models.³⁰⁹ This method enables the direct determination of an activation energy from simulations at a single temperature,^{13,58,309} by computing the analytical derivative of a timescale or rate constant with respect to temperature at a single temperature and pressure, in contrast to the numerical derivative obtained in an Arrhenius analysis.

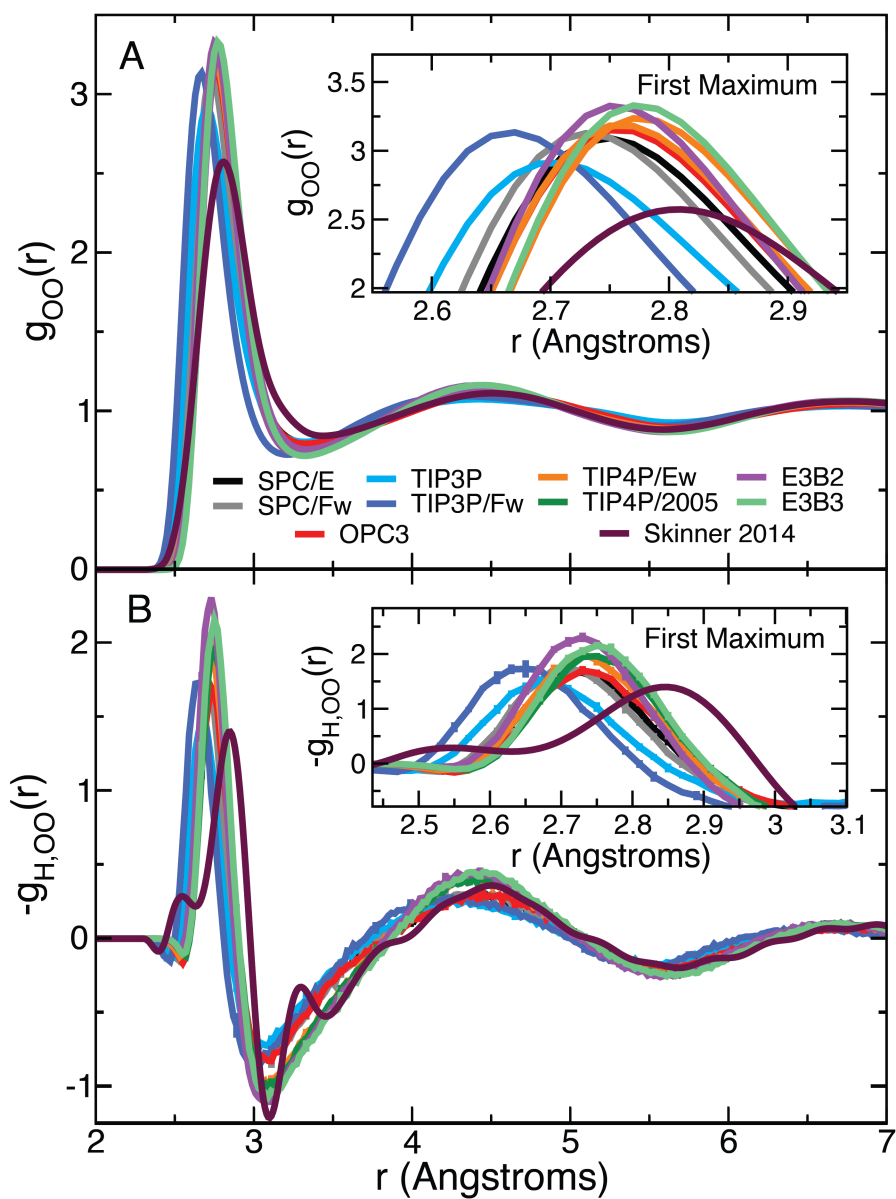


Figure 12.1: Plots of the liquid water OO a) radial distribution function and b) the β derivative of the RDF, $-g_{H,OO}(r)$, for each model. Insets show a closer view of the first maximum.

The same approach can be used to calculate the temperature dependence of static equilibrium properties.^{147,270,271} In liquids, the pair-distribution function (RDF) is frequently used to characterize liquid structure,²⁷² as

$$g_{OO}(r) = \frac{V}{N^2} \left\langle \sum_i \sum_j \delta(r - |\vec{r}_{ij}|) \right\rangle, \quad (12.4)$$

where $\vec{r}_{ij} = \vec{r}_j - \vec{r}_i$ is the distance between sites i and j , N is the number of molecules, r is the distance along the $O \cdots O$ coordinate, and V is the volume. Experimentally, RDFs are obtained as the Fourier transform of the structure factor measured by either neutron^{231,273,274} or X-ray scattering.^{12,275} Using fluctuation theory, we have previously demonstrated that the derivative of the RDF with respect to β can be expressed in terms of fluctuation theory as,

$$\begin{aligned} \frac{\partial g_{OO}(r)}{\partial \beta} &= -\frac{V}{N^2} \left\langle \delta H \sum_i \sum_j \delta(r - |\vec{r}_{ij}|) \right\rangle \\ &= -g_{H,OO}(r). \end{aligned} \quad (12.5)$$

Here we have neglected the $p\delta V$ contribution to the derivative present in the NpT ensemble, which is negligible at 1 bar. This derivative is evaluated directly at a single T and p .

We have calculated the RDF for each water model listed in the first column of Table 12.1 and plotted the in Fig 12.1a. The studied models represent a wide range of parametrizations, that span 3-site and 4-site models, and include flexible, and 3-body interactions. In this figure, we have also included the experimental radial distribution function at 295.1 K as measured by Skinner and Benmore using X-ray diffraction.¹² Each model exhibits moderate agreement with the experimental RDF, but all overestimate the height of the first peak. The models generally agree on the peak's location along r , with the exception of the TIP3P-PME and TIP3P-PME/Fw models which predict a more contracted liquid structure.

We have also directly calculated the β derivative of the RDF at 298.15 K for each water model using Eq. (12.5) and have used the experimentally measured RDFs at 307 K and 284.5 K to evaluate this derivative numerically.¹² The results are plotted in Fig 12.1b. The model and the experimental derivatives are in general qualitative agreement though the models exhibit slightly less structure than the experimental result. Interestingly the 4-site models are in general agreement with experiment after the first minimum (located at about 3.1 Å); however, only TIP3P-PME is in good agreement with the height of the first maximum with the other models slightly overestimating the T -dependence of the peak.

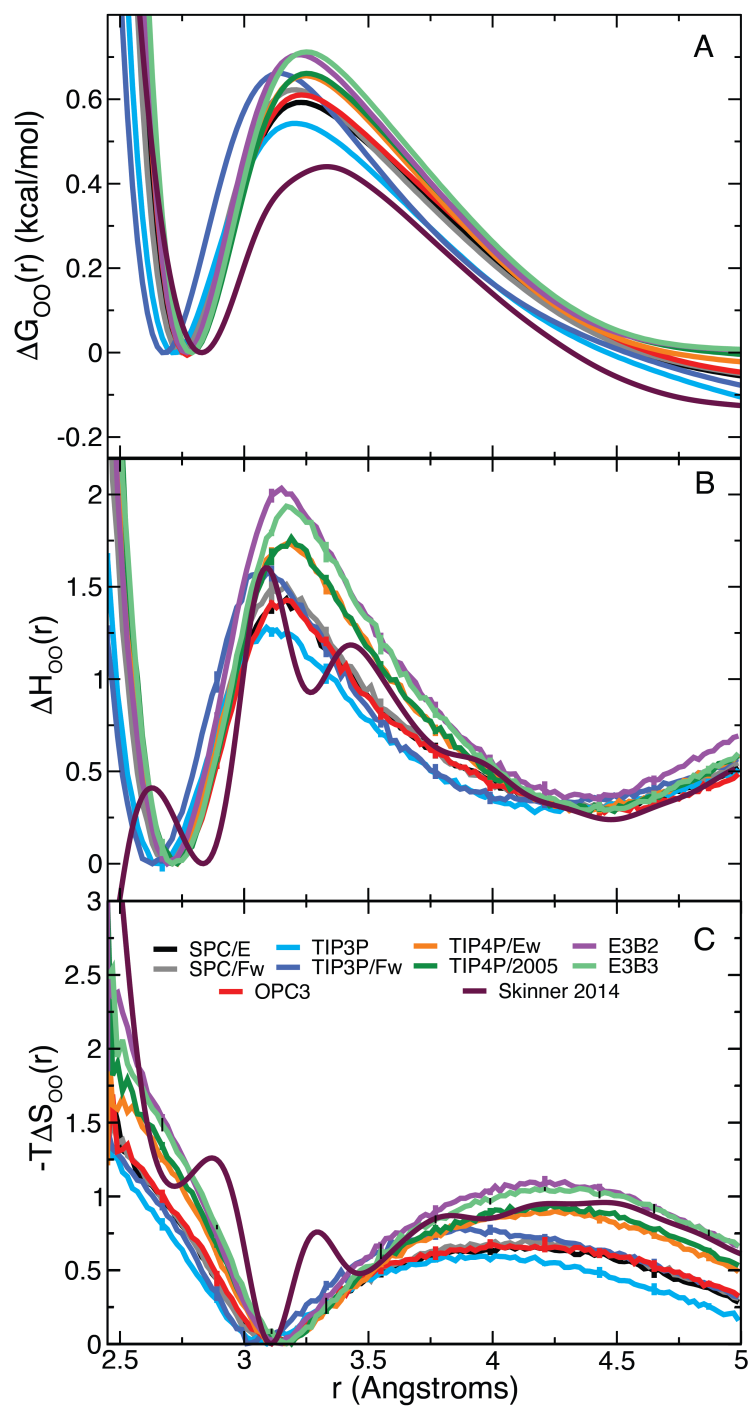


Figure 12.2: Water OO (a) Gibbs free energy, (b) enthalpy, and (c) entropy profiles. (The first minimum is set to zero in each case.)

The Gibbs free energy can be calculated from the RDF as,

$$\Delta G_{OO}(r) = -k_b T \ln g_{OO}(r) - 2k_b T \ln r, \quad (12.6)$$

where the first term is the potential of mean force and the second term is the entropy associated with the increasing volume with r . The calculated $\Delta G_{OO}(r)$ for each model and the experimental results of Ref. 12 are shown in Fig. 12.2. We find that the free energy barrier to move from the first to the second solvation shell is overestimated by each model compared with experiment. Generally, we observe that a higher barrier between the first and second solvation shell corresponds with an overall shallower minimum in the second solvation shell, though the two flexible models do not follow this pattern.

It is straightforward to show¹⁴⁷ that the derivative $g_{H,OO}(r)$ can be used to determine the corresponding enthalpy,

$$\Delta H_{OO}(r) = \frac{g_{H,OO}(r)}{g_{OO}(r)}, \quad (12.7)$$

and the entropic contribution to the Gibbs free energy as,

$$-T\Delta S_{OO}(r) = \Delta G_{OO}(r) - \Delta H_{OO}(r), \quad (12.8)$$

using $\Delta G_{OO}(r) = \Delta H_{OO}(r) - T\Delta S_{OO}(r)$ and assuming ΔH and ΔS are independent of temperature. The enthalpy and entropy contributions to the free energy calculated in this way are shown in Fig. 12.2. Both quantities exhibit more structuring in the experimental results than in the simulations. The experimental enthalpic barrier for moving from the first to second solvation shell is in best agreement with the E3B models, though the measured second solvation shell minimum is shallower than predicted by any of the models. The experimental entropy profile is similar to that predicted by all of the water models and agrees best with the 4-site models studied. However, at short distances the measured $-T\Delta S_{OO}(r)$ increases more steeply than in any of the models.

We have previously reported calculations of the diffusion, reorientation, and the jump activation

energies for the models considered here (Chapter 11).³⁰⁹ We will now examine the relationship between the enthalpic (and entropic) change associated with exchanging an H-bond and the observed activation energy for each of these three timescales.

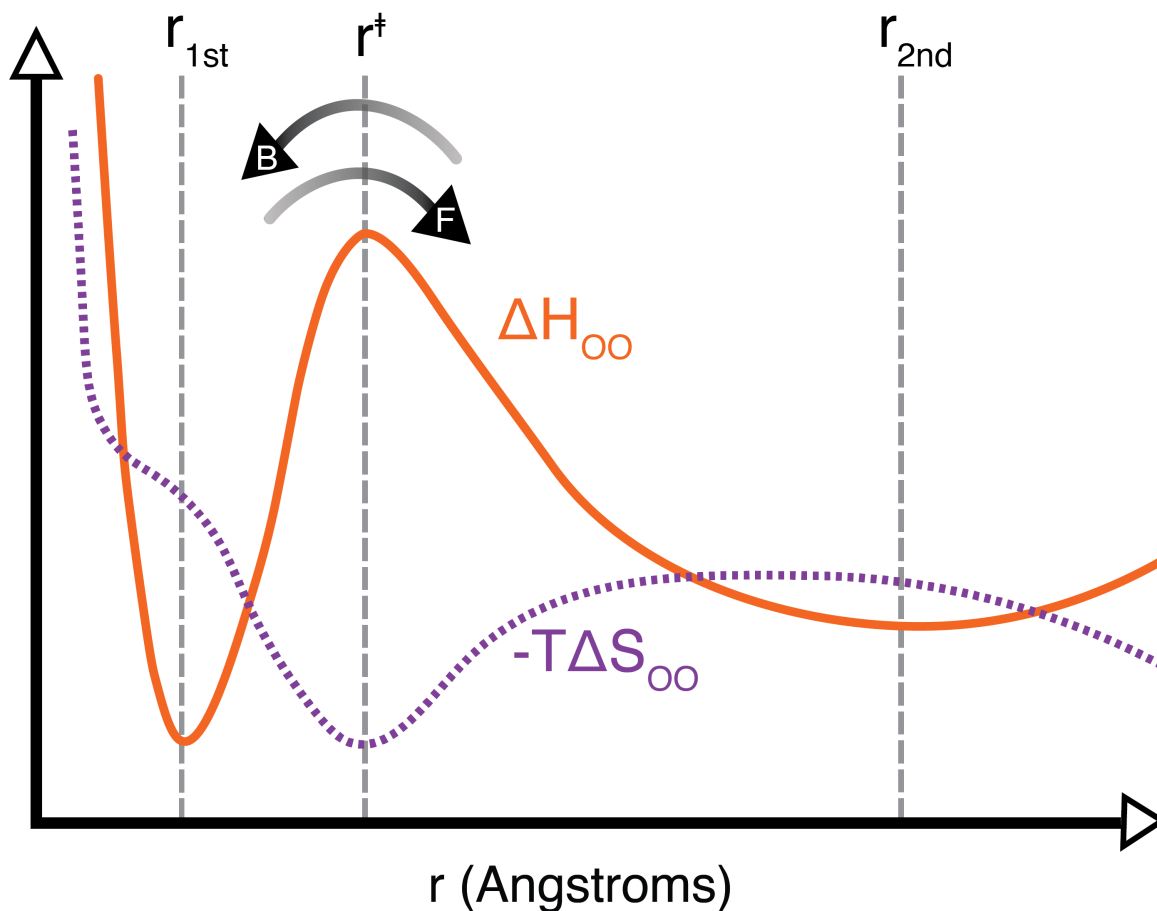


Figure 12.3: Schematic of the liquid water OO a) enthalpic and b) entropic contributions to the free energy. Indicated on the plot are the positions r_{1st} , r^{\ddagger} , and r_{2nd} as well as marking the forward and backward directions over the enthalpic barrier.

At this point, it should be pointed out that the hydrogen bond jump involves the breakage of, at a minimum, two H-Bonds, in order to free both an acceptor and a donor. Thus, we can consider the quantity $\Delta\Delta H = \Delta H_f + \Delta H_b$ which corresponds to the sum of the enthalpy barrier in both directions. Here we define ΔH_f and ΔH_b as the enthalpy required to cross the barrier in the

| Model | $E_{a,0}^\ddagger$ | $\Delta\Delta H$ | $\Delta\Delta H^\theta$ | $-T\Delta\Delta S$ |
|---------------------------------|--------------------|--------------------|-------------------------|---------------------|
| SPC/E ⁴² | 3.09 ₄ | 2.58 ₅ | 0.51 ₇ | -1.50 ₁₀ |
| SPC/Fw ³⁰³ | 3.27 ₆ | 2.72 ₉ | 0.55 ₁₁ | -1.57 ₁₄ |
| TIP3P-PME ^{304,305} | 2.71 ₅ | 2.28 ₃ | 0.43 ₆ | -1.39 ₄ |
| TIP3P-PME/Fw ^{304,305} | 3.38 ₆ | 2.82 ₇ | 0.56 ₁₀ | -1.63 ₉ |
| OPC3 ³⁰⁶ | 3.26 ₆ | 2.58 ₈ | 0.68 ₁₀ | -1.45 ₁₁ |
| E3B2 ¹⁹⁴ | 4.11 ₆ | 3.71 ₈ | 0.40 ₁₀ | -2.54 ₈ |
| E3B3 ¹⁹⁵ | 4.03 ₂ | 3.58 ₁₃ | 0.45 ₁₅ | -2.40 ₁₆ |
| TIP4P/2005 ⁵ | 3.63 ₅ | 3.25 ₅ | 0.38 ₈ | -2.10 ₅ |
| TIP4P/Ew ³⁰⁷ | 3.52 ₆ | 3.18 ₈ | 0.34 ₉ | -2.03 ₁₃ |
| Expt ³³² | 3.43 | 2.97 | 0.46 | -2.16 |

† values have been reproduced from Ref. 309.

Table 12.1: $E_{a,0}$, $\Delta\Delta H$, $\Delta\Delta H^\theta$, and $-T\Delta\Delta S$ for each water model and experiment.¹²

forward and backward directions, respectively. These are calculated as

$$\begin{aligned}\Delta H_f &= \Delta H_{OO}(r^\ddagger) - \Delta H_{OO}(r_{1st}) \\ \Delta H_b &= \Delta H_{OO}(r^\ddagger) - \Delta H_{OO}(r_{2nd}),\end{aligned}\tag{12.9}$$

where r^\ddagger , r_{1st} , and r_{2nd} are the positions of the transition state, the first solvation shell, and second solvation shell, respectively. A schematic diagram of $\Delta H_{OO}(r)$ and $-T\Delta S_{OO}(r)$ with these positions overlaid has been included in Figure 12.3. A similar approach has previously been successfully used with the RDF to estimate the jump time, though it relies on information only available from simulations.¹²⁷

Laage and Hynes have suggested previously that the jump activation energy can be expressed as $E_{a,0} = \Delta\Delta H + \Delta\Delta H^\theta$ where the second term corresponds to a separate barrier along an angular coordinate.⁸⁵ From our present calculations, we find that the SPC/E model $\Delta\Delta H$ is 2.58 kcal/mol \pm 0.06 kcal/mol, and its $E_{a,0}$ is 3.09 kcal/mol \pm 0.04 kcal/mol. Using these values, we then find $\Delta\Delta H^\theta = 0.51 \pm 0.07$ kcal/mol in close agreement with Laage's result of 0.50 kcal/mol. In the fourth column of Table 12.1 we have included our calculated values of $\Delta\Delta H^\theta = E_{a,0} - \Delta\Delta H$ for each water model. Interestingly, 4-site models have generally larger values of $\Delta\Delta H$ and smaller values of $\Delta\Delta H^\theta$ than their 3-site brethren, leading to higher values of $E_{a,0}$.

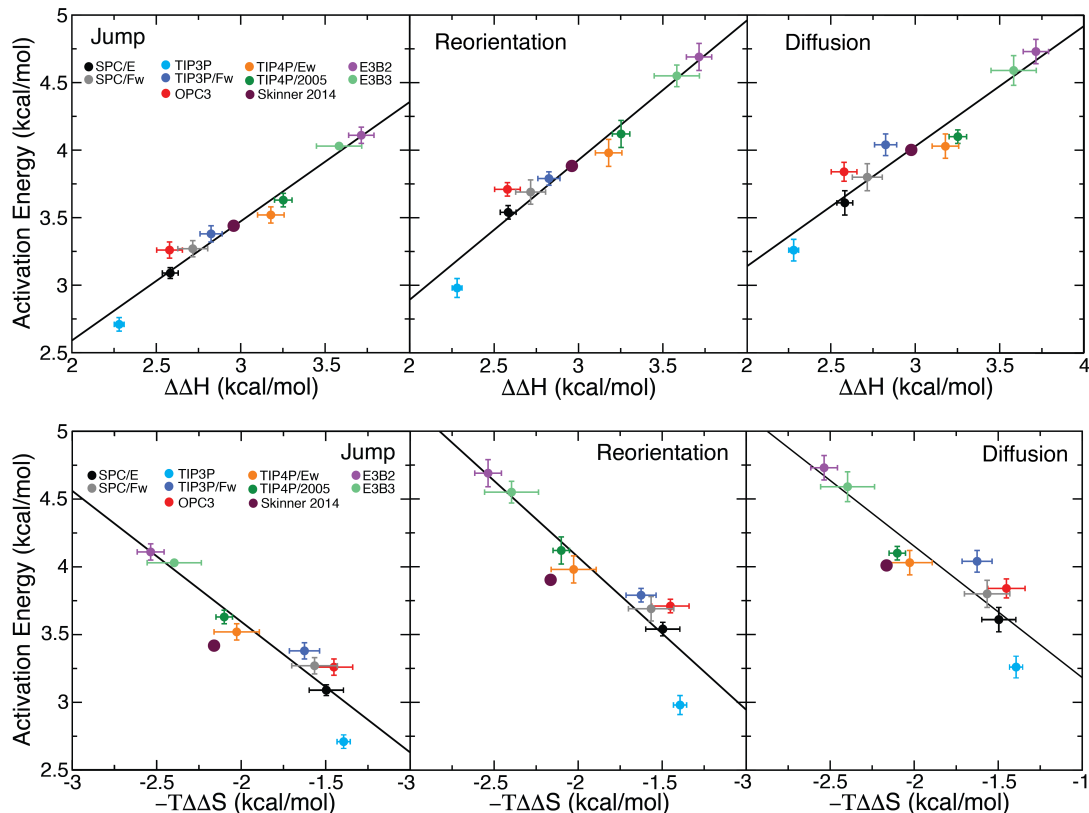


Figure 12.4: Plot of the jump, reorientation, and diffusion activation energies plotted for each water model as a function of $\Delta\Delta H$ (top panels) and $\Delta\Delta S$ (bottom panels). Linear fits are included for each panel as a dashed line in the same color. The predicted activation energies from Skinner’s X-ray data generated using the correlations of $\Delta\Delta H$ are included on each plot.

It is useful to consider instead that there may be a linear dependence of a given activation energy on the enthalpic barrier $\Delta\Delta H$, such that

$$E_{a,X} = m_{H,X} (\Delta\Delta H) + b_{H,X}, \quad (12.10)$$

where here $b_{H,X}$ is the y-intercept, the value $m_{H,X}$ is the slope, and X represents the timescale (either 0, 2, or D).

We have plotted the jump, reorientation and diffusion activation energies of each water model as a function of their corresponding values of $\Delta\Delta H$ in Figure 12.4a. We have included the linear fit described by Eq. (12.10). For all three timescales $E_{a,X}$ and $\Delta\Delta H$ have a strong linear correlation (R^2 between 0.916 and 0.957).

We have also calculated $-T\Delta\Delta S$, the entropic contribution to the free energy barrier corresponding to an H-Bond exchange, which we have included in the fifth column of Table 12.1. With this a similar linear equation may be obtained, as

$$E_{a,X} = m_{S,X} (-T\Delta\Delta S) - b_{S,X}. \quad (12.11)$$

Here $m_{S,X}$ and $b_{S,X}$ are again the slope and the y-intercept.

As with above, we have plotted $E_{a,X}$ as a function of $-T\Delta\Delta S$ for each water model in Figure 12.4b and fitted these correlations to Eq. (12.11). We have gain found that while these correlations remain strong (R^2 between 0.842 and 0.887), they are weaker than what we found for the enthalpic correlations. The strong linear correlations of the activation energies with both $\Delta\Delta H$ and $-T\Delta\Delta S$ is likely a direct result of enthalpy-entropy compensation between water models - this may also explain why the RDF of SPC/E meshes well with experimental RDFs, but performs so poorly at describing the T-dependence of dynamics.

From Skinner and Benmore's experiments,¹² we have followed a similar procedure to numerically evaluate $\Delta\Delta H^{SB} = 2.97$ kcal/mol and $-T\Delta\Delta S^{SB} = -2.16$ kcal/mol. Both results fall within the range predicted by simulations, with $\Delta\Delta H^{SB}$ falling in between the values predicted by the 3-site and 4-site models. The value of $\Delta\Delta S^{SB}$ falls very near the value predicted by the TIP4P/2005 model.

As the correlation for $\Delta\Delta H$ is stronger than the entropic correlation, we use our calculated $\Delta\Delta H^{SB}$ and our fitted parameters in Table S1 to infer the experimental activation energies. We will begin by first using this technique to predict $E_{a,2}$ and $E_{a,D}$ as we have experimental measurements to which we can compare. We find $E_{a,2} = 3.89$ kcal/mol which is in good agreement with both the value measured by Petersen (4.1 ± 0.5 kcal/mol) and Nicodemus (3.7 ± 0.5 kcal/mol).^{7,105} Following the same procedure, we find that $E_{a,D} = 4.00$ kcal/mol, which is close to the experimental range (4.2-4.6 kcal/mol).^{3,4,54,322} We have repeated the above using the entropic correlations and $-T\Delta\Delta S^{HB}$ and found that those predict values of 4.26 kcal/mol and 4.30 kcal/mol for $E_{a,2}$ and

$E_{a,D}$ respectively. While these values are also reasonable, the correlation is stronger for $\Delta\Delta H$ and thus likely provides the better estimate of the activation energy.

As the estimations of $E_{a,2}$ and $E_{a,D}$ appear to be in accord with experiment, we can then apply the same technique applied to the jump activation energy. We find that $E_{a,0} = 3.43$ kcal/mol, which to the best of our knowledge is the first estimate of this value. Due to the factors involved (mixture of experiments, simulations *etc.*), it is difficult to directly calculate the uncertainty in this value; however, error propagation suggests it is near 0.60 kcal/mol. As with above, if we utilize the entropic correlations instead we find that the jump activation energy is 3.76 kcal/mol which is within uncertainty of our above calculated value, but suffers from the same weaker correlation mentioned above.

Furthermore, a two step process using the experimental $E_{a,D}$ and $E_{a,2}$ in reverse to first predict $\Delta\Delta H$, and then using that value to predict $E_{a,0}$ produces viable values for this activation energy in relatively good agreement with our value reported above. Furthermore, for the TIP4P/2005 model we find $E_{a,0} = 3.63$ kcal/mol which is close to our value. This is significant as this particular model describes $E_{a,2}$ and $E_{a,D}$ to high accuracy compared to experiment, and thus likely does for $E_{a,0}$ as well. Furthermore, from Skinner's value of the jump activation energy, we find that $\Delta\Delta H^\theta = 0.46$ kcal/mol, which is right in the range calculated for the four-site models.

12.4 Conclusions

In summary, we have used molecular dynamics simulations of nine commonly used water models to evaluate the connection between liquid structure and dynamics. Presently, we have calculated the RDF, the Gibbs free energy, the enthalpy, and the entropic contribution to the free energy along the OO coordinate in water using fluctuation theory for each of the water models. We then discovered a strong linear dependence between the activation energies of three dynamical timescales (hydrogen bond exchanges, reorientation, and diffusion) and enthalpic barriers involved in a hydrogen bond exchange through calculations with nine commonly used water models. We have then used experimental T -dependent RDFs measured by Skinner and co-workers to estimate

the jump activation energy for the first time, which we find to be 3.43 kcal/mol.

Chapter 13

A Dynamical Maxwell Relation

13.1 Introduction

Practically every undergraduate physical chemistry student learns about the Maxwell relations that provide important connections between thermodynamic variables³³³ (and some of the students even remember them!). These relationships arise naturally from the fact that thermodynamic functions like enthalpy and free energy are state functions. And they are used to provide a deeper understanding of the properties of chemical systems, *e.g.*, how entropy changes with volume at constant temperature.³³³

In examining chemical dynamics, one often faces the same issue that motivates the Maxwell relations: How does a property change with the independent thermodynamic variables like pressure (p) and temperature (T). The difference is that the fundamental quantities of interest are dynamical, *e.g.*, reaction rate constants, timescales, or transport coefficients. Indeed, the temperature dependence of a reaction rate constant, expressed as the activation energy,^{14,17,18} is a central feature of reaction rate theory. Similarly, while significantly less attention has been paid to it, the activation volume characterizes the change of a rate constant with pressure.^{60,61}

In the Arrhenius perspective, the activation energy is assumed to be constant and provides insight into the magnitude of the (fixed) underlying energetic barrier of the process.^{18,333} However, for some processes non-Arrhenius behavior is quantitatively and qualitatively important. The dynamics of liquid water is one such case, where temperature-dependent activation energies have been observed for diffusion,^{1-4,10,160} reorientation dynamics,^{52,138,160} and viscosity;^{141,334} these processes have a common underlying barrier associated with the exchange of hydrogen-bond (H-

bond) acceptors, which itself exhibits non-Arrhenius behavior that are largely attributed to changes in the H-bond network. Other cases are reactions in which quantum mechanical tunneling represents a significant contribution (typically at lower temperatures) and enzymatic reactions.⁵⁷

The effect of pressure on dynamical processes is typically much more modest than that of temperature and can often only be resolved by varying p by hundreds or thousands of bar.^{1,3,4,221} In many cases, this behavior is Arrhenius-like, *i.e.*, the activation volume is constant with pressure. Then, the activation volume can be obtained from an Arrhenius analysis based on measurement or simulation of the rate constant, or other dynamical timescale, at a few (widely different) pressures. In other systems, however, the activation volume can change significantly, even in the sign, as the pressure is varied. Because the activation volume represents the relative space taken up by the transition state configuration compared to that of the reactants, this suggests a change in the mechanistic details. Note that the “volume” difference here applies to the entire system, including any arrangements of the solvent, whether it is innocent in the reaction or not.⁶²

In cases where the activation energy is not constant with thermodynamic conditions, a full understanding of the dynamics requires a description of how the energy required to carry out the process of interest changes with the temperature and pressure. The same is certainly true of the activation volume. In this Chapter we explore this issue theoretically, in the context of an effective Maxwell relation for a dynamical variable such as a rate constant, and computationally, through simulations of the water diffusion coefficient. We also propose a method for global fitting of a dynamical timescale based on these ideas that is parameterized only by physically meaningful quantities and demonstrate it by analysis of the extensive existing experimental data for the water diffusion coefficient.

13.2 Theory

13.2.1 Maxwell Relation for a Dynamical Variable

In the isobaric-isothermal (NpT) ensemble, we can consider a generic rate constant, transport coefficient, or (inverse) timescale – which we will denote as k – as a function of the independent thermodynamic variables such that its total differential is given by

$$dk = \left(\frac{\partial k}{\partial T} \right)_{p,N} dT + \left(\frac{\partial k}{\partial p} \right)_{T,N} dp + \left(\frac{\partial k}{\partial N} \right)_{p,T} dN. \quad (13.1)$$

In the following, we will assume that N is fixed and it will be convenient to consider $\ln k$ rather than the diffusion coefficient itself and to use $\beta = 1/k_B T$ rather than T as an independent variable (where k_B is Boltzmann's constant). Then, we have

$$d \ln k = \left(\frac{\partial \ln k}{\partial \beta} \right)_p d\beta + \left(\frac{\partial \ln k}{\partial p} \right)_\beta dp, \quad (13.2)$$

as the total differential of interest.

The partial derivatives appearing in Eq. (13.2) can be identified as physically meaningful, measurable quantities in reaction rate theory (and in the theory of transport coefficients). Namely, the activation energy, E_a , is given by the first derivative as

$$\left(\frac{\partial \ln k}{\partial \beta} \right)_p = -E_a, \quad (13.3)$$

i.e., a measure of the temperature dependence of k . Similarly,

$$\left(\frac{\partial \ln k}{\partial p} \right)_\beta = -\beta \Delta V^\ddagger, \quad (13.4)$$

gives the activation volume, ΔV^\ddagger , reflecting how k is influenced by pressure. Thus, the total differ-

ential of k , can be written as

$$d \ln k = -E_a d\beta - \beta \Delta V^\ddagger dp, \quad (13.5)$$

which suggests that we can think of β and p as natural variables of the rate constant (or transport coefficient).

We can then proceed in complete analogy to the derivation of a thermodynamic Maxwell relation, by noting that

$$\left(\frac{\partial^2 \ln k}{\partial p \partial \beta} \right) = \left(\frac{\partial^2 \ln k}{\partial \beta \partial p} \right). \quad (13.6)$$

Evaluating these cross-derivatives yields the Maxwell relation

$$\left(\frac{\partial E_a}{\partial p} \right)_\beta = \Delta V^\ddagger + \beta \left(\frac{\partial \Delta V^\ddagger}{\partial \beta} \right)_p. \quad (13.7)$$

This equation demonstrates the relationship between the pressure dependence of the activation energy to the temperature dependence of the activation volume. Because the meaning of k is general, this equation should hold for rate constants, transport coefficients, and other dynamical timescales. In the following, we examine the underpinnings of this Maxwell relation.

13.2.2 Fluctuation Theory and the Maxwell Relation

It is instructive to examine how the Maxwell relation in Eq. (13.7) arises naturally within fluctuation theory. We can consider an ensemble of NpT trajectories, each with a different (fixed) energy and volume, such that the rate constant is given by

$$k = \langle k_i \rangle = \frac{1}{\Delta(N, p, T)} \text{Tr} \left[e^{-\beta(H_i + pV_i)} k_i \right], \quad (13.8)$$

where H_i and V_i are the fixed energy and volume of the i^{th} trajectory and Tr indicates a sum over all the trajectories, $\Delta(N, p, T) = \text{Tr}[e^{-\beta(H_i + pV_i)}]$ is the isobaric-isothermal partition function, and thus $\langle \dots \rangle$, indicates an ensemble average. Note that k_i is itself an average over the i^{th} constant energy and volume trajectory, typically a time correlation function, *e.g.*, for a reaction rate constant

$\lim_{t \rightarrow \text{long}} \langle F_s(0) \theta[s(t)] \rangle_i$ where F_s is the flux across the transition state dividing surface defined by $s = 0$ and θ is the Heaviside step function. Recall, however, that k can also be a transport coefficient or other dynamical quantity, which are also expressible as averaged time correlation functions.

We have earlier shown^{13,44,58,59,136,147,160,168,184,309} that the derivatives of Eq. (13.8) with respect to the independent thermodynamic variables can be expressed in terms of fluctuations. Namely, it is straightforward to show that

$$\frac{\partial k}{\partial \beta} = -\langle [\delta H_i + p \delta V_i] k_i \rangle, \quad (13.9)$$

where $\delta H_i = H_i - \langle H_i \rangle$ and $\delta V_i = V_i - \langle V_i \rangle$ are the fluctuations in energy and volume respectively of the i^{th} trajectory from the average of all the trajectories in the NpT ensemble. Similarly, the pressure derivative is given by

$$\frac{\partial k}{\partial p} = -\beta \langle \delta V_i k_i \rangle. \quad (13.10)$$

Both of these quantities can be directly calculated from an ensemble of isobaric-isothermal trajectories.

The activation energy can be obtained by combining Eqs. (13.9) and (13.3) to yield

$$E_a = \frac{\langle [\delta H_i + p \delta V_i] k_i \rangle}{\langle k_i \rangle}. \quad (13.11)$$

This fluctuation theory result has a straightforward and useful physical interpretation. The activation energy is the correlation of the enthalpy of the system, $\mathcal{H}_i = H_i + pV_i$ with the rate constant. Thus, if, when the enthalpy is larger (smaller) than average the process is faster (slower), E_a is positive and, the greater the effect of an enthalpy fluctuation on the rate constant, the bigger the magnitude of the activation energy. This activation energy includes, as one component, the activation volume. This can be seen by using Eqs. (13.9) and (13.4), to find

$$\Delta V^\ddagger = \frac{\langle \delta V_i k_i \rangle}{\langle k_i \rangle}. \quad (13.12)$$

This is the first term on the right-hand-side (*rhs*) of the Maxwell relation, Eq. (13.7). It also has an analogous interpretation to the activation energy in that it measures the effect of the volume on the rate constant.

The remaining terms in the Maxwell relation are more challenging as they involve higher, cross-derivatives. However, the second term on the *rhs* of Eq. (13.7) can be obtained by taking the derivative of Eq. (13.12) with respect to β . This gives

$$\frac{\partial \Delta V^\ddagger}{\partial \beta} = \frac{1}{\langle k_i \rangle} \frac{\partial \langle \delta V_i k_i \rangle}{\partial \beta} + \Delta V^\ddagger E_a. \quad (13.13)$$

The derivative in the first term is more explicitly written as

$$\frac{\partial \langle \delta V_i k_i \rangle}{\partial \beta} = \frac{\partial}{\partial \beta} \frac{1}{\Delta} \text{Tr} \left[e^{-\beta(H_i + pV_i)} \delta V_i k_i \right], \quad (13.14)$$

which involves three terms due to the temperature dependence of Δ , the Boltzmann weighting, and the average volume in ΔV_i . Evaluating the derivative yields

$$\begin{aligned} \frac{\partial \langle \delta V_i k_i \rangle}{\partial \beta} &= \langle H_i + pV_i \rangle \langle \delta V_i k_i \rangle - \langle [H_i + pV_i] \delta V_i k_i \rangle \\ &\quad - \frac{\partial \langle V_i \rangle}{\partial \beta} \langle k_i \rangle \\ &= -\langle [\delta H_i + p\delta V_i] \delta V_i k_i \rangle - \frac{\partial \langle V_i \rangle}{\partial \beta} \langle k_i \rangle. \end{aligned} \quad (13.15)$$

Thus, we find that

$$\begin{aligned} \beta \frac{\partial \Delta V^\ddagger}{\partial \beta} &= -\beta \frac{\langle [\delta H_i + p\delta V_i] \delta V_i k_i \rangle}{\langle k_i \rangle} \\ &\quad - \beta \frac{\partial \langle V_i \rangle}{\partial \beta} + \beta \Delta V^\ddagger E_a, \end{aligned} \quad (13.16)$$

for the second term on the *rhs* of the Maxwell relation.

The left-hand-side (*lhs*) of Eq. (13.7) can be derived in a completely analogous fashion. From

Eq. (13.11), we have

$$\frac{\partial E_a}{\partial p} = \frac{1}{\langle k_i \rangle} \frac{\partial \langle [\delta H_i + p \delta V_i] k_i \rangle}{\partial p} + E_a \beta \Delta V^\ddagger, \quad (13.17)$$

using Eq. (13.10). The first term has three pressure-dependent quantities and proceeding as before, it is straightforward to show that

$$\begin{aligned} \frac{\partial E_a}{\partial p} &= -\beta \frac{\langle [\delta H_i + p \delta V_i] \delta V_i k_i \rangle}{\langle k_i \rangle} + \Delta V^\ddagger \\ &+ \beta \Delta V^\ddagger E_a - \frac{\partial \langle H_i \rangle}{\partial p} - p \frac{\partial \langle V_i \rangle}{\partial p}. \end{aligned} \quad (13.18)$$

represents the *lhs* of the Maxwell relation in Eq. (13.7).

Comparing the fluctuation theory results for the *lhs* and *rhs* of the Maxwell relation using Eqs. (13.18) and (13.16), it is clear that it holds if

$$\frac{\partial \langle H_i \rangle}{\partial p} + p \frac{\partial \langle V_i \rangle}{\partial p} = \beta \frac{\partial \langle V_i \rangle}{\partial \beta}. \quad (13.19)$$

This equation does not involve any dynamical property and is a purely thermodynamic relationship that involves the averages present in the fluctuations. It is not hard to show that it is equivalent to the connection, derived using a Maxwell relation, between the pressure derivative of the enthalpy, $\mathcal{H} = \langle H_i + pV_i \rangle$, and the temperature derivative of the volume

$$\left(\frac{\partial \mathcal{H}}{\partial p} \right)_T = T \left(\frac{dS}{dp} \right)_T + V = \beta \left(\frac{dV}{d\beta} \right)_p + V, \quad (13.20)$$

where S is the entropy.

Thus, we have evaluated the Maxwell relation for a dynamical quantity, Eq. (13.7), within the context of fluctuation theory. A key result is that the central quantity is the second-order correlation of the fluctuations,

$$-\beta \frac{\langle [\delta H_i + p \delta V_i] \delta V_i k_i \rangle}{\langle k_i \rangle}, \quad (13.21)$$

that describes both the pressure dependence of the activation energy and the temperature depen-

dence of the activation volume.

In the following, we evaluate and examine the different elements of the Maxwell relation from the fluctuation theory expressions. We consider as a particular example the case of liquid water self-diffusion. It is known that water diffusion exhibits interesting temperature dependence of ΔV^\ddagger (and consequently pressure dependence of E_a). The generality of the equations shown above for a nominal rate constant k are straightforwardly applied to the case of the water diffusion coefficient D . Practically, we evaluate the fluctuation theory quantities as they are described above by generating an isobaric-isothermal ensemble of constant energy and volume trajectories, from each of which we extract a diffusion coefficient D_i .

13.3 Computational Methods

We have evaluated the quantities in the Maxwell relation using LAMMPS⁸¹ molecular dynamics simulations of 343 TIP4P/2005⁵ water molecules. A 200 ns NpT trajectory at 1 bar and 298.15 K was propagated using a three-chain Nosé-Hoover thermostat and barostat.^{83,84} A simulation timestep of 1 fs was used, and the thermostat and barostat damping parameters were 100 fs and 1 ps, respectively. The molecules were held rigid using the SHAKE algorithm with a 1.0×10^{-4} tolerance parameter. The Particle-Particle-Particle-Mesh (PPPM) method^{119,120} was used to calculate long-range electrostatic interactions (tolerance parameter of 1.0×10^{-4}). Tail corrections were included to achieve the correct density. From this simulation, 200,000 configurations, each separated by 1 ps, were used as starting points for 50 ps NVE trajectories. From each trajectory, the mean-squared-displacement, $MSD(t) = \langle |\vec{r}(t) - \vec{r}(0)|^2 \rangle$, was calculated for $t = 0$ to 20 ps with multiple time origins separated by 1 ps, the last 5 ps of which was fit to a line to compute $D_i = \text{slope}_i/6$. All uncertainties were calculated over 4 blocks and represent a 95% confidence interval based on the Student's t -distribution.¹²²

13.4 Results and Discussion

The remainder of this Chapter focuses on two objectives. First, we use the fluctuation theory for dynamics to calculate each of the terms involved in the Maxwell relation for the water self-diffusion coefficient from simulations at a single phase point (298.15 K and 1 bar). Second, we suggest that the Maxwell relation suggests a physically motivated, (relatively) global mathematical description for the water diffusion coefficient as a function of pressure and temperature and demonstrate its utility by fitting existing experimental data in the literature.

13.4.1 Contributions to the Maxwell Relation

From our simulations, we have evaluated the diffusion coefficient to be $(2.030 \pm 0.001) \times 10^{-5}$ cm²/s with our periodic boundary condition simulations. Using the correction for finite-size effects proposed by others,^{247,323} based on the shear viscosity of 0.855 cP for the TIP4P/2005 water model,³³⁵ we get $D = 2.332 \times 10^{-5}$ cm²/s. (The calculated quantities from the present simulations are included in Table 13.1.) which is in good agreement with our previously reported values,^{50,160}. Furthermore, we have used Eq. (13.12) to directly evaluate the activation energy and the activation volume from our simulations, and we find $E_a = 4.14 \pm 0.02$ kcal/mol and $\Delta V^\ddagger = -1.32 \pm 0.02$ cm³/mol, in good agreement with our previously reported results.^{59,309}

Hydrogen bond-exchanges are the primary mechanism for diffusion in liquid water,¹⁷⁸ and both the activation parameters reported here are consistent with that picture. The diffusion activation energy reported here is very close to the hydrogen bond exchange activation energy that we have calculated for TIP4P/2005 water, which we have found from an NVT simulation to be 3.79 ± 0.06 kcal/mol.¹³⁶ The negative activation volume for diffusion is related to the reduction of volume associated with moving towards the transition state of a hydrogen bond-exchange, when considering the three water molecules involved within that exchange.

The *rhs* of the Maxwell Relation involves the temperature derivative of the activation volume, $\beta(\partial\Delta V^\ddagger/\partial\beta)$. Of the three terms that contribution to this derivative as expressed in Eq. (13.16),

the last depends only on the product of the activation parameters discussed above which yield $\beta\Delta V^\ddagger E_a = -9.23 \pm 0.12 \text{ cm}^3/\text{mol}$. The second term, $-\beta(\partial\langle V_i\rangle/\partial\beta)$ is calculated as $\langle[\delta H_i + p\delta V_i] V_i\rangle$, obtained from the NpT simulation described in Sec. 13.3, and found to be $509.63 \pm 14.48 \text{ cm}^3/\text{mol}$. This term, within a factor of $1/(T\langle V_i\rangle)$, is the thermal expansion coefficient, α , which we find to be $(27.6 \pm 0.8) \times 10^{-5} \text{ K}^{-1}$, in reasonable agreement with the previously reported value of $28 \times 10^{-5} \text{ K}^{-1}$.⁵

The final term contributing to $\beta(\partial\Delta V^\ddagger/\partial\beta)$ is the cross-correlation term given in Eq. (13.21). The present calculations give this as $-521.33 \pm 17.13 \text{ cm}^3/\text{mol}$. Combined with the two terms discussed in the preceding paragraph, we see that the change in activation energy with temperature is determined by a significant cancellation between this cross-correlation term and the temperature dependence of the average volume, $-\beta\partial\langle V_i\rangle/\partial\beta$. The total result obtained for $\beta(\partial\Delta V^\ddagger/\partial\beta)$ from all three terms is $-20.93 \pm 3.49 \text{ cm}^3/\text{mol}$. Unfortunately, at present this value does not appear to be consistent with those described by the experiments that we will detail below; however, it is possible that in the future advanced sampling techniques will make it simpler to resolve this derivative. Note that the smaller error bars on $\beta(\partial\Delta V^\ddagger/\partial\beta)$, compared to those for the contributing terms, arises because the canceling terms have error that is correlated. Within the uncertainty of the components, there is still room for this value to change significantly in a way that would bring it into better agreement with the remainder of the results presented in this chapter.

This result indicates that as temperature increases, the activation volume should likewise increase (*i.e.*, the transition state structure for the H-bond exchange increases in size). This is consistent with previous measurements^{3,10} and our prior calculations⁵⁹ of the activation volume. For example, our calculations found that when the temperature increases from 283.15 to 473.15 K at 100 bar, ΔV^\ddagger increases from -2.43 to 6.13 cm^3/mol .

As expressed in the Maxwell relation, Eq. (13.7), the derivative of the activation energy with respect to pressure, $\partial E_a/\partial p$, contains the same information. We have evaluated it using Eq. (13.18), where the only terms involved that have not been discussed above are $-\partial\langle H_i\rangle/\partial p = \beta\langle\delta V_i H_i\rangle$ and $-\partial\langle V_i\rangle/\partial p = \beta p\langle\delta V_i V_i\rangle$. The calculations yield 509.35 ± 14.48 and $0.285 \pm 0.001 \text{ cm}^3/\text{mol}$,

respectively. Within a factor of $1/\langle V_i \rangle$, the latter term is the isothermal compressibility, κ_T , which we find to be $4.61 \pm 0.02 \text{ bar}^{-1}$, in good agreement with the reported value of $4.65 \pm 0.1 \text{ bar}^{-1}$.⁵

Combining the terms in Eq. (13.18) gives $\partial E_a/\partial p = -22.25 \pm 3.49 \text{ cm}^3/\text{mol}$. This is identical to what we obtain from the sum $\Delta V^\ddagger + \beta(\partial\Delta V^\ddagger/\partial\beta)$, as expected. Interpreting this value is may be simplified by expressing it as $(-5.32 \pm 0.83) \times 10^{-4} \text{ kcal}/(\text{mol bar})$. This makes it clear that increases in pressure lead to slight decreases in the diffusion activation energy, with substantial (on the order of kbar) changes required to significantly affect E_a .

13.4.2 Physically Motivated Description of $D(p, T)$

The Maxwell relation given in Eq. (13.7) and its origins suggest a way to describe the pressure and temperature dependence of a dynamical quantity in a physically motivated way. Here, we explore this approach for the particular case of the water self-diffusion coefficient, but it is completely general and could be equally well applied to reaction rate constants or dynamical timescales, as long as they are measures of activated processes.

The water diffusion coefficient (like other dynamical properties of liquid water) is well-known to be significantly non-Arrhenius.^{1-4,10,160} We can describe this behavior by a Taylor series expansion in p and β about a set of reference values

$$\begin{aligned} \ln D(p, \beta) &= \ln D(p_0, \beta_0) + \left. \frac{\partial \ln D}{\partial \beta} \right|_0 (\beta - \beta_0) \\ &+ \left. \frac{\partial \ln D}{\partial p} \right|_0 (p - p_0) + \frac{1}{2} \left. \frac{\partial^2 \ln D}{\partial \beta^2} \right|_0 (\beta - \beta_0)^2 \\ &+ \frac{1}{2} \left. \frac{\partial^2 \ln D}{\partial p^2} \right|_0 (p - p_0)^2 \\ &+ \left. \frac{\partial^2 \ln D}{\partial p \partial \beta} \right|_0 (p - p_0) (\beta - \beta_0), \end{aligned} \quad (13.22)$$

where the subscript "0" on the derivatives indicates evaluation at the reference point, p_0 and β_0 . However, we can identify the derivatives of $\ln D$ as the activation energy and volume so that this

can be written as,

$$\begin{aligned} \ln \frac{D(p, \beta)}{D(p_0, \beta_0)} &= -E_{a,0} \Delta\beta - \beta \Delta V_0^\ddagger \Delta p - \frac{1}{2} \left. \frac{\partial E_a}{\partial \beta} \right|_0 \Delta\beta^2 \\ &\quad - \frac{\beta}{2} \left. \frac{\partial \Delta V^\ddagger}{\partial p} \right|_0 \Delta p^2 - \left. \frac{\partial E_a}{\partial p} \right|_0 \Delta p \Delta\beta, \end{aligned} \quad (13.23)$$

with $\Delta\beta = \beta - \beta_0$ and $\Delta p = p - p_0$. Here, we have noted that, in this explicitly non-Arrhenius description, the activation energy and volume are functions of p and β so that $E_{a,0}$ and ΔV_0^\ddagger indicate their values at p_0 and β_0 .

Note that the Maxwell relation, Eq. (13.7) can be used to express the last term in Eq. (13.23), which, after some rearrangement, gives

$$\begin{aligned} \ln \frac{D(p, \beta)}{D(p_0, \beta_0)} &= -E_{a,0} \Delta\beta - \beta_0 \Delta V_0^\ddagger \Delta p - 2\Delta V_0^\ddagger \Delta\beta \Delta p \\ &\quad - \frac{1}{2} \left. \frac{\partial E_a}{\partial \beta} \right|_0 \Delta\beta^2 - \frac{\beta}{2} \left. \frac{\partial \Delta V^\ddagger}{\partial p} \right|_0 \Delta p^2 \\ &\quad - \beta_0 \left. \frac{\partial \Delta V^\ddagger}{\partial \beta} \right|_0 \Delta p \Delta\beta. \end{aligned} \quad (13.24)$$

These two formulas, Eqs. (13.23) and (13.24), can both be used to fit experimental measurements of the diffusion coefficient as a function of temperature and pressure. An advantage of these expressions is that the fitting parameters represent physically meaningful properties: the activation energy and volume and their first derivatives with respect to β and pressure that are the clearest measures of non-Arrhenius behavior.

We can illustrate and test the global description of the pressure and temperature dependence of the water diffusion coefficient by using Eq. (13.24), or its equivalent Eq. (13.23), to fit existing measurement data in the literature.¹⁻⁴ We consider results from four separate studies that have examined $D(p, T)$ for H₂O, primarily using NMR measurements, over different ranges of pressure and temperature.

We first consider the NMR tracer measurements by Woolf of THO diffusion in H₂O.⁴ Temperatures from 277 to 318 K and pressures from 1 to ~ 2400 bar were considered and the results

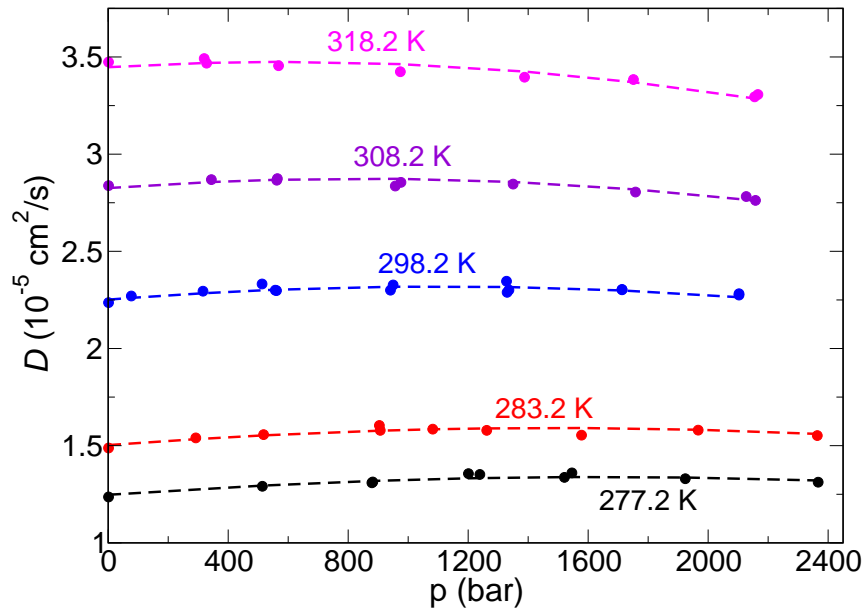


Figure 13.1: Comparison of measured $D(p, T)$ from Woolf⁴ (circles) compared to its fit (dashed lines) to Eq. (13.24).

are shown in Fig. 13.1 and compared to the fit to Eq. (13.24). The resulting fitting parameters are given in Table 13.1 and will be discussed below; note that six of the parameters are unique while $\partial E_a/\partial p$ and $\beta(\partial\Delta V^\ddagger/\partial\beta)$ are related through Eq. (13.7). Woolf fit the diffusion data to an eight-parameter expression that has the characteristics of a polynomial in $1/T$ and obtained a root-mean-squared deviation (RMSD) from the data of $0.014 \times 10^{-5} \text{ cm}^2/\text{s}$. The present fitting approach gives a comparable RMSD of $0.017 \times 10^{-5} \text{ cm}^2/\text{s}$ with two fewer parameters. Overall, Fig. 13.1 shows that Eq. (13.24) does an excellent job of describing the experimental data with an even representation of the data at all p and T .

One of the largest data sets for water diffusion was provided by Krynicki *et al.* based on proton spin echo NMR measurements.³ These data extend from 1 to 1700 bar and 275 to 498 K and are plotted in Fig. 13.2 where they are compared to their fit to Eq. (13.24). In this case, the fit is not as good as that in Fig. 13.1, with the most marked deviations occurring in the 298.2 and 472.2 K isotherms. In particular, the fit underestimates D at room temperature for all pressures and do so at 323.2 K for pressures above ~ 400 bar. At 472.2 K the fit underestimates the rate of decrease of D

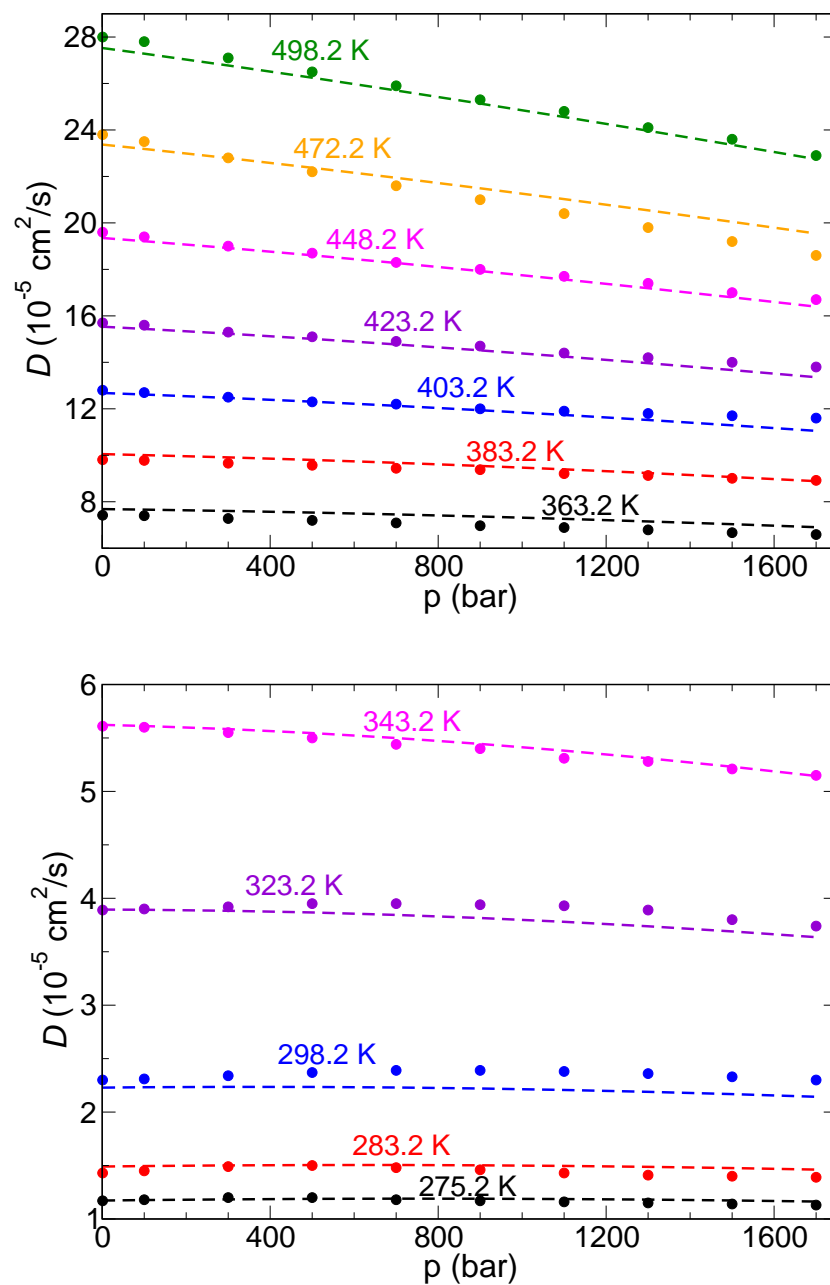


Figure 13.2: Comparison of measured $D(p, T)$ from Krynicki³ (circles) compared to its fit (dashed lines) to Eq. (13.24) at high (top panel) and low (bottom panel) temperatures.

| Quantity | Ref. 4 | Ref. 3 | Ref. 1 | Ref. 2 | TIP4P/2005 ^a | Units |
|---|--------|--------|--------|--------|-------------------------|--|
| D | 2.25 | 2.23 | 2.30 | 2.26 | 2.332 ± 0.001 | $10^{-5} \text{ cm}^2/\text{s}$ |
| E_a | 4.29 | 4.41 | 4.22 | 4.08 | 4.14 ± 0.02 | kcal/mol |
| ΔV^\ddagger | -1.33 | -0.43 | -0.77 | -1.33 | -1.32 ± 0.02 | cm^3/mol |
| $\frac{\partial E_a}{\partial \beta}$ | 5.15 | 2.07 | 3.40 | 4.20 | 4.33 ± 1.07 | $(\text{kcal/mol})^2$ |
| $\frac{\partial \Delta V^\ddagger}{\partial p}$ | 1.20 | 1.18 | 0.81 | 1.07 | 1.12 ± 0.20 | $10^{-3} \text{ cm}^3/\text{mol}/\text{bar}$ |
| $\frac{\partial E_a}{\partial p}$ | -5.29 | -3.25 | -3.52 | -2.86 | -22.25 ± 3.49 | cm^3/mol |
| $\beta \frac{\partial \Delta V^\ddagger}{\partial \beta}$ | -3.96 | -2.83 | -2.75 | -1.52 | -20.93 ± 3.49 | cm^3/mol |

^aThis work

Table 13.1: Summary of fits of Eqs. (13.23) and (13.24) to experimental measurements¹⁻⁴ and direct simulation results for TIP4P/2005 water. Values are for 298.15 K and 1 bar.

with increasing pressure. Beyond these deficiencies, however, the agreement is good for most of the temperatures and pressures explored; the average absolute error is 2.3%, on the same order of the error estimates of the measurements of 1.5-4%.

Harris and Woolf reported measurements of D for 277-333 K and for pressures up to 3000 bar.¹ It is worth noting that they observed some significant differences with the measurements of Krynicky *et al.*,³ the primary one being that the latter observed the maximum in D with increasing p at lower pressures than Harris and Woolf. The data from Ref. 1 are presented in Fig. 13.3 and compared to the result of fitting to Eq. (13.24). The fit is in excellent agreement with the measured D across the range of pressures and temperatures, with an average absolute error of $< 1\%$.

Finally, we consider NMR spin-echo measurements by Harris and Newitt aimed primarily at T below room temperature extending to pressures around 3500 bar.² Their results are plotted in Fig. 13.4 and compared to the present fit, which is in excellent agreement, even down to the lowest temperature of 253.2 K. It is important to note that the expansion in Eq. (13.23) or (13.24) is based on an assumption of a relatively smooth variation of D with pressure and temperature. It is thus not expected that it would accurately describe the dramatic slowdown in the diffusion coefficient (divergence of $1/D$) as the Widom line is approached upon lowering the temperature.^{6,145,146} We anticipate that the fitting approach described here will not be adequate at significantly lower temperatures. It is therefore all the more encouraging that the approach works satisfactorily down

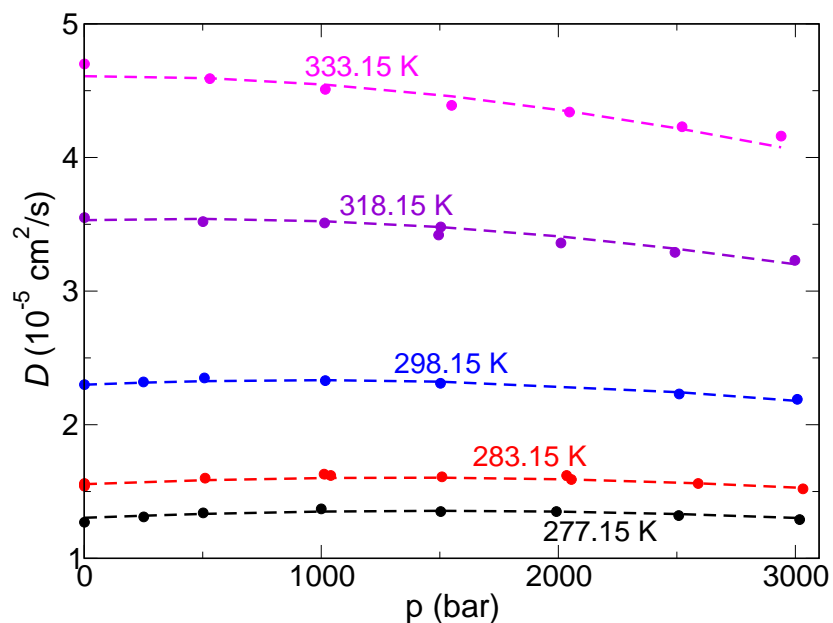


Figure 13.3: Comparison of measured $D(p, T)$ from Harris 1980¹ (circles) compared to its fit (dashed lines) to Eq. (13.24).

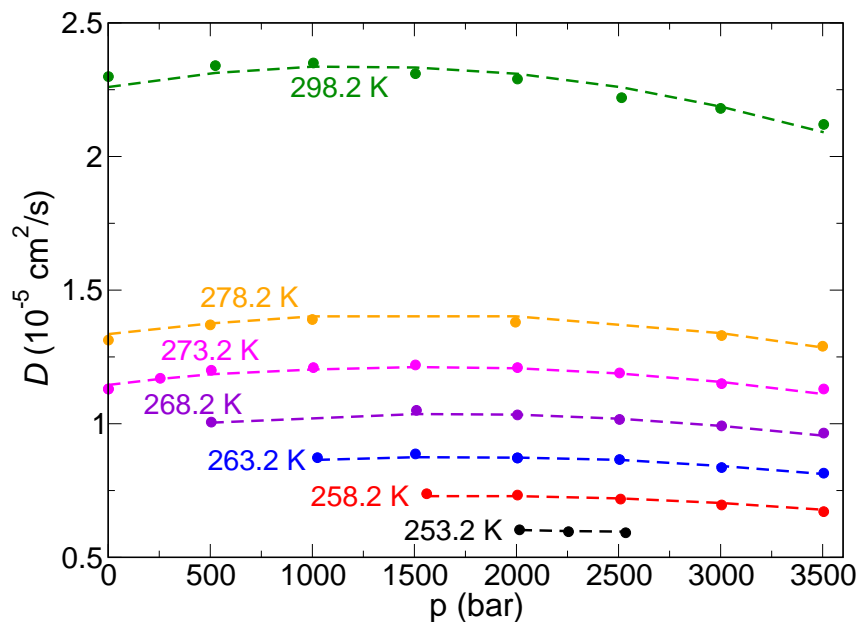


Figure 13.4: Comparison of measured $D(p, T)$ from Harris 1997² compared to its proposed fit to Eq. (13.24).

to such low T . The average absolute error with the data of Harris and Newitt is $< 1\%$ and the maximum error is $< 2\%$.

We now turn to an examination of the results of the fitting, namely, the optimized parameters obtained for each data set that are provided in Table 13.1. All the fits naturally give values of $D(1 \text{ bar}, 298.15 \text{ K})$ that are the same or close to the actual measured value. More interesting is the activation energy, for which values between 4.08-4.41 kcal/mol are obtained. These are close to the values of $E_a = 4.37$ and 4.33 found directly by Arrhenius analyses in Refs.⁴ and³, respectively. The results are also in good agreement with the present simulations. There is a greater spread in the values obtained for the activation volume. All of the fits give $\Delta V^\ddagger < 0$, as do our simulations, but with magnitudes that vary from -0.43 to -1.33 cm³/mol.

The other fitting parameters represent higher derivatives of the diffusion coefficient with respect to β and p . The non-Arrhenius behavior is most directly expressed in $\partial E_a / \partial \beta$, which has values of 2.07 to 5.15 (kcal/mol)² at 298.15 K and 1 bar based on the fitting. We note that this quantity can be written as

$$\frac{\partial E_a}{\partial \beta} = E_a^2 - \frac{1}{D} \frac{\partial^2 D}{\partial \beta^2}, \quad (13.25)$$

which indicates that it is determined by the cancellation of two opposing terms that are both significant in magnitude. It is this cancellation that makes it more challenging to determine with our fluctuation theory approach such that the current calculations cannot distinguish its sign outside of error bars (Table 13.1). Nevertheless, the TIP4P/2005 simulation results do overlap, with the lowest of the values obtained by fitting.

The situation is a bit clearer for the pressure dependence of the activation volume. This dependence is weak and found to be $(0.81 - 1.20) \times 10^{-3} \text{ cm}^3/(\text{mol bar})$. The TIP4P/2005 model gives a result, $(1.15 \pm 0.62) \times 10^{-3} \text{ cm}^3/(\text{mol bar})$, that is in good agreement with these values. Note that this derivative and the value of $\Delta V^\ddagger(p_0, \beta_0)$ indicate that the activation volume changes in sign as the pressure is increased, but this requires an increase of the pressure by $\sim 1000 \text{ bar}$.

Finally, the key elements of the Maxwell relation, Eq. (13.7), are also obtained from the fitting. Namely, $\partial E_a / \partial p$ is negative with values of -2.86 to -5.29 cm³/mol. This is related to $\beta(\partial \Delta V^\ddagger / \partial \beta)$

by ΔV^\ddagger and so is also negative with values of -1.52 to -3.96 cm³/mol.

Taken as a whole, while these fits do not quantitatively determine all the pressure and temperature dependencies of $D(p, T)$ to high precision due to differences between the data sets, they do present a consistent semi-quantitative physical picture across. The diffusion coefficient and activation energy are quite well determined and in agreement across the different measurements. Greater uncertainty exists in the activation volume and the higher derivatives, but the fitting approach illustrates how these fundamental properties of the diffusion coefficient can be determined given sufficiently extensive and accurate measurements.

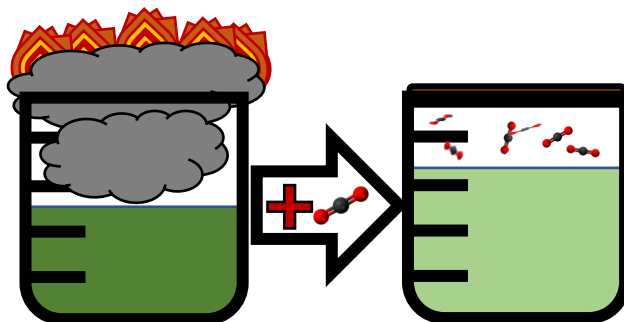
13.5 Conclusions

Thus, we have demonstrated the existence of a Maxwell relation for the diffusion coefficient and used it to create a global fitting function made up of physically motivated parameters. We found that this fitting function was able to describe experimental observables (*e.g.* activation energies, and activation volumes) with relatively high accuracy. We then demonstrated that many of these parameters were consistent with results calculated from simulations (with the exception of the simulation cross-derivative, which was difficult to calculate to high accuracy with present techniques). To the best of our knowledge, this is the first such global fitting function to describe diffusion temperature and pressure dependence in liquid water using only physically motivated parameters. Should the cross-derivative become easier to resolve with increased computational power in the future, this approach would provide the ability to predict the diffusion coefficient over a wide range of temperatures and pressures.

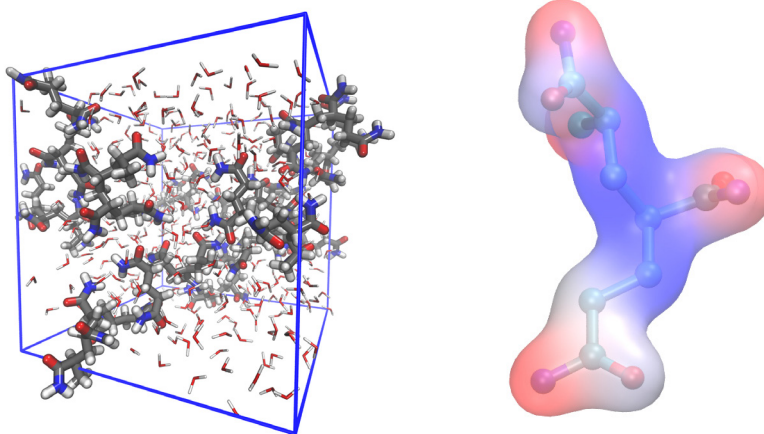
Part IV

Complex Systems

CO₂-Expanded Electrolytes



Polyacrylamide Hydrogels



In Part 4, we consider two systems that are not neat water. In Chapter 14 we describe the calculation of phase equilibria, shear viscosities, diffusion coefficients and diffusion activation energies in CO₂-expanded electrolytes and how they can be used to further our understanding of the role of electrolyte in those systems. Chapter 15 develops a simple model that demonstrates that water reorientation times are invariant with acrylamide polymer chain length in hydrogels.

Chapter 14

Vapor-Liquid Equilibria and Diffusion in CO₂-Expanded Electrolytes

14.1 Introduction

Recently, a class of reaction media for catalysis called carbon-dioxide (CO₂) expanded liquids (CXLs), in which a gas is dissolved in an organic solvent, has attracted significant and growing interest.^{336–338} Experimental studies have shown that CXLs provide the advantages of both traditional organic solvents and super-critical fluids, while reducing many disadvantages of both media.^{337–339} Specifically, CXLs have been seen to have pressure-tunable solubility of CO₂, a volume expansion effect that can result in a five-fold reduction in the amount of solvent as well as a decrease in viscosity and an increase in diffusion.^{337,339–342}

Recently, Shaughnessy *et al.* demonstrated the use of a CXL-based electrolyte (CXE) for the conversion of CO₂ to carbon monoxide (CO) could provide an order of magnitude enhancement in the reaction rate.³⁴³ Their experimental and simulation studies have demonstrated that this reaction rate enhancement occurs at an optimum CO₂ concentration, rather than increasing monotonically with CO₂ pressure due to increased electrical resistance at higher pressures. Recent work with a Re(CO)₃(bpy)Cl catalyst has demonstrated that reasonably low pressures of CO₂ lead to significant enhancements in the reaction rate.³⁴²

While CXLs have been studied in great detail both by experiment and simulation, to the best of our knowledge the COMSOL simulations by Shaughnessy and co-workers represent the bulk of the modeling work that has been done on CO₂-expanded electrolytes, there has been as of yet no

atomistic simulations of these systems.³⁴⁴ Experiments have shown that the addition of electrolyte decreases the volume expansion effect; however, it is not well understood whether this is a direct effect of the electrolyte or if it is a secondary effect of a reduction in the CO₂ solubility driven by the addition of electrolyte. Furthermore, currently little is known about the specific influence of the electrolyte on the transport of specific species within the liquid phase.

In the present work, we present molecular dynamics (MD) simulations of a model CO₂-expanded Acetonitrile (MeCN) electrolyte solution at constant CO₂ concentrations as a function of electrolyte concentration. Specifically, we have calculated the shear viscosity and the diffusion coefficients and have demonstrated that the addition of electrolyte leads to a higher overall viscosity and slower diffusion of both CO₂ and MeCN. We then use dynamical fluctuation theory to calculate the diffusion activation energy and use it and our diffusion results to demonstrate that the decrease in MeCN diffusion with increasing electrolyte concentration is well described by changes in the activation energy; however, the slowed CO₂ diffusion is due to a decreased activation entropy caused by preferential solvation.

14.2 Methods

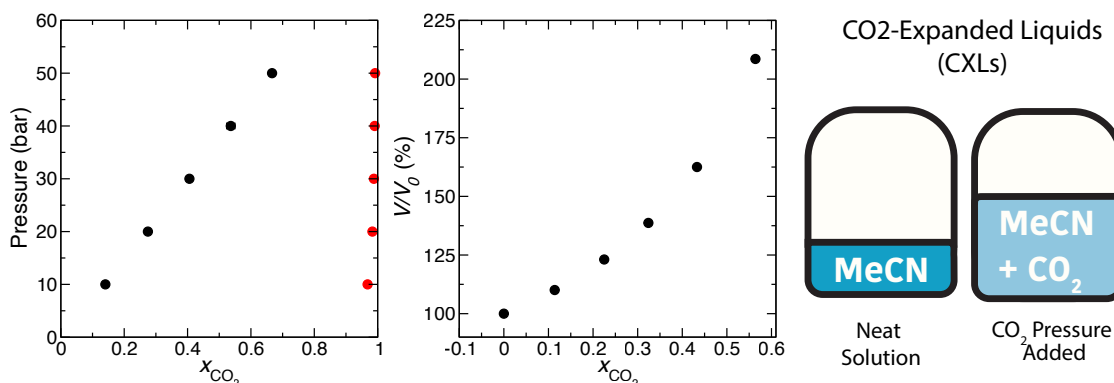


Figure 14.1: Left Panel: The vapor-liquid equilibrium for the binary MeCN-CO₂ mixture is presented. The liquid phase compositions are presented in black, the vapor phase compositions are presented in red. Middle Panel: The volume expansion for the binary mixture is presented. Right Panel: Schematic diagram of the volume expansion observed during the CO₂ expansion process.

14.2.1 Transport Properties

The shear viscosity, η_s , was calculated using the Green-Kubo (GK) relation,

$$\begin{aligned}\eta_s &= \frac{V}{k_B T} \int_0^\infty \langle P_{\alpha\beta}(0) P_{\alpha\beta}(t) \rangle dt \\ &\equiv \beta V \int_0^\infty C_{\eta_s}(t) dt,\end{aligned}\quad (14.1)$$

where $\langle \dots \rangle$ indicates an ensemble average, t is time, V is the simulation box volume, and $\beta = 1/(k_B T)$. The term $P_{\alpha\beta}$ represents the average of the five autocorrelation functions constructed from the anisotropic contributions to the stress tensor: P_{xy} , P_{yz} , P_{xz} , $(P_{xx} - P_{yy})/2$, and $(P_{yy} - P_{zz})/2$. In our simulations shear viscosities were averaged over time origins separated by 1.0 ps, and were calculated up to 5.0 ps. $C_{\eta_s}(t)$ were integrated using the trapezoid rule with a spacing between successive steps of 10.0 fs. Final values of η_s were extracted from an average over the last picosecond of the correlation function, in which it has already reached linearity.

Diffusion coefficients are calculated from MD simulations from the mean-squared displacement (MSD),

$$MSD(t) = \langle |\vec{r}(t) - \vec{r}(0)|^2 \rangle. \quad (14.2)$$

Here, $\vec{r}(t)$ is the time-dependent position vector corresponding to the molecular center of mass. From the MSD the diffusion coefficient can be extracted from our simulations through the relationship,

$$D_{PBC} = \lim_{t \rightarrow long} \frac{MSD(t)}{6t}, \quad (14.3)$$

where D_{PBC} is the diffusion coefficient extracted from our simulations under periodic boundary conditions. We have further calculated the finite-size corrections to the diffusion using our calculated values of the viscosity in the manner described by Yeh and Hummer.²⁴⁷ Thus, diffusion coefficients were reported as,

$$D = D_{PBC} + \frac{k_B T \xi}{6\pi\eta_s L} \quad (14.4)$$

where we have used the value $\xi \approx 2.837297$ as is reported in that work.

14.2.2 Activation Energies

In general, the activation energy of a dynamical quantity (*e.g.*, the diffusion coefficient) may be expressed as a derivative of that timescale with respect to $\beta = \frac{1}{k_b T}$, as

$$E_{a,D} = -\frac{\partial \ln[D]}{\partial \beta} = -\frac{1}{D} \frac{\partial D}{\partial \beta}, \quad (14.5)$$

where this derivative would generally be evaluated through a numerical derivative using the Arrhenius equation, $D = Ae^{-E_{a,D}\beta}$. This numerical method is not valid; however, for systems with a temperature-dependent chemical potential as is the case of CXEs, where the CO₂-composition is temperature dependent.

Recently, an extension of statistical mechanical fluctuation theory applied to dynamics has provided a means by which activation energies may be evaluated directly from simulations at a single temperature. This new technique avoids the requirement of running simulations at other temperatures, and thus avoids the above mentioned compositional challenges. Within the fluctuation theory description, the activation energy of the diffusion coefficient in Eq. 14.3 can be written as,

$$E_{a,D} = \frac{\lim_{t \rightarrow \text{long}} MSD_H(t)}{\lim_{t \rightarrow \text{long}} MSD(t)}, \quad (14.6)$$

where here $MSD_H(t)$ is the derivative of Eq. 14.2 with respect to β . This derivative can be written down directly as,

$$\begin{aligned} \frac{\partial MSD(t)}{\partial \beta} &= -\left\langle \delta H(0) |\vec{r}(t) - \vec{r}(0)|^2 \right\rangle \\ &= -MSD_H(t). \end{aligned} \quad (14.7)$$

Here $\delta H(0) = H(0) - \langle H \rangle$ is the fluctuation in energy from the average energy. Generally, the ratio in Eq. (14.6) is calculated as the ratio of the long time limit slopes of $MSD_H(t)$ and $MSD(t)$.

| MeCN | | | |
|--|----------|------------|----------|
| $k_{\theta} = 20 \text{ kcal}/(\text{mol } \text{Å}^2), \theta = 180^{\circ}$ | | | |
| Atom | σ | ϵ | Q |
| CH3 | 3.6 | 0.37955 | 0.269 |
| C | 3.4 | 0.09936 | 0.129 |
| N | 3.3 | 0.09936 | -0.398: |
| CO ₂ | | | |
| $k_{\theta} = 58 \text{ kcal}/(\text{mol } \text{Å}^2), \theta = 180^{\circ}$ | | | |
| Atom | σ | ϵ | Q |
| C | 3.033 | 0.15998 | 0.6512 |
| O | 2.757 | 0.05589 | -0.3256 |
| Electrolyte | | | |
| $k_{\theta} = 227 \text{ kcal}/(\text{mol } \text{Å}^2), \theta = 109.5^{\circ}$ | | | |
| Atom | σ | ϵ | Q |
| Li ⁺ | 2.2742 | 0.01828 | 0.8 |
| Cl | 3.996 | 0.2500 | 0.77984 |
| O | 3.5918 | 0.1561 | -0.39496 |

Table 14.1: Force Field Parameters

It should be noted that it has been shown previously that $E_{a,D} = E_{a,D_{PBC}}$.

14.3 Simulation Details

14.3.1 Force Fields

The MeCN force field developed by Edwards *et al.*³⁴⁵ and the EPM2 CO₂ force field³⁴⁶ were used for all simulations as the Edwards force field has previously been used successfully to describe electrolyte solutions^{347,348} and the EPM2 force-field has been typically been used in studies involving gas expansion.^{340,341,349–353} We have taken the AMBER force-field parameters for lithium,³⁵⁴ and the Ottoson *et al.*³⁵⁵ parameters for perchlorate and scaled the charges by a factor of 0.8 to prevent aggregation at the highest CO₂ concentrations. The aim of the present work is to determine a qualitative, rather than quantitative, description of the effect of inclusion of electrolyte in CXEs, thus such a scaling is reasonable. Force-field parameters for these models have been included in Table 14.1.

Intermolecular interactions were treated via a Lennard-Jones potential with a cutoff of 12.0 Å.

Long-range tail corrections were included and the Lorentz-Berthelot combining rules were used for unlike intramolecular interactions.^{79,80} For VLE simulations, the Ewald summation method was used to calculate long-range electrostatic interactions. A real space cutoff of 10 Å and 20 Å were used for the liquid and vapor phases, respectively. For molecular dynamics (MD) simulations, the Particle-Particle-Particle Mesh Ewald (PPPM) method used a real-space cutoff of 10 Å.^{119,120} For all simulations, the Ewald/PPPM accuracy parameter was set to 10^{-5} .

14.3.2 Vapor Liquid Equilibrium

Vapor-liquid equilibrium (VLE) were calculated from constant pressure Gibbs Ensemble Monte Carlo (μPT -GEMC)³⁵⁶ simulations using the open-source software *GPU-Optimized Monte Carlo* (GOMC).^{357,358} All VLE simulations consist of 1,000 CXL molecules, configurations were generated using PACKMOL.¹⁶² All VLE coexistence curves were calculated at a temperature of 298.15 K and were run in 10 bar increments from 10-50 bar for each ion concentration. Monte Carlo (MC) move frequencies of 0.35, 0.34, 0.01, and 0.30 were used for translation, rotation, volume, and swap moves, respectively. Simulations were equilibrated for 50,000 cycles, with a cycle being equivalent to 1,000 MC steps. Average compositions and densities were calculated over a 250,000 cycle production run. Reported uncertainties represent a 95% confidence interval taken from Student's t-distribution calculated by averaging over 5 blocks.¹²²

14.3.3 MD Simulations

Initial conditions for MD diffusion and mobility calculations are generated from the average density and CO₂ concentration calculated from the binary μPT -GEMC simulations using PACKMOL.¹⁶² The Large-scale Atomic/Molecular Massively Parallel Simulator (LAMMPS) was used for all Molecular Dynamics simulations.⁸¹

The MD simulations in the present work fall into three categories: 1) simulations of the volume expansion, 2) simulations of the dynamics, and 3) simulations to calculate activation energies. All MD simulations have been carried out at 1, 10, 20, 30, 40, and 50 bar, and at room temperature.

For all simulations involving a thermostat, a Nosé -Hoover thermostat of chain-length 3 was used with a thermostat damping parameter of 100.0 fs.^{83,84} For all constant pressure simulations, a barostat damping parameter of 1000.0 fs was used.^{226,227} All simulations were run with a simulation timestep of 1.0 fs, and the bonds of both MeCN and CO₂ were held rigid with the SHAKE algorithm.⁸² As with the VLE simulations above, reported uncertainties represent a 95% confidence interval taken from Student's *t*-distribution calculated by averaging over 5 blocks.¹²²

14.3.3.1 Volume Expansion Simulations

For the volume expansion MD simulations, a simulation cell consisting of 1,000 MeCN molecules was generated. For each volume expansion point an appropriate number of CO₂ were added to reach the CO₂ concentrations appropriate for the pressure, as calculated from the VLE simulations (see Table 14.2). Electrolyte molecules were added to reach mole fractions of 0.0, 0.02, 0.04, and 0.07. Each simulation was equilibrated for 1 nanosecond, following which a 5.0 nanosecond simulation was used as a production run. From this trajectory, average volumes were calculated at each pressure and volume expansions were calculated as $V/V_0 = V(P)/V(1\text{bar})$.

14.3.3.2 Transport Calculations

For the transport property calculations, MD simulations were run with 1,000 solvent molecules in the presence of 0, 1, 10, 20, and 40 pairs of the lithium perchlorate model electrolyte, where the 0 case corresponds to the binary system. Simulations were first equilibrated in the canonical ensemble (*NVT*) for 500 ps, followed by a 2 ns equilibration in the isothermal isobaric ensemble (*NPT*), the last half of which was used to determine the average density. The box size and coordinates were then remapped to this density and equilibrated in the *NVT* ensemble for a further 500 ps. Following equilibration, a 50 ns *NVT* trajectory was propagated from which dynamical and structural quantities were calculated.

| P | x_{CO_2} | N_{CO_2} | N_{MeCN} |
|-----|---------------------|-------------------|-------------------|
| 1 | 0.0 | 1 | 999 |
| 10 | 0.114 ₇ | 114 | 886 |
| 20 | 0.225 ₉ | 225 | 775 |
| 30 | 0.324 ₁₄ | 324 | 676 |
| 40 | 0.433 ₂₀ | 433 | 567 |
| 50 | 0.564 ₂₁ | 564 | 436 |

Table 14.2: GEMC concentrations and volume expansions, as well as solvent numbers. Uncertainties are included as subscripts.

| P | V/V_0 (%) | | | |
|-----|------------------------|---------------------------|---------------------------|---------------------------|
| | $x_{\text{LiClO}_4}=0$ | $x_{\text{LiClO}_4}=0.02$ | $x_{\text{LiClO}_4}=0.04$ | $x_{\text{LiClO}_4}=0.07$ |
| 1 | 100.0 | 100.0 | 100.0 | 100.0 |
| 10 | 110.0 ₁ | 110.1 ₁ | 110.1 ₁ | 110.1 ₁ |
| 20 | 123.1 ₁ | 123.1 ₁ | 123.1 ₁ | 123.1 ₁ |
| 30 | 139.7 ₁ | 138.6 ₁ | 138.6 ₁ | 138.5 ₁ |
| 40 | 162.5 ₁ | 162.4 ₁ | 162.2 ₁ | 162.2 ₂ |
| 50 | 208.6 ₂ | 208.3 ₁ | 208.0 ₁ | 208.0 ₂ |

Table 14.3: Volume expansions calculated as a function of pressure for each electrolyte concentration, x_{LiClO_4} .

14.3.3.3 Activation Energy Calculations

Configurations and momenta were saved every picosecond from each of the above described 50 ns trajectories. 20,000 of these configurations were used as initial conditions for 20 ps *NVE* trajectories, from which the derivative TCF was calculated as described above and activation energies were evaluated. Activation energies were calculated by fitting the derivative TCF and the unweighted TCF from 10-20 ps, and taking the ratio of the slopes in Eq. 14.6.

14.4 Results and Discussion

We have calculated the phase equilibria of CO₂-expanded MeCN without the inclusion of electrolyte from our GEMC simulations. These calculations have been explored previously for other combinations of force-fields^{340,359,360} however, we have included them here for completeness as the CO₂ concentrations calculated are necessary for the MD simulations that will be discussed

throughout the remainder of this Chapter. The binary phase diagram is included in Figure 14.1, and the system information is included in Table 14.2.

Furthermore, we have calculated the volume expansions of both the binary system, as well as the system with electrolyte. Interestingly, we found that adding electrolyte did not significantly quantitatively change the degree of expansion. As such, we have tabulated the values for the all electrolyte concentrations in Table 14.3, but have only plotted the binary volume expansion in Figure 14.1b. It should be noted that this is not consistent with the decrease in the volume expansion observed by Shaughnessy *et al.*;³⁴³ however, it has long been understood that the volume expansion is directly dependent on the concentration of CO₂.³⁶¹ Thus, this disagreement likely comes from the presence of electrolyte decreasing the solubility of CO₂ in the liquid phase in the experiments which is not a feature captured within the present simulations.

In the present investigation, we explore the dependence of the shear viscosity, the diffusion coefficient, and the diffusion activation energy on electrolyte concentration in order to better understand the effect of electrolyte on these properties under conditions of constant CO₂ concentration. Furthermore, we will demonstrate that electrolyte affects the diffusion of MeCN and CO₂ differently.

14.4.1 Viscosity and Diffusion

We have calculated the viscosity using Eq. (14.1) for each electrolyte concentration, the results of which are plotted in Figure 14.2a. The trends with CO₂ concentration are nearly identical for each electrolyte concentration, with the value of decreasing essentially linearly over the concentration range. Interestingly, at 50 bar, the viscosity value is essentially a factor of 2 smaller for every electrolyte concentration considered. On the other hand, the viscosity increases significantly as electrolyte concentration is increased, going from 0.243 cP in the binary system to 0.387 ± 0.004 cP at the highest electrolyte concentration for the simulations at 50 bar.

We have also calculated the viscosities for “neutralized” systems in which the electrolyte molecule net charges have been set to zero. These simulations, as described in detail in Support-

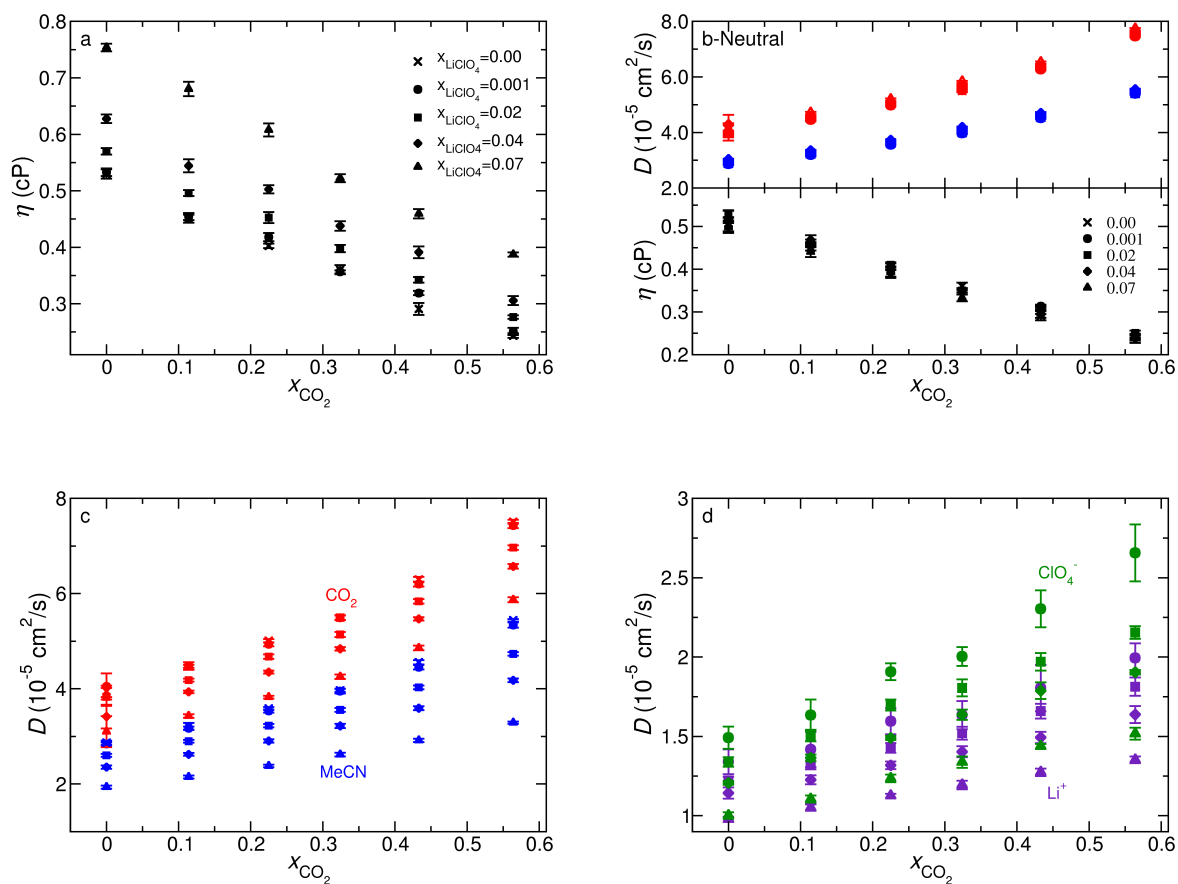


Figure 14.2: a) Shear viscosities as a function of CO₂ concentration. b) Diffusion coefficients for MeCN (blue) and CO₂ (red) and shear viscosities (black) for the "Neutralized" system. c) Diffusion coefficients for the "Charged" system for MeCN (blue) and CO₂ (red). d) Diffusion coefficients for the "Charged" system for Li⁺ (indigo) and ClO₄⁻ (green). Electrolyte concentrations are indicated in the figure legends.

ing Information, demonstrate essentially the same dependence of the viscosity on x_{CO_2} ; however, we find no significant dependence of the viscosity on the electrolyte concentration in those simulations. Thus, it is clear that it is the charge-charge interactions between the electrolyte and solvent that are causing the increased viscosity observed in our regular electrolyte system, rather than another colligative effect.

We have also calculated the diffusion coefficient using Eq. (14.2-14.3) as described in Methods and have included them in Figure 14.2b and Figure 14.2c. Reported diffusion coefficients also include the finite size corrections proposed by Yeh and Hummer as described in Eq. 14.4. These corrections are very important when examining diffusion in these systems due to the large changes in the shear viscosity with both CO_2 and electrolyte concentration described above.

For the “charged” system, we again find distinct trends with CO_2 and electrolyte concentration. As CO_2 concentration increases, there is a significant increase in the diffusion coefficient of all four species. Similarly, as electrolyte concentration is increased the diffusion coefficient of all species, including the electrolyte, is slowed. This has important implications for electrochemical experiments as it indicates that the presence of the electrolyte not only directly impacts the conductivity, but it also affects how quickly CO_2 is able to reach the reaction site in electrochemical experiments using this media. It also indicates that the electrolyte transport through the system is also very dependent on the electrolyte concentration.

We also consider the unitless quantities $D/D_{0,C} = D(P)/D(1 \text{ bar})$, $\eta/\eta_{0,C} = \eta(P)/\eta(1 \text{ bar})$, and $D/D_{0,E} = D(x_{\text{LiClO}_4})/D(x_{\text{LiClO}_4} = 0.0)$ which allow for direct comparison of the effects electrolyte and CO_2 concentration on the diffusion and viscosity. We have included plots of these ratios in Figure 14.3a and Figure 14.3b, respectively.

The ratio for the diffusion coefficients provides key mechanistic insight into the interplay between CO_2 -expansion and electrolyte concentration. For MeCN, both $D/D_{0,C}$ and $D/D_{0,E}$ are more widely spread than for CO_2 . Specifically, our results indicate that CO_2 -expansion enhances CO_2 -diffusion uniformly causing relatively little, to no, change to overall degree of the expansion effect on the diffusion coefficient. Alternatively, we find that as electrolyte is added the enhance-

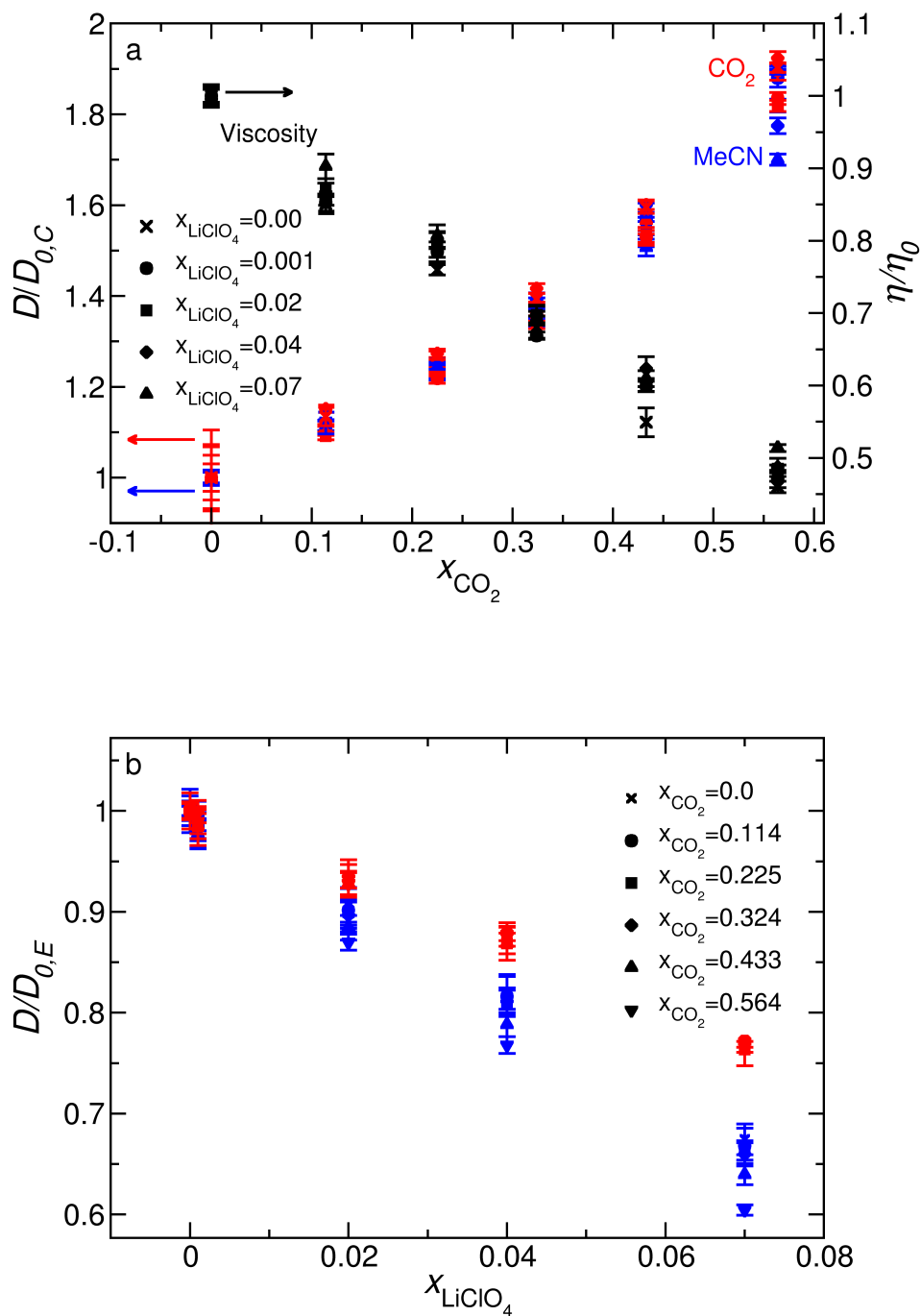


Figure 14.3: a) The ratio $D/D_{0,C}$ is shown on the primary axis. The ratio η/η_0 is shown in black. CO_2 results are shown in red, and MeCN results are shown in blue. Electrolyte concentrations are indicated in the figure legend. b) The ratio $D/D_{0,E}$ is shown. CO_2 results are shown in red, and MeCN results are shown in blue. CO_2 concentrations are indicated in the figure legend.

| MeCN | | | | | | | | | | | | | | | |
|---------|--------------------|--------------------|--------------------|-----------------------|-------------------|-------------------|-----------------------|-------------------|-------------------|------------------------|-------------------|-------------------|-------------------------|-------------------|-------------------|
| P (bar) | E_a^H (kcal/mol) | | | E_a^{LJ} (kcal/mol) | | | E_a^{KE} (kcal/mol) | | | E_a^{Ang} (kcal/mol) | | | E_a^{Elec} (kcal/mol) | | |
| | 0 | 20 | 40 | 0 | 20 | 40 | 0 | 20 | 40 | 0 | 20 | 40 | 0 | 20 | 40 |
| 1 | 1.17 ₈ | 1.27 ₁₁ | 1.46 ₁₀ | 0.23 ₄ | 0.22 ₄ | 0.31 ₆ | 0.57 ₅ | 0.62 ₈ | 0.68 ₆ | 0.15 ₃ | 0.19 ₃ | 0.19 ₄ | 0.22 ₃ | 0.24 ₄ | 0.29 ₄ |
| 10 | 1.19 ₈ | 1.21 ₇ | 1.39 ₉ | 0.22 ₅ | 0.19 ₄ | 0.26 ₆ | 0.62 ₅ | 0.62 ₅ | 0.65 ₇ | 0.17 ₄ | 0.15 ₃ | 0.19 ₄ | 0.18 ₄ | 0.25 ₄ | 0.29 ₇ |
| 20 | 1.05 ₅ | 1.20 ₅ | 1.31 ₁₀ | 0.18 ₅ | 0.21 ₆ | 0.23 ₅ | 0.55 ₅ | 0.59 ₅ | 0.63 ₅ | 0.14 ₃ | 0.15 ₃ | 0.15 ₅ | 0.18 ₄ | 0.24 ₄ | 0.30 ₄ |
| 30 | 1.05 ₉ | 1.10 ₆ | 1.24 ₈ | 0.18 ₃ | 0.17 ₄ | 0.21 ₆ | 0.56 ₈ | 0.59 ₇ | 0.60 ₄ | 0.12 ₃ | 0.11 ₃ | 0.14 ₄ | 0.19 ₄ | 0.22 ₃ | 0.29 ₅ |
| 40 | 0.93 ₁₁ | 1.11 ₁₂ | 1.14 ₁₀ | 0.15 ₄ | 0.16 ₅ | 0.16 ₄ | 0.49 ₈ | 0.57 ₆ | 0.54 ₆ | 0.11 ₃ | 0.15 ₄ | 0.16 ₄ | 0.18 ₄ | 0.24 ₅ | 0.29 ₃ |
| 50 | 0.94 ₅ | 0.99 ₁₂ | 1.19 ₁₁ | 0.10 ₃ | 0.14 ₅ | 0.13 ₆ | 0.54 ₄ | 0.54 ₅ | 0.58 ₈ | 0.11 ₃ | 0.09 ₆ | 0.13 ₄ | 0.19 ₄ | 0.23 ₅ | 0.33 ₄ |

| CO ₂ | | | | | | | | | | | | | | | |
|-----------------|--------------------|--------------------|--------------------|-----------------------|-------------------|-------------------|-----------------------|--------------------|--------------------|------------------------|-------------------|-------------------|-------------------------|-------------------|-------------------|
| P (bar) | E_a^H (kcal/mol) | | | E_a^{LJ} (kcal/mol) | | | E_a^{KE} (kcal/mol) | | | E_a^{Ang} (kcal/mol) | | | E_a^{Elec} (kcal/mol) | | |
| | 0 | 20 | 40 | 0 | 20 | 40 | 0 | 20 | 40 | 0 | 20 | 40 | 0 | 20 | 40 |
| 10 | 1.16 ₁₂ | 1.08 ₁₄ | 1.26 ₁₀ | 0.27 ₆ | 0.14 ₆ | 0.24 ₈ | 0.54 ₈ | 0.59 ₁₁ | 0.61 ₁₁ | 0.19 ₆ | 0.13 ₅ | 0.13 ₅ | 0.15 ₈ | 0.21 ₉ | 0.28 ₇ |
| 20 | 0.85 ₄ | 1.10 ₁₀ | 1.11 ₁₁ | 0.15 ₆ | 0.17 ₈ | 0.20 ₇ | 0.47 ₆ | 0.55 ₇ | 0.53 ₆ | 0.10 ₃ | 0.15 ₄ | 0.16 ₅ | 0.14 ₅ | 0.22 ₅ | 0.21 ₆ |
| 30 | 0.97 ₈ | 0.94 ₆ | 1.01 ₁₁ | 0.15 ₄ | 0.15 ₅ | 0.18 ₄ | 0.54 ₉ | 0.49 ₇ | 0.51 ₇ | 0.11 ₄ | 0.10 ₄ | 0.12 ₅ | 0.16 ₄ | 0.21 ₄ | 0.21 ₆ |
| 40 | 0.87 ₇ | 0.92 ₇ | 0.86 ₇ | 0.13 ₄ | 0.14 ₅ | 0.11 ₄ | 0.45 ₆ | 0.48 ₆ | 0.44 ₆ | 0.11 ₂ | 0.13 ₄ | 0.11 ₄ | 0.18 ₄ | 0.18 ₅ | 0.20 ₅ |
| 50 | 0.78 ₈ | 0.73 ₇ | 0.79 ₉ | 0.11 ₃ | 0.08 ₃ | 0.11 ₄ | 0.43 ₄ | 0.41 ₆ | 0.45 ₇ | 0.11 ₃ | 0.09 ₃ | 0.08 ₃ | 0.14 ₄ | 0.16 ₃ | 0.15 ₄ |

Table 14.4: Activation energy decompositions for both MeCN and CO₂ diffusion as a function of pressure and number of ions. Uncertainties in the final digits are included as subscripts.

ment of the MeCN diffusion coefficient is lessened. These results are consistent with a picture of MeCN preferentially solvating the electrolyte, thus weakening the expansion-induced enhancement of its transport. This can also be seen in Figure 14.3b where for a particular electrolyte concentration the ratio $D/D_{0,E}$ is independent of CO₂ concentration for CO₂ diffusion, but decreases for MeCN.

14.4.2 Activation Energies

To better understand these CXEs, we have used dynamical fluctuation theory to directly calculate the activation energy from our room temperature simulations as a function of CO₂ and electrolyte concentration as described in Methods. The dynamical fluctuation theory approach is ideally suited for application to CXEs as the solubility of CO₂ is dependent on temperature, thus calculation of activation energies through a traditional Arrhenius approach implicitly includes a contribution from this temperature dependent solubility.

Beginning with the binary system we present the total activation energy of MeCN diffusion as a function of CO₂ concentration in Figure 14.4a. As concentration of CO₂ is increased the MeCN diffusion activation energy decreases from 1.17 ± 0.08 kcal/mol when $x_{\text{CO}_2}=0.0$ to 0.94 ± 0.05 kcal/mol when $x_{\text{CO}_2}=0.564$. Figure 14.4b presents similar results for the diffusion activation energy

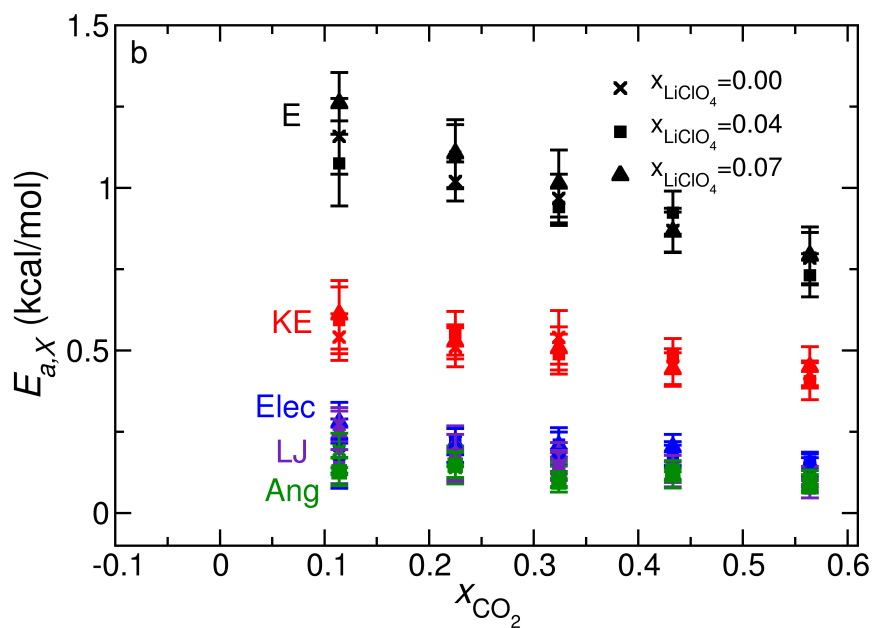
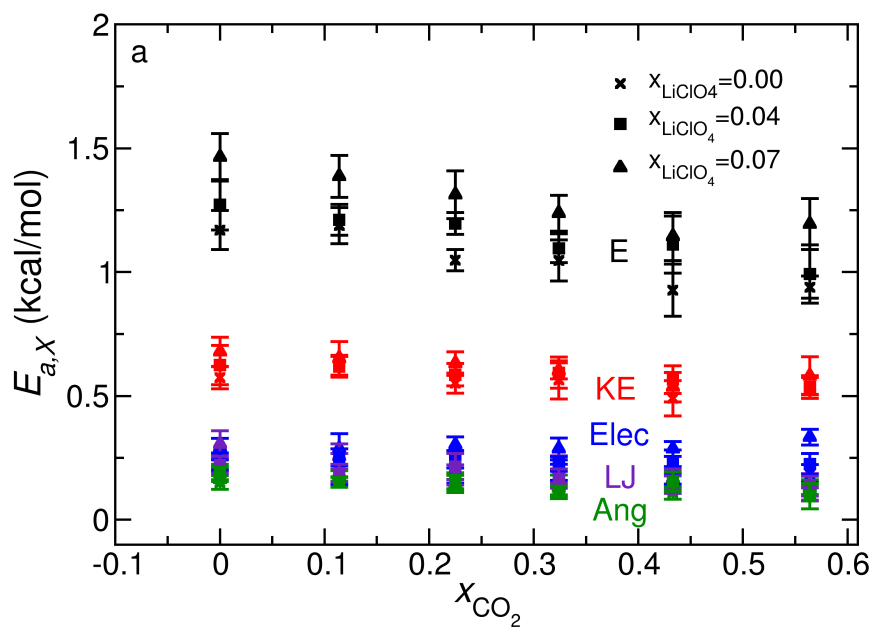


Figure 14.4: Activation energies for the highest concentration of electrolyte of a) MeCN, b) CO_2 as a function of pressure. The decomposition of the activation energy is presented in the figure legend.

of CO₂ over the same range of CO₂ concentrations. At the lowest concentration with CO₂ present ($x_{\text{CO}_2}=0.114$) the diffusion activation energy is 1.16 ± 0.12 kcal/mol, which then decreases to a value of 0.78 ± 0.08 kcal/mol as CO₂ concentration is increased. In both cases, these results are consistent with past and present observations that diffusion of both CO₂ and MeCN is enhanced within CO₂-expanded media. The larger decrease in the CO₂ activation energy over this range of pressures is consistent with the faster increase in D/D_0 observed for CO₂ diffusion compared to that of MeCN.

As the focus of this study is on the effect of electrolyte concentration on the transport properties within these CO₂-expanded electrolytes, we have also calculated the total activation energies for systems with 20 and 40 ion pairs present in addition to the binary system discussed above and included these in Figure 14.4a and 14.4b. We again observe that there is a decrease in both the MeCN and CO₂ activation energies as a function of increasing CO₂ concentration. As concentration of the ions increases the MeCN activation energy increases significantly (*e.g.*, from 1.17 kcal/mol in the binary to 1.46 kcal/mol with 40 ions) corresponding with the drop in the diffusion coefficients that we observe with increasing ion concentration. Interestingly, we do not observe this for the activation energies of CO₂ diffusion. Instead, we find that the CO₂ activation energies are essentially independent of ion concentration even though we observe similar slowdowns in the diffusion coefficient to what we observed for MeCN.

Within the fluctuation theory approach, activation energies can be decomposed according to the different types of molecular interactions in the system.¹³ In the present CO₂-expanded electrolyte system the activation energies can be subdivided into contributions from the Lennard-Jones potential energy, the electrostatic potential energy, the angle bending potential energy, and the kinetic energy, as

$$E_a = E_{a,\text{LJ}} + E_{a,\text{Elec}} + E_{a,\text{Ang}} + E_{a,\text{KE}}. \quad (14.8)$$

This decomposition can be understood within the context of the Tolman interpretation of activation energies, where activation energies are thought of as the amount of excess energy compared to "reactants" required to surmount the barrier to diffusion rather than being the electronic barrier

itself.¹⁸

Our activation energy decompositions are also included in Figure 14.4a and Figure 14.4b. At all pressures, we find that the largest contribution to both the MeCN and CO₂ diffusion activation energy comes from the kinetic energy. The other contributions from the Lennard-Jones potential energy, the angular bending potential energy, and the electrostatic potential energy contribute relatively similar amounts. Upon addition of electrolyte, the electrostatic contribution to the MeCN activation energy increases (*e.g.*, this contribution at 50 bar increases from 0.18 kcal/mol in the binary system to 0.33 kcal/mol at the highest electrolyte concentration). Over this same range the CO₂ electrostatic contribution doesn't increase within uncertainty (0.14 kcal/mol in the binary, 0.15 kcal/mol at the highest electrolyte concentration). In the following section, we will demonstrate that this increase is likely consistent with preferential solvation of the electrolyte by MeCN.

14.5 Discussion

In the remainder of this work, we will demonstrate using activation energies and activation entropies that the observed slowdown of CO₂ diffusion is consistent with preferential solvation of the electrolyte by MeCN creating an excluded volume into which CO₂ cannot diffuse.

14.5.1 Entropic Origin of Slowed CO₂ Diffusion

Activation energies in the NVT ensemble (as is the case in our simulations) can be described in terms of transition state theory as coming from the internal energy barrier (or enthalpic barrier) underlying the reaction coordinate. To better understand this, we turn to an Eyring-Polyani equation to look at the ratio between diffusion coefficients D_f/D_{ref} (here the subscripts indicate a state f , and a reference state ref),

$$\frac{D_f}{D_{\text{ref}}} = \exp \left\{ -\frac{\Delta\Delta A^\ddagger}{k_b T} \right\}, \quad (14.9)$$

where here $\Delta\Delta A^\ddagger = \Delta A_f^\ddagger - \Delta A_{\text{ref}}^\ddagger$ is the difference Helmholtz free energy of activation between f and ref . This can be further subdivided into a term related to the difference in activation entropies, $\Delta\Delta S^\ddagger$,

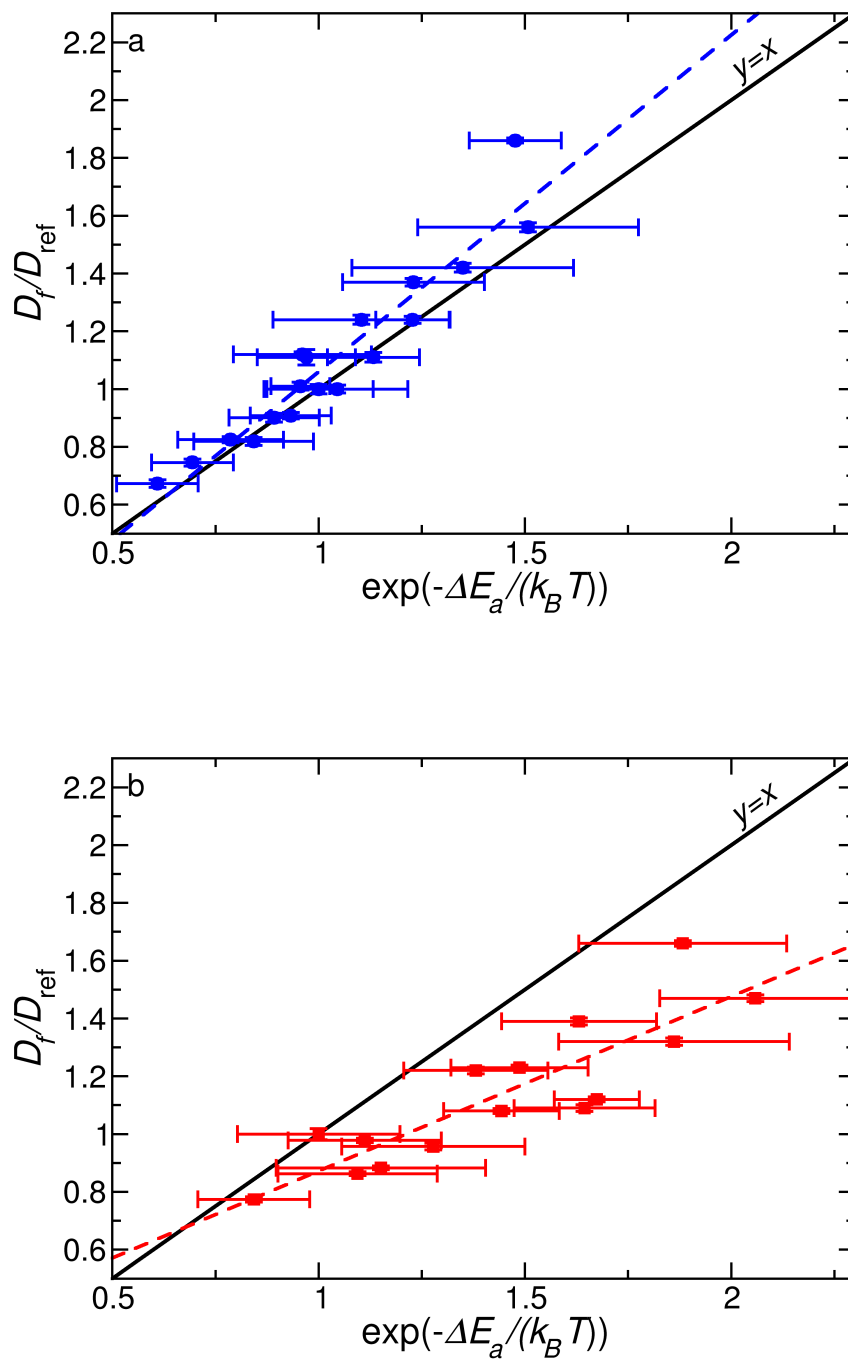


Figure 14.5: Comparison of D_f/D_{ref} and the arrhenius exponent corresponding to $\Delta E_a = E_{a,f} - E_{a,\text{ref}}$. MeCN results are included in panel a, CO_2 results are included in panel b. Linear fits are included as dashed lines. The line of constant entropy ($y = x$) is included as a solid black line.

and activation internal energies, $\Delta\Delta U^\ddagger$, between states f and ref, as

$$\frac{D_f}{D_{\text{ref}}} = \exp \left\{ -\frac{\Delta E_a}{k_b T} + \frac{\Delta\Delta S^\ddagger}{k_b} \right\} \quad (14.10)$$

where here we have made the replacement $\Delta\Delta U^\ddagger = \Delta E_a$ (and have made the assumption that there is minimal recrossing).

To explore this, we have selected our diffusion coefficient at 1 bar and no electrolyte, $D_{\text{ref}} = D(P = 1\text{bar}, x_{\text{LiClO}_4} = 0)$, as our reference state, and then mapped the ratio D_f/D_{ref} (here $D_f = D(P, x_{\text{LiClO}_4})$) against the corresponding exponential of the activation energy difference, $\exp \left\{ -\frac{\Delta E_a}{k_b T} \right\}$. We have included this in Figure 14.5 for both the diffusion of MeCN in panel a, and CO₂ in panel b for the entire pressure and electrolyte dependence of the diffusion coefficients investigated in the present study. This mapping scheme is convenient as it provides a measure of the differences in activation entropies between states f and "ref", values above the line $y = x$ indicate that state f has a larger activation entropy, whereas values below indicate that the activation entropy is reduced.

For MeCN diffusion, we find that that these quantities have a strong, linear correlation ($R^2 = 0.90$) with a slope greater than one (1.16), indicating that in general increasing either electrolyte concentration or pressure leads to an increased activation entropy for MeCN diffusion. With that said, the uncertainties in our calculated values for MeCN include the line $y = x$, indicating that the differences between observed diffusion coefficients comes primarily from the differences in the activation energy (and thus activation internal energy).

For CO₂ diffusion, we find a weaker linear correlation ($R^2 = 0.76$) with a slope significantly less than one (0.60), indicating that increasing electrolyte concentration or pressure leads to a decrease in the activation entropy. Importantly, unlike MeCN, many of the calculated values are resolved within uncertainty as not including the line $y = x$. Our present results indicate that increasing the electrolyte concentration decreases the activation entropy while the activation energy remains unchanged, leading to a slowdown of the diffusion coefficient. This decrease in the activation entropy likely comes from an excluded volume effect caused by MeCN molecules preferentially

solvating electrolyte molecules.

14.5.2 Activation Energy Decomposition

Importantly, our decomposition of the activation energy lends further support to our interpretation that the decreased activation entropy is responsible for the observed slowdown in the CO_2 diffusion coefficient as electrolyte concentration increases. Above, we found that the MeCN electrostatic contribution to the diffusion activation energy increases as electrolyte concentration is increased. This increase is consistent with a picture of MeCN preferentially solvating the electrolyte through attractive electrostatic interactions. To diffuse, MeCN needs to break free from these attractive charge-charge interactions leading to the higher electrostatic contribution to the activation energy. CO_2 on the other hand, has weaker interactions with the electrolyte and thus do not have the same attractive interactions to overcome to diffuse freely. Instead, the MeCN-electrolyte clusters act as excluded volumes into which CO_2 cannot diffuse.

14.6 Conclusions

In this Chapter, we have studied the viscosity and diffusion of a model CO_2 -expanded electrolyte. We have applied dynamical fluctuation theory to these systems in order to directly calculate the activation energies within this electrolyte at a single temperature over a range of pressures.

In particular, we have demonstrated that the addition of electrolyte leads to strong electrostatic interactions between MeCN and the electrolyte that leads to a significant increase in the shear viscosity. These same interactions lead to an increase in the MeCN diffusion activation energy, and an overall slowdown of MeCN diffusion. While CO_2 exhibits a similar slowdown, the present calculations indicate that this slowdown is likely related to a decrease in the available space for CO_2 to diffuse as seen by a decreasing activation entropy.

Chapter 15

Water Reorientation Times are Invariant with Acrylamide Chain Length

15.1 Introduction

Hydrogels are polymer materials that are heavily crosslinked by a combination of hydrogen and chemical bonds. These crosslinked polymers are able to absorb a significant amount of water, which has led to them being used for a wide range of applications in commercial products³⁶² (e.g. diapers, grow-in-water toys, and fire-retardant gels) and in biomedical applications^{363–366} (e.g. drug delivery, wound dressings, and contact lenses).

Hydrogels are a unique example of the nanoscale confinement of liquid water.³⁶⁷ Instead of confinement within a spherical cavity as is found in reverse micelles or within a cylindrical pore as found in nanoporous silica, hydrogels form a networked series of polymer threads with multiple channels in which water is confined.^{368,369} The mean channel diameter in a polyacrylamide (PAAm) hydrogel can range from 73–139 Å at low concentrations to 15–38 Å at higher concentrations.³⁶⁷

Recently, Yan and coworkers have studied PAAm hydrogels using ultrafast Infrared (IR) spectroscopy and have demonstrated that water confined in hydrogels exhibit generally slower dynamics than neat water, water molecules in hydrogels exhibit significantly faster dynamics than they do in reverse micelles of similar diameter.³⁶⁷ In reverse micelles (and in nanopores), dynamics of water are part of essentially two ensembles with interfacial waters exhibiting slowed dynamics, whereas the waters in the core of the confined region retain bulk-like character.^{201,368} In their ex-

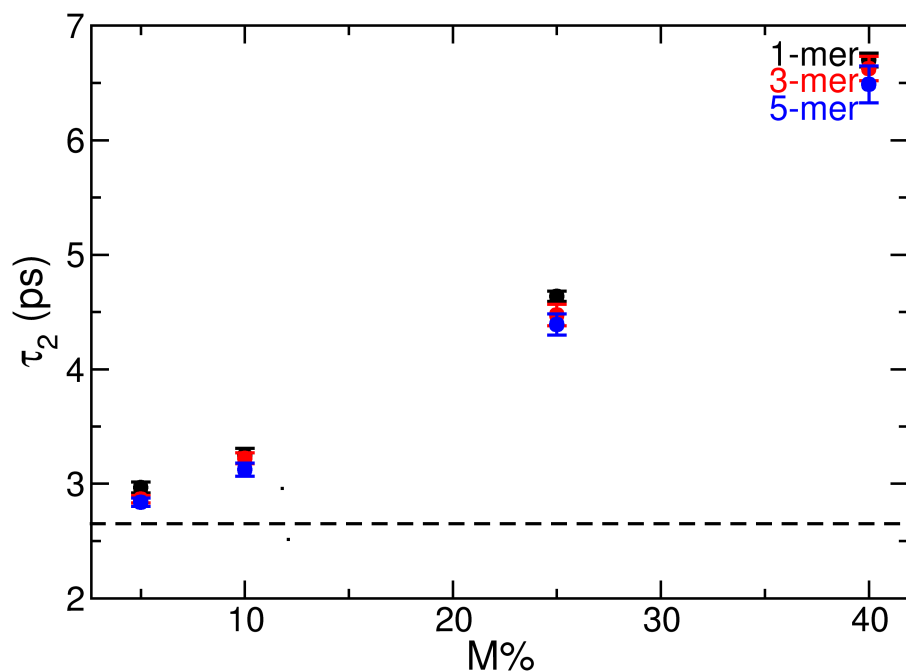


Figure 15.1: The reorientation time (τ_2) is presented for the 1-mer (black circles), 3-mer (red circles), and the 5-mer (blue circles). The neat water reorientation time ($\tau_{2,neat}=2.65$ ps) is included as a dashed black line.

periments with PAAm hydrogels, Yan and coworkers did not find evidence of this two-ensemble behavior and instead found that the presence of hydrogel acts to slow down dynamics of the confined waters as a single ensemble. They posited that this behavior was caused by the presence of sites on the polymer that are able to accept and donate hydrogen bonds (H-Bonds) with water, thus having a smaller impact on the hydrogen bond network than the anionic sulfonate groups inside reverse micelles or hydroxyl groups on the inside of silica pores.

Recent, currently unpublished, experiments from the same group (Michael Fayer - Stanford University) have found that water molecules at the same PAAm concentration exhibit similar orientational relaxation times whether or not polymer crosslinks are present. Indeed, for a range of polymer chain lengths, including the monomer, they find that the orientational relaxation time is essentially independent of the chain-length. The present simulation results, illustrated in Figure

| % | 1-mer | | | 3-mer | | | 5-mer | | |
|----|------------|-------|-------|------------|-------|-------|------------|-------|-------|
| | N_{PAAm} | N_w | L | N_{PAAm} | N_w | L | N_{PAAm} | N_w | L |
| 5 | 5 | 395 | 23.09 | 2 | 450 | 24.09 | 1 | 395 | 23.02 |
| 10 | 11 | 396 | 23.46 | 4 | 432 | 24.05 | 2 | 353 | 22.47 |
| 25 | 31 | 369 | 24.14 | 12 | 432 | 25.14 | 6 | 357 | 23.52 |
| 40 | 57 | 343 | 25.11 | 22 | 396 | 24.09 | 12 | 361 | 24.92 |

Table 15.1: Compositions and simulation cell side lengths for each of the polymer concentrations and chain-lengths.

15.1, demonstrate the same chain-length independence of the reorientation time. To this point, the origin of this chain length independence, and the above-described ensemble-like confined behavior of water dynamics are not well understood.

In the present work, we have undertaken molecular dynamics simulations of various concentrations of PAAm (with no crosslinks) in order to better understand the behavior of water dynamics within these unique confined materials. We will demonstrate that simulation results over the available experimental vibrational lifetime exhibit similar invariance of the orientational timescales with respect to chain-length; however, we will demonstrate that significant differences are observed after this vibrational lifetime. In the present work, we demonstrate that dynamics within these systems, including the longer time dynamics, are well described by a three-ensemble model where water molecules exhibit differing dynamics when hydrogen bonded to the polymer, when in the first solvation shell of the polymer, and when in the bulk.

15.2 Methods

15.2.1 System Details

We have simulated the 1-mer, 3-mer, and 5-mer variants of the PAAm polymer in aqueous solution at four mass concentrations (5%, 10%, 25%, and 40%). We have used the OPLS/All-Atom force field, built using the LiParGen Server, to describe PAAm Lennard-Jones parameters, charges, bond lengths and equilibrium angles, bond and angle force constants, dihedral, and improper parameters. Bond stretches and angle bends are described within this model by a harmonic potential function,

dihedrals and impropers are described in the usual way for OPLS.³⁷⁰⁻³⁷²

15.2.2 Solvation Shell Calculations

We have calculated the radial distribution function (RDF) between each of the sites on our PAAM molecules and the surrounding water molecules for each of the above described systems. The RDF can be calculated as,

$$g(r) = \frac{V}{N^2} \left\langle \sum_i \sum_{j \neq i} \delta(r - |\vec{r}_{ij}|) \right\rangle, \quad (15.1)$$

where here V is the volume, N is the number of molecules, and r is the distance. We have then used the first minimums calculated from the RDF to determine the occupancy of the solvation shell by counting molecules for the closest site that they are near.

We have roughly calculated the radial distribution functions between water oxygen atoms and the oxygen, carbon and nitrogen atoms on PAAM. We then used these to calculate the location of the minimum separating the first and second solvation shells, which we found to be largely independent of chain length and polymer concentration. As such, have selected a uniform criteria for calculating the cutoff distances based of a single set of parameters to define this solvation shell. For a water to be defined as part of the the solvation shell, one of the following is defined is true: $r_{O_{PAAM}O_w} \leq 3.25 \text{ \AA}$, $r_{N_{PAAM}O_w} \leq 3.5 \text{ \AA}$, or $r_{C_{PAAM}O_w} \leq 4.75 \text{ \AA}$.

We have then used this definition, as well as H-bonding criteria ($r_{O_wX} \leq 3.5 \text{ \AA}$, $r_{H_wX} \leq 2.45$, and $\theta_{H_wO_wX} \leq 30.0 \text{ deg}$, where X is a PAAM H-bond acceptor), to categorize the water OH groups into "HB" OHs that are H-bonded to PAAM, "1st" OHs that are not H-bonded to PAAM but are present in the first solvation shell, and "bulk" OHs that do not belong to either category. Clearly, there are further categorizations that could be added (for instance, OHs in the first solvation shell of two PAAM molecules); however, for simplicity in this work we consider only the above described categories.

15.2.3 Reorientation Correlation Function

The reorientation correlation function describes the loss of memory of particular OH orientation over time, and can be written in the form of a time-correlation function (TCF), as

$$C_2(t) = \langle P_2[\vec{e}(0) \cdot \vec{e}(t)] \rangle \quad (15.2)$$

where here, P_2 is the second legendre polynomial, and $\vec{e}(t)$ is the orientation of a unit vector pointing along the OH bond of water at time t . This TCF describes, within a factor of 0.4, the orientational relaxation measured from pump-probe IR spectroscopy.

In the present work, we calculate the reorientation correlation function for all water OHs in our simulations; however, we also calculate individual reorientation correlation functions for the "1st", "HB", and "bulk" categories described in the previous section. To accomplish this, we check the occupancy of the OH at $t = 0$ and then subdivide the reorientation TCFs based on this occupancy.

15.2.4 Simulation Details

We have built systems at the compositions described in Table 15.1 of PAAm and spc/e water using PACKMOL,¹⁶² and used a custom program to build a data file compatible with the Large Scale Atomic/Molecular Massively Parallel Simulator (LAMMPS) program,⁸¹ which we have used for all simulations in the present study.

All simulations in the NVT ensemble were undertaken using a Nosè-Hoover thermostat with a damping parameter of 100.0 fs at 298.15 K.^{83,84} All simulations in the NpT ensemble utilize the same thermostat along with a barostat with a 1000.0 fs damping parameter.^{226,227} All water molecules were held rigid using the SHAKE algorithm with a tolerance of 1.0×10^{-4} .⁸² All simulation cells were fully periodic. Electrostatic interactions were calculated using the Particle-Particle-Particle Mesh Ewald method, with a tolerance of 1.0×10^{-4} . All uncertainties reported are calculated over 5-blocks and represent 95% confidence intervals based on Student's t -distribution.¹²² All initial velocities (selected at any point) were chosen randomly from the Maxwell-Boltzmann

distribution.

Starting configurations were generated by equilibrating in the NVT ensemble for 1 nanosecond, before switching to the NpT ensemble for 2 nanoseconds, the last nanosecond of which was used to calculate the average volume. The simulation cell was then remapped to this average volume and simulated in the NVT ensemble again for a further 2 nanoseconds.

The above configurations were then used as the starting point for five separate simulations in which all of the atoms were given new velocities selected randomly from the Maxwell-Boltzmann distribution. Following this, a 2 ns NVT trajectory was propagated with only the last half used for calculating solvation shell occupancy, hydrogen bonding, and time-correlation functions. TCF time origins were separated by 1 picosecond, configurations were dumped every 10 fs, and correlation functions were calculated out for 50 ps.

15.3 Theoretical Model

Within our subdivision of the reorientation times into the categories of “HB”, “1st”, and “bulk” described above, the total observed reorientation time can be written as

$$\frac{1}{\tau_2} = \frac{f_{HB}}{\tau_{2,HB}} + \frac{f_{1st}}{\tau_{2,1st}} + \frac{f_{bulk}}{\tau_{2,bulk}} \quad (15.3)$$

where f_{HB} , f_{1st} , and f_{bulk} are the fraction of water OHs in each category.

The fraction of water OHs H-bonded to PAAm can be calculated as

$$f_{HB} = \frac{sN_{PAAm}n_{HB}}{2N_w}, \quad (15.4)$$

where N_{PAAm} is the number of PAAm molecules, s is the chain length, \tilde{n}_{HB} is the average number of OHs H-bonded to PAAm per monomer unit, and N_w is the number of waters.

To calculate f_{1st} , we turn to a simple model where PAAm mers are thought up of being made up of “end”, or “middle” groups. In this model, the 1-mer is made up of two halves of an end unit

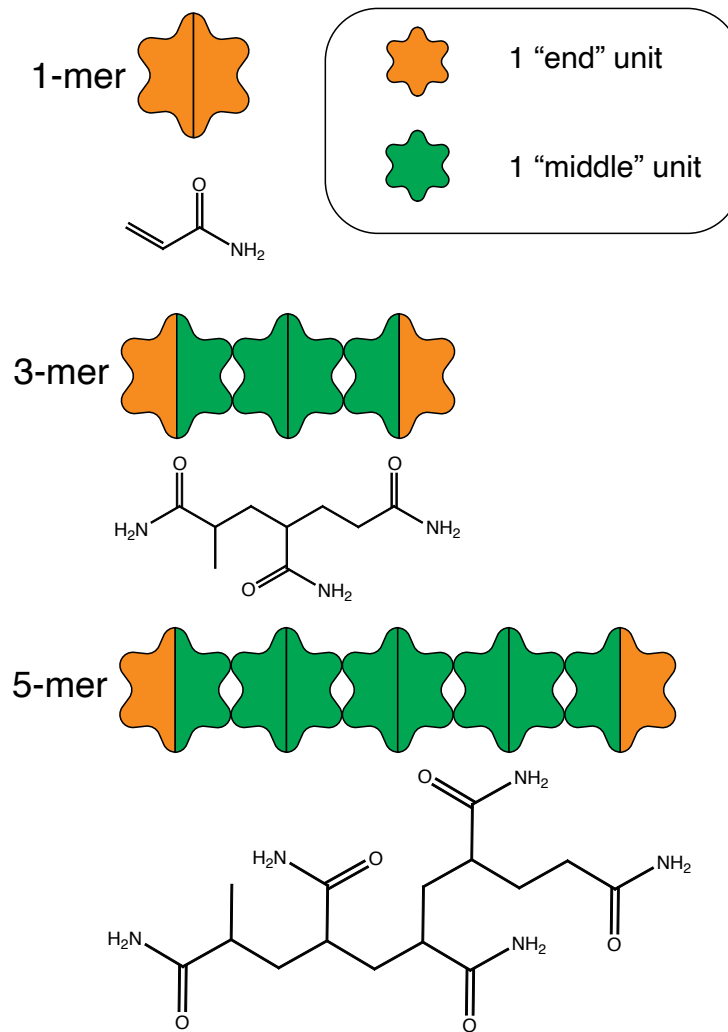


Figure 15.2: A schematic diagram of the simplified PAAm model, separating the mers into "end" groups (orange) and "middle" groups (green).

($1\tilde{n}_{end}$), the 3-mer is made up of one "end" unit and two "middle" units ($1\tilde{n}_{end} + 2\tilde{n}_{mid}$), and the 5-mer is made up of one "end" unit and four "middle" units ($1\tilde{n}_{end} + 4\tilde{n}_{mid}$). A schematic diagram of this model is included in Figure 15.2. Then, the total number of OH groups in the first solvation shell of PAAm can be written as $N_{1st} = N_{PAAm}(\tilde{n}_{end} - \tilde{n}_{mid}) + sN_{PAAm}\tilde{n}_{mid}$, giving the fraction of OHs in the first solvation shell to be

$$f_{1st} = \frac{N_{PAAm}(\tilde{n}_{end} - \tilde{n}_{mid})}{2N_w} + \frac{sN_{PAAm}\tilde{n}_{mid}}{2N_w}. \quad (15.5)$$

The fraction of bulk OHs may then be calculated as $f_{bulk} = 1 - f_{HB} - f_{1st}$, or

$$f_{bulk} = 1 - \frac{N_{PAAm}(\tilde{n}_{end} - \tilde{n}_{mid})}{2N_w} + \frac{sN_{PAAm}(\tilde{n}_{HB} + \tilde{n}_{mid})}{2N_w}. \quad (15.6)$$

Equations (15.4-15.6) can then be combined with equation (15.3) to find,

$$\begin{aligned} \frac{1}{\tau_2} &= \frac{1}{\tau_{2,bulk}} + \frac{N_{PAAm}}{2N_w}(\tilde{n}_{end} - \tilde{n}_{mid}) \left(\frac{1}{\tau_{2,1st}} - \frac{1}{\tau_{2,bulk}} \right) \\ &+ \frac{sN_{PAAm}}{N_w} \left[\tilde{n}_{HB} \left(\frac{1}{\tau_{2,HB}} - \frac{1}{\tau_{2,bulk}} \right) + \tilde{n}_{mid} \left(\frac{1}{\tau_{2,1st}} - \frac{1}{\tau_{2,bulk}} \right) \right]. \end{aligned} \quad (15.7)$$

Here, the chain length dependence appears only in the third term. However, by recognizing that,

$$M\% = \frac{M_{PAAm}(s)}{M_w} 100\% = \frac{sN_{PAAm}m_{PAAm,u}}{N_w m_w}, \quad (15.8)$$

where $M\%$ is the mass concentration, m_w is the molar mass of water, and $m_{PAAm,u}$ is the molar mass of the PAAm monomer. Then Eq. (15.7) can be re-written as,

$$\begin{aligned} \frac{1}{\tau_2} &= \frac{1}{\tau_{2,bulk}} + \frac{M\%m_w}{2m_{PAAm,u}s100\%}(\tilde{n}_{end} - \tilde{n}_{mid}) \left(\frac{1}{\tau_{2,1st}} - \frac{1}{\tau_{2,bulk}} \right) \\ &+ \frac{M\%m_w}{2m_{PAAm,u}100\%} \left[\tilde{n}_{HB} \left(\frac{1}{\tau_{2,HB}} - \frac{1}{\tau_{2,bulk}} \right) + \tilde{n}_{mid} \left(\frac{1}{\tau_{2,1st}} - \frac{1}{\tau_{2,bulk}} \right) \right], \end{aligned} \quad (15.9)$$

where here the chain length dependence is only found in the denominator of the second term, indicating that the chain length dependence of τ_2 is biggest for the monomer, and then becomes less significant as the chain length increases.

15.4 Results and Discussion

In the remainder of this work, we will demonstrate that the above-described theoretical model demonstrates qualitatively the origin of the chain-length independence, and that it describes the low-concentration behavior observed in our simulations quantitatively.

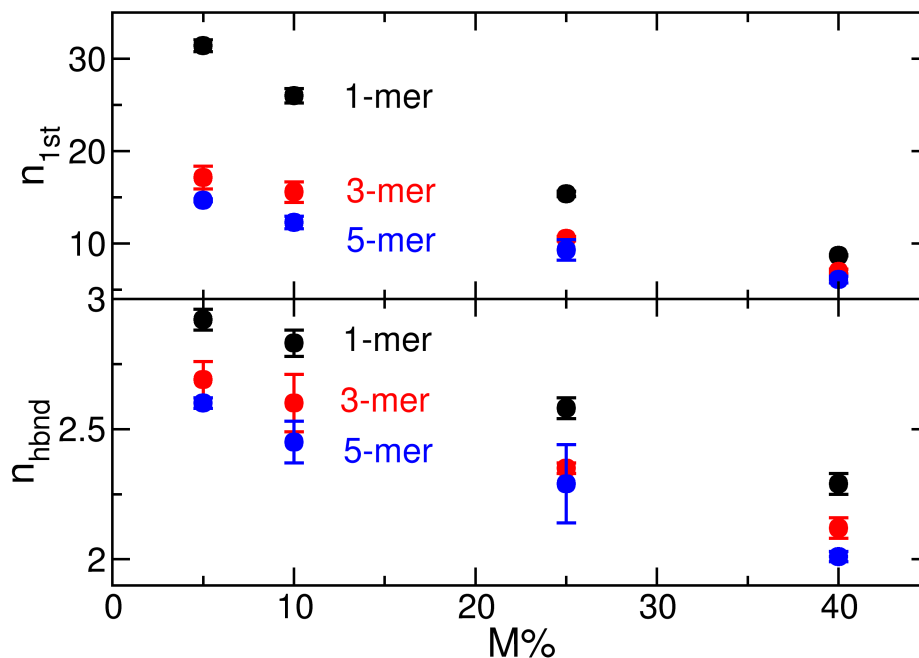


Figure 15.3: Counts (per monomer unit) of (top panel) OHs in the first solvation shell (but not H-bonded to PAAm) and (bottom panel) OHs H-bonded to PAAm. Results are presented for the 1-mer (black), 3-mer (red), and 5-mer (blue).

15.4.1 Categorization of OH groups

We have included our average values for the number of OHs that are H-bonded per-monomer unit (n_{HB}), as well as the average number of OHs in the first solvation shell of PAAm per monomer unit (n_{1st}) and have included both in Table 15.2 and in Figure 15.3. Both quantities decrease with increasing concentration; for example in the 3-mer n_{HB} decreases from 2.69 to 2.12 and n_{1st} decreases from 17.15 to 6.96.

15.4.2 Reorientation Times

The reorientation correlation function has been calculated for each of the PAAm chain lengths and concentrations. These have been fit to a single exponential function from 2-10 picoseconds (the range observable in experiment) to extract the reorientation time, τ_2 . The fitted timescales

| M% | n_{HB} | | | n_{1st} | | |
|-----|-------------------|--------------------|--------------------|---------------------|-----------------------|----------------------|
| | 1-mer | 3-mer | 5-mer | 1-mer | 3-mer | 5-mer |
| 5% | 2.92 ₄ | 2.69 ₇ | 2.60 ₂ | 31.42 ₆₅ | 17.15 _{1,24} | 14.67 ₁₆ |
| 10% | 2.83 ₅ | 2.61 ₁₁ | 2.45 ₈ | 26.00 ₇₉ | 15.57 _{1,1} | 12.28 ₆₈ |
| 25% | 2.58 ₄ | 2.35 ₂ | 2.29 ₁₅ | 15.37 ₃ | 10.53 ₂₆ | 9.31 _{1,12} |
| 40% | 2.29 ₄ | 2.12 ₄ | 2.01 ₂ | 8.72 ₆ | 6.96 ₂₆ | 6.11 ₃₆ |

Table 15.2: Counts (per monomer unit) of OHs H-bonded to PAAm and OHs in the first solvation shell.

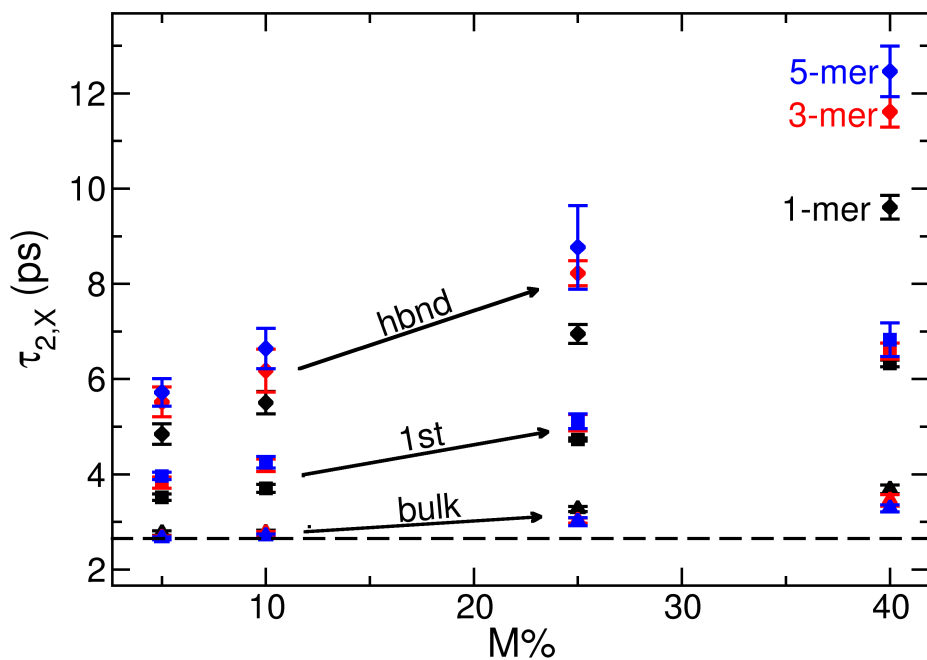


Figure 15.4: The categorized reorientation correlation times are presented for the 1-mer (black), the 3-mer (red), and the 5-mer (blue). 1st solvation shell values ($\tau_{2,1st}$) are included as squares, H-bonded values ($\tau_{2,HB}$) are included as diamonds, and bulk values ($\tau_{2,bulk}$) are included as upwards triangles. The neat water value ($\tau_{2,neat}=2.65$ ps) is included as a dashed black line.

| M% | τ_2 (ps) | | | $\tau_{2,1st}$ (ps) | | | $\tau_{2,hbond}$ (ps) | | | $\tau_{2,bulk}$ (ps) | | |
|-----|-------------------|--------------------|--------------------|---------------------|--------------------|--------------------|-----------------------|---------------------|---------------------|----------------------|--------------------|-------------------|
| | 1-mer | 3-mer | 5-mer | 1-mer | 3-mer | 5-mer | 1-mer | 3-mer | 5-mer | 1-mer | 3-mer | 5-mer |
| 5% | 2.97 ₅ | 2.87 ₄ | 2.84 ₄ | 3.52 ₇ | 3.83 ₁₂ | 3.96 ₈ | 4.84 ₂₂ | 5.52 ₃₂ | 5.72 ₂₉ | 2.77 ₅ | 2.67 ₄ | 2.66 ₃ |
| 10% | 3.25 ₇ | 3.22 ₅ | 3.12 ₆ | 3.71 ₉ | 4.19 ₁₄ | 4.25 ₁₂ | 5.51 ₂₄ | 6.18 ₄₅ | 6.64 ₄₂ | 2.77 ₆ | 2.76 ₄ | 2.70 ₅ |
| 25% | 4.64 ₅ | 4.47 ₁₀ | 4.39 ₁₀ | 4.73 ₄ | 5.09 ₁₈ | 5.11 ₁₅ | 6.95 ₂₀ | 8.22 ₂₆ | 8.77 ₈₈ | 3.27 ₅ | 3.03 ₆ | 3.01 ₉ |
| 40% | 6.70 ₇ | 6.63 ₁₁ | 6.49 ₁₆ | 6.33 ₈ | 6.59 ₁₈ | 6.83 ₃₆ | 9.61 ₂₅ | 11.61 ₃₂ | 12.46 ₅₃ | 3.68 ₁₀ | 3.45 ₁₂ | 3.28 ₈ |

Table 15.3: OH reorientation times calculated for each concentration and chain length of PAAm. Included are reorientation of all OHs (τ_2), OHs in the 1st solvation shell ($\tau_{2,1st}$), OHs H-bonded to PAAm ($\tau_{2,hbond}$), and OHs that are neither H-bonded to PAAm or in the first solvation shell ($\tau_{2,bulk}$).

are included in Figure 15.1. As the PAAm concentration increases the reorientation time gets increasingly slower; however, we see minimal dependence on chain length regardless of PAAm concentration. For instance, moving from a PAAm concentration of 5% to 40% τ_2 increases from 2.97 ps to 6.70 ps for the 1-mer and we see an almost identical increase from 2.84 ps to 6.49 ps for the 5-mer. These reorientation times have been tabulated in Table 15.3. All of these are longer than the reorientation time of neat water, which for SPC/E is about 2.65 picoseconds.

Using the information calculated in the previous section, we have calculated the reorientation correlation function for OHs that are in the first solvation shell of PAAm (but not H-Bonded) at $t = 0$ ps. We have included the timescales, hereafter referred to as $\tau_{2,1st}$, obtained by the same fitting procedure described above in Table 15.3. We find that these are all significantly slower than the neat reorientation time, and that like the results described above these increase significantly as PAAm concentration increases. Unlike the total results, we find that there is a moderate dependence on the chain length with higher chain lengths resulting in slightly slower reorientation in the first solvation shell (*e.g.*, 6.33 ps for the 1-mer and 6.83 ps for the 5-mer at 40%).

We have similarly calculated the reorientation correlation functions for OHs that are H-Bonded to PAAm at $t = 0$ ps. We have again extracted the timescales (hereafter referred to as $\tau_{2,HB}$) and included them in Table 15.3. These timescales exhibit the largest increase with chain length, increasing from 9.61 ps to 12.46 ps at 40% going from the 1-mer to the 5-mer. Lastly, we have calculated the reorientation correlation functions for OHs that are involved with neither of these categories (hereafter referred to as $\tau_{2,bulk}$). These results are generally independent of the chain

| Model Parameters | | | | |
|----------------------|-------------------|-------------------|---------------|----------------------|
| \tilde{n}_{HB} | \tilde{n}_{end} | \tilde{n}_{mid} | m_w (g/mol) | $m_{PAAm,u}$ (g/mol) |
| 2.60 | 31.42 | 10.02 | 18.01 | 71.08 |
| $\tau_{2,HB}(M\%)$ | = | 4.39 | + | 0.1639M% |
| $\tau_{2,1st}(M\%)$ | = | 3.26 | + | 0.0793M% |
| $\tau_{2,bulk}(M\%)$ | = | 2.55 | + | 0.0226M% |

Table 15.4: Model parameters used for Eq. 15.9.

length, with the exception of the highest concentrations due to a decreasing occupancy of this category. Furthermore, they are all relatively close to the neat value of 2.65 ps (for instance 2.77 ps for the 1-mer at 5% and 10%). We do see a slight increase of the bulk timescale as concentration increases indicating that this category isn't exactly bulk-like, likely because we have not consider water molecules in higher solvation shells.

Importantly, our results presently indicate that there are distinct populations of water molecules that exhibit different reorientation times surrounding PAAm molecules. Our simulation results do not exhibit the uniform slowdown noted by experiment;³⁶⁷ however, this could be related to issues with experimental resolution of these timescales.

15.4.3 Model Parameters

With the data calculated in the previous two subsections, we now have nearly all the pieces required by Eq. 15.9, with the exception of the three parameters (\tilde{n}_{HB} , \tilde{n}_{end} , and \tilde{n}_{mid}), as well as as a general set of timescales to use for the prediction. We can use the OH counts in Table 15.2 to calculate the average number of hydrogen bonds per monomer unit, \tilde{n}_{HB} , directly from our simulations at 5% (where there are relatively few water molecules bridging two PAAm molecules). We do this by averaging the 5% results for the 1-mer, the 3-mer, and the 5-mer which we find to be $\tilde{n}_{HB} = 2.74$.

Similarly, the value of \tilde{n}_{end} may be calculated from this data by recognizing that in the 1-mer, $\tilde{n}_{end} = n_{1st} = 31.42$, as the 1-mer is essentially made up of a single end unit. \tilde{n}_{mid} can then be calculated using the 3-mer as $\tilde{n}_{mid} = (sn_{1st} - \tilde{n}_{end})/(s - 1) = 10.02$ (for the 5-mer, this is 10.48 which is relatively close).

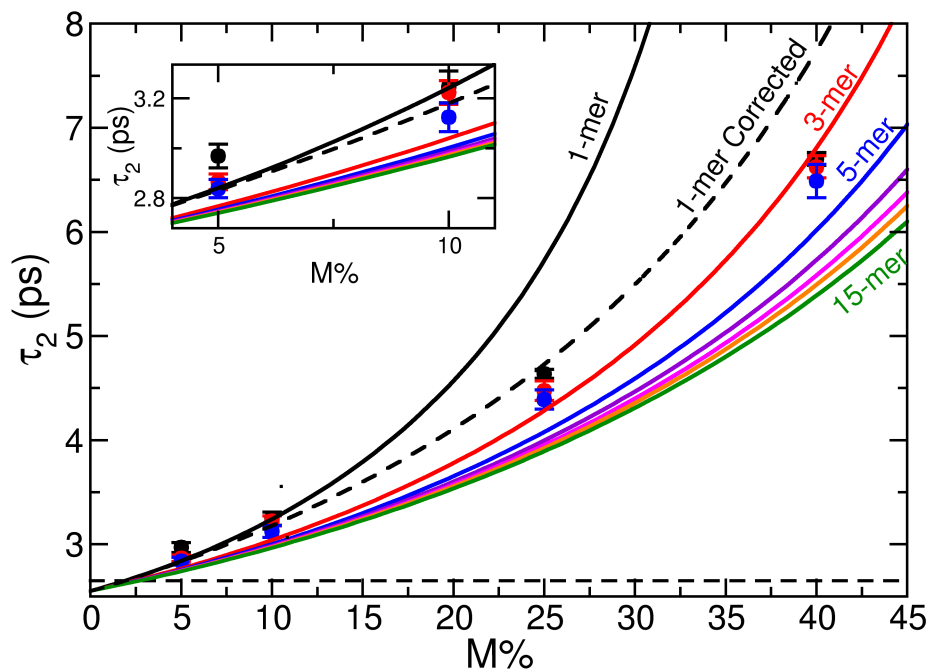


Figure 15.5: The total reorientation correlation times (τ_2) are presented for the 1-mer (black), the 3-mer (red), and the 5-mer (blue). The neat water value ($\tau_{2,neat}=2.65$ ps) is included as a dashed black line. We have included the results from our simple model, described by Eq. 15.9 using the parameters from Table 15.4 for the 1-mer (black), 3-mer (red), 5-mer (blue), 7-mer (purple), 9-mer (magenta), 11-mer (orange), and 15-mer (green). The inset figure shows the low concentration data, the main figure shows high concentrations. The 1-mer result corrected by s_{eff} is included as a black dashed line.

In order to create a simplified model, we have averaged the rate constants (inverse timescales) of each category to get values for $\tau_{2,HB}$, $\tau_{2,1st}$, and $\tau_{2,Bulk}$ that are independent of chain length. We have then linearly fit these values versus concentration (using all four concentrations) to develop our model. We have included a summary of the final selected model parameters in Table 15.4.

15.4.4 Chain Length-Independence

In Figure 15.5 we have plotted our model as a function of $M\%$ for varying chain lengths. Our model results demonstrate some dependence on the chain length moving from the 1-mer to the 5-mer; however, at higher chain-lengths this dependence becomes insignificant as the second term

of Eq. 15.9 gets smaller. This also demonstrates the likely origin of the experimental findings that PAAm hydrogels with polymer crosslinks and PAAm molecules without these crosslinks have similar reorientation times. Our model and simulation results demonstrate that the chain-length dependence is strongest at the shortest chain lengths; however, the observed differences in our simulation results are likely smaller than what could be observed experimentally.

Our model fails most significantly for the 1-mer at higher concentrations; however, it performs fairly well at the lowest concentrations (5% and 10%). Our model does not consider the influence of overlapping solvation shells, *e.g.* water molecules located within the first solvation shell of two different PAAm molecules. At the lowest concentrations these are quite rare; in the 5% solution of the 1-mer, 91.9% of non-bulk waters are in the solvation shell of exactly one PAAm molecule, 7.7% are in the solvation shell of exactly two PAAm molecules, and 0.4% are in the solvation shell of exactly three PAAm molecules. This changes only slightly for the 10% solution, with these numbers changing to 78.3%, 18.8%, and 2.6%, respectively. For this concentration, we see that a fourth population corresponding to waters in four or more solvation shells appears at around 0.3%. At the highest concentration, however, the fractions of waters in more than a single PAAm solvation shells increases significantly with 34% in exactly two, 24.3% in exactly three, 14.3% in four or more solvation shells, and only 27.4% in exactly one solvation shell.

This increasing population of water molecules in the first solvation shell of more than one PAAm molecule likely explains the failure of our model at higher concentrations. One way of thinking about this is that water molecules may be acting effectively as bridges between polymer molecules at higher concentrations, leading to faster timescales than our model predicts at these concentrations due to these “bridged” monomers having an *effective* chain length longer than the monomer by itself. This effect is present in the higher chain lengths that we have observed; however, to not the same extent. For instance, the 5-mer doesn’t have any population in three or more shells until the 25% solution, where this population is still small (2.4% in three shells, 0.3% in four or more). We can make a slight modification to our model, by calculating this effective chain length for the 1-mer as $s_{eff} = f_1 + 2f_2 + 3f_3 + 4f_4$, where f_X is the fraction of water molecules in

exactly X solvation shells. We have included a corrected 1-mer model result using this effective chain length as a dashed line in Figure 15.5, we see that it significantly corrects the behavior of the 1-mer bringing the model prediction at even 40% into relatively good agreement with our simulation results. This could potentially be improved further by the inclusion of fractions in larger numbers of solvation shells.

15.5 Conclusions

We have presented a simple model for the experimentally observed independence of the reorientation time in PAAm solutions on chain length. Within the proposed model, the total reorientation time is a combination of the reorientation times of OHs that are in the first solvation shell, hydrogen bonded to PAAm, and bulk. These timescales are scaled by the fraction of OHs in each of these categories. Specifically, we demonstrate that chain length dependence appears in the denominator of a single term involved in the model leading to independence for longer chains, consistent with experimental observations that the crosslinked polymer exhibits similar water dynamics to solutions without crosslinks. We also demonstrated that deviations in the model prediction for the 1-mer can be corrected by considering an effective chain length longer than the monomer.

Part V

End Matter

Chapter 16

Concluding Remarks, Outlook, and Technological Impediments

Overall, in this thesis we have presented the dynamical fluctuation theory approach which allows for the calculation of temperature and pressure derivatives of dynamical timescales from simulations at a single temperature and pressure. A key advantage of this approach is the fact that it allows for the direct decomposition of the activation energy into contributions from specific molecular interactions, providing deeper insight into the driving forces that underly these timescales. In the remainder of this chapter, we will summarize each part of my thesis and then provide a future outlook on where we believe the future work should be directed. In the final section, we will outline current technological limitations as well as a roadmap for looking at systems once they are overcome.

16.1 Activation Energies of Dynamical Timescales

In the first part of the thesis, we developed the dynamical fluctuation theory method, which allows for activation energies to be evaluated directly using simulations at a single temperature and pressure. We then applied this technique to calculate activation energies in liquid water for the diffusion coefficient, the OH and average reorientation times, the “jump” H-Bond exchange time, the reorientation of the H-Bond “frame” time, and the spectral diffusion time. Across this part, we were able to delve into the driving forces that underly these processes and found that all of these activation energies share a common theme of competition between a positive electrostatic contribution to the activation energy winning out over a negative contribution from the Lennard-Jones potential energy. This competition originates from the requirement of breaking an H-bond where

the water molecule moves from the first solvation shell to the second solvation shell, moving down from the repulsive wall of the Lennard-Jones potential and moving up from the attractive well of the Coulombic interactions.

Using these techniques, we were able to demonstrate that there is a resolvable difference in the activation energies of OH reorientation (measured by Infrared Pump-Probe Anisotropy) and average reorientation (measured by Nuclear Magnetic Resonance). We also demonstrated that the extended-jump model which outlines “jump” reorientation as an essential component of OH-reorientation, is consistent not only on the level of timescales but also is consistent on the level of activation energies, as well as mechanistically *via* their decompositions. We have also demonstrated that the “jump” time (and activation energy) are separately resolvable from the spectral diffusion time (and activation energy), indicating that these are two separate timescales found within liquid water rather than the same timescale as has been previously thought.

16.2 Water Under Extreme Conditions

In the second part, we discussed water at pressures and temperatures away from standard conditions. In particular, we demonstrated that dynamical fluctuation theory can be used to evaluate pressure derivatives in addition to the temperature derivatives calculated in the previous part. These pressure derivatives were then used to evaluate activation volumes, which measure the relative size of the transition state of a dynamical timescale compared to the reactant state, over a wide-range of temperatures and pressures in liquid water. We were able to demonstrate that these activation volumes were consistent with experimental results.

The remainder of this part has focused on the use of the calculated derivatives to predict the temperature and pressure dependence of dynamical and structural properties. We first demonstrated an extension to our developed fluctuation theory approach to calculate the second temperature derivative of dynamical timescales at room temperature, and then used them to predict the temperature dependence of these timescales deep into the supercooled regime. We developed methods for using a Van’t Hoff approach for using the first temperature derivative of the liquid

structure and the water infrared spectrum to predict their temperature dependence to high accuracy. We furthermore showed that a similar approach could be used to predict the pressure dependence by direct calculation of the molar volume using the derivative with respect to pressure.

16.3 Toward a Unified Picture of Water Dynamics

In the third part we expanded on the themes of the first two parts focusing on the H-Bond “jump” as the key underlying mechanism for most dynamical timescales in liquid water alongside the desire to predict these timescales over a wide range of temperatures and pressures. In particular, we discovered that the enthalpy change associated with an H-Bond exchange could be calculated from the oxygen-oxygen radial distribution function, and is strongly correlated with the activation energies observed for diffusion, reorientation, and H-Bond “jumps”. We then developed a physically motivated global fitting function using a dynamical Maxwell relation and used this function to fit a broad range of experimental data over T and P.

16.4 Complex Systems

In the final part we apply the dynamical fluctuation theory approach to a variety of systems outside of pure water in order to demonstrate its flexibility to study other systems. With it, we were able to identify a different role for enthalpy and entropy within the diffusion of CO₂-expanded electrolyte systems that originates from preferential solvation of electrolyte by acetonitrile. We furthermore developed a simple model for understanding the origin of chain-length independence in hydrogels in terms of the reorientation of water molecules in hydrogen bonded to the polymer, in the first solvation shell, and in the bulk. We demonstrated that it is only at longer chain lengths that the reorientation becomes essentially independent of the chain length.

16.5 Outlook

In this Section, some *low-hanging fruit* is briefly described that could provide interesting avenues of research. Many of these aspects will be discussed in greater detail in the next Chapter.

16.5.1 Maxwell Relations

A similar Maxwell relation to that derived in the third part of this thesis can be written for other dynamical timescales, and structural properties, and could potentially lead to further insights into these properties. Importantly, this could provide an avenue into developing a global fitting function for the liquid structure and other quantities. Furthermore, there is nothing in that derivation that requires the system to be liquid water. It would be interesting, for instance, to consider binary mixtures and dynamical Maxwell relations that depend on concentration.

16.5.2 Jump Diffusion Model

The present results within this thesis have furthered evidence that H-Bond exchanges play an integral role to diffusion; however, currently no theoretical framework like the extended-jump model which describes the relationship of these exchanges to reorientation exists presently for diffusion. Future work should continue to examine the underlying mechanisms of diffusion to look for such a diffusive “jump” model.

16.5.3 Other Quantities

There are a wide range of other quantities for which derivatives could be calculated, specifically, nearly anything that can be written as a thermal average can have fluctuation theory applied to it. In the next Chapter, a few of these quantities will be outlined; however, the list is not (yet) exhaustive. The software developed over the course of this thesis is fairly flexible and is likely able to calculate a fair number of additional quantities that have not been considered in the present study with minimal additional modification.

16.5.4 Other Derivatives

In the present thesis, we presented approaches for taking temperature and pressure derivatives. There are other derivatives that are possible with respect to chemical potential and potential parameters that could provide interesting directions for future study. For instance, could potential parameter derivatives be used to create an improved water model? Could the concentration dependence of the liquid structure in aqueous electrolytes be predicted from simulations at a single concentration? These, and more, are open questions that could be interesting to consider in the future.

16.5.5 Other Systems

There are a wide variety of systems that could, and should, be studied through the presently described approaches. Systems that should especially be of interest are those in which activation parameters are normally difficult to obtain because they change in nature with temperature or pressure (*e.g.* phase transitions, solutions, nanoconfinement), systems in which activation energy decompositions could provide unique insight (*e.g.* water around particular sites of biomolecules), and systems in which high accuracy resolution of the activation energy is desired.

16.6 Technological Impediments

16.6.1 Size Effects

The present approach that has been described throughout this work has performed generally well for the systems that have been studied thus far (on the order of 300 molecules, in general). There are two issues with the present formulation of the method that lead to non-ideal effects that prevent scaling the present methods to larger systems. The first is related to Computational Power and data storage, the second is related to the effect of system size on thermal fluctuations.

16.6.2 Computational Power and Data Storage

A key recurring issue with the current implementation of the method is that it requires the generation of anywhere between 4-20 separate files for each *NVE* trajectory. As future additions to the code are added it is likely that these numbers could increase significantly. Presently, for 50,000 trajectories this can lead to a million files (not including the other files required for the calculation to run - in general it can exceed 1.5 million). Effort should be made to create a more efficient method of storing these files in a compact way. Higher trajectory counts are possible, but place considerable strain on the file system. In addition to file counts, the storage space is also a frequent issue. Data is presently stored in python "pickle" files; however, care needs to be taken with these files as they are subject to changes in python version that can lead to incompatibilities. At some point, the log files from the trajectories should also be converted to these types of files as the logs are the largest source of used storage space.

A deeper issue is that presently the length of possible *NVE* trajectories is limited by the available computational power. Even 50 picosecond trajectories can significantly increase the length of time that the calculation takes. In general, it would be ideal if the present approaches could be incorporated directly within a Molecular Dynamics simulation package in order to better utilize storage and processing power.

16.6.2.1 *Ab Initio* Molecular Dynamics

At the time of the present study, the computational power is not available to study the present systems using *ab initio* molecular dynamics (AIMD) simulations due to the high computational expense of these types of simulations. Similarly, simulation methods that incorporate many-body effects and nuclear quantum effects are likewise computationally straining. Twenty years ago the available computational power would not have been enough to run many of the simulations involved in the present work. Hopefully computational power will continue to improve to such a point that fluctuation theory can feasibly be applied to *AIMD* simulations (which I estimate to be approximately the point where a 5 ns *AIMD* can be run in around a month).

16.6.3 Thermal Fluctuations

It is a well known quality from statistical mechanics that the relative size of the energy fluctuations, $\sqrt{\langle \delta E^2 \rangle} / \langle E \rangle$, decrease as $1/\sqrt{N}$ as the number of molecules are increased.²⁶ This presents an issue in our present approach which couples the fluctuation in energy to the diffusion coefficient as the system size is increased the energy fluctuations are less and less related to the motions of a particular molecule. A potentially improved approach would be to consider the energy fluctuations within a spherical shell around each molecule individually and weight the individual process, rather than the average over all molecules.

Chapter 17

Future Work

In this Chapter we present further details on avenues for future study, including the calculation of derivatives of other quantities (*e.g.* other time-correlation functions), other derivatives (*e.g.* derivatives with respect to potential parameters), and other systems (*e.g.* biomolecules).

17.1 Other Quantities

A wide range of other time correlation functions and distributions exist that have not been examined in the present work. In this thesis, derivatives of the mean-squared displacement, the first three orders of the reorientation correlation function (and the integrated reorientation correlation function), the jump (side-side) correlation function, the reactive-flux (flux-side) correlation function, the infrared spectrum, the frequency-frequency correlation function, and the radial distribution function were all calculated. This has also been demonstrated for the shear-viscosity Green Kubo relation in Ref. 50.

17.1.1 Raman Spectroscopy

There are however a significant number of remaining correlation functions that could be calculated. For instance, the Raman spectra is typically calculated through the relation

$$I_{iso}(\omega) = \frac{1}{2\pi} \int_{-\infty}^{\infty} e^{-\omega t} \phi_{iso}(t) dt \quad (17.1)$$

where

$$\phi_{iso}(t) = \left\langle \alpha_{01}(0) \alpha_{01}(t) e^{i \int_0^t \omega(\tau) d\tau} \right\rangle e^{-\frac{|t|}{2T_1}}. \quad (17.2)$$

Here, ω is the frequency, T_1 is the vibrational energy relaxation time, and α_{01} is the transition polarizability between the ground and first-excited vibrational states. $\alpha = (\alpha_{xx} + \alpha_{yy} + \alpha_{zz})/3$ for the isotropic lineshape. Thus, the derivative of the isotropic Raman lineshape can be written as

$$\frac{\partial I_{iso}(\omega)}{\partial \beta} = -\frac{1}{2\pi} \int_{-\infty}^{\infty} e^{-i\omega t} \phi_{iso,H}(t) dt, \quad (17.3)$$

where

$$\phi_{iso,H} = -\frac{\partial \phi(t)}{\partial \beta} = \left\langle \delta H(0) \alpha_{01}(0) \alpha_{01}(t) e^{i \int_0^t \omega(\tau) d\tau} \right\rangle e^{-\frac{|t|}{2T_1}}. \quad (17.4)$$

A similar approach could be used to calculate derivatives of lineshapes from other types of spectroscopies, for instance two-dimensional infrared spectroscopy, and sum-frequency generation.

17.1.2 Dielectric Relaxation

Another time-correlation that may be of interest is the dipole-moment correlation function³⁷³ which describes dielectric relaxation through the relation

$$\frac{\epsilon' + i\epsilon''}{\Delta\epsilon} = 1 - i\omega \int_0^{\infty} P_1(t) e^{-i\omega t} dt, \quad (17.5)$$

where ϵ' is the frequency dielectric constant, ϵ'' is the dielectric loss, and $\Delta\epsilon$ is the dielectric strength. Here,

$$P_1(t) = \frac{\langle \mathbf{M}(0) \mathbf{M}(t) \rangle - \langle \mathbf{M}(0) \rangle^2}{\langle \mathbf{M}(0) \mathbf{M}(0) \rangle - \langle \mathbf{M}(0) \rangle^2}, \quad (17.6)$$

where $\mathbf{M}(t)$ is the dipole moment of the simulation box at time t . The derivative of $P_1(t)$ is

$$\begin{aligned} \frac{\partial P_1(t)}{\partial \beta} &= \frac{2\langle \mathbf{M}(0) \rangle \langle \delta H \mathbf{M}(0) \rangle + \langle \delta H \mathbf{M}(0) \rangle}{\langle \mathbf{M}(0) \mathbf{M}(0) \rangle - \langle \mathbf{M}(0) \rangle^2} \\ &+ \frac{\langle \mathbf{M}(0) \rangle^2 [2\langle \mathbf{M}(0) \rangle \langle \delta H \mathbf{M}(0) \rangle - \langle \delta H \mathbf{M}(0) \mathbf{M}(0) \rangle]}{[\langle \mathbf{M}(0) \mathbf{M}(0) \rangle - \langle \mathbf{M}(0) \rangle^2]^2} \\ &+ \frac{\langle \mathbf{M}(0) \mathbf{M}(t) \rangle [\langle \delta H \mathbf{M}(0) \mathbf{M}(0) \rangle - 2\langle \mathbf{M}(0) \rangle \langle \delta H \mathbf{M}(0) \rangle]}{[\langle \mathbf{M}(0) \mathbf{M}(0) \rangle - \langle \mathbf{M}(0) \rangle^2]^2}, \end{aligned} \quad (17.7)$$

where only the final term is time-dependent. As we did above for the Raman spectrum, we can take the derivative of Eq. 17.5 as

$$\frac{\partial}{\partial \beta} \left[\frac{\varepsilon' + i\varepsilon''}{\Delta \varepsilon} \right] = -i\omega \int_0^\infty e^{-i\omega t} \frac{\partial P_1(t)}{\partial \beta} dt. \quad (17.8)$$

Here, it should be noted that the dielectric strength can be expressed as

$$\Delta \varepsilon = \frac{4\beta\pi \langle \mathbf{M}(0) \rangle^2}{3V} \quad (17.9)$$

where here V is the volume. Thus, the derivative of this dielectric strength can be written as

$$\frac{\partial \Delta \varepsilon}{\partial \beta} = \frac{4\pi [\langle \mathbf{M}(0) \rangle^2 - \beta \langle \delta H \mathbf{M}(0) \rangle^2]}{3V}. \quad (17.10)$$

Thus this provides a means of studying the temperature dependence of the dielectric relaxation as a function of frequency.

17.1.3 Non-Equilibrium Methods

There are many other TCFs that could benefit from such temperature derivatives, for instance those involved in non-equilibrium methods and reverse nonequilibrium molecular dynamics methods. These could potentially provide an approach for a better estimate of the viscosity activation energy (instead of the Green-Kubo approach).

17.1.4 Weighted Histogram Analysis Method

The weighted histogram analysis is a key method for determining the potential of mean force (PMF) along a particular coordinate (or set of coordinates).³⁷⁴ The method operates running a set of simulations with bias potentials each placed at a different location along the coordinate of interest. For instance, in the case of a distance coordinate the total unbiased distribution can be calculated using the equations,

$$\langle p(r) \rangle = \frac{\sum_{i=1}^{N_w} N_i \langle p(r) \rangle^{(i)}}{\sum_{i=1}^{N_w} N_i e^{-\beta [U_{bias}^{(i)}(r) - F_i]} \quad (17.11)$$

and

$$F_i = -\frac{1}{\beta} \ln \left[\sum_{r_{bins}} e^{-\beta U_{bias}^{(i)}(r)} \langle p(r) \rangle \right]. \quad (17.12)$$

Here, $\langle p(r) \rangle$ is the unbiased distribution, N_w is the number of simulation windows run along the coordinate r , $\langle \tilde{p}_i(r) \rangle$ is the unbiased distribution calculated from window i , N_i is the total number of measurements of the collective variable in window i , $U_{bias}^{(i)}(r)$ is the value of the bias potential of window i at a distance r , and F_i is the free energy shift of window i . Beginning with an initial guess for the set of free energy shifts, $\{F_i\}$, the calculation works by using these to calculate the distribution in Eq. 17.11, which is then used to calculate a new set of $\{F_i\}$ using Eq. 17.12. This is then iterated until the distribution is converged.

Using fluctuation theory, the derivative of the unbiased distribution function can be calculated as

$$\frac{\partial \langle p(r) \rangle}{\partial \beta} = \frac{\sum_{i=1}^{N_w} N_i \frac{\partial \langle p(r) \rangle^{(i)}}{\partial \beta} - \langle p \rangle \sum_{i=1}^{N_w} N_i e^{-\beta [U_{bias}^{(i)}(r) - F_i]} \left[\beta \frac{\partial F_i}{\partial \beta} + F_i - U_{bias}^{(i)}(r) \right]}{\sum_{i=1}^{N_w} N_i e^{-\beta [U_{bias}^{(i)}(r) - F_i]}}, \quad (17.13)$$

where here $\partial F_i / \partial \beta$ is the derivative of the free energy shift of window i . $\partial \langle p(r) \rangle^{(i)} / \partial \beta$ is the

temperature derivative of the biased distribution function, which can be calculated as,

$$\frac{\partial \langle p(r) \rangle^{(i)}}{\partial \beta} = - \langle \delta \tilde{H}(r) p(r) \rangle^{(i)} \quad (17.14)$$

where here $\delta \tilde{H} = \tilde{H} - \langle \tilde{H} \rangle$ is the fluctuation in the energy of the biased simulation (including the component that comes from the biasing potential). With these equations, the final unbiased derivative may be re-expressed as,

$$\frac{\partial \langle p(r) \rangle}{\partial \beta} = \frac{-\sum_{i=1}^{N_w} N_i \langle \delta \tilde{H}(r) p(r) \rangle^{(i)} - \langle p \rangle \sum_{i=1}^{N_w} N_i e^{-\beta [U_{bias}^{(i)}(r) - F_i]} \left[\beta \frac{\partial F_i}{\partial \beta} + F_i - U_{bias}^{(i)}(r) \right]}{\sum_{i=1}^{N_w} N_i e^{-\beta [U_{bias}^{(i)}(r) - F_i]}}. \quad (17.15)$$

Finally, the derivative of the free energy shift, $\partial F_i / \partial \beta$, can be calculated as

$$\frac{\partial F_i}{\partial \beta} = -\frac{F_i}{\beta} - \frac{\sum_{r_{bins}} \left(\frac{\partial \langle p(r) \rangle}{\partial \beta} - U_{bias}^{(i)}(r) \langle p(r) \rangle \right) e^{-\beta U_{bias}^{(i)}(r)}}{\beta \sum_{r_{bins}} e^{-\beta U_{bias}^{(i)}(r)} \langle p(r) \rangle}. \quad (17.16)$$

Thus, a new iterative process using these equations could be undertaken where the original wham procedure is followed to calculate $\langle p(r) \rangle$, and $\{F_i\}$. Following this procedure, a second self-consistent calculation of Eq. 17.15 and Eq. 17.16 is followed to determine the derivative of the potential of mean force. It should be noted that this approach is likely not only restricted to temperature derivatives, but similar expressions may be derived for potential parameter derivatives, pressure derivatives, and chemical potential derivatives as well.

17.2 Other Derivatives

17.2.1 Potential Parameter Derivatives

A consistent problem in molecular dynamics simulation is the need to choose the correct molecular model to describe experiment with qualitative accuracy. Indeed, new force-fields are frequently created to match a certain set of experimental observables. This can be challenging as it is not

always clear exactly how changing a particular parameter of the force-field will influence structural and dynamical quantities, so instead frequently it becomes a computationally expensive optimization problem where parameters are varied independently and then simulations are run to see whether they improve the behavior of the model. We long considered whether derivatives with respect to the potential parameters could be used to predict the dependence of dynamical timescales on, for example, the Lennard-Jones σ parameter. Unfortunately, such a derivative for a time-dependent quantity like the diffusion coefficient ends up requiring a derivative of the Liouville operator which renders the problem computationally difficult.

However, for a quantity that is *time-independent*, for instance liquid structure, the derivative of the Liouville operator is not needed. For a given time independent distribution, $P(x) = \langle \delta(x - \tilde{x}(\mathbf{Q})) \rangle$, where x is a coordinate in the system that is time-independent, then the derivative of $P(x)$ with respect to a general potential parameter α can be written as,

$$\frac{\partial P(x)}{\partial \alpha} = -\beta \left\langle \delta \left(\frac{\partial V}{\partial \alpha} \right) \delta(x - \tilde{x}) \right\rangle. \quad (17.17)$$

Then, for the Lennard-Jones parameters ($\alpha = \epsilon, \sigma$ and Q) the derivatives can be written as,

$$\frac{\partial P(x)}{\partial \epsilon} = -\frac{\beta}{\epsilon} \langle \delta V_{LJ} \delta(x - \tilde{x}) \rangle, \quad (17.18)$$

$$\frac{\partial P(x)}{\partial \sigma} = -\beta \left\langle \delta \left[\frac{6V_{LJ}}{\sigma} + \frac{24\epsilon}{\sigma} \left(\frac{\sigma}{r} \right)^{12} \right] \delta(x - \tilde{x}) \right\rangle, \quad (17.19)$$

and

$$\frac{\partial P(x)}{\partial Q} = -\frac{2\beta}{Q} \langle \delta V_{coul} \delta(x - \tilde{x}) \rangle \quad (17.20)$$

where δV_{LJ} is the fluctuation in the Lennard-Jones potential energy, and V_{coul} is the fluctuation in the Coulombic potential energy. Conveniently, for derivatives with respect to ϵ and Q all the information required for such a calculation is already typically output from a molecular dynamics simulation, thus to calculate all three derivatives only the σ derivative requires extra information to be provided in the output file. It is possible that in the future advanced sampling techniques could

enhance the calculation of these higher derivatives and make them more reasonable to resolve.

17.2.2 Chemical Potential Derivatives

During my graduate work, we have discussed a number of times the approach for calculating the derivative with respect to the chemical potential, which could then be used to understand the dependence of dynamical quantities and timescales on concentration. One such model system where such derivatives may provide useful information is the CO₂-expanded electrolyte system discussed in Chapter 15, where the dynamics of the solvent are strongly concentration-dependent. Furthermore, a question to consider is whether such derivatives could be used to predict the concentration dependence as we have predicted the temperature and pressure dependence of timescales and structural properties throughout the second part of this thesis?

In the Grand Canonical Ensemble ($\mu_i VT$) the diffusion coefficient can be expressed as

$$\langle D \rangle = \frac{1}{\Omega} \text{Tr} \left\{ e^{-\beta(H + \sum_{\text{species}} N_i \mu_i)} D \right\} \quad (17.21)$$

where here Ω is the Grand Canonical partition function, N_i is the number of molecules of species i , and μ_i is the chemical potential of species i . In the same manner described in Chapter 6 Eq. (6.9), the derivative with respect to μ_i can be written as

$$\frac{\partial D}{\partial \mu_i} = -\beta \langle \delta N_i(0) D \rangle \quad (17.22)$$

where here $\delta N_i(0) = N_i(0) - \langle N_i \rangle$ is the fluctuation in the number of species i . In a molecular dynamics simulation, such an approach could likely be achieved by examining the diffusion coefficient within a sub-volume of the simulation cell and then weighting by the fluctuation in the number of i within that sub-volume compared to the average number. This is an ongoing problem that should be fairly easy to implement in the future.

17.2.3 High-Order Derivatives

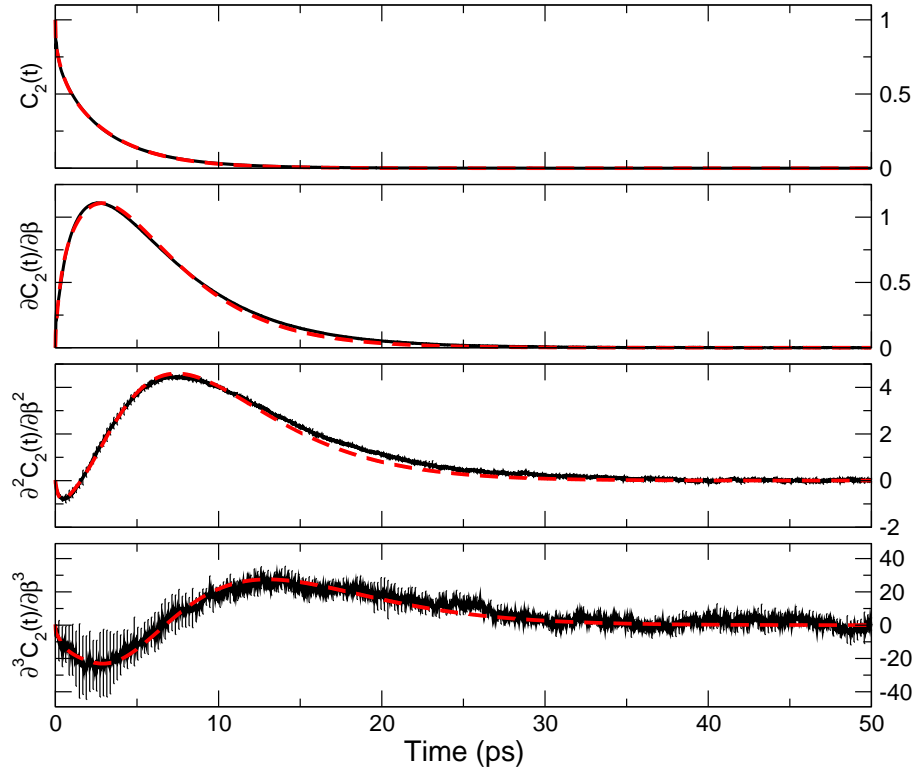


Figure 17.1: The first three derivatives of the reorientation correlation function are included (black) along with their fits (red) for TIP4P/2005 water at room temperature.

In the work described in this thesis, we have demonstrated the calculation of up to the second derivative with respect to temperature and pressure. Here, I briefly outline the third and fourth derivatives with respect to temperature. Recall that the first derivative of a time-dependent quantity $\langle f(t) \rangle$ can be expressed as,

$$\frac{\partial \langle f(t) \rangle}{\partial \beta} = -\langle \delta H(0) f(t) \rangle \quad (17.23)$$

where here the mark ' indicates a temperature derivative. The second derivative is

$$\frac{\partial^2 \langle f(t) \rangle}{\partial \beta^2} = \langle [\delta H(0)^2 - \langle \delta H^2 \rangle] \rangle. \quad (17.24)$$

This procedure can be continued to calculate the third derivative,

$$\frac{\partial^3 \langle f(t) \rangle}{\partial \beta^3} = -\langle \delta H(0)^3 f(t) \rangle + \langle \delta H^3 \rangle \langle f(t) \rangle - 3 \langle \delta H^2 \rangle \frac{\partial \langle f(t) \rangle}{\partial \beta}, \quad (17.25)$$

and the fourth derivative,

$$\frac{\partial^4 \langle f(t) \rangle}{\partial \beta^4} = \langle [\delta H(0)^4 - \langle \delta H^4 \rangle] f(t) \rangle - 6 \langle \delta H^2 \rangle \frac{\partial^2 \langle f(t) \rangle}{\partial \beta^2} + 4 \langle \delta H^3 \rangle \frac{\partial \langle f(t) \rangle}{\partial \beta} \quad (17.26)$$

As an example, we have calculated the first three derivatives of the C_2 reorientation correlation function for TIP4P/2005 water at room temperature from 1 million NVE trajectories and plotted them in figure 17.1. More simulations would be needed to resolve the fourth derivative. These can be fit by taking successive derivatives of the triple exponential fitting. For more information on the simulation setup, see Chapter 7.

17.3 Other Systems

The advantage of the fluctuation theory approach is that it is not mathematically bound to a particular system, and is instead applicable to a wide-variety of systems. In this thesis, we have considered primarily applications to liquid water; however, we have also applied it to the CO₂-expanded electrolyte system successfully. Other members of our group have successfully applied similar approaches to aqueous electrolyte solutions,³⁷⁵ and alanine dipeptide conformational equilibria.³⁷⁶ Ongoing work in our group is working on applying these methods to reactions involving Criegee intermediate reactions.

17.3.1 Activation Parameters Near Phase Transitions

A key drawback of traditional Arrhenius analysis is the wide-range of temperatures needed to extract an activation energy. Near the boiling point, or any other phase transition, this required temperature range prevents calculation of the activation energies using traditional approaches. A

key feature of dynamical fluctuation theory is the ability to determine activation parameters from simulations at a single temperature and pressure, and thus provides the ability to calculate the activation energy without this issue.

17.3.2 Liquids at Interfaces

A key system where activation energies could provide important information is the solid-liquid interface as the presence of an interface both slows the dynamics of the water molecules in the interfacial region, and likely also modifies the temperature dependence of these dynamics. It would potentially be of interest to study the dependence of the diffusion activation energy as a function of distance from the interface both a slab surface, but also in nanopores under confinement. Activation energies would provide a window into the specific molecular interactions that drive slowed diffusion in the interfacial region and would allow for the decomposition of the activation energies into contributions from different sites on the surface of the interface. Furthermore, work with the nanoporous silica model developed by the Thompson group would be a natural next step for studying a combination of interfacial and confinement effects.

17.3.3 Biomolecules

With a large heterogeneity of sites available to interact with water molecules, it is possible that fluctuation theory could present a useful technique for understanding the effect of these sites on dynamical timescales. Recently, Laage and co-workers have developed site-specific methods for mapping water dynamics within the first solvation layer (similar to the maps we generated earlier in this thesis).⁸⁹ In their work, they demonstrated that there is not uniform slowdown in the first hydration layer but instead that associated with the heterogeneity of sites there is also a heterogeneity of water reorientation times associated with those sites. Unfortunately, biomolecules can undergo conformational changes with respect to temperature making mapping activation energies using traditional techniques complicated. It is likely; however, that the fluctuation theory approach could be used to better understand these systems as a temperature range is not required for this approach.

Furthermore, the decomposition of the activation energies could provide otherwise unobtainable insight into the driving forces underlying water dynamics in the first hydration layer.

17.3.4 Lithium Fluoride Ion Pairing

We have recently been working with Chris Mundy and Gregory Schenter at Pacific Northwest National Laboratory to develop the first ever application of the fluctuation theory approach to *Ab Initio* Molecular Dynamics (AIMD) simulations. Due to the computational limitations at the time of writing this thesis, we have selected *Lithium Fluoride* ion pairing in liquid water. Ion pairing is an ideal system for testing the method as each *NVE* trajectory is only required to be 2 picoseconds; rather than the 20 picosecond (or longer) trajectories required for other dynamical timescales.

17.3.4.1 Theory

The reactive flux (or flux-side) time-correlation function (TCF) can be written as

$$C_{fs}(t) = \langle F_s(0) \theta [s(t) - s^\ddagger] \rangle. \quad (17.27)$$

Here, $F_s(0) = \delta [s(0) - s^\ddagger] v_s(0)$ is the classical flux at $t = 0$ through the dividing surface $s = s^\ddagger$, where $s < s^\ddagger$ describes reactants, and $s > s^\ddagger$ describes products. $v_s(0)$ is the velocity along the reaction coordinate at $t = 0$, $\theta(s)$ is the Heaviside step function, and $\langle \dots \rangle$ indicates a thermal average.

From the flux-side TCF, the reaction rate constant can be written as the long time limit, as

$$k = \lim_{t \rightarrow \text{long}} C_{fs}(t) \quad (17.28)$$

where this limit is taken to a long enough time that the reaction has occurred, but not so long that the reaction can go to products and then return again to reactants.

The activation energy can be written in terms of the flux-side TCF, giving

$$E_a = -\frac{1}{k} \lim_{t \rightarrow \text{long}} \frac{\partial C_{fs}(t)}{\partial \beta}. \quad (17.29)$$

This derivative may be easily calculated by recognizing that the thermal average may be rewritten as,

$$C_{fs}(t) = \frac{1}{Q_r} \text{Tr} \left[e^{-\beta H} F_s(0) \theta \left[s(t) - s^\ddagger \right] \right] \quad (17.30)$$

where here Q_r is the reactant partition function, H is the Hamiltonian, and Tr is an average over all coordinates and momenta. Of these parameters, it should be noted that only the reactant partition function, Q_r , and the Boltzmann factor, $e^{-\beta H}$ depend upon temperature. Thus, the derivative in Eq. 17.29 can be expressed as,

$$\frac{\partial C_{fs}(t)}{\partial \beta} = -\frac{1}{Q_r} \text{Tr} \left[e^{-\beta H} H(0) F_s(0) \theta \left[s(t) - s^\ddagger \right] \right] - \frac{\partial \ln Q_r}{\partial \beta} C_{fs}(t), \quad (17.31)$$

where $-\frac{\partial \ln Q_r}{\partial \beta} = \langle H \rangle_r$ is the average energy of the reactants. This expression can then be simplified, as

$$\frac{\partial C_{fs}(t)}{\partial \beta} = -\langle \delta H(0) F_s(0) \theta \left[s(t) - s^\ddagger \right] \rangle, \quad (17.32)$$

where now the derivative is expressed as a new TCF that resembles the original flux-side TCF but is now weighted by the fluctuation of the energy from the average reactant energy, $\delta H(0) = H(0) - \langle H \rangle_r$. Combined with Eq. 17.29, the activation energy is written as

$$E_a = \lim_{t \rightarrow \text{long}} \frac{\langle \delta H(0) F_s(0) \theta \left[s(t) - s^\ddagger \right] \rangle}{\langle F_s(0) \theta \left[s(t) - s^\ddagger \right] \rangle}. \quad (17.33)$$

17.3.4.2 Methods

A simulation of 96 water molecules and one lithium fluoride ion pair was simulated using the CP2K software in the NVT ensemble at a temperature of 298.15 K. In this simulation, the ion pair was constrained to be at the transition state determined from the maximum separating the

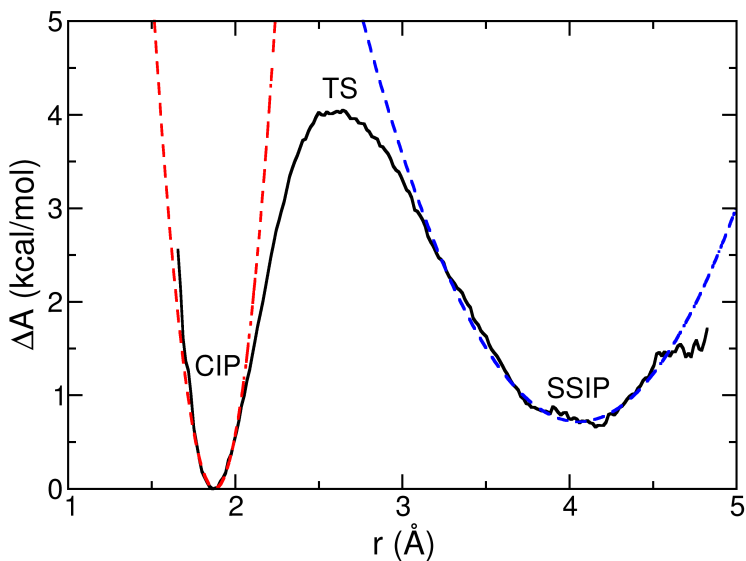


Figure 17.2: The potential of mean force calculated from the AIMD simulations. Harmonic fits of the CIP and SSIP wells are included as red and blue dashed lines, respectively.

contact ion pair (CIP) and the solvent-separated ion pair (SSIP) along the $r_{Li^+ \cdots F^-}$ coordinate. From this simulation, 1391 separate configurations and momenta were saved as starting points for separate, short 2 picosecond NVE trajectories. In these NVE trajectories, the relative velocity along the $Li^+ \cdots F^-$ were randomly re-selected from the Maxwell-Boltzmann distribution. For these simulations, a simulation timestep of 0.5 fs was chosen and configurations were output every 5 fs.

17.3.4.3 Preliminary Results

AIMD PMF

We have used the Weighted Histogram Analysis Method (WHAM) to calculate the potential of mean force along the $\vec{r} = r_{Li^+ \cdots F^-}$ coordinate for our AIMD system. The contact ion pair (CIP) well is at a minimum value at $\vec{r} = 1.86 \text{ \AA}$, the transition state (TS) occurs at $\vec{r} = 2.58 \text{ \AA}$, and the solvent-separated ion pair (SSIP) well is at its minimum value at $\vec{r} = 4.15 \text{ \AA}$. Relative to the CIP, the Helmholtz free energy of the TS is 4.0 kcal/mol, and for the SSIP it is 0.66 kcal/mol.

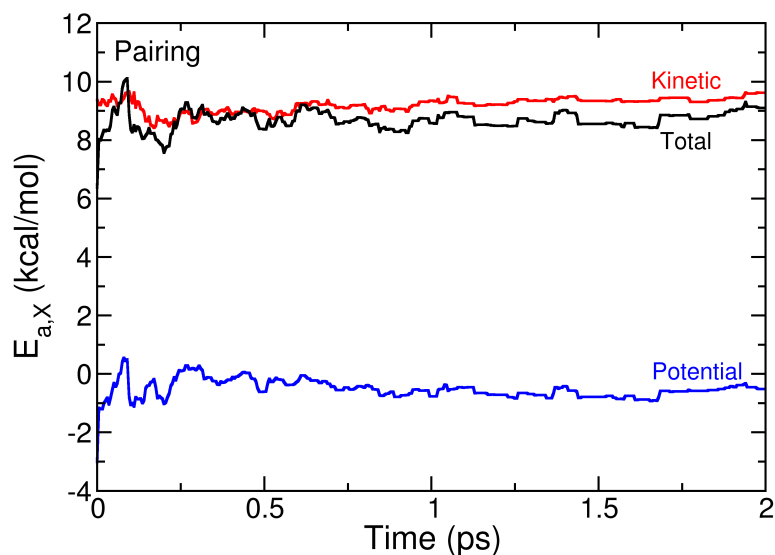


Figure 17.3: Activation energy decompositions for ion pairing. The total activation energy, the kinetic contribution to the activation energy, and the potential contribution to the activation energy are included in black, red, and blue, respectively.

| $E_{a,H}$ | $E_{a,KE}$ | $E_{a,U}$ |
|-----------|------------|-----------|
| 8.75 | 9.40 | -0.65 |

Table 17.1: Activation energies (in kcal/mol) for ion pairing.

As is required to obtain the activation energies, we have calculated the average energy in each of these reactant basins. We find that the SSIP average reactant energy is 2.11 kcal/mol larger than that of the CIP, corresponding to an entropy change of 5.4 cal/mol/K moving from the CIP to the SSIP.

AIMD TCFs

In Figure 17.3a and 17.3b we have calculated the activation energy decomposition for ion pairing. We have included these in Table 17.1, calculated as a fit to a horizontal line over the last 500 femtoseconds. We find that the activation energy is significantly higher than the free energy barrier, indicating a large role of entropy in the ion pairing process.

In the future, more detailed calculations are necessary to determine whether the above described behavior is physical. Ongoing work is looking at developing a classical LiF model that

adequately describes the potential of mean force in order to do a corresponding classical molecular dynamics calculation to see if these same entropic behavior is witnessed. As such, the present calculations should be interpreted as a proof of principle for the time being.

17.4 Summary

As was the case for the present thesis, this Chapter only a small subset of the possibilities for future development of dynamical fluctuation theory have been presented. Nearly any dynamical system could likely benefit from various applications of the developed approaches. Future technological and theoretical innovations will likely make these approaches less expensive and more feasible for future implementation of this method.

Chapter 18

References

- [1] Harris, K. R.; Woolf, L. A. Pressure and temperature dependence of the self diffusion coefficient of water and oxygen-18 water. *J. Chem. Soc.* **1980**, *76*, 377–385.
- [2] Harris, K. R.; Newitt, P. J. Self-diffusion of water at low temperatures and high pressure. *J. Chem. Eng. Data* **1997**, *42*, 346–348.
- [3] Krynicky, K.; Green, C. D.; Sawyer, D. W. Pressure and temperature dependence of self-diffusion in water. *Faraday Discuss. Chem. Soc.* **1978**, *66*, 199–208.
- [4] Woolf, L. A. Tracer Diffusion of Tritiated Water (THO) in Ordinary Water (H₂O) under Pressure. *J. Chem. Soc., Faraday Trans. 1* **1975**, *71*, 784–796.
- [5] Abascal, J. L. F.; Vega, C. A general purpose model for the condensed phases of water: TIP4P/2005. *J. Chem. Phys.* **2005**, *123*, 234505.
- [6] Xu, Y.; Petrik, N. G.; Smith, R. S.; Kay, B. D.; Kimmel, G. A. Growth rate of crystalline ice and the diffusivity of supercooled water from 126 to 262 K. *Proc. Natl. Acad. Sci.* **2016**, *113*, 14921–14925.
- [7] Petersen, C.; Tielrooij, K. J.; Bakker, H. J. Strong temperature dependence of water reorientation in hydrophobic hydration shells. *J. Chem. Phys.* **2009**, *130*.
- [8] Moilanen, D. E.; Fenn, E. E.; Lin, Y.-S.; Skinner, J. L.; Bagchi, B.; Fayer, M. D. Water inertial reorientation: Hydrogen bond strength and the angular potential. *Proc. Natl. Acad. Sci.* **2008**, *105*, 5295–5300.

- [9] Ramasesha, K.; Roberts, S. T.; Nicodemus, R. A.; Tokmakoff, A. No Title. *J. Chem. Phys.* **2011**, *135*, 054509.
- [10] Weingartner, H. Self-Diffusion in liquid water. A reassessment. *Z. Phys. Chem.* **1982**, *132*, 129–149.
- [11] Fanetti, S.; Lapini, A.; Pagliai, M.; Citroni, M.; Di Donato, M.; Scandolo, S.; Righini, R.; Bini, R. Structure and dynamics of low-density and high-density liquid water at high pressure. *J. Phys. Chem. Lett.* **2014**, *5*, 235–240.
- [12] Skinner, L. B.; Benmore, C. J.; Neufeind, J. C.; Parise, J. B. The structure of water around the compressibility minimum. *J. Chem. Phys.* **2014**, *141*.
- [13] Piskulich, Z. A.; Mesele, O. O.; Thompson, W. H. Activation energies and beyond. *J. Phys. Chem. A* **2019**, *123*, 7185–7194.
- [14] Arrhenius, A. Über die reaktionsgeschwindigkeit bei der inversion von rohrzucker durch säuren. *Z. physik. Chem.* **1889**, *4*, 226–248.
- [15] Menzinger, M.; Wolfgang, R. The Meaning and Use of the Arrhenius Activation Energy. *Angew. Chem. Intl. Ed.* **1969**, *8*, 438–444.
- [16] Logan, S. R. The Origin and Status of the Arrhenius Equation. *J. Chem. Educ.* **1982**, *59*, 279–281.
- [17] Laidler, K. J. The development of the Arrhenius equation. *J. Chem. Educ.* **1984**, *61*, 494–5.
- [18] Tolman, R. C. Statistical mechanics applied to chemical kinetics. *J. Am. Chem. Soc.* **1920**, *42*, 2506–2528.
- [19] Truhlar, D. G. Interpretation of the activation energy. *J. Chem. Educ.* **1978**, *55*, 309–311.
- [20] Levine, R. D.; Bernstein, R. B. *Molecular Reaction Dynamics and Chemical Reactivity*; Oxford University Press: New York, 1987.

- [21] Blais, N. C.; Truhlar, D. G.; Garrett, B. C. Dynamical calculation of the temperature dependence of the activation energy for a chemical reaction from 444 to 2400 K. *J. Phys. Chem.* **1981**, *85*, 1094–1096.
- [22] Rafatijo, H.; Thompson, D. L. General Application of Tolman's Concept of Activation Energy. *J. Chem. Phys.* **2017**, *147*, 224111.
- [23] Miller, W. H.; Schwartz, S. D.; Tromp, J. W. Quantum Mechanical Rate Constants for Bimolecular Reactions. *J. Chem. Phys.* **1983**, *79*, 4889–4898.
- [24] Eyring, H. The Activated Complex in Chemical Reactions. *J. Chem. Phys.* **1935**, *3*, 107–115.
- [25] Wigner, E. The Transition State Method. *Trans. Faraday Soc.* **1938**, *34*, 29–41.
- [26] Hill, T. L. *Statistical Mechanics. Principles and Selected Applications*; Dover: New York, 1956.
- [27] Landau, L. D.; Lifshitz, E. M. *Statistical Physics*; Addison-Wesley: Reading, MA, 1969.
- [28] Greene, R. F.; Callen, H. B. On the Formalism of Thermodynamic Fluctuation Theory. *Phys. Rev.* **1951**, *83*, 1231–1235.
- [29] An analogous direct analysis of classical trajectories based on the Tolman expression for the activation energy has been previously applied²¹ to the gas phase H + H₂ reaction to differentiate the contributions of relative translational motion and internal energy.
- [30] Wilbur, D. J.; DeFries, T.; Jonas, J. Self-Diffusion in Compressed Liquid Heavy-Water. *J. Chem. Phys.* **1976**, *65*, 1783–1786.
- [31] Mesele, O. O.; Thompson, W. H. Removing the barrier to the calculation of activation energies. *J. Chem. Phys.* **2016**, *145*, 13410.

- [32] Chandler, D. Statistical Mechanics of Isomerization Dynamics in Liquids and the Transition State Approximation. *J. Chem. Phys.* **1978**, *68*, 2959–2970.
- [33] Northrup, S. H.; Hynes, J. T. The stable states picture of chemical reactions. I. Formulation for rate constants and initial condition effects. *J. Chem. Phys.* **1980**, *73*, 2700–2714.
- [34] Grote, R. F.; Hynes, J. T. The Stable States Picture of Chemical Reactions. II. Rate Constants for Condensed Phase and Gas Phase Reaction Models. *J. Chem. Phys.* **1980**, *73*, 2715–2732.
- [35] Dellago, C.; Bolhuis, P. G. Activation energies from transition path sampling simulations. *Mol. Simul.* **2004**, *30*, 795–799.
- [36] Lo, C. S.; Radhakrishnan, R.; Trout, B. L. Application of Transition Path Sampling Methods in Catalysis: A New Mechanism for CC Bond Formation in the Methanol Coupling Reaction in Chabazite. *Catalysis Today* **2005**, *105*, 93–105.
- [37] Borrero, E. E.; Dellago, C. Overcoming Barriers in Trajectory Space: Mechanism and Kinetics of Rare Events via Wang–Landau Enhanced Transition Path Sampling. *J. Chem. Phys.* **2010**, *133*, 134112–12.
- [38] Drechsel-Grau, C.; Sprik, M. Activation Energy for a Model Ferrous-Ferric Half Reaction from Transition Path Sampling. *J. Chem. Phys.* **2012**, *136*, 034506–11.
- [39] Moqadam, M.; Riccardi, E.; Trinh, T. T.; Lervik, A.; van Erp, T. S. Rare Event Simulations Reveal Subtle Key Steps in Aqueous Silicate Condensation. *Phys. Chem. Chem. Phys.* **2017**, *19*, 13361–13371.
- [40] Moqadam, M.; Lervik, A.; Riccardi, E.; Venkatraman, V.; Alsberg, B.; van Erp, T. S. Local Initiation Conditions for Water Autoionization. *Proc. Natl. Acad. Sci.* **2018**, *115*, E4569–e4576.
- [41] Bolhuis, P. G.; Csányi, G. Nested Transition Path Sampling. *Phys. Rev. Lett.* **2018**, *120*, 250601.

- [42] Berendsen, H. J.; Grigera, J. R.; Straatsma, T. P. The missing term in effective pair potentials. *J. Phys. Chem* **1987**, *91*, 6269–6271.
- [43] Gordon, R. G. Relations between Raman spectroscopy and nuclear spin relaxation. *J. Chem. Phys.* **1965**, *42*, 3658–3665.
- [44] Piskulich, Z. A.; Thompson, W. H. The activation energy for water reorientation differs between IR pump-probe and NMR measurements. *J. Chem. Phys.* **2018**, *149*, 164504.
- [45] Zwanzig, R. Time-Correlation Functions and Transport Coefficients in Statistical Mechanics. *Annu. Rev. Phys. Chem.* **1965**, *16*, 67–102.
- [46] Sakaguchi, S.; Ishiyama, T.; Morita, A. Theory and efficient computation of differential vibrational spectra. *J. Chem. Phys.* **2014**, *140*, 144109.
- [47] Sakaguchi, S.; Ishiyama, T.; Morita, A. Theory and Efficient Computation of Differential Vibrational Spectra (vol 140, 144109, 2014). *J. Chem. Phys.* **2014**, *141*.
- [48] Joutsuka, T.; Morita, A. Efficient computation of difference vibrational spectra in isothermal–isobaric ensemble. *J. Phys. Chem. B* **2016**, *120*, 11229–11238.
- [49] Joutsuka, T.; Morita, A. Improved theory of difference vibrational spectroscopy and application to water. *J. Chem. Theor. Comp.* **2016**, *12*, 5026–5036.
- [50] Mendis, C. H.; Piskulich, Z. A.; Thompson, W. H. Tests of the Stokes-Einstein relation through the shear viscosity activation energy of water. *J. Phys. Chem. B* **2019**, *123*, 5857–5865.
- [51] Ludwig, R.; Weinhold, F.; Farrar, T. C. Experimental and theoretical determination of the temperature dependence of deuteron and oxygen quadrupole coupling constants of liquid water. *J. Chem. Phys.* **1995**, *103*, 6941–6950.
- [52] Qvist, J.; Mattea, C.; Sunde, E. P.; Halle, B. Rotational dynamics in supercooled water from nuclear spin relaxation and molecular simulations. *J. Chem. Phys.* **2012**, *136*, 204505.

- [53] Pruppacher, H. R. Self-diffusion coefficient of supercooled water. *J. Chem. Phys.* **1972**, *56*, 101–107.
- [54] Gillen, K. T.; Douglass, D. C.; Hoch, M. J. Self-diffusion in liquid water to -31°C . *J. Chem. Phys.* **1972**, *57*, 5117–5119.
- [55] Angell, C. A.; Finch, E. D.; Woolf, L. A.; Bach, P. Spin-echo diffusion coefficients of water to 2380 Bar and -20°C . *J. Chem. Phys.* **1976**, *65*, 3063–3074.
- [56] Prielmeier, F. X.; Lang, E. W.; Speedy, R. J.; Lüdemann, H. D. The pressure-dependence of self-diffusion in supercooled light and heavy-water. *Ber. Bunsen. Phys. Chem.* **1988**, *92*, 1111–1117.
- [57] Truhlar, D. G.; Kohen, A. Convex Arrhenius plots and their interpretation. *Proc. Natl. Acad. Sci.* **2001**, *98*, 848–851.
- [58] Piskulich, Z. A.; Mesele, O. O.; Thompson, W. H. Removing the barrier to the calculation of activation energies: Diffusion coefficients and reorientation times in liquid water. *J. Chem. Phys.* **2017**, *147*, 134103.
- [59] Piskulich, Z. A.; Mesele, O. O.; Thompson, W. H. Expanding the calculation of activation volumes: Self-diffusion in liquid water. *J. Chem. Phys.* **2018**, *148*, 134105.
- [60] van Eldik, R.; Asano, T.; le Noble, W. J. Activation and reaction volumes in solution. 2. *Chem. Rev.* **1989**, *89*, 549–688.
- [61] Drljaca, A.; Hubbard, C. D.; van Eldik, R.; Asano, T.; Basilevsky, M. V.; le Noble, W. J. Activation and reaction volumes in solution. 3. *Chem. Rev.* **1998**, *98*, 2167–2290.
- [62] Ladanyi, B. M.; Hynes, J. T. Transition-state solvent effects on atom transfer rates in solution. *J. Am. Chem. Soc.* **1986**, *108*, 585–593.
- [63] Kerisit, S.; Rosso, K. M. Transition Path Sampling of Water Exchange Rates and Mechanisms around Aqueous Ions. *J. Chem. Phys.* **2009**, *131*, 114512–15.

- [64] Dang, L. X.; Schenter, G. K. Solvent exchange in liquid methanol and rate theory. *Chem. Phys. Lett.* **2016**, *643*, 142–148.
- [65] Wiebe, H.; Spooner, J.; Boon, N.; Deglint, E.; Edwards, E.; Dance, P.; Weinberg, N. Calculation of Molecular Volumes and Volumes of Activation Using Molecular Dynamics Simulations. *J. Phys. Chem. C* **2012**, *116*, 2240–2245.
- [66] Kubo, R.; Toda, M. *Statistical Physics II*; Springer-Verlag: New York, 1978.
- [67] Chandler, D. *Introduction to Modern Statistical Mechanics*; Oxford University Press: New York, 1987.
- [68] Zwanzig, R. *Nonequilibrium Statistical Mechanics*; Oxford: New York, 2001.
- [69] Miller, W. H. Quantum mechanical transition state theory and a new semiclassical model for reaction rate constants. *J. Chem. Phys.* **1974**, *61*, 1823–1834.
- [70] Drechsel-Grau, C.; Sprik, M. Activation energy for a model ferrous-ferric half reaction from transition path sampling. *Journal of Chemical Physics* **2012**, *136*.
- [71] Lin, Y. S.; Pieniazek, P. A.; Yang, M.; Skinner, J. L. On the calculation of rotational anisotropy decay, as measured by ultrafast polarization-resolved vibrational pump-probe experiments. *J. Chem. Phys.* **2010**, *132*.
- [72] Bakker, H. J.; Skinner, J. L. Vibrational spectroscopy as a probe of structure and dynamics in liquid water. *Chem. Rev.* **2010**, *110*, 1498–1517.
- [73] Laage, D.; Stirnemann, G.; Sterpone, F.; Rey, R.; Hynes, J. T. Reorientation and allied dynamics in water and aqueous solutions. *Ann. Rev. Phys. Chem.* **2011**, *62*, 395–416.
- [74] Smith, D. W.; Powles, J. G. Proton spin-lattice relaxation in liquid water and liquid ammonia. *Molecular Physics* **1966**, *10*, 451–463.

- [75] Zeidler, M. D. A Comparative Study of Quasielastic Neutron Scattering and NMR Relaxation in Liquid Acetonitrile. *Berichte der Bunsengesellschaft für physikalische Chemie* **1971**, *75*, 769–776.
- [76] Jonas, J.; DeFries, T.; Wilbur, D. J. Molecular motions in compressed liquid water. *The Journal of Chemical Physics* **1976**, *65*, 582–588.
- [77] See, *e.g.*, Ref. 73.
- [78] It can be shown that the inertial dynamics give an initial Gaussian decay (see, *e.g.*, D. A. McQuarrie, *Statistical Mechanics*, Harper-Collins, New York, 1976). However, it is more convenient to fit this component as an exponential decay like that associated with the librational and H-bond exchange dynamics. While this yields an approximate timescale for the inertial dynamics (which are not a focus of the present analysis), it does not affect the values obtained for τ_{lib} or τ_2 , as we have verified by different fitting approaches.
- [79] Lorentz, H. Ueber die anwendung des satzes vom virial in der kinetischen theorie der gase. *Annalen der Physik* **1881**, *248*, 127–136.
- [80] Berthelot, D. Si la fonction doit etre continue par rapport a l'ensemble (xy), elle doit etre constante sur les caracteristiques. *Academie des Sciences* **1898**, *126*, 1703–1855.
- [81] Plimpton, S. Fast parallel algorithms for short-range molecular dynamics. *J. Comput. Phys.* **1995**, *117*, 1–19.
- [82] Ryckaert, J. P.; Ciccotti, G.; Berendsen, H. J. Numerical integration of the cartesian equations of motion of a system with constraints: molecular dynamics of n-alkanes. *J. Comput. Phys.* **1977**, *23*, 327–341.
- [83] Nosé, S. A unified formulation of the constant temperature molecular dynamics methods. *J. Chem. Phys.* **1984**, *81*, 511–519.

- [84] Hoover, W. G. Canonical dynamics: Equilibrium phase-space distributions. *Phys. Rev. A* **1985**, *31*, 1695–1697.
- [85] Laage, D.; Hynes, J. T. On the molecular mechanism of water reorientation. *J. Phys. Chem. B* **2008**, *112*, 14230–14242.
- [86] Vartia, A. A.; Mitchell-Koch, K. R.; Stirnemann, G.; Laage, D.; Thompson, W. H. On the reorientation and hydrogen-bond dynamics of alcohols. *J. Phys. Chem. B* **2011**, *115*, 12173–12178.
- [87] We have not accounted for finite-size effects²⁴⁷ in calculating the diffusion constants. At the time of publication, we thought that this could have an effect on the activation energies, but Mendis, Piskulich, and Thompson, *J. Phys. Chem. B.*, **123**, p. 5857-5865, (2019) shows that activation energies do not suffer from finite size effects.⁵⁰.
- [88] Laage, D.; Hynes, J. T. A molecular jump mechanism of water reorientation. *Science* **2006**, *311*, 832–835.
- [89] Laage, D.; Elsaesser, T.; Hynes, J. T. Water dynamics in the hydration shells of biomolecules. *Chem. Rev.* **2017**, *117*, 10694–10725.
- [90] Ando, K.; Hynes, J. T. HCl acid ionization in water: A theoretical molecular modeling. *J. Mol. Liq.* **1995**, *64*, 25–37.
- [91] Ando, K.; Hynes, J. T. Molecular Mechanism of HCl Acid Ionization in Water: Ab Initio Potential Energy Surfaces and Monte Carlo Simulations. *J. Phys. Chem. B.* **1997**, *101*, 10464–10478.
- [92] Gertner, B. J.; Whitnell, R. M.; Wilson, K. R.; Hynes, J. T. Activation to the Transition State: Reactant and Solvent Energy Flow for a Model SN2 Reaction in Water. *J. Am. Chem. Soc* **1991**, *113*, 74–87.

- [93] Roy, S.; Baer, M. D.; Mundy, C. J.; Schenter, G. K. Marcus Theory of Ion-Pairing. *J. Chem. Theor. Comp.* **2017**, *13*, 3470–3477.
- [94] Roy, S.; Galib, M.; Schenter, G. K.; Mundy, C. J. On the relation between Marcus theory and ultrafast spectroscopy of solvation kinetics. *Chem. Phys. Lett.* **2017**, *692*, 407–415.
- [95] Okada, M.; Ibuki, K.; Ueno, M. Pressure Effect on the Reorientational Correlation Time of Water in N,N-Diethylformamide - Water Mixtures at 25C. *Bull. Chem. Soc. Jpn.* **2012**, *85*, 1192–1202.
- [96] Nakahara, M.; Wakai, C. Effect of solvent, temperature, and pressure on hydrogen bonding and reorientation of water molecules. *J. Mol. Liq.* **1995**, *66*, 149–155.
- [97] Struis, R. P. W. J.; De Bleijser, J.; Leyte, J. C. Dynamic behavior and some of the molecular properties of water molecules in pure water and in magnesium chloride solutions. *J. Phys. Chem.* **1987**, *91*, 1639–1645.
- [98] Van Der Post, S. T.; Bakker, H. J. Femtosecond mid-infrared study of the reorientation of weakly hydrogen-bonded water molecules. *J. Phys. Chem. B* **2014**, *118*, 8179–8189.
- [99] Woutersen, S.; Emmerichs, U.; Bakker, H. J. Femtosecond Mid-IR Pump-Probe Spectroscopy of Liquid Water : Evidence for a Two-Component Structure Femtosecond Mid-IR Pump-Probe Spectroscopy of Liquid Water : Evidence for a Two-Component Structure. *Science* **1997**, *278*, 658–660.
- [100] Bakker, H. J.; Woutersen, S.; Nienhuys, H. K. Reorientational motion and hydrogen-bond stretching dynamics in liquid water. *Chem. Phys.* **2000**, *258*, 233–245.
- [101] Rezus, Y. L. A.; Bakker, H. J. On the orientational relaxation of HDO in liquid water. *J. Chem. Phys.* **2005**, *123*.
- [102] Ramasesha, K.; Roberts, S. T.; Nicodemus, R. A.; Mandal, A.; Tokmakoff, A. Ultrafast

- 2D IR anisotropy of water reveals reorientation during hydrogen-bond switching. *J. Chem. Phys.* **2011**, *135*.
- [103] Piletic, I. R.; Moilanen, D. E.; Spry, D. B.; Levinger, N. E.; Fayer, M. D. Testing the Core/Shell Model of Nanoconfined Water in Reverse Micelles Using Linear and Nonlinear IR Spectroscopy. *J. Phys. Chem. A* **2006**, *110*, 4985–4999.
- [104] Bakker, H. J.; Rezus, Y. L. A.; Timmer, R. L. A. Molecular reorientation of liquid water studied with femtosecond midinfrared spectroscopy. *J. Phys. Chem. A* **2008**, *112*, 11523–11534.
- [105] Nicodemus, R. A.; Corcelli, S. A.; Skinner, J. L.; Tokmakoff, A. Collective hydrogen bond reorganization in water studied with temperature-dependent ultrafast infrared spectroscopy. *J. Phys. Chem. B* **2011**, *115*, 5604–5616.
- [106] Hindman, J. C.; Svirnickas, A.; Wood, M. Relaxation processes in water. A study of the proton spin-lattice relaxation time. *J. Chem. Phys.* **1973**, *59*, 1517–1522.
- [107] van der Maarel, J.; Lankhorst, D.; De Bleijser, J.; Leyte, J. On the Single-Molecule Dynamics of Water from Proton, Deuterium and Oxygen-17 Nuclear Magnetic Relaxation. *Chem. Phys. Lett.* **1985**, *122*, 541–544.
- [108] Stirnemann, G.; Laage, D. Communication: On the origin of the non-Arrhenius behavior in water reorientation dynamics. *J. Chem. Phys.* **2012**, *137*, 031101.
- [109] Ropp, J.; Lawrence, C.; Farrar, T. C.; Skinner, J. L. Rotational motion in liquid water is anisotropic: A nuclear magnetic resonance and molecular dynamics simulation study. *J. Am. Chem. Soc.* **2001**, *123*, 8047–8052.
- [110] Lankhorst, D.; Schrieffer, J.; Ley, Determination of the Rotational Correlation Time of Water by Proton NMR Relaxation in H₂¹⁷O and Some Related Results. *Ber. Bunsen-Ges. Phys. Chem.* **1982**, *86*, 215–220.

- [111] Ivanov, E. N. Theory of rotational brownian motion. *Sov. Phys. JETP-USSR* **1964**, *18*, 1041–1045.
- [112] Debye, P. *Polar Molecules*; Dover Publications, Inc.: New York, 1928.
- [113] Nienhuys, H. K.; Woutersen, S.; van Santen, R. A.; Bakker, H. J. Mechanism for Vibrational Relaxation in Water Investigated by Femtosecond Infrared Spectroscopy. *J. Chem. Phys.* **1999**, *111*, 1494–1500.
- [114] Fecko, C. J.; Loparo, J. J.; Roberts, S. T.; Tokmakoff, A. Local hydrogen bonding dynamics and collective reorganization in water: ultrafast infrared spectroscopy of HOD/D₂O. *J. Chem. Phys.* **2005**, *122*, 54506.
- [115] Kropman, M. F.; Nienhuys, H. K.; Woutersen, S.; Bakker, H. J. Vibrational relaxation and hydrogen-bond dynamics of HDO:H₂O. *J. Phys. Chem. A* **2001**, *105*, 4622–4626.
- [116] Chase, Jr., M. W. *NIST-JANAF Thermochemical Tables*; American Institute of Physics: New York, 1998.
- [117] We have calculated the constant pressure heat capacity, $C_p = 21.4 \text{ cal mol}^{-1} \text{ K}^{-1}$, from the energy and volume fluctuations of our simulations. This value agrees well with that previously reported for the TIP4P/2005 water model⁵ used here. It should be noted that these results are larger than that obtained experimentally¹¹⁶ as they ignore both intramolecular vibrations (due to the rigidity of the model) and quantum nuclear effects. Corrections for these effects⁵ have been found to give a result in good agreement with measurements.
- [118] Ciccotti, G.; Ryckaert, J. Molecular Dynamics of Rigid Molecules. *Comp. Phys. Rep.* **1986**, *4*, 346–392.
- [119] Darden, T.; York, D.; Pedersen, L. Particle mesh Ewald: An N·log(N) method for Ewald sums in large systems. *J. Chem. Phys.* **1993**, *98*, 10089–10092.

- [120] Pollock, E. L.; Glosli, J. Comments on PPPM, FMM, and the Ewald method for large periodic Coulombic systems. *Comput. Phys. Comm.* **1995**, *95*, 93–110.
- [121] Hockney, R.; Eastwood, J. In *Computer Simulation Using Particles*, 1st ed.; Hilger, A., Ed.; Taylor and Francis: Ny, 1989.
- [122] Shoemaker, D. P.; Garland, C. W.; Nibler, J. W. *Experiments in Physical Chemistry*; McGraw-Hill: New York, 1989.
- [123] Ni, Y.; Skinner, J. L. Ultrafast Pump-probe and 2DIR Anisotropy and Temperature-dependent Dynamics of Liquid Water within the E3B Model. *J. Chem. Phys.* **2014**, *141*, 024509.
- [124] Paesani, F. Temperature-Dependent Infrared Spectroscopy of Water from a First-Principles Approach. *J. Phys. Chem. A* **2011**, *115*, 6861–6871.
- [125] Values of $E_{a,\langle\tau_2\rangle}$ were obtained from Refs. 96 and 51 by an Arrhenius analysis of their reported $\langle\tau_2\rangle$ values using five temperatures centered around 298.15 K. For the results from Ref. 52, Eq. (2.5) in that work was used.
- [126] Nienhuys, H. K.; Van Santen, R. A.; Bakker, H. J. Orientational relaxation of liquid water molecules as an activated process. *J. Chem. Phys.* **2000**, *112*, 8487–8494.
- [127] Wilkins, D. M.; Manolopoulos, D. E.; Pipolo, S.; Laage, D.; Hynes, J. T. Nuclear Quantum Effects in Water Reorientation and Hydrogen-Bond Dynamics. *J. Phys. Chem. Lett.* **2017**, *8*, 2602–2607.
- [128] Pieniazek, P. A.; Lin, Y.-S.; Chowdhary, J.; Ladanyi, B. M.; Skinner, J. L. Vibrational Spectroscopy and Dynamics of Water Confined inside Reverse Micelles. *J. Phys. Chem. B* **2009**, *113*, 15017–15028.
- [129] Stirnemann, G.; Wernersson, E.; Jungwirth, P.; Laage, D. Mechanisms of acceleration and retardation of water dynamics by ions. *J. Am. Chem. Soc.* **2013**, *135*, 11824–11831.

- [130] Park, S.; Moilanen, D. E.; Fayer, M. D. Water dynamics - The effects of ions and nanoconfinement. *J. Phys. Chem. B* **2008**, *112*, 5279–5290.
- [131] Tielrooij, K. J.; van der Post, S. T.; Hunger, J.; Bonn, M.; Bakker, H. J. Anisotropic Water Reorientation around Ions. *J. Phys. Chem. B* **2011**, *115*, 12638–12647.
- [132] Tielrooij, K. J.; Garcia-Araez, N.; Bonn, M.; Bakker, H. J. Cooperativity in Ion Hydration. *Science* **2010**, *328*, 1006–1009.
- [133] Harpham, M. R.; Ladanyi, B. M.; Levinger, N. E.; Herwig, K. W. Water motion in reverse micelles studied by quasielastic neutron scattering and molecular dynamics simulations. *J. Chem. Phys.* **2004**, *121*, 7855–7868.
- [134] Moilanen, D. E.; Wong, D.; Rosenfeld, D. E.; Fenn, E. E.; Fayer, M. D. Ion-water hydrogen-bond switching observed with 2D IR vibrational echo chemical exchange spectroscopy. *Proc. Natl. Acad. Sci.* **2009**, *106*, 375–380.
- [135] Abel, S.; Galamba, N.; Karakas, E.; Marchi, M.; Thompson, W. H.; Laage, D. On the structural and dynamical properties of DOPC reverse micelles. *Langmuir* **2016**, *32*, 10610–10620.
- [136] Piskulich, Z. A.; Laage, D.; Thompson, W. H. Activation energies and the extended jump model: How temperature affects reorientation and hydrogen-bond exchange dynamics in water. *J. Chem. Phys.* **2020**, *153*, 074110.
- [137] Lang, E.; Lüdemann, H.-D. Pressure and temperature dependence of the longitudinal proton relaxation times in supercooled water to -87°C and 2500 bar. *J. Chem. Phys.* **1977**, *67*, 718–723.
- [138] Nicodemus, R. A.; Ramasesha, K.; Roberts, S. T.; Tokmakoff, A. Hydrogen bond rearrangements in water probed with temperature-dependent 2D IR. *J. Phys. Chem. Lett.* **2010**, *1*, 1068–1072.

- [139] Perakis, F.; Hamm, P. Two-dimensional infrared spectroscopy of supercooled water. *J. Phys. Chem. B* **2011**, *115*, 5289–5293.
- [140] Rønne, C.; Thrane, L.; Astrand, P.-O.; Wallqvist, A.; Mikkelsen, K. V.; Keiding, S. R. Investigation of the temperature dependence of dielectric relaxation in liquid water by THz reflection spectroscopy and molecular dynamics simulation. *J. Chem. Phys.* **1997**, *107*, 5319–5331.
- [141] Cho, C. H.; Urquidi, J.; Singh, S.; Robinson, G. W. Thermal offset viscosities of liquid H₂O, D₂O, and T₂O. *J. Phys. Chem. B* **1999**, *103*, 1991–1994.
- [142] Eicher, L. D.; Zwolinski, B. J. High-precision viscosity of supercooled water and analysis of the extended range temperature coefficient. *J. Phys. Chem.* **1971**, *75*, 2016–2024.
- [143] Teixeira, J.; Bellissent-Funel, M.-C.; Chen, S.-H.; Dianoux, A. J. Experimental determination of the nature of diffusive motions of water molecules at low temperatures. *Phys. Rev. A* **1985**, *31*, 1913–1917.
- [144] Qvist, J.; Schober, H.; Halle, B. Structural dynamics of supercooled water from quasielastic neutron scattering and molecular simulations. *J. Chem. Phys.* **2011**, *134*, 144508.
- [145] Gallo, P. et al. Water: A tale of two liquids. *Chem. Rev.* **2016**, *116*, 7463–7500.
- [146] Hestand, N. J.; Skinner, J. L. Perspective: Crossing the Widom line in no man’s land: Experiments, simulations, and the location of the liquid-liquid critical point in supercooled water. *J. Chem. Phys.* **2018**, *149*, 140901.
- [147] Piskulich, Z. A.; Thompson, W. H. On the temperature dependence of liquid structure. *J. Chem. Phys.* **2020**, *152*, 011102.
- [148] Boisson, J.; Stirnemann, G.; Laage, D.; Hynes, J. T. Water reorientation dynamics in the first hydration shells of F- and I-. *Phys. Chem. Chem. Phys.* **2011**, *13*, 19895–19901.

- [149] Laage, D.; Stirnemann, G. Effect of Ions on Water Dynamics in Dilute and Concentrated Aqueous Salt Solutions. *J. Phys. Chem. B* **2019**, *123*, 3312–3324.
- [150] Laage, D.; Stirnemann, G.; Hynes, J. T. Why water reorientation slows without iceberg formation around hydrophobic solutes. *J. Phys. Chem. B* **2009**, *113*, 2428–2435.
- [151] Sterpone, F.; Stirnemann, G.; Hynes, J. T.; Laage, D. Water hydrogen-bond dynamics around amino acids: The key role of hydrophilic hydrogen-bond acceptor groups. *J. Phys. Chem. B* **2010**, *114*, 2083–2089.
- [152] Stirnemann, G.; Sterpone, F.; Laage, D. Dynamics of water in concentrated solutions of amphiphiles: Key roles of local structure and aggregation. *J. Phys. Chem. B* **2011**, *115*, 3254–3262.
- [153] Xiao, S.; Figge, F.; Stirnemann, G.; Laage, D.; McGuire, J. A. Orientational dynamics of water at an extended hydrophobic interface. *J. Am. Chem. Soc.* **2016**, *138*, 5551–5560.
- [154] Fogarty, A. C.; Laage, D. Water dynamics in protein hydration shells: the molecular origins of the dynamical perturbation. *J. Phys. Chem. B* **2014**, *118*, 7715–7729.
- [155] Laage, D.; Stirnemann, G.; Sterpone, F.; Hynes, J. T. Water jump reorientation: From theoretical prediction to experimental observation. *Acc. Chem. Res* **2012**, *45*, 53–62.
- [156] Rahman, A.; Stillinger, F. Molecular dynamics study of liquid water. *J. Chem. Phys.* **1971**, *55*, 3336–3359.
- [157] Rossky, P. J.; Karplus, M. Solvation. A molecular dynamics study of a dipeptide in water. *J. Am. Chem. Soc.* **1979**, *101*, 1913–1937.
- [158] Svishchev, I. M.; Kusalik, P. G. Dynamics in liquid H₂O, D₂O, and T₂O: A comparative simulation study. *J. Phys. Chem.* **1994**, *98*, 728–733.
- [159] In fitting, $C_n(t)$ it is assumed that $\sum_{\alpha} A_{\alpha} = 1$. As a consequence, in fitting $C_{n,H}(t)$ it is required that $\sum_{\alpha} (\partial A_{\alpha} / \partial \beta) = 0$.

- [160] Piskulich, Z. A.; Thompson, W. H. The dynamics of supercooled water can be predicted from room temperature simulations. *J. Chem. Phys.* **2020**, *152*, 074505.
- [161] Previous work has typically considered only the long timescale of this decay, however, a global fit of the time correlation function is helpful in obtaining an accurate determination of the activation energies.
- [162] Martinez, L.; Andrade, R.; Birgin, E.; Martinez, J. Packmol: A package for building initial configurations. *J. Comput. Chem.* **2009**, *30*, 2157–2164.
- [163] Sciortino, F.; Geiger, A.; Stanley, H. E. Isochoric differential scattering functions in liquid water: The fifth neighbor as a network defect. *Phys. Rev. Lett.* **1990**, *65*, 5–8.
- [164] Endom, L.; Hertz, H. G.; Thül, B.; Zeidler, M. D. A microdynamic model of electrolyte solutions as derived from nuclear magnetic relaxation and self-diffusion data. *Ber. Bunsenges Phys. Chem.* **1967**, *71*, 1008–1031.
- [165] Vartia, A. A. Reorientation and Solvation Dynamics of Bulk and Confined Alcohols. Ph.D. thesis, University of Kansas, 2012.
- [166] We note that there may be some systematic error involved in our fits of the $n = 1$ results for the frame reorientation as the fitted timescale is longer than the range of our data.
- [167] Ji, M.; Odellius, M.; Gaffney, K. J. Large angular jump mechanism observed for hydrogen bond exchange in aqueous perchlorate solution. *Science* **2010**, *328*, 1003–1005.
- [168] Piskulich, Z. A.; Laage, D.; Thompson, W. H. On the role of hydrogen bond exchanges in the spectral diffusion of water. *J. Chem. Phys.* **2021**, *154*, 064501.
- [169] Fayer, M. D. Dynamics of liquids, molecules, and proteins measured with ultrafast 2D IR vibrational echo chemical exchange spectroscopy. *Annu. Rev. Phys. Chem.* **2009**, *60*, 21–38.
- [170] Hamm, P.; Zanni, M. *Concepts and methods of 2D infrared spectroscopy*; Cambridge Univ Press: Cambridge, UK, 2011.

- [171] Elsaesser, T. Two-dimensional infrared spectroscopy of intermolecular hydrogen bonds in the condensed phase. *Acc Chem Res* **2009**, *42*, 1220–1228.
- [172] Rey, R.; Møller, K. B.; Hynes, J. T. Hydrogen bond dynamics in water and ultrafast infrared spectroscopy. *Journal of Physical Chemistry A* **2002**, *106*, 11993–11996.
- [173] Rey, R.; Møller, K. B.; Hynes, J. T. Ultrafast vibrational population dynamics of water and related systems: A theoretical perspective. *Chem. Rev.* **2004**, *104*, 1915–1928.
- [174] Møller, K. B.; Rey, R.; Hynes, J. T. Hydrogen bond dynamics in water and ultrafast infrared spectroscopy: A theoretical study. *Journal of Physical Chemistry A* **2004**, *108*, 1275–1289.
- [175] Lawrence, C. P.; Skinner, J. L. Ultrafast infrared spectroscopy probes hydrogen-bonding dynamics in liquid water. *Chem. Phys. Lett.* **2003**, *369*, 472–477.
- [176] Fecko, C. J.; Eaves, J. D.; Loparo, J. J.; Tokmakoff, A.; Geissler, P. L. Ultrafast hydrogen-bond dynamics in the infrared spectroscopy of water. *Science* **2003**, *301*, 1698–1702.
- [177] Garrett-Roe, S.; Hamm, P. Three-point frequency fluctuation correlation functions of the OH stretch in liquid water. *J. Chem. Phys.* **2008**, *128*, 104507.
- [178] Glasstone, S.; Laidler, K. J.; Eyring, H. In *The Theory of Rate Processes*; McGraw-Hill, Ed.; 1941.
- [179] Shimizu, S.; Matubayasi, N. Ion hydration: Linking self-diffusion and reorientational motion to water structure. *Phys. Chem. Chem. Phys.* **2018**, *20*, 5909–5917.
- [180] Kramer, P. L.; Nishida, J.; Giammanco, C. H.; Tamimi, A.; Fayer, M. D. Observation and theory of reorientation-induced spectral diffusion in polarization-selective 2D IR spectroscopy. *J. Chem. Phys.* **2015**, *142*, 184505.
- [181] Laenen, R.; Rauscher, C.; Laubereau, A. Dynamics of local substructures in water observed by ultrafast infrared hole burning. *Phys Rev Lett* **1998**, *80*, 2622.

- [182] Woutersen, S.; Bakker, H. J. Hydrogen bond in liquid water as a Brownian oscillator. *Phys Rev Lett* **1999**, *83*, 2077.
- [183] Bakker, H. J.; Nienhuys, H.-K.; Gallot, G.; Lascoux, N.; Gale, G. M.; Leicknam, J.-C.; Bratos, S. Transient absorption of vibrationally excited water. *J. Chem. Phys.* **2002**, *116*, 2592.
- [184] Piskulich, Z. A.; Thompson, W. H. Temperature dependence of the water infrared spectrum: Driving forces, isosbestic points, and predictions. *J. Phys. Chem. Lett.* **2020**, *11*, 7762–7768.
- [185] Gale, G. M.; Gallot, G.; Hache, F.; Lascoux, N.; Bratos, S.; Leicknam, J. C. Femtosecond dynamics of hydrogen bonds in liquid water: A real time study. *Phys. Rev. Lett.* **1999**, *82*, 1068–1071.
- [186] Laenen, R.; Simeonidis, K.; Laubereau, A. Subpicosecond spectroscopy of liquid water in the infrared: Effect of deuteration on the structural and vibrational dynamics. *J. Phys. Chem. B* **2002**, *106*, 408–417.
- [187] Lawrence, C. P.; Skinner, J. L. Vibrational spectroscopy of HOD in liquid D₂O. VI. Intramolecular and intermolecular vibrational energy flow. *J. Chem. Phys.* **2003**, *119*, 1623–1633.
- [188] Lawrence, C. P.; Skinner, J. L. Vibrational spectroscopy of HOD in liquid D₂O. VII. Temperature and frequency dependence of the OH stretch lifetime. *J. Chem. Phys.* **2003**, *119*, 3840.
- [189] Stenger, J.; Madsen, D.; Hamm, P.; Nibbering, E. T. J.; Elsaesser, T. Ultrafast vibrational dephasing of liquid water. *Phys. Rev. Lett.* **2001**, *87*, 027401.
- [190] Asbury, J. B.; Steinel, T.; Stromberg, C.; Corcelli, S. A.; Lawrence, C. P.; Skinner, J. L.; Fayer, M. D. Water dynamics: Vibrational echo correlation spectroscopy and comparison to molecular dynamics simulations. *J. Phys. Chem. A* **2004**, *108*, 1107–1119.

- [191] Kwak, K.; Rosenfeld, D. E.; Fayer, M. D. Taking apart the two-dimensional infrared vibrational echo spectra: More information and elimination of distortions. *J. Chem. Phys.* **2008**, *128*, 204505.
- [192] Levenberg, K. A method for the solution of certain non-linear problems in least squares. *Q. Appl. Math.* **1944**, *2*, 164–168.
- [193] Marquardt, D. W. An algorithm for least-squares estimation of nonlinear parameters. *Math., J. Soc. Indust. Appl.* **1963**, *11*, 431–441.
- [194] Tainter, C. J.; Pieniazek, P. A.; Lin, Y. S.; Skinner, J. L. Robust three-body water simulation model. *J. Chem. Phys.* **2011**, *134*, 184501.
- [195] Tainter, C. J.; Shi, L.; Skinner, J. L. Reparametrized E3B (explicit three-body) water model using the TIP4P/2005 model as a reference. *J. Chem. Theory Comput.* **2015**, *11*, 2268–2277.
- [196] Corcelli, S. A.; Lawrence, C. P.; Skinner, J. L. Combined electronic structure/molecular dynamics approach for ultrafast infrared spectroscopy of dilute HOD in liquid H₂O and D₂O. *J. Chem. Phys.* **2004**, *120*, 8107–8117.
- [197] Corcelli, S. A.; Skinner, J. L. Infrared and Raman line shapes of dilute HOD in liquid H₂O and D₂O from 10 to 90°C. *J. Phys. Chem. A* **2005**, *109*, 6154–6165.
- [198] Auer, B. M.; Skinner, J. L. IR and Raman spectra of liquid water: Theory and interpretation. *J. Chem. Phys.* **2008**, *128*, 224511.
- [199] Gruenbaum, S. M.; Tainter, C. J.; Shi, L.; Ni, Y.; Skinner, J. L. Robustness of frequency, transition dipole, and coupling maps for water vibrational spectroscopy. *J. Chem. Theor. Comp.* **2013**, *9*, 3109–3117.
- [200] Schmidt, J. R.; Roberts, S. T.; Loparo, J. J.; Tokmakoff, A.; Fayer, M. D.; Skinner, J. L. Are water simulation models consistent with steady-state and ultrafast vibrational spectroscopy experiments? *Chem Phys* **2007**, *341*, 143–157.

- [201] Burris, P. C.; Laage, D.; Thompson, W. H. Simulations of the infrared, Raman, and 2D-IR photon echo spectra of water in nanoscale silica pores. *J. Chem. Phys.* **2016**, *144*, 194709.
- [202] Our f -test for the FFCF gives a value of $F=25.79$ which is greater than the critical f -value of 3.85 corresponding to the present degrees of freedom and a 95% confidence interval, indicating that the 4-exponential fit is a statistically significant improvement over the 3-exponential fit. The corresponding f -test for the fit of the derivative FFCF gives a value of $F=1802.86$, which is again greater than the critical f -value.
- [203] This is true even if one assumes that the spectral diffusion time is obtained from the sum of forward and backward exchange rate constants, *i.e.*, $1/\tau_\omega = k_\omega = k_f + k_b$. That is, it is straightforward to show that $E_{a,\omega} = -\partial(\ln k_\omega)/\partial\beta = (k_f/k_\omega)E_{a,f} + (k_b/k_\omega)E_{a,b}$. Then, assuming the forward and backward H-bond exchange processes have the same rate constant and activation energies by symmetry, namely the values associated with the H-bond jump time, $k_f = k_b = 1/\tau_0$ and $E_{a,f} = E_{a,b} = E_{a,0}$, it is clear that $E_{a,k} = E_{a,0}$.
- [204] We have verified, for the SPC/E model, that an Arrhenius analysis over a narrow temperature range (290, 298.15, and 310 K) gives a spectral diffusion activation energy ($E_a = 2.61 \pm 0.21$ kcal/mol) in agreement with our value directly calculated from simulations at 298.15 K ($E_a = 2.24 \pm 0.51$ kcal/mol).
- [205] Stirnemann, G.; Hynes, J. T.; Laage, D. Water hydrogen bond dynamics in aqueous solutions of amphiphiles. *Journal of Physical Chemistry B* **2010**, *114*, 3052–3059.
- [206] McQuarrie, D. A. *Statistical Mechanics*; Harper Collins: New York, 2001.
- [207] Evans, M. G.; Polanyi, M. Some applications of the transition state method to the calculation of reaction velocities, especially in solution. *Transactions of the Faraday Society* **1935**, *31*, 875–894.
- [208] Neumaier, S.; Büttner, M.; Bachmann, A.; Kiefhaber, T. Transition state and ground state properties of the helix-coil transition in peptides deduced from high-pressure studies. *Pro-*

- ceedings of the National Academy of Sciences of the United States of America* **2013**, *110*, 20988–20993.
- [209] Ducommun, Y.; Newman, K. E.; Merbach, A. E. High-Pressure O17 NMR Evidence for a Gradual Mechanistic Changeover from Ia to Id for Water Exchange on Divalent Octahedral Metal Ions Going from Manganese(II) to Nickel(II). *Inorg. Chem.* **1980**, *19*, 3696–3703.
- [210] Hugi, A. D.; Helm, L.; Merbach, A. Variable-Temperature, -Pressure, and -Frequency Oxygen-17 NMR Study of Water Exchange on Hexaaquatitanium(III): A Limiting Associative Mechanism. *Inorg. Chem.* **1987**, *26*, 1763–1768.
- [211] Cossy, C.; Helm, L.; Merbach, A. E. Water-Exchange Mechanisms on the Terbium to Thulium Octaaqualanthanide(III) Ions: A Variable-Pressure O17 NMR Study. *Inorg. Chem.* **1989**, *28*, 2699–2703.
- [212] Balogh, E.; Casey, W. H. High-pressure 17O NMR studies on some aqueous polyoxoions in water. *Progress in Nuclear Magnetic Resonance Spectroscopy* **2008**, *53*, 193–207.
- [213] Spångberg, D.; Wojcik, M.; Hermansson, K. Pressure dependence and activation volume for the water exchange mechanism in NaCl(aq) from MD simulations. *Chemical Physics Letters* **1997**, *276*, 114–121.
- [214] Hermansson, K.; Wojcik, M. Water exchange around Li+ and Na+ in LiCl(aq) and NaCl(aq) from MD simulations. *Journal of Physical Chemistry B* **1998**, *102*, 6089–6097.
- [215] Spångberg, D.; Rey, R.; Hynes, J. T.; Hermansson, K. Rate and mechanisms for water exchange around Li+(aq) from MD simulations. *Journal of Physical Chemistry B* **2003**, *107*, 4470–4477.
- [216] Rustad, J. R.; Stack, A. G. Molecular dynamics calculation of the activation volume for water exchange on Li+. *Journal of the American Chemical Society* **2006**, *128*, 14778–14779.

- [217] Dang, L. X.; Annapureddy, H. V. Computational studies of water exchange around aqueous Li^+ with polarizable potential models. *Journal of Chemical Physics* **2013**, *139*.
- [218] Annapureddy, H. V. R.; Dang, L. X. Water exchange rates and molecular mechanism around aqueous halide ions. *J. Phys. Chem. B* **2014**, *118*, 7886–7891.
- [219] Dang, L. X. Computational studies of water-exchange rates around aqueous Mg^{2+} and Be^{2+} . *Journal of Physical Chemistry C* **2014**, *118*, 29028–29033.
- [220] Wilkins, D. M.; Manolopoulos, D. E.; Dang, L. X. Nuclear quantum effects in water exchange around lithium and fluoride ions. *Journal of Chemical Physics* **2015**, *142*.
- [221] Prielmeier, F. X.; Lang, E. W.; Speedy, R. J.; Lüdemann, H. D. Diffusion in supercooled water to 300 Mpa. *Phys. Rev. Lett.* **1987**, *59*, 1128–1131.
- [222] Starr, F. W.; Harrington, S.; Sciortino, F.; Stanley, H. E. Slow dynamics of water under pressure. *Physical Review Letters* **1999**, *82*, 3629–3632.
- [223] Singh, L. P.; Issenmann, B.; Caupin, F. Pressure dependence of viscosity in supercooled water and a unified approach for thermodynamic and dynamic anomalies of water. *Proc. Natl. Acad. Sci.* **2017**, *114*, 4312–4317.
- [224] This expression is accurate as long as $MSD(t)$ and $MSD_V(t)$ are linear with intercepts close to zero. This is typically well-satisfied for the cases considered here, but if it is not the ratio of the slopes can be used.
- [225] It should be noted that alternatively one could calculate both $MSD(t)$ and $MSD_V(t)$ from the equilibrium NpT trajectory itself, in a manner analogous to that we previously used for activation energies.³¹ However, this approach yields dynamics (and associated activation volumes) that are modified by the presence of both the thermostat and barostat, the effects of which can be difficult to determine *a priori*. The method used in the present work avoids this issue.

- [226] Martyna, G. J.; Tobias, D. J.; Klein, M. L. Constant pressure molecular dynamics algorithms. *The Journal of Chemical Physics* **1994**, *101*, 4177–4189.
- [227] Shinoda, W.; Shiga, M.; Mikami, M. Rapid estimation of elastic constants by molecular dynamics simulation under constant stress. *Physical Review B - Condensed Matter and Materials Physics* **2004**, *69*, 16–18.
- [228] Few papers report activation volumes^{3,4} and we have found that the values can vary with the analysis used. Here, when ΔV_d^\ddagger is not reported directly, we use values obtained by a cubic fit to $D(p, T)$ for each fixed temperature (similar to the global fitting approach of Woolf⁴).
- [229] Debenedetti, P. G. *Metastable Liquids: Concepts and Principles*; Princeton University Press: New Jersey, 1996; Chapter 1, pp 1–62.
- [230] Debenedetti, P. G. Supercooled and glassy water. *J. Phys.-Condens. Mat.* **2003**, *15*, R1669–r1726.
- [231] Soper, A. K.; Ricci, M. A. Structures of high-density and low-density water. *Phys. Rev. Lett.* **2000**, *84*, 2881–2884.
- [232] Huang, C. et al. The inhomogeneous structure of water at ambient conditions. *Proc. Natl. Acad. Sci.* **2009**, *106*, 15214–15218.
- [233] Taschin, A.; Bartolini, P.; Eramo, R.; Righini, R.; Torre, R. Evidence of two distinct local structures of water from ambient to supercooled conditions. *Nat. Comm.* **2013**, *4*, 1–8.
- [234] Russo, J.; Tanaka, H. Understanding water’s anomalies with locally favoured structures. *Nat. Commun.* **2014**, *5*, 1–11.
- [235] Pettersson, L. G. M.; Nilsson, A. The structural origin of anomalous properties of liquid water. *Nat. Commun.* **2015**, *6*, 1–11.
- [236] Saito, S.; Bagchi, B.; Ohmine, I. Crucial role of fragmented and isolated defects in persistent relaxation of deeply supercooled water. *J. Chem. Phys.* **2018**, *149*, 124504.

- [237] Soper, A. K. Is water one liquid or two? *J. Chem. Phys.* **2019**, *150*, 234503.
- [238] Poole, P. H.; Sciortino, F.; Essmann, U.; Stanley, H. E. Phase behaviour of metastable water. *Nature* **1992**, *360*, 324–328.
- [239] Palmer, J. C.; Martelli, F.; Liu, Y.; Car, R.; Panagiotopoulos, A. Z.; Debenedetti, P. G. Metastable liquid-liquid transition in a molecular model of water. *Nature* **2014**, *510*, 385–388.
- [240] Palmer, J. C.; Poole, P. H.; Sciortino, F.; Debenedetti, P. G. Advances in Computational Studies of the Liquid-Liquid Transition in Water and Water-Like Models. *Chem. Rev.* **2018**, *118*, 9129–9151.
- [241] Tanaka, H. Simple physical model of liquid water. *J. Chem. Phys.* **2000**, *112*, 799–809.
- [242] Montero de Hijes, P.; Sanz, E.; Joly, L.; Valeriani, C.; Caupin, F. Viscosity and self-diffusion of supercooled and stretched water from molecular dynamics simulations. *J. Chem. Phys.* **2018**, *149*, 094503.
- [243] Ni, Y.; Hestand, N. J.; Skinner, J. L. Communication: Diffusion constant in supercooled water as the Widom line is crossed in no man's land. *J. Chem. Phys.* **2018**, *148*, 191102.
- [244] Price, W. S.; Ide, H.; Arata, Y. Self-diffusion of supercooled water to 238 K using PGSE NMR diffusion measurements. *J. Phys. Chem. A* **1999**, *103*, 448–450.
- [245] Chitnelawong, P.; Sciortino, F.; Poole, P. H. The stability-limit conjecture revisited. *J. Chem. Phys.* **2019**, *150*, 234502.
- [246] Speedy, R. J. Stability-limit conjecture. An interpretation of the properties of water. *J. Phys. Chem.* **1982**, *86*, 982–991.
- [247] Yeh, I.-C.; Hummer, G. System-size dependence of diffusion coefficients and viscosities from molecular dynamics simulations with periodic boundary conditions. *J. Phys. Chem. B* **2004**, *108*, 15873–15879.

- [248] Bengtzelius, U.; Gotze, W.; Sjolander, A. Dynamics of supercooled liquids and the glass transition. *J. Phys. C: Solid State Phys.* **1984**, *17*, 5915–5934.
- [249] Yoshida, K.; Matubayasi, N.; Uosaki, Y.; Nakahara, M. Scaled polynomial expression for self-diffusion coefficients for water, benzene, and cyclohexane over a wide range of temperatures and densities. *J. Chem. Eng. Data* **2010**, *55*, 2815–2823.
- [250] Vogel, H. Das temperaturabhängigkeit gesetz der viskosität von flüssigkeiten. *Phys. Z.* **1921**, *22*, 149.
- [251] Fulcher, G. Analysis of Recent Measurements of the Viscosity of Glasses. *J. Am. Ceram. Soc.* **1925**, *8*, 339.
- [252] Tamman, V.; Hesse, W. Die Abhängigkeit der Viskosität von der Temperatur bei unterkühlten Flüssigkeiten. *Anorganische und Allgemeine Chemie* **1926**, *68*, 245.
- [253] Xu, L.; Kumar, P.; Buldyrev, S. V.; Chen, S. H.; Poole, P. H.; Sciortino, F.; Stanley, H. E. Relation between the Widom line and the strong-fragile dynamic crossover in systems with a liquid-liquid phase transition. *Proc. Natl. Acad. Sci.* **2005**, *102*, 16558–16562.
- [254] Sokolov, A. P.; Hurst, J.; Quitmann, D. Dynamics of supercooled water: Mode-coupling theory approach. *Phys. Rev. B* **1995**, *51*, 12865–12868.
- [255] De Marzio, M.; Camisasca, G.; Rovere, M.; Gallo, P. Mode coupling theory and fragile to strong transition in supercooled TIP4P/2005 water. *J. Chem. Phys.* **2016**, *144*.
- [256] Torre, R.; Bartolini, P.; Righini, R. Structural relaxation in supercooled water by time-resolved spectroscopy. *Nature* **2004**, *428*, 296–299.
- [257] Hardy, R.; Cottingham, R. Viscosity of deuterium oxide and water in the range 5 to 125°C. *J. Res. Natl. Bur. Std.* **1949**, *42*, 573–578.
- [258] Simpson, J.; Carr, H. Diffusion and nuclear spin relaxation in water. *Phys. Rev.* **1958**, *111*, 1201–1202.

- [259] Angell, C. A. *Supercooled and superheated water*; 1979; pp 1–36.
- [260] Gallo, P.; Sciortino, F.; Tartaglia, P.; Chen, S.-H. Slow dynamics of water molecules in supercooled states. *Phys. Rev. Lett.* **1996**, *76*, 2730–2733.
- [261] Galamba, N. On the hydrogen-bond network and the non-Arrhenius transport properties of water. *J. Phys.: Condens. Matter* **2017**, *29*, 015101.
- [262] Vignes, A. Diffusion in binary solutions. Variation of diffusion coefficient with composition. *Ind. Eng. Chem. Fund.* **1966**, *5*, 189–199.
- [263] Cullinan Jr., H. T. Concentration dependence of the binary diffusion coefficient. *Ind. Eng. Chem. Fund.* **1966**, *5*, 281–283.
- [264] Matthiesen, J.; Smith, R. S.; Kay, B. D. Mixing it up: Measuring diffusion in supercooled liquid solutions of methanol and ethanol at temperatures near the glass transition. *J Phys Chem Lett* **2011**, *2*, 557–561.
- [265] Andersen, H. C.; Kob, W. Testing mode-coupling theory for a supercooled binary Lennard-Jones mixture: The van Hove correlation function. *Phys. Rev. E* **1995**, *51*, 4134–4153.
- [266] Shi, R.; Russo, J.; Tanaka, H. Origin of the emergent fragile-to-strong transition in supercooled water. *Proc. Natl. Acad. Sci.* **2018**, *115*, 9444–9449.
- [267] Chen, S.-H.; Mallamace, F.; Mou, C.-Y.; Broccio, M.; Corsaro, C.; Faraone, A.; Liu, L. The violation of the Stokes-Einstein relation in supercooled water. *Proc. Natl. Acad. Sci.* **2006**, *103*, 12974–12978.
- [268] Ni, Y.; Skinner, J. L. IR spectra of water droplets in no man’s land and the location of the liquid-liquid critical point. *J. Chem. Phys.* **2016**, *145*.
- [269] Note that because water at 1 bar is in the supercritical region of the liquid-liquid phase transition, water at this pressure *does have* a continuous temperature dependence across the

range of temperatures we consider, *i.e.*, across the Widom line; see also Refs. 146 and 6. This would not be the case when changing the temperature passes through a first-order phase transition and it is not expected that one could make predictions with the present approach across a phase coexistence boundary.

- [270] Monroe, J. I.; Hatch, H. W.; Mahynski, N. A.; Shell, M. S.; Shen, V. K.; Mahynski, N. A. Extrapolation and interpolation strategies for efficiently estimating structural observables as a function of temperature and density Extrapolation and interpolation strategies for efficiently estimating structural observables as a function of temperature. *J. Chem. Phys.* **2020**, *144101*, 144101.
- [271] Mahynski, N. A.; Jiao, S.; Hatch, H. W.; Blanco, M. A.; Shen, V. K. Predicting structural properties of fluids by thermodynamic extrapolation. *J. Chem. Phys.* **2018**, *148*, 194105.
- [272] Allen, M. P.; Tildesley, D. J. *Computer Simulation of Liquids*; Oxford: New York, 2017.
- [273] Narten, A. H.; Thiessen, W. E.; BLUM, L. Atom pair distribution functions of liquid water at 25°C from neutron diffraction. *Science* **1982**, *217*, 1033–1034.
- [274] Head-Gordon, T.; Hura, G. Water Structure from Scattering Experiments and Simulation. *Chem. Rev.* **2002**, *102*, 2651–2670.
- [275] Narten, A. H.; Levy, H. A. Liquid Water: Molecular correlation functions from X-ray diffraction. *J. Chem. Phys.* **1971**, *55*, 2263–2269.
- [276] Pathak, H.; Späh, A.; Kim, K. H.; Tsironi, I.; Mariedahl, D.; Blanco, M.; Huotari, S.; Honkimäki, V.; Nilsson, A. Intermediate range O–O correlations in supercooled water down to 235 K. *J. Chem. Phys.* **2019**, *150*, 224506.
- [277] Bosio, L.; Chen, S.-H.; Teixeira, J. Isochoric temperature differential of the X-ray structure factor and structural rearrangements in low-temperature heavy water. *Phys. Rev. A* **1983**, *27*, 1468–1475.

- [278] Ferrenberg, A. M.; Swendsen, R. H. New Monte Carlo Technique for Studying Phase Transitions. *Phys. Rev. Lett.* **1988**, *61*, 2635–2638.
- [279] Pinkley, L. W.; Sethna, P. P.; Williams, D. Optical constants of water in the infrared: Influence of temperature. *J. Opt. Soc. Am.* **1977**, *67*, 494–499.
- [280] Cunningham, K.; Lyons, P. A. Depolarization ratio studies on liquid water. *J. Chem. Phys.* **1973**, *59*, 2132–2139.
- [281] Wyss, H. R.; Falk, M. Infrared spectrum of HDO in water and in NaCl solution. *Can. J. Chem.* **1970**, *48*, 607–614.
- [282] Senior, W. A.; Verrall, R. E. Spectroscopic evidence for the mixture model in HOD solutions. *J. Phys. Chem.* **1969**, *73*, 4242–4249.
- [283] Falk, M.; Ford, T. A. Infrared spectrum and structure of liquid water. *Can. J. Chem.* **1966**, *44*, 1699–1707.
- [284] Hare, D. E.; Sorensen, C. M. Raman spectroscopic study of dilute HOD in liquid H₂O in the temperature range -31.5 to 160°C. *J. Chem. Phys.* **1990**, *93*, 6954–6961.
- [285] Maréchal, Y. Infrared spectra of water. I. Effect of temperature and of H/D isotopic dilution. *J. Chem. Phys.* **1991**, *95*, 5565–5573.
- [286] Libnau, F. O.; Toft, J.; Christy, A. A.; Kvalheim, O. M. Structure of liquid water determined from infrared temperature profiling and evolutionary curve resolution. *J. Am. Chem. Soc.* **1994**, *116*, 8311–8316.
- [287] Iwata, T.; Koshoubu, J.; Jin, C.; Okubu, Y. Temperature dependence of the mid-infrared OH spectral band in liquid water. *Appl Spectrosc* **1997**, *51*, 1269–1275.
- [288] Walrafen, G. E.; Fisher, M. R.; Hokmabadi, M. S.; Yang, W. H. Temperature dependence of the low- and high-frequency Raman scattering from liquid water. *J. Chem. Phys.* **1986**, *85*, 6970–6982.

- [289] Walrafen, G. E. Effects of equilibrium H-bond distance and angle changes on Raman intensities from water. *J. Chem. Phys.* **2004**, *120*, 4868–4876.
- [290] Walrafen, G. E. Dispersion of the Raman depolarization ratio of HDO in water and heavy water from 295 to 368 K, and from concentrated NaClO₄/D₂O/H₂O. *J. Chem. Phys.* **2005**, *122*, 174502–9.
- [291] Smith, J.; Cappa, C.; Wilson, K.; Cohen, R.; Geissler, P.; Saykally, R. Unified description of temperature-dependent hydrogen-bond rearrangements in liquid water. *Proc. Natl. Acad. Sci.* **2005**, *102*, 14171–14174.
- [292] Geissler, P. L. Temperature dependence of inhomogeneous broadening: On the meaning of isosbestic points. *J. Am. Chem. Soc.* **2005**, *127*, 14930–14935.
- [293] Geissler, P. L. Water interfaces, solvation, and spectroscopy. *Annu. Rev. Phys. Chem.* **2013**, *64*, 317–337.
- [294] Pattenaude, S. R.; Streacker, L. M.; Ben-Amotz, D. Temperature and polarization dependent Raman spectra of liquid H₂O and D₂O. *J Raman Spectrosc* **2018**, *49*, 1860–1866.
- [295] Morawietz, T.; Marsalek, O.; Pattenaude, S. R.; Streacker, L. M.; Ben-Amotz, D.; Markland, T. E. The interplay of structure and dynamics in the Raman spectrum of liquid water over the full frequency and temperature range. *J. Phys. Chem. Lett.* **2018**, *9*, 851–857.
- [296] Hestand, N. J.; Strong, S. E.; Shi, L.; Skinner, J. L. Mid-IR spectroscopy of supercritical water: From dilute gas to dense fluid. *J. Chem. Phys.* **2019**, *150*, 054505.
- [297] Kubo, R.; Toda, M.; Hashitsume, N. *Statistical Physics II*; Springer-Verlag, New York, 1978.
- [298] Urquidi, J.; Singh, S.; Cho, C. H.; Robinson, G. W. Origin of temperature and pressure effects on the radial distribution function of water. *Phys. Rev. Lett.* **1999**, *83*, 2348–2350.

- [299] Singh, R. S.; Biddle, J. W.; Debenedetti, P. G.; Anisimov, M. A. Two-state thermodynamics and the possibility of a liquid-liquid phase transition in supercooled TIP4P/2005 water. *J. Chem. Phys.* **2016**, *144*.
- [300] Li, Y.; Li, J.; Wang, F. Liquid-liquid transition in supercooled water suggested by microsecond simulations. *Proc. Natl. Acad. Sci.* **2013**, *110*, 12209–12212.
- [301] Nilsson, A.; Pettersson, L. G. M. The structural origin of anomalous properties of liquid water. *Nature Communications* **2015**, *6*, 8998.
- [302] Camisasca, G.; Pathak, H.; Wikfeldt, K. T.; Pettersson, L. G. M. Radial distribution functions of water: Models vs experiments. *The Journal of Chemical Physics* **2019**, *151*, 044502.
- [303] Wu, Y.; Tepper, H. L.; Voth, G. A. Flexible simple point-charge water model with improved liquid-state properties. *J. Chem. Phys.* **2006**, *124*, 024503.
- [304] Jorgensen, W. L.; Chandrasekhar, J.; Madura, J. D.; Impey, R. W.; Klein, M. L. Comparison of simple potential functions for simulating liquid water. *J. Chem. Phys.* **1983**, *79*, 926–935.
- [305] Price, D. J.; Brooks, C. L. A modified TIP3P water potential for simulation with Ewald summation. *J. Chem. Phys.* **2004**, *121*, 10096–10103.
- [306] Izadi, S.; Onufriev, A. V. Accuracy limit of rigid 3-point water models. *J. Chem. Phys.* **2016**, *145*, 074501.
- [307] Horn, H. W.; Swope, W. C.; Pitera, J. W.; Madura, J. D.; Dick, T. J.; Hura, G. L.; Head-Gordon, T. Development of an improved four-site water model for biomolecular simulations: TIP4P-Ew. *J. Chem. Phys.* **2004**, *120*, 9665–9678.
- [308] Teng, X.; Liu, B.; Ichiye, T. Understanding how water models affect the anomalous pressure dependence of their diffusion coefficients. *Journal of Chemical Physics* **2020**, *153*.

- [309] Piskulich, Z. A.; Thompson, W. H. Examining the Role of Different Molecular Interactions on Activation Energies and Activation Volumes in Liquid Water. *J. Chem. Theor. Comput.* **2020**, *17*, 2659–2671.
- [310] Joung, I. S.; Cheatham, T. E. Determination of alkali and halide monovalent ion parameters for use in explicitly solvated biomolecular simulations. *J. Phys. Chem. B.* **2008**, *112*, 9020–9041.
- [311] Nutt, D. R.; Smith, J. C. Molecular dynamics simulations of proteins: Can the explicit water model be varied? *J. Chem. Theory Comput.* **2007**, *3*, 1550–1560.
- [312] Best, R. B.; Mittal, J. Protein simulations with an optimized water model: Cooperative helix formation and temperature-induced unfolded state collapse. *J. Phys. Chem. B.* **2010**, *114*, 14916–14923.
- [313] Laage, D.; Hynes, J. T. In *Ultrafast Infrared Vibrational Spectroscopy*; Fayer, M. D., Ed.; CRC Press, 2013; pp 73–98.
- [314] Cisneros, G. A.; Wikfeldt, K. T.; Ojamäe, L.; Lu, J.; Xu, Y.; Torabifard, H.; Bartók, A. P.; Csányi, G.; Molinero, V.; Paesani, F. Modeling molecular interactions in water: From pairwise to many-body potential energy functions. *Chem. Rev.* **2016**, *116*, 7501–7528.
- [315] Brini, E.; Fennell, C. J.; Fernandez-Serra, M.; Hribar-Lee, B.; Lukšič, M.; Dill, K. A. How water's properties are encoded in its molecular structure and energies. *Chem. Rev.* **2017**, *117*, 12385–12414.
- [316] Lata, N. N.; Zhou, J.; Hamilton, P.; Larsen, M.; Sarupria, S.; Cantrell, W. Multivalent surface cations enhance heterogeneous freezing of water on muscovite mica. *J. Phys. Chem. Lett.* **2020**, *11*, 8682–8689.
- [317] Bellissent-Funel, M. C.; Hassanali, A.; Havenith, M.; Henchman, R.; Pohl, P.; Sterpone, F.;

- Van Der Spoel, D.; Xu, Y.; Garcia, A. E. Water determines the structure and dynamics of proteins. *Chem. Rev.* **2016**, *116*, 7673–7697.
- [318] Kohagen, M.; Pluhařová, E.; Mason, P. E.; Jungwirth, P. Exploring ion-ion interactions in aqueous solutions by a combination of molecular dynamics and neutron scattering. *J. Phys. Chem. Lett.* **2015**, *6*, 1563–1567.
- [319] Harpham, M. R.; Ladanyi, B. M.; Levinger, N. E. The effect of the counterion on water mobility in reverse micelles studied by molecular dynamics simulations. *J. Phys. Chem. B.* **2005**, *109*, 16891–16900.
- [320] Yamada, S. A.; Shin, J. Y.; Thompson, W. H.; Fayer, M. D. Water dynamics in nanoporous silica: Ultrafast vibrational spectroscopy and molecular dynamics simulations. *J. Phys. Chem. C.* **2019**, *123*, 5790–5803.
- [321] Sun, H. Compass: An ab initio force-field optimized for condensed-phase applications - Overview with details on alkane and benzene compounds. *Journal of Physical Chemistry B* **1998**, *102*, 7338–7364.
- [322] Mills, R. Self-diffusion in normal and heavy water in the range 1 – 45°. *J. Phys. Chem.* **1973**, *77*, 685–688.
- [323] Dunweg, B.; Kremer, K. Molecular dynamics simulation of a polymer chain in solution. *J. Chem. Phys.* **1993**, *99*, 6983–6997.
- [324] Linke, M.; Köfinger, J.; Hummer, G. Rotational Diffusion Depends on Box Size in Molecular Dynamics Simulations. *Journal of Physical Chemistry Letters* **2018**, *9*, 2874–2878.
- [325] Mark, P.; Nilsson, L. Structure and dynamics of the TIP3P, SPC, and SPC/E water models at 298 K. *J. Phys. Chem. A* **2001**, *105*, 9954–9960.
- [326] van der Spoel, D.; van Maaren, P. J.; Berendsen, H. J. C. A systematic study of water models

- for molecular simulation: Derivation of water models optimized for use with a reaction field. *J. Chem. Phys.* **1998**, *108*, 10220–10230.
- [327] Kawasaki, T.; Kim, K. Identifying time scales for violation/preservation of Stokes-Einstein relation in supercooled water. *Sci. Adv.* **2017**, *3*, e1700399.
- [328] Pinilla, C.; Irani, A. H.; Seriani, N.; Scandolo, S. Ab initio parameterization of an all-atom polarizable and dissociable force field for water. *J. Chem. Phys.* **2012**, *136*, 114511.
- [329] Reddy, S. K.; Straight, S. C.; Bajaj, P.; Huy Pham, C.; Riera, M.; Moberg, D. R.; Morales, M. A.; Knight, C.; Götz, A. W.; Paesani, F. On the accuracy of the MB-pol many-body potential for water: Interaction energies, vibrational frequencies, and classical thermodynamic and dynamical properties from clusters to liquid water and ice. *J. Chem. Phys.* **2016**, *145*, 194504.
- [330] Seki, T.; Chiang, K. Y.; Yu, C. C.; Yu, X.; Okuno, M.; Hunger, J.; Nagata, Y.; Bonn, M. The Bending Mode of Water: A Powerful Probe for Hydrogen Bond Structure of Aqueous Systems. *The journal of physical chemistry letters* **2020**, *11*, 8459–8469.
- [331] Ortiz De Urbina, J.; Sesé, G. Influence of hydrogen bonds and temperature on dielectric properties. *Physical Review E* **2016**, *94*, 1–7.
- [332] Skinner, L. B.; Galib, M.; Fulton, J. L.; Mundy, C. J.; Parise, J. B.; Pham, V. T.; Schenter, G. K.; Benmore, C. J. The structure of liquid water up to 360 MPa from x-ray diffraction measurements using a high Q-range and from molecular simulation. *J. Chem. Phys.* **2016**, *144*.
- [333] McQuarrie, D. A.; Simon, J. D. *Physical Chemistry: A Molecular Approach*; University Science Books: Sausalito, CA, 1997.
- [334] Horne, R. A.; Courant, R. A.; Johnson, D. S.; Margosian, F. F. The activation energy of

- viscous flow of pure water and sea water in the temperature region of maximum density. *Journal of Physical Chemistry* **1965**, *69*, 3988–3991.
- [335] González, M. A.; Abascal, J. L. F. The shear viscosity of rigid water models. *J. Chem. Phys.* **2010**, *132*, 096101–2.
- [336] Subramaniam, B. Enhancing the stability of porous catalysts with supercritical reaction media. *Applied Catalysis A: General* **2001**, *212*, 199–213.
- [337] Subramaniam, B. Gas-expanded liquids for sustainable catalysis and novel materials: Recent advances. *Coordination Chemistry Reviews* **2010**, *254*, 1843–1853.
- [338] Akien, G. R.; Poliakoff, M. A critical look at reactions in class I and II gas-expanded liquids using CO₂ and other gases. *Green Chemistry* **2009**, *11*, 1083.
- [339] Jessop, P. G.; Subramaniam, B. Gas-expanded liquids. *Chemical Reviews* **2007**, *107*, 2666–2694.
- [340] Houndonougbo, Y.; Jin, H.; Rajagopalan, B.; Wong, K.; Kuczera, K.; Subramaniam, B.; Laird, B. Phase equilibria in carbon dioxide expanded solvents: Experiments and molecular simulations. *Journal of Physical Chemistry B* **2006**, *110*, 13195–13202.
- [341] Palafox-Hernandez, J. P.; Mendis, C. H.; Thompson, W. H.; Laird, B. B. Pressure and Temperature Tuning of Gas-Expanded Liquid Structure and Dynamics. *Journal of Physical Chemistry B* **2019**, *123*, 2915–2924.
- [342] Sconyers, D. J.; Shaughnessy, C. L.; Lee, H.-J.; Subramaniam, B.; Leonard, K. C.; Blakemore, J. D. Enhancing Molecular Electrocatalysis of CO₂ Reduction With Pressure-Tunable CO₂-Expanded Electrolytes. *Chem. Sus. Chem.* **2020**, *13*, 6338–6345.
- [343] Shaughnessy, C. I.; Sconyers, D. J.; Kerr, T. A.; Lee, H.; Subramaniam, B.; Leonard, K. C.; Blakemore, J. D. Intensified Electrocatalytic CO₂ Conversion in Pressure-Tunable CO₂-Expanded Electrolytes. *ChemSusChem* **2019**, *12*, 3761–3768.

- [344] Shaughnessy, C. I.; Sconyers, D. J.; Lee, H. J.; Subramaniam, B.; Blakemore, J. D.; Leonard, K. C. Insights into pressure tunable reaction rates for electrochemical reduction of CO₂ in organic electrolytes. *Green Chemistry* **2020**, *22*, 2434–2442.
- [345] Edwards, D.; Madden, P.; McDonald, I. A computer simulation study of the dielectric properties of a model of methyl cyanide. *Mol. Phys.* **1984**, *51*, 1141–1161.
- [346] Harris, J. G.; Yung, K. H. Carbon Dioxide 's Liquid-Vapor Coexistence Curve and Critical Properties As Predicted by a Simple Molecular Model. **1995**, 12021–12024.
- [347] Wang, Z.; Olmsted, D. L.; Asta, M.; Laird, B. B. Electric potential calculation in molecular simulation of electric double layer capacitors. *Journal of Physics Condensed Matter* **2016**, *28*.
- [348] Fries, P. M.; Kunz, W.; Calmettes, P.; Turq, P. Pictorial intuition of the correlation between structure and properties in liquid solutions: acetonitrile as a strongly structured solvent of dissociated ions. *Journal of Molecular Structure: THEOCHEM* **1995**, *330*, 287–300.
- [349] Li, H.; Arzhantsev, S.; Maroncelli, M. Solvation and solvatochromism in CO₂-expanded liquids. 2. Experiment-simulation comparisons of preferential solvation in three prototypical mixtures. *Journal of Physical Chemistry B* **2007**, *111*, 3208–3221.
- [350] Swalina, C.; Arzhantsev, S.; Li, H.; Maroncelli, M. Solvation and solvatochromism in CO₂-expanded liquids. 3. The dynamics of nonspecific preferential solvation. *Journal of Physical Chemistry B* **2008**, *112*, 14959–14970.
- [351] Laird, B.; Houndonougbo, Y.; Kuczera, K. Phase Equilibrium, Structure, and Transport Properties of Carbon-Dioxide Expanded Liquids: A Molecular Simulation Study. *ACS symposium series* **2009**,
- [352] Granero-Fernandez, E.; Lacaze-Dufaure, C.; Condoret, J. S.; Gerbaud, V.; Medina-Gonzalez, Y. Controlling Solvation and Mass Transport Properties of Biobased Solvents

- through CO₂ Expansion: A Physicochemical and Molecular Modeling Study. *Industrial and Engineering Chemistry Research* **2019**, *58*, 18942–18964.
- [353] Cai, L.; Li, W.; Tan, G.; Lei, D.; Liu, Z. Effect of graphene sheet size on exfoliation process in CO₂-expanded organic solvent: A molecular dynamics simulation. *Journal of Applied Physics* **2020**, *128*.
- [354] Cornell, W. D.; Cieplak, P.; Bayly, C. I.; Gould, I. R.; Merz, K. M.; Ferguson, D. M.; Spellmeyer, D. C.; Fox, T.; Caldwell, J. W.; Kollman, P. A. A Second Generation Force Field for the Simulation of Proteins, Nucleic Acids, and Organic Molecules. *J. Am. Chem. Soc.* **1995**, *117*, 5179–5197.
- [355] Ottosson, N.; Vácha, R.; Aziz, E. F.; Pokapanich, W.; Eberhardt, W.; Svensson, S.; Öhrwall, G.; Jungwirth, P.; Björneholm, O.; Winter, B. Large variations in the propensity of aqueous oxychlorine anions for the solution/vapor interface. *J. Chem. Phys.* **2009**, *131*, 124706.
- [356] Panagiotopoulos, A. Z. Gibbs Ensemble Techniques BT - Observation, Prediction and Simulation of Phase Transitions in Complex Fluids. *Observation, Prediction and Simulation of Phase Transitions in Complex Fluids* **1995**, *460*, 463–501.
- [357] Nejahi, Y.; Soroush Barhaghi, M.; Mick, J.; Jackman, B.; Rushaidat, K.; Li, Y.; Schwiebert, L.; Potoff, J. GOMC: GPU Optimized Monte Carlo for the simulation of phase equilibria and physical properties of complex fluids. *SoftwareX* **2019**, *9*, 20–27.
- [358] Soroush Barhaghi, M.; Potoff, J. J. Prediction of phase equilibria and Gibbs free energies of transfer using molecular exchange Monte Carlo in the Gibbs ensemble. *Fluid Phase Equilibria* **2019**, *486*, 106–118.
- [359] Houndonougbo, Y.; Laird, B. B.; Kuczera, K. Transport properties of CO₂-expanded acetonitrile from molecular dynamics simulations. *Journal of Chemical Physics* **2007**, *126*.

- [360] Maroncelli, M. Computer simulations of solvation dynamics in acetonitrile. *The Journal of Chemical Physics* **1991**, *94*, 2084–2103.
- [361] Kordikowski, A.; Schenk, A. P.; Van Nielen, R. M.; Peters, C. J. Volume expansions and vapor-liquid equilibria of binary mixtures of a variety of polar solvents and certain near-critical solvents. *The Journal of Supercritical Fluids* **1995**, *8*, 205–216.
- [362] Chung, C.; Degner, B.; Decker, E. A.; McClements, D. J. Oil-filled hydrogel particles for reduced-fat food applications: Fabrication, characterization, and properties. *Innovative Food Science and Emerging Technologies* **2013**, *20*, 324–334.
- [363] Murphy, S. V.; Skardal, A.; Atala, A. Evaluation of hydrogels for bio-printing applications. *Journal of Biomedical Materials Research - Part A* **2013**, *101 A*, 272–284.
- [364] Caló, E.; Khutoryanskiy, V. V. Biomedical applications of hydrogels: A review of patents and commercial products. *European Polymer Journal* **2015**, *65*, 252–267.
- [365] Ahmed, E. M. Hydrogel: Preparation, characterization, and applications: A review. *Journal of Advanced Research* **2015**, *6*, 105–121.
- [366] Cascone, S.; Lamberti, G. Hydrogel-based commercial products for biomedical applications: A review. *International Journal of Pharmaceutics* **2020**, *573*, 118803.
- [367] Yan, C.; Kramer, P. L.; Yuan, R.; Fayer, M. D. Water Dynamics in Polyacrylamide Hydrogels. *Journal of the American Chemical Society* **2018**, *140*, 9466–9477.
- [368] Thompson, W. H. Perspective : Dynamics of confined liquids. *J. Chem. phys.* **2018**, *149*, 170901.
- [369] Cleary, J.; Bromberg, L. E.; Magner, E. Diffusion and Release of Solutes in Pluronic-g-poly(acrylic acid) Hydrogels. *Langmuir* **2003**, *19*, 9162–9172.

- [370] Dodda, L. S.; De Vaca, I. C.; Tirado-Rives, J.; Jorgensen, W. L. LigParGen web server: An automatic OPLS-AA parameter generator for organic ligands. *Nucleic Acids Research* **2017**, *45*, W331–w336.
- [371] Jorgensen, W. L.; Tirado-Rives, J. Potential energy functions for atomic-level simulations of water and organic and biomolecular systems. *Proceedings of the National Academy of Sciences of the United States of America* **2005**, *102*, 6665–6670.
- [372] Dodda, L. S.; Vilseck, J. Z.; Tirado-Rives, J.; Jorgensen, W. L. 1.14CM1A-LBCC: Localized Bond-Charge Corrected CM1A Charges for Condensed-Phase Simulations. *Journal of Physical Chemistry B* **2017**, *121*, 3864–3870.
- [373] Borodin, O.; Bedrov, D.; Smith, G. D. Molecular dynamics simulation study of dielectric relaxation in aqueous poly(ethylene oxide) solutions. *Macromolecules* **2002**, *35*, 2410–2412.
- [374] Kumar, S.; Rosenberg, J. M.; Bouzida, D.; Swendsen, R. H.; Kollman, P. A. THE weighted histogram analysis method for free-energy calculations on biomolecules. I. The method. *J. Comput. Chem.* **1992**, *13*, 1011–1021.
- [375] Borkowski, A. K.; Piskulich, Z. A.; Thompson, W. H. Examining the Hofmeister Series through Activation Energies: Water Diffusion in Aqueous Alkali-Halide Solutions. *The Journal of Physical Chemistry B* **2020**, *125*, 350–359.
- [376] Katiyar, A.; Thompson, W. H. Temperature Dependence of Peptide Conformational Equilibria from Simulations at a Single Temperature. *The Journal of Physical Chemistry A* **2021**,